Quantifying rates of active extension and seismic hazard in the upper plate of subduction zones

Department of Earth and Planetary Sciences, Birkbeck University

Quantifying rates of active extension and seismic hazard in the upper plate of subduction zones

A thesis submitted to Birkbeck University

for the degree of Doctor of Philosophy in the

Faculty of Science

Marco Meschis

(marco.meschis.14@ucl.ac.uk – marco.meschis@gmail.com)

First supervisor: Prof. Gerald Roberts, gerald.roberts@ucl.ac.uk

Second supervisor: Dr. Rebecca Briant, b.briant@bbk.ac.uk

September 2018

Declaration of Authorship

I, Marco Meschis, confirm that the work presented in this thesis is my own. Where information has been derived from other sources, I confirm that this has been indicated in the thesis.

Signed:

Date:

Abstract

To test the hypothesis that crustal deformation within the deforming upper plate of the Ionian Subduction Zone, influences uplift in the Calabrian Arc (CA), sequences of tectonically-deformed uplifted palaeoshorelines have been mapped, dated and assigned ages. These regions have historically experienced damaging earthquakes, yet, crustal deformation rates spanning the Late Quaternary are unclear and poorly-constrained. Uplifted Quaternary palaeoshorelines are preserved: (i) on the hangingwalls and footwalls of major Quaternary normal faults deforming the CA and (ii) within the deforming foreland region. This thesis constrains the relationship between historical seismicity, "regional" uplift and upper plate crustal deformation, quantifying both the "local" signal due to the normal faulting and the "regional" uplift. To assign ages to palaeoshorelines, a synchronous correlation approach is applied, driven by new absolute age controls alongside those available in the literature. This assigns ages to un-dated palaeoshorelines, suggesting: (i) new uplift rate scenarios and (ii) new long-term fault slip-rates. Uplift rate variations are mapped: (i) along the strike of the upper plate normal faults and (ii) along the foreland region, either constant and fluctuating through time. The deformation rates are used to discuss seismic hazard in southern Italy. Moreover, elastic half-space modelling is used to replicate levelling data from 1907 – 1909 to test if the Messina Strait fault is the seismogenic source of the 1908 Mw 7.1 Messina Earthquake, the most destructive earthquake recorded in Europe.

Overall, this thesis shows that: (i) critically-assigning ages to un-dated palaeoshorelines by applying synchronous correlation approach is crucial to obtain reliable long-term deformation rates and (ii) upper plate crustal vertical rates should be removed if observations from deforming upper plates are used to derive slip distribution on the subduction interface.

Table of Contents

List of Figures

Figures in Chapter 2

Figure 2.4: Modified picture from Gvirtzman and Nur, (2001) showing at the top a picture of the evolution of the Ligur-Provenzal and Tyrrhenian Basins from the Early Miocene associated with the presence of the Jurassic Tethyan Ocean. In the lower picture, a schematic lithospheric section crossing the actual Tyrrhenian Basin is shown; furthermore, asthenospheric wedging is shown under the Calabrian Arc probably associated with the detaching of the retreating slab from the overriding plate.

Figure 2.5: Sketched cartoon amended from Nalin, Massari and Zecchin, 2007 showing the formation of marine terraces as the result of the interaction between regional uplift and sea level changes through time (Bianca et al., 2011).

Figure 2.6: Figure from Lambeck, Esat and Potter, (2002) showing Δ 18O over the time from two sediment cores. Curve A from the Caribbean Sea (Raymo, 1992) shows the variation since the Upper Neogene; curve B from the Equatorial Atlantic (Haug and Tiedemann, 1998) shows variation since the Upper Pliocene.

Figure 2.7: Cartoon showing how an uplifted marine terrace forms in an uplifting region.

Figure 2.8: Simplified tectonic sketch showing regions with estimated Late Quaternary uplift rates in mm/yr by various authors, measured over the last 125 ka (dark red dots): 1 Giunta, et al., (2012) and Scicchitano, et al., (2011) – 2 Bordoni & Valensise 1998 – 3 Antonioli, Ferranti, et al. 2006 – 4 Monaco et al. (2014) – 5 Roberts, et al., (2013) – 6 Miyauchi, et al., (1994) – 7

Westway, (1993) – 8 Catalano & De Guidi (2003) – 9 Bianca et al. (1999). Blue squares show investigated area. CDOF: Capo D'Orlando Fault, TF: Taormina Fault, AcF: Acireale Fault, RCF: Reggio Calabria Fault, AF: Armo Fault, CF: Cittanova Fault, SF: Serre Fault, VF: Vibo Fault, TrF: Tropea Fault, CoF: Coccorino Fault, MF: Mileto Fault, RoF: Rossano Fault, CrF: Crati Fault, MrF: Maratea Fault.

Figure 2.9: Examples of "sequential correlation approach" by Armijo et al., (1996) and Giunta et al., (2012) modelling a sequence of marine terraces starting from a dated horizon and assume that the next higher and un-dated terrace belongs to the next higher and older sea level highstand.

Figure 2.10: Examples of modelled (or expected) shoreline elevations showing two different uplift rate scenarios. The top graph shows that the 175 ka and 217 ka palaeoshorelines will be eroded by the 125 ka and the 200 ka palaeoshorelines if an uplift rate of 0.2 mm/yr is mapped. The bottom graph shows that an uplift rate of 1.5 mm/yr is needed for the preservation of the 175 ka and 217 ka palaeoshorelines.

Figure 2.11: Historical earthquake locations occurred along the Calabrian Arc. Note that the 1693 earthquake (M 7.4), SE Sicily, is perhaps related to a fault thrusting activity produced by the SBT. Data from Basili et al., (2008) and Stucchi et al., (2013).

Figure 2.12: Co-seismic geodetic-based vertical movements measured during the normal faulting-related 2009 l'Aquila earthquake (Mw 6.2) on top (Papanikolaou et al., 2010) and 1983 Borah Peak earthquake (Ms 7.3) on bottom (Stein and Barrientos, 1985).

Figure 2.13: Simplified picture from Pace et al., (2014) showing prominent geometric features of a normal fault. L= Half-length of faulting surface rupture, D= Depth of seismogenic layer (around 15 km), W= Down-Dip Width and S= the slip direction of fault.

Figure 2.14: Graph from Schlische et al. (1996) with X-Y logarithmic axis plotting displacement (d) against length (L) values for several published fault dataset. Sources of data are indicated showing the type of fault. (T= Thrust fault, N= Normal fault and SS= strike-slip fault) and the number of data.

Figure 2.15: Graphs from Wells and Coppersmith, (1994) showing (i) the relationship between the fault length that can be ruptured during an earthquake and the associated possible produced magnitude (a) and (ii) the relationship between the magnitude of an earthquake and the maximum surface displacement produced by the associated earthquake (b).

Figure 2.16: Bennett et al. (2004) show that ~70% of the total plate motion, between Pacific and North America Plates, has been partitioned between the San Jacinto and the southernmost part of San Andreas fault transferring around 35mm/yr from Imperial Fault to Mojave fault segment. However, this example is related to a strike-slip faults system.

Figure 2.17: Previous fault models proposed for the 1908 Messina Earthquake (Schick, 1977; Mulargia and Boschi, 1983; Bottari et al., 1986; Capuano et al., 1988; Valensise, 1988; Boschi, Pantosti and Valensise, 1989; De Natale and Pingue, 1991; Aloisi et al., 2013).

Figures in Chapter 3

Figure 3.1: Map showing locations of age controls. Orange dots show locations where corals have been mapped and collected for $^{234}U/^{230}Th$ dating. Pink dots show locations where WCPs have been sampled for ^{36}Cl cosmogenic dating. White dots show locations of well-known age controls from literature. Dashed blue square are the investigated regions and the number is referred to the chapter.

Figure 3.2: In (a) and (b) marine abrasion platforms made of Mesozoic limestone unconformably overlain by marine conglomeratic deposits are shown. In places lithophagid borings (a) into Mesozoic limestone have been mapped close this area. In (c) a sketched wave-cut platform cut into Neogene limestone with a fault scarp-like palaeocliff and presence of litophagid borings (d) and mill-holes (e) are shown. In (f) a wave-cut platform is sampled for ^{36}Cl dating with associated beach pebbles (g) confirming a rocky palaeoshoreline next to a beach pebble. In (h) location of sampling is shown next to beach pebbles. In (I) the equivalent sampled flat-surface cut by river incision.

Figure 3.3: In (a) a topographic profile derived by using a 10m high resolution DEM is shown. Marine terraces are modelled by applying a synchronous correlation approach. In (b) the same

location in the field of the topographic profile in (a) is shown. It is possible to appreciate how the GIS-based mapping is robust showing a very "similar topography" if compared to the field.

Figure 3.4: Sketch of an ideal linear regression analysis between field-based measurements and GIS-based mapping to assess that GIS analysis is robust and reliable.

Figure 3.5: An *in-situ* coral colony is collected for dating where a wave-cut platform showing lithophagid borings is mapped (top). A death assemblage of bioclastic materials with presence of corals is mapped within a Quaternary calcarenite-made boulder embedded on marine terrace deposits (bottom). Coral locations shown in Figure 3.1.

Figure 3.6: Graph used to plot obtained results from U/Th analysis. All data lying on the right part of this diagram will show open system diagenesis, not allowing an age estimation. The 1.145-curve represents the $^{234}U/^{238}U$ initial activity ratio of the modern seawater.

Figure 3.7: Sketched cartoon of the process of spallation (a) modified from (http://www3.telus.net/lejgeology/etrain/htmls/36cl.htm, 2008). In (b) a graph showing a decrease of ^{36}Cl concentration vs depth adapted from Schlagenhauf et al., (2010).

Figure 3.8: Picture from Darvill, (2013) showing six of the most used cosmogenic nuclide and the associated summarized properties for dating. Age ranges have shown with data from Ivy-Ochs & Kober (2008); 10Be from Chmeleff et al. (2010) and Korschinek et al. (2010).

Figure 3.9: Sample locations from south of Syracuse town as shown in Figure 3.1. Dashed red lines show cm-depth millholes indicating minimal erosion next to the sample locations. Dashed dark blue circle show lithophagid borings next to the sample locations, indicating that sampled WCPs represent the palaeo sea-level at time of their formation. Dashed yellow lines show the sampled WCP. Magenta arrows with associated dashed lines show the flat sampled surfaces. Ages estimated by using submerged palaeoshorelines at -20m and -40m respectively associated to the 76ka and 50ka highstands (Dutton et al., 2009) as age controls driving a synchronous correlation approach as shown in Chapter 6. Black dashed lines used to separate different sample photos. Note that sample locations have chosen next to mill-holes and/or lithophagid borings implying minimal erosion.

Figure 3.10: Palaeoshorelines on a topographic profile are modelled by applying a synchronous correlation approach (see top panel). Coloured lines represent the predicted elevations of sea-level highstands (see table for values) iteratively-calculated driven by an age control value for the 51 m palaeoshoreline. The bottom left graph shows which palaeoshorelines are overprinted given the implied low and constant through time. The bottom right panel shows a linear regression analysis between "predicted" and "measured" elevations. The predicted elevations, representing the synchronously calculated sea-level highstand elevations, have been derived by defining a constant uplift rate through time, and iterating this value to find the best match to the measured and mapped paleoshorelines elevations with a R^2 value >0.99, confirming that the correlation is robust and reliable.

Figure 3.11: Sketch of an ideal linear regression analysis between "predicted" elevations iteratvely-calculated driven by age controls and "measured" elevations from GIS analysis. R^2 values >0.99 confirm that the synchronous correlation analysis is robust and reliable.

Figure 3.12: Co-seismic elevation changes measured after the 1908 Messina Earthquake in Sicily and Calabria.

Figures in Chapter 4

Figure 4.1: Location maps for palaeoshorelines around the Vibo active normal fault. (a) Map amended from Bianca et al. (2011) showing the investigated area from Pizzo Calabro to Briatico. The locations of the studied 29 topographic profiles are shown, as are locations with age control from coral dates. The ages given in the lower panel are from Bianca et al. (2011), with the refined ages indicated in the upper panel and map with coloured dots, and again in (b). (b) Palaeoshorelines from this study shown on a 10 m DEM. Dashed lines link palaeoshoreline locations interpreted to be the same age from the synchronous correlation method.

Figure 4.2: Graph adapted from Tortorici et al., (2003) showing a dramatic uplift rate chages through time in the Capo Vaticano peninsula. Note that this section is parallel to profiles 26 and 28 shown in Figure 4.1.

Figure 4.3: In (a) marine terraces are shown outcropping on the hangingwall of the Vibo Fault. The footwall cut-off at ~ 500 m is mapped to derive Quaternary fault displacement. In (b) view of the marine terraces and palaeoshoreline indicators along Profile 4 (figure 4.1) are shown through Vibo Marina. Breaks of slope at 21, 60, 115, and 147 m are interpreted as the 100 ka, 125 ka, 240 ka, 310 ka and 340 ka palaeoshorelines. Modelling shown in Figure 4a for Profile 4 shows that we would expect the 240 ka and 310 ka to be within a few metres of each other in elevation, given the differences in global sea-level at those times.

Figure 4.4: Graph showing the relationship between DEM-based and field-based measurements of palaeoshoreline elevations. The R^2 value >0.99 confirms that mapped palaeoshoreline elevations agree with those from Bianca et al. (2011). Figure 4.1 shows how age determinations differ from Bianca et al. (2011).

Figure 4.5: Profiles showing mapped and modelled palaeoshoreline elevations. The topographic profile is from the 10 m DEM. The numbers with arrows mark the elevations of palaeoshorelines mapped in the field. The coloured lines indicate palaeoshoreline elevations predicted by an uplift rate that has been changed iteratively to produce the best match with the mapped palaeoshorelines; goodness of fit is indicated by the value for slope and the R^2 values in Figure 4.4. Profiles are located on Figure 4.1.

Figure 4.6: Graph showing linear regression between measured and predicted palaeoshoreline elevations. The predicted elevations have been generated by defining a constant uplift rate

through time and iterating this value to produce a best fit to the measured palaeoshorelines. Best fit is quantified by R^2 values that are >0.99 for all 29 graphs with slopes close to 1.

Figure 4.7: Profiles showing tilting of palaeoshorelines whose ages are defined by the modelling in Figures 4.5 and 4.6. Solid lines show extrapolations between modelled topographic profiles 1-29.

Figure 4.8: Profile showing how uplift rates derived from modelling shown in figures 4.2 and 4.4.

Figure 4.9: Tilt angles measured along the studied along-strike profiles showing that tilt increases with age for palaeoshorelines.

Figure 4.10: Elevations of the hangingwall and footwall cut-offs of the palaeoshoreface surface associated with the 340 ka palaeoshoreline. The difference in elevation of these cut-offs define the throw-rate across the Vibo Fault.

Figures in Chapter 5

Figure 5.1: Database of Individual Seismogenic Source (DISS) (INGV - DISS Working Group, 2018) showing "capable" active faults which can produce seismic events in southern Italy. White square shows the investigated area where two historical earthquakes have been located from the Italian catalogues (Guidoboni et al., 2007). Note that the CDF (Capo D'Orlando Fault) has not been reported within DISS.

Figure 5.2: Location maps for palaeoshorelines within the hangingwall of the Capo d'Orlando active normal fault. A 10-m resolution DEMs with the associated coloured slope to highlight breaks of slopes is used as base-map. (a) shows a map amended from Giunta et *al.*, (2012) showing the investigated area from Capo d'Orlando town to Santa Agata di Militello town. The locations and ages of marine terraces from Giunta et *al.*, (2012) have shown as well as locations of U/Th and OSL dating by Scicchitano et al., (2011) and Giunta et *al.*, (2012). In (b) inner edges of marine terraces (palaeoshorelines) with our revised ages are presented (see numbered dots and the associated age within Legends panel). The "tip zone" area for the fault is marked in the SW with a red-coloured dashed line. Additionally, 15-topographic profile locations are shown from this study.

Figure 5.3: Graph showing the relationship between field-based and DEM-based inner edge elevations. The R^2 value > 0.99 confirms a very robust relationship suggesting that elevations measured elsewhere in the DEM are likely to be accurate.

Figure 5.4: (a) View of interpreted marine terraces in the field (shaded polygons) associated with Profile 8, with the inner edge elevations and the synchronously-assigned ages. The synchronous correlation approach allowed us to reassign the age of 240 ka to the palaeoshoreline at 96 m, which was previously sequentially-assigned to the 200 ka sea-level highstand by Giunta et al. (2012). (b) Field evidence, from along Profile 6, of an inner edge showing an upper palaeoshoreface depositional environment. The picture shows a marine abrasion platform made of Mesozoic limestone unconformably overlain by marine conglomeratic deposits already well-described by Scicchitano et al. (2011) and Giunta et al.

(2012). In places lithophagid borings into Mesozoic limestone and scattered evidence of beach cobbles have been mapped close to this area, suggesting the presence of the 125ka-dated palaeoshoreline. This inner edge could have not been mapped in the DEMs due to its small size and the resolution of the DEM, reinforcing the need for field work to check palaeoshorelines in the field. In (c) a flat surface cut into Mesozoic-aged limestone is shown with the associated sloping break interpreted as an inner edge. In (d) and (e) evidence of a shallow marine paleoenvironment are shown with presence of a flat surface cut into Mesozoic-aged limestone (d) and beach pebbles/cobbles associated with a palaeorocky beach. Note that this WCP (d) was sampled to be dated (Sample 15 and 16 in Table 5.2) and interpreted as the same with respect to the one shown in "c", before the river cutting activity.

Figure 5.5: Profiles showing mapped and modelled palaeoshoreline elevations. The topographic profile is from the 10 m DEM. The numbers with arrows mark the elevations of palaeoshorelines mapped in the field. The coloured lines indicate palaeoshoreline elevations predicted by an uplift rate that has been changed iteratively to produce the best match with the mapped palaeoshorelines; goodness of fit is indicated by the value for slope and the R^2 values in Figure 5.4. Profiles are located on Figure 5.2.

Figure 5.6: Graph showing linear regression analysis between our measured and predicted elevations. The predicted elevations, representing the synchronously-calculated sea-level highstand elevations, have been derived by defining a constant uplift rate through time, and iterating this value to find the best match to the measured and mapped palaeoshorelines. Note that "measured" elevations represent palaeoshoreline elevations mapped in the 10-m high

resolution DEMs. Coefficient of determination, R^2 value, has been used between these two datasets to quantify the best fit for all 15 topographic profiles with a value.

Figure 5.7: Palaeoshoreline elevations are changing along the strike of the Capo D'Orlando Fault. Solid lines represent mapped and measured palaeoshoreline elevations mapped by using DEMs and checked in the field; closely-dashed coloured lines represent m odelled iteratively-calculated sea-level highstand elevations (or the expected elevations) mostly matching with the solid lines. Uplift/Subsidence ratio (U:S) value of 1/3.5 has been applied to the oldest (340 ka) palaeoshoreline mapped within the hangingwall to estimate the expected elevation on the footwall and derive long-term fault slip-rate. A black dashed arrowed line shows the displacement between terraces mapped in the hangingwall and footwall cut-offs. The grey box identifies the "tip zone" discussed in the text.

Figure 5.8: Profile showing that uplift rates vary spatially along strike the Capo D'Orlando Fault.

Figure 5.9: The faulting activity of the Capo D'Orlando Fault over the Late Quaternary has tilted the investigated marine terraces; in fact, older and higher palaeoshorelines show higher tilt angle values because they have been experiencing a longer history of faulting activity.

Figure 5.10: In (a) uplift gradients are shown derived from Giunta et al., (2012) (orange-coloured dashline) and this study (blue line). The orange-coloured dash line shows an exponential growth of the uplift gradient through time driven by an absolutely-dated

palaeoshoreline (125 ka). Instead, the blue-coloured line shows a constant growth of the uplift gradient through time also driven by an absolutely-dated palaeshoreline (125 ka). Note that changing uplift rates through time is also shown in Figure 7 (section 2) in Giunta et al., (2012).

Figures in Chapter 6

Figure 6.1: In (a) a tectonic sketch map of the mainland Sicily is shown. The white-coloured dashed square shows the investigated area lying in the HP. Black dots show the location of historical earthquakes; yellow dots show values of Holocene uplift rates. Inset "a" shows a map with the seismogenic sources mapped within the DISS (INGV - DISS Working Group, 2018). In (b) a sketch cross-section shows (i) the seismicity distribution and the Moho discontinuity along the transect A-B adapted from Chiarabba and Palano, (2017). Note that the sketched geological section (adapted from Mattia et al., (2012)) shows the SBT where the Maghrebide Chain is southwardly overthrusting on the HP, producing a forebulge zone.

Figure 6.2: Modified map by Bianca et al., (1999) where marine terraces are mapped and proposed ages for un-dated terraces are assigned by a "sequential" correlation approach.

Figure 6.3: Location maps for palaeoshorelines within the HP, SE Sicily. A 2-m resolution DEM with the associated coloured slope to highlight breaks of slop is used as base-map. Dashed coloured lines represent the inner edge of successive mapped palaeoshorelines. Locations for ^{36}Cl cosmogenic dating are shown alongside the unpublished data from

Spampinato, (2011). Locations where corals for U/Th dating have been collected are shown. Numbered black lines indicate the 10 topographic profiles within the investigated area.

Figure 6.4: GPS measurements of horizontal velocities (Mattia et al., 2012; Palano et al., 2012; Mastrolembo Ventura et al., 2014) along the N-S oriented investigated transect in this thesis showing contraction process near the mapped trace of the SBT.

Figure 6.5: Topographic profile constructed along the sequence of palaeoshorelines attemped to date by Spampinato (2011) and this thesis. The sample location of "C5" from Spampinato, (2011) lies near (~ 300 m apart) where "Sample 1, 2 and 3" are mapped and collected.

Figure 6.6: (a) Field photo, locating Samples 1, 2 and 3 for ^{36}Cl cosmogenic dating. Note that these three samples have collected ~300 m away from those unpublished by Spampinato, (2011), and on the same geomorphic surface. Details of geomorphic features of the sampled WCP, confirming wave action, such as mill-holes are shown in (b), (c) and (d). (e) A perspective view of successive marine terrace inner edges is shown. In (f) a profile shows the topography and geomorphology of the sampled palaeoshorelines with associated inner edges and the spatial relationship with samples collected by Spampinato (2011). Note that samples "C5" and "C9" in panel (f) are from Spampinato, (2011) PhD thesis.

Figure 6.7: Top image shows a perspective view of the area where a coral colony has been sampled for U/Th age determination, with a sketch stratigraphic log. Bottom image shows details of the coral colony in-situ.

Figure 6.8: Graph showing the relationship between field-based and DEM-based inner edge elevation measurements. The R^2 value > 0.99 confirms a very robust relationship suggesting that elevations measured elsewhere in the DEM are likely to be accurate.

Figure 6.9: Profiles showing mapped and modelled palaeoshoreline elevations. The topographic profiles are from the 2 m DEM. The numbers with arrows mark the elevations of palaeoshorelines mapped in the field. The coloured lines indicate palaeoshoreline elevations predicted by an uplift rate that has been changed iteratively to produce the best match with the mapped palaeoshorelines; goodness of fit is indicated by the value for the R^2 value in Figure 6.10. Profiles are located on Figure 6.3.

Figure 6.10: Graph showing linear regression analysis between our measured and predicted elevations. The predicted elevations, representing the synchronously-calculated sea-level highstand elevations, have been derived by defining a constant uplift rate through time, and iterating this value to find the best match to the measured and mapped palaeoshorelines. Note that "measured" elevations represent palaeoshoreline elevations mapped in the 2-m high resolution DEMs. Coefficient of determination, R^2 value, has been used between these two datasets to quantify the best fit for all 15 topographic profiles with a value > 0.99.

Figure 6.11: On top a topographic profile is constructed onshore with respect the locations of the dated submerged palaeoshorelines by Dutton et al., (2009). On the bottom, outcomes of a synchronous correlation approach which models the un-dated mapped palaeoshorelines, claiming a constant uplift rate through time, showing a robust linear regression analysis (R^2 >

0.99). Red coloured values are the age controls from the submerged dated palaeoshoreline. Note that the dated coral presented in Table 6.3 has been sampled along the same topographic profile, at 14 m. Sample 21 location is shown in Figure 6.3 and 6.7.

Figure 6.12: The top panel (a) shows calculated exposure ages, from the unpublished data (Spampinato, 2011), within the sea level curve by Siddall et al., (2003). Note that, even though the relatively large uncertainty, all these ages lie close to the age of the LIM, confirming the age of a prominent palaeoshoreline in the geomorphology which is most likely to be that from MIS 5e derived by using different age controls. In panel (b) a topographic profile derived from 2m high resolution DEMs data, and located on Figure 6.3 shows the inner edge of mapped palaeoshorelines in details. Note that in the table outcomes results from a synchronous correlation are shown, by using these new exposure ages.

Figure 6.13: Profiles showing tilting of palaeoshorelines whose ages are defined by the modelling in Figures 6.9 and 6.10. Solid lines show extrapolations between modelled topographic profiles 1-10.

Figure 6.14: Profile showing that uplift rates vary spatially along the N-S oriented transect within the HP.

Figure 6.15: Tilt angle values are calculated for each mapped palaeoshorelines in this chapter, where older and higher palaeoshorelines show higher tilt angle values because they have been experiencing a longer history of crustal deformation.

Figure 6.16: Number of preserved palaeoshorelines from south to north. Note that where higher uplift rates are mapped a higher number of palaeoshorelines is preserved.

Figure 6.17: Higher values of uplift (a) and uplift rates (b) are mapped northwardly where deeper values of Moho discontinuity are mapped (c) and lower values of horizontal GPS velocities (d) are mapped. Note that the uplift is slightly affected by the doming effect from Mt Etna (e), suggesting that the differential uplifting process is describing a forebulge process affecting the HP.

Figures in Chapter 7

Figure 7.1: Location map showing the major Quaternary normal faults bordering the Messina Strait. The black dashed-squares outline locations of subsequent figures (see labels). Coloured dots represent mapped palaeoshorelines with newly-assigned ages from synchronous correlation. MSF: Messina Strait Fault; AF: Armo Fault; RCF: Reggio Calabria Fault; MF: Messina Fault.

Figure 7.2abcd: Location maps for palaeoshorelines within the footwall of the offshore Messina Strait Fault. A 10-m resolution DEM with the associated shaded relief to highlight breaks of slope is used as base-map. Panels a,b,c and d show palaeoshorelines with newly-assigned ages (see numbered dots and the associated age within Legends panel) and the 13-topographic profile locations from Messina town in the northern fault tip to Taormina town in the southern tip, E Sicily.

Figure 7.3: Location map for palaeoshorelines within the hangingwall of the Reggio Calabria Fault. A 10-m resolution DEM with the associated shaded relief, used to highlight breaks of slope is used as base-map. Palaeoshorelines with reviewed ages (see numbered dots and the associated age within Legends panel) and 4-topographic profile locations along the strike of this fault, S Calabria, are shown from this thesis. "7.19" refers to Figure 7.19 which shows where a marine terrace is offset by the RCF in the field.

Figure 7.4: Location map for palaeoshorelines within the hangingwall of the Armo Fault. A 10-m resolution DEM with the associated shaded relief, used to indicate breaks of slopes, is used as base-map. Inner edges of marine terraces with reviewed ages (see numbered dots and the associated age within Legends panel) and 5-topographic profile locations along the strike of this fault, S Calabria, are shown from this thesis. "7.26" refers to Figure 7.26 which shows where a marine terrace is offset by the RCF in the field.

Figure 7.5: Profiles showing mapped and modelled palaeoshoreline elevations along the strike of the offshore Messina Strait Fault. The topographic profile is from a 10 m DEM. The numbers with arrows mark the elevations of palaeoshorelines mapped in the field. The coloured lines indicate palaeoshoreline elevations predicted by an uplift rate that has been changed iteratively to produce the best match with the mapped palaeoshorelines; goodness of fit is indicated by the value for slope and the R^2 values in Figure 7.8. Profiles are located in Figure 7.1 and 7.2.

Figure 7.6: (a) A sequence of uplifted marine terraces is shown on the Sicilian coast. Marine terrace inner edges have been mapped (blue dots) and refined ages are assigned using a synchronous correlation approach. In places, shallow marine deposits have been mapped unconformably overlying wave-cut platforms (b). In (c) and (d) lithophagid borings in Mesozoic limestone formation have been mapped close to inner edge of the 125 ka-dated palaeoshoreline.

Figure 7.7: The graph shows the relationship between field-based and DEM-based inner edge elevations. The R^2 value > 0.99 confirms a very robust relationship suggesting that elevations measured elsewhere in the DEM are likely to be accurate.

Figure 7.8: Graph showing linear regression analysis between measured and predicted elevations. The predicted elevations, representing the synchronously-calculated sea-level highstand elevations, have been derived by defining a fluctuating uplift rate through time (increase in rate at ~50 ka), and iterating this value to find the best match to the measured and mapped palaeoshorelines. Note that "measured" elevations represent palaeoshoreline elevations mapped in the 10-m high resolution DEMs. Coefficient of determination, R^2 value, has been used between these two datasets to quantify the best fit for all 13 topographic profiles with a value > 0.99 achieved. Inset "a" shows the changing uplift rate through time measured in the centre of fault.

Figure 7.9: Profiles showing tilting of palaeoshorelines whose ages are defined by the modelling in Figure 7.2 and 7.5. Solid lines represent mapped and measured palaeoshoreline

elevations mapped by using DEMs and checked in the field across topographic profiles 1-13. Profile locations shown in Figure 7.1 and 7.2.

Figure 7.10: Profile showing that uplift rates are spatially varying along the strike the offshore Messina Strait Fault, both before and after 50 ka.

Figure 7.11: The faulting activity of the Messina Strait Fault over the Late Quaternary has tilted the investigated palaeoshorelines; in fact, older and higher palaeoshorelines show higher tilt angle values because they have experienced a longer history of faulting activity.

Figure 7.12: X-Y graphs showing good match between uplift rates and the number of preserved palaeoshorelines along the strike of the Messina Strait Fault; higher uplift rates allow.

Figure 7.13: Profiles showing mapped and modelled palaeoshoreline elevations along the strike of the Reggio Calabria Fault. The topographic profiles are from a 10 m DEM. The numbers with arrows mark the elevations of palaeoshorelines mapped in the field and DEMs. The coloured lines indicate palaeoshoreline elevations predicted by an uplift rate that has been changed iteratively to produce the best match with the mapped palaeoshorelines; goodness of fit is indicated by the value for slope and the R^2 values in Figure 7.15. Profiles are located on Figure 7.3.

Figure 7.14: Graph showing the relationship between field-based and DEM-based inner edge elevations. The R^2 value > 0.99 confirms a very robust relationship suggesting that elevations measured elsewhere in the DEM are likely to be robust.

Figure 7.15: Graph showing linear regression analysis between measured and predicted elevations. The predicted elevations, representing the synchronously-calculated sea-level highstand elevations, have been derived by defining a fluctuating uplift rate through time, and iterating this value to find the best match to the measured and mapped palaeoshorelines. Note that "measured" elevations represent palaeoshoreline elevations mapped in the 10-m high resolution DEMs. Coefficient of determination, R^2 value, has been used between these two datasets to quantify the best fit for all 4 topographic profiles with a value > 0.99. Inset "a" shows the uplift rate versus time measured along Profile 1.

Figure 7.16: Palaeoshoreline elevations vary along the strike of the Reggio Calabria Fault. Solid lines represent mapped and measured palaeoshoreline elevations mapped by using DEMs and checked in the field across topographic Profiles 1-4 shown in Figure 7.3.

Figure 7.17: Profile showing that uplift rates are spatially varying along the strike of the Reggio Calabria Fault before and after 50 ka.

Figure 7.18: The faulting activity of the Reggio Calabria Fault over the Late Quaternary has tilted the investigated marine terraces; in fact, older and higher palaeoshorelines show higher

tilt angle values because they have been experiencing a longer history of faulting activity. Note that a flex point is shown, suggesting a changing uplift rate through time.

Figure 7.19: Cartoon sketch showing the Reggio Calabria Fault offsetting terraced shallow marine deposits over 125 ka. On the footwall terrace a boulder made of cemented bioclastic sands containing corals with ages given in Table 3.1 (Samples 15,16 and 17) and Table 7.1, and the significance of the ages described in the text.

Figure 7.20: Profiles showing mapped and modelled palaeoshoreline elevations along the strike of the Armo Fault. The topographic profile is from a 10 m DEM. The numbers with arrows mark the elevations of palaeoshorelines mapped in the field and on DEMs. The coloured lines indicate palaeoshoreline elevations predicted by an uplift rate that has been changed iteratively to produce the best match with the mapped palaeoshorelines; goodness of fit is indicated by the value for slope and the R^2 values in Figure 7.22. Profiles are located on Figure 7.1 and 7.4.

Figure 7.21: Graph showing the relationship between field-based and DEM-based inner edge elevations. The R^2 value > 0.99 confirms a very robust relationship suggesting that elevations measured elsewhere in the DEM are likely to be accurate.

Figure 7.22: Graph showing linear regression analysis between measured and predicted elevations. The predicted elevations, representing the synchronously-calculated sea-level highstand elevations, have been derived by defining a fluctuating uplift rate through time, and

iterating this value to find the best match to the measured and mapped palaeoshorelines. Note that "measured" elevations represent palaeoshoreline elevations mapped in the 10-m high resolution DEMs. Coefficient of determination, R^2 value, has been used between these two datasets to quantify the best fit for all 4 topographic profiles with a value > 0.99. Inset "a" shows the changing uplift rate through time measured along the Profile 1.

Figure 7.23: Palaeoshoreline elevations along the strike of the Armo Fault. Solid lines represent mapped and measured palaeoshoreline elevations mapped by using DEMs and checked in the field across Topographic Profiles 1-4 shown in Figure 7.1 and 7.4.

Figure 7.24: Profile showing that uplift rates are spatially varying along the strike of the Armo Fault, but with higher rates after 50 ka.

Figure 7.25: The faulting activity of the Armo Fault over the Late Quaternary has tilted the investigated palaeoshorelines; older and higher palaeoshorelines show higher tilt angle values because they have been experiencing a longer history of faulting activity. Note that a flex point is shown, suggesting a change in uplift rate through time.

Figure 7.26: Photograph showing mapped uplifted palaeoshorelines on the hangingwall of the Armo Fault cut into Plio-Pleistocene marine deposits. It is also shown the Armo Fault offsetting the sycnrhonously-derived 478-aged marine terrace, suggesting faulting activity over the Late Quaternary. Bottom photo shows some of the palaeoshorelines mapped on the hangingwall of the Armo Fault along the Profile 3 "Amendolea". Profile location is shown in Figure 7.4.

Figures in Chapter 8

Figure 8.1: Map showing a tectonic sketch of the Messina Strait with well-known Quaternary normal faults (Monaco and Tortorici, 2000; Doglioni et al., 2012). Coloured dots represent the coseismic vertical movement mapped by Loperfido, (1909). Messina Fault (MF); Messina Strait Fault (MSF); Armo Fault (AF); Reggio Calabria Fault (RCF); Sant'Eufemia Fault (SEF); Cittanova Fault (CF); Scilla Fault (SF). Panel (a) is located in (b). (c) Levelling data used in the modelling. (d) Port of Messina town affected by coastal slumping after the earthquake.

Figure 8.2: Comparison of observed coseismic elevation changes for three normal faulting earthquakes, where the dip direction of the surface rupture is known for only two of the examples. (a) The 2009 L'Aquila Earthquake; (b) the 1983 Borah Peak Earthquake; (c) the 1908 Messina Earthquake.

Figure 8.3: In (a) the characteristic earthquake model is shown where the same amount of slip occurs along the strike of the fault on successive earthquakes. In (b) the variable earthquake slip model is shown where successive earthquakes can rupture partially the same fault and with a different amount of slip along-strike.

Figure 8.4: Well-plots showing misfits for various models and the preferred model.

Figure 8.5: Regression analysis to compare measured and modelled values of co-seismic elevation change for the preferred model; R^2 value = 0.925.

Figure 8.6: (a) Coseismic elevation changes projected onto an E-W transect. (b) Coseismic elevation changes projected onto a N-S transect. Elevation changes for other dip and slip scenarios are shown in Appendix 8.1, but all show higher values of misfit and hence have been rejected.

Figure 8.7: (a) 3D view of the slip distribution for the preferred model of the Messina Strait Fault. (b) Co-seismic uplift/subsidence contours produced by the preferred model.

Figure 8.8: Calculated linear regressions between "predicted" uplift elevations and "measured" elevations to drive the characteristic earthquake modelling, showing the "m" value from the y=mx equation equals to 1.

Figure 8.9: Graphs showing "measured" and "predicted" elevations along-strike the Messina Strait Fault. Black arrows highlight the difference in uplift in northern part of the fault.

Figure 8.10: Cartoon sketch showing disturbance of the long-term footwall uplift of the MSF by the tectonic subsidence produced by the MF (a) and the RCF (b). (c) Tectonic sketch of the Messina Strait where the deficit shown in Figure 8.9 is mapped (dashed-grey square).

Figures in Chapter 9

Figure 9.1: Regional extension accommodated by normal faults within the upper plate of the Ionian Subduction Zone, along the geological domain of Calabrian Arc. (a) Spatially-varying uplift rates from GPS analysis (light blue values; Serpelloni et al., 2013) are shown along the Calabrian Arc. (b) Spatially-varying Late Quaternary uplift rates change by up to a factor of 4 across the Calabrian Arc, with large variations between the footwalls and hangingwalls of faults, and along the strike of faults toward fault tips. Light blue values in (b) are reported by Catalano and De Guidi, (2003) and Ferranti et al., (2006), and black values are reported from this thesis, Roberts et al. (2013) and Meschis et al. (2018).

Figure 9.2: Top map shows a tectonic map modified from Roberts et al., (2009) for the Gulf of Corinth. The black square indicates the location of marine terraces mapped by De Gelder et al. (submitted). Bottom map shows detailed swath profiles mapping the inner edges of marine terraces on the footwall of the Xylokastro Fault.

Figure 9.3: Linear regression between "predicted" and "measured" elevations by applying a synchronous correlation approach to model the sequence of marine terraces presented in Table 9.1 and Figure 9.2. Note that 9 palaeoshorelines out of 11 are modelled assuming a constant uplift rate through time as initial hypothesis.

Figure 9.4: Linear regression between "predicted" and "measured" elevations by applying a synchronous correlation approach to model the sequence of marine terraces presented in Table 9.1 and Figure 9.2. Note that 10 palaeoshorelines out of 11 are modelled assuming a changing uplift rate through time as second tested hypothesis.

Figure 9.5: The difference between constant (a) and time-varying uplift rates (b). Coloured horizontal lines show the elevations of mapped palaeoshorelines from De Gelder et al. (submitted). Blue lines show the uplift rate histories with diamond symbols showing the expected elevations for expected palaeoshorelines.

Figure 9.6: Coseismic surface uplift variation with distance from the subduction interface after different megathrust earthquakes occurring in active subduction zones. Dashed green line shows the co-seismic subsidence modelled after the 1908 Messina earthquake shown in Chapter 8 at the same scale.

Figure 9.7: Tectonic sketch of the Calabrian Arc showing the Ionian slab trace and the normal faults modelled for Coulomb Stress Changes calculations (white square).

Figure 9.8: Coulomb Stress Change calculations showing different megathrust earthquakes scenarios with differing slip at depth (5 m to 20 m, increased of 5 m per model). Note that an increasing magnitude is derived for each change in slip at depth. The upper panels show the slip distribution. The lower panels show Coulomb stress transfer onto receiver normal faults in the upper plate and stress transferred onto un-slipped or weakly-slipped patches on the subduction interface. The result is that upper plate normal faults are positively stressed with values of 0.5 bars to 20 bars. IS: Ionian Slab, CDF: Capo D'Orlando Fault, MSF: Messina Strait Fault, RCF: Reggio Calabria Fault, AF: Armo Fault, CF: Cittanova Fault, SF: Serre Fault, VF: Vibo Fault, MF: Messina Faul

List of Tables

Tables in Chapter 2

Tables in Chapter 3

Tables in Chapter 4

Table 4.1: Measurements of U/Th isotope ratios of a coral sample collected near Vibo Marina town. The location of the collected corals is shown in Figure 4.1.

Table 4.2: All mapped inner edges from DEM and fieldwork with age assigned via synchronous correlation are shown. Note that not all the locations for inner edges mapped by DEM analysis with GPS in the field have been checked because the investigated area is in places thickly-vegetated and densely-populated with private properties.

Tables in Chapter 5

Table 5.1: Previous dating of palaeoshorelines lying within the investigated area by Scicchitano et al. (2011), Giunta et al. (2012) and Sulli et al. (2013). Note that different dating methods have confirmed the age (125 ky) of a prominent marine terrace along the strike of fault and over its tip. The samples are located in Figure 5.1.

Table 5.2: Exposure ages from ^{36}Cl cosmogenic dating are shown in the table. Sampling locations are shown in Figure 5.2b and in Chapter 3.

Table 5.3: All mapped inner edges from DEM and fieldwork with age assigned via synchronous correlation are shown. Note that not all the locations for inner edges mapped by

DEM analysis with GPS in the field have been checked because the investigated area is in places thickly-vegetated and densely-populated with private properties.

Tables in Chapter 6

Table 6.1: Samples from an un-published PhD thesis (Spampinato, 2011) for ^{36}Cl cosmogenic dating but discarded because initially thought to be affected by high erosion rates. These three samples are re-analysed and re-interpreted in this thesis. Sample locations are shown in Figure 6.3.

Table 6.2: Age controls derived from two submerged palaeoshorelines available in the literature. Locations are shown in Figure 6.3.

Table 6.3: Measurements of U/Th isotope ratios of a coral sample collected near Syracuse town. The location of the collected corals is shown in Figure 6.3.

Table 6.4: Exposure ages from ^{36}Cl cosmogenic dating are shown in the table. Sampling locations are shown in Figure 6.3 and in Chapter 3.

Table 6.5: All mapped inner edges from DEM and fieldwork with age assigned via synchronous correlation are shown. Note that not all the locations for inner edges mapped by DEM analysis have been checked with GPS in the field because the investigated area is in places thickly-vegetated and densely-populated with private properties. However, see Figure 6.8 for a check of consistency between the two databases.

Table 6.6: Exposure ages from 36Cl cosmogenic dating are shown in the table. These samples have been collected by Spampinato, (2011) but never published. Sampling locations are shown in Figure 6.3.

Tables in Chapter 7

Table 7.1: Measurements of U/Th isotope ratios of coral sample collected near Reggio Calabria town. Location of collected corals is shown in Figure 7.1 and 7.3.

Table 7.2: Available well-accepted age controls from literature. Locations of age controls are shown in Figures 7.1, 7.2, 7.3 and 7.4.

Table 7.3: Data collected for the Messina Strait Fault. All mapped inner edges from DEM and fieldwork with ages assigned via synchronous correlation. Note that not all the locations for inner edges mapped by DEM have been checked analysis with GPS in the field because the investigated area is in places thickly-vegetated and densely-populated with private properties.

Table 7.4: Exposure ages from in situ ^{36}Cl cosmogenic exposure dating are shown in the table. Sampling locations are shown in Figure 7.1, 7.2c and in Chapter 3.

Table 7.5: Data collected for the Reggio Calabria Fault. All mapped inner edges from DEM and fieldwork with age assigned via synchronous correlation are shown. Note that not all the locations for inner edges mapped by DEM analysis with GPS in the field have been checked

because the investigated area is in places thickly-vegetated and densely-populated with private properties.

Table 7.6: Data collected for the Armo Fault All mapped inner edges from DEM and fieldwork with age assigned via synchronous correlation are shown. Note that not all the locations for inner edges mapped by DEM analysis with GPS in the field have been checked because the investigated area is in places thickly-vegetated and densely-populated with private properties.

Tables in Chapter 8

Table 8.1: (A) Profile numbers from Chapter 7, (B) Latitude in UTM, (C) Elevation of the 76 ka palaeoshoreline (m), (D) Elevation of the 125 ka palaeoshoreline (m), (E) Elevation of the 240 ka palaeoshoreline (m), (F) Elevation of the 340 ka palaeoshoreline (m), (G) Uplift from best fit elastic model for the 76 ka palaeoshoreline (mm), (H) Uplift from best fit elastic model for the 125 ka palaeoshoreline (mm), (I) Uplift from best fit elastic model for the 240 ka palaeoshoreline (mm), (J) Uplift from best fit elastic model for the 340 ka palaeoshoreline (mm), (K) Number of earthquakes needed to replicate the 76 ka data, (L) Number of earthquakes needed to replicate the 125 ka data, (M) Number of earthquakes needed to replicate the 240 ka data, (N) Number of earthquakes needed to replicate the 340 ka data, (O) Predicted uplift (m) for the 76 ka data by multiplying the number of earthquakes to the co-seismic uplift (mm) in column G, (P) Predicted uplift (m) for the 125 ka data by multiplying the number of earthquakes to the co-seismic uplift (mm) in column H, (Q) Predicted uplift (m) for the 240 ka data by multiplying the number of earthquakes to the co-seismic uplift

(mm) in column I, (R) Predicted uplift (m) for the 340 ka data by multiplying the number of earthquakes to the co-seismic uplift (mm) in column.

Tables in Chapter 9

Table 9.1: Elevation of mapped inner edges shown in Figure 9.2 (bottom) by using a very high resolution DEMs (De Gelder et al., submitted), confirming and updating a previous mapping (Armijo et al., 1996). Age control is from Armijo et al., (1996).

Table 9.2: "Predicted" and "measured" elevations are shown with an assigned age assuming a constant uplift rate through time of 1.2 mm/yr. Note that two palaeoshorelines could not be modelled with the assumed constant uplift rate scenario. Red coloured elevation represents the age control used to drive the synchronous correlation. Note that it was not possible to identify the 340 ka palaeoshoreline using constant uplift rates.

Table 9.3: "Predicted" and "measured" elevations are shown with an assigned age assuming a changing uplift rate through time (0.35 mm/yr pre-175ka and 1.2 mm/yr post 175 ka). Red coloured elevation represents the age control used to drive the synchronous correlation approach. Importantly, the prominent highstand at 340 ka is successfully modelled, in contrast to the results in Table 9.2.

Acknowledgements

I find very easy to overstate my gratitude to my mentor and supervisor Prof. Gerald Roberts. Since I met him in 2012, when I had the wonderful opportunity to start working with him supported by a merit scholarship awarded me by the University of Palermo (Italy), he has been an inspiration to me; with his constant enthusiasm he has always encouraged me during all the "ups" and "downs" of my PhD. The time spent either in his office or in the field has always been fun and fulfilling. I have learnt something each time I had a scientific discussion with him, in front of his laptop, during a field campaign or eating a pizza in Sicily. He has always supported me with amazing advice, good teaching and constructive ideas. I cannot tell him enough "GRAZIE (thank you)" for that.

I also want to thank my second supervisor Dr. Rebecca Briant; with her expertise on OSL dating technique she has been decisive for my first published paper as a first author. She has always been supportive and kind.

Jenni Robertson has been my colleague since I have started my PhD. Her project on marine terraces and Active Tectonics topics in Greece has been parallel and complementary to mine. Being her "work-husband" in the field in Greece and Sicily allowed me to learn many things from her; discussion with her either in the evenings after amazing field days spent mapping in the Mediterranean or in the office in front our laptops have been crucial for my PhD development. Usually doing a PhD is a "solitary journey" for a student, I have never felt alone working with her alongside.

I want to thank Francesco Iezzi, Elisa Guerro-Moreno, Edoardo Villalobos-Seguira, Simon Maxwell, Claudia Sgambato, Lucy Buck and Sally Collins for being the best PhD colleagues that I could have asked for. I firstly knew them as PhD colleagues of "Room 6.11"

of the Earth and Planetary Sciences Department at Birkbeck University, now I am honoured to be their friend.

I want to thank Dr. Zoe Mildon for her kindness, time and help supporting the use of the Coulomb 3.3 software.

I want to thank Maz Iqbal for his immense help throughout my PhD; a pillar of the Earth and Planetary Sciences Department.

I want to thank Dr. Joanna Faure Walker who was the examiner of my PhD transfer. During the viva, we had a stimulating discussion, where she made many useful suggestions that helped me to develop this thesis.

Dr. Gianfranco Scicchitano is thanked for his help during my fieldwork in SE Sicily, near to Syracuse town. He showed me useful locations for mapping and sampling in that area. His presence was crucial for me to develop Chapter 6 in this thesis.

NERC is immensely thanked for having funded my PhD, field campaigns and conferences.

I want to thank my parents who have always helped me and supported my studies. Without them, I could not have had this amazing opportunity.

The last but not the least of thanks, is a special GRAZIE for my wife Vanessa who has always supported me. She has been my best friend, my partner, my fiancé and now wife in each moment of this journey. A person that I knew was there for me to celebrate when I have succeeded by publishing my first paper and to comfort me during my “down” moments. This thesis is dedicated to her.

A little thought is also for a kid called "Pietro Di Gregorio Stagnitta". His body was not found; in this photo a tomb is dedicated to his memory by his parents. He was 12 and killed by the 1908 Messina Earthquake. He was a simple student, enjoying his life and loved by his parents. Pietro, we are working to honour you.

This photo is from a field campaign close to Taormina with my supervisor Prof. Gerald Roberts. We were mapping a sequence of terraces when we found a small cemetery, near Forza D'Agro' town (Chapter 7).

Chapter 1: Introduction

The processes that produce long-term uplift of the upper plates of subduction zones relative to sea-level have been extensively studied by investigating uplifted Late Quaternary sequences of marine terraces and Holocene coastal notches (e.g. Armijo, Lyon-Caen and Papanastassiou, 1992; Miyauchi, Dai Pra and Sylos Labini, 1994; Balescu *et al.*, 1997; Tortorici *et al.*, 2003; Catalano and De Guidi, 2003; De Guidi *et al.*, 2003; Antonioli *et al.*, 2006; Pedoja *et al.*, 2006, 2014; Ferranti *et al.*, 2007; Shaw *et al.*, 2008, 2010; Giunta *et al.*, 2012; Roberts *et al.*, 2013; Gallen *et al.*, 2014; Boulton and Stewart, 2015; Jara-Muñoz and Melnick, 2015; Melnick, 2016). Uplift data from upper plates have been driving geoscientists worldwide to derive new scientific knowledge aimed at deriving a better understanding of subduction processes and the associated seismic hazard due to the occurrence of megathrust earthquakes. New insights into coupling and earthquake slip distributions on the subduction interface, as well as inferences about mantle upwelling processes, are useful to improve our understanding of the geodynamics and seismic hazard associated with subduction zones, and are commonly assessed using geological, geomorphological, geodetic and geophysical observations on overriding plates (e.g. McCloskey, Nalbant and Steacy, 2005; Meltzner *et al.*, 2006; Nalbant *et al.*, 2013; Nic Bhloscaidh *et al.*, 2015). However, although slip on the subduction interface and mantle upwelling are clearly important factors influencing uplift, it is becoming increasingly clear that active crustal deformation also occurs within the upper plates of subduction zones (e.g. Meltzner *et al.*, 2006; Mouslopoulou *et al.*, 2015, 2016). There is a growing body of evidence that indicates the presence of active faults in the upper crust that influence uplift (Armijo, Lyon-Caen and Papanastassiou, 1992a; Armijo *et al.*, 1996; Hasegawa *et al.*, 2000; Monaco and Tortorici, 2000; Jacques *et al.*, 2001; Tortorici *et al.*, 2003; Nicol and Beavan, 2003; Papanikolaou, Alexandri and Nomikou, 2006; Giunta *et al.*, 2012; Roberts *et al.*, 2013; Gallen

et al., 2014). The effect of the recognition of active faults within upper plates has been that uplift rate values, which were previously thought to be "regional" in extent, have been influenced by local tectonics due to the presence of active faults within the crust of the upper plate, which tectonically deform uplifted Late Quaternary palaeoshorelines (Catalano and De Guidi, 2003; Tortorici *et al.*, 2003; Giunta *et al.*, 2012; Roberts *et al.*, 2013; Gallen *et al.*, 2014; Pavano, Pazzaglia and Catalano, 2016; Roda-Boluda and Whittaker, 2017). The evidence for this takes the form of uplift rates that can be demonstrated to change along the strike of active faults (Roberts *et al.*, 2013).

This thesis aims to elucidate interactions between "regional" uplift due either to subduction processes and/or mantle upwelling processes, and processes related to active crustal deformation over the Late Quaternary, to constrain: (i) the nature of upper plate processes, (ii) quantify long-term deformation rates for upper plate faulting, that might otherwise be attributed erroneously to slip on the subduction interface and/or mantle upwelling, and (iii) identify the nature of any remaining signals, not attributable to upper plate faulting, that might be used to make inferences about subduction processes and/or mantle upwelling.

The investigated area of the Calabrian Arc (southern Italy), which represents the link between the NW-SE oriented Italian southern Apennines thrust belt and the E-W oriented Maghrebide chain in north Sicily (Malinverno and Ryan, 1986; Tortorici *et al.*, 1995), has long been thought to be undergoing uplift due, at least in part, to the ongoing Ionian subduction process supported by the presence of prominent sequences of uplifted marine terraces (Malinverno and Ryan, 1986; Dewey *et al.*, 1989; Boccaletti *et al.*, 1990; Selvaggi and Chiarabba, 1995; Chiarabba, De Gori and Speranza, 2008; Roberts *et al.*, 2013). Also, where

limited collision between continental fragments has occurred, crustal thickening and the formation of a forebulge have been suggested to produce differential uplift, for example within the foreland represented by the Hyblaean Plateau (HP), SE Sicily (DeCelles and Giles, 1996; Bianca *et al.*, 1999; DeCelles, 2012). In addition, long-term crustal extension processes have been occurring within the upper plate accommodated by active normal faults which have been seismically deforming sequences of Late Quaternary palaeoshorelines (Monaco and Tortorici, 2000; Jacques *et al.*, 2001; Catalano and De Guidi, 2003; Bianca *et al.*, 2011; Giunta *et al.*, 2012; Roberts *et al.*, 2013; Roda-Boluda and Whittaker, 2017). The extension is evidenced by the locations of damaging historical normal faulting earthquakes, collated within Italian catalogues such as the Database of Individual Seismogenic Source (DISS) (Guidoboni *et al.*, 2007; Basili *et al.*, 2008; Stucchi *et al.*, 2013). These earthquakes occur where the traces of normal faults are mapped within the deforming upper plate of the Ionian subduction zone (Monaco and Tortorici, 2000; Galli, Galadini and Pantosti, 2008) (Figure 2.1). Nonetheless, some of these extension-related seismogenic sources, and the associated long-term deformation rates, are either poorly known/constrained or considered not active because no Holocene activity is mapped (Roberts *et al.*, 2013; Meschis *et al.*, 2018). This contrasts with the approach used elsewhere, for example, where it is considered that for a better and improved long-term seismic hazard assessment, it is important to take into account the notion that any evidence of fault movement in the last 500 ky can be used to define a structure as an "active fault" (Yeats, 2012; Chapman *et al.*, 2014).

It is important to identify active faults because quantitative insights from Late Quaternary upper-crustal vertical movements and their associated deformation rates is critical for a long-term seismic hazard assessment (Roberts *et al.*, 2013). Consequently, it is essential

to constrain deformation over long timescales, such as over the period of time since the Middle Pleistocene, for example by investigating sequences of palaeoshorelines. The results can be used to: (i) differentiate long-term uplift patterns from transitory strain-rates produced by a single seismic event or temporal earthquake cluster, and (ii) judge how strain-rates derived by short term investigations at the timescale of individual seismic cycles or temporal earthquake clusters relate to the longer-term Quaternary deformation (Yeats and Prentice, 1996; Ward, 1998; Papanikolaou, Roberts and Michetti, 2005; Faure Walker *et al.*, 2010; Roberts *et al.*, 2013). To do that, studying tectonically-deformed Late Quaternary marine terraces is perhaps the only way to derive crustal deformation rates spanning timescales long enough to average out deformation over multiple seismic cycles (Roberts *et al.*, 2013), and this is the approach taken in this thesis. However, a problem exists in that it is commonly the case that the long-term crustal vertical movements on upper plates of subduction zones have been previously derived by investigating sequences of palaeoshorelines and applying a "sequential" correlation approach (e.g. Armijo *et al.*, 1996; Tortorici *et al.*, 2003; Giunta *et al.*, 2012; Gallen *et al.*, 2014). This thesis, along with published work that derives from it, will show that such sequential correlation is prone to fail in tectonically active regions affected by low uplift rates (Roberts *et al.*, 2013; Meschis *et al.*, 2018; Pedoja *et al.*, 2018). Furthermore, it will be shown that the uplift rates derived from this method commonly suggest temporally varying-uplift rates (Tortorici *et al.*, 2003; Bianca *et al.*, 2011; Giunta *et al.*, 2012; Gallen *et al.*, 2014), which this thesis and papers derived from it will show are not robust (Roberts *et al.*, 2013; Meschis *et al.*, 2018). The thesis will develop an alternative approach to correlating palaeoshorelines with the Quaternary sea-level curve, based on the observation that sea-level highstands during this time were not

evenly spaced in time, suggesting that, for a constant uplift-rate, uplifted palaeoshorelines will not be evenly spaced in elevation as explained below.

Several authors have studied the occurrence of flights of marine terraces in tectonically active regions as the result of the interaction between Quaternary eustatic sea-level changes and tectonic uplifting processes (Lajoie, 1986; Carobene and Dai Pra, 1991; Westaway, 1993; Cinque, De Pippo and Romano, 1995; Armijo *et al.*, 1996; Bosi, Carobene and Sposato, 1996; Bianca *et al.*, 1999; Roberts *et al.*, 2009; Giunta *et al.*, 2012; Roberts *et al.*, 2013; Gallen *et al.*, 2014; Meschis *et al.*, 2018). More importantly, inner edges of marine terraces provide the actual elevation of palaeoshorelines which represent the principal eustatic highstands of the global eustatic curve (e.g. Siddall *et al.*, 2003; Rohling *et al.*, 2014), produced mostly during interglacials (Bloom, 1974; Lajoie, 1986; Bosi, Carobene and Sposato, 1996; Caputo, 2007; Roberts *et al.*, 2013). However, as noted above, it is important to note that sea-level highstands in the Quaternary period are not equally-spaced over the time, so sequences of paleoshorelines formed as a consequence of constant uplift rates will not be equally-spaced in elevation (Westaway, 1993; Houghton et al. 2003, Roberts et al. 2009, Roberts *et al.*, 2013). Taking this into account the latter, a "synchronous correlations approach" (as opposed to a sequential correlation; see above) can be used to estimate long-term crustal deformation rates. The synchronous correlation approach investigates sequences of Quaternary palaeoshorelines through iteration of the uplift rate, with linear regression between the measured palaeoshorelines and predicted palaeoshoreline elevations for each iteration, searching for a best-fit scenario that minimises misfit. The approach takes into account the "overprinting problem" where-by older palaeoshorelines, that are lower than given elevation such as present-day sea-level, may be destroyed and/or overprinted by younger highstands that are at the given

elevation. This is important because this scenario would suggest that the next higher or lower palaeoshoreline on a coastal hillside does not necessarily correlate with the next older or younger sea-level highstand (Westaway, 1993; Roberts *et al.*, 2009; Roberts *et al.*, 2013; Meschis *et al.*, 2018). The uplift-rate can be held constant through time or varied through time, with the former being the first approach that is attempted, before more complicated uplift histories are investigated if the constant uplift hypothesis is rejected. If the uplift can be directly related to an active fault, for example where uplift-rates vary along the strike of a fault, the synchronous correlation approach can allow derivation of long-term fault slip-rates and information on whether these slip-rates have been constant or fluctuating through time. In turn, it may be possible to investigate whether high slip-rate pulses on neighbouring faults are simultaneous or anti-correlated, giving information that can be used to investigate fault interactions within the upper plate (Roberts *et al.*, 2009; Roberts *et al.*, 2013; Meschis *et al.*, 2018). Furthermore, the long-term uplift may then also be compared with geodetic data for single earthquakes that have affected the same coastlines, such as the 1908 Messina Mw 7.0 earthquake, to whether long-term uplift field is a good guide to the uplift and hence slip distributions of single earthquakes.

In this thesis the following scientific questions are examined:

- Is the uplift rate, mapped within the upper plate of the Ionian Subduction Zone (ISZ), simply regional, controlled by large-scale subduction zone processes such as subduction interface slip and mantle upwelling, and not controlled by upper plates active faults?
- Does the uplift rate vary over the Late Quaternary? If so, why?
- Does the uplift rate vary along the strike of major upper plate active faults?

- Is the uplift rate related to slip-rate on faults of the upper plate?
- Do slip-rates on faults control seismic hazard of tectonically-active regions?
- Is the slip distribution on subduction interfaces affected by upper plate crustal deformation?

These questions test the hypothesis that uplift is simply related to subduction and not associated with deformation within the upper plate. This test is important because if the hypothesis is rejected it will not be possible to invert uplift data to derive details of slip on the subduction interface such as mega-thrust earthquake slip distributions, or coupling (the ratio of slip and far-field shortening implied by plate motions), or mantle upwelling, without removing the uplift signal produced by deformation within the upper plate.

To test the above hypothesis, investigations of sequences of palaeoshorelines along the uplifting Calabrian Arc have been undertaken to: (i) temporally and spatially constrain long-term uplift rates on the upper plate of the ISZ, (ii) constrain seismic hazard related both to subduction zone earthquake and active crustal faults, (iii) constrain continental deformation relating to collision of microcontinental fragments by using uplift rates, and (iv) differentiating local fault-controlled uplift processes, mantle upwelling, and subduction-controlled uplift due to mega-thrust earthquake slip distributions or aseismic creep. Furthermore, due to the geometric relationships between candidate active faults and uplifted palaeoshorelines this thesis applies the synchronous correlations approach to sequences of Late Quaternary palaeoshorelines outcropping both on the hangingwalls and footwalls of upper plate active faults. This allow quantification of: (i) uplift rates in the framework of the structural geometries of the active faults such as fault tip gradients, en echelon relay zones and across strike geometries such as horst and graben, and (ii) estimates of the associated long-

term fault slip-rates which have fundamental tectonic and seismic hazard implications (Cowie *et al.*, 2012).

The methods that facilitate the above approach are based on detailed geomorphological field mapping of palaeoshorelines that have been supported by mapping in a GIS environment using both a 10-m, high-resolution, Digital Elevation Model (DEM) (Tarquini *et al.*, 2012) and 2-m high-resolution DEMs provided by the Regional Sicilian government (Regione Siciliana). In particular, palaeoshoreline elevations have been mapped in the field and correlated with those mapped on the DEMs, with regression analysis used to check the robustness of these correlations. Wave-cut platforms (WCPs) in limestone and corals associated with the palaeoshorelines have been sampled in an attempt to date them by applying absolute age dating methods such as ^{36}Cl cosmogenic dating and $^{234}U/^{230}Th$ dating to gain new age controls for marine terraces modelling. Correlations made by applying the synchronous correlation approach have been driven either by the above-described new obtained age controls where possible, or ages available already in the literature (Antonioli, Ferranti, *et al.*, 2006; Antonioli, Kershaw, *et al.*, 2006; Dutton *et al.*, 2009; Bianca *et al.*, 2011; Scicchitano *et al.*, 2011; Giunta *et al.*, 2012; Sulli *et al.*, 2013).

New results from this thesis give new insights into the relationship between "regional" uplift signal due either to the subduction process and the mantle upwelling and the local tectonic signal associated with the upper plate active faults. Local and regional tectonic implications depicted by investigating uplifted Late Quaternary marine terraces, applying a synchronous correlation technique, are discussed alongside possible future scientific questions that can be addressed based on this thesis.

1.1 Thesis layout

A brief outline of the thesis is described as follows:

Chapter 2 provides the geological background of the Calabrian Arc region and the associated "undeformed" uplifted foreland area of the Hyblaean Plateau, SE Sicily. A literature review is presented outlining the state-of-the-art about subduction zones, sea level curves, marine terraces, age determination for Quaternary palaeoshorelines and its associated gaps, seismic hazard calculations in Italy, normal faulting activity and continental deformation by deriving long-term Quaternary fault slip-rates, all of which represent key-components for the present study.

Chapter 3 describes the methods and approach adopted to map tectonically-deformed marine terraces within the investigated areas. DEM-based mapping and field-based mapping approaches for palaeoshorelines are described. The synchronous correlation approach, which takes into account the "overprinting problem" common in regions affected by low uplift rates, is described. Absolute dating techniques such the $^{234}U/^{230}Th$ dating on corals and *in situ* ^{36}Cl cosmogenic exposure dating on WCPs on limestone to obtain age controls to drive the synchronous correlation are described. In particular, emphasis is placed on obtaining detailed geomorphological and paleoenvironmental site characterizations because it is argued that these are essential to gain suitable samples for dating.

Chapter 4 provides results and associated local tectonic implications related to the Late Quaternary faulting activity of the Vibo Fault, Calabria, where for the first-time long-term slip rate on faults and Earthquake Recurrence Interval (or T_{mean}) are derived. The Vibo Fault, lying within the uplifting forearc of the ISZ in Calabria, has been deforming a sequence of Late Quaternary uplifted palaeoshorelines with constant rate through time, suggesting that this fault has been active during the last 340 ky. A paper has been published in *Quaternary Science*

Reviews (Roberts *et al.*, 2013), with the PhD candidate as the second of five authors, having been responsible for much of the fieldwork and modelling in this paper.

Chapter 5 provides results and associated local tectonic implications related to the Late Quaternary faulting activity of the Capo D'Orlando Fault, NE Sicily, where for the first-time long-term slip rate on faults and Earthquake Recurrence Interval (or T_{mean}) are derived. This fault, lying at the southernmost part of the Calabrian Arc, has been deforming a sequence of Late Quaternary uplifted palaeoshorelines with constant rate through time, implying that this fault has been active during the last 340 ky. Previous authors claimed that this fault has been inactive because no Holocene activity was mapped (Giunta *et al.*, 2012). A paper has been published on this topic in *Tectonics* (Meschis *et al.*, 2018).

Chapter 6 provides results and associated local implications related to the differential uplift occurring in the HP, representing the foreland of the continental collision between Eurasia and Africa plates. Long-term process of forebulging seems to be the cause of the differential uplift studied by investigating and refining Late Quaternary uplifted marine terraces in SE Sicily. A manuscript intended for eventual publication with the PhD candidate as first author is in preparation.

Chapter 7 provides results and associated local implications related to the Messina Strait Fault activity in NE Sicily and the activity of the Reggio Calabria Fault and the Armo Fault in Calabria. By investigating Late Quaternary uplifted marine terraces outcropping on footwalls and hangingwalls of these faults, a swapping faulting activity through time is revealed within the fault systems controlling the Messina Strait formation and the associated seismic hazard. A manuscript intended for eventual publication with the PhD candidate as first author is in preparation.

Chapter 8 describes elastic half-space modelling or a geodetic dataset for the 1908 Messina Mw 7.1 earthquake that occurred in the Messina Strait, and comparison with uplift and deformation of Late Quaternary palaeoshorelines. This provides new results and evidence for a high-angle east dipping normal fault as a seismogenic source for this, one of the most destructive earthquakes in Italy. In particular, levelling data obtained a year later since the earthquake occurred show co-seismic subsidence on the Calabrian side of the Messina Strait. The tectonically-deformed sequence of marine terraces outcropping between Messina town and Taormina town has been tectonically-deformed by the tectonic uplift of the Messina Strait Fault (Chapter 7), and it is suggested that the same seismogenic source produced the 1908 Messina Earthquake. The chapter also details an investigation of whether this earthquake can be considered to be a "characteristic earthquake" for this fault, by trying to find a correlation between the co-seismic tectonic uplift through time due to the occurrence of a "characteristic earthquake" and the long-term uplift measured by investigating the Late Quaternary palaeoshorelines. A manuscript on this topic (Meschis et al. in review) has been submitted for publication.

Chapter 9 discusses the regional tectonic implications and generic inferences which can be drawn about subduction zones. In particular, the role of faulting activity on the upper plate of the ISZ is discussed. Furthermore, the importance of long-term slip rates on fault systems through time and their relevance for gaining new insights for an improved long-term seismic hazard approach are discussed.

Chapter 10 highlights general concluding remarks for this thesis.

To re-iterate the suitability of this material for publication, this thesis with its methods and obtained results has either led and contributed to the following scientific publications:

1) The implications of revised Quaternary palaeoshoreline chronologies for the rates of active extension and uplift in the upper plate of subduction zones. Roberts, Meschis et al., 2013, *Quaternary Science Reviews, 78, 169-187* (covered in Chapters 3 and 4).

2) The relationships between regional Quaternary uplift, deformation across active normal faults and historical seismicity in the upper plate of subduction zones: The Capo D'Orlando Fault, NE Sicily. Meschis et al., 2018, *Tectonics* (Covered in Chapters 3 and 5).

3) A 70° east-dipping offshore normal fault with 5 m dip-slip as the source of the 28th December 1908 Messina earthquake (Mw 7.1), Italy, revealed by levelling data. Meschis et al., (submitted), *Scientific Reports* (Covered in Chapter 8).

4) Neogene – Quaternary slow coastal uplift of Western Europe through the perspective of sequences of strandlines from the Cotentin Peninsula (Normandy, France). Pedoja et al., 2018, *Geomorphology, 303, 338-356.* I have co-authored this publication.

5) Temporally constant uplift rates observed along south-central Crete, Greece, and their relationship to active normal faults in the upper plate of the Hellenic subduction zone, constrained with in situ 36Cl cosmogenic exposure dating. Robertson, et al., (submitted) *Tectonics.*

6) Long-term active normal faulting interaction by investigating tectonically-deformed Late Quaternary marine terraces: the Messina Strait as a case-study. Meschis et al., *(in prep.)* (Covered in Chapters 3 and 7).

Chapter 2: Literature review

This chapter provides an overview of previous research on key-components of this thesis. Furthermore, an overview about the geological context will be introduced to provide a general overview of the investigated area.

2.1 Geological background of the Calabrian Arc and the foreland area in SE Sicily

2.1.1. The geological domain of the Calabrian Arc

Calabria and NE Sicily, southern Italy, form the geological domain of the Calabrian Arc. Many authors have investigated the origin and evolution of this area (Figure 2.1). The general accepted view is that the Calabrian Arc marks the geological link between the NW-SE oriented southern Italian Apennines thrust belt and the E-W oriented Maghrebide chain of northern Sicily as a result of tectonic convergence between the Eurasian and African paleo-margins and the associated progressive closure of the Tethys Ocean since the Late Cretaceous (Malinverno and Ryan, 1986; Tortorici *et al.*, 1995; Monaco and Tortorici, 2000; McClusky *et al.*, 2003; Serpelloni *et al.*, 2007).

Regional uplift processes affecting the Calabrian Arc are associated with ongoing subduction, with the Ionian Basin oceanic crust subducting beneath the Calabrian Arc as a result of the northward ongoing progression of the African paleo-margin and the progressive south-eastward movement of the Calabrian Arc with the associated opening of the Tyrrhenian Extensional Basin (Rehault, Boillot and Mauffret, 1984; Malinverno and Ryan, 1986; Dewey *et al.*, 1989). Since Late Miocene/Pliocene thrust belt structures have been overprinted and dissected by extensional processes due to the Tyrrhenian Basin opening, accommodated by active normal faults along the entire Calabrian Arc, producing structural highs (horst

structures) and sedimentary basins (graben structures) fragmenting the Tertiary thrust belts (Ghisetti and Vezzani, 1982; Monaco and Tortorici, 2000; Pepe *et al.*, 2003).

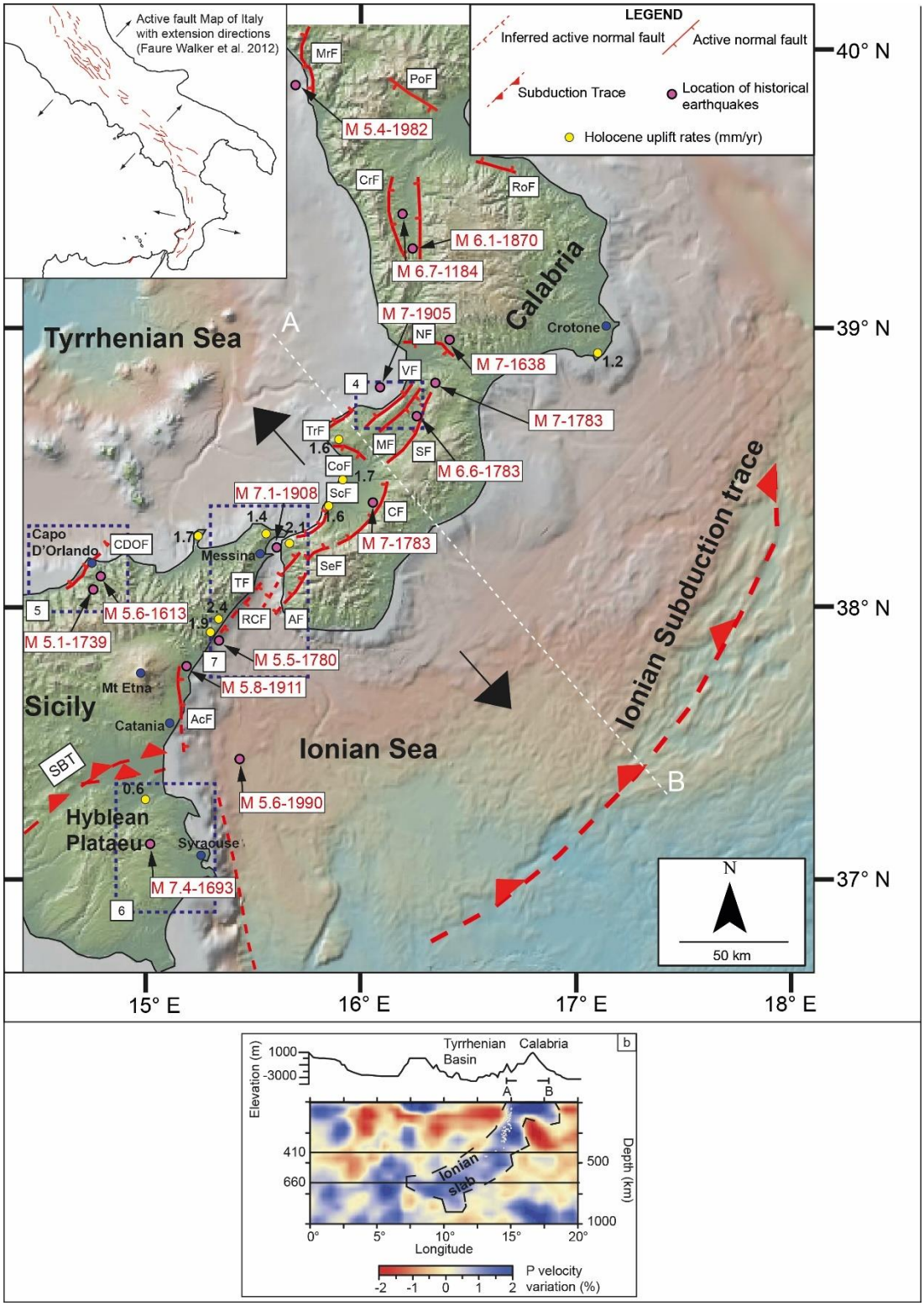

***Figure 2.1**: Location map showing the tectonic setting of Calabria and NE Sicily. In (a) yellow dots show Holocene uplift-rate values (Antonioli, Ferranti, et al., 2006; Antonioli, Kershaw, et al., 2006) from coastal notches. Black dots represent locations for historical earthquakes with the associated earthquake magnitude from Guidoboni et al. [2007]. Blu squares show the investigated areas of this thesis (related numbers represent Result chapters). Reported active*

normal faults are from Monaco and Tortorici, (2000), Database of Individual Seismogenic Sources (INGV - DISS Working Group, 2018), *Bianca et al., 2011 and Giunta et al., 2012: MrF: Maratea Fault, PoF: Pollino Fault, RoF: Rossano Fault, CrF: Crati Fault, NF: Nicastro Fault, VF: Vibo Fault, TrF: Tropea Fault, CoF: Coccorino Fault, MF: Mileto Fault, SeF: Serre Fault, CF: Cittanova Fault, SEF: Sant'Eufemia Fault, SF: Scilla Fault, AF: Armo Fault, RCF: Reggio Calabria Fault, TF: Taormina Fault, CDF: Capo D'Orlando Fault. In (b) amended tomographic cross-section from the Gulf of Lion to the Calabrian Arc by Lucente et al., (2006). Section trace A-B shows the Ionian slab beneath the Calabrian Arc characterized by intermediate and deep earthquakes (white dots).*

Active extension along the Calabrian Arc, with rates between 2mm/yr and 3mm/yr (Serpelloni *et al.*, 2005; Mastrolembo Ventura *et al.*, 2014), has been demonstrated by the presence of historical seismicity in the overriding plate (Monaco and Tortorici, 2000). Moreover, some geoscientists have proposed a cessation or slowing of the rolling-back process and the associated extension within the Tyrrhenian Basin due to the de-coupling of the Ionian slab from the Calabrian Arc since 700 ka (Gvirtzman and Nur, 1999b; Wortel and Spakman, 2000; Goes *et al.*, 2004; Serpelloni *et al.*, 2005, 2007; Palano *et al.*, 2012). This suggested slab detachment process is thought to have produced both the sinking of the slab itself with the related isostatic rebound and the lithospheric tearing-related faulting process in the SW and NE tips of the NW-dipping Ionian slab, producing flow of mantle material through slab windows just beneath the crust of the Calabrian Arc. All these processes have produced significant uplift and crustal extension within the upper plate of the Ionian subduction zone since the Middle Pleistocene (Gvirtzman and Nur, 1999b; Faccenna *et al.*, 2011).

Sequences of marine terraces record the uplift process and the local extensional tectonics accommodated by active normal faults in the Calabrian Arc (Dumas *et al.*, 1981; Miyauchi, Dai Pra and Sylos Labini, 1994; Monaco and Tortorici, 2000; Catalano *et al.*, 2003, 2008; Roberts *et al.*, 2013). In fact, the Calabrian Arc represents one of the best locations worldwide to investigate the relationship between uplift and active faulting due to the presence of dramatic flights of marine terraces developed since the Late Quaternary (Ghisetti, 1981;

Dumas *et al.*, 1988; Westaway, 1993; Catalano *et al.*, 2003; Tortorici *et al.*, 2003; Roberts *et al.*, 2013).

In this thesis, sequences of marine terraces along the Calabrian Arc have been investigated to better understand the relationship between "regional" uplift and local active normal faults to derive long-term crustal deformation rates critical to: (i) improve the long-term seismic hazard analysis and (ii) differentiate the regional signal of uplifting and local tectonics.

2.1.2. The "undeformed" foreland area in SE Sicily

The Hyblean Plateau (HP), which extends from Catania to south of Syracuse town in SE Sicily (Figure 2.1), represents the onshore portion of a larger foreland area so-called the Pelagian Block (Burollet, Mugniot and Sweeney, 1978; Ben-Avraham and Grasso, 1991; Cultrera *et al.*, 2015). More particularly, the HP represents an onshore carbonate promontory of the larger African paleo-margin. It extends from NE Tunisia region to SE Sicily abruptly interrupted by the Malta Escarpment in the East which separates the geological domain of continental crust of the African paleo-margin and the geological domain of oceanic crust of the subducting Ionian Basin (Torelli *et al.*, 1998; Nicolich *et al.*, 2000; Cultrera *et al.*, 2015).

The HP, representing the "undeformed" foreland of the northern Sicilian Maghrebide chain, lies within the so-called "Siculo-Calabrian rift zone" at its southernmost tip (Monaco and Tortorici, 2000; Dutton *et al.*, 2009). Geological and seismic studies have shown Meso-Cenozoic-aged 6 km thick sedimentary carbonate with volcanic intercalated layers, which overlie the Palaeozoic basement, which in places has been overlain by Quaternary marine deposits associated with sequences of palaeoshorelines (Lentini *et al.*, 1987; Bianca *et al.*, 1999).

Neogene-aged tectonic shortening has affected the HP producing a NE-SW oriented SE-verging thrust and fold system, forming the so-called the "Sicilian Collision Zone" (SCZ) (Cultrera *et al.*, 2015). This stage has caused thrust sheets piling at the NW margin of the underthrusted HP producing a foreland-bulging of the HP caused by tectonic overload (Faccenna *et al.*, 2001; Billi *et al.*, 2006; Musumeci *et al.*, 2014; Cultrera *et al.*, 2015). During the Late Miocene to Early Pliocene, as a result of the bulging process, a NE-SW oriented hinge zone has been produced on the HP accommodated by extensional normal faulting (Grasso *et al.*, 1995; Cultrera *et al.*, 2015). Quaternary processes related to the interaction between sea level changes, regional uplift and crustal deformation are represented by the presence of sequences of marine terraces mostly outcropping on the eastern part of the HP (Bianca *et al.*, 1999; Monaco *et al.*, 2002). Recent studies have shown that the HP is undergoing contraction processes slightly deforming the "undeformed" Sicilian foreland, possibly due to the compressional activity of the Sicilian Basal Thrust (SBT) (Lavecchia *et al.*, 2007; Mattia *et al.*, 2009; Palano *et al.*, 2012; Mastrolembo Ventura *et al.*, 2014; Musumeci *et al.*, 2014).

In this thesis, tectonically-deformed marine terraces have been mapped in SE Sicily to better understand if long-term contraction processes have been recorded by palaeoshorelines and compare crustal vertical rates at different timescales such as in the Late Quaternary, the Holocene and geodetic timescales.

2.2. Subduction process

The Ionian oceanic crust is subducting beneath the overriding plate represented by the Calabria Arc, which is the fore-arc associated with the subduction process. In this section, subduction processes and associated tectonic features will be reviewed.

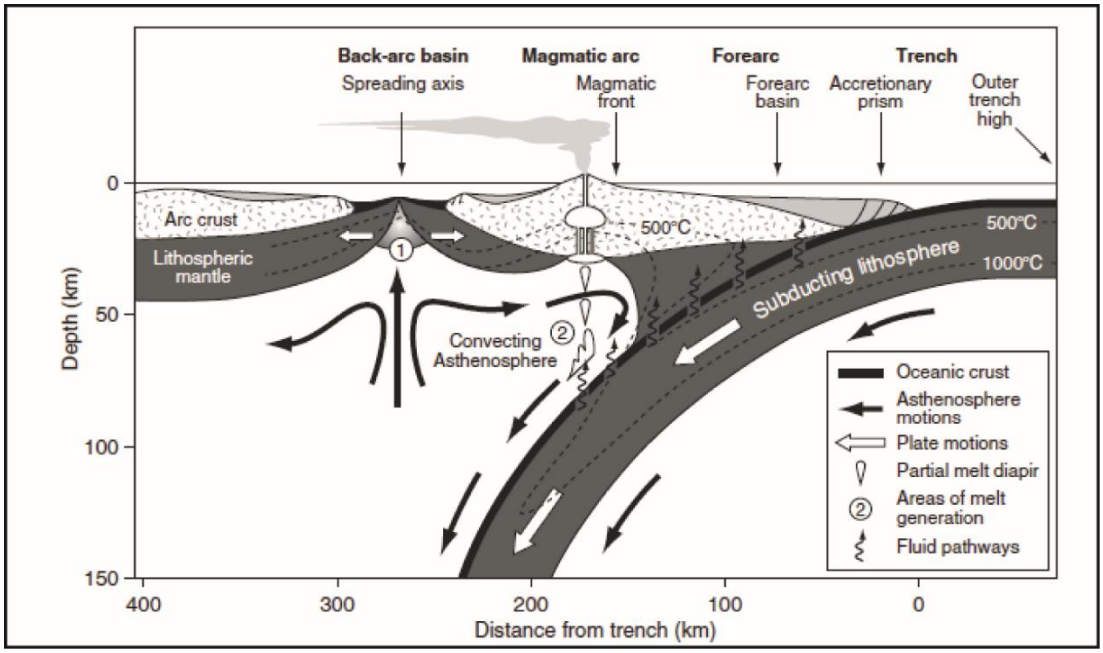

Figure 2.2: *Section of a subduction zone. From the book Global Tectonics (Kearey, Klepeis and Vine, 2013).*

Tectonic plates move along active margins such as divergent margins where new oceanic crust is formed and convergent margins where oceanic crust is consumed. Convergent active margins lie where tectonic plates meet leading to descending of oceanic lithosphere into asthenosphere mantle under an overriding plate defining a so-called subduction zone as shown in Figure 2.2 (Peacock, 1986; Doglioni *et al.*, 1999). In particular, subduction processes take place when: (i) two tectonic plates show an initial convergent component of relative plate movements and (ii) one of the involved plates is denser, thinner and overridden (Doglioni *et al.*, 2007). These tectonically active zones have been documented through the study of seismicity (Doglioni *et al.*, 1999). After Wadati, 1935 and Benioff, 1949, investigations on subduction zones have been carried out using geophysical, vulcanological, surface geology, petrological and geochemical studies (e.g. Menard, 1964; Bally, 1983; Giardini and Woodhouse, 1986; Fowler, 1990; Bebout *et al.*, 1996; Doglioni *et al.*, 1999), allowing the identification of a well-defined zone, called the *Benioff-Wadati zone*, where earthquake

hypocentres are distributed defining the geometry of the subducting slab as shown in Figure 2.3 (Jarrard, 1986; Doglioni *et al.*, 1999).

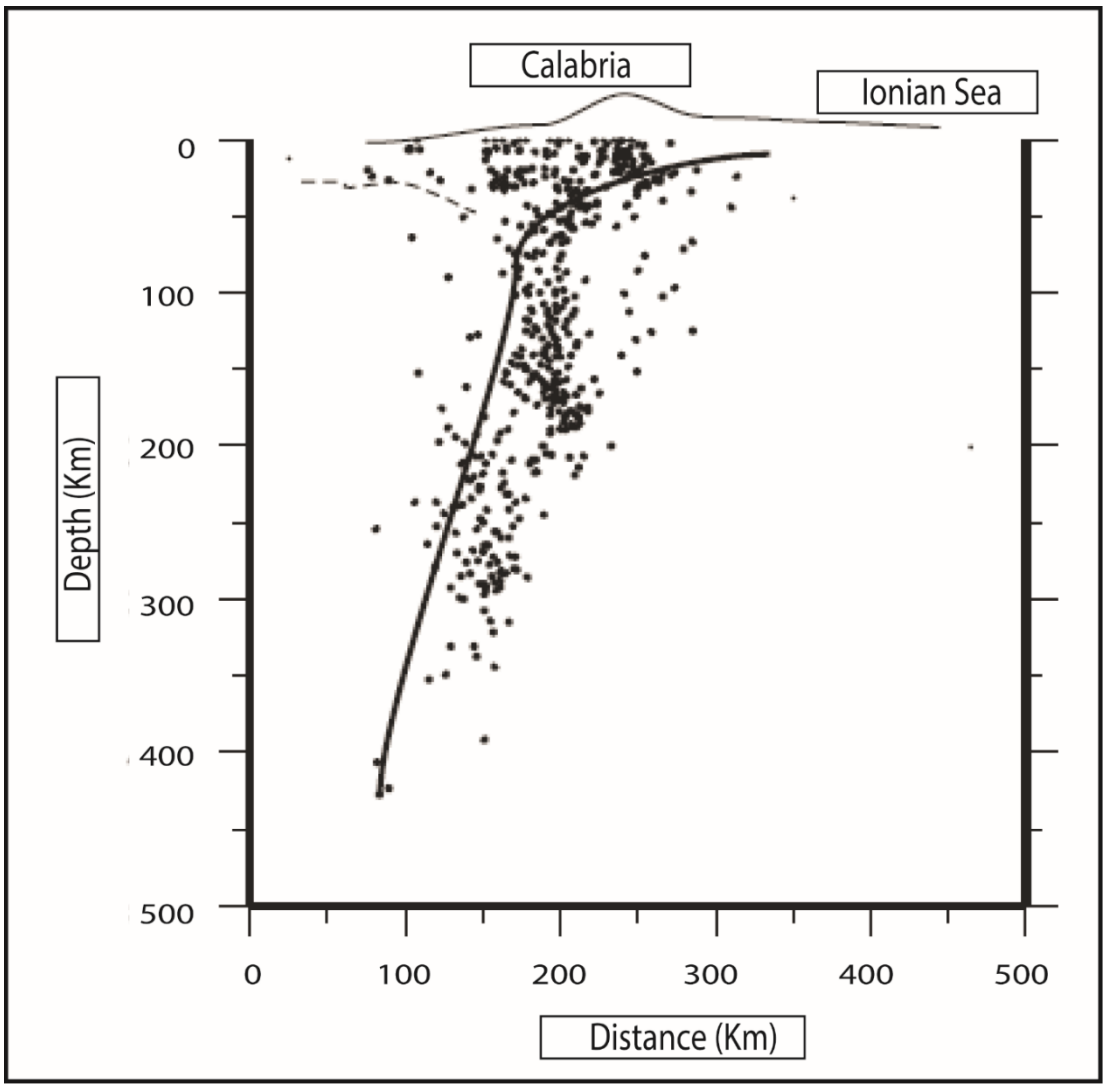

Figure 2.3: *Picture from Chiarabba, Jovane and DiStefano, (2005) showing the intermediate-deep earthquake hypocentres which define the WNW oriented Benioff-Wadabi slab under the Calabrian Arc.*

Back-arc active extension is thought to be either the result of the trench retreat or the motion of the overriding plate away from the trench itself (Magni *et al.*, 2014). In the central Mediterranean region, the retreating slab of the Ionian oceanic lithosphere subducting under the Calabrian Arc has led to the diachronous formation of two back-arc basins such as the Ligur-Provenzal basin between 30 and 16 Ma and the Tyrrhenian basin between 12 and 10 Ma (Magni *et al.*, 2014) which are thought to be formed as episodic processes with pulses of

extension and oceanic spreading (Malinverno and Ryan, 1986; Faccenna *et al.*, 2001; Magni *et al.*, 2014). The Ionian subduction zone involves the remains of the Jurassic Neotethys Ocean (Dewey *et al.*, 1989) identified by the actual Ionian Sea formed by oceanic crust covered by Meso-Cenozoic sedimentary deposits (Catalano and Sulli, 2006).

Extension processes accommodated by crustal normal faults, within the upper plate of the subduction zone, have been intensely studied in the Ionian subduction zone, revealing a coeval uplifting process probably also associated with asthenospheric wedging beneath the Calabrian Arc, and additionally suggesting a lack of asthenospheric mantle as shown in Figure 4 (e.g. Doglioni, 1995; Selvaggi and Chiarabba, 1995; Gvirtzman and Nur, 2001). The onset of the afore-mentioned uplift process is thought to have started around the Middle Pleistocene. This would be associated with the asthenospheric wedging, which is thought to result from the decoupling/detaching process of overriding plates from the roll-back of the Ionian slab (Figure 2.4) (Cucci and Cinti, 1998; Gvirtzman and Nur, 1999b, 2001). It has been suggested that this has resulted in unusually high forearc elevations in the Calabrian Arc relative to other forearc zones associated with subduction zones on Earth (Gvirtzman and Nur, 1999a, 2001). Moreover, it is still debated if the Ionian subduction process is still active (Cucci and Cinti, 1998; Gutscher *et al.*, 2017) because some authors emphasise that there is no evidence of major seismicity at ~ 100 km depth (Anderson and Jackson, 1987; Westaway, 1993). However, other studies of the seismicity show a 60°-70° W–NW dipping slab, interpreted from intermediate-deep earthquake hypocentres between 40 and 80 km depth, suggesting the subduction process is still active, as already shown in Figure 2.3 (e.g. Selvaggi and Chiarabba, 1995; Chiarabba, Jovane and DiStefano, 2005; Chiarabba, De Gori and Speranza, 2008).

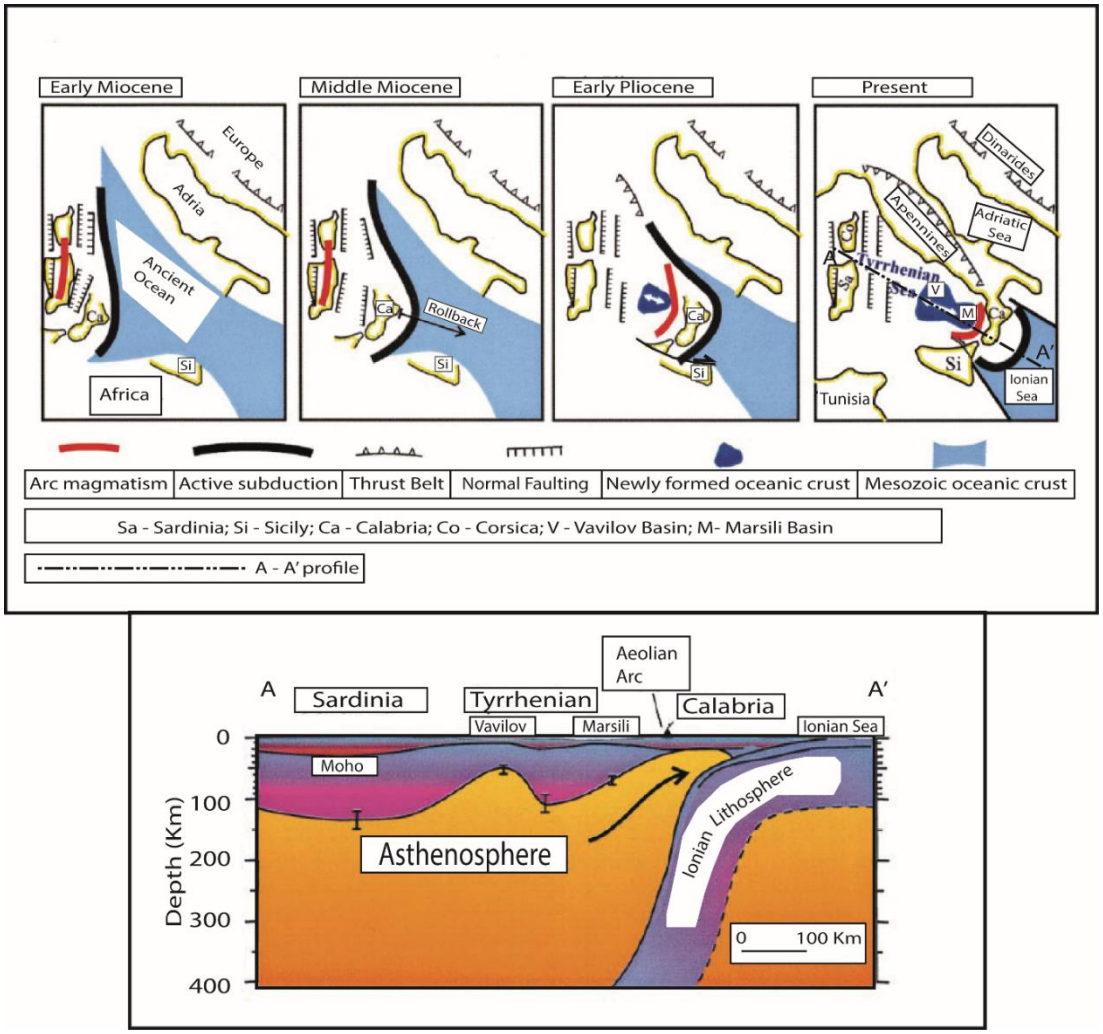

Figure 2.4: *Modified picture from Gvirtzman and Nur, (2001) showing at the top a picture of the evolution of the Ligur-Provenzal and Tyrrhenian Basins from the Early Miocene associated with the presence of the Jurassic Tethyan Ocean. In the lower picture, a schematic lithospheric section crossing the actual Tyrrhenian Basin is shown; furthermore, asthenospheric wedging is shown under the Calabrian Arc probably associated with the detaching of the retreating slab from the overriding plate.*

Slip distribution on subduction interface have been attempted to be derived with observations from uplifting upper plates on active subduction zones such as the Sumatra subduction (Meltzner *et al.*, 2006; Nalbant *et al.*, 2013). However, it is unclear if this upper plate is affected by active faulting, suggesting that more studies are needed to investigate if the uplift signal mapped on the upper plate is "disturbed" by "local" faulting.

In this thesis, uplift rates have been quantified in order to better understand if these uplift rates are simply "regional" or are controlled by crustal active faults lying in the extension

zone. Studying tectonically-deformed sequences of marine terraces allows the differentiation of "regional" uplift rates and local fault-controlled uplift rates within a subduction zone.

2.3. Sea Level curves

Studies of active tectonics have shown that uplifted sequences of marine terraces represent the interaction between regional uplifting processes, local crustal deformation and Quaternary sea-level changes (Lajoie, 1986; Carobene and Dai Pra, 1991; Westaway, 1993; Cinque, De Pippo and Romano, 1995; Armijo *et al.*, 1996; Bosi, Carobene and Sposato, 1996; Bianca *et al.*, 1999; Roberts *et al.*, 2009; Giunta *et al.*, 2012; Roberts *et al.*, 2013; Gallen *et al.*, 2014; Pedoja *et al.*, 2018). The inner edges of marine terraces represent the actual elevation of past sea-level identifying the principal highstands of the global eustatic curve, associated with interglacial periods, as shown in Figure 2.5 (Bloom, 1974; Lajoie, 1986; Bosi, Carobene and Sposato, 1996; Caputo, 2007; Bianca *et al.*, 2011; Roberts *et al.*, 2013).

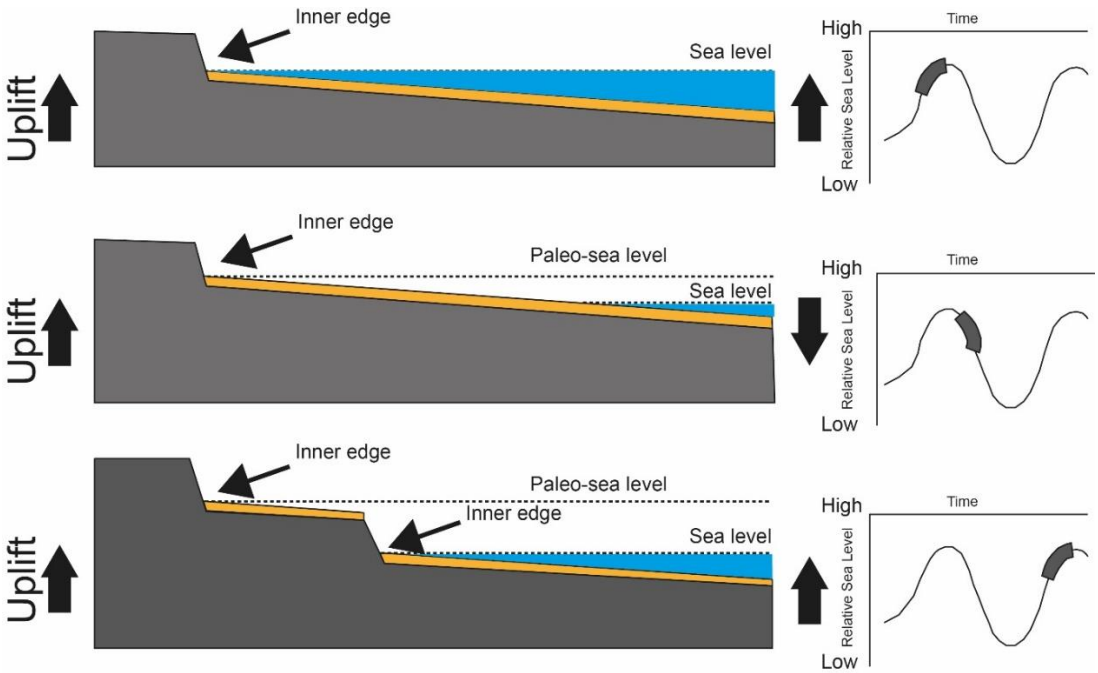

Figure 2.5: *Sketched cartoon amended from Nalin, Massari and Zecchin, 2007 showing the formation of marine terraces as the result of the interaction between regional uplift and sea level changes through time* (Bianca *et al.*, 2011).

Complex interaction between ice sheets, solid earth, atmosphere and oceans produce a combined configuration defining rapid changes in sea level, responding at different timescales (Lambeck, Esat and Potter, 2002). The global climate of the Quaternary period has been affected by small changes in active solar insolation provoked by varying the geometry of Earth's orbit around the sun (Peltier, 1998, 1999). These small changes in geometry of the Earth's orbit seem to be enough to cause the "Ice Ages" which have controlled climate system variability in the second half of the Pleistocene period (Hays, Imbrie and Shackleton, 1976), triggering sea-level fluctuations. It has been suggested that the main sea-level cycles have happened every ~ 100kyr over the last 1Myr, showing maximum amounts around 120-140 meters sea-level fluctuation, produced by changes in ice volume of around 55 million km^3 (Peltier, 1998; Lambeck, Esat and Potter, 2002).

Benthic calcareous foraminifera shells have been considered as a proxy indicator for knowledge on ice volume and associated global sea-level changes (Shackleton, 1987; Lambeck, Esat and Potter, 2002); this calcareous marine material records the geochemical signatures of the water in which the foraminifera lived, underlying the importance of the $^{18}O/^{16}O$ ratio because, during main glaciations, the oceanic water shows reduced, that is lighter, oxygen isotope values (Lambeck, Esat and Potter, 2002; Waelbroeck *et al.*, 2002). This ratio leads allows quantification of the variation associated with the heavier oxygen isotope defined as $\Delta^{18}O = \{(^{18}O/^{16}O)sample /(^{18}O/^{16}O)standard - 1\}$ which indicates the global ice volume (Lambeck, Esat and Potter, 2002), expressed as parts per thousand as shown in Figure 2.6. The Figure shows that high values of $\Delta^{18}O$ indicate large ice sheets associated with low temperatures, and low values of $\Delta^{18}O$ indicate small ice sheets associated globally warm conditions (Shackleton, 1967; Mix, 1985; Lambeck, Esat and Potter, 2002).

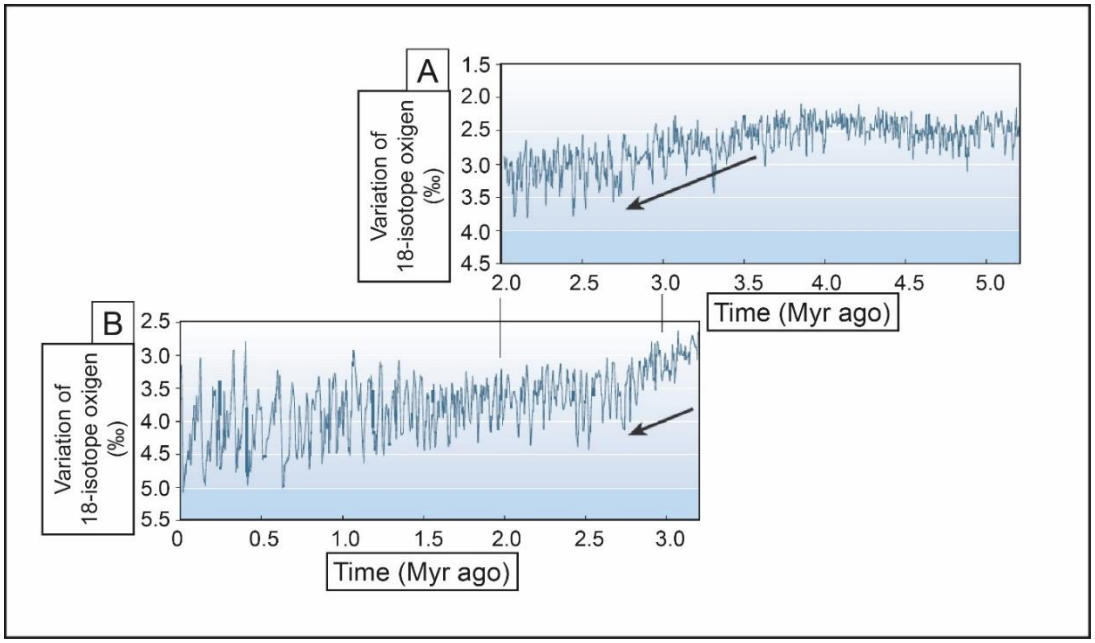

Figure 2.6: *Figure from Lambeck, Esat and Potter, (2002) showing Δ ^{18}O over the time from two sediment cores. Curve A from the Caribbean Sea* (Raymo, 1992) *shows the variation since the Upper Neogene; curve B from the Equatorial Atlantic* (Haug and Tiedemann, 1998) *shows variation since the Upper Pliocene*

Oxygen isotopes ratios, derived from the calcite shells of benthic foraminifera, have been used to estimate sea levels (Chappell and Shackleton, 1986; Waelbroeck *et al.*, 2002). However, clear incongruities have been shown (Fig.1 from Shackleton 1987 for detailed review) between this ratio and another proxy used to derive paleo-sea levels which are dated (Chappell and Shackleton, 1986; Stirling *et al.*, 1998). This fact could be explained as the result of deep water temperature changes of Pacific Ocean (Chappell and Shackleton, 1986; Shackleton, 1987). Nonetheless, some authors (e.g. Clarke & Marshall 2002; Waelbroeck et al. 2002) proposed that it is challenging to estimate sea-levels from $^{18}O/^{16}O$ ratios not only due to deep ocean water temperature changes, but also because temporal variations in the isotopic composition of the melted ice.

For the Mediterranean area, a well-constrained sea level curve describing the last half million years of sea fluctuations is available, based on investigations in the Red Sea (Siddall *et al.*, 2003). In fact, the Red Sea has shown higher water residence times magnifying the sea-level changes which have been recorded in Δ ^{18}O of benthic microfossil (Δ $^{18}O_b$) through

sediment cores of the Red Sea (Siddall *et al.*, 2003). Furthermore, past investigations (Rohling *et al.*, 1998; Waelbroeck *et al.*, 2002) have individually supported these magnifications to estimate sea level lowstands during the maximum glaciations periods over the Middle Pleistocene (Siddall *et al.*, 2003). Additionally, to gain improved knowledge about global sea-level fluctuations a hydraulic model which simulates flow exchanges between the open ocean and the Red Sea has been proposed providing a better resolution for the last 70kyr temporally constraining magnitudes and rates of sea-level variations within +/- 12m (Siddall *et al.*, 2003).

Different independent methods have been applied to infer the sea-level curves over the last 500 kyr (e.g. Waelbroeck *et al.*, 2002; Rohling *et al.*, 2009; Grant *et al.*, 2012). Following the "Red Sea approach" (Siddall *et al.*, 2003), relying on hydraulic control of water exchange with open ocean, the Mediterranean Sea has been proposed as a study-area to expand back in time the sea level curve by using independent proxies (Rohling *et al.*, 2014). In fact, for older periods than the last 500 kyr there was no validation, with independent methodologies, due to the fact that all existing sea-level data were associated with deep-sea oxygen isotope data from benthic foraminifera ($\Delta\,^{18}O_b$) affected by processes unlinked to sea level (Rohling *et al.*, 2014). For this reason, a sea-level reconstruction spanning the last ~5 Myr, looking at independent proxies such as planktonic foraminiferal ($\Delta\,^{18}O_f$) which has been produced into a 5.3-Myr "Mediterranean stack", has been proposed by using the Mediterranean Sea (Rohling *et al.*, 2014). The Mediterranean basin shows more complex variables than the Red Sea to take into account such as: (i) its hydrological cycle which is more complicated than in the Red Sea and (ii) the larger connection at Gibraltar, with respect to Bab-el-Mandab Strait for the Red Sea, due to the lower signal-to-noise ratio, which shows Mediterranean glacial-interglacial $\Delta\,^{18}O_f$ amplitudes of ~ 3‰ which the half if compared those from the Red Sea (~6‰) (Rohling *et al.*,

2014). However, the Mediterranean Sea, in fact, represents another evaporative peripheral sea with limited linkage to the open ocean (Rohling *et al.*, 2014). This implies that lowering of sea level reduces the above-mentioned exchange and the increases water residence times in highly evaporative sea, like in the Red Sea. This causes strong increases in salinity and $\Delta\ ^{18}O$ of basin waters, which recorded also by carbonate microfossil $\Delta\ ^{18}O_f$. A quantification between change in microfossil $\Delta\ ^{18}O_f$ and sea level change permits a conversion into sea level data from such $\Delta\ ^{18}O$ records (Rohling *et al.*, 2014).

It is also important to consider the rates at which sea-level can rise and fall. For example, between 350/345 ka and 340ka, sea level rose by 120m, implying an average rate of sea-level rise of ~ 20 mm/yr. When compare with the rates of vertical motions of the crust caused by normal faulting, which lie in the range of 3 mm/yr (Lajoie, 1986; Lambeck, Esat and Potter, 2002), it is clear that sea-level rise can outpace uplift allowing a geomorphic and sedimentary signature to be preserved on the footwall and hangingwall of the fault.

Age (ka)	**Elevation of highstands (mm)**
0	0
30	-80000
50	-60000
76	-30000
100	-25000
115	-21000
119	-5000
125	5000
175	-30000

200	-5000
217	-30000
240	-5000
285	-30000
310	-22000
340	5000
410	-5000
478	0
525	20000
550	10000
560	3000
590	20000
620	20000
695	10000
740	5000
800	20000
855	20000
980	25000

Table 2.1: *Values of sea-level highstands derived from Siddall et al. (2003) and Rohling et al., (2014) used to calculate predicted palaeoshoreline elevations given a value for uplift rate.*

With the above in mind, this thesis uses sea level curves by *Siddall et al.,* (2003) and *Rohling et al.,* (2014) (Table 2.1) to model sequences of marine terraces describing uplifting processes and crustal deformation along the Calabrian Arc. The curve is shown in Figure 2.8.

2.4. Sequences of marine terraces as indicators of active tectonics

Marine terraces have been described as a result of interaction between uplift and Quaternary sea level changes through time (e.g. Lajoie 1986; Westaway 1993; Armijo et al. 1996; Roberts et al. 2009; Giunta et al. 2012; Roberts et al. 2013). The Calabrian Arc is affected by uplift, and represents a natural geological laboratory to investigate sequences of palaoeshorelines deformed by upper plate crustal deformation (Malinverno & Ryan 1986; Monaco & Tortorici 2000; Roberts et al. 2013).

Palaeoshorelines are associated with marine terraces, which are relatively flat gently-sloping seaward-inclined geomorphic surfaces mostly outcropping close to the actual coastlines, also identified as palaeoshoreface surfaces cut by the action of sea-wave forming abrasion marine platform, in places overlay by palaeoshoreface deposits (e.g. Bianca et al. 1999; Bianca et al. 2011; Roberts et al. 2013). The sediments represent the geological record of past sea level highstands (e.g. Armijo et al. 1996; Houghton, 2010; Giunta et al. 2012; Roberts et al. 2013). The palaeoshorelines themselves are located at the highest point of the sedimentary dip and are marked by palaeo-sea-level indicators, such as shorelines deposits (beach deposits) and landforms indicating former rocky shorelines (palaeo-sea-cliffs, coastal notches, wave-cut platforms) (Figure 2.7).

A long-standing problem has been the identification of so-called "regional" uplift, usually associated with underlying subduction processes (McCloskey, Nalbant and Steacy, 2005; Nalbant *et al.*, 2013; Bhloscaidh *et al.*, 2015), and more local uplift variations, attributable to active faults and gradients in deformation along active faults (Roberts *et al.*, 2009; Roberts *et al.*, 2013; Meschis *et al.*, 2018). One of the key claims in this thesis is that the study of raised and deformed palaeoshorelines allows differentiation between "purely-regional" uplift rates and "local-fault-controlled" uplift rates values (Roberts *et al.*, 2009; Roberts *et al.*, 2013).

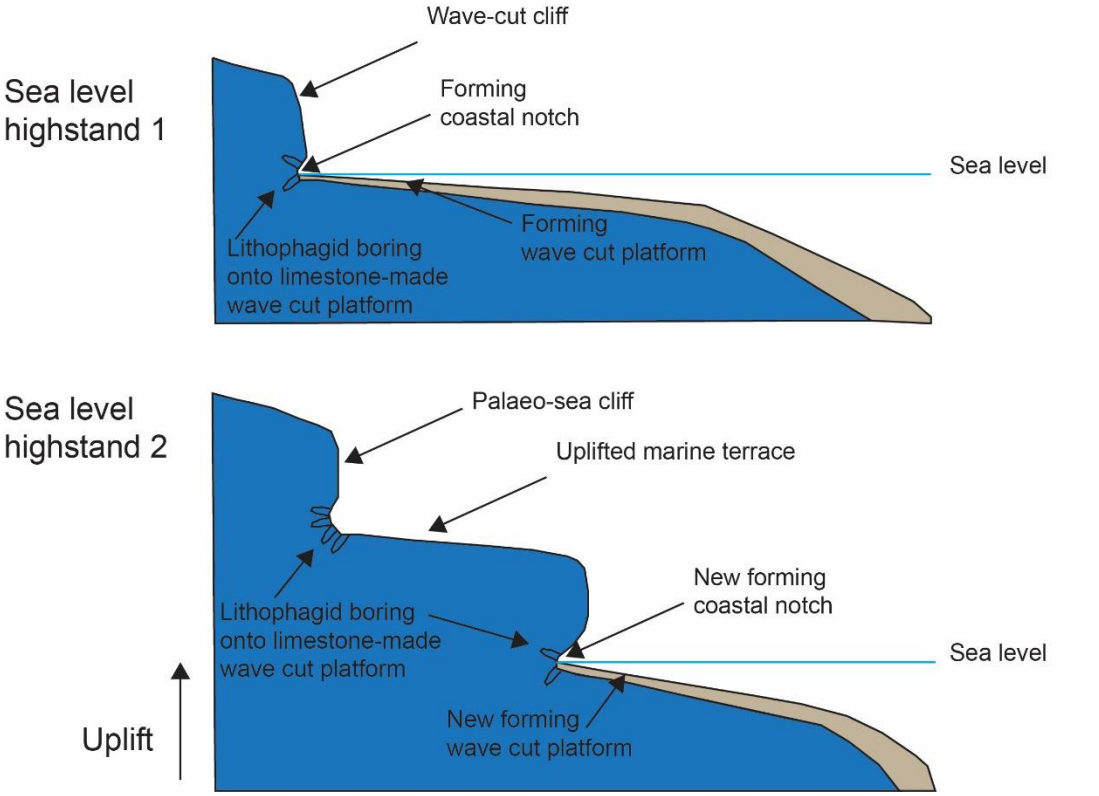

Figure 2.7: *Cartoon showing how an uplifted marine terrace forms in an uplifting region*

Moreover, it will be emphasised that Late Quaternary uplift rate values can be used to estimate long-term fault slip-rates, that can in turn be used to better define the geography of seismic hazard (Roberts *et al.*, 2009; Roberts *et al.*, 2013). For example, Quaternary "regional" uplift rate values have been derived within regions affected by active crustal normal faulting (e.g. Westaway 1993; Miyauchi et al. 1994; Tortorici et al. 2003). However, it is important to view these "regional" uplift rate values stated in the literature in a framework that includes active normal fault systems. Active faults are widespread within the Calabrian Arc, with a higher density of such faults on the Tyrrhenian side, possibly due to the Tyrrhenian Basin opening (Malinverno and Ryan, 1986; Monaco and Tortorici, 2000), compared to the Ionian side as shown in Figure 2.1 and 2.8 (Monaco and Tortorici, 2000) (Figure 2.8).

This thesis uses and approach that explicitly includes variations due to active faulting, and how this varies spatially and temporally through the Quaternary.

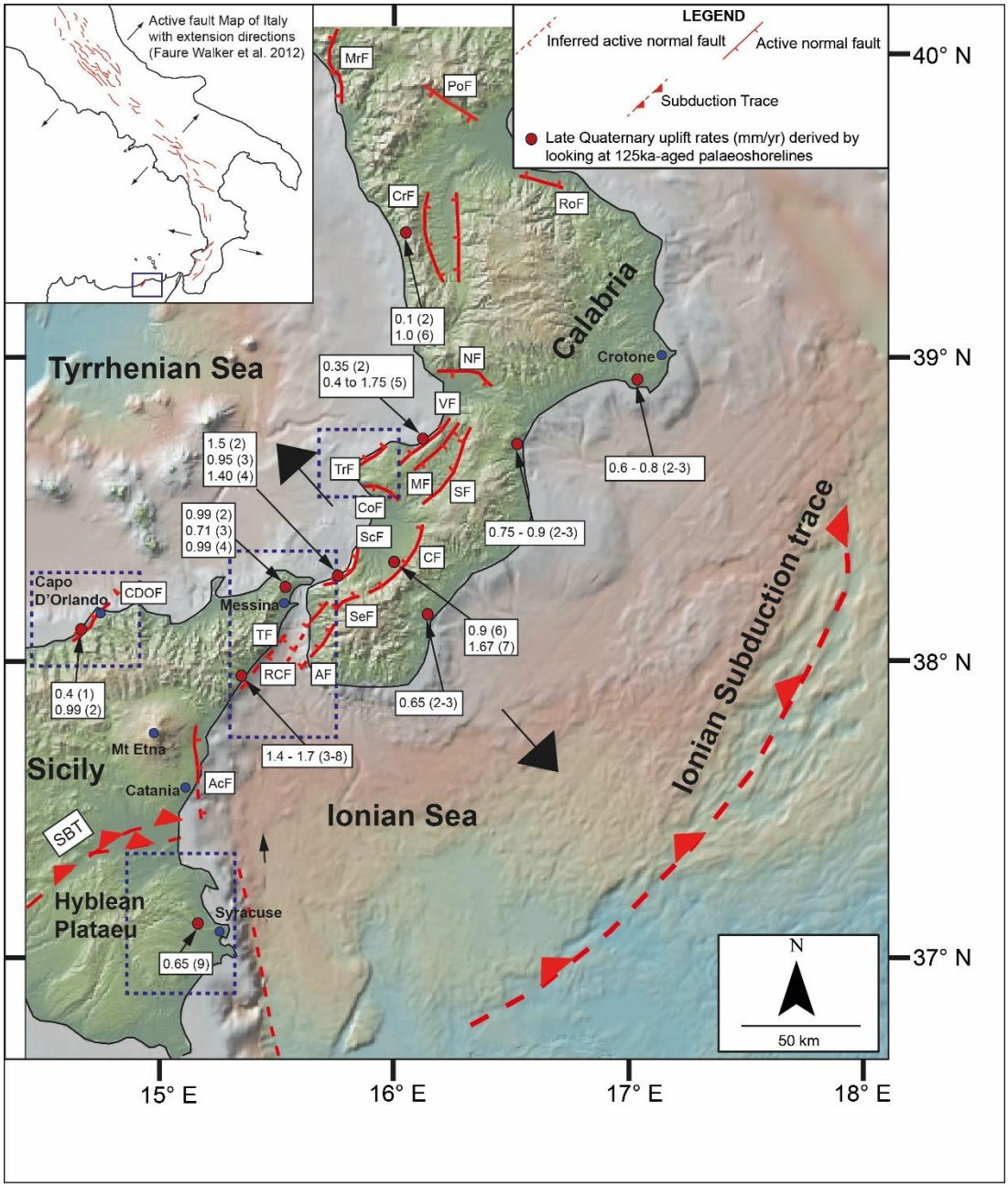

Figure 2.8: *Simplified tectonic sketch showing regions with estimated Late Quaternary uplift rates in mm/yr by various authors, measured over the last 125 ka (dark red dots): 1 Giunta, et al., (2012) and Scicchitano, et al., (2011) – 2 Bordoni & Valensise 1998 – 3 Antonioli, Ferranti, et al. 2006 – 4 Monaco et al. (2014) – 5 Roberts, et al., (2013) – 6 Miyauchi, et al., (1994) – 7 Westway, (1993) – 8 Catalano & De Guidi (2003) – 9 Bianca et al. (1999). Blue squares show investigated area. CDOF: Capo D'Orlando Fault, TF: Taormina Fault, AcF: Acireale Fault, RCF: Reggio Calabria Fault, AF: Armo Fault, CF: Cittanova Fault, SF: Serre Fault, VF: Vibo Fault, TrF: Tropea Fault, CoF: Coccorino Fault, MF: Mileto Fault, RoF: Rossano Fault, CrF: Crati Fault, MrF: Maratea Fault, NF: Nicastro Fault.*

2.5. Age determination for sequences of marine terraces: the synchronous correlation approach

Determination of the ages of palaeoshorelines is a crucial step for any kind of sea-level and uplift modelling aimed at temporally constraining long-term crustal vertical movements. The two commonly-used methods for their modelling, the sequential correlation method and the synchronous correlation method will be reviewed in the following. This thesis has developed the application of the synchronous method, developing both the data input preferences and the calculation since its introduction by Houghton et al. (2003) and Roberts et al. (2009), and strongly advocates its application over that of the sequential correlation approach, which is perhaps more widely accepted at present; this is one of the major achievements of the thesis.

A recurring theme in studies of palaeoshorelines and their associated marine terraces, is the lack of age control from absolute dating (e.g. Lajoie 1986; Bloom 1974; Bosi et al. 1996; Caputo 2007; Giunta et al. 2012; Roberts et al. 2013). This is because material that is suitable for absolute dating can be scarce and hard to find and collect. It is therefore common that age control exists for only a few dated palaeoshorelines within an investigated sequence of marine terraces (Roberts et al. 2009; Roberts et al. 2013). To deal with this problem the traditional approach has been to adopt a "sequential" correlation technique (e.g. Armijo et al. 1996; Bianca et al. 1999; Tortorici et al. 2003; Bianca et al. 2011; Giunta et al. 2012; Gallen et al. 2014). The "sequential" correlation approach has been used to estimate ages by considering one preferred age-constrained palaeoshoreline, that may or may not have an absolute age, and correlating the next higher/lower palaeoshoreline to the next older/younger sea-level highstand "sequentially" (e.g. Armijo et al. 1996; Bianca et al. 2011; Giunta et al. 2012) as shown in Figure 2.9. However, this approach tends to fail because the sea level highstands are not at the same elevation (Roberts *et al.*, 2009; Roberts *et al.*, 2013; Pedoja *et al.*, 2018). For

example, in Table 2.1 it is shown that the 175 ka and 217 ka are -30 m relative to modern sea level whereas the 125 ka, 200 ka and 240 ka are higher, at + 5 m, -5 m and -5 m respectively.

If uplift between for example the 217 ka and 200 ka is less than the difference in sea level elevations (-35 m), sea level rise towards the 200 ka highstand will overwhelm and erode the deposits from the 217 ka (Figure 2.10). So, in regions with low uplift rates, realistically lower than 2 mm/yr which seems a threshold to have all the sea level highstands preserved (more investigations with real data are needed), the sequential correlation approach tends to fail. In other words, if the next and younger sea level highstand, due to a new rise of the sea level, will be higher than the previous one, then the previous marine terrace will be obliterated by a new younger marine terrace with fossiliferous material and reworked shoreline deposits from older and previous palaeoshoreline; this process is well-known as "overprinting problem" (Westaway, 1993; Roberts *et al.*, 2013; Pedoja *et al.*, 2018).

To overcome the afore-explained problems with the "sequential" correlation approach, a so-called "synchronous" correlation method has been proposed and adopted to investigate uplifting processes in Greece and southern Italy (Houghton et al. 2003, Roberts et al. 2009; Roberts et al. 2013). This approach makes use of the fact that sea-level highstands are not perfectly spaced in time, and so for constant uplift rate, resultant flights of palaeoshorelines will not be perfectly spaced in terms of elevation. In fact, for any given uplift rate history, whether constant rate or with changing rates through time, a characteristic signature of vertical spacings between successive palaeoshorelines is produced; this is analogous to the finger-printing technique used to correlate tree-ring records (number of rings; thickness and hence spacing of rings) with records of fluctuating climate promoting rapid or supressed tree growth (personal communication with Gerald Roberts who first described the synchronous correlation approach).

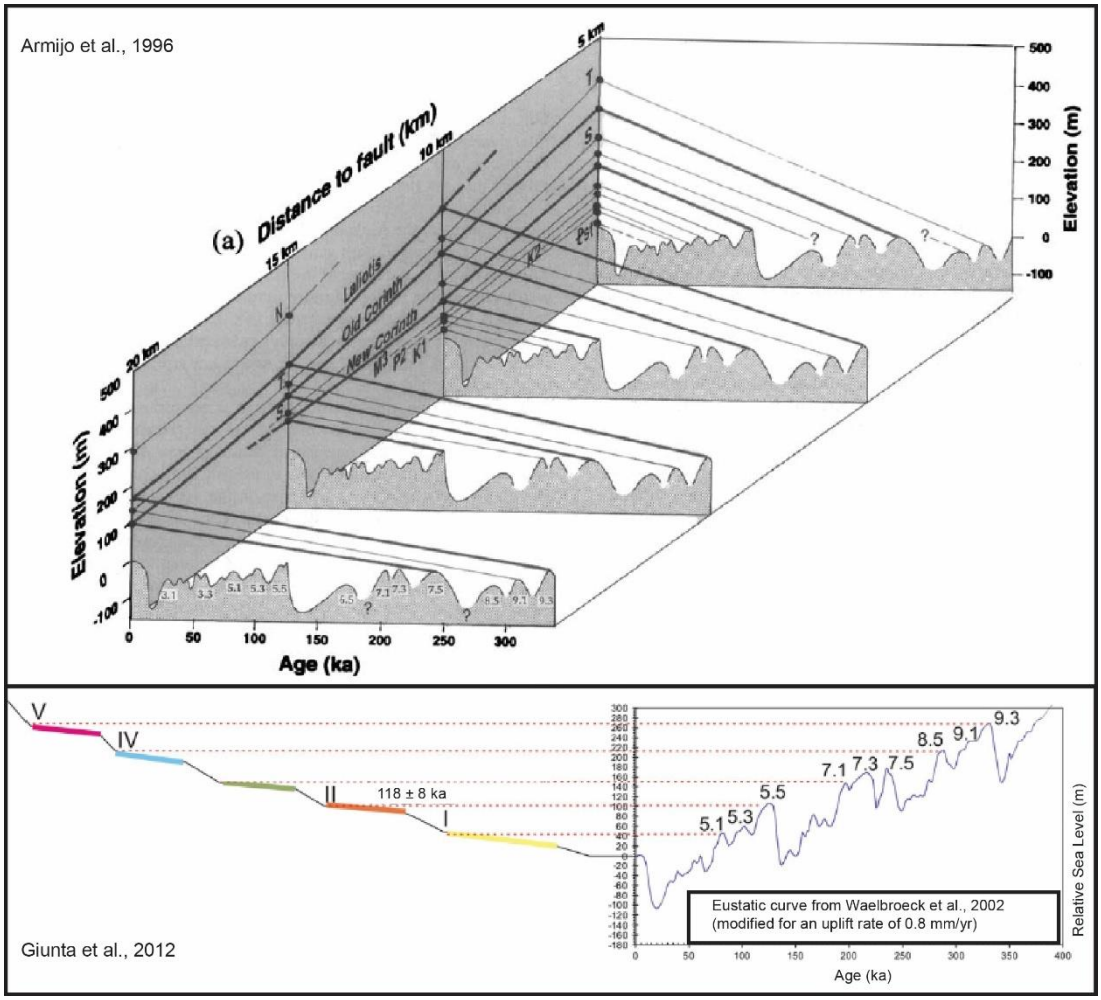

Figure 2.9: *Examples of "sequential correlation approach" by Armijo et al., (1996) and Giunta et al., (2012) modelling a sequence of marine terraces starting from a dated horizon and assume that the next higher and un-dated terrace belongs to the next higher and older sea level highstand.*

Thus, the synchronous correlation approach attempts to compare all mapped palaeoshorelines with predicted sea-level highstands elevations, with the latter calculated iteratively by changing the uplift rate. Modelling should start by considering only constant uplift rate scenarios, which are the simplest scenarios, progressing to more complex varying uplift rate through time scenarios only when a satisfactory fit to the observed palaeoshoreline elevation cannot be found. Satisfaction with the model results is verified through linear regressions between observed and predicted palaeoshoreline elevations, with R^2 values quantifying the goodness of fit (Roberts *et al.*, 2009; Roberts *et al.*, 2013; Pedoja *et al.*, 2018).

By using a "Terrace Age Calculator" excel spreadsheet (see Methods for more details), the synchronous correlation method allows estimation of ages for un-dated palaeoshorelines iteratively calculating uplift rates to find the best match between palaeoshoreline elevations mapped on Digital Elevation Models using GIS software, ground truthing their real presence in the field, and predicted highstand elevations given an initially constant uplift rate driven by age controls using known sea-level curves.

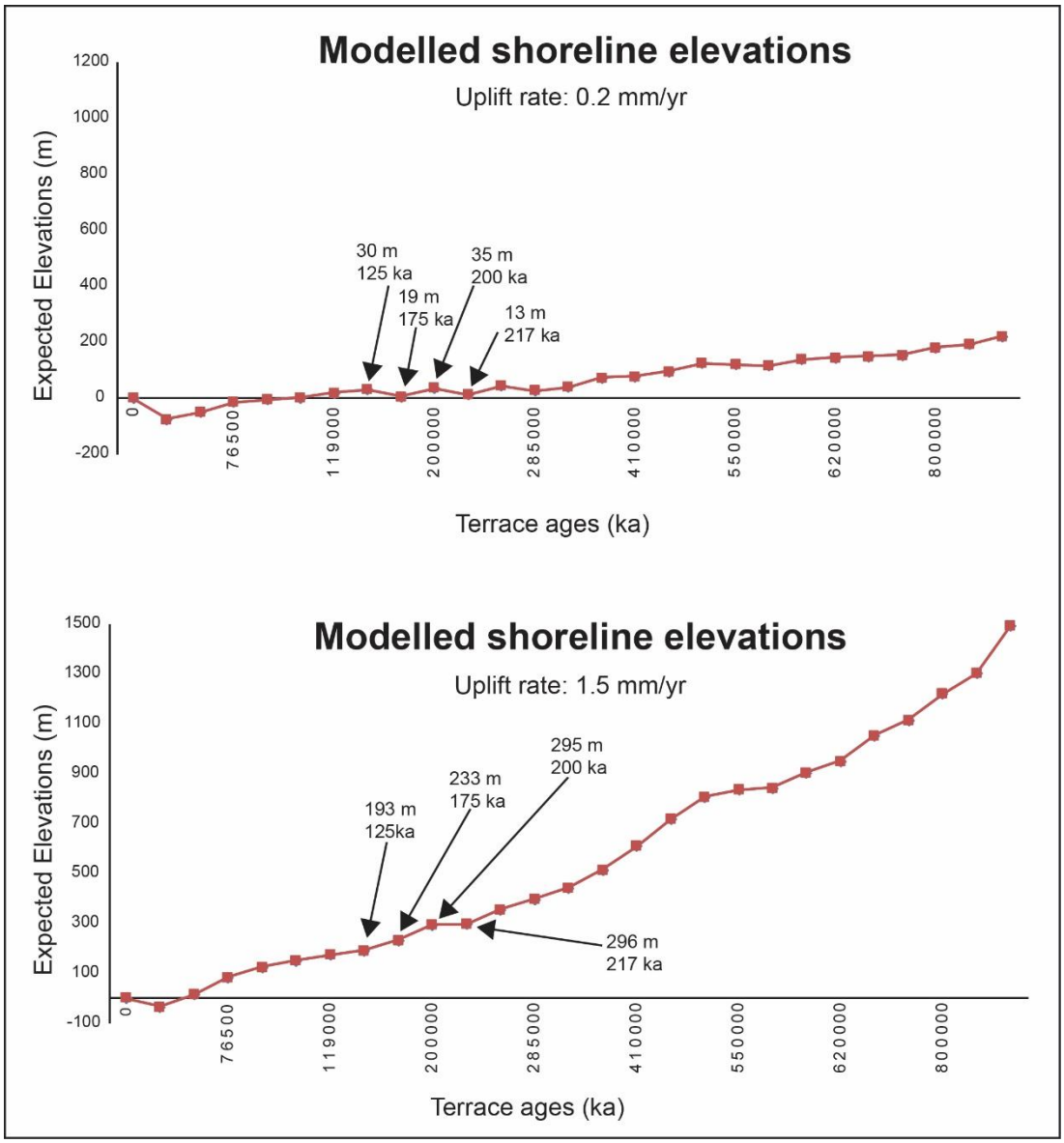

Figure 2.10: *Examples of modelled (or expected) shoreline elevations showing two different uplift rate scenarios. The top graph shows that the 175 ka and 217 ka palaeoshorelines will be eroded by the 125 ka and the 200 ka palaeoshorelines if an uplift rate of 0.2 mm/yr is mapped. The bottom graph shows that an uplift rate of 1.5 mm/yr is needed for the preservation of the 175 ka and 217 ka palaeoshorelines.*

In practise, the calculator should be applied to serial topographic profiles along the strike of the investigated area to investigate spatial variation and/or continuity, forcing the user to consider all the palaeoshoreline locations in a region at the same time (synchronously) (Roberts *et al.*, 2009; Roberts *et al.*, 2013). The input data to the "Terrace Age Calculator" are values for the elevations of mapped palaeoshorelines, best presented on an annotated topographic profile across the strike of the marine terrace sequence, and the palaeo-elevations of sea-level highstand taken from sea-level curves; in this thesis, sea-level curves by Siddall et al., (2003) and Rohling et al., (2014) have been used spanning the last 1 Myrs (Table 2.1 and Appendix 2). With these inputs, the user simply iterates the uplift rate to identify the best fit of predicted palaeoshoreline elevations to observed palaeoshoreline elevations; the characteristic signature of vertical spacings between successive palaeoshorelines for the actual uplift scenario mentioned above.

In this thesis, sequences of marine terraces have been mapped and modelled by using a synchronous correlations approach to derive and refine improved crustal vertical movements driven by new absolute age controls.

2.6. Seismic Hazard Calculations in Italy using fault slip-rates, earthquake recurrence interval (T_{mean}) and Coefficient of Variation (CV) parameters

One of the reasons for constraining uplift rates from sequences of uplifted palaeoshorelines is that it may be possible to convert uplift-rates to fault slip-rates, a parameter is being increasingly used in seismic hazard assessments (e.g. Roberts *et al.*, 2004; Pace *et al.*, 2006; Papanikolaou and Roberts, 2007; Peruzza, Pace and Cavallini, 2010; Cowie *et al.*, 2012; Papanikolaou *et al.*, 2013; Deligiannakis, Papanikolaou and Roberts, 2018). This approach

utilises the fact that there will be an inverse relationship between the slip-rate on a fault and the recurrence interval for a given earthquake magnitude; recurrence may be difficult to measure with slip-rate more accessible, so this provides a pragmatic way to estimate recurrence. The relationship between uplift-rates and faults slip-rates, and how the latter is used in seismic hazard assessments will be reviewed in this section.

The reason that fault slip-rates are being increasingly used in seismic hazard assessments is that some authors (e.g. Pace 2006; Cowie et al. 2012) showed that historical seismicity catalogues provide insufficient information for analysis of seismic hazard mapping if time dependency is required. This is because historical records are generally too short (a few hundred years at most for the interval of completeness for given magnitudes of interest) compared to the recurrence intervals of large magnitude damaging earthquakes (e.g. >Mw 5.8) on specific active faults (10^3 - 10^5 years; Pace *et al.*, 2006). This means that some active faults will not have ruptured in historical times, so they will be missed off maps of potential seismic sources, and it will not be possible to constrain the earthquake recurrence intervals for the large, damaging events of interest. This is particularly important for relatively low slip-rate normal faults such as those in the area investigated herein, where some active faults have not experienced faulting rupture within the historical time due to low fault slip rates (lower than 1mm/yr) (Roberts *et al.*, 2002; Pace *et al.*, 2006, Meschis et al. 2018). Slip rates on faults, and Earthquake Recurrence Interval (or T_{mean}) which is defined as the inter-seismic event time, are crucial to better investigate the seismic hazard of a region (Cowie *et al.*, 2012). The slip rate on fault is defined as the value of slip on a fault averaged over time. Empirical relationships allow the estimation of T_{mean} from the knowledge of crucial parameters such as the length of fault rupture, the associated potential maximum earthquake magnitude, the co-seismic maximum

displacement expected for that magnitude (Wells and Coppersmith, 1994). In other words, the amount of slip in a given time interval can be divided by the slip expected in a damaging earthquake (or magnitude range) to define expected earthquake recurrence intervals. A complication exists in that fault slip-rates obtained by different investigations spanning different timescales (for instance, geological $10^{4\text{-}6}$ years, palaeoseismological $10^{2\text{-}3}$ years and geodetic measurements of slip-rates 10-10^2 years) show incongruities through time (e.g. Friedrich et al. 2003; Oskin et al. 2008; Cowgill et al. 2009) due to temporal earthquake clustering and temporal slip-rate changes. Nevertheless, historical catalogues of earthquakes as well as GPS and palaeoseismic investigations provide an incomplete understanding because they span a limited temporal window (10 to 10^3 years) which is, in general, much shorter than an earthquake cycle (Papanikolaou et al. 2005; Visini et al. 2009; Roberts et al. 2013). The integrating of the afore-mentioned investigations with longer timescale deformation rates, such as those since the Middle Pleistocene, using tectonically-deformed sequences of marine terraces (Roberts et al. 2009; Roberts et al. 2013), is a key step in order to attain more temporally constrained factors useful to better describe seismic hazard due to upper crustal deformation (Visini *et al.*, 2009). To gain data providing long earthquakes sequences on active faults is crucial to define T_{mean} and their temporal variability which represents a critical step for calculating earthquake probabilities (Visini and Pace, 2014). Robust temporally-constrained long term fault slip rates provide the baseline to better outline the T_{mean} on active faults allowing one to better define the CV value, which is an important parameter for seismic hazard calculations, describing the variability of T_{mean} defined by the ratio between Standard Deviation of T_{mean} and the T_{mean} itself for a sequence of earthquakes (Cowie *et al.*, 2012; Pace, Bocchini and Boncio, 2014; Visini and Pace, 2014). However, past studies (Ellsworth *et al.*,

1999) show that CV values are poorly-constrained for recurrence of earthquakes showing that slight differences in the CV values can lead to significant differences in earthquake probability forecasts (Cowie *et al.*, 2012; Visini and Pace, 2014). A further complication is that, associated with this latter point of CV, Cowie et al., (2012) have proposed and defined another important parameter, which takes into account the magnitude and the temporal ordering of single slip events (see Fig. 1 from Cowie et al., 2012 for more details), termed "slip rate variability" (SRV), defined by the ratio between standard deviation of short-term slip rates over a sliding time window of fixed length and SR_{mean} which is the long-term average slip rate. Together, CV and SRV values allow the exploration of how elastic interaction influences the temporal and spatial variability in fault slip rates and recurrence of earthquakes (Cowie *et al.*, 2012).

A summary of how faults are used to map seismic hazard is as follows. Seismically-active fault scarps are the result of several earthquakes occurred through time deforming Middle Pleistocene deposits (Papanikolaou and Roberts, 2007; Yeats, 2012; Chapman *et al.*, 2014). It is crucial to constrain all active faults in order to identify all possible seismic sources (Papanikolaou and Roberts, 2007). To do that, fault lengths have to be measured by field mapping: (i) deriving fault slip direction (Roberts, 1996; Roberts and Ganas, 2000; Papanikolaou and Roberts, 2007), (ii) observing geomorphic offsets such as marine terraces (Roberts *et al.*, 2013; Meschis *et al.*, 2018) and palaeoseismological studies. Furthermore, geological cross-sections derived from published geological maps and topographic analysis are critical steps. Moreover, throw-rate values through time are gained and alongside throws profile and fault lengths, throw-length profiles can be derived spanning a given temporal window (Papanikolaou and Roberts, 2007). This allows the conversion of throw rate profiles into frequency of earthquakes, assuming an earthquake surface rupture and a triangular throw

profile for the faults (Cowie and Shipton, 1998; Papanikolaou and Roberts, 2007). Building on this approach temporal variations in earthquake recurrence are now being included. For example around the world, time-dependence and new fault-based probabilistic seismic hazard analysis and earthquake rupture forecast methods have been suggested including tectonically-active regions showing low strain-rates (Pace *et al.*, 2006; Akinci, Malagnini and Sabetta, 2010; Peruzza, Pace and Cavallini, 2010). Prominent parameters within these models are the: (i) elapsed time since the last seismic event (T_{elap}) has occurred and (ii) the effects triggered by stress changes of earthquakes on neighbouring faults (Pace, Bocchini and Boncio, 2014). These, alongside earthquake probabilities and previously described parameters, such as slip rates on faults, CV value, T_{mean}, elapsed time are related by:

$$P(t) = \sqrt{\frac{T_{\text{mean}}}{2\pi\alpha^2 t^3}} e^{-\frac{(t-T_{\text{mean}})^2}{2T_{\text{mean}}\alpha^2 t}}$$

$$P(T_{\text{elap}} \leqslant T \leqslant T_{\text{elap}} + \Delta T | T > T_{\text{elap}}) = \frac{P(T_{\text{elap}} \leqslant T \leqslant T_{\text{elap}} + \Delta T)}{1 - P(0 \leqslant T \leqslant T_{elap})}$$

presented by Pace et al., (2014) to calculate the conditional probability (P(t)) of occurrence of a seismic event for each fault by Brownian passage-time distributions. Furthermore, they calculated the conditional probability (*P*) of having an event in the next 50 years. They also pointed out that this approach provides important insights into local seismic hazard defining priority areas for monitoring. Additionally, Pace et al (2014), following Stein, (1999), has quantified how to include the effects of stress transfer into seismic hazard assessments. This approach also showed that a relationship between positive Coulomb Stress changes (dCFF) and expected PGA (Peak Ground Acceleration by USGS definition) could increase the

expected seismic hazard of investigated areas (Pace, Bocchini and Boncio, 2014). Indeed, the effect of dCFF on the probability of the maximum expected earthquake, and on the T_{mean} can be approached by applying the following equation:

$$T^{1}_{mean} = T_{mean} - (dCFF/\tau),$$

where τ is the rate of shear stress accumulation on the fault, and the Coulomb Stress change (dCFF) is considered equivalent to a modification of T_{mean} (Pace, Bocchini and Boncio, 2014). Furthermore, a positive relationship between dCFF and the time advance or delay to the next earthquake has been discussed (Wedmore *et al.*, 2017)

In this thesis, emphasis is placed on gaining the long term slip rates on faults by studying tectonically-deformed palaeoshorelines over a time period long enough to cancel out earthquake clustering which can lead to misleading interpretations concerning deformation rates; associated earthquake recurrence intervals (T_{mean}) have been calculated to improve understanding of: (i) the geography of seismic hazard in the seismically-deforming upper plate, and (ii) the subduction slip distribution taking into account deformation on the upper plate.

2.7. Normal faulting activity

Since the Pliocene-Pleistocene the geological domain of the Calabrian Arc has been affected by active extensional processes causing the formation of syn-rift basins bordered by active normal faults (Malinverno and Ryan, 1986; Monaco and Tortorici, 2000). Details of the extension will be reviewed below.

Plate tectonic movements produce stress which accumulates in the Earth ‘s crust until the failure point producing earthquakes. Along the Calabrian Arc, active crustal extensional processes are accommodated by normal faulting activity producing devastating earthquakes

such as the 1783 earthquake sequences between Cittanova Fault and Serre Fault (Jacques *et al.*, 2001; Galli and Bosi, 2002; Galli, Galadini and Pantosti, 2008), the 1905 Vibo Valentia earthquake (Jacques et al. 2001; Roberts et al. 2013), the 1908 Messina Strait earthquake (Baratta, 1910; Valensise and Pantosti, 1992; Monaco and Tortorici, 2000; Aloisi *et al.*, 2013) (Figure 2.11).

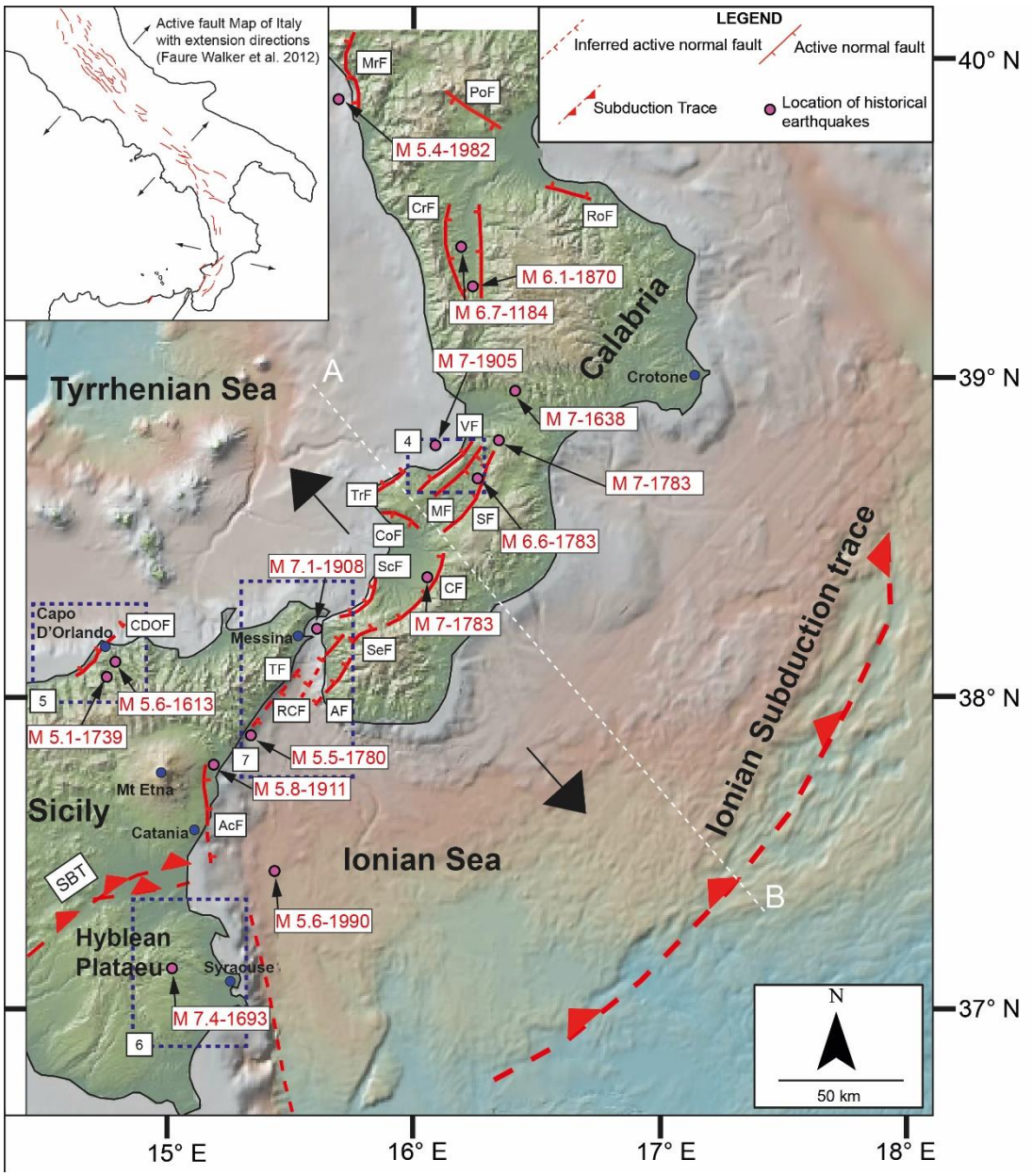

Figure 2.11: *Historical earthquake locations occurred along the Calabrian Arc. Note that the 1693 earthquake (M 7.4), SE Sicily, is perhaps related to a fault thrusting activity produced by the SBT. Data from Basili et al., (2008) and Stucchi et al., (2013).*

Previous studies (Walsh and Watterson, 1991; Roberts and Yielding, 1994) showed that active normal faults generating surface ruptures, produced by medium-large earthquakes with Mw > 6.0 or greater, displayed enough down-dip width to rupture the entire 15-km seismogenic layer associated with strike-length of 20-40 km (Molnar and Chen, 1983; Jackson and White, 1989). The slip on normal faults produces vertical movements such as uplift in the footwall and subsidence in the hangingwall, with associated tilting, producing an area affected by crustal deformation whose effect proportionally decreases with distance from the fault itself (Jackson and White, 1989) (Figure 2.12). These vertical motions, which can be geodetically measurable (Stein and Barrientos, 1985), are thought to be as the result of two temporal phases: (i) an immediate crustal deformation caused by co-seismic movements with an associated footwall uplift to hangingwall subsidence ratio of around 1:5 and 1:7 (Stein and Barrientos, 1985; Galli, Giaccio and Messina, 2010), followed by (ii) a long-term rearrangement phase probably due to the elastic rebound and viscoelastic relaxation at depth (Stein and Barrientos, 1985; King, Stein and Rundle, 1988) with an associated change in the finite ratios to around 1:3 and 1:4 (Armijo *et al.*, 1996; McNeill and Collier, 2004; Kent *et al.*, 2016). Unfortunately, this picture is complicated by the fact that shallow afterslip in the fault zone itself can contribute to the deformation that is also at least partly attributable to viscoelastic relaxation in the lower crust and mantle, and it is not trivial to separate the effects of these different processes (e.g. compare Wilkinson *et al.*, (2010) with D'Agostino *et al.*, (2012) for the 2009 Mw 6.3 L'Aquila normal faulting earthquake in central Italy). There is also some evidence that the ratio between coseismic slip and postseismic slip may not be constant for all earthquakes, for example compare the doubling of slip across the 2009 L'Aquila ruptures when the postseismic slip is added to the coseismic slip (Wilkinson et al. 2010) with the almost complete

lack of postseismic slip reported for the 30th October 2016 Mw 6.5 Mt. Vettore earthquake (see Ferrario and Livio, 2018). Thus, it is unclear whether the footwall uplift to hangingwall subsidence ratio of around 1:5 and 1:7 is always degraded to 1:3 and 1:4 through time. If this ratio could be better defined, it could be used to estimate slip rate on faults from measurements of footwall uplift to better describe the normal faulting history; this thesis attempts to do this using observation of deformed palaeoshorelines.

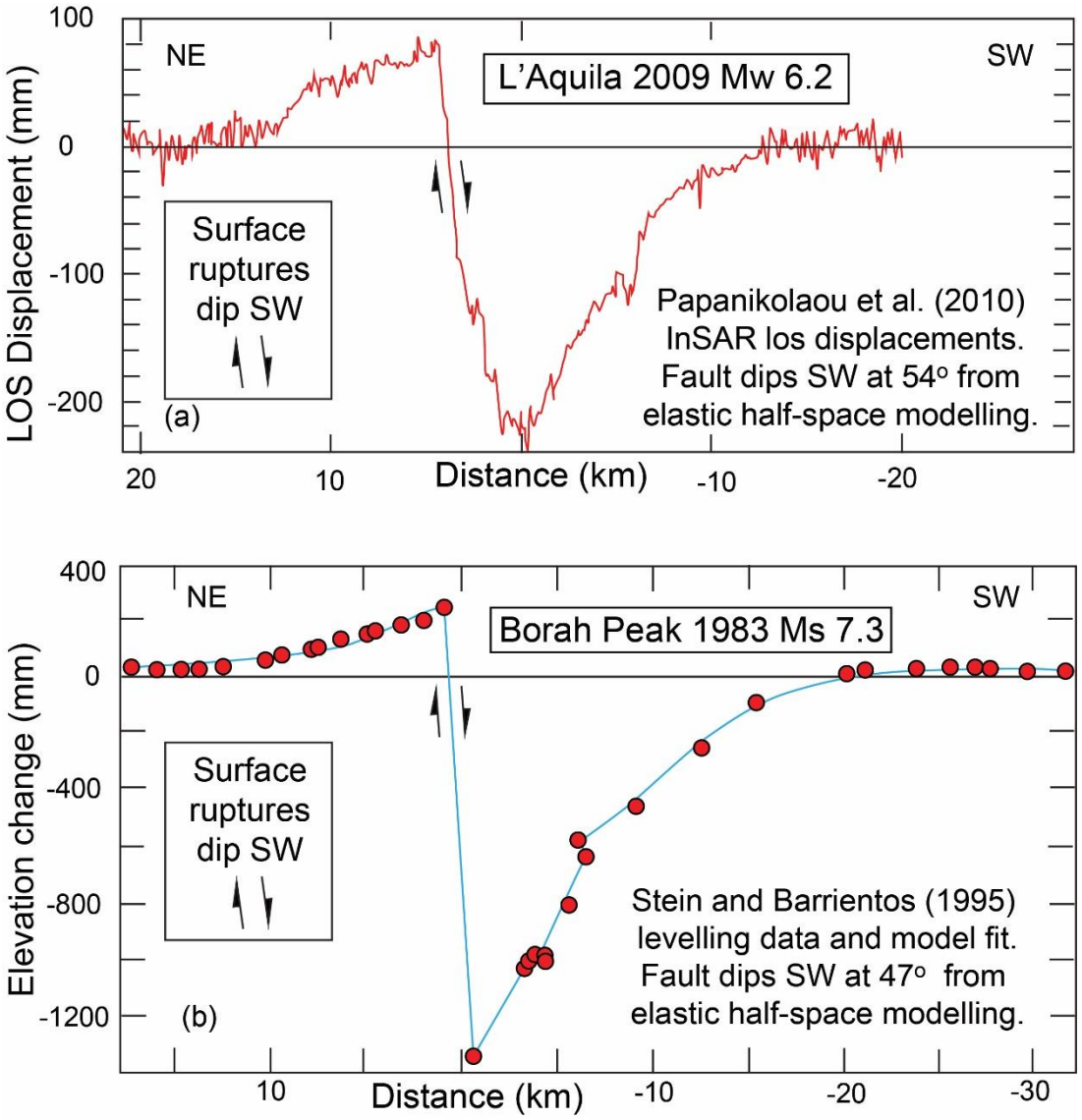

Figure 2.12: *Co-seismic geodetic-based vertical movements measured during the normal faulting-related 2009 l'Aquila earthquake (Mw 6.2) on top (Papanikolaou et al., 2010) and 1983 Borah Peak earthquake (Ms 7.3) on bottom (Stein and Barrientos, 1985).*

Ground displacements, produced by normal faulting activity, can be investigated immediately after earthquakes using geodetic techniques such as GPS and SAR interferometry (InSAR) (e.g. Stramondo et al. 1999) to derive short-term crustal deformation (Figure 2.12). More particularly, InSAR investigations can explore co-seismic and post-seismic ground displacements detected by using satellites with well-known temporal regular intervals obtaining times series images during and after earthquakes occurring without an advance knowledge of an earthquake's location. Figure 2.12 shows measured co-seismic tectonic subsidence of the hangingwall and co-seismic tectonic uplift of the footwall consistent with the ratio mentioned in the previous paragraph. The second phase can also be monitored geodetically, but as the postseismic period can last years to decades (Ingleby and Wright, 2017) there are few dataset of this kind. Therefore this thesis takes a pragmatic approach and uses the long-term signal recorded by tectonically-deformed marine terraces (Roberts et al. 2013), geomorphological features, for instance, such as footwall relief (Kent *et al.*, 2016; Roda-Boluda and Whittaker, 2017) and longitude river profiles (Whittaker and Boulton, 2012; Roda-Boluda and Whittaker, 2017); this long-term signal will contain both coseismic and postseismic effects from hundreds to thousands of earthquake, but it may be that this is the only realistic way to study uplift and subsidence related to faulting given the uncertainties in annual, decadal and centennial timescale postseismic deformation.

Active extension produces crustal thinning accommodated by normal faulting activity associated with moderate/large earthquakes, for instance, such as the 1905 Vibo earthquake (Mw 7) and 1908 Messina earthquake (Mw 7.1) in the Calabrian Arc (Faure Walker *et al.*, 2012; Roberts *et al.*, 2013). This seismically-related crustal extension process produces elongated normal fault-bounded sedimentary basins, so-called syn-rift basins, defined by

normal faults systems which characterise active extension regions (Burchfiel, 1980; Neumann and Ramberg, 2012) exist in several regions around the world such as the Basin and Range Province in Nevada (e.g. Bennett et al. 2003), the East African Rift (e.g. Morley et al. 1990), the Gulf of Corinth (e.g. Roberts et al. 2009) and central/southern Italy (e.g. Roberts and Michetti, 2004; Papanikolaou and Roberts, 2007; Roberts *et al.*, 2013). Individual earthquake segments within these fault systems are geometrically defined by the length of surface rupture (L) and the down-dip Width (W) as shown in Figure 2.13. Furthermore, it has been observed that displacement amount (d) is proportional to the surface rupture length (L) as d = f(L) (Figure 2.14) with f lying within a range of 0,001 < d=f(L) <0.1 (e.g. Cowie & Scholz 1992; Cowie & Roberts 2001). Moreover, Wells & Coppersmith, (1994) and Loreto et al. (2013) show that surface rupture length (L) is positively related to the magnitude of an earthquake if the entire investigated fault length is seismically ruptured. For instance, a Mw 6 earthquake can be produced by a 15-20 km long fault which have ruptured along its entire length (Figure 2.15a), producing a maximum surface displacement of 10-20 cm (Figure 2.15b).

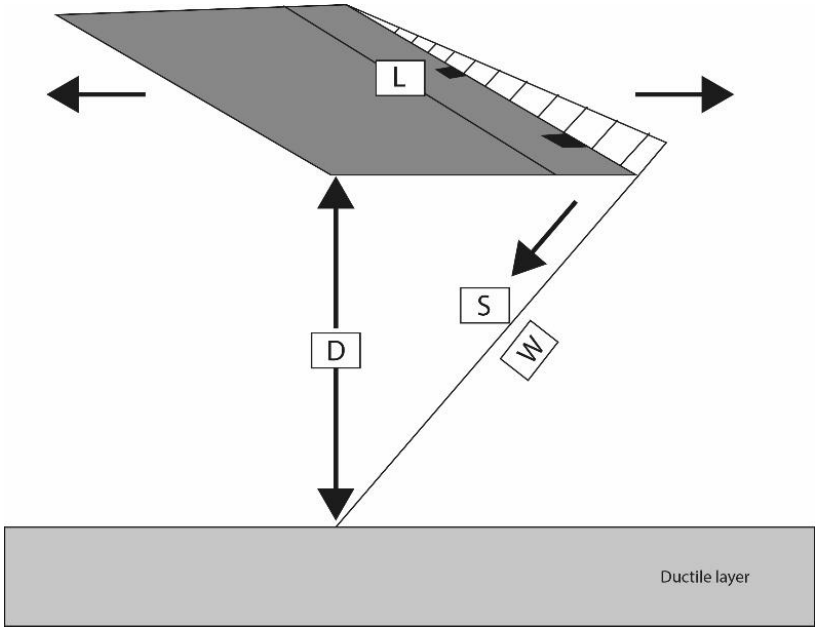

Figure 2.13: *Simplified picture from Pace et al., (2014) showing prominent geometric features of a normal fault. L= Half-length of faulting surface rupture, D= Depth of seismogenic layer (around 15 km), W= Down-Dip Width and S= the slip direction of fault.*

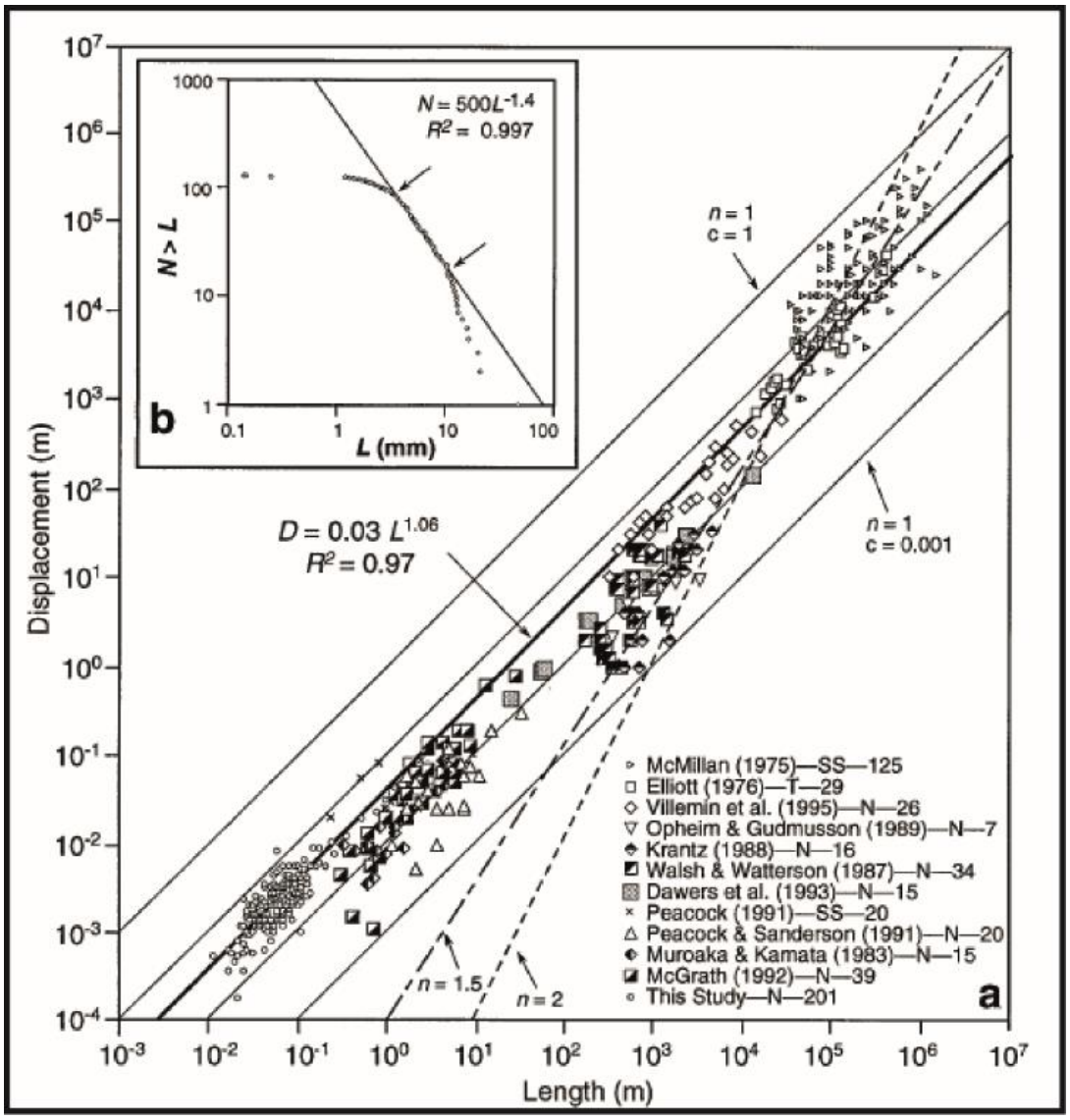

Figure 2.14: *Graph from Schlische et al. (1996) with X-Y logarithmic axis plotting displacement (d) against length (L) values for several published fault dataset. Sources of data are indicated showing the type of fault. (T= Thrust fault, N= Normal fault and SS= strike-slip fault) and the number of data.*

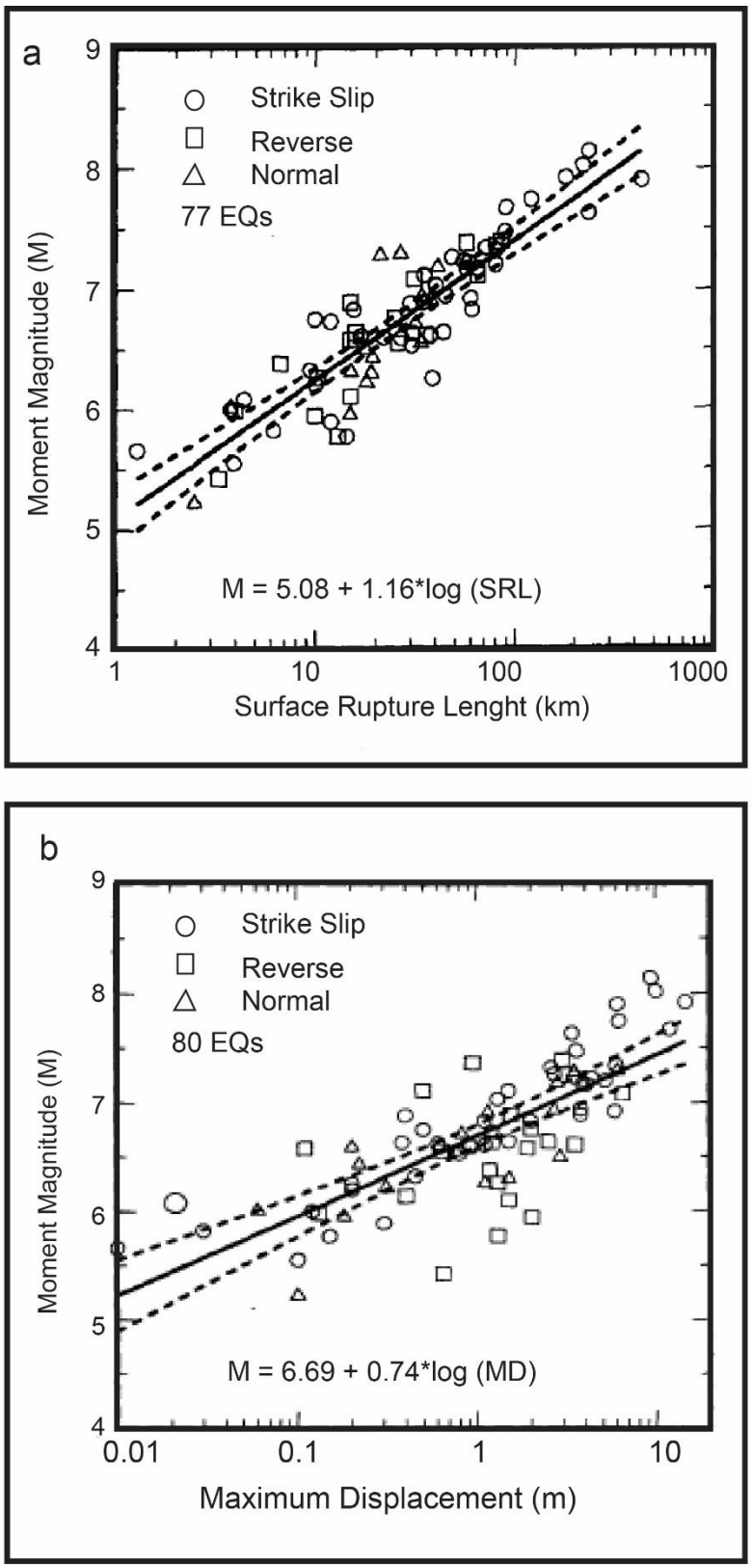

Figure 2.15: *Graphs from Wells and Coppersmith, (1994) showing: (i) the relationship between the fault length that can be ruptured during an earthquake and the associated possible produced magnitude (a) and (ii) the relationship between the magnitude of an earthquake and the maximum surface displacement produced by the associated earthquake (b).*

Seismically-active crustal extension accommodated by normal fault systems, between tectonic plate boundaries, needs to accommodate regional deformation rates (e.g. Roberts et al. 2002). This implies that summed deformation rates (slip rates on faults) across all the involved fault segments: (i) will equal the regional deformation rates associated with the plate motions and (ii) will be temporally constant if all the same number of faults remains active through the time (Roberts *et al.*, 2002). However, it also has been demonstrated that slip rates on faults can change through time within normal fault systems (Cowie and Roberts, 2001; Roberts *et al.*, 2002; Roberts and Michetti, 2004; Roberts *et al.*, 2009) (Figure 2.16).

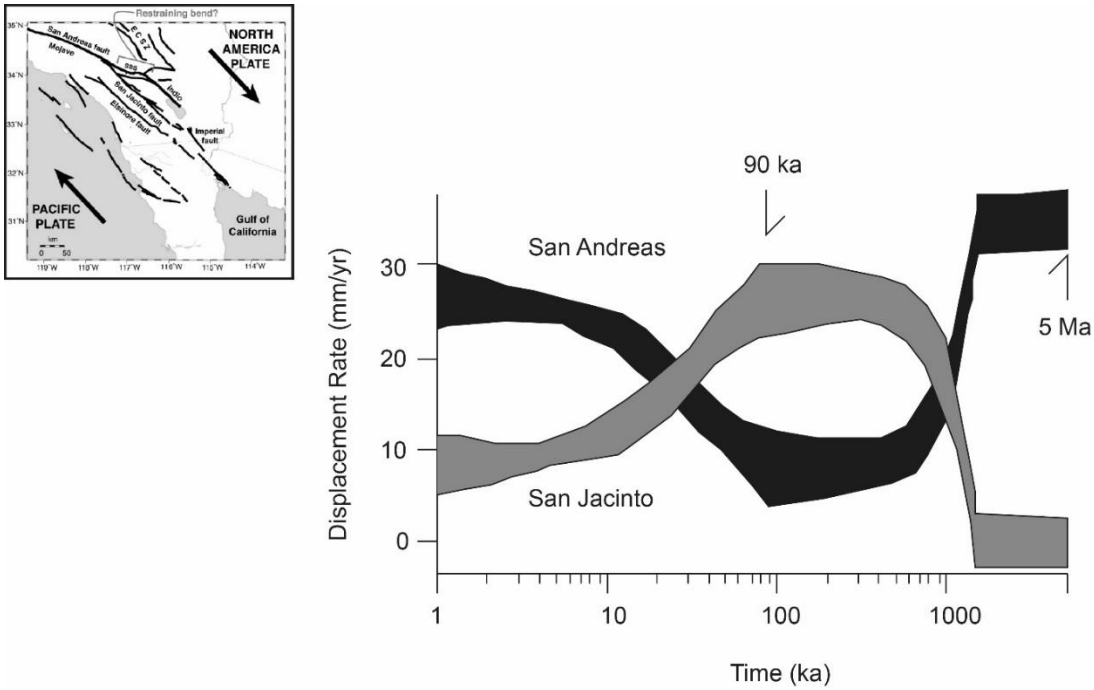

Figure 2.16: *Bennett et al. (2004) show that ~70% of the total plate motion, between Pacific and North America Plates, has been partitioned between the San Jacinto and the southernmost part of San Andreas fault transferring around 35mm/yr from Imperial Fault to Mojave fault segment. However, this example is related to a strike-slip faults system.*

This implies that deformation rates increase on faults active upon those inactive (Dawers and Underhill, 2000; Roberts *et al.*, 2002; Bennett, Friedrich and Furlong, 2004; McLeod, Dawers and Underhill, 2008). For instance, normal fault slip rates within syn-rift basins can increase up to a factor 3 derived by studying deformed palaeoshorelines temporally constraining the normal faulting history over the Late Quaternary (Roberts *et al.*, 2009). Similarly, tectonically-

deformed sequences of marine terraces show constant slip rates on normal faults over the Middle Pleistocene (Roberts et al. 2013), temporally constraining faulting activity allowing a better approach to long term seismic hazard analysis.

In this study, large normal faults have been investigated through tectonically-deformed sequences of palaeoshorelines allowing the estimation of long-term constant and/or fluctuating fault slip rates through time.

2.7.1. Co-seismic uplift/subsidence scenarios for the 1908 Messina Earthquake modelled by using Coulomb 3.3 software

Another aspect of normal faulting that should be considered is how deformation of the Earth's surface produced by a single earthquake relates to longer-term deformation through repeated earthquakes; this section reviews this topic. Geodetic investigations have utilised levelling data, Global Positioning System (GPS) and INSAR data to derive new insights into deformation of the Earth's surface produced by single earthquakes (Stein and Barrientos, 1985; Valensise and Pantosti, 1992; Massonnet and Feigl, 1995; Jackson, 2001; Papanikolaou *et al.*, 2010; Aloisi *et al.*, 2013). The aim has been to: (i) constrain the nature of co-seismic ground displacements close to active faults, and (ii) how these faults slip and affect the landscape through repeated earthquakes.

Of particular relevance to this thesis is that coseismic vertical motions have also been measured after the damaging Mw 7.1 1908 seismic event that occurred in the Messina Strait. In particular, benchmark elevations were mapped 1 yr before, and immediately after the above earthquake, documenting down-throw of the Messina Strait and coastal uplift (Loperfido, 1909; Valensise and Pantosti, 1992; Aloisi *et al.*, 2013). Inversion of these levelling data have

been performed, showing possible different seismogenic sources (Schick, 1977; Mulargia and Boschi, 1983; Ghisetti, 1984; Bottari *et al.*, 1986; Valensise, 1988; Boschi, Pantosti and Valensise, 1989; Aloisi *et al.*, 2013) all in agreement with dominant normal faulting on planes oriented nearly parallel to the Messina Strait (Aloisi *et al.*, 2013). However, dip direction and dip angle of the seismogenic source for the 1908 Messina earthquake is still debated.

Later in this thesis (Chapter 8), vertical ground motions for the Messina earthquake are modelled using an elastic half-space model provided by the Coulomb 3.3 software (Toda *et al.*, 2011) to better understand and define the geometry of the possible seismogenic source for the 1908 Messina earthquake within the Messina Strait. In particular, vertical displacements have been modelled to find the best match between the levelling data by Loperfido, (1909), where benchmarks has been measured before and after the earthquake, and modelled co-seismic uplift/subsidence scenarios. The relationship between the coseismic vertical motions and the faulting model revealed by the Coulomb modelling are discussed in terms of the longer-term vertical motions revealed by mapping of deformed late-Quaternary palaeoshorelines. This discussion is used to help conclude on how the Quaternary deformation can be used to place constraints on the likely patterns of future coseismic deformation that may occur.

Chapter 3: Methods and approach

This chapter presents methodologies used to investigate tectonically-deformed marine terraces in this thesis. In particular, the approach used in this thesis involves: (i) fieldwork to examine the nature and elevations of palaeoshorelines and their associated marine terraces (Section 3.1), (ii) detailed geormophological analysis using 2 m and 10 m high resolution DEMs to collect palaeoshoreline elevations (Section 3.1), (iii) an attempt to gain absolute age control on terrace deposits associated with palaeoshorelines using $^{234}U/^{230}Th$ dating on corals (Section 3.2), (iv) an attempt to gain absolute age control on wave-cut platforms associated with palaeoshorelines using *in situ* ^{36}Cl cosmogenic exposure dating on wave-cut platforms cut into limestones (Section 3.3), (v) a synchronous correlation approach to investigate how sequences of uplifted marine terraces relate to the Quaternary sea-level curve (Section 3.4), and (vi) elastic half-space modelling in an attempt to replicate measured geodetic vertical motions for the 1908 Mw 7.1 Messina earthquake (Section 3.5). Each of these six methods are explained in detail in the following sections. More details on coral dating, *in situ* ^{36}Cl cosmogenic exposure dating on WCPs and the "terrace calculator" in Excel format are shown in the Appendix 3.1 and 3.2. Locations of investigated marine terraces with sample locations for *in situ* ^{36}Cl cosmogenic exposure dating and $^{234}U/^{230}Th$ dating on corals are shown in Figure 3.1.

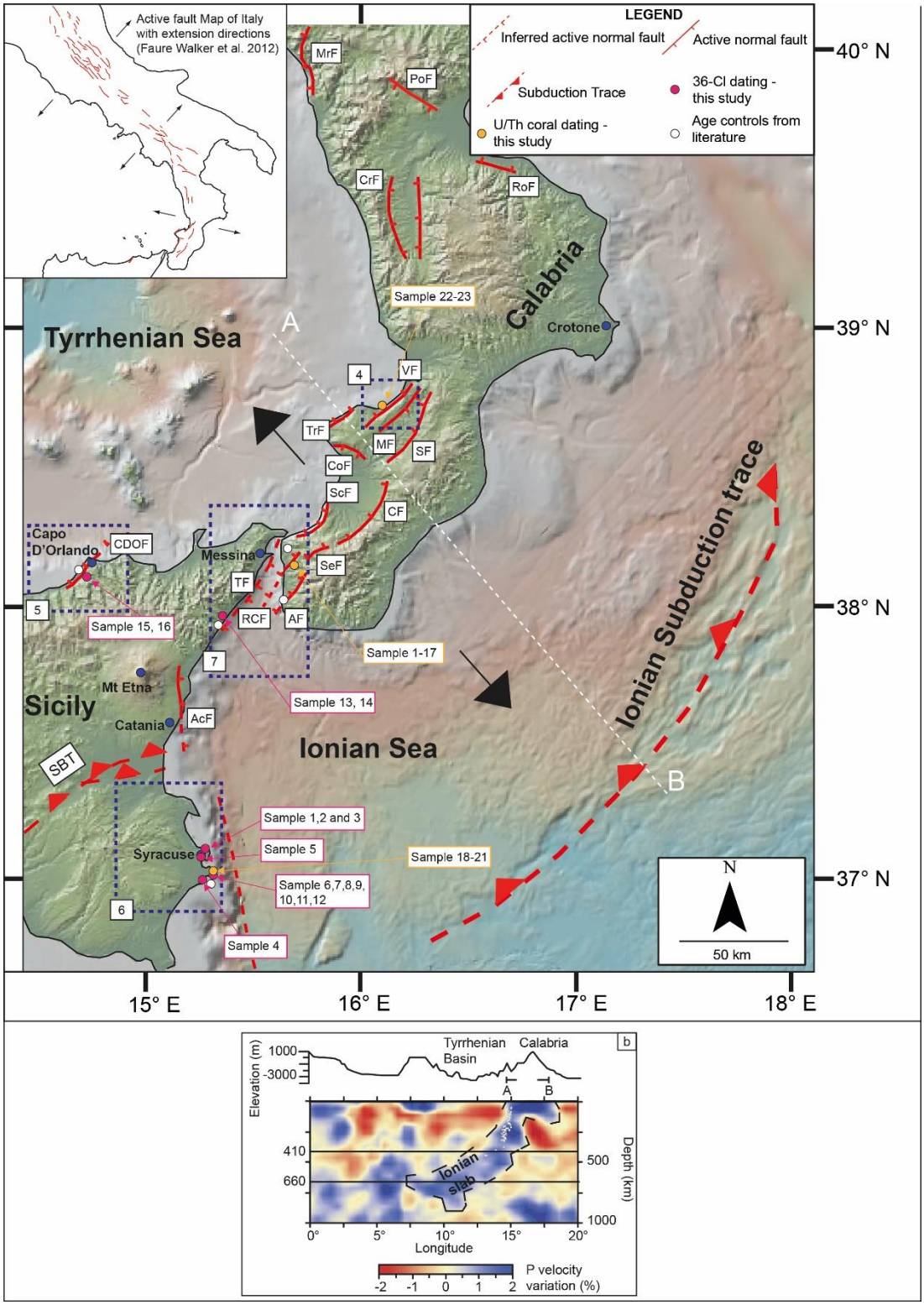

Figure 3.1: *Map showing locations of age controls. Orange dots show locations where corals have been mapped and collected for $^{234}U/^{230}Th$ dating. Pink dots show locations where WCPs have been sampled for ^{36}Cl cosmogenic dating. White dots show locations of well-known age controls from literature. Dashed blue square are the investigated regions and the number is referred to the chapter.*

3.1. Palaeoshoreline elevation data: DEM-based topographic analysis and fieldwork

The key data that this thesis investigates is the presence of flights of palaeoshorelines and their associated marine terraces and wave-cut platforms, because their deformation constrains the fault activity over the Late Quaternary. Thus, the basis of the thesis is underpinned by mapping in the field supported by mapping on DEMs. In particular this has involved topographic analysis using 2 m and 10 m high resolution Digitial Elevation Models (DEMs) (Tarquini *et al.*, 2012), constructing a number of topographic profiles along each active structure identified in the literature and in the field, such as the NE-SW oriented Vibo Fault (Chapter 4) the Capo D'Orlando Fault (Chapter 5), structures encountered along a N-S oriented transect in SE Sicily on the foreland (Chapter 6), and the offshore Messina Strait Fault and along-strike and across the Reggio Calabria Fault and the Armo Fault (Chapter 7), In detail, individual topographic profiles were picked where the geomorphology of the marine terraces is suitable, as identified during fieldwork and during study of the DEMs, where their preservation is of suitable quality, and also where profiles can be located to help interpretation of existing published maps of marine terraces and palaeoshorelines (Bianca *et al.*, 1999, 2011; Catalano *et al.*, 2003; Giunta *et al.*, 2012).

In general, an attempt has been made to locate topographic profiles where they can constrain displacement gradients along the faults, such as from the fault centre towards their tips. This follows the approach of previous geoscientists who have investigated marine terraces (Armijo *et al.*, 1996; Tortorici *et al.*, 2003; Roberts *et al.*, 2009; Roberts *et al.*, 2013; Giunta *et al.*, 2012; Gallen *et al.*, 2014; Pedoja *et al.*, 2018). Areas with prominent river incision have, in general, been avoided to ensure that studied geomorphic features were marine and not fluvial,

however in some instances preservation of palaeoshorelines in high river incision does exist and some example have been mapped on interfluve areas.

The presence of marine terraces and their associated shallow marine deposits were corroborated by extensive fieldwork deriving x, y and z coordinates using a handheld GPS with a built-in barometric altimeter, In particular, it was found to be advantageous to attempt to re-visit locations mapped by previous authors (e.g. Bianca *et al.*, 1999, 2011; Catalano *et al.*, 2003; Giunta *et al.*, 2012) and those mapped on DEMs. Extensive field observations of the sedimentary sequences and geomorphology of the palaeoshorelines were also made during the fieldwork and these are reported where necessary.

The following text describes the key observations made in the field and whilst studying the DEMs. The key aspects that define palaeoshorelines and their associated marine terrace deposits and wave-cut platforms are summarised in Figure 3.2. The key feature that must be identified is the palaeoshoreline itself which in the Calabrian Arc are characterised either by palaeo-beach deposits or palaeo-rocky shorelines. The key features that allow one to identify palaeo-beach deposits are shallow marine deposits, such as symmetrical ripples, bar-forms, truncation surfaces, beach pebbles/cobbles and marine conglomerates that suggest deposition and re-working in a shoreface environment, unconformably overlie the Palaeozoic crystalline basement and/or Mesozoic/Neogene limestones (Figure 3.2 a, b, g and h). The key features that allow one to identify palaeo-rocky shorelines are: (i) flat-surfaces cut into bedrock alongside shallow marine deposits by erosion of wave action (Roberts *et al.*, 2009; Meschis *et al.*, 2018), (ii) caves, lithophagid borings and notches (Firth and Stewart, 1996; Ferranti *et al.*, 2006; Roberts *et al.*, 2013; Meschis *et al.*, 2018), and (iii) millholes (or marine erosion pan) which are quasi-circular depressions lying in the wave-cut platform formed by the scouring

action of pebbles onto the terrace-forming surface as a result of wave action (Miller and Mason, 1994) Figure 3.2 c, d, e, f and i).

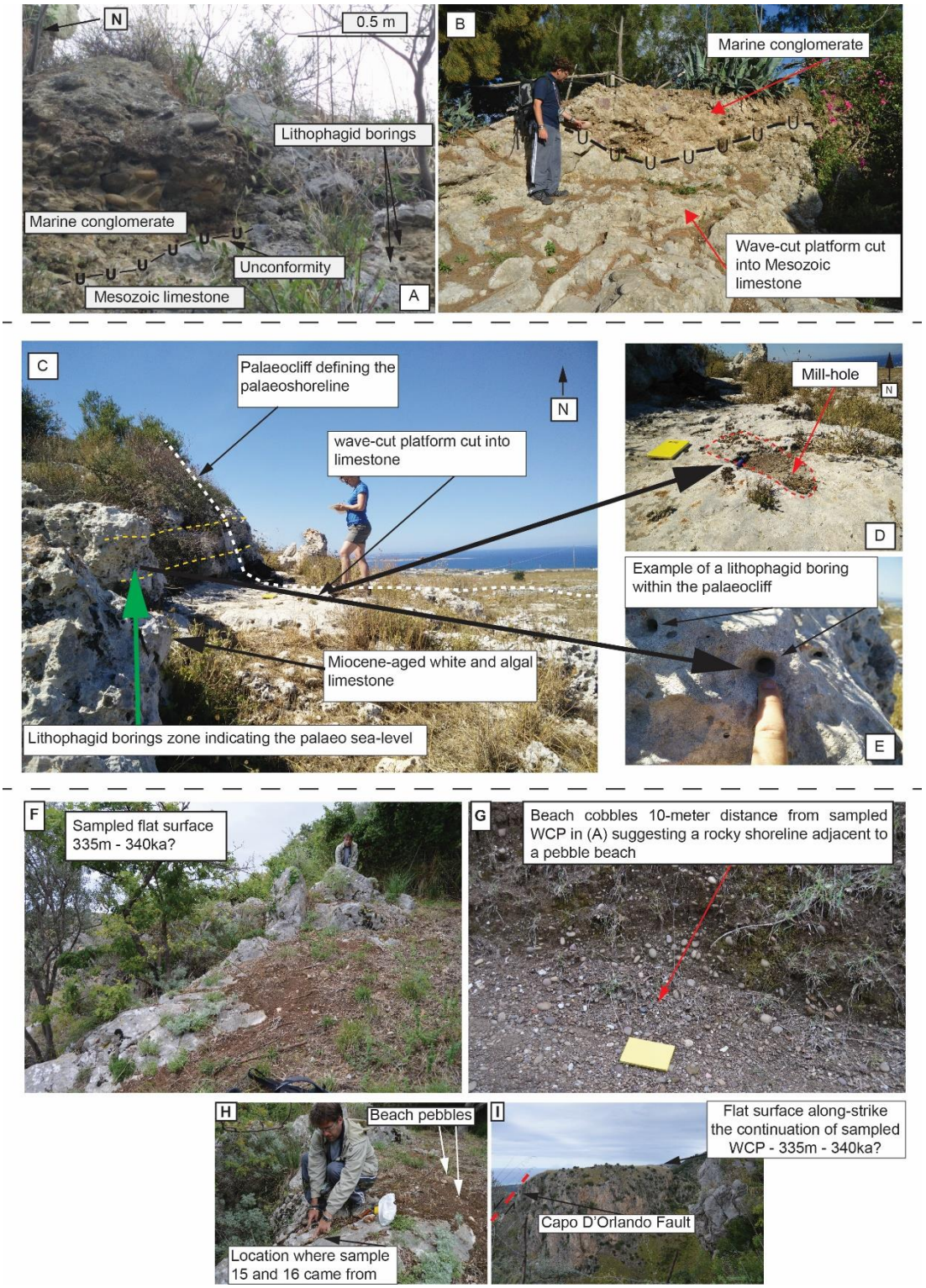

Figure 3.2: *In (a) and (b) marine abrasion platforms made of Mesozoic limestone unconformably overlain by marine conglomeratic deposits are shown. In places lithophagid borings (a) into Mesozoic limestone have been mapped close this area. In (c) a sketched wave-cut platform cut into Neogene limestone with a fault scarp-like palaeocliff and presence of litophagid borings (d) and mill-holes (e) are shown. In (f) a wave-cut platform is sampled for ^{36}Cl dating*

with associated beach pebbles (g) confirming a rocky palaeoshoreline next to a beach pebble. In (h) location of sampling is shown next to beach pebbles. In (I) the equivalent sampled flat-surface cut by river incision.

It is important to highlight that all these features form within the subtidal/intertidal zone a few decimetres to metres down-dip of the inner edge of the marine terrace.

The palaeoshorelines described above are generally located up-dip of palaeoshoreface surfaces marked by sedimentary deposits or wave-cut platforms. For example, gently-sloping surfaces have been interpreted as palaeoshoreface surfaces cut by wave-action and bounded up-dip by fault scarp-like resembling palaeo-sea-cliffs, following previous marine terraces investigations (Armijo *et al.*, 1996; Roberts *et al.*, 2009; Roberts *et al.*, 2013; Bianca *et al.*, 2011; Giunta *et al.*, 2012; Gallen *et al.*, 2014; Pedoja *et al.*, 2018) (Figure 3.3).

Once palaeoshorelines and their associated palaeoshoreface deposits and wave-cut platforms were identified, their x, y and z coordinates were recorded. Field-based palaeoshoreline elevations were georeferenced onto DEMs to confirm their reliability. It is important to highlight that in places the access to the palaeoshoreline locations was difficult due to the thick vegetation and private land. Field mapping was crucial because some marine terraces were clear on the DEM and in the field, but others were less clear to map on the DEM because detailed geomorphological fieldwork showed that: (i) breaks of slope identified as palaeo-sea-cliffs were rather small in height above the sloping terraced surface (less or equal to few meters) and (ii) the geographic extent of the terrace surfaces and wave-cut platforms were limited (a few metres across) and too small to resolve on DEMs. In general, the combined approach of mapping of palaeoshoreline elevations from DEMs analysis and fieldwork allows extensive regional coverage. To confirm that observations of the locations and elevations of palaeoshorelines made on the DEMs were robust and consistent with field measurements, crossplots were made with linear regression analysis used to measure R^2 values, with a value

of 1 indicating a perfect correlation between palaeoshorelines measured in the field and palaeoshorelines measured on the DEMs; examples are shown in Chapter 4, 5, 6 and 7 (Figure 3.4). It is important to note that error bars on linear regression analysis are assigned taking into account that errors associated with hand-held barometric altimeter is 5 m and the resolution of DEM from TINITALY used in Chapter 4, 5 and 7 is 10 m.

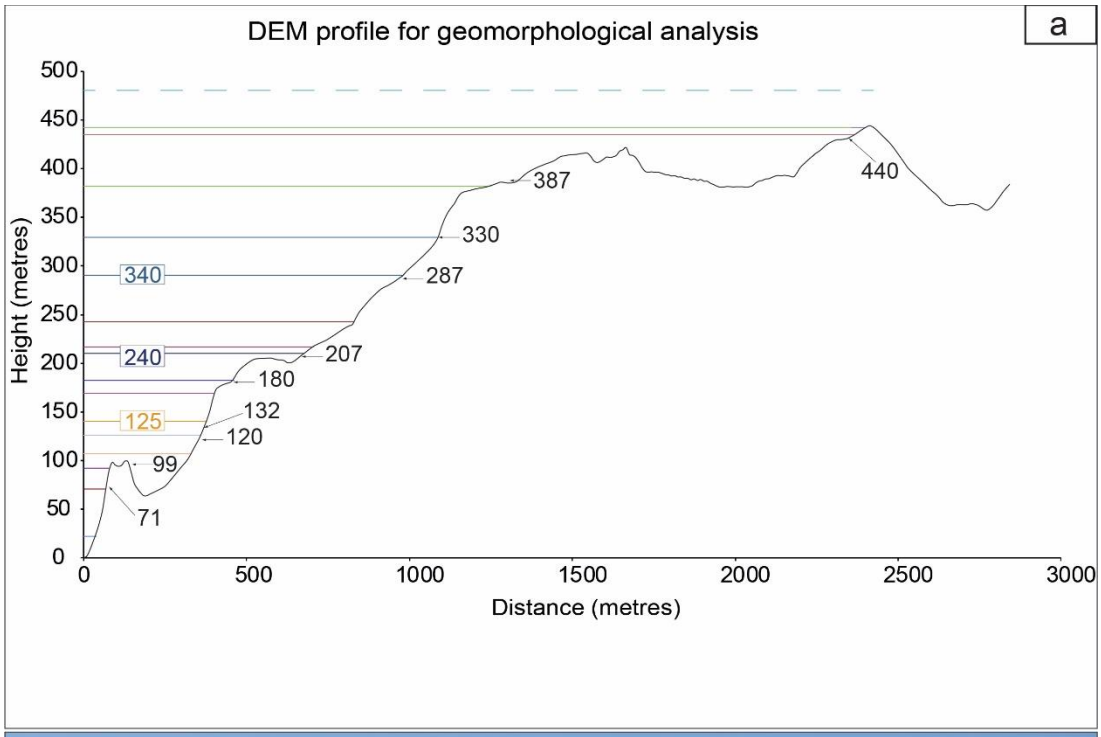

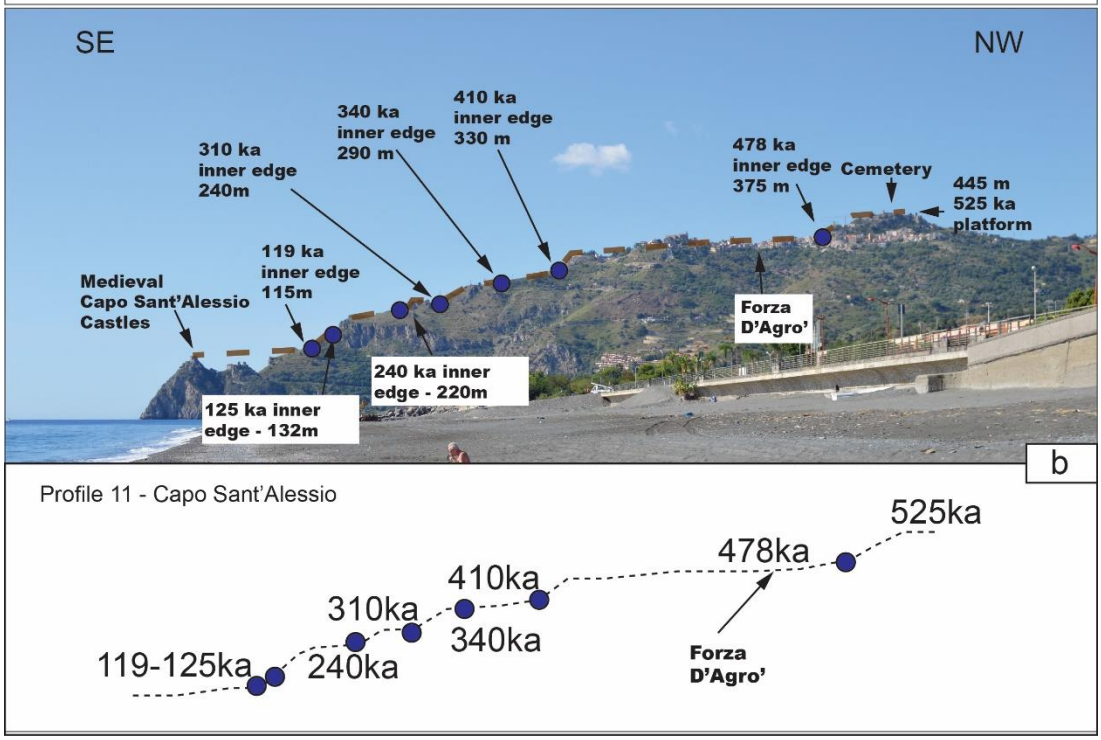

Figure 3.3: *In (a) a topographic profile derived by using a 10m high resolution DEM is shown. Marine terraces are modelled by applying a synchronous correlation approach. In (b) the same location in the field of the topographic profile in (a) is shown. It is possible to appreciate how the GIS-based mapping is robust showing a very "similar topography" if compared to the field.*

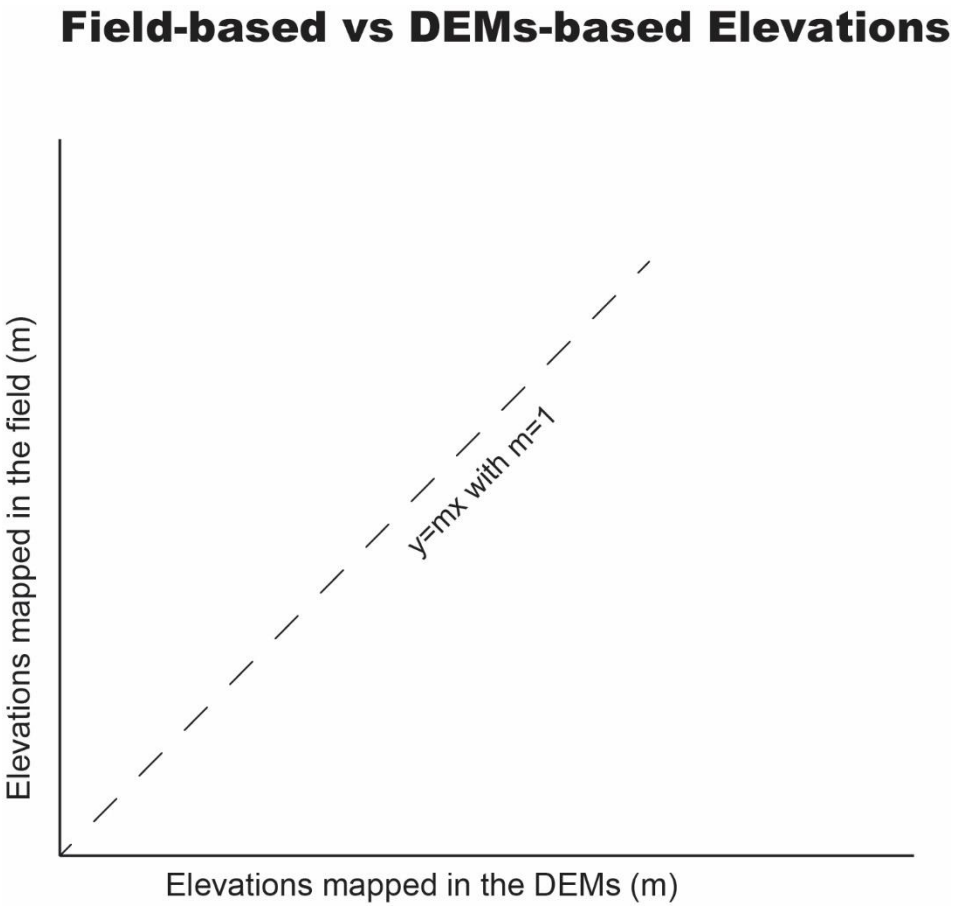

Figure 3.4: *Sketch of an ideal linear regression analysis between field-based measurements and GIS-based mapping to assess that GIS analysis is robust and reliable.*

3.2. U/Th dating on corals

This section describes the method used in an attempt to gain absolute ages of palaeoshoreface deposits, exposed immediately down-dip and correlatable with palaeoshorelines, using $^{234}U/^{230}Th$ dating of corals. Corals were targeted because they concentrate U in their walls and septa to an extent that allows the use of this method (> ~2-3 ppm U is, in general, required).

3.2.1. Background

$^{234}U/^{230}Th$ dating is a method that allows calculation of ages from the radioactive decay process linking ^{238}U, ^{234}U and ^{230Th}. The method can resolve the ages of samples from the Late Quaternary and Holocene (Ivanovich and Harmon, 1982; Edwards, Chen and Wasserburg, 1987; Edwards, 1988; Edwards *et al.*, 1993; Stirling *et al.*, 2007; Andersen *et al.*, 2008).

The method relies on the fact that Uranium is a very soluble chemical element in oxygenated water (Langmuir, 1978; Houghton, 2010), with a long ocean residence time in modern seawater around 5×10^5 years (Ku, Knauss and Mathieu, 1977). A common type of sample to select are fossils formed of marine aragonite, such as corals because they will have assimilated high uranium concentrations, and preservation of primary aragonite indicates the absence of diagenetic alteration and hence a closed system (Stirling *et al.*, 1998, 2007; Roberts *et al.*, 2009; Houghton, 2010). In contrast, marine fossils made of calcite such as molluscs lose uranium from their skeleton structure, especially during diagenesis and open-system behaviours, so they are less useful and precise for dating (Stirling *et al.*, 1998, 2007; Houghton, 2010). In this thesis, a common coral species in the Mediterranean, that is, *Cladocora caespistosa* (Houghton *et al.*, 2003; Roberts *et al.*, 2009; Roberts *et al.*, 2013) has been sampled and dated, although some other species have also been sampled in places known as "solitary coral".

Coral ages from $^{234}U/^{230}Th$ dating are obtained when a disequilibrium in the ^{238}U-^{234}U-^{230}Th decay chain is measured (Edwards, Chen and Wasserburg, 1987; Houghton *et al.*, 2003; Houghton, 2010). Aragonitic corals commonly preserve U at concentrations of ~ 2-3 ppm. If a closed system operates, ^{234}U undergoes radioactive decay to ^{230}Th (Lawrence Edwards, Chen and Wasserburg, 1987; Houghton, 2010). There is no Th present in the corals as they grow

because Th is insoluble in seawater; this implies that the presence of ^{230}Th indicates a daughter isotope, allow the possibility that an age determination of the coral age can be achieved (Edwards, Chen and Wasserburg, 1987; Houghton, 2010). Emission of alpha particles as a product of decay is the base of the Uranium-Thorium dating method through mass spectrometry of both the parent ^{234}U and daughter ^{230}Th (Edwards, Chen and Wasserburg, 1987). In particular, it is also necessary to know or calculate the initial ratio of ^{230}Th/^{234}U in sea-water; 230-Thorium will be stored in the investigated sample through radiometric decay (Edwards, Chen and Wasserburg, 1987; Houghton, 2010). Assuming that the investigated sample has not undergone interchange with the surrounding environment, for example during open system diagenesis, the age of the sample will be derived by the difference between the initial ratio of ^{230}Th/^{234}U and the ratio obtained by the investigated sample itself (Lawrence Edwards, Chen and Wasserburg, 1987; Houghton *et al.*, 2003; Houghton, 2010). In particular, data should be plotted on a graph like Figure 3.6. This graph shows fields within isotopic space that are possible given closed-system decay from ^{230}Th to ^{234}U, given knowledge of the original ^{234}U/^{238}U initial activity ratio of the modern seawater (Figure 3.6), and fields within isotopic space where the measured concentrations can only have resulted from open system diagenetic alteration. Data resulting from this thesis are presented on this graph in Chapters 4, 6 and 7. It will be shown that not all samples collected in PhD were suitable, with some exhibiting open system behaviour and this is discussed in Chapters 4, 6 and 7.

3.2.2. Methods for U-Th series isotopes measurement

In general, advances of mass spectrometry analytical techniques have led to development of new techniques in U-series analysis.

Figure 3.5: *An in-situ coral colony is collected for dating where a wave-cut platform showing litophagid borings is mapped (top). A death assemblage of bioclastic materials with presence of corals is mapped within a Quaternary calcarenite-made boulder embedded on marine terrace deposits (bottom). Coral locations shown in Figure 3.1.*

In particular, Inductively Coupled Plasma Multicollector Mass Spectrometry (ICP-MC-MS; Seth *et al.*, 2003) has been used in an attempt to obtain the ages of corals in this thesis.

In total, 21 $^{234}U/^{230}Th$ series analyses (Table 3.1) have been carried out at the NERC Isotope Geosciences Laboratory (NIGL), British Geological Survey, Keyworth, UK. Specifically, data are obtained on a ICP-MC-MS which follow procedures modified by some (Hellstrom, McCulloch and Stone, 1998; Andersen *et al.*, 2008; Hiess *et al.*, 2012) and applied to other studies (e.g. Nehme *et al.*, 2015; Crémière *et al.*, 2016).

3.2.3. Coral sample preparation

Preparation of coral samples was a crucial step before the U-series analysis in Keyworth. In particular, samples were cleaned systematically and each corallite was selected cautiously. Some corallites were already separated from cemented sediments, occurring as death-assemblage individual corallites that were easily-separated from the sediment. Other corallites were collected in the field as a cemented colony embedded in Quaternary calcarenite and also within a boulder embedded in marine terrace deposits (Figure 3.5). These examples were more difficult to work with as they had to be separated from the cemented sediment and cleaned.

The cleaning process is described below. After that corallites were physically removed from the sediment, millimetre-sized fragments of corallites were isolated. Any material providing evidence for alteration and/or detrital matrix on the outside of the corallite wall was removed both physically by scraping using a scalpel working under a microscope, and chemically by washing the wall with HCl (10% diluted) for 5-10 seconds. Furthermore, coral septa were separated from the wall because they are thinner and more prone to diagenetic alteration processes; only walls are used for analysis in this thesis. Even after the above cleaning, some wall fragments still showed impurities and alteration after visual examination

(e.g. brown and discoloured relative to the white material of modern corals, and other parts of the altered specimens), which was very difficult to remove; therefore, a 200 micron-sized driller is used to sample the purest part of corallites, avoiding the altered portions.

Samples with obtained ages are shown in Table 3.1. The table shows that some samples appear to be closed system and un-altered by diagenesis, and have provided dates, However, other samples cannot be dated because they exhibit high ratio values of $^{230}Th/^{238}U$ (>1.2), indicating open-system diagenesis and alteration (Figure 3.6). The individual samples, sample locations, isotopic compositions and viability for providing ages are discussed in later chapters. However, in summary, Samples 1-14 cannot be dated, whilst samples 15-17 do provide dates and hence constraints on the age of a terrace (see Chapter 7). Sample 18-21 also provide dates, and these are used to constrain the age of a WCP, supported by age controls from the literature (see Chapter 6).

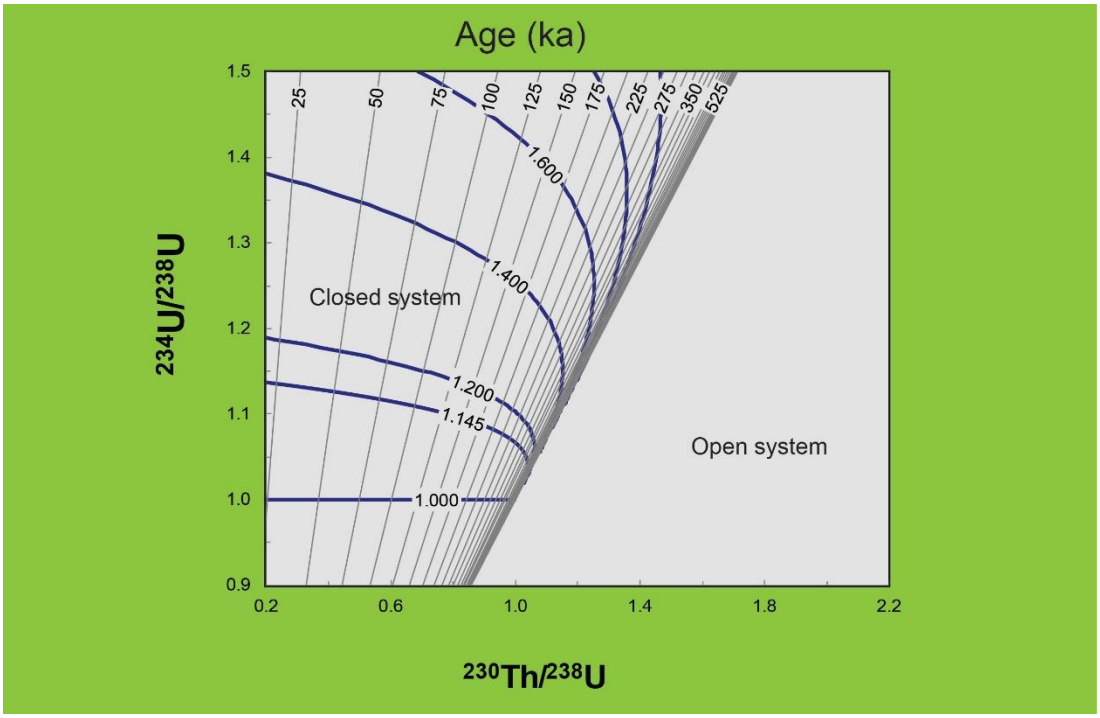

Figure 3.6: *Graph used to plot obtained results from U/Th analysis. All data lying on the right part of this diagram will show open system diagenesis, not allowing an age estimation. The 1.145-curve represents the $^{234}U/^{238}U$ initial activity ratio of the modern seawater.*

Sample	(230Th/234U)	Uncertainty (2 s.e.)	(234U/238U)	Uncertainty (2 s.e.)	Age (ka)	+	-
1	1.23218	0.22	1.1095	0.12	-	-	-
2	1.20263	0.23	1.0899	0.14	-	-	-
3	1.31008	0.25	1.1206	0.19	-	-	-
4	1.31259	0.25	1.1225	0.17	-	-	-
5	1.21234	0.23	1.1020	0.13	-	-	-
6	1.19235	0.23	1.0965	0.12	-	-	-
7	1.61180	0.23	1.2496	0.14	-	-	-
8	1.19885	0.22	1.0966	0.14	-	-	-
9	1.88163	0.23	1.3990	0.14	-	-	-
10	1.41548	0.22	1.2486	0.11	-	-	-
11	1.44911	0.22	1.2987	0.11	-	-	-
12	1.47943	0.23	1.1141	0.13	-	-	-
13	1.49121	0.23	1.1190	0.13	-	-	-
14	1.44556	0.23	1.1240	0.13	-	-	-
15	1.0042	0.22	1.0532	±0.003	449.068	17.342	-17.342
16	1.0007	0.26	1.0677	±0.004	384.123	11.465	-11.465
17	1.0095	0.23	1.0612	±0.004	480.295	25.100	-25.100
18	1.29855	0.32	1.0955	0.24	-	-	-
19	1.22119	0.32	1.0965	0.21	-	-	-
20	1.31970	0.33	1.1040	0.26	-	-	-
21	0.6610	0.85	1.1032	±0.008	102.042	1.706	-1.706
22	0.7148	0.00425	1.114	0.00390	132	1.62	-1.62
23	0.7411	0.00431	1.113	0.00392	142	1.78	-1.78

Table 3.1: *Dated coral samples in red. In black coral samples that could not have been possible to date because they describe an open system. In green coral dates derived from a previous investigation (Roberts et al., 2013) but in this thesis used in Chapter 4 to model a sequence of marine terraces. Samples 15, 16 and 17 are used in Chapter 7.*

3.3. In situ ^{36}Cl cosmogenic exposure dating to date wave-cut platforms cut into limestone

3.3.1. Background

In situ ^{36}Cl cosmogenic exposure dating is a technique which allows derivation of the exposure age of rocks at the Earth's surface (Dunai, 2010; Schlagenhauf *et al.*, 2010; Vermeesch *et al.*, 2010). In particular, the age of exposure is determined by measuring the abundance of cosmogenic isotopes which are mainly produced because of interaction involving spallation between high energy cosmic particles, such as neutrons and muons and target elements present in the rock itself such Ca, K, Ti and Fe, with Ca mainly in limestone rocks (Gosse and Phillips, 2001; Dunai, 2010; Schlagenhauf *et al.*, 2010) (Figure 3.7). Most of the production in limestone rocks occurs by spallation of ^{40}Cl atoms largely within the top 2 m of exposed surfaces (Dunai, 2010), exponentially decreasing with depth (Figure 3.7). In general, the production rate from spallation process lies within a range between 48.8 ± 3.5 to 76 ± 5 atoms of ^{36}Cl/g Ca yr^{-1} (Stone *et al.*, 1996; Schimmelpfennig *et al.*, 2009; Dunai, 2010). With this technique the measured concentration (number of atoms per gram) of the cosmogenic nuclide allows the estimation of exposure age, given information on erosion rates, magnetic field variations and shielding from cosmic radiation, spanning a temporal window of hundreds to million years (Darvill, 2013).

The maximum exposure age which can be obtained by applying this technique is generally limited to the Quaternary and depends on the half-life of the cosmogenic nuclide and on the well preservation of the surface that needs to be dated (Dunai, 2010; Schlagenhauf *et al.*, 2010). Indeed, after 2-3 times the half-life of exposure time the decay rate and the rate of cosmogenic nuclide production become similar, approaching to the saturation (Dunai,

2010). However, the half-life of ^{36}Cl is 3.01×10^5 years, making it suitable for studying exposure ages for Quaternary wave-cut platforms described in this thesis.

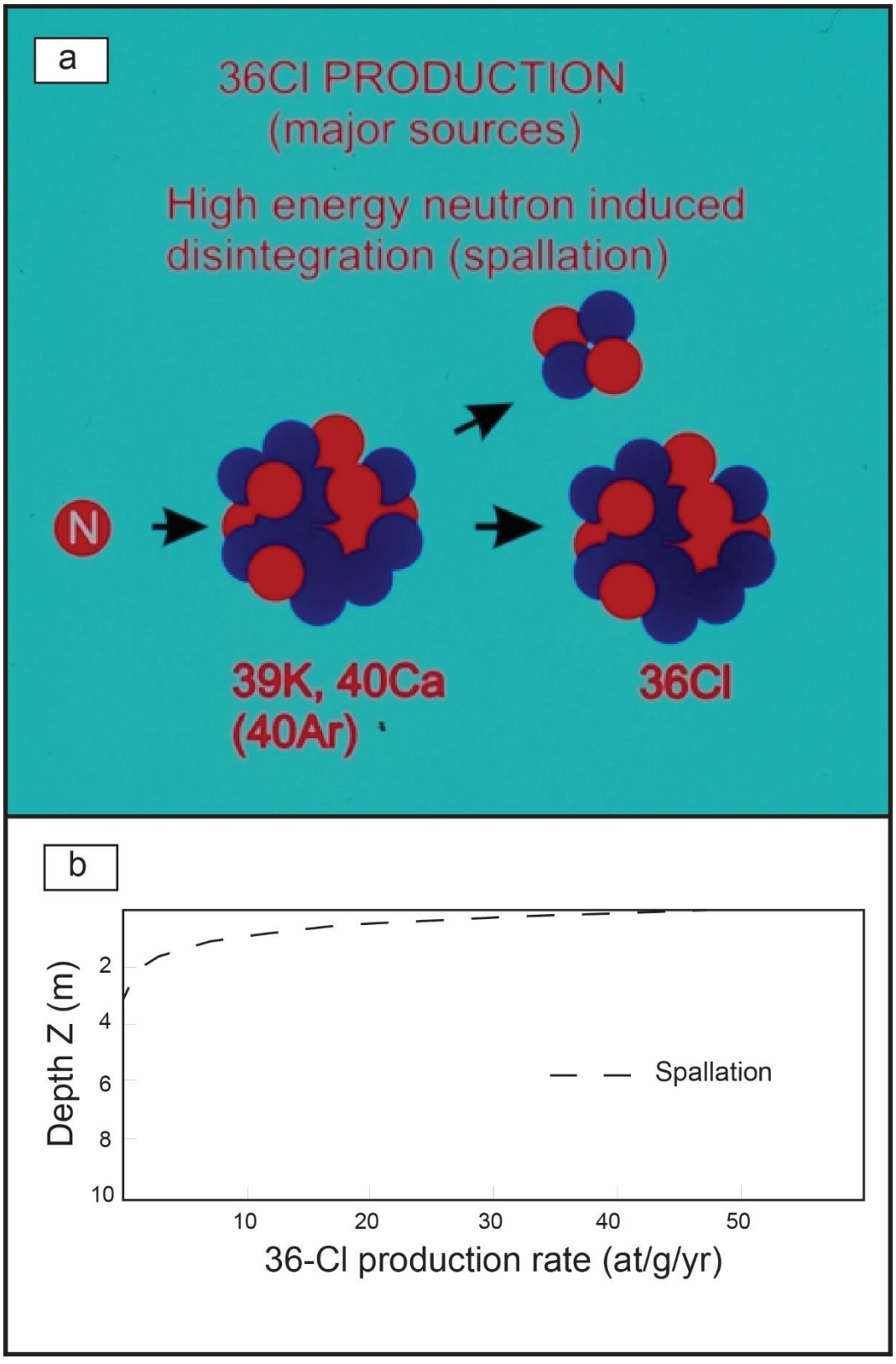

Figure 3.7: *Sketched cartoon of the process of spallation (a) modified from (http://www3.telus.net/lejgeology/etrain/htmls/36cl.htm,* 2008). *In (b) a graph showing a decrease of 36-Cl concentration versus depth adapted from Schlagenhauf et al., (2010).*

In more detail, the common isotopes and the related t1/2 (the isotope half-life) investigated, over the afore-mentioned noble-gas isotopes, for most common crustal rocks are ^{10}Be (t1/2 = 1.5×10^6 years), ^{26}Al (t1/2 = 7.5×10^5 years) and ^{36}Cl (t1/2 = 3.01×10^5 years) (Dunai, 2010; Schlagenhauf *et al.*, 2010; Darvill, 2013) (Figure 3.8). In general, assuming negligible erosion rates, measurements of isotope concentration in a rock can vary as a function of the time of rock exposure (t) and burial depth (z) defined as $dN(z, t)/dt = P(z, t) - \lambda \times N(z, t)$ where N is the number of atoms of investigated isotope, P is the isotope production rate, λ is the decay constant and dN/dt is the rate of change.

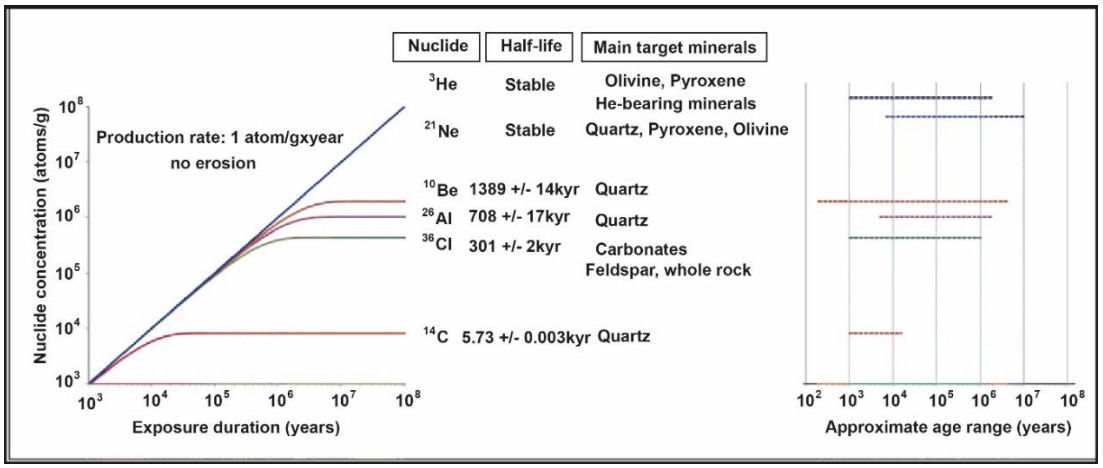

Figure 3.8: *Picture from Darvill, (2013) showing six of the most used cosmogenic nuclide and the associated summarized properties for dating. Age ranges have shown with data from Ivy-Ochs & Kober (2008); ^{10}Be from Chmeleff et al. (2010) and Korschinek et al. (2010).*

Scaling factors are important on describing how the cosmic-ray flux varies and affects the cosmogenic nuclide production; indeed, this production varies as a function of topographic elevation, latitude, magnetic fields and shielding (Dunai, 2010; Marrero, Phillips, Borchers, *et al.*, 2016). For instance, the flux of cosmic-ray increases from the equator towards higher latitude because of the geometry of the magnetic field of Earth (McElhinny and

McFadden, 1997). Moreover, particles from cosmic flux will interact with atoms in the atmosphere, loosing energy and implying that the difference in sampling location elevation (or thicker atmosphere) plays an important role on the production rate; lower elevations of sampling location would imply that the cosmic-flux will lose more energy (Dunai, 2010; Schlagenhauf *et al.*, 2010). Furthermore, the topographic shielding is a critical factor because it will affect the flux of cosmic rays hitting the WCP and then the production rate (Dunai, 2010).

Exposure ages are derived by using the "CRONUScalc" which is programmed to be used with the common used nuclides, including ^{10}Be, ^{26}Al, ^{3}He and ^{36}Cl (Marrero, Phillips, Caffee, *et al.*, 2016). In particular, CRONUScalc presents an easy input interface (Marrero *et al.*, 2015) which allows: (i) the user to copy from spreadsheets (Excel format) and (ii) run synchronously several samples (Marrero, Phillips, Caffee, *et al.*, 2016). One of the peculiarity of this calculator is the possibility to specify uncertainties within the input parameters, allowing to propagate them to the resulting exposure age (Marrero, Phillips, Caffee, *et al.*, 2016). Indeed, this calculator can: (i) calculate accumulation and production for a given sample and (ii) make depth-profile exposure ages, providing either depth-profile and surface sample dating which are based on the same code (Marrero *et al.*, 2015; Marrero, Phillips, Caffee, *et al.*, 2016).

In this thesis, wave-cut platforms formed by wave erosion at Quaternary sea-level highstands were studied.

3.3.2. Field sampling and sample preparation

Detailed geomorphological mapping is a crucial step for sampling uplifted wave-cut platforms (WCPs) cut into limestone, by identifying locations with preserved palaeoshoreline

indicators such as mill-holes and lithophagid borings, which support the idea of minimal values of erosion. Marine terrace surfaces from Holocene have been dated by using this technique in Scotland (Stone *et al.*, 1996), however, for Quaternary examples in the Mediterranean Basin has rarely been applied. For instance, Late Quaternary uplifted WCPs cut into Mesozoic limestone had been initially investigated by trying to date them, using the *in situ* ^{36}Cl cosmogenic exposure dating technique but because of high erosion rate obtained exposure ages have been discarded (Strobl *et al.*, 2014). In this thesis, sampling locations have been carefully selected using criteria that show they have been barely affected by erosion process (Figure 3.9). In particular, lithophagid borings are 5 to 10 centimetres deep when formed by boring bivalves, so their preservation limits erosion to less than 5-10 cm, a value that makes sample sites with lithophagids suitable for *in situ* ^{36}Cl cosmogenic exposure dating because the ~2 m extent of ^{36}Cl production is implied by Figure 3.7. Additionally, mill-holes, formed by agitation of pebbles by wave action to form incised depressions, are typically a few centimetres to 10 cm deep, so again their preservation suggest ^{36}Cl exposure dating is possible. Ideally, the presence of both lithophagid borings and millholes suggest that the WCP has been affected only by a few centimetres of erosion since their formation. In this thesis, sampling locations have been chosen where lithophagid borings and millholes occur within a few metres of a mapped palaeoshoreline. Once locations were selected, detailed photogrpahs were taken of each site to record the geomorphology, and measurements of shielding were made every 30 degrees as suggested by Dunai (2010) to calculate the percentage of the sky that could contribute to ^{36}Cl production. Samples were physically removed using a chisel and mallet, noting the top of the sample. Once samples were collected in the field, they were analysed by preparing thin sections to check their lithological composition. Because some of the samples

have been collected close to the splash zone, where natural ^{35}Cl exists due to the presence of sea-salt, samples have been washed using an ultrasonic bath in distilled water to remove the sea-salt. Additionally, the density of each sample has been calculated by applying the Archimedes principle, used by some (Schimmelpfennig *et al.*, 2009). Care was taken to try to isolate samples from the top surface of outcrops to obtain a 3 cm sample thickness, ensuring that the most concentrated part of the sample in terms of ^{36}Cl is analysed.

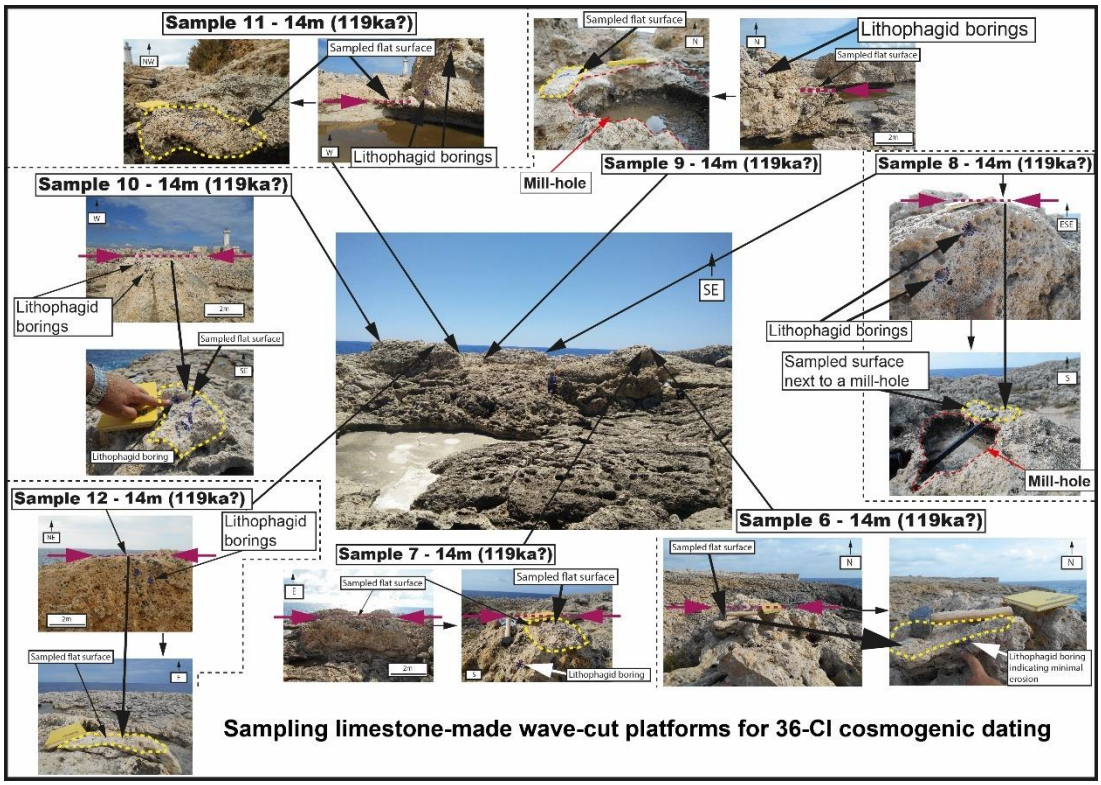

Figure 3.9: *Sample locations from south of Syracuse town as shown in Figure 3.1. Dashed red lines show cm-depth millholes indicating minimal erosion next to the sample locations. Dashed dark blue circle show lithophagid borings next to the sample locations, indicating that sampled WCPs represent the palaeo sea-level at time of their formation. Dashed yellow lines show the sampled WCP. Magenta arrows with associated dashed lines show the flat sampled surfaces. Ages estimated by using submerged palaeoshorelines at -20m and -40m respectively associated to the 76ka and 50ka highstands (Dutton et al., 2009) as age controls driving a synchronous correlation approach as shown in Chapter 6. Black dashed lines used to separate different sample photos. Note that sample locations have chosen next to mill-holes and/or lithophagid borings implying minimal erosion.*

All samples have been crushed to obtain 50-70 g of powder, 125-250 micron-sized, which has been used following sample preparation guidelines described by Schimmelpfennig *et al.*, (2009). Samples were sent to the Cosmogenic Isotope Analysis Facility (CIAF) at the Scottish Universities Environmental Research Centre (SUERC) for chemical preparation. Accelerator

Mass Spectrometry (AMS) has been used to calculate the concentration of the ^{36}Cl and then by using CRONUS calculator (Marrero, Phillips, Caffee, *et al.*, 2016) exposure ages of samples have been calculated assuming minimal erosion rate values between 0 and 0.8 mm/ky.

Table 3.2 shows the obtained outcomes where the calculated ages (green column) with results discussed in subsequent chapters. In general, it appears that ^{36}Cl concentrations are unexpectedly low in the samples, perhaps implying higher than expected erosion rates. An alternative explanation could be related to the fact that marine deposits could have covered the investigated WCPs after their formation, shielding the process of accumulation and suddenly eroded in more recent time. The implications of this, and the fidelity of the derived ages are discussed.

Sample	Latitude (°)	Longitude (°)	Elevation (m)	Inner-edge Elevation (m)	Erosion rate (mm/kyr)	Total erosion (mm)	Cl (p.p.m)	±	^{36}Cl (g of rock)	±	CaO (wt%)	±	Age (kyr)	Total uncertainty (kyr)	Expected Age (kyr)
1	37.10722	15.28194	36	36	0.8	1000	12.90734877	1.464896928	444512.7971	18923.13941	46.3061386	0.264826622	**31.1**	7.4	**125**
2	37.10733	15.2819	36	36	0.8	1000	7.308453526	0.128564994	501752.7274	15240.42317	48.35125366	0.294170252	**35.2**	8.6	**125**
3	37.10731	15.28184	35	36	0.8	1000	11.49816224	0.208932376	529940.5325	14145.0171	49.93505428	0.245345642	**35.7**	8.6	**125**
5	37.09123	15.22756	139	139	0.8	4200	2.579227656	0.070041331	377426.451	9038.991922	53.64140928	0.273960211	**22.5**	5.5	**525**
6	37.00256	15.33581	14	14	0.8	952	21.92532333	0.405078167	435056.1338	10839.32981	47.98090507	0.197268973	**29.1**	6.5	**119**
8	37.00248	15.33588	14	14	0.8	952	17.16254582	0.296099013	378052.1812	10217.02566	49.3866029	0.232807276	**25.1**	5.6	**119**
9	37.0025	15.33592	14	14	0.8	952	12.99885928	0.213200221	144167.6404	4881.27009	43.72119983	0.193124318	**14.3**	3.2	**119**
10	37.00253	15.33596	14	14	0.8	952	19.22341174	0.335758027	452615.3345	12256.66806	46.09799497	0.239719163	**32.5**	7.5	**119**
11	37.00251	15.33593	14	14	0.8	952	28.46100317	0.563611338	113835.1077	3921.114504	44.5719683	0.227830693	**10.7**	2.3	**119**
12	37.00253	15.33595	14	14	0.8	952	16.94316159	0.283669832	413138.7467	11554.61222	49.51359051	0.270216349	**27.7**	6.3	**119**
13	37.74167	15.33748	369	380	0.8	3824	104.0866379	4.332998319	318214.6695	13319.06311	29.90252017	0.134797236	**15.5**	2.4	**478**
14	37.74167	15.33748	369	380	0.8	3824	95.28837925	3.791788876	240052.4105	9742.785211	28.10244797	0.179843156	**11.2**	1.8	**478**
15	38.08083	14.69753	335	335	0.8	2720	8.134415882	0.138888242	97743.14203	3051.706025	43.35093037	0.249847152	**5.5**	1.2	**340**
16	38.08083	14.69753	335	335	0.8	2720	8.990053144	0.150356843	98034.67934	2724.83255	45.21286323	0.222343466	**5.3**	1.1	**340**
3	37.10731	15.28184	35	36	0.8	1000	11.49816224	0.208932376	529940.5325	14145.0171	49.93505428	0.245345642	**35.7**	8.6	**125**
C2	37.2444182	15.2474674	46	46	0.8	1000	20	0	1250000	33761	55.15	0	**109**	46	**125**
C5	37.1041	15.2766	37	37	0.8	1000	16	0	1220000	37359.79	56.09	0	**105**	43	**125**
C9	37.0853106	15.2995998	27	27	0.8	952	8	0	1090000	26679.57431	55.42	0	**97**	39	**119**

Table 3.2: *WCP samples used for ^{36}Cl cosmogenic dating in this thesis. Red coloured samples are from an unpublished study (Spampinato, 2011), collected close to Sample 3 in Syracuse (Chapter 6). Note that the obtained ages (green column) from the unpublished data confirm the expected ages (yellow column) for a prominent palaeoshoreline modelled by applying a synchronous correlation approach driven by an age control obtained by Dutton et al., 2009.*

3.4. The synchronous correlation approach to allocate ages for un-dated uplifted palaeoshorelines

The synchronous correlation technique is built on the concept that sea-level highstands, which are thought to produce marine terraces (Lajoie, 1986; Armijo *et al.*, 1996), are unequally-spaced in time implying that for a constant uplift rate through time marine terraces are unequally-spaced in elevation (Houghton *et al.*, 2003; Roberts *et al.*, 2009, 2013; Meschis *et al.*, 2018). To apply this approach, it is important to obtain at least one dated marine terrace across the investigated transect/topographic profile.

The traditional approach to this problem, which is not used in this thesis for reasons described in section 2.5 (Chapter 2) (so-called sequential correlation technique, for further details Roberts *et al.*, 2009, 2013; Meschis *et al.*, 2018), correlates a single palaeoshoreline with a single sea-level highstand and assumes that the next higher and older palaeoshoreline belongs to the next older sea-level highstands, and so on (Armijo *et al.*, 1996; Bianca *et al.*, 2011; Giunta *et al.*, 2012; Gallen *et al.*, 2014). However, it is important to note that not all the sea-level highstands with the associated palaeoshorelines are preserved within a profile because either they have been eroded or as a result of overprinting of older palaeoshorelines by younger sea-level highstands (Westaway, 1993; Roberts *et al.*, 2013; Jara-Muñoz and Melnick, 2015; Meschis *et al.*, 2018; Pedoja *et al.*, 2018). Indeed, the "overprinting problem" is typical in region affected by low uplift and is not taken into account when marine terraces are modelled by applying the "sequential" correlation approach (Westaway, 1993; Roberts *et al.*, 2009, 2013; Meschis *et al.*, 2018) (Figure 3.10).

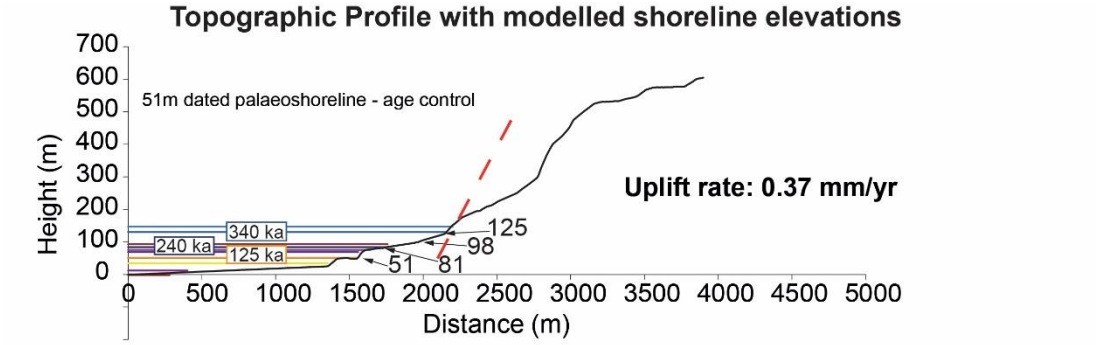

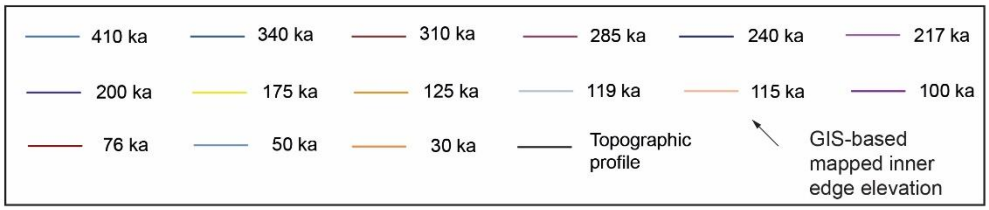

Uplift rate (mm/yr)	Highstand age (ka)	Predicted Elevations (m)	Measured Elevations (m)
0.37	30	-69	
0.37	50	-42	
0.37	76.5	-2	
0.37	100	12	
0.37	115	22	
0.37	119	39	
0.37	125	51	51
0.37	178	35	
0.37	200	69	
0.37	217	50	
0.37	240	84	81
0.37	275	75	
0.37	310	93	98
0.37	340	131	125
0.37	410	147	

← Dated palaeoshoreline

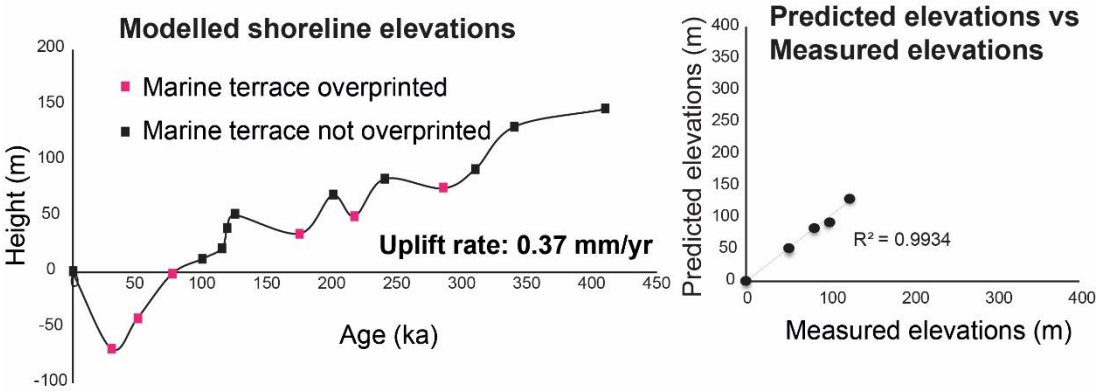

Figure 3.10: *Palaeoshorelines on a topographic profile are modelled by applying a synchronous correlation approach (see top panel). Coloured lines represent the predicted elevations of sea-level highstands (see table for values) iteratively-calculated driven by an age control value for the 51 m palaeoshoreline. The bottom left graph shows which palaeoshorelines are overprinted given the implied low and constant through time. The bottom right panel shows a linear regression analysis between "predicted" and "measured" elevations. The predicted elevations, representing the synchronously calculated sea-level highstand elevations, have been derived by defining a constant uplift rate through time, and iterating this value to find the best match to the measured and mapped paleoshorelines elevations with a R^2 value >0.99, confirming that the correlation is robust and reliable.*

Instead, the so-called synchronous correlation approach forces the user to maximise the coefficient of determination (R^2 value) for a linear regression analysis through data including the "measured" elevations of all marine terrace inner edges on a topographic profile and the "predicted" elevations which represent the sea-level highstand elevations implied by iterating uplift rate values driven by age controls and using well-accepted and known sea-level curves in the Late Quaternary (Siddall *et al.*, 2003; Rohling *et al.*, 2014) (Figure 3.10 and 3.11); this is explained in detail below. It is important to note that error bars on this linear regression analysis are assigned considering that DEMs used from TINITALY (Tarquini *et al.*, 2007, 2012) have a 10 m resolution and the "predicted" elevations iteratively-calculated using well-known sea level curves (Siddall *et al.*, 2003; Rohling *et al.*, 2014) have 12 m of error on each sea level highstand.

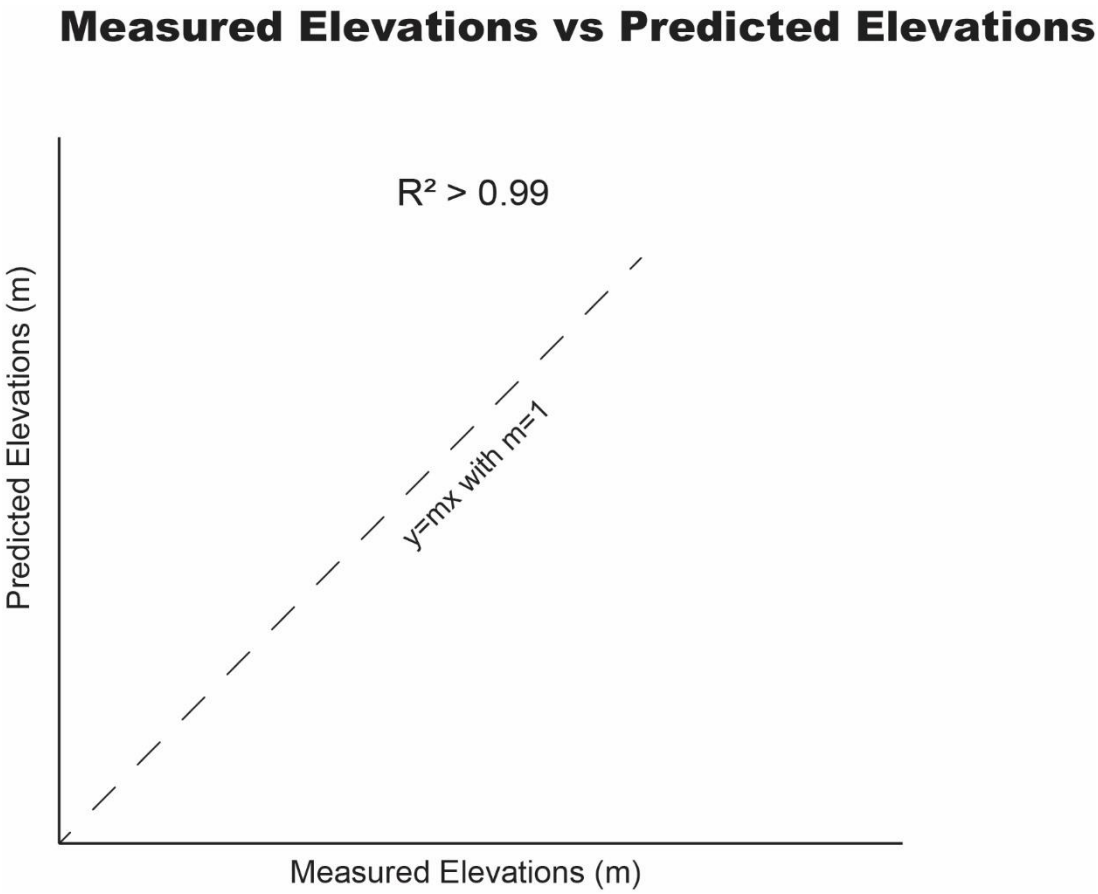

Figure 3.11: *Sketch of an ideal linear regression analysis between "predicted" elevations iteratvely-calculated driven by age controls and "measured" elevations from GIS analysis. R^2 values >0.99 confirm that the synchronous correlation analysis is robust and reliable.*

In particular, the age control drives the iteration of uplift rate to the entire topographic profile, modelling at the same time all mapped and measured palaeoshorelines. This approach tests if un-dated palaeoshorelines can be modelled by the uplift rates implied by the dated palaeoshorelines. This iteration is enabled by a "Terrace Calculator" built in Excel where data from sea-level highstands are input (Siddall *et al.*, 2003; Rohling *et al.*, 2014). The calculator uses an input uplift rate (UR), which is iterated to calculate the predicted elevations (PE) of all sea-level highstands using the age of the highstands (T) and the sea level elevations of the highstands relative to the sea level of today (SLT) following this formula:

$$PE = (UR \times T) + SLT$$

The table within Figure 3.10 shows an example of the output of the "Terrace Calculator". Values for a constant uplift rate through time have been iterated. A set of "predicted" elevations are synchronously calculated for all sea-level highstands and plotted on a topographic profile. The iteration procedure attempts to find the best match with "measured" palaeoshoreline elevations. This assigns ages to the un-dated palaeoshorelines. The same procedure is used for serial topographic profiles, chosen at suitable locations along the strike of faults, to study how uplift rates change spatially.

It is important to emphasise that the approach described above always assumes, as an initial and simplest hypothesis, that the value of uplift rate has been constant through time (Roberts *et al.*, 2009, 2013; Meschis *et al.*, 2018). If the first hypothesis is supported by the data and synchronous correlation, and a single uplift rate fits the data, confirmed by a high value for the coefficient of determination, R^2, (for example higher than 0.99) (Figure 3.11), then modelling ceases to that point (examples are given in Chapters 4, 5 and 6). However, if the initial hypothesis of constant uplift rate through time cannot be verified, for example with

some observed palaeoshorelines remaining unexplained, and with a relatively low R^2 value, the modelling is extended to explore temporally-varying uplift rates (see Chapter 7 for examples, and also Roberts *et al.*, 2009). Note that when uplift rates are calculated error bars are assigned taking into account the equation used by some (e.g. see Gallen *et al.*, 2014):

$$SE\ (u)^2 = u^2((\sigma H^2/(Ht-Hsl)^2)+(\sigma T^2/T^2))$$

where u is the uplift, σH is the combined uncertainty for sea level elevation and terrace (inner edge) elevation, Ht is the elevation of the inner edge, Hsl is the elevation of the sea level relative to today, T is the age of the sea level highstand and σT is the uncertainty of the age of the sea level highstand.

3.5. Elastic half-space modelling to reproduce vertical motions derived from levelling data produced during the Mw 7.1 Messina earthquake

Levelling data (Loperfido, 1909) have been projected across-strike the mapped Quaternary active faults affecting the Messina Strait. Figure 3.12 leads to hypothesise that the geometry of the possible seismogenic source producing the 1908 Messina Earthquake (Mw 7.1) should be different from those already proposed by some and shown in Figure 2.17 in Chapter 2 (Schick, 1977; Mulargia and Boschi, 1983; Bottari *et al.*, 1986; Capuano *et al.*, 1988; Valensise, 1988; Boschi, Pantosti and Valensise, 1989; De Natale and Pingue, 1991; Aloisi *et al.*, 2013); it suggests an east-dipping high dip angle normal fault has to be claimed.

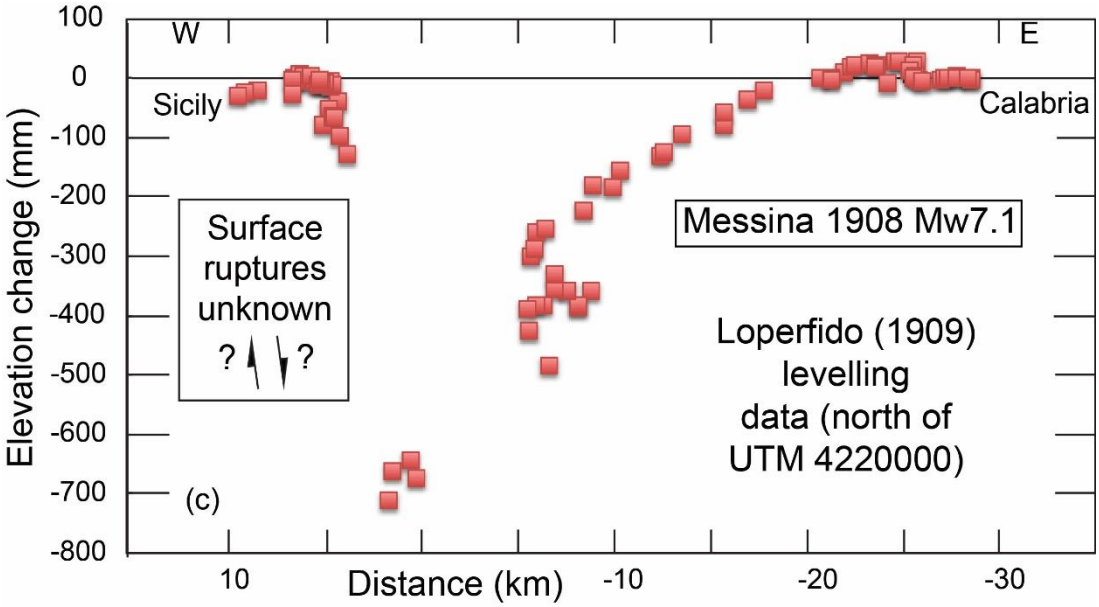

Figure 3.12: *Co-seismic elevation changes measured after the 1908 Messina Earthquake in Sicily and Calabria*

Following the classic example of the 1983 Borah Peak Earthquake (Stein and Barrientos, 1985), to test this hypothesis faults embedded in an elastic half-space are modelled by using Coulomb 3.3 software (Toda *et al.*, 2011) with a new code provided by Mildon *et al.*, (2016). It is important to note that only mapped and well-known active normal faults have used for the inversion modelling of the levelling data, discarding all the previous attempts where levelling data are modelled trying to find the best match with fictitious not-mapped faults (see section 2.7.1 and Figure 2.17 in Chapter 2). Different dip angle and slip distribution scenarios are tested to find the lowest misfit between the "modelled" and the "measured" co-seismic vertical elevation changes. Moreover, a critical filtering of the levelling data has been done trying to take out the benchmarks which have been affected by secondary effects such as slumping and landsliding processes.

More details on the approach used are shown in Chapter 8 where it is also investigated the possibility that the 1908 Messina Earthquake could represent a "characteristic earthquake" as described by Schwartz and Coppersmith, (1984).

3.6. Summary of applied approach and methods

Long-term tectonic uplift in the Calabrian Arc is investigated in this thesis by investigating several kilometres of uplifted Late Quaternary marine terraces. For the first time, the uplift has been investigated along the strike of the major mapped Quaternary active faults on the upper plate of the Ionian Subduction Zone (ISZ), testing if the "regional" uplift is affected by local tectonic activity (Chapter 4, 5 and 7). Furthermore, uplift and the associated palaeoshorelines have been investigated in a forebulge region within a convergence tectonic boundary (Chapter 6).

For the first time, new refined ages for un-dated palaeoshorelines can be estimated by applying a synchronous correlation approach which overcome the "overprinting problem" affecting region showing low uplift rates. This allows to refine uplift and uplift rates over the Late Quaternary investigated on footwalls and hangingwalls of active normal faults, and consequently, to refine long-term fault slip rates.

A multidisciplinary approach has been applied to test the scientific questions stated in Chapter 1 by: (i) field mapping supported by detailed GIS-based geomorphological analysis, (ii) absolute dating by applying U/Th dating on corals and ^{36}Cl cosmogenic dating on limestone-made wave-cut platform in the same tectonic region and (iii) a synchronous correlation approach driven by new obtained age controls alongside those available in the literature. Nonetheless, refined long-term uplift has been compared with co-seismic footwall uplift in the Messina Strait to find a relationship which could explain if the 1908 Messina Earthquake is a "characteristic earthquake" (Chapter 8).

For the first time, long-term slip rates on faults can be derived by using refined ages of palaeoshorelines across active faults. Furthermore, rates of forebulge uplift are associated

with the ongoing convergence of Eurasia-Africa plates, suggesting new scenarios for the high historical seismicity affecting the Hyblean Plateau.

The next Chapters (4, 5, 6, 7 and 8) show results obtained in this thesis, highlighting how crucial an improved approach to investigate long-term uplift can be if related to the long-term seismic hazard affecting the seismically-deforming upper plate of a subduction zone.

Chapter 4: The implications of revised Quaternary palaeoshoreline chronologies for the rates of active extension and uplift in the upper plate of subduction zones

4.1. Abstract

In this chapter, results from testing interaction between tectonic activity, climate and sea-level changes by adopting a synchronous correlation method to refine ages of dated and un-dated Late Quaternary uplifted palaeoshorelines are presented. Mapping and measurements of palaeoshorelines, tectonically-deformed by a Quaternary active normal fault (the Vibo Fault) has been carried out. The results show that within the Calabrian Arc, the uplift process outpaced the local effect of the hangingwall tectonic subsidence from the Vibo Fault allowing the uplift and preservation above the present-day sea-level of a well-exposed sequence of marine terraces; a correlation of palaeoshorelines across and around the tip of the NE-SW oriented Vibo Fault has been mapped. New long-term uplift rates are suggested, displaying a constant rate through time instead of fluctuating through time as claimed by previous authors. Values of uplift, produced by combined hangingwall subsidence and regional uplift, increase from the centre of the fault hangingwall towards the fault tip, suggesting faulting activity over the Late Quaternary. This suggests that perturbations of uplift mapped within active fault systems are key observations that help to identify and map active faults, their deformation rates and the associated seismic hazard above subduction zones.

4.2. Introduction

Rates of uplift resulting from the study of uplifted Late Quaternary marine terraces are generally the only way to derive rates of crustal deformation from plate boundary zones

over the timescales long-enough to average out deformation over several seismic cycles (10^4 – 10^5 years) (Roberts *et al.*, 2013). This is needed to cancel out transient strain-rates associated with individual seismic events or temporal earthquakes clustering, with the intention of using the obtained results for long-term seismic hazard analysis. However, age controls for sequences of marine terraces unfortunately exist only for a few palaeoshorelines in many examples. As described earlier in this thesis (see Chapter 2, section 2.5), a common way to derive ages for un-dated palaeoshorelines adjacent to dated palaeoshorelines is to assume that the next topographically higher or lower palaeoshoreline belongs to the next older or younger sea-level highstand (Armijo *et al.*, 1996; Tortorici *et al.*, 2003; Bianca *et al.*, 2011; Giunta *et al.*, 2012; Gallen *et al.*, 2014). However, this method, the so-called "sequential correlation method", is prone to fail in tectonically-active regions affected by low uplift rates (Roberts *et al.*, 2009; Roberts *et al.*, 2013; Pedoja *et al.*, 2018). This is because it has been recognized that in these regions palaeoshorleines representing sea-level highstands that were lower than present-day sea level are destroyed and/or overprinted by younger, higher sea-level highstands (Westaway, 1993; Roberts *et al.*, 2013) (see Chapter 2, section 2.5 – Figure 2.9 and 2.10). In this chapter, new results concerning long-term uplift rates, derived from Late Quaternary uplifted marine terraces, along the strike of the Vibo Fault (Calabria) are presented obtained by exploiting the new synchronous correlation approach described in the Methods chapter (see Chapter 3, section 3.4) (Figure 4.1).

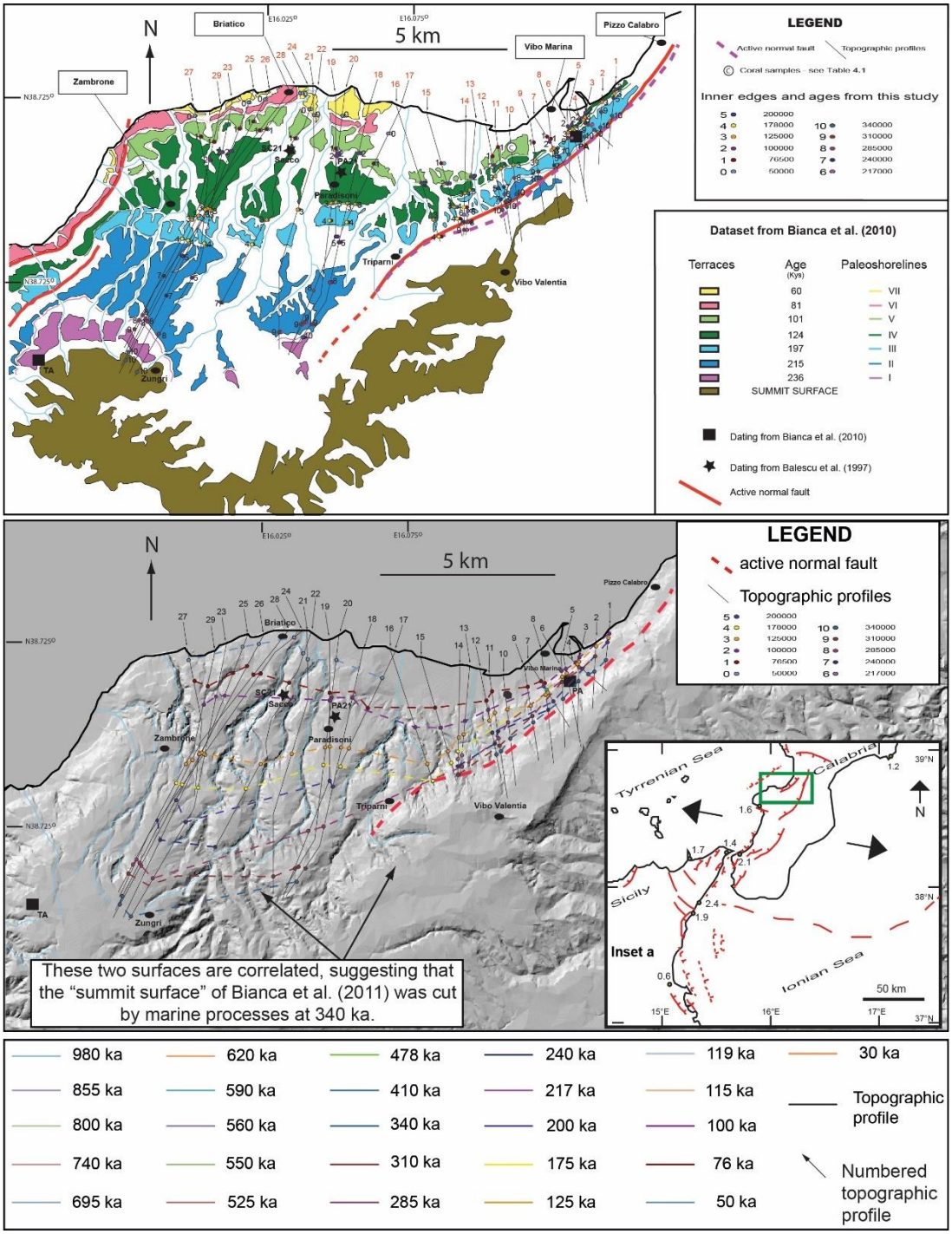

Figure 4.1: *Location maps for palaeoshorelines around the Vibo active normal fault. (a) Map amended from Bianca et al. (2011) showing the investigated area from Pizzo Calabro to Briatico. The locations of the studied 29 topographic profiles are shown, as are locations with age control from coral dates. The ages given in the lower panel are from Bianca et al. (2011), with the refined ages indicated in the upper panel and map with coloured dots, and again in (b). (b) Palaeoshorelines from this study shown on a 10 m DEM. Dashed lines link palaeoshoreline locations interpreted to be the same age from the synchronous correlation method.*

The case-study location lies within the upper plate of the subduction system (Calabrian Arc), that is affected by crustal extension confirmed by the presence of historical

seismicity (Gvirtzman and Nur, 1999a; Monaco and Tortorici, 2000), associated with the ongoing Ionian subduction process (Gutscher *et al.*, 2017). In particular, the Capo Vaticano promontory provides a well-exposed sequence of uplifted Late Quaternary palaeoshorelines along the strike of a normal fault (Vibo Fault), outcropping on both its hangingwall and footwall (Figure 4.1). This special set circumstances, with palaeoshorelines on the footwall and hangingwall, allows study of the slip-rate on the fault and how the fault-related vertical motion relate to more regional processes associated with subduction process. Some authors have investigated this sequence of palaeoshorelines claiming fluctuating uplift rates from 0.9mm/yr to 4mm/yr within the last 240ka (Tortorici *et al.*, 2003; Bianca *et al.*, 2011) (Figure 4.2).

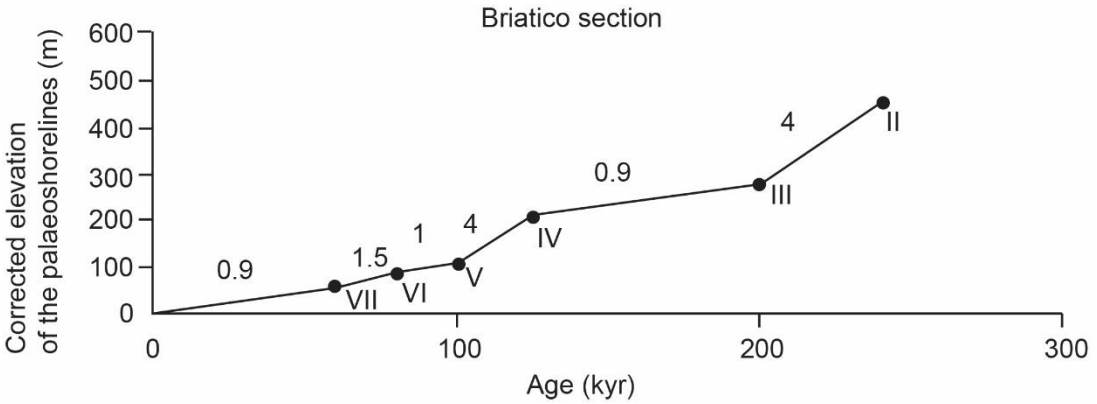

Figure 4.2: *Graph adapted from Tortorici et al., (2003) showing a dramatic uplift rate chages through time in the Capo Vaticano peninsula. Note that this section is parallel to profiles 26 and 28 shown in Figure 4.1.*

However, a lack of absolute ages for all palaeoshorelines has presumably driven these authors to assign ages for the un-dated palaeoshorelines by using a "sequential correlation approach". Furthermore, the role of the Vibo Fault activity within the investigated region is still unclear due to the fact that evidence of seismic activity from Holocene has not been clearly observed. However, historical earthquakes have occurred confirming the ongoing active extension which seem to have ruptured some faults around the investigated area. This chapter describes evidence that the Vibo Fault is also active (see Loreto *et al.*, 2013; Roberts *et al.*, 2013). For example, it is still debated if the 1905 AD earthquake, which caused extensive damage and loss

of life (Roberts *et al.*, 2013) could have ruptured the Vibo Fault, with an epicentre located a few kilometres NW from the investigated area. The earthquake produced more than 500 victims and prominent damage was recorded in many small towns such as Cessaniti, Vibo Valentia, Briatico and Bivona (Jacques *et al.*, 2001).

The aim of this chapter is testing the following scientific questions:

- Are the assigned ages for the un-dated marine terraces possibly in error due to the adopted "sequential correlation" method?
- Is the associated long-term uplift rate fluctuating or constant through time?
- Is this sequence of Late Quaternary palaeoshorelines and the associated uplift rates tectonically-controlled by the long-term activity on the Vibo Fault?

To address these scientific questions, detailed geomorphological mapping of palaeoshorelines and marine terraces have been undertaken using new high resolution Digital Elevation Models (DEMs) with 10 m resolution (Tarquini *et al.*, 2012) and an extensive field campaign. The work has exploited knowledge of the Quaternary sea-level curve and an iterative investigation of uplift rates, applying the "synchronous correlation approach" to predict expected sea-level highstands. Existing and new U/Th absolute dating of corals, confirming the age of a prominent palaeoshorelines, have been exploited. It is emphasised that this region provides an excellent opportunity because palaeoshorelines and the associated shallow marine deposits outcrop both on the hangingwall and the footwall of the Vibo Fault and around its tip (Figure 4.1). Moreover, the work has been exploited the fact that: (i) the fault is parallel to the present-day shoreline along its strike and (ii) hangingwall subsidence of the fault is outpaced by uplift, which is generally thought to have a "regional" origin (Balescu *et al.*, 1997; Jacques *et al.*, 2001; Tortorici *et al.*, 2003).

4.3. Methods and approach

In this chapter the approach used to test the scientific questions mentioned in Section 4.2 has been already explained in detail in Chapter 3. In this chapter, new U/Th dating on corals (Table 4.1) and previous Thermo-luminiscence dating (Balescu et al., 1997) have been used to drive the synchronous correlation approach.

4.3.1. Palaeoshoreline elevation data: DEM-based topographic analysis and fieldwork

Geomorphological analysis, by using 10 m high resolution DEMs (Tarquini *et al.*, 2007, 2012), and the associated fieldwork have been already explained in Chapter 3 (Section 3.1) (Figure 4.3). For this region, 29 topographic profiles have been derived (Figure 4.1) along the strike and on the hangingwall of the Vibo Fault, from its centre, towards and beyond its lateral fault tip. In particular, the field campaign has covered an area between Pizzo Calabro town and Briatico from NE to SW; palaeoshorelines have been mapped around the fault tip (Figure 4.1). The mapping also re-checked and partially re-mapped features studies by previous authors mapping (Tortorici et al., 2003; Bianca et al., 2011), focussing the attention on the 29 topographic profiles across the DEM.

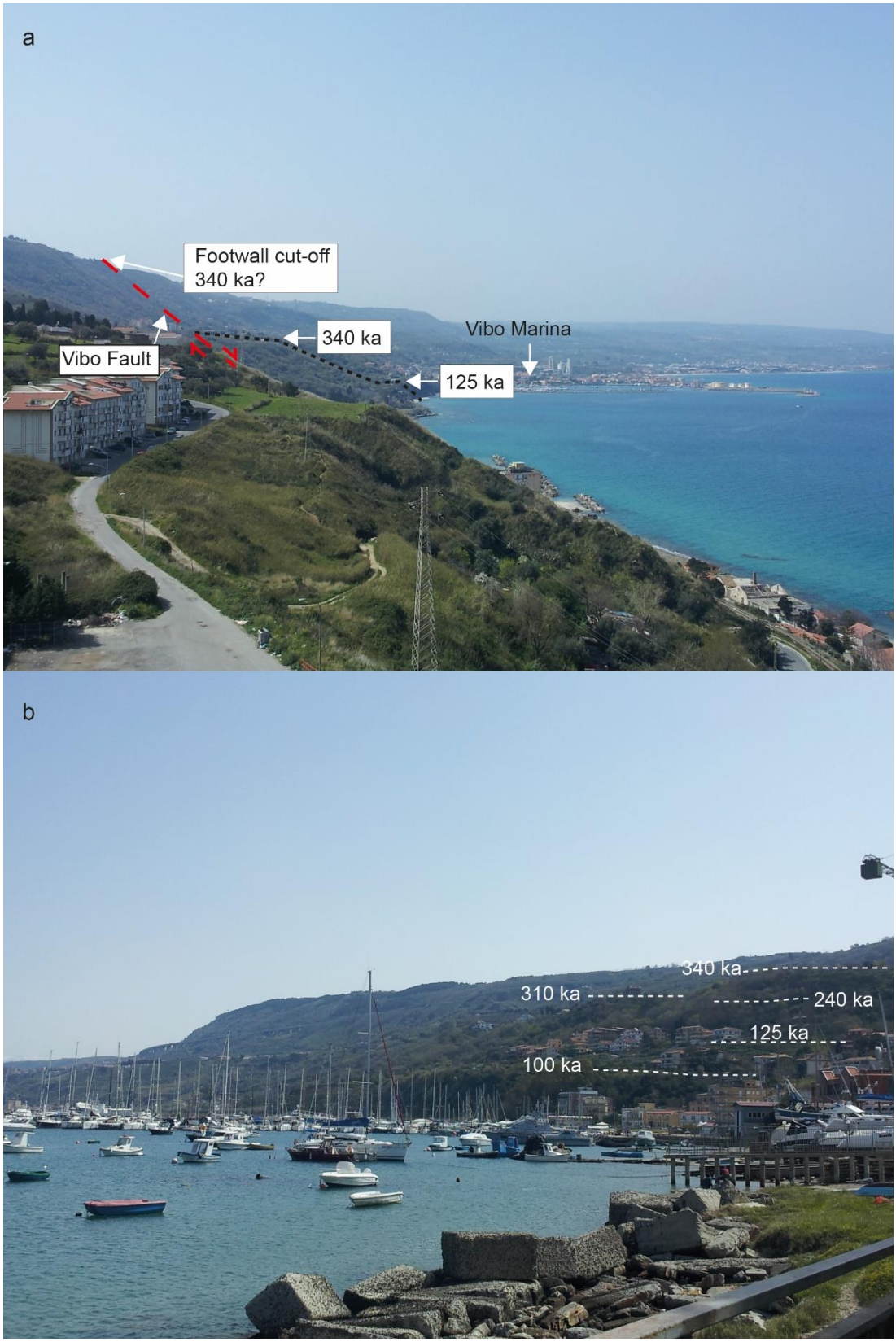

Figure 4.3: *In (a) marine terraces are shown outcropping on the hangingwall of the Vibo Fault. The footwall cut-off at ~ 500 m is mapped to derive Quaternary fault displacement. In (b) view of the marine terraces and palaeoshoreline indicators along Profile 4 (figure 4.1) are shown through Vibo Marina. Breaks of slope at 21, 60, 115, and 147 m are interpreted as the 100 ka, 125 ka, 240 ka, 310 ka and 340 ka palaeoshorelines. Modelling shown in Figure 4a for Profile 4 shows that we would expect the 240 ka and 310 ka to be within a few metres of each other in elevation, given the differences in global sea-level at those times.*

4.3.2. A synchronous correlation approach of multiple sea-level highstands with multiple Late Quaternary palaeoshorelines

An exhaustive and complete explanation of the synchronous correlation approach has been provided in the Methods chapter (see Section 3.4).

In general, this approach allows the correlation between multiple uplifted Late Quaternary palaeoshoreline elevations (measured elevations) and multiple sea-level highstands (predicted elevations), forcing the user to maximise the value R^2 achieved through multiple iterations of the uplift rate and linear regression. The approach forces geoscientists to investigate a sequence of marine terraces at the same time (or synchronously); this implies that the investigation is not biased to one preferred interpretation for a particular marine terrace age (Roberts *et al.*, 2013; Meschis et al. 2018; Pedoja *et al.*, 2018).

A new age control from absolute U/Th dating on corals (Table 4.1) has confirmed the age of a prominent palaeoshoreline (125 ka) in agreement with previous Thermo-luminescence dating by Balescu *et al.*, (1997). The obtained ages mark the onset of the "5e stage", as shown by previous studies, suggesting that corals grow and flourish during slow rise of sea level (Hearty *et al.*, 2007).

Sample	(230Th/234U)	Uncertainty (2 s.e.)	(234U/238U)	Uncertainty (2 s.e.)	Age (ka)	+	-
22	0.7148	0.00425	1.114	0.00390	132	1.62	1.62
23	0.7411	0.00431	1.113	0.00392	142	1.78	1.78

Table 4.1: *Measurements of U/Th isotope ratios of a coral sample collected near Vibo Marina town. The location of the collected corals is shown in Figure 4.1.*

This new date existed before this PhD, produced by a former PhD student, Dr. Sarah Houghton, but the date was not used during that PhD, and finally published in Roberts et al. (2013) with the present PhD candidate as a co-author. The new date, combined with the previous ones, have been used to drive the synchronous correlation approach allowing the

identification of new ages for the un-dated palaeoshorelines as shown in Figure 4.1; this suggests new insights into the uplift rate history spanning the Late Quaternary.

Assigning new palaeoshoreline ages by synchronously-predicting their elevations also allowed the correlation between the preserved and newly-dated palaeoshorelines outcropping on the hanginwall of the Vibo Fault with those outcropping in its footwall by mapping them around the lateral fault tip and linking them with the footwall cut-off of the 340 ka marine terrace. This has allowed the estimation of throw and throw-rate for the Vibo Fault over the Late Quaternary.

The elevation data used to help derive uplift rates were derived both from observations of DEMs and field observations using a hand-held barometric altimeter. The use of data from DEMs was necessary because thick vegetation and limited access on private houses meant that not all locations of interest could be visited in the field.

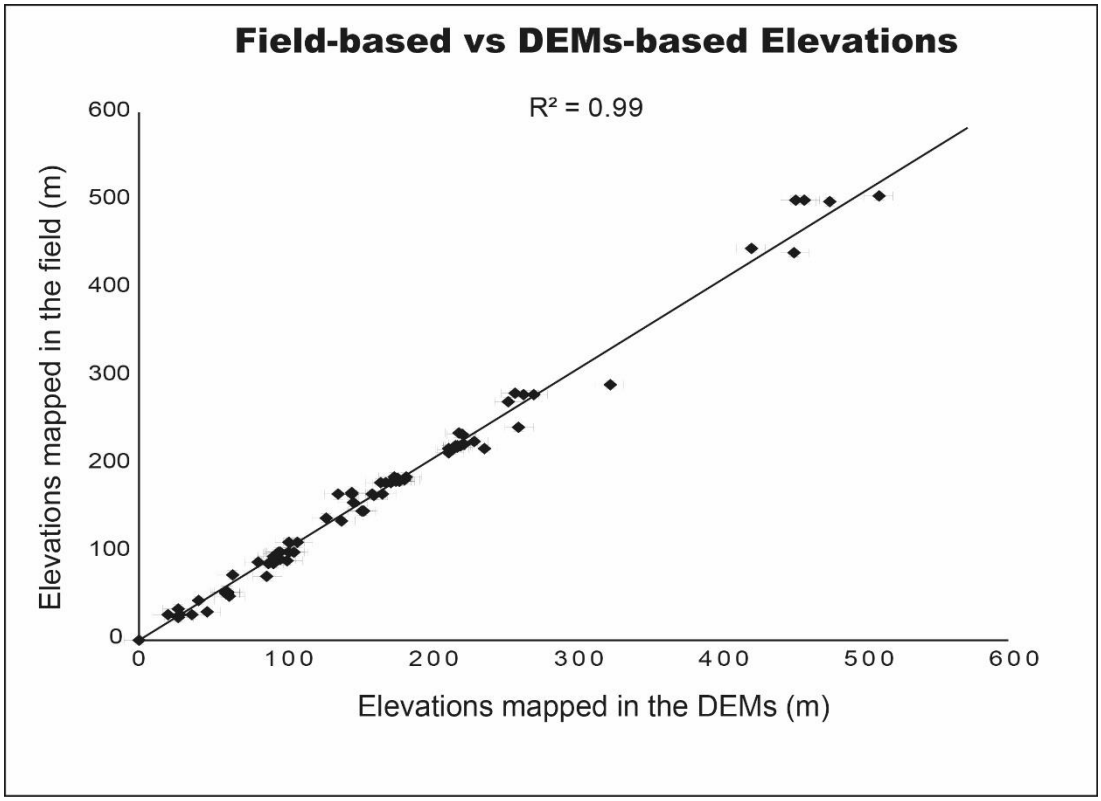

Figure 4.4: *Graph showing the relationship between DEM-based and field-based measurements of palaeoshoreline elevations. The R^2 value >0.99 confirms that mapped palaeoshoreline elevations agree with those from Bianca et al. (2011). Figure 4.1 shows how age determinations differ from Bianca et al. (2011).*

In particular, the field observations were used to ground truth identification of palaeoshoreline inner edges made on the DEM, and to check the elevations derived from the DEM were robust. A correlation between field and DEM-based elevation data demonstrates that elevations from DEM appear to be robust and appropriate to use in uplift rate calculations (Figure 4.4).

4.4. Results

In this section, firstly the approach adopted above allows the correlation between multiple palaeoshorelines and multiple sea-level highstands along the strike of the Vibo Fault. Then, temporal and spatial constrains on the marine terrace geometries are used to estimate and calculate long-term uplift rates and their relationship with displacements on the active Vibo normal fault.

Newly-mapped palaeoshoreline elevations with ages refined by applying a synchronous correlation approach are shown in Table 4.2; it is important to note that many palaeoshoreline locations were checked but not all due to thick vegetation and limited access on private houses. Detailed topographic analysis on high-resolution DEMs has allowed to derive exhaustive and complete topographic profiles that show gently sloping terraced surfaces bounded by steeper palaeo-seacliffs, interpreted as marine terraces as previous geoscientists (Armijo *et al.*, 1996; Roberts *et al.*, 2013).

Palaeoshoreline (Profile number)	Latitude	Longitude	Elevation from DEM	Elevation from barometric altimeter	Age assigned (Years)
2(1)	38°42'18,722"N	16°8'13,705"E	20		100000
3(1)	38°42'14,608"N	16°8'12,679"E	62	55	125000
5(1)	38°42'11,443"N	16°8'11,889"E	84		200000
10(1)	38°41'48,850"N	16°7'59,960"E	147	165	340000

3(2)	38°42'7,422"N	16°7'56,847"E	61	52	125000
9(2)	38°41'59,744"N	16°7'55,546"E	115		310000
10(2)	38°41'44,389"N	16°7'52,943"E	147	168	340000
2(3)	38°41'56,912"N	16°7'36,291"E	22		100000
3(3)	38°41'54,028"N	16°7'35,913"E	60	55	125000
8(3)	38°41'51,144"N	16°7'35,536"E	86		285000
10(3)	38°41'38,967"N	16°7'33,942"E	138	165	340000
2(4)	38°41'52,823"N	16°7'30,931"E	21		100000
3(4)	38°42'45,5913"N	16°7'48,9121"E	60	52	125000
9(4)	38°41'48,14"N	16°7'36,591"E	115		310000
10(4)	38°41'42,287"N	16°7'43,664"E	147	166	340000
2(5)	38°41'49,202"N	16°7'19,083"E	23		100000
3(5)	38°41'45,04"N	16°7'19,679"E	60	52	125000
2(6)	38°41'47,226"N	16°7'13,354"E	23		100000
3(6)	38°41'43,034"N	16°7'13,189"E	63	50	125000
4(6)	38°41'43,356"N	16°7'13,202"E	46		178000
9(6)	38°41'37,552"N	16°7'12,973"E	110		310000
10(6)	38°41'20,138"N	16°7'12,289"E	161	165	340000
1(7)	38°41'38,14"N	16°6'47,937"E	24		76500
2(7)	38°41'34,414"N	16°6'50,397"E	46		100000
3(7)	38°41'27,821"N	16°6'54,748"E	95	90	125000
5(7)	38°41'18,077"N	16°7'1,181"E	146		200000
1(8)	38°41'38,441"N	16°6'52,155"E	22		76500
3(8)	38°41'27,499"N	16°6'52,616"E	98	92	125000
7(8)	38°41'9,157"N	16°6'53,39"E	167	178	240000
1(9)	38°41'33,345"N	16°6'31,441"E	17		76500
3(9)	38°41'17,618"N	16°6'32,906"E	90	87	125000
9(9)	38°41'7,989"N	16°6'33,804"E	178	180	310000
10(9)	38°41'1,249"N	16°6'34,432"E	222	220	340000
3(10)	38°41'15,181"N	16°6'4,494"E	92	90	125000
8(10)	38°41'3,609"N	16°6'5,194"E	171	178	285000
10(10)	38°40'47,214"N	16°6'6,185"E	231	225	340000
1(11)	38°41'31,823"N	16°5'47,652"E	25		76500
3(11)	38°41'13,175"N	16°5'49,346"E	93	87	125000
7(11)	38°40'56,777"N	16°5'50,836"E	158		240000
9(11)	38°40'50,347"N	16°5'51,42"E	176	185	285000
9(11)	38°40'41,344"N	16°5'52,238"E	203		310000
10(11)	38°40'33,627"N	16°5'52,939"E	238	217	340000
1(12)	38°41'25,851"N	16°5'40,105"E	23		76500
2(12)	38°41'16,906"N	16°5'41,667"E	42	45	100000
3(12)	38°41'4,448"N	16°5'43,843"E	104	100	125000
5(12)	38°40'53,906"N	16°5'45,684"E	160		200000
7(12)	38°40'43,044"N	16°5'47,581"E	185	185	240000
10(12)	38°40'29,946"N	16°5'49,868"E	263		340000
2(13)	38°41'7,78"N	16°5'14,018"E	65	73	100000
3(13)	38°40'56,03"N	16°5'11,524"E	110	110	125000
6(13)	38°40'36,658"N	16°5'7,414"E	155	147	217000
8(13)	38°40'23,003"N	16°5'4,517"E	220		285000
3(14)	38°40'51,295"N	16°5'3,98"E	130	138	125000
4(14)	38°40'38,143"N	16°5'2,146"E	148	156	178000
6(14)	38°40'29,481"N	16°5'0,939"E	176		217000
7(14)	38°40'23,066"N	16°5'0,045"E	232		240000
9(14)	38°40'13,442"N	16°4'58,703"E	287		310000
1(15)	38°41'19,718"N	16°4'38,143"E	45		76500
2(15)	38°41'4,884"N	16°4'42,177"E	93	95	100000

3(15)	38°40'39,95"N	16°4'48,957"E	140	135	125000
4(15)	38°40'29,219"N	16°4'51,875"E	168	165	178000
2(16)	38°41'5,727"N	16°4'12,428"E	94	92	100000
3(16)	38°40'27,73"N	16°4'23,571"E	162	164	125000
4(16)	38°40'11,401"N	16°4'28,359"E	202		178000
0(17)	38°41'55,715"N	16°3'40,489"E	22		50000
1(17)	38°41'27,921"N	16°3'19,639"E	77		76500
3(17)	38°40'51,231"N	16°2'52,125"E	180	181	125000
4(17)	38°40'32,608"N	16°2'38,162"E	221	235	178000
2(18)	38°41'33,077"N	16°2'59,19"E	93	91	100000
3(18)	38°40'52,949"N	16°2'43,692"E	174	178	125000
5(18)	38°40'15,907"N	16°2'29,39"E	278		200000
8(18)	38°39'39,173"N	16°2'15,213"E	355		285000
9(18)	38°39'1,179"N	16°1'48,473"E	394		310000
10(18)	38°38'46,095"N	16°1'32,992"E	452	440	340000
1(19)	38°41'42,934"N	16°2'33,294"E	72		76500
2(19)	38°41'36,826"N	16°2'32,66"E	107	99	100000
3(19)	38°40'53,106"N	16°2'28,123"E	179	183	125000
5(19)	38°40'22,307"N	16°2'24,635"E	262	242	200000
9(19)	38°38'58,572"N	16°1'33,7"E	406		310000
0(20)	38°42'10,444"N	16°2'43,894"E	28	25	50000
2(20)	38°41'32,187"N	16°2'34,235"E	97	100	100000
3(20)	38°40'54,562"N	16°2'24,739"E	184	182	125000
4(20)	38°40'34,642"N	16°2'19,713"E	223	233	178000
9(20)	38°38'56,706"N	16°1'34,079"E	414		310000
0(21)	38°42'22,146"N	16°2'10,776"E	29	28	50000
3(21)	38°40'43,649"N	16°1'37,635"E	180	180	125000
9(21)	38°38'54,219"N	16°1'9,525"E	422	445	310000
0(22)	38°42'26,247"N	16°2'9,3"E	21		50000
1(22)	38°41'57,105"N	16°1'49,633"E	83	88	76500
3(22)	38°40'41,653"N	16°1'5,085"E	214	212	125000
4(22)	38°40'19,421"N	16°0'45,861"E	255	270	178000
7(22)	38°39'24,564"N	16°0'1,253"E	375		240000
2(23)	38°42'5,631"N	16°0'24,939"E	154		100000
3(23)	38°40'55,327"N	15°59'58,956"E	224	222	125000
4(23)	38°40'23,426"N	15°59'47,172"E	272	278	178000
5(23)	38°39'50,604"N	15°59'28,382"E	345		200000
7(23)	38°39'1,89"N	15°58'45,993"E	477	498	285000
0(24)	38°42'38,434"N	16°1'58,561"E	20	28	50000
1(24)	38°42'4,87"N	16°1'11,261"E	98	100	76500
3(24)	38°40'54,256"N	15°59'57,747"E	220	219	125000
4(24)	38°40'26,619"N	15°59'29,422"E	266	278	178000
7(24)	38°39'55,171"N	15°58'57,296"E	390		240000
8(24)	38°39'19,513"N	15°58'26,612"E	443		285000
0(25)	38°42'27,803"N	16°0'50,353"E	37	28	50000
1(25)	38°42'7,923"N	16°0'38,604"E	104	110	76500
2(25)	38°41'47,75"N	16°0'26,685"E	163		100000
3(25)	38°40'56,148"N	15°59'54,808"E	219	220	125000
7(25)	38°39'39,473"N	15°58'58,615"E	413		240000
10(25)	38°38'26,426"N	15°58'5,121"E	570		340000
0(26)	38°42'23,563"N	16°1'4,562"E	47	32	50000
1(26)	38°42'13,202"N	16°0'56,189"E	89	72	76500
3(26)	38°40'54,663"N	15°59'52,756"E	219	220	125000
5(26)	38°40'13,207"N	15°59'19,294"E	325	290	200000
8(26)	38°39'15,926"N	15°58'33,083"E	459	500	285000

10(26)	38°38'35,825"N	15°58'0,747"E	571		340000
0(27)	38°42'24,993"N	15°59'47,704"E	27	35	50000
1(27)	38°42'2,336"N	15°59'51,427"E	109		76500
3(27)	38°40'54,24"N	15°59'51,511"E	216	216	125000
1(28)	38°42'6,017"N	16°1'5,017"E	96	98	76500
3(28)	38°40'46,54"N	15°59'41,06"E	214	218	125000
8(28)	38°39'20,454"N	15°58'33,637"E	453	500	285000
10(28)	38°38'42,769"N	15°58'4,141"E	572		340000
1(29)	38°42'0,933"N	16°0'8,91"E	103	90	76500
2(29)	38°41'41,455"N	16°0'1,462"E	154	147	100000
3(29)	38°40'48,886"N	15°59'36,501"E	220	220	125000
4(29)	38°40'30,624"N	15°59'21,762"E	260	280	178000
8(29)	38°39'21,113"N	15°58'25,687"E	442		285000
9(29)	38°39'8,028"N	15°58'15,135"E	510	505	310000

Table 4.2: *All mapped inner edges from DEM and fieldwork with age assigned via synchronous correlation are shown. Note that not all the locations for inner edges mapped by DEM analysis with GPS in the field have been checked because the investigated area is in places thickly-vegetated and densely-populated with private properties.*

It is important to note that for a few marine terraces mapped over the fault tip, where higher uplift is recorded, some discrepancies between "measured" and "expected" elevations" are evidenced. This could be related to the sum of the margin of errors associated to DEMs (10 m), the hand-held barometric altimeter (5 m) and the longer action of erosion through time for higher and older raised palaeoshorelines such as the ones associated to the 285 ka and the 340 ka highstands. Nonetheless, it is not yet proved that the area over the tip where Profile 26, 27, 28 and 29 intercept marine terraces could be affected by local footwall uplift from other normal faults which bound the Capo Vaticano peninsula.

Figure 4.5 shows interpreted palaeoshoreline locations on each topographic profile. It is important to highlight that the interpreted locations are in a very good agreement with those of Tortorici et al., (2003) and Bianca et al., (2011) who have already studied this area; however, age of palaeoshorelines needed to be reviewed (Figure 4.4).

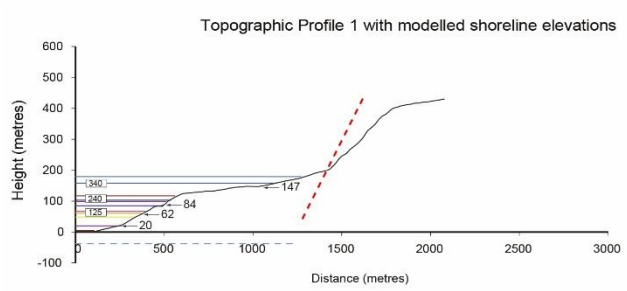
Topographic Profile 1 with modelled shoreline elevations
Height (metres)
Distance (metres)
340
240
125
147
84
62
20

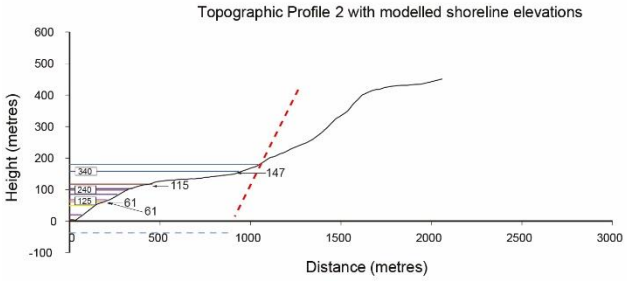
Topographic Profile 2 with modelled shoreline elevations
Height (metres)
Distance (metres)
340
240
125
147
115
61
61

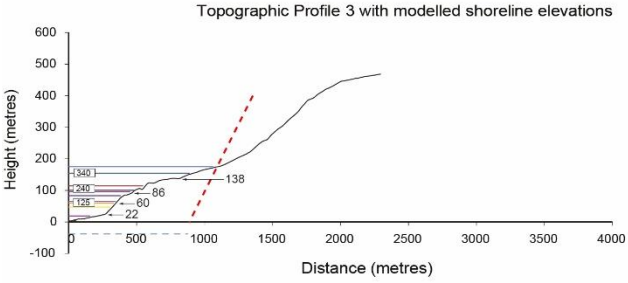
Topographic Profile 3 with modelled shoreline elevations
Height (metres)
Distance (metres)
340
240
125
138
86
60
22

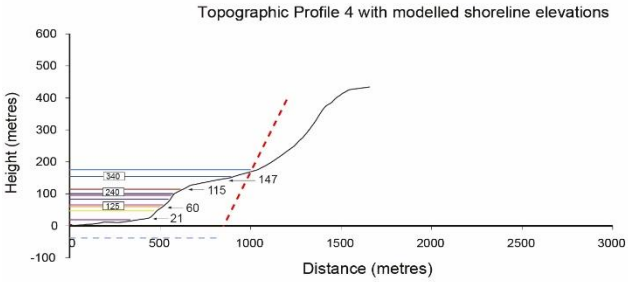
Topographic Profile 4 with modelled shoreline elevations
Height (metres)
Distance (metres)
340
240
125
147
115
60
21

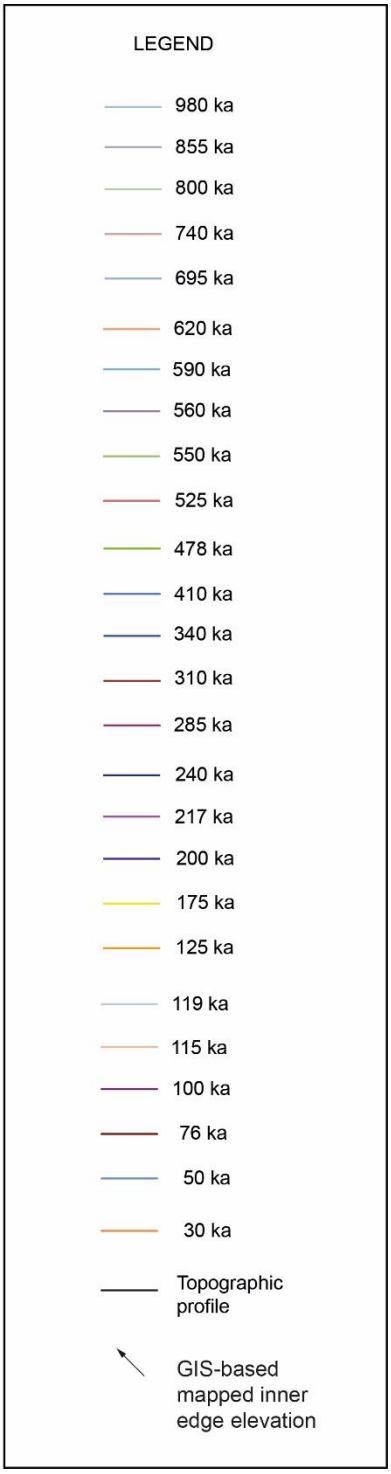
LEGEND
980 ka
855 ka
800 ka
740 ka
695 ka
620 ka
590 ka
560 ka
550 ka
525 ka
478 ka
410 ka
340 ka
310 ka
285 ka
240 ka
217 ka
200 ka
175 ka
125 ka
119 ka
115 ka
100 ka
76 ka
50 ka
30 ka
Topographic profile
GIS-based mapped inner edge elevation

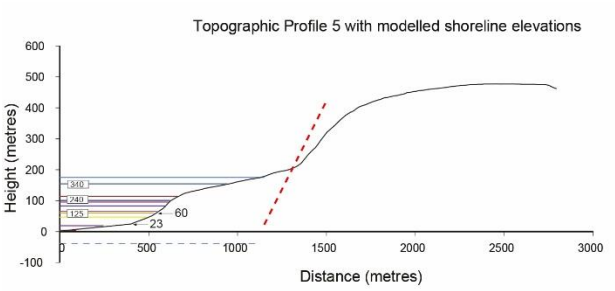
Topographic Profile 5 with modelled shoreline elevations
Height (metres)
Distance (metres)
340
240
125
60
23

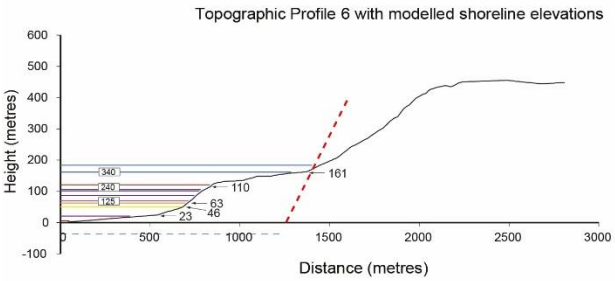
Topographic Profile 6 with modelled shoreline elevations
Height (metres)
Distance (metres)
340
240
125
161
110
63
46
23

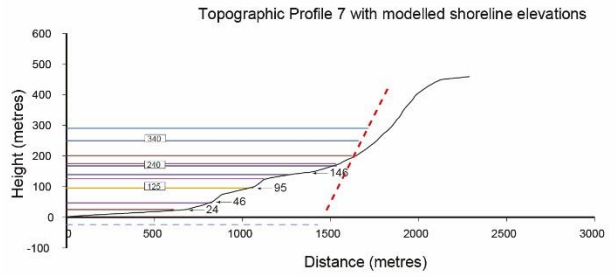
Topographic Profile 7 with modelled shoreline elevations
Height (metres)
Distance (metres)
340
240
125
146
95
46
24

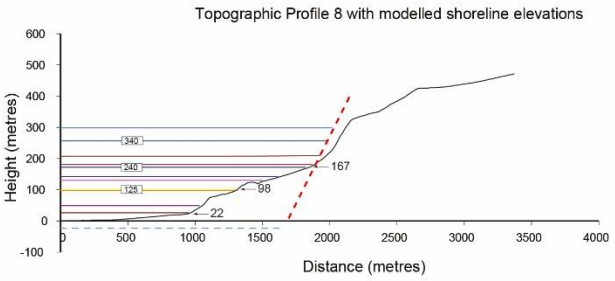
Topographic Profile 8 with modelled shoreline elevations
Height (metres)
Distance (metres)
340
240
125
167
98
22

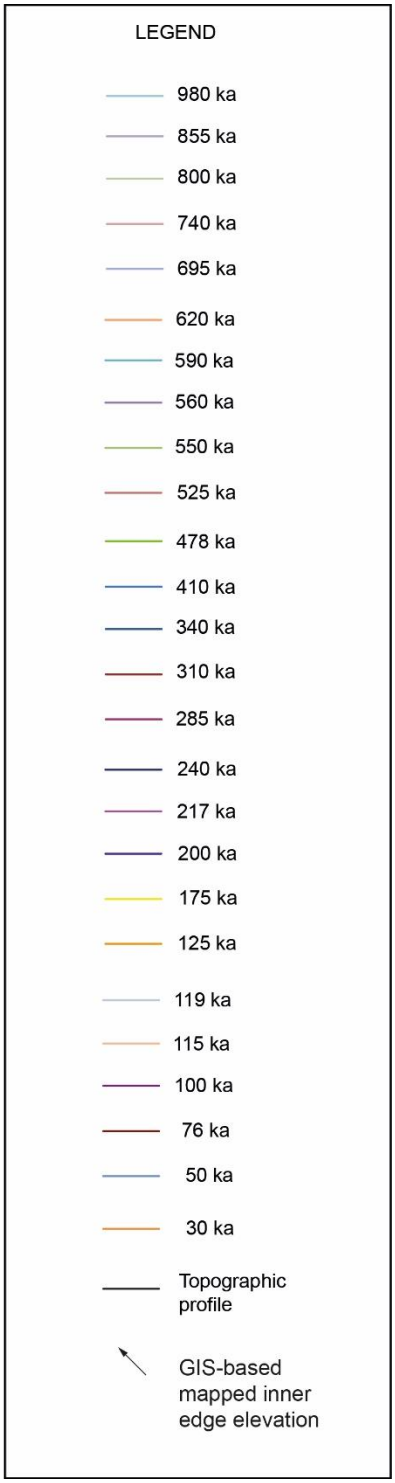
LEGEND
980 ka
855 ka
800 ka
740 ka
695 ka
620 ka
590 ka
560 ka
550 ka
525 ka
478 ka
410 ka
340 ka
310 ka
285 ka
240 ka
217 ka
200 ka
175 ka
125 ka
119 ka
115 ka
100 ka
76 ka
50 ka
30 ka
Topographic profile
GIS-based mapped inner edge elevation

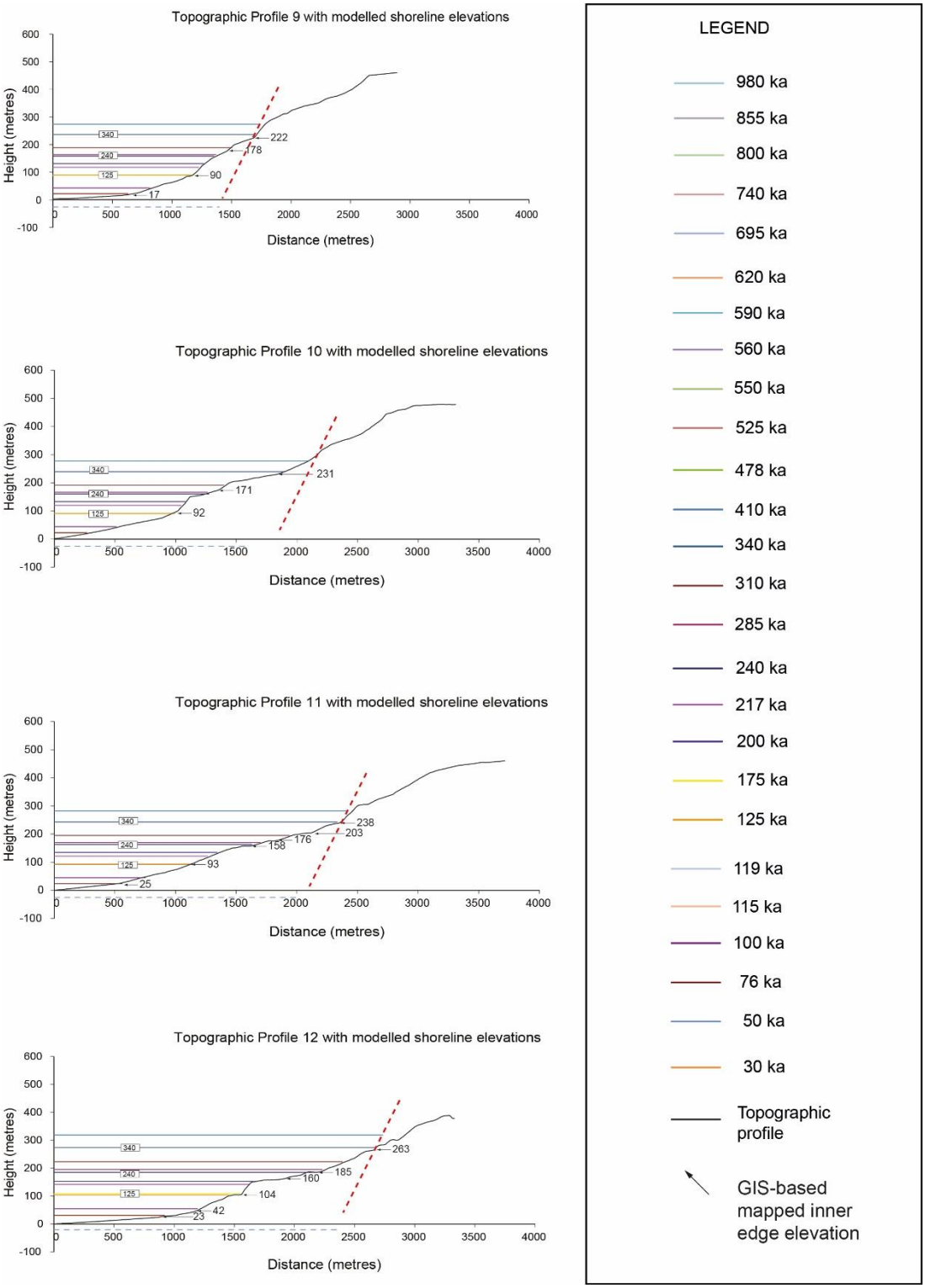
Topographic Profile 9 with modelled shoreline elevations
Height (metres)
Distance (metres)
340
240
125
222
178
90
17
Topographic Profile 10 with modelled shoreline elevations
231
171
92
Topographic Profile 11 with modelled shoreline elevations
238
203
176
158
93
25
Topographic Profile 12 with modelled shoreline elevations
263
185
160
104
42
23
LEGEND
980 ka
855 ka
800 ka
740 ka
695 ka
620 ka
590 ka
560 ka
550 ka
525 ka
478 ka
410 ka
340 ka
310 ka
285 ka
240 ka
217 ka
200 ka
175 ka
125 ka
119 ka
115 ka
100 ka
76 ka
50 ka
30 ka
Topographic profile
GIS-based mapped inner edge elevation

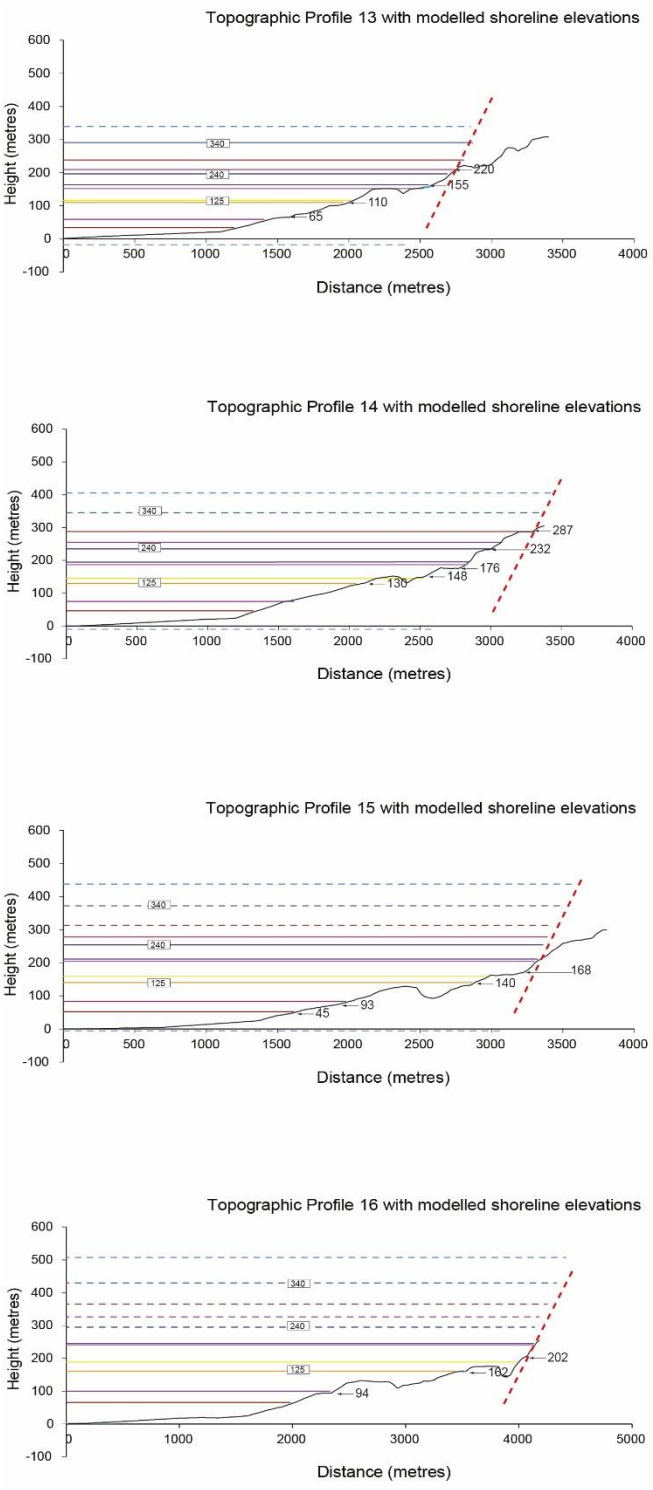
Topographic Profile 13 with modelled shoreline elevations
Height (metres)
Distance (metres)
340
240
125
220
155
110
65
Topographic Profile 14 with modelled shoreline elevations
Height (metres)
Distance (metres)
340
240
125
287
232
176
148
130
Topographic Profile 15 with modelled shoreline elevations
Height (metres)
Distance (metres)
340
240
125
168
140
93
45
Topographic Profile 16 with modelled shoreline elevations
Height (metres)
Distance (metres)
340
240
125
202
182
94

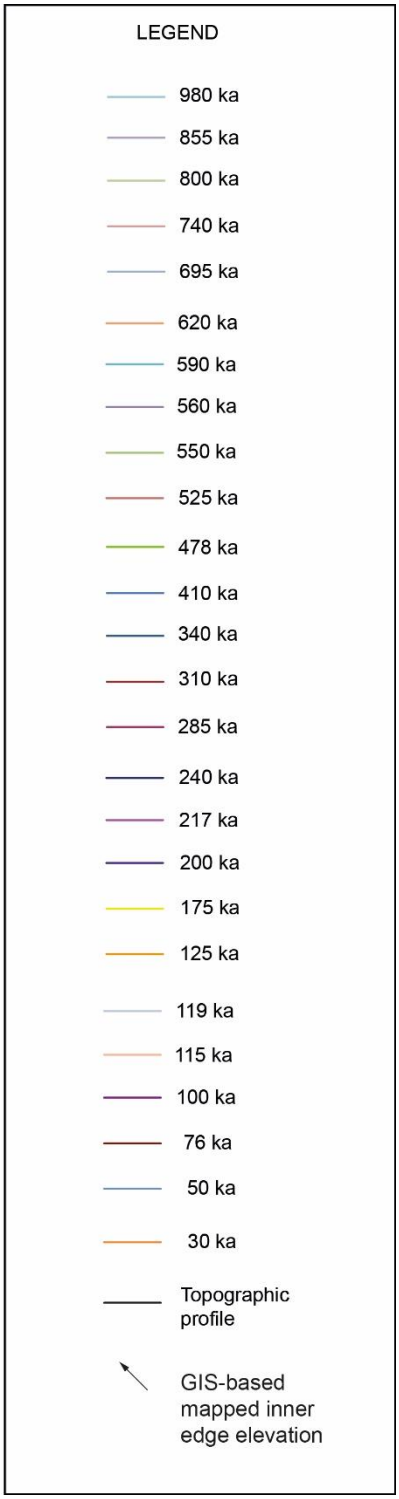
LEGEND
980 ka
855 ka
800 ka
740 ka
695 ka
620 ka
590 ka
560 ka
550 ka
525 ka
478 ka
410 ka
340 ka
310 ka
285 ka
240 ka
217 ka
200 ka
175 ka
125 ka
119 ka
115 ka
100 ka
76 ka
50 ka
30 ka
Topographic profile
GIS-based mapped inner edge elevation

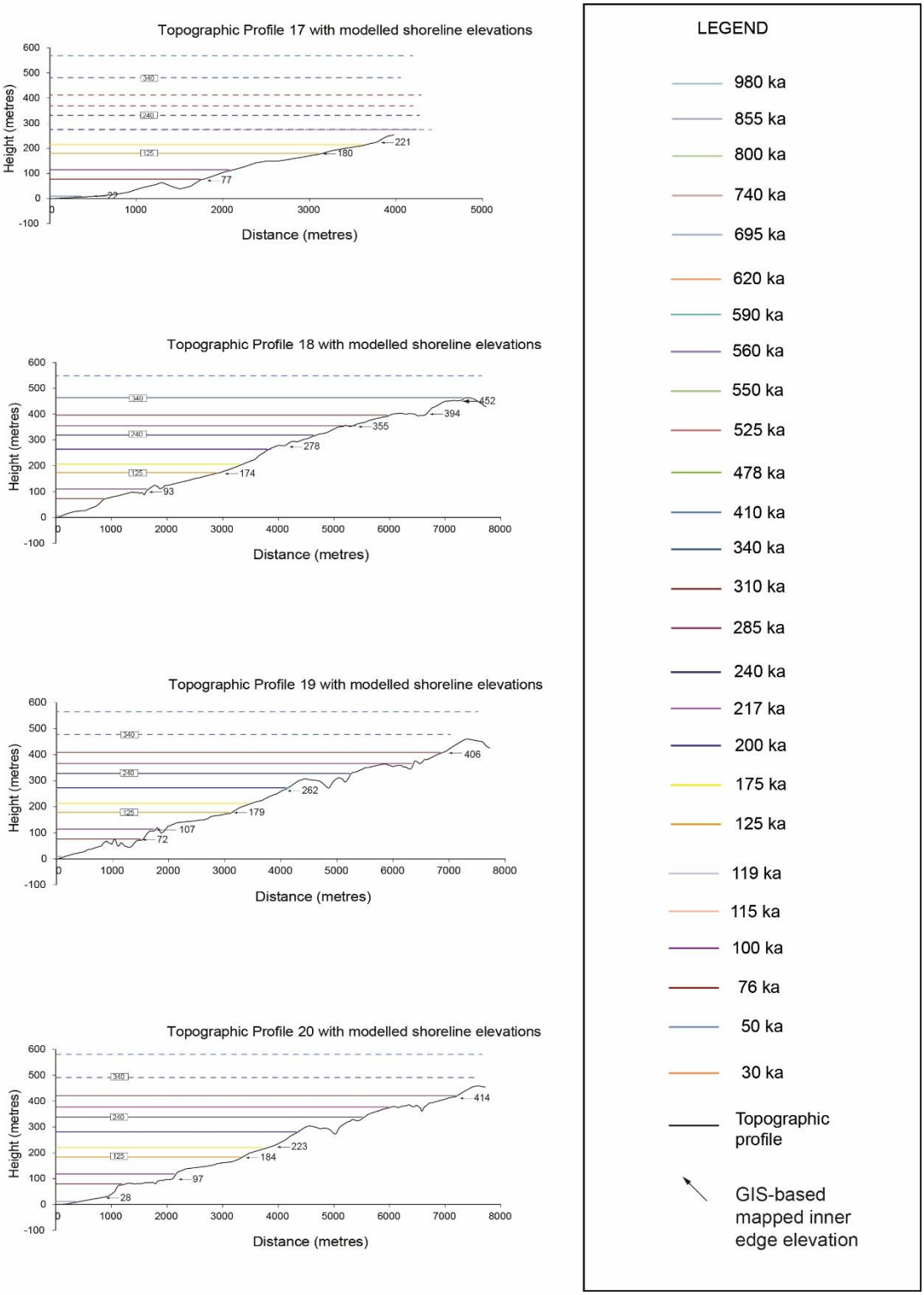
Topographic Profile 17 with modelled shoreline elevations
Height (metres)
Distance (metres)
340
240
125
221
180
77
22
Topographic Profile 18 with modelled shoreline elevations
452
394
355
278
174
93
Topographic Profile 19 with modelled shoreline elevations
406
262
179
107
72
Topographic Profile 20 with modelled shoreline elevations
414
223
184
97
28
LEGEND
980 ka
855 ka
800 ka
740 ka
695 ka
620 ka
590 ka
560 ka
550 ka
525 ka
478 ka
410 ka
340 ka
310 ka
285 ka
240 ka
217 ka
200 ka
175 ka
125 ka
119 ka
115 ka
100 ka
76 ka
50 ka
30 ka
Topographic profile
GIS-based mapped inner edge elevation

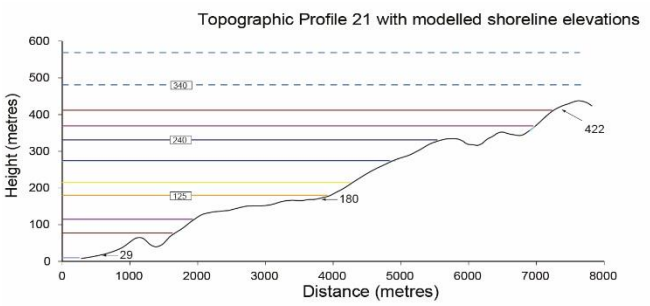
Topographic Profile 21 with modelled shoreline elevations
Height (metres)
Distance (metres)
340
240
125
422
180
29

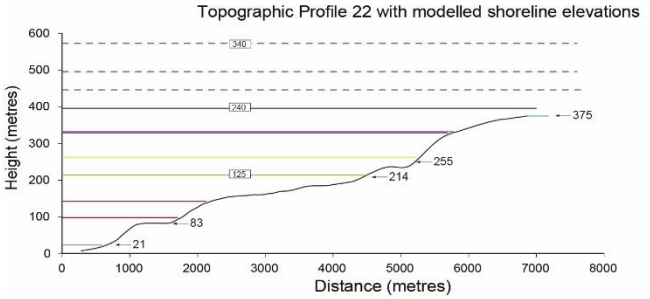
Topographic Profile 22 with modelled shoreline elevations
Height (metres)
Distance (metres)
340
240
125
375
255
214
83
21

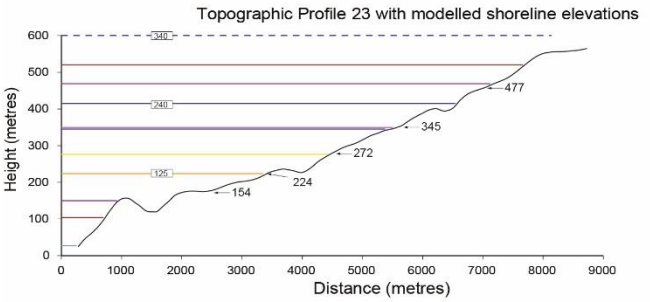
Topographic Profile 23 with modelled shoreline elevations
Height (metres)
Distance (metres)
340
240
125
477
345
272
224
154

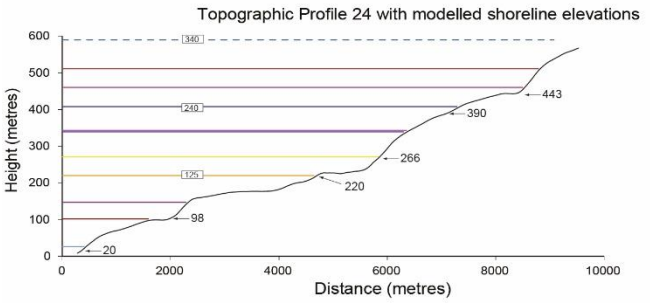
Topographic Profile 24 with modelled shoreline elevations
Height (metres)
Distance (metres)
340
240
125
443
390
266
220
98
20

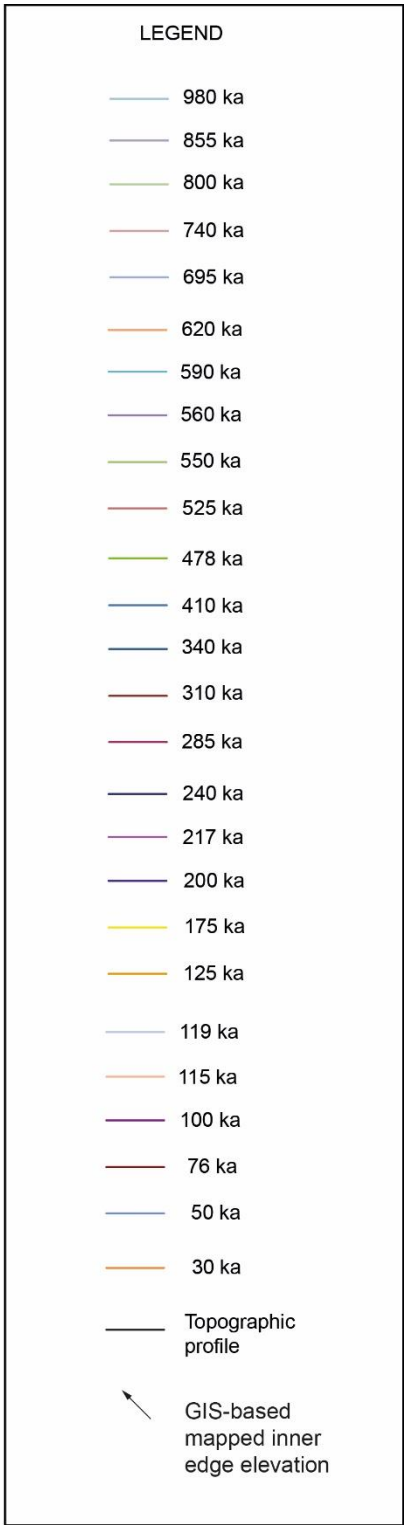
LEGEND
980 ka
855 ka
800 ka
740 ka
695 ka
620 ka
590 ka
560 ka
550 ka
525 ka
478 ka
410 ka
340 ka
310 ka
285 ka
240 ka
217 ka
200 ka
175 ka
125 ka
119 ka
115 ka
100 ka
76 ka
50 ka
30 ka
Topographic profile
GIS-based mapped inner edge elevation

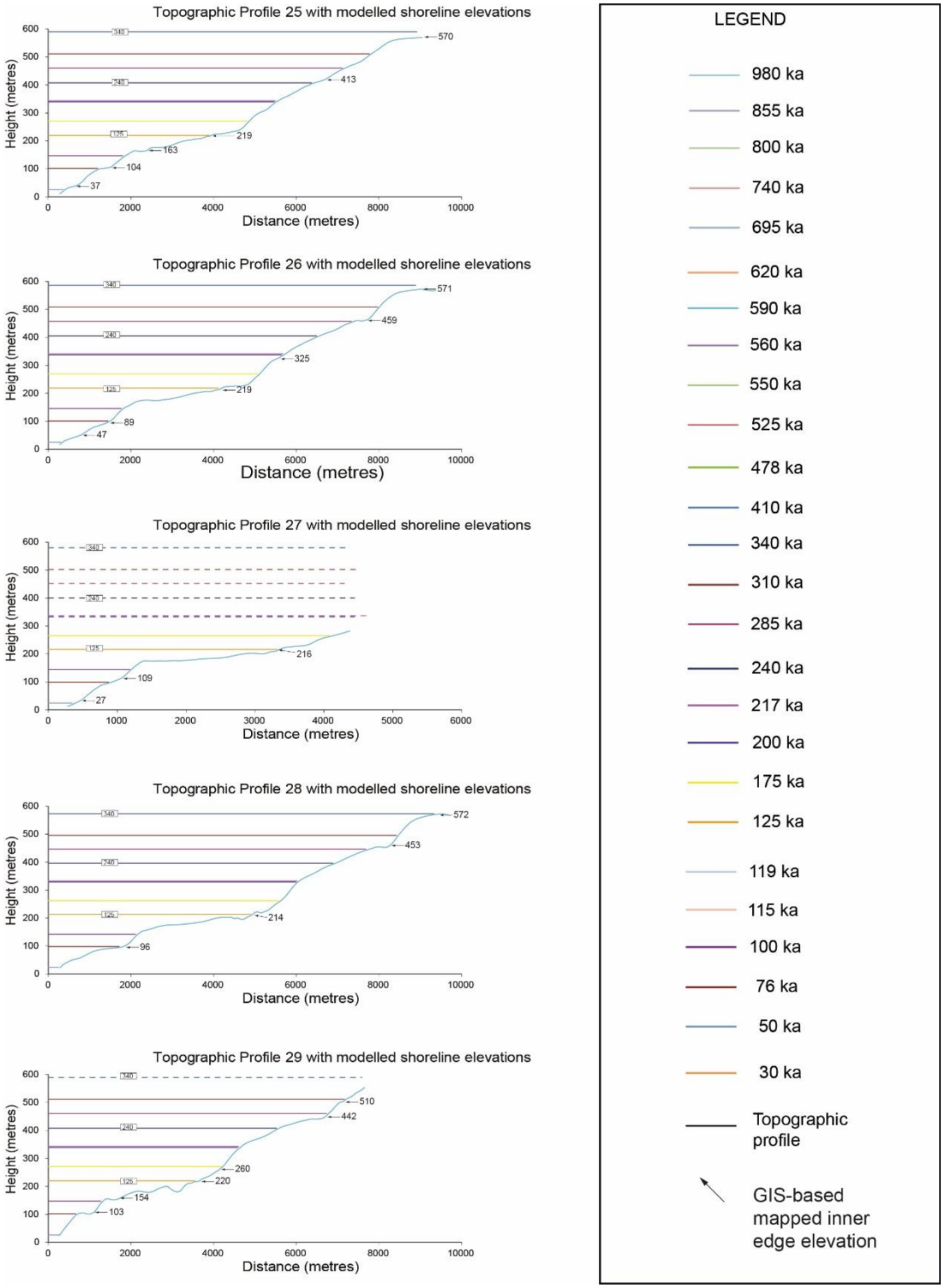

Figure 4.5: *Profiles showing mapped and modelled palaeoshoreline elevations. The topographic profile is from the 10 m DEM. The numbers with arrows mark the elevations of palaeoshorelines mapped in the field. The coloured lines indicate palaeoshoreline elevations predicted by an uplift rate that has been changed iteratively to produce the best match with the mapped palaeoshorelines; goodness of fit is indicated by the value for slope and the R^2 values in figure 4.4. Profiles are located on figure 4.1.*

Figure 4.6 is constructed to show the robustness (R^2 values close to 1) of the correlation between the measured palaeoshoreline elevations and the those iteratively

calculated (predicted elevations) given: (i) an uplift rate value driven by new age controls and (ii) fixed values for sea-level relative to present-day sea-level for several highstands presented by Siddall *et al.*, (2003) (Table 2.1, Chapter 2).

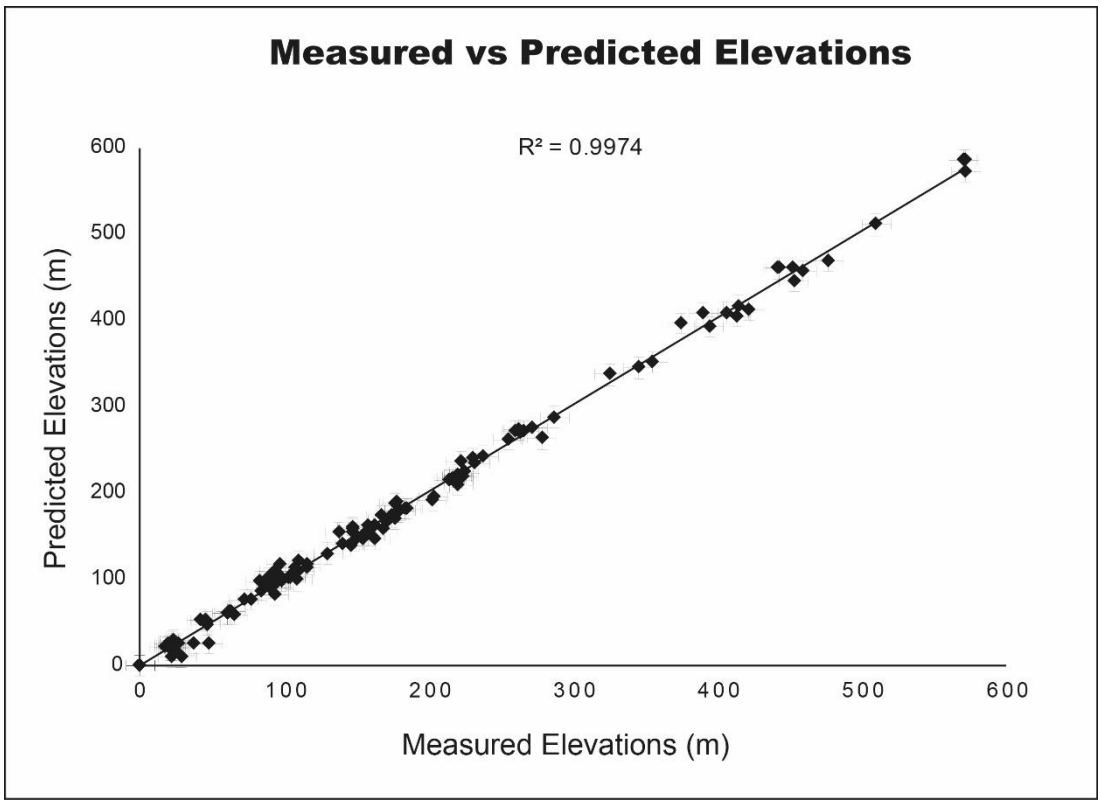

Figure 4.6: *Graph showing linear regression between measured and predicted palaeoshoreline elevations. The predicted elevations have been generated by defining a constant uplift rate through time and iterating this value to produce a best fit to the measured palaeoshorelines. Best fit is quantified by R^2 values that are >0.99 for all 29 graphs with slopes close to 1.*

In particular, values of R^2 >0.99 between "predicted" and "measured" elevations also imply that the uplift rate has not fluctuated through time as previously claimed (Tortorici *et al.*, 2003; Bianca *et al.*, 2011; see Figure 4.2) using a "sequential correlation approach". Moreover, this correlation indicates the presence of marine terraces belonging to the 50ka 76ka, 100 ka, 125 ka, 178 ka, 200 ka, 217 ka, 240 ka, 285 ka 310 ka and 340 ka highstands. The identification of such a large number of palaeoshorelines is perhaps surprising, as some studies that rely on sequential correlation tend to identify fewer examples. However, where detailed mapping has been carried out, and in some examples where the synchronous correlation forces the user to

consider all late Quaternary sea-level highstands, the above sequence of ages appears to be distinctive for marine terraces mapped in the Mediterranean and elsewhere (Roberts *et al.*, 2009; Roberts *et al.*, 2013; Binnie *et al.*, 2016; Pedoja *et al.*, 2018). It is important to note that implied, newly-assigned age for the un-dated palaeoshorelines are different to those assigned by Tortorici et al., (2003) and Bianca et al., (2011). For instance, along topographic Profile 2 they assign, by using a sequential correlation approach, an age of 197 ka (light blue colour, Terrace V) to the highest mapped marine terrace outcropping on the hangingwall of the Vibo Fault; the synchronous correlation approach allows the identification of a new age for the same terrace, suggesting instead that their "Terrace V" belongs to the 340 ka highstand, implying a different uplift rate history.

Figures 4.7 and 4.8 summarise the along strike variation in uplift implied by the synchronous correlations made in this thesis.

Figure 4.7 shows that palaeoshorelines identified on individual topographic profiles can be correlated along strike. The correlation shows that individual palaeoshorelines can be traced along strike, changing in elevation. This tilted geometry suggests that uplift rates increase towards the SW, towards the SW tip of the Vibo Fault (Figure 4.8). It is remarkable to note that the tilting has occurred for each and every palaeoshoreline, with tilt angles increasing for progressively-older palaeoshorelines (Figure 4.9). The uplift rates increase from ~0.45 mm/yr to ~1.75 mm/yr over the ~12.5 km extent of the study (Figure 4.8). The tilt angles increase from 0.75 degrees for the 125 ka palaeoshoreline to 2.25 degrees for the 340 ka palaeoshoreline.

The above observations are remarkable because they occur in the hangingwall of the Vibo Fault where, at first sight, one might expect subsidence. Uplift in the hangingwall of the

Vibo Fault presumably results from a combination of "regional" uplift, related to larger scale tectonic processes (discussed later in the thesis; Chapter 9), and local fault-controlled tectonic subsidence. This suggests that the Vibo Fault is active, and its activity is counteracting the "regional" uplift signal.

Another important feature is the progressive increase in tilt angle for successively older palaeoshorelines. Figures 4.7 and 4.9 show that higher and older palaeoshorelines show higher value of titling angle. This observation is explained herein by the suggestion that older and higher palaeoshorelines have experienced a longer history of faulting, accruing higher tilt angles, and implying activity for the Vibo Fault throughout the Late Quaternary. This pattern of higher tilt angles is suggested to be characteristic of active faulting (e.g. Armijo *et al.*, 1996; Roberts *et al.*, 2009; Roberts *et al.*, 2013; Meschis *et al.*, 2018). However, note that not all of these ages are identified on each profile, because where uplift rates are at lower values, fewer palaeoshorelines are preserved.

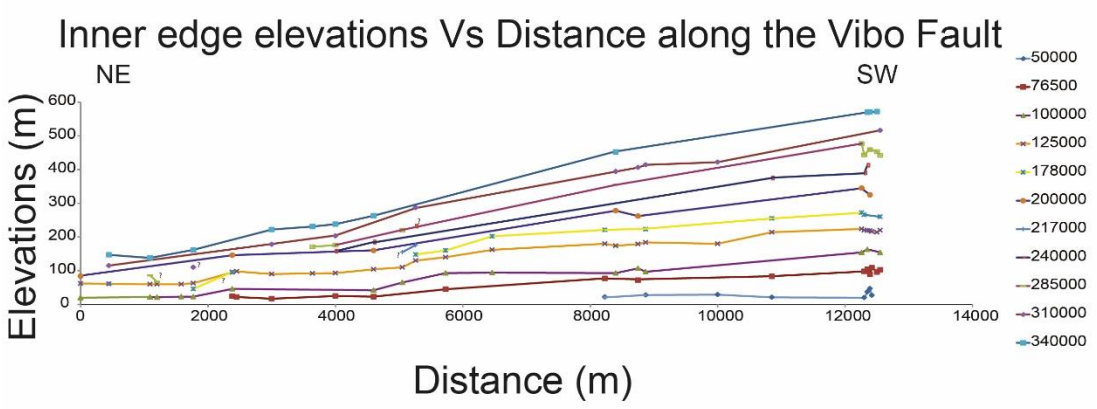

Figure 4.7: *Profiles showing tilting of palaeoshorelines whose ages are defined by the modelling in figures 4.5 and 4.6. Solid lines show extrapolations between modelled topographic profiles 1-29.*

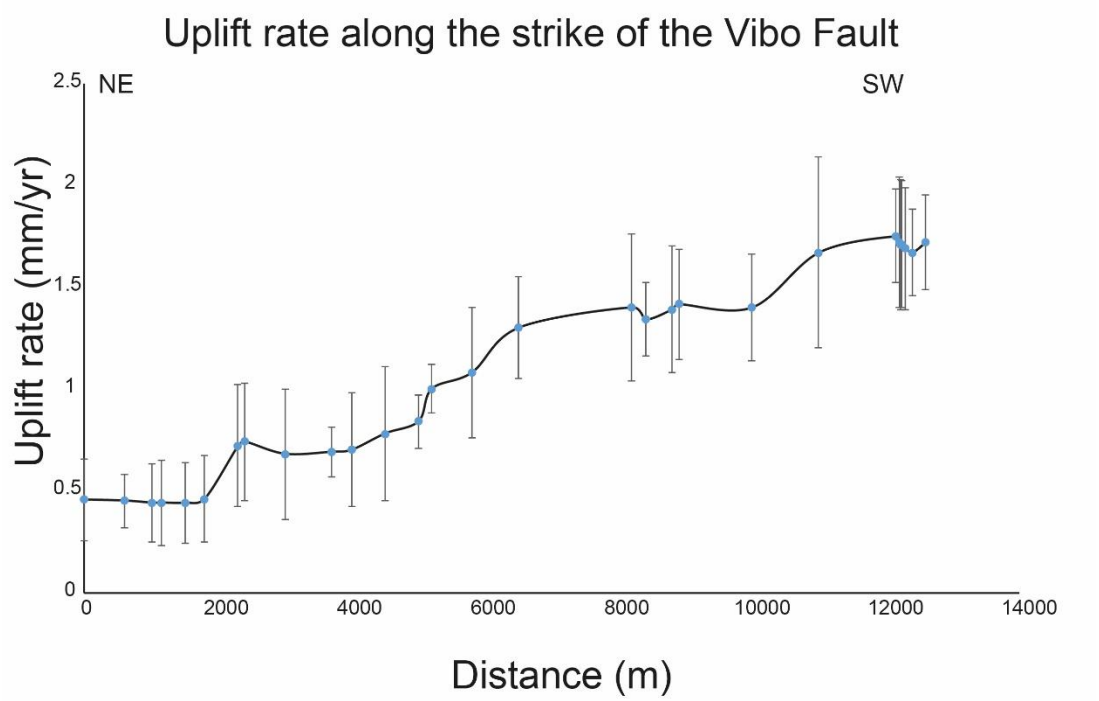

Figure 4.8: *Profile showing how uplift rates derived from modelling shown in figures 4.2 and 4.4*

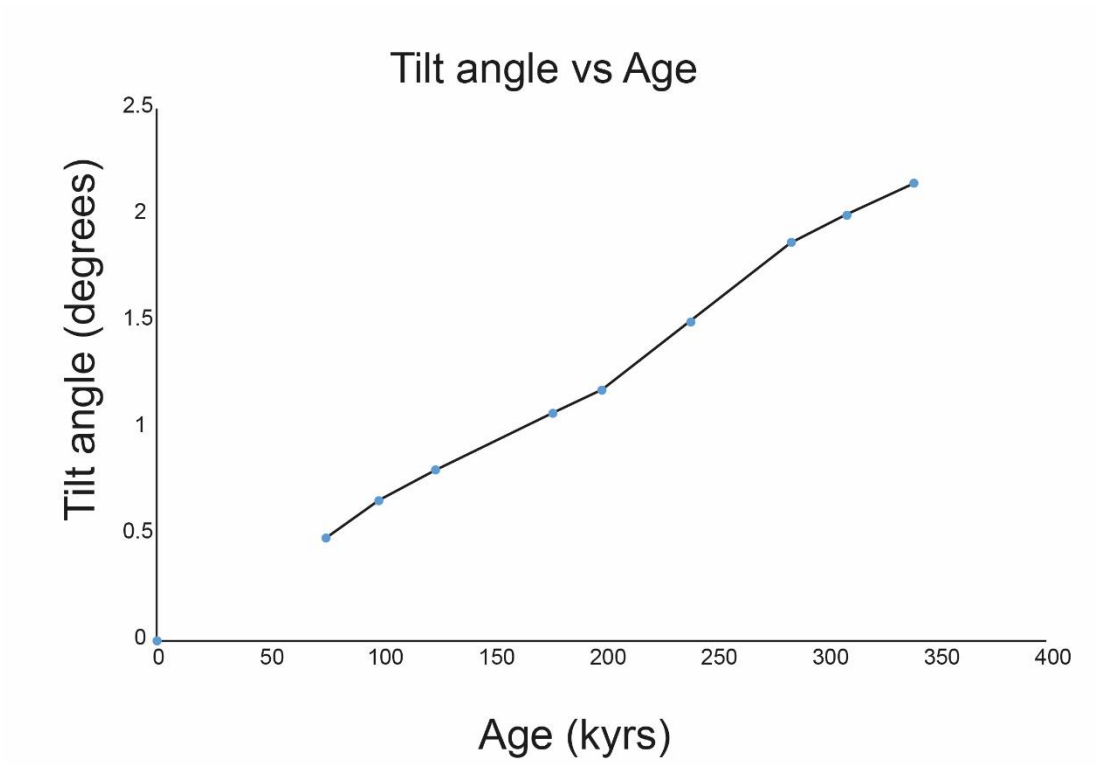

Figure 4.9: *Tilt angles measured along the studied along-strike profiles showing that tilt increases with age for palaeoshorelines.*

Furthermore, a special set of circumstances allows the slip rate of the Vibo fault to be calculated. It is unusual for palaeoshorelines to be preserved both in the footwall and the

hangingwall of an active fault. Although use of the synchronous correlation has not been attempted herein on topographic profiles that cross the active Vibo fault, because the uplift rate will change across the fault, the mapping herein shows that one can trace the palaeoshoreline that we assign an age of 340 ka around the fault tip and correlate it with a palaeoshoreline mapped on the footwall. This has allowed, for the first time, correlation to derive throw and the related throw-rate spanning the Late Quaternary between footwall and hanginwall across the Vibo Fault. In particularly, a maximum throw of ~360 m mapped in the vicinity of the fault centre (Figure 4.10) between the hangingwall (~140 m) and footwall cut-offs (~500 m), over 340 ka, implies a value of 1.06 mm/yr for the throw rate (Figure 4.10). Uplift also occurs beyond the tip of the Vibo fault. Figure 4.10 shows that the 340 ka palaeoshoreline continues SW of the point where the hangingwall and footwall portions of the palaeoshoreline coincide at an elevation of ~450-475 m at ~8500 m along strike.

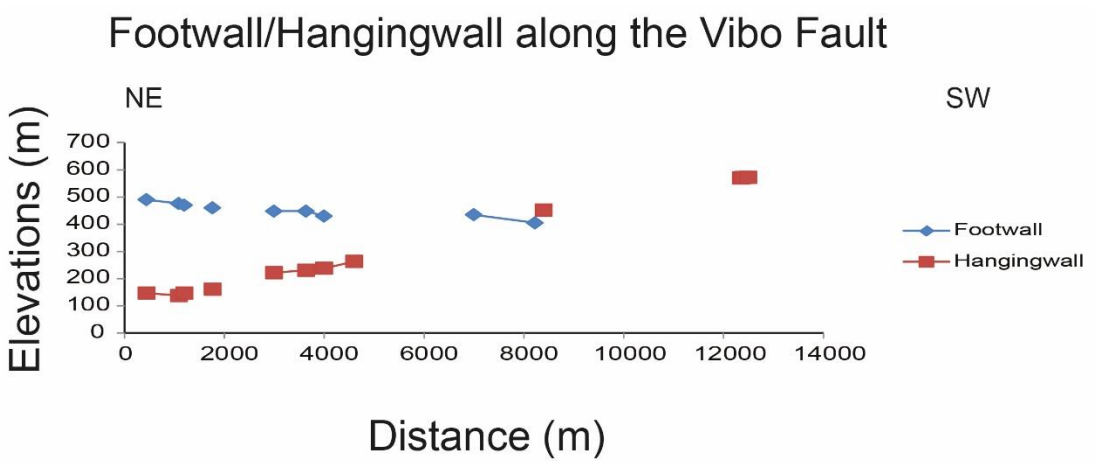

Figure 4.10: *Elevations of the hangingwall and footwall cut-offs of the palaeoshoreface surface associated with the 340 ka palaeoshoreline. The difference in elevation of these cut-offs define the throw-rate across the Vibo fault.*

The palaeoshorelines increases from an elevation of ~450-475 m to ~550 m at ~12500 m along strike. Note that the ~550 m elevation is greater than that for the footwall at ~ 0 m along strike where a value of ~500 m elevation has been measured; it is interesting to speculate on what

has caused this pattern. Firstly, it is noted that the footwall of the Vibo fault may be affected by fault related subsidence from the parallel fault only ~9 km to the SE shown in Figure 4.1. The location at ~550 m at ~12500 m along strike on Figure 4.10 is ~18 km to the NW of the parallel fault to the SE and hence may be too far away to be affected by its hangingwall subsidence. Taken together, this suggests that the point at ~550 m elevation at ~12500 m along strike (see Figure 4.10), may provide what is probably the best available measure of the uplift away from the influence of faults, an uplift that we term "regional" herein and discuss in Chapter 9. Thus, the "regional" uplift is here measured to be 550 m uplift since 340 ka, that is 1.62 mm/yr.

In summary, by applying a synchronous correlation approach between multiple sea level highstands and multiple uplifted palaeoshorelines, it has been shown that uplift rates mapped in the hangingwall of the Vibo Fault has been constant over the Late Quaternary and has changed along the strike the fault, suggesting that the Vibo Fault has to be considered an active fault. Indeed, the geometry of the investigated palaeoshorelines has been affected by long-term faulting activity showing higher tilt angle for older marine terraces.

4.5. Discussion

By performing detailed mapping and a synchronous correlation approach, refined ages of marine palaeoshorelines have been proposed. These suggest a simple constant uplift rate rather than a fluctuating uplift-rate over the Late Quaternary. These results are remarkable because it has been shown that the sequential correlation approach appears not to work well in this situation, yet the sequential correlation approach has been used in many locations worldwide (e.g. Armijo *et al.*, 1996; Bianca *et al.*, 1999, 2011; Grant *et al.*, 1999;

Saillard *et al.*, 2011; Gallen *et al.*, 2014). The new results herein raise the question as to whether a review of palaeoshoreline chronologies around the world should take place. This issue is highlighted again where more examples are provided (Chapters 5, 6 and 7), and discussed in Chapter 9.

Identifying that the "regional" uplift signal has been perturbed by the local effect of the Vibo Fault activity over the Late Quaternary implies important tectonic implications for the tectonically-deforming upper plate of the Ionian subduction. In fact, for the first time, uplift rate changes along the NE-SW oriented Vibo Fault have been mapped implying that this fault has been active over the Late Quaternary. This fact is no surprising considering that several historical earthquakes have been occurring close to the investigated region, producing widespread damage and fatalities; for instance, the 1905 seismic event (Me 6.7) occurred near Vibo Valentia killed >500 people (Jacques *et al.*, 2001; Cucci *et al.*, 2006; Roberts *et al.*, 2013). Indeed, establishing that the Vibo Fault has shown evidence of faulting movement by investigating tectonically-deformed marine terraces since at least since 340 ka implies that it has to be considered "active" according to the definition of an "active fault" by some (Yeats, 2012; Chapman *et al.*, 2014), even though no clear evidence of Holocene activity has been mapped. In fact, these results highlight the importance of this active fault if compared to other active faults in Italy in terms of seismic hazard, allowing for the first the estimation of its Earthquake Recurrence Interval or T_{mean} implied for an assumed value of co-seismic slip. The long-term value of 1 mm/yr of throw rate derived across the active Vibo normal fault is more than reasonable given that 2 mm/yr of geodetically-derived crustal extension have been suggested in this area (Serpelloni *et al.*, 2005), taking into account that some geoscientists have mapped another onshore active normal fault across strike (Jacques *et al.*, 2001). Furthermore,

range of throw rates of 0.3 mm/yr – 2 mm/yr have been measured in the Central Apennines (Roberts and Michetti, 2004) and in the southern Apennines (Jacques *et al.*, 2001; Galli and Bosi, 2002; Papanikoloau and Roberts 2007), implying that the 1 mm/yr derived for the Vibo Fault is not unusual. More importantly, a throw rate of 1 mm/yr produced by assuming a maximum 1000 mm slip events in M 6.5 earthquakes (Wells and Coppersmith, 1994), implies a T_{mean} of 1 ky, or 2 ky for 2000 mm slip events in earthquakes with magnitude > 6.5. These values of T_{mean} for the Vibo Fault are similar to those that characterise active normal faults in Italy derived from historical records and palaeoseismological investigations (Jacques *et al.*, 2001; Galli, Galadini and Pantosti, 2008).

4.6. Conclusion

A new uplift rate history has been presented within the tectonically-deforming upper plate of the Ionian subduction zone by refining the chronology of tectonically-deformed Late Quaternary palaoshorelines, by applying a synchronous correlation approach, suggesting a simpler and more robust uplift estimation. Use of the "sequential correlation" approach by others has suggested dramatic fluctuations in uplift rates for the last 240 ka, 4 order of magnitude (Tortorici *et al.*, 2003; Bianca *et al.*, 2011), for the same investigated area (see Figure 4.2). However, the results presented herein suggest that this is incorrect and uplift rates, and implied fault slip-rates on active faults, have been constant. This has important implications for seismic hazard (see discussion in Chapter 9). In terms of uplift the results herein suggest that uplift rates from other locations worldwide may need to be reviewed, especially when poor or scarce age controls exist, allowing to obtain new insights when investigations link sea-level, climate and tectonics are carried out (see Chapter 9 for discussion).

In summary, the Calabrian Arc, changes of uplift rates along-strike the active Vibo normal fault confirm the hangingwall tectonic subsidence which has been presumably counteracting the "regional" uplift signal possibly associated either with the Ionian subduction process (Malinverno and Ryan, 1986; Tortorici *et al.*, 2003) or with mantle upwelling (Gvirtzman and Nur, 1999b). Synchronous correlations between multiple, tectonically-deformed, Late Quaternary palaeoshorelines with global sea-level highstands, reinforced by detailed terrace mapping in the field and on 10 m high-resolution DEMs unravel that the Vibo Fault have been active over the Late Quaternary with a throw rate value of 1 mm/yr close to its centre; uplift rate gradient has been mapped in the centre of the fault with a value of 0.4 mm/yr and over its tip with a value of 1.75 mm/yr. Detailed topographic analysis and fieldwork have shown that the mapped uplift rate field has been constant since the last 340 ka. Finally, tilted palaeoshorelines along-strike the fault have been mapped with higher tilt angle values associated with older palaeoshorelines, implying that they have been affected by a longer history of faulting activity. Thus, according to the definition of "active fault" by some (Yeats, 2012; Chapman *et al.*, 2014), the Vibo Fault has to be considered active even though no clear evidence of Holocene activity has been mapped.

Chapter 5: The relationships between regional Quaternary uplift, deformation across active normal faults and historical seismicity in the upper plate of subduction zones: The Capo D'Orlando Fault, NE Sicily

5.1. Abstract

In this chapter, rates of crustal deformation within the upper plate of the Calabrian subduction zone are investigated by mapping and modelling sequences of Late Quaternary palaeoshorelines tectonically-deformed by the Capo D'Orlando normal fault, NE Sicily. This region has experienced damaging earthquakes probably associated with the Capo D'Orlando Fault activity, such as the 1613 and 1739 earthquakes, in addition to the 1908 Messina Strait earthquake (~ Mw 7), however, this is not considered by some to be a potential seismogenic source in Italian national databases of active faults. It will be shown that in a similar manner to the Vibo Fault studied in Chapter 4, a "regional" uplift signal appears to have been counteracting the subsidence experienced in the hangingwall of the Capo D'Orlando normal fault, possibly due to the subduction/collision process. The aim of this chapter is to constrain the relationship between historical seismicity, upper plate crustal extensional processes and "regional" uplift and quantifying the rates of both the regional and extensional deformation. By applying a synchronous correlation technique ages for un-dated palaeoshorelines have been refined relative to those in the literature, allowing calculation of new uplift-rates along the strike of the fault and the related fault slip-rate. It is shown that palaeoshoreline elevations change along the strike of the Capo D'Orlando Fault, evidencing an increase in uplift rates in the hangingwall from 0.4 mm/yr in the centre of the fault to 0.89 mm/yr beyond its SW fault tip. Mapping of the palaeoshorelines onto the footwall and measuring the implied offset of the

340 ka palaeoshoreline, implies a throw rate of 0.63 mm/yr ± 0.02mm/yr, suggesting significant seismic hazard. The results are discussed in terms of tectonic processes and seismic hazard.

This work is published in the paper Meschis, M., Roberts, G. P., Robertson, J., & Briant, R. M. (2018). The relationships between regional Quaternary uplift, deformation across active normal faults, and historical seismicity in the upper plate of subduction zones: The Capo D'Orlando Fault, NE Sicily. *Tectonics*, 37. https://doi.org/10.1029/2017TC004705.

5.2. Introduction

In order to better understand the geodynamics and the associated seismic hazard of subduction zones new insights into the relationships between local long-term fault slip rates within subduction/collision zones, far-field plate motion and slip distributions for subduction zone earthquake are needed. Slip distributions in single earthquakes, and the relationship between convergence rates and seismicity are commonly investigated through modelling based on observations of deformation of the upper plate of subduction zones such as coastal uplift (McCloskey, Nalbant and Steacy, 2005; Meltzner *et al.*, 2006; Nalbant *et al.*, 2013; Nic Bhloscaidh *et al.*, 2015). Also, in some cases, uplift of the upper plate of subduction zones can be modified by mantle upwelling (D'Agostino *et al.*, 2001; Faure Walker *et al.*, 2012; Faccenna *et al.*, 2014). However, several new lines of evidence show that the uplifting upper plates of subduction zones can also be affected and deformed by normal faults and this is wide spread in example from southern Italy, Japan, Central Greece, Crete island and south America (Armijo, Lyon-Caen and Papanastassiou, 1992; Hasegawa *et al.*, 2000; Jacques *et al.*, 2001; Nicol and Beavan, 2003; Papanikolaou, Alexandri and Nomikou, 2006; Saillard *et al.*, 2011;

Spampinato *et al.*, 2012; Roberts *et al.*, 2013 (which arises from the previous chapter); Gallen *et al.*, 2014; Binnie *et al.*, 2016), suggesting that this deformation must be accounted and removed if the observed coastal uplift and associated rates are to be used to constrain both mantle dynamics-related topography and slip-distribution on the subduction interface.

For example the Capo D'Orlando fault lies in an area where it is well known that crustal extension processes over the Late Quaternary occurring in Calabria and NE Sicily (Calabrian Arc) have been accommodated by active normal faults, seismically deforming sequences of Middle/Late Pleistocene palaeoshorelines (Monaco and Tortorici, 2000; Jacques *et al.*, 2001; Catalano and De Guidi, 2003; Giunta *et al.*, 2012; Roberts *et al.*, 2013). However, the Capo D'Orlando fault is not considered by some to be an active fault capable of hosting damaging earthquakes. In particular, the locations of damaging historical seismic events noted in Italian catalogues (Guidoboni *et al.*, 2007; Stucchi *et al.*, 2013) lie along mapped normal faults in some instances (Monaco and Tortorici, 2000; Galli, Galadini and Pantosti, 2008; Roberts *et al.*, 2013) (see Chapter 2 - Figure 2.1), but some earthquakes have not been allocated to a particular active fault. Examples include the 1613 (M 5.6) and the 1739 (M 5.1) earthquakes, that occurred close to Capo D'Orlando. The active faults (or if preferred seismogenic sources) have been collected within the so-called Database of Individual Seismogenic Source (DISS) (Basili *et al.*, 2008), providing a base from which to define the geography of the seismic hazard in Italy. Nevertheless, it is important to ask if the locations of all such normal faults are known and mapped (Figure 5.1). For instance, the aforementioned two well-documented medium-magnitude historical earthquakes have been described (Guidoboni *et al.*, 2007) in NE Sicily, around the Capo D'Orlando area (Figure 5.1 and 5.2)

but only a few studies (Scicchitano *et al.*, 2011; Giunta *et al.*, 2012) have tried to recognize conceivable potential faults, such as the Capo D'Orlando Fault.

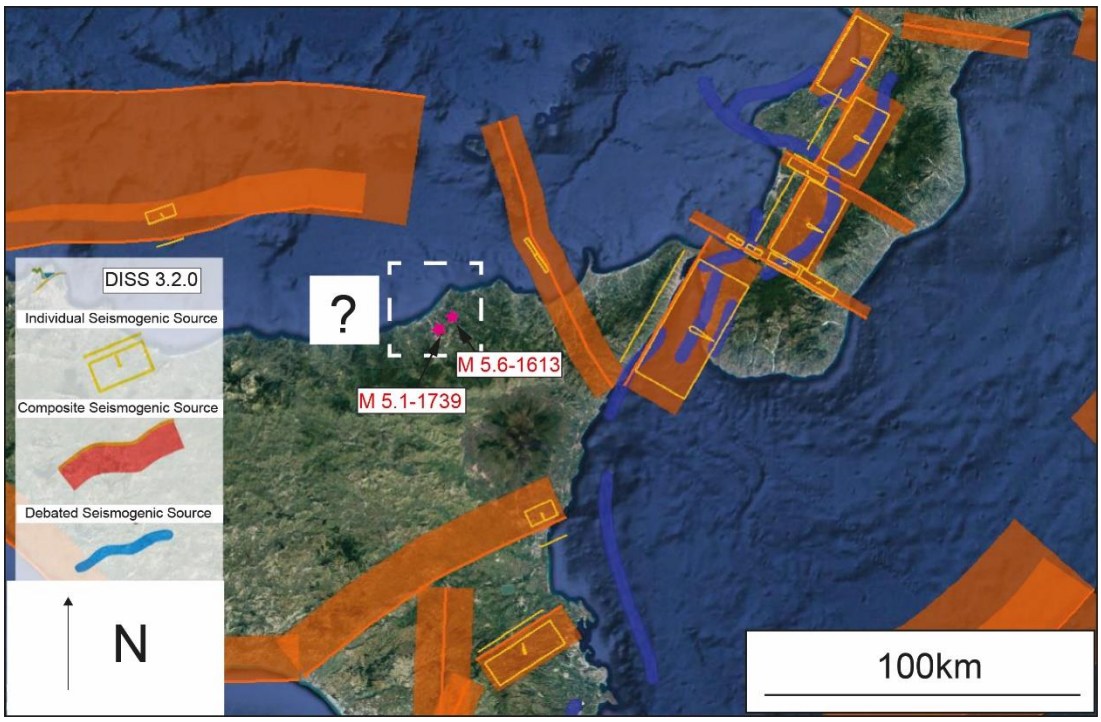

Figure 5.1: *Database of Individual Seismogenic Source (DISS) (INGV - DISS Working Group, 2018) showing "capable" active faults which can produce seismic events in southern Italy. White square shows the investigated area where two historical earthquakes have been located from the Italian catalogues (Guidoboni et al., 2007). Note that the CDF (Capo D'Orlando Fault) has not been reported within DISS.*

However, the results from Scicchitano *et al.*, (2011) and Giunta *et al.*, (2012) are either considered vague or not considered by some, with no active faults reported within the DISS (INGV - DISS Working Group, 2018) for the NE Sicily (Figure 5.1). The case-study area contains raised marine terraces outcropping in the hangingwall and footwall of the Capo D'Orlando Fault (Giunta *et al.*, 2012). These outcrops form the basis of the study in this chapter.

A summary of previous work on the Capo D'Orlando Fault (Figure 5.2), suggests that some faulting activity possibly occurred, but this fault is no longer active because there is a lack of observations suggesting Holocene activity (Giunta *et al.*, 2012). Furthermore, due to the common problem affecting many studies involving marine terraces investigations

(Roberts *et al.*, 2013), a lack of absolute dating for all mapped palaeoshorelines led previous geoscientists (Scicchitano *et al.*, 2011; Giunta *et al.*, 2012) to derive ages for the un-dated terraces by applying a "sequential correlation approach" (see Methods chapter and Chapter 4 for more details) exploiting some obtained absolute age controls (OSL dating and U/Th dating) (Scicchitano *et al.*, 2011; Giunta *et al.*, 2012).

The aim of this chapter is testing the following scientific questions:

- Are the sequentially-derived ages for the un-dated palaeoshoreline in error?
- Is the uplift rate constant or fluctuating through the Late Quaternary?
- Is the Capo D'Orlando Fault active?
- Are the Late Quaternary palaeoshorelines controlled by the activity on the Capo D'Orlando Fault?
- If the Capo D'Orlando is active, is its slip rate fluctuating through time constrained by deformation of the palaeoshorelines?
- Should the Capo D'Orlando Fault be added within the DISS?

The above scientific questions are investigated by undertaking new detailed topographic analysis exploiting a 10 m high resolution Digital Elevation Model (Tarquini *et al.*, 2012) alongside new field mapping to check palaeoshoreline locations previously mapped by others (Giunta *et al.*, 2012) (Figure 5.2).

As shown in the previous chapter (Chapter 4), knowledge of Quaternary sea-level curves and the application of a synchronous correlation technique allows iteration of the uplift rate, aided by the availability of existing age controls from the literature (Scicchitano *et al.*, 2011; Giunta *et al.*, 2012; Sulli *et al.*, 2013).

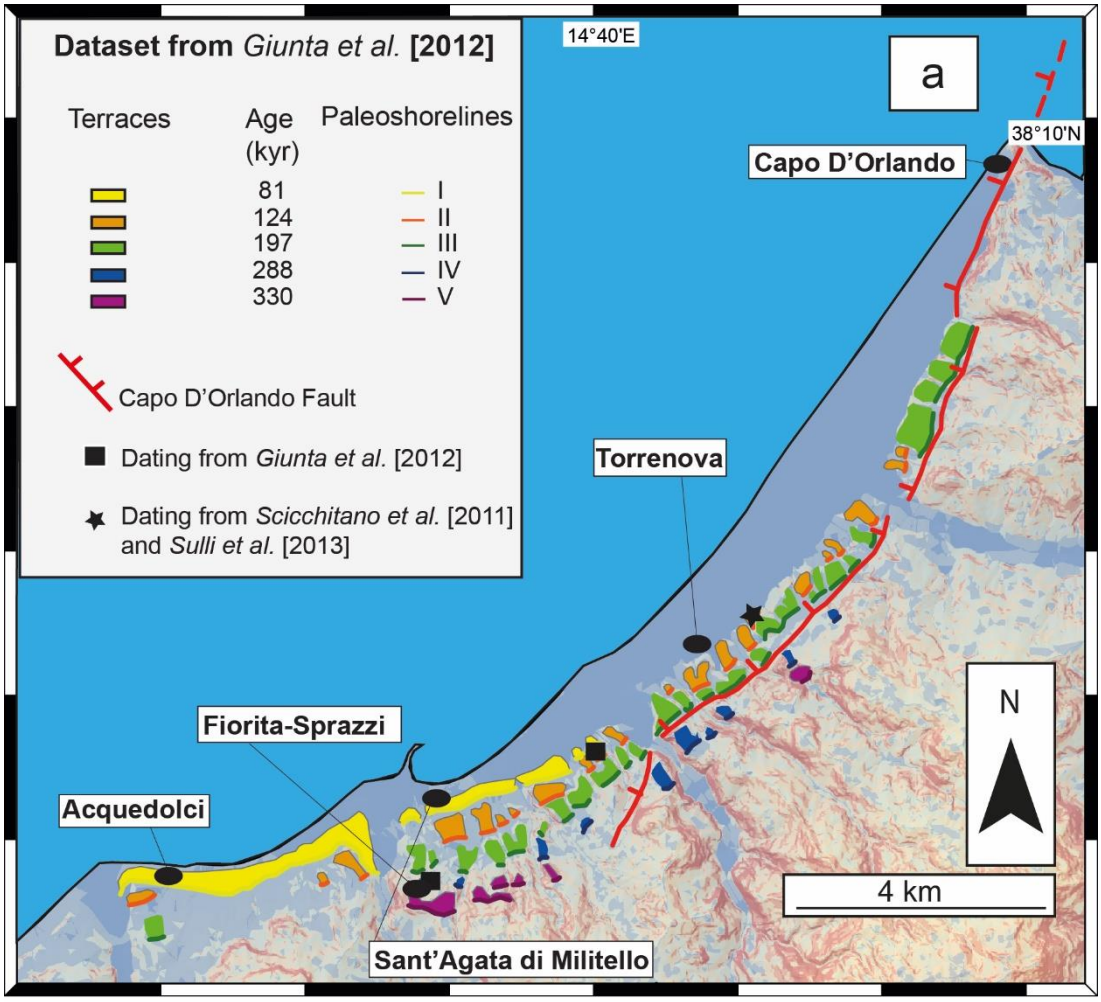
Dataset from Giunta et al. [2012]
Terraces
Age (kyr)
Paleoshorelines
81
124
197
288
330
I
II
III
IV
V
Capo D'Orlando Fault
Dating from Giunta et al. [2012]
Dating from Scicchitano et al. [2011] and Sulli et al. [2013]
14°40'E
a
38°10'N
Capo D'Orlando
Torrenova
Fiorita-Sprazzi
Acquedolci
Sant'Agata di Militello
N
4 km

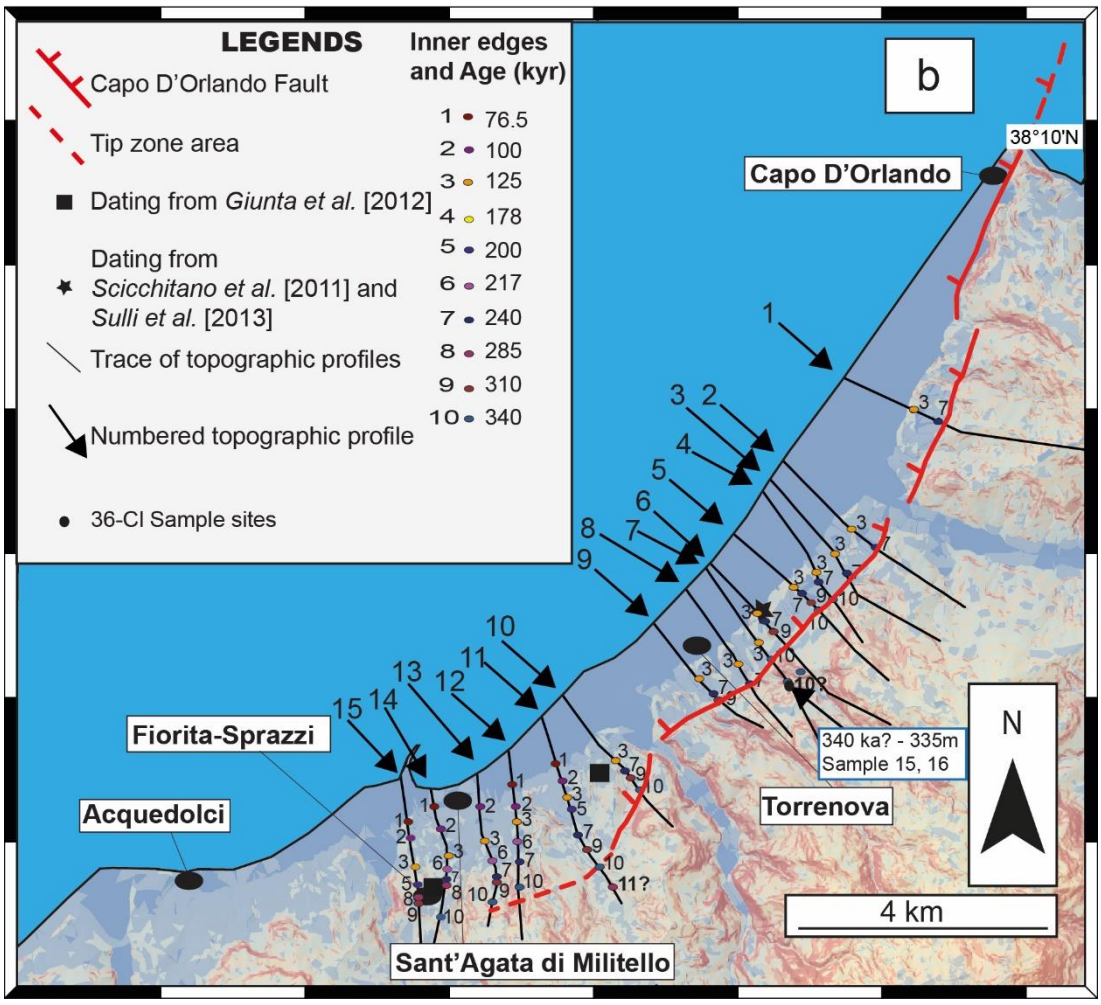
LEGENDS
Capo D'Orlando Fault
Tip zone area
Dating from Giunta et al. [2012]
Dating from Scicchitano et al. [2011] and Sulli et al. [2013]
Trace of topographic profiles
Numbered topographic profile
36-Cl Sample sites
Inner edges and Age (kyr)
1 76.5
2 100
3 125
4 178
5 200
6 217
7 240
8 285
9 310
10 340
b
38°10'N
Capo D'Orlando
Fiorita-Sprazzi
Acquedolci
Torrenova
Sant'Agata di Militello
340 ka? - 335m
Sample 15, 16
N
4 km

Figure 5.2: *Location maps for palaeoshorelines within the hangingwall of the Capo d'Orlando active normal fault. A 10-m resolution DEMs with the associated coloured slope to highlight breaks of slopes is used as base-map. (a) shows a map amended from Giunta et al., (2012) showing the investigated area from Capo d'Orlando town to Santa Agata di Militello town. The locations and ages of marine terraces from Giunta et al. (2012) have shown as well as locations of U/Th and OSL dating by Scicchitano et al., (2011) and Giunta et al. (2012). In (b) inner edges of marine terraces (palaeoshorelines) with our revised ages are presented (see numbered dots and the associated age within Legends panel). The "tip zone" area for the fault is marked in the SW with a red-coloured dashed line. Additionally, 15-topographic profile locations are shown from this study.*

5.3. Methods and approach

In this chapter the approach used to test the scientific questions mentioned in Section 5.2 are very similar to Chapter 4. Palaeoshoreline elevations have been mapped on DEMs by constructing 15 topographic profiles and conducting a detailed topographic analysis along the strike of the Capo D'Orlando Fault (Figure 5.2). The palaeoshorelines mapped on the DEMs have been checked in the field, using as a guide previous mapping by Giunta *et al.*, (2012).

5.3.1. Age controls to drive the synchronous correlation approach

Available age controls (Table 5.1) have been used to drive the synchronous correlation (for details see Method chapter) to refine ages for the un-dated marine terraces. In particular, Giunta *et al. (2012)* dated two palaeoshorelines by using Optically Stimulated Luminescence (OSL) dating on shallow marine sand deposits (their II and IV in Figure 5.2). The more robust of these is the one on "palaeoshoreline II", sampled at an elevation of ~ 50 m, close the SW fault tip area between Torrenova and Sant'Agata di Militello town (Figure 5.2a). Indeed, this sample shows robust luminescence behaviour, using a widely-applied protocol, and gives an age of 118 ± 7 ka (Giunta *et al.*, 2012), presumably suggesting the presence of the 125 ka highstand-related palaeoshoreline. Furthermore, an *in-situ* shell of *Spondylus* sp. from sediments just above the marine deposit overlying palaeoshoreline II in the Rocca Scodoni' area was dated by U/Th to c. 125 ka (Scicchitano *et al.*, 2011; Sulli *et al.*, 2013), confirming this

age. There is also another absolute age available from palaeoshoreline IV sampled at 208 m over the fault tip close to Fiorita-Sprazzi village. However, the luminescence characteristics of this sample are not shown, and large error bars suggest that the analysis may be close to saturation.

Reference	Dating Method	Dated sample description	Profile number	Reported Age (ky)	Assigned Highstand (ka)	Palaeo-shoreline Elevation (m a.s.l)
Scicchitano et al., 2011 and Sulli et al., 2013	U/Th dating	*"A shell of Spondylus sp collected within thick marine deposit constituted by coarse polygenic conglomerates, micro-conglomerates and crossed lamination sands."*	6	100 - 125	125	53
Giunta et al., 2012	OSL dating	*"Yellow shore sands from unconsolidated marine sands."*	10	118 ± 7	125	61
Giunta et al., 2012	OSL dating	*"Sandy levels from unconsolidated marine sands."*	14/15	283 ± 22	285	208

Table 5.1: *Previous dating of palaeoshorelines lying within the investigated area by Scicchitano et al. (2011), Giunta et al. (2012) and Sulli et al. (2013). Note that different dating methods have confirmed the age (125 ky) of a prominent marine terrace along the strike of fault and over its tip. The samples are located in Figure 5.1.*

As described in Chapter 3, ^{36}Cl cosmogenic dating has been attempted to date a WCP mapped in the footwall of this fault to resolve the fault slip-rate over 340 ka. However, it will be shown that the sample site appears to have been subject to erosion as the obtained exposure ages are low (Table 5.2); this is actually confirmed by the fact that no lithophagid boring and

millholes were found when sample 15 and 16 were collected. It is also important to say that this location was the only one accessible to WCPs on the footwall. It may be that these ages need to be discarded for present purposes.

Sample	36-Cl Conc. (Atoms of 36-Cl/g of sample)	Erosion rate (mm/ky)	Age (kyr)	Total uncertainty (kyr)	Elevation (m)	Expected Age (ka)
15	97743.14203	8	5.5	1.2	335	340
16	98034.67934	8	5.3	1.1	335	340

Table 5.2: *Exposure ages from ^{36}Cl cosmogenic dating are shown in the table. Sampling locations are shown in Figure 5.2b and in Chapter 3.*

Data of palaeoshoreline elevations used to derive uplift rates were obtained both from field observations using a hand-held barometric altimeter and GIS-based detailed DEMSs analysis, similarly to Chapter 4 for the Vibo Fault. Furthermore, DEMs analysis was crucial and necessary because in places heavily-vegetated areas and limited access on private houses were not possible to be checked in the field.

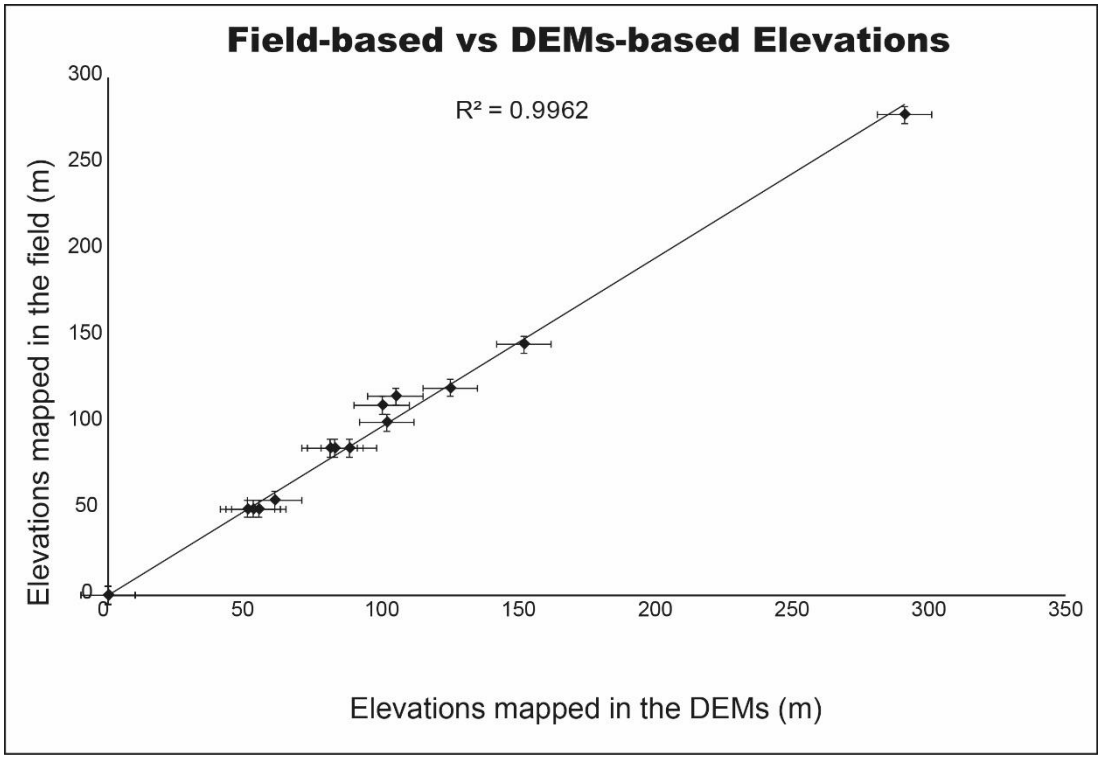

Figure 5.3: *Graph showing the relationship between field-based and DEM-based inner edge elevations. The R^2 value > 0.99 confirms a very robust relationship suggesting that elevations measured elsewhere in the DEM are likely to be accurate.*

More particularly, observations in the field were used to ground truth identification of marine terrace inner edges made on the DEMs, and to check the elevations derived from the DEMs were robust. Figure 5.3 shows a robust correlation between field-based elevations and DEMs-based elevations, demonstrating that elevations from DEM analysis appear to be robust and reliable to use in uplift rate calculations.

5.3.2. Long-term uplift/subsidence ratio and footwall palaeoshorelines to derive slip-rate on Capo D'Orlando Fault

In more detail, a terraced surface cut on Mesozoic limestone by wave action (wave-cut platform, WCP) has been mapped on the footwall close to where it would form a footwall cut-off against the fault. Shallow marine deposits (conglomerates) have been mapped associated with the WCP close to the supposed centre of the onshore fault segment at ~ 345 m above the sea level (Figure 5.2b). Indeed, evidence for an upper shoreface marine environment have been recognized such as rounded marine beach cobbles and pebble, probably associated with a palaeo-rocky beach. The geomorphology of the footwall includes deep ravines that are tens of metres deep. These impeded an attempt to map the footwall palaeoshorelines along strike in the field, but it is clear from view through binoculars and on the DEM that the footwall palaeoshorelines are continuous along strike (Figure 5.4c, d and e). Even though a detailed mapping of the footwall WCPs has not been completed in the field, an attempt has been made to estimate the long-term fault throw-rate by applying a well-known long-term uplift/subsidence ratio already proposed by several geoscientists in the past (King, Stein and Rundle, 1988; Armijo *et al.*, 1996; McNeill and Collier, 2004). A value of 1/3.5 (Uplift/Subsidence) ratio has been applied taking into account the elevation of the oldest 340 ka-aged palaeoshoreline mapped close the centre of fault on the hangingwall at 129 m and

within the fault "tip zone" at 291 m. This ratio suggests that mapped palaeoshoreline in the footwall (Figure 5.2b and 5.4c) is the correlative surface with the highest WCP on the hangingwall (Figure 5.2b).

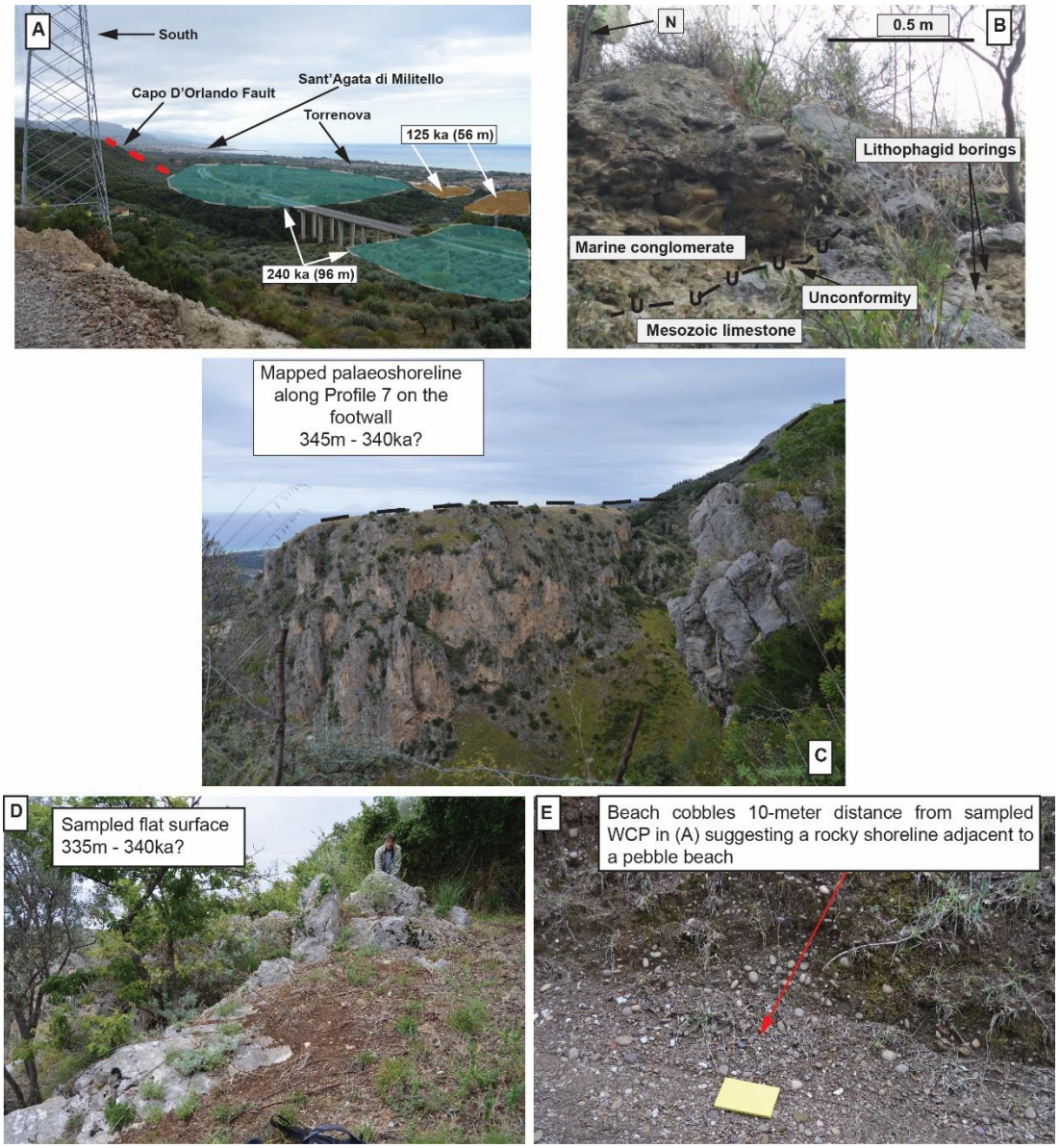

Figure 5.4: *(a) View of interpreted marine terraces in the field (shaded polygons) associated with Profile 8, with the inner edge elevations and the synchronously-assigned ages. The synchronous correlation approach allowed us to reassign the age of 240 ka to the palaeoshoreline at 96 m, which was previously sequentially-assigned to the 200 ka sea-level highstand by Giunta et al. (2012). (b) Field evidence, from along Profile 6, of an inner edge showing an upper palaeoshoreface depositional environment. The picture shows a marine abrasion platform made of Mesozoic limestone unconformably overlain by marine conglomeratic deposits already well-described by Scicchitano et al. (2011) and Giunta et al. (2012). In places lithophagid borings into Mesozoic limestone and scattered evidence of beach cobbles have been mapped close to this area, suggesting the presence of the 125ka-dated palaeoshoreline. This inner edge could have not been mapped in the DEMs due to its small size and the resolution of the DEM, reinforcing the need for field work to check palaeoshorelines in the field. In (c) a flat surface cut into Mesozoic-aged limestone is shown with the associated sloping break interpreted as an inner edge. In (d) and (e) evidence of a shallow marine paleoenvironment are shown with presence of a flat surface cut into Mesozoic-aged limestone (d) and beach*

pebbles/cobbles associated with a palaeorocky beach. Note that this WCP (d) was sampled to be dated (Sample 15 and 16 in Table 5.2) and interpreted as the same with respect to the one shown in "c", before the river cutting activity.

5.4. Results

In this section, results describing observations of the palaeoshorelines are presented. The palaeoshorelines that are identified are correlated with sea-level highstands using a synchronous correlation approach are shown. Then, temporal and spatial constraints on this sequence of uplifted marine terraces are used to derive uplift rates and how these relate to displacements on the Capo D'Orlando normal fault.

Table 5.3 presents all marine terrace elevations with a refined age by using a synchronous correlation approach. A common problem for palaeoshoreline investigations already described in the Chapter 4 is that not all mapped palaeoshoreline locations were checked in the field due to limited access on private land and heavily-vegetated area. However, Figure 5.3 shows that those that were visited have elevations measured with a hand-help barometric altimeter that are in good agreement with those made form the DEM. This suggests measurements made solely on the DEM are likely to be robust.

Palaeoshoreline (Profile number)	DEMs Elevations (m)	Expected Elevations (m)	Field Elevations (m)	Giunta's Elevations (m)	Our proposed Age (kyrs)	Age proposed by Giunta et al., 2012 (kyrs)	UTM Coordinate
3 (1)	57	59	-	57	125	125	33 S 0475871 4219672
7 (1)	99	99	-	99	240	200	33 S 0476308 4219436
3 (2)	57	59	-	57	125	125	33 S 0474722 4217578
7 (2)	98	98	-	98	240	200	33 S 0475083 4217269
3 (3)	54	54	-	54	125	125	33 S 0474353 4217219

7 (3)	87	89	-	87	240	200	33 S 0474511 4216876
3 (4)	49	50	-	49	125	125	33 S 0473994 4216902
7 (4)	80	79	-	-	240	-	33 S 0474049 4216761
10 (4)	124	124	-	124	340	200	33 S 0474265 4216425
3 (5)	51	51	50	51	125	125	33 S 0473639 4216783
7 (5)	81	84	85	-	240	-	33 S 0473912 4216612
9 (5)	98	93	-	98	310	200	33 S 0473868 4216424
10 (5)	125	131	120	-	340	-	33 S 0473996 4216277
3 (6)	53	53	50	53	125	125	33 S 0472871 4216042
7 (6)	83	86	85	-	240	-	33 S 0473005 4215984
9 (6)	100	96	110	100	310	200	33 S 0473260 4215861
3 (7)	54	51	-	54	125	125	33 S 0472915 4215755
10 (7)	129	131	-	129	340	200	33 S 0473105 4215415
3 (8)	56	56	-	56	125	125	33 S 0472539 4215404
7 (8)	96	93	-	96	240	200	33 S 0472701 4215060
3 (9)	55	54	54	55	125	125	33 S 0471586 4215093
7 (9)	88	89	75	88	240	200	33 S 0471462 4214794
9 (9)	102	99	100	-	310	-	33 S 0471767 4214611
3 (10)	61	63	-	61	125	125	33 S 0470269 4213855
7 (10)	105	105	115	105	240	200	33 S 0470442 4213664
9 (10)	123	121	-	-	310	-	33 S 0470528 4213527

10 (10)	152	161	145	-	340	-	33 S 0470823 4213768
1 (11)	26	21	-	-	76	-	33 S 0469214 4213892
2 (11)	50	42	-	50	100	76	33 S 0469289 4213580
3 (11)	87	89	-	87	125	125	33 S 0469370 4213279
5 (11)	125	129	-	125	200	200	33 S 0469435 4213057
7 (11)	150	156	-	-	240	-	33 S 0469528 4212622
9 (11)	190	186	-	-	310	-	33 S 0469673 4212322
10 (11)	230	233	-	-	340	-	33 S 0469861 4212020
11 (11)	274	270	-	-	410?	-	33 S 0470076 4211665
1 (12)	25	28	-	25	76	76 (?)	33 S 0468440 4213543
2 (12)	50	51	-	50	100	76 (?)	33 S 0468458 4213177
3 (12)	100	100	-	100	125	125	33 S 0468478 4212907
6 (12)	143	147	-	-	200	-	33 S 0468480 4212536
7 (12)	180	177	-	180	240	200	33 S 0468453 4212205
10 (12)	264	263	-	264	340	340	33 S 0468424 4211752
2 (13)	52	57	-	52	100	76	33 S 0467832 4213228
3 (13)	105	108	-	105	125	125	33 S 0467886 4212584
6 (13)	149	159	-	140 (?)	200	200 (?)	33 S 0467996 4212239
7 (13)	200	192	-	-	240	-	33 S 0468052 4211966
9 (13)	228	232	-	-	310	-	33 S 0468046 4211866
10 (13)	291	284	278	300	340	340	33 S 0467955 4211523

1 (14)	27	33	-	40	76	76 (?)	33 S 0467030 4213264
2 (14)	64	57	-	64	100	76 (?)	33 S 0467078 4212875
3 (14)	109	108	-	109	125	125	33 S 0467227 4212394
6 (14)	155	159	-	146 (?)	200	200 (?)	33 S 0467206 4212147
7 (14)	187	192	-	-	240	-	33 S 0467153 4211987
8 (14)	208	204	-	208	285	285	33 S 0467140 4211866
10 (14)	288	284	-	288	340	340	33 S 0467020 4211313
1 (15)	40	38	-	40	76	76 (?)	33 S 0466553 4213014
2 (15)	61	64	-	61	100	76 (?)	33 S 0466577 4212733
3 (15)	112	116	-	112	125	125	33 S 0466629 4212216
5 (15)	174	173	-	174	200	200	33 S 0466644 4211888
8 (15)	225	224	-	225	285	285	33 S 0466664 4211696
9 (15)	253	254	-	253	310	340	33 S 0466677 4211574

Table 5.3: *All mapped inner edges from DEM and fieldwork with age assigned via synchronous correlation are shown. Note that not all the locations for inner edges mapped by DEM analysis with GPS in the field have been checked because the investigated area is in places thickly-vegetated and densely-populated with private properties.*

Detailed topographic analysis with 15 topographic profiles along the strike of the Capo D'Orlando Fault (Figure 5.2 and 5.5), by using 10 m high resolution DEMs (Tarquini *et al.*, 2012), is shown. In particular, seaward-dipping planar terraced surfaces, with dips of a few degrees have been interpreted as palaeoshoreface surfaces cut by wave-action. Shallow palaeoshoreface marine sediments are in places present on these terraced surfaces (Figure 5.4), in agreement with previous authors (Bianca *et al.*, 1999; Tortorici *et al.*, 2003; Giunta *et al.*,

2012; Roberts *et al.*, 2013). Furthermore, these terraced surfaces are bounded up-dip by steeper breaking slope features that are interpreted as palaeo-sea cliffs, defining palaeoshorelines. As described in Chapter 4, some of these palaeoshorelines are indistinct on the topographic profiles due to their small lateral extent in the field and the resolution of the DEM. Nonetheless, the field work conducted in this study has confirmed the existence of these in the field (Figure 5.3).

In order to assess past sea-level highstands interpretations in Figure 5.5, the elevation dataset is used to construct linear regression previously shown in Figure 5.6 to validate the robustness of the correlation between mapped (measured) palaeoshorelines and expected (or predicted) palaeoshoreline elevations. The regression makes full use of the corrected sea-level values relative to the present-day sea level shown by Siddall *et al.*, (2003) and Rohling *et al.*, (2014) (see Table 2.1 in Chapter 2). Uplift rates were iterated for all 15 topographic profiles to gain the best fit between measured and predicted palaeoshoreline elevations and investigate if strike-variations in uplift/subsidence can be mapped due to the Capo D'Orlando Fault activity. Constant uplift rates were applied in the first instance, with a plan to use time-varying uplift if needed. However, as shown below, it appears that the observed uplift is best explained by constant uplift rates.

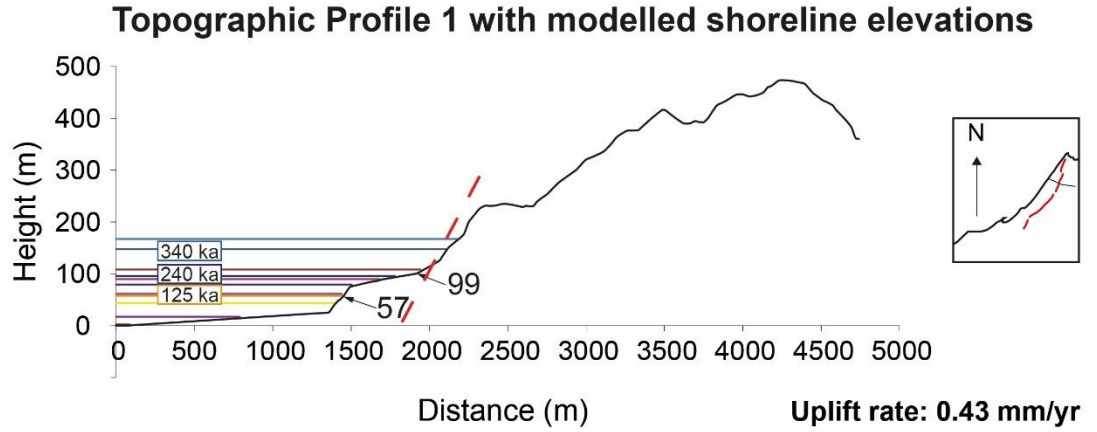
Topographic Profile 1 with modelled shoreline elevations
Height (m)
500
400
300
200
100
0
340 ka
240 ka
125 ka
99
57
0 500 1000 1500 2000 2500 3000 3500 4000 4500 5000
Distance (m)
N
Uplift rate: 0.43 mm/yr

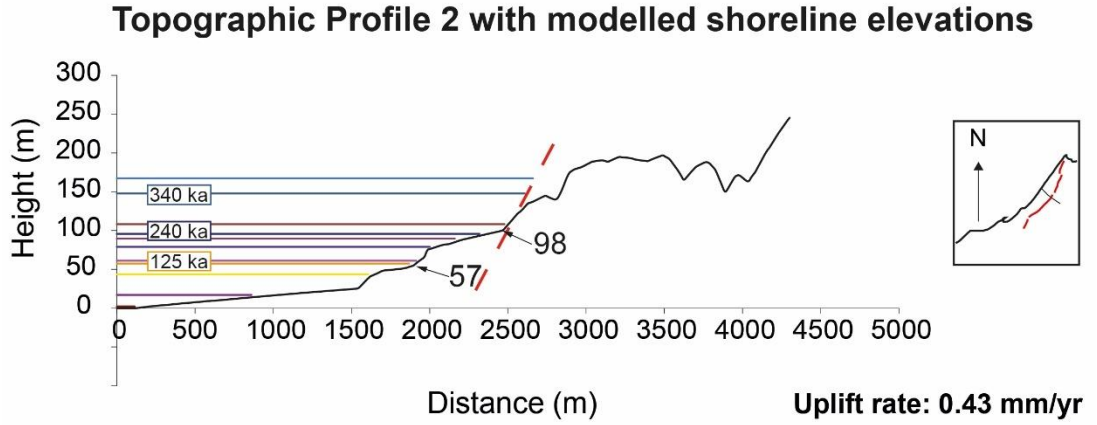
Topographic Profile 2 with modelled shoreline elevations
Height (m)
300
250
200
150
100
50
0
340 ka
240 ka
125 ka
98
57
0 500 1000 1500 2000 2500 3000 3500 4000 4500 5000
Distance (m)
N
Uplift rate: 0.43 mm/yr

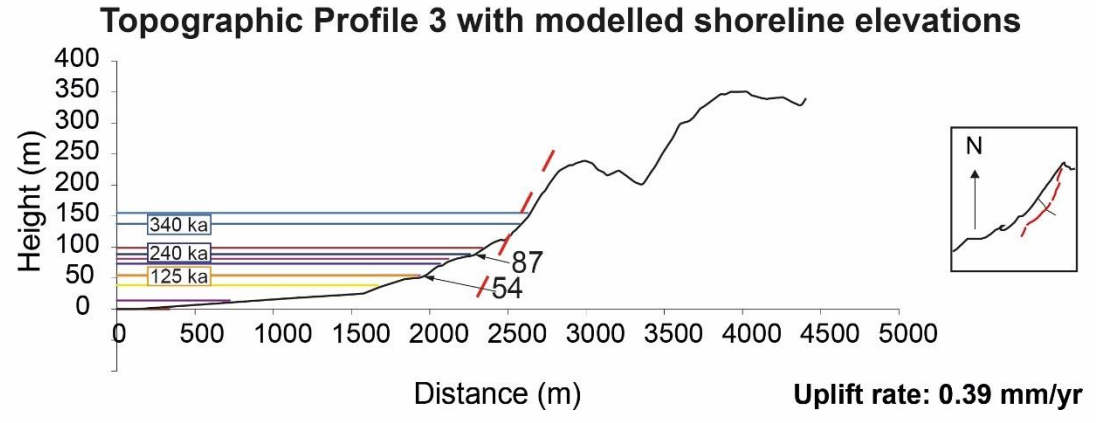
Topographic Profile 3 with modelled shoreline elevations
Height (m)
400
350
300
250
200
150
100
50
0
340 ka
240 ka
125 ka
87
54
0 500 1000 1500 2000 2500 3000 3500 4000 4500 5000
Distance (m)
N
Uplift rate: 0.39 mm/yr

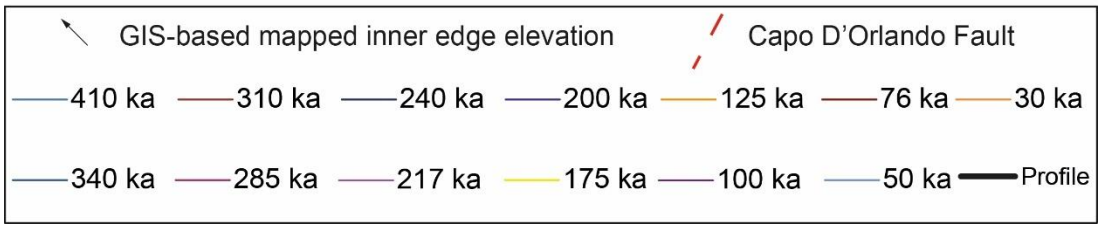
GIS-based mapped inner edge elevation
Capo D'Orlando Fault
410 ka
310 ka
240 ka
200 ka
125 ka
76 ka
30 ka
340 ka
285 ka
217 ka
175 ka
100 ka
50 ka
Profile

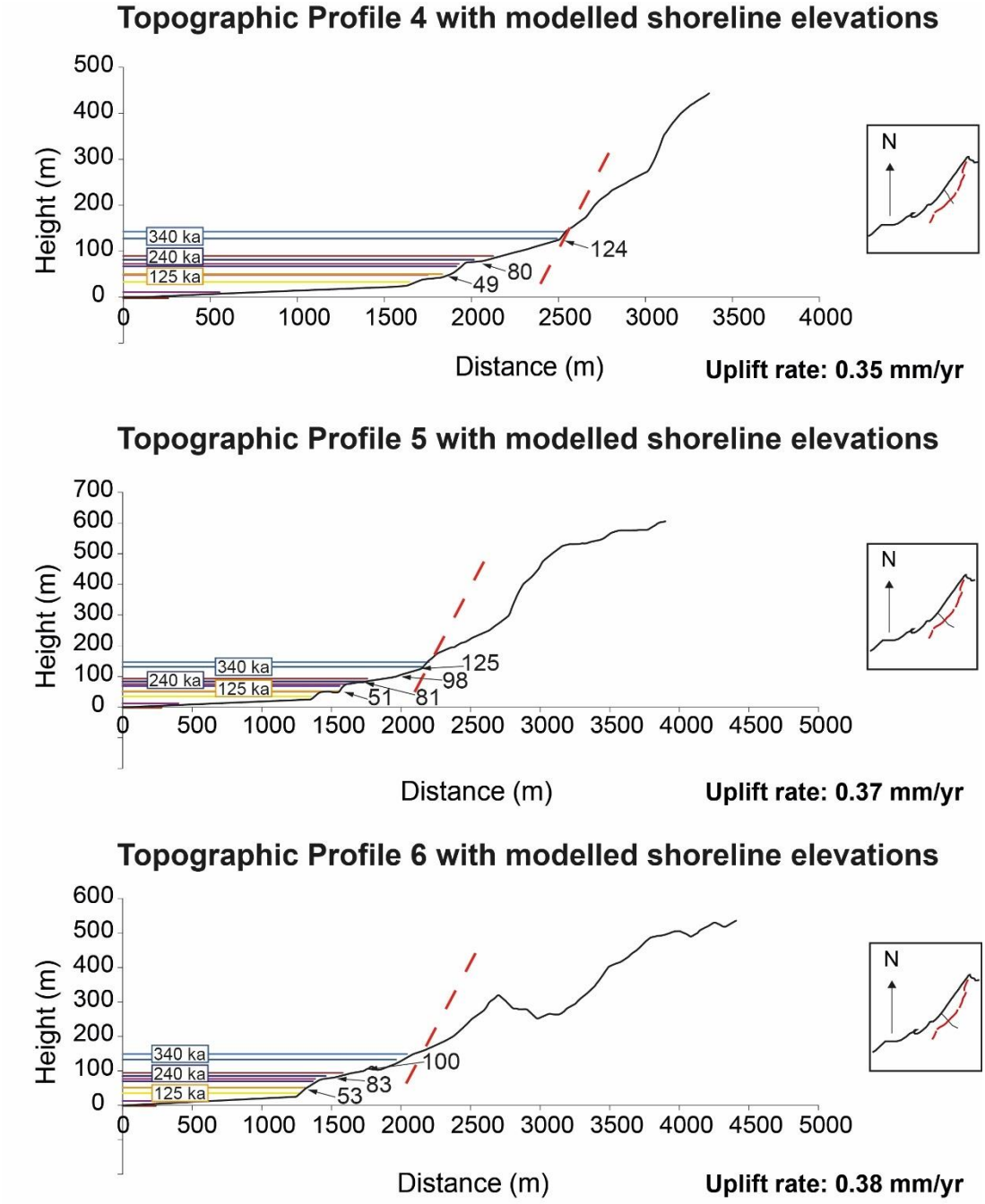
Topographic Profile 4 with modelled shoreline elevations
Height (m)
Distance (m)
340 ka
240 ka
125 ka
124
80
49
N
Uplift rate: 0.35 mm/yr
Topographic Profile 5 with modelled shoreline elevations
Height (m)
Distance (m)
340 ka
240 ka
125 ka
125
98
51
81
N
Uplift rate: 0.37 mm/yr
Topographic Profile 6 with modelled shoreline elevations
Height (m)
Distance (m)
340 ka
240 ka
125 ka
100
83
53
N
Uplift rate: 0.38 mm/yr
GIS-based mapped inner edge elevation
Capo D'Orlando Fault
410 ka
310 ka
240 ka
200 ka
125 ka
76 ka
30 ka
340 ka
285 ka
217 ka
175 ka
100 ka
50 ka
Profile

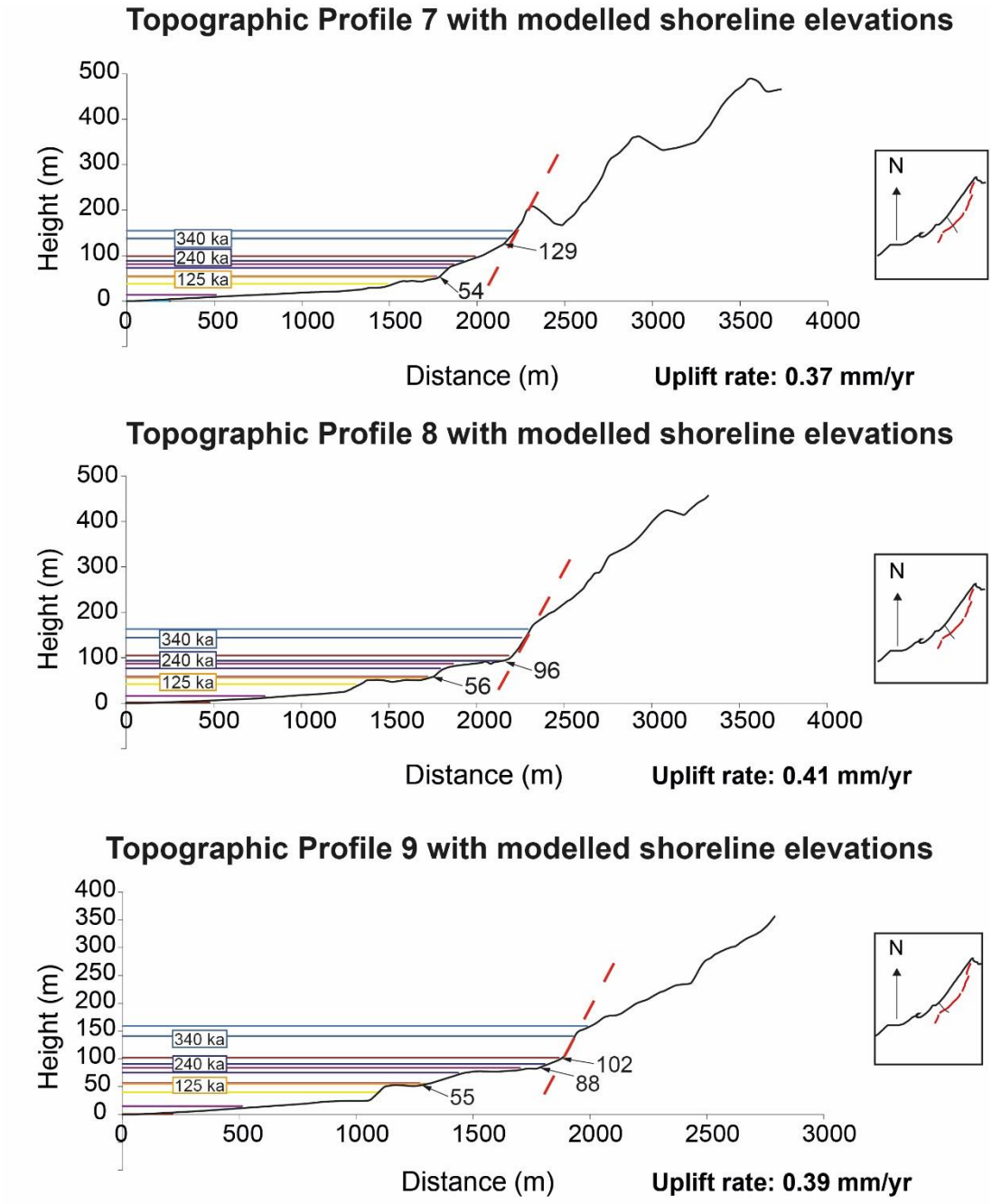
Topographic Profile 7 with modelled shoreline elevations
Height (m)
500
400
300
200
100
0
340 ka
240 ka
125 ka
129
54
0
500
1000
1500
2000
2500
3000
3500
4000
Distance (m)
Uplift rate: 0.37 mm/yr
N
Topographic Profile 8 with modelled shoreline elevations
Height (m)
500
400
300
200
100
0
340 ka
240 ka
125 ka
96
56
0
500
1000
1500
2000
2500
3000
3500
4000
Distance (m)
Uplift rate: 0.41 mm/yr
N
Topographic Profile 9 with modelled shoreline elevations
Height (m)
400
350
300
250
200
150
100
50
0
340 ka
240 ka
125 ka
102
88
55
0
500
1000
1500
2000
2500
3000
Distance (m)
Uplift rate: 0.39 mm/yr
N
GIS-based mapped inner edge elevation
Capo D'Orlando Fault
410 ka
310 ka
240 ka
200 ka
125 ka
76 ka
30 ka
340 ka
285 ka
217 ka
175 ka
100 ka
50 ka
Profile

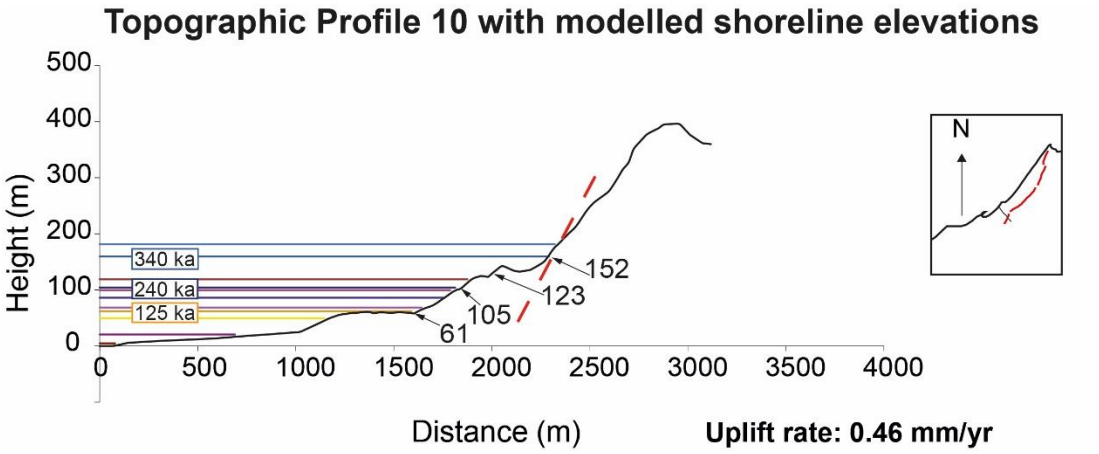
Topographic Profile 10 with modelled shoreline elevations
Height (m)
500
400
300
200
100
0
340 ka
240 ka
125 ka
152
123
105
61
0
500
1000
1500
2000
2500
3000
3500
4000
Distance (m)
N
Uplift rate: 0.46 mm/yr

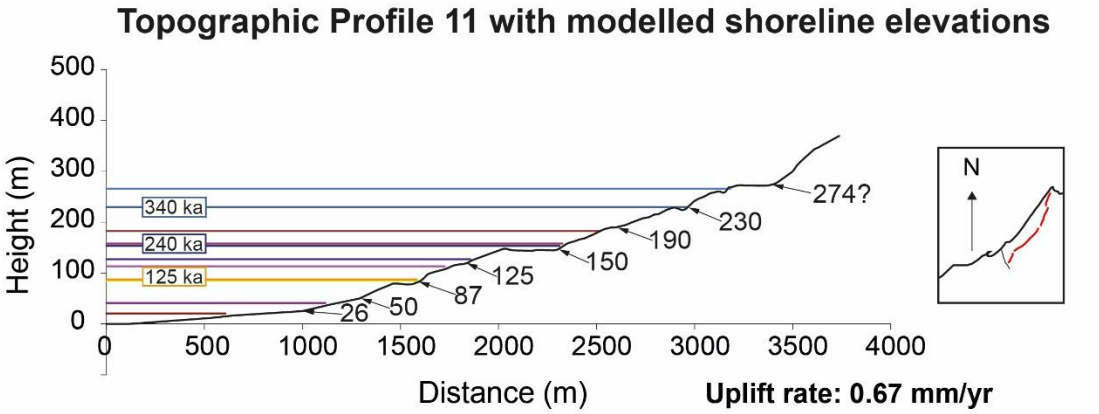
Topographic Profile 11 with modelled shoreline elevations
Height (m)
500
400
300
200
100
0
340 ka
240 ka
125 ka
274?
230
190
150
125
87
50
26
0
500
1000
1500
2000
2500
3000
3500
4000
Distance (m)
N
Uplift rate: 0.67 mm/yr

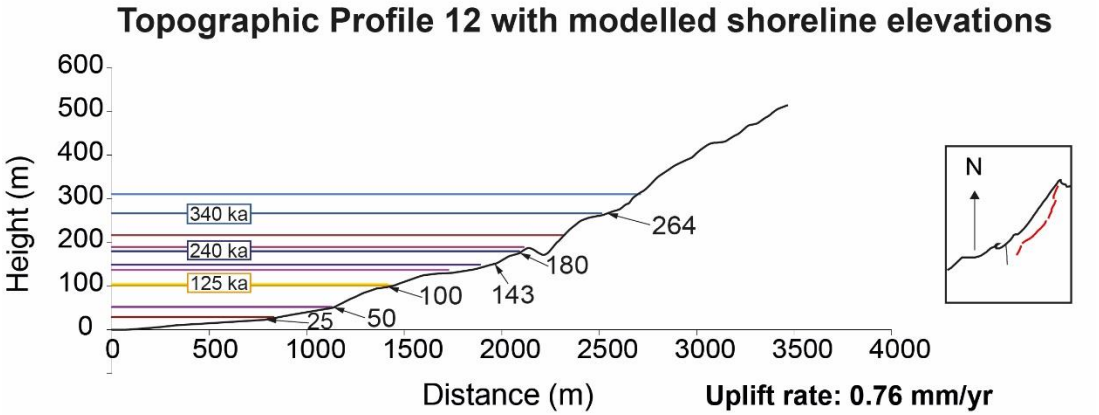
Topographic Profile 12 with modelled shoreline elevations
Height (m)
600
500
400
300
200
100
0
340 ka
240 ka
125 ka
264
180
143
100
50
25
0
500
1000
1500
2000
2500
3000
3500
4000
Distance (m)
N
Uplift rate: 0.76 mm/yr

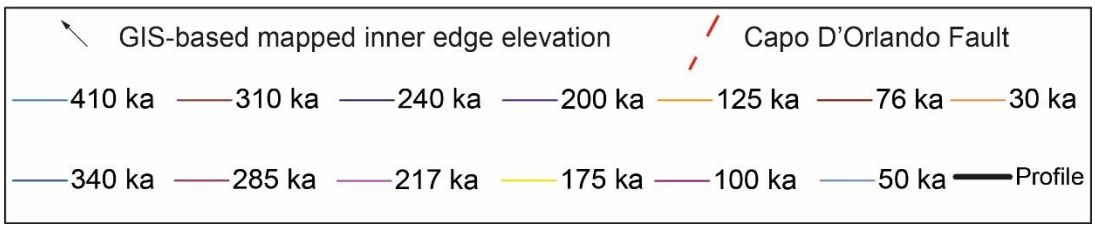
GIS-based mapped inner edge elevation
Capo D'Orlando Fault
410 ka
310 ka
240 ka
200 ka
125 ka
76 ka
30 ka
340 ka
285 ka
217 ka
175 ka
100 ka
50 ka
Profile

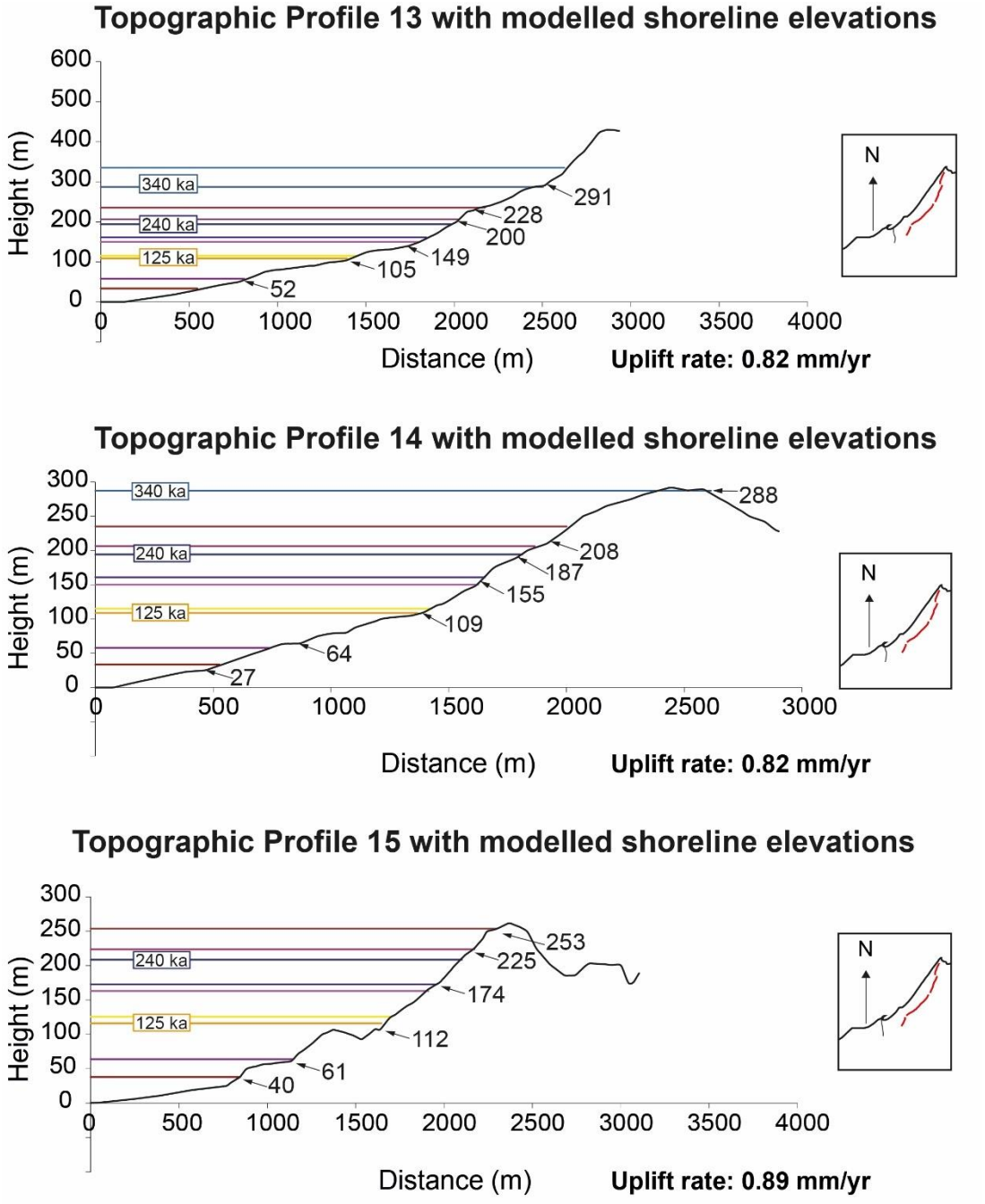

Figure 5.5: *Profiles showing mapped and modelled palaeoshoreline elevations. The topographic profile is from the 10 m DEM. The numbers with arrows mark the elevations of palaeoshorelines mapped in the field. The coloured lines indicate palaeoshoreline elevations predicted by an uplift rate that has been changed iteratively to produce the best match with the mapped palaeoshorelines; goodness of fit is indicated by the value for slope and the R^2 values in Figure 5.4. Profiles are located on Figure 5.2.*

Figure 5.6 shows a linear regression analysis between "measured" and "predicted" elevations (see Chapter 3 – Methods for more details) with a value of the coefficient of determination > 0.99 (R^2 values of ~0.99), implying a strong, synchronous correlation between multiple marine terrace elevations and multiple sea-level highstands. As in the previous chapter for the Vibo Fault, this approach has allowed the correlation between multiple uplifted Late Quaternary palaeoshoreline elevations (or measured elevations) and multiple sea-level highstands (or predicted elevations), forcing the user to maximise the value R^2 through a linear regression.

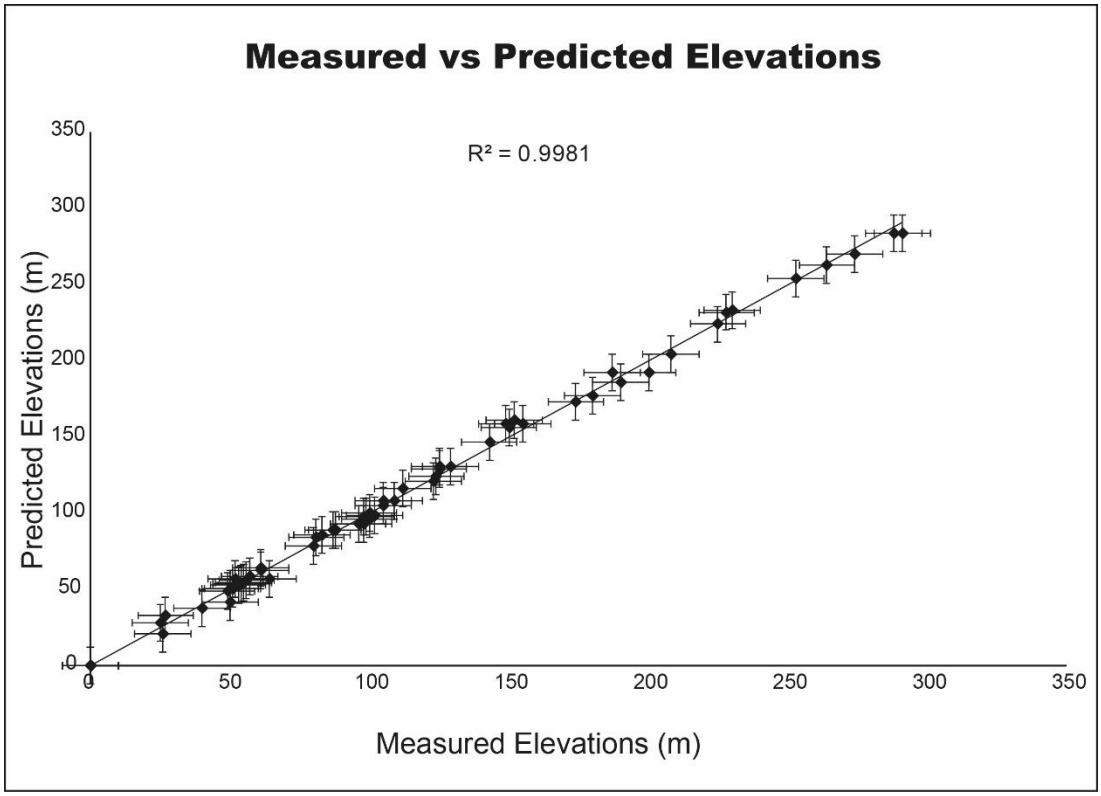

Figure 5.6: *Graph showing linear regression analysis between our measured and predicted elevations. The predicted elevations, representing the synchronously-calculated sea-level highstand elevations, have been derived by defining a constant uplift rate through time, and iterating this value to find the best match to the measured and mapped palaeoshorelines. Note that "measured" elevations represent palaeoshoreline elevations mapped in the 10-m high resolution DEMs. Coefficient of determination, R^2 value, has been used between these two datasets to quantify the best fit for all 15 topographic profiles with a value.*

The approach forces geoscientists to investigate a sequence of marine terraces at the same time (or synchronously); this implies that the investigation is not biased to one preferred interpretation for a particular marine terrace age (Roberts *et al.*, 2013; Pedoja *et al.*, 2018).

Moreover, the correlation suggests that uplift rates have been constant through time, instead of fluctuating as claimed by previous authors (Giunta *et al.*, 2012) (see Figure 5.5). As in Chapter 4, the palaeoshorelines related with the following sea-level highstands have been identified; 76 ka, 100 ka, 125 ka, 175 ka, 200 ka, 217 ka, 240 ka, 285 ka, 310 ka, 340 ka and 410 ka. However, note that not all of these ages are identified on each profile, because where uplift rates are at lower values, fewer palaeoshorelines are preserved. As mentioned in Chapter 4, note that these synchronously-derived ages of marine terraces have been identified elsewhere in the Mediterranean area (Roberts *et al.*, 2009; Roberts *et al.*, 2013). The results suggest that the mapping by Giunta *et.*, (2012) is reliable and robust, but that the ages of marine terraces suggested in that paper needed to be reviewed; the ages assigned in this chapter are preferred compared to those suggested by Giunta et al. (2012).

Palaeoshoreline elevations on individual topographic profiles can be combined to produce a correlation of inner edges of marine terraces along the strike of the Capo D'Orlando Fault (see Figure 5.2). Figure 5.7 shows that spatially-varying fault-related uplift along the strike of the fault, with lower palaeoshoreline elevation values mapped in the centre of the hangingwall fault, suggesting that the Capo D'Orlando Fault has been controlling the geometry of the palaeoshorelines, implying faulting activity over the Late Quaternary. Figure 5.8 shows that uplift rates, mapped in the hangingwall of the Capo D'Orlando Fault, change spatially along the strike of the fault and are constant through time, instead of fluctuating as claimed previously (Giunta *et al.*, 2012). Uplift-rate values vary from 0.35 mm/yr in the centre of fault hangingwall, increasing with distance towards the fault tip and beyond to 0.89 mm/yr (Figure 5.8). This suggests that rates of uplift in the hangingwall of the fault are produced by a

combination of local fault-controlled subsidence and a "regional" uplift. Moreover, the spatial variation in uplift rate along strike suggests that the Capo D'Orlando Fault is an active fault.

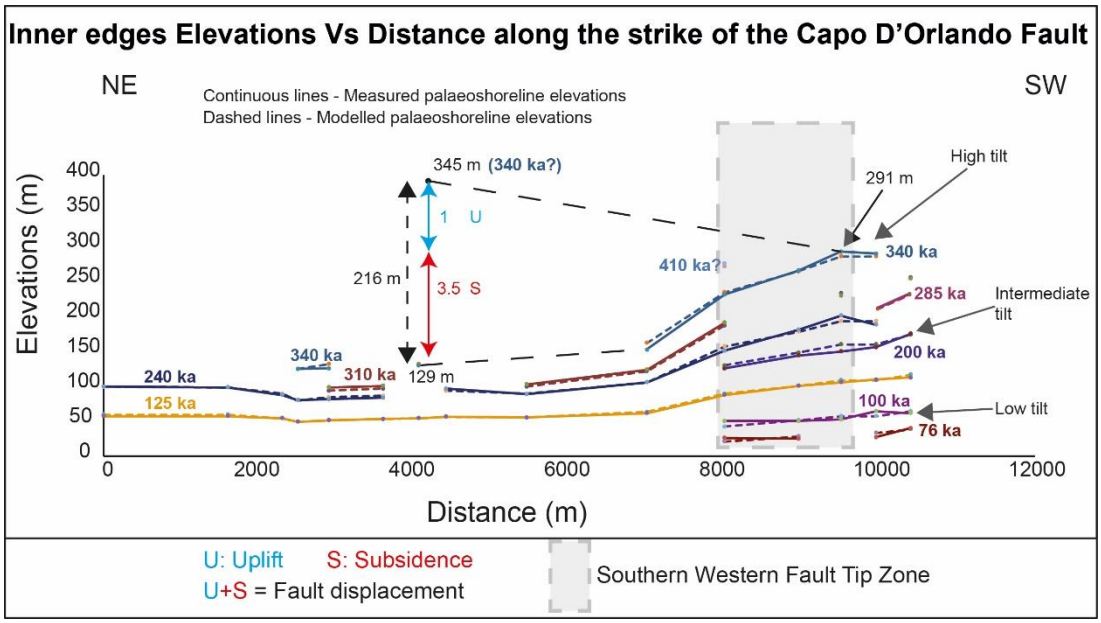

Figure 5.7: *Palaeoshoreline elevations are changing along the strike of the Capo D'Orlando Fault. Solid lines represent mapped and measured palaeoshoreline elevations mapped by using DEMs and checked in the field; closely-dashed coloured lines represent m odelled iteratively-calculated sea-level highstand elevations (or the expected elevations) mostly matching with the solid lines. Uplift/Subsidence ratio (U:S) value of 1/3.5 has been applied to the oldest (340 ka) palaeoshoreline mapped within the hangingwall to estimate the expected elevation on the footwall and derive long-term fault slip-rate. A black dashed arrowed line shows the displacement between terraces mapped in the hangingwall and footwall cut-offs. The grey box identifies the "tip zone" discussed in the text.*

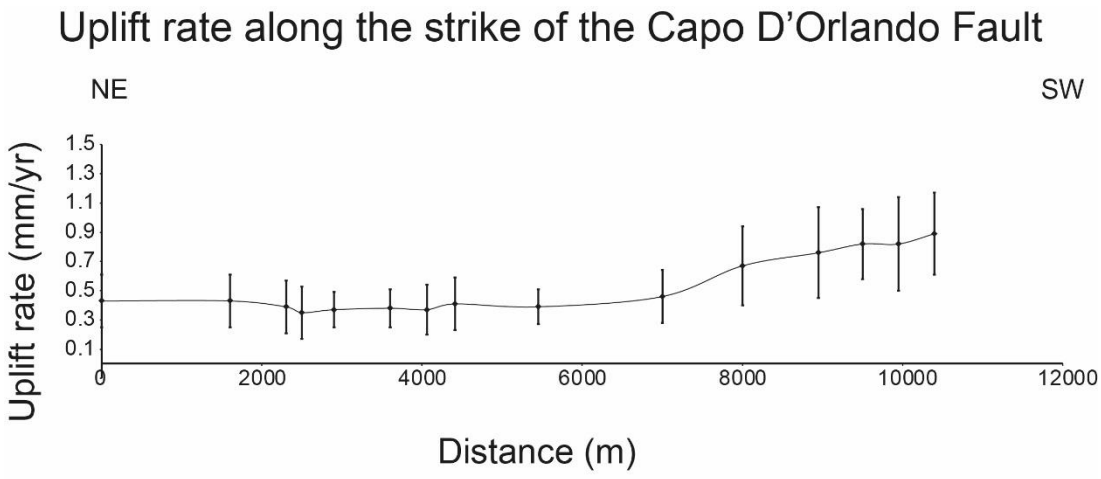

Figure 5.8: *Profile showing that uplift rates vary spatially along strike the Capo D'Orlando Fault.*

An observation that is consistent with progressive faulting through the Late Quaternary is the increase in along-strike tilt angle for successively older palaeoshorelines (Figure 5.9). Tilt angle

values for each investigated palaeoshoreline have been calculated, as a $\tan^{-1}$ of a gradient "m" of straight line equation (y=mx). It is important to highlight that these values have been derived considering the tilting measured parallel to the strike of the fault. The increase in tilt angle with age implies that older palaeoshorelines have experienced a longer history of faulting activity, again confirming that the Capo D'Orlando Fault has been active throughout the late Quaternary.

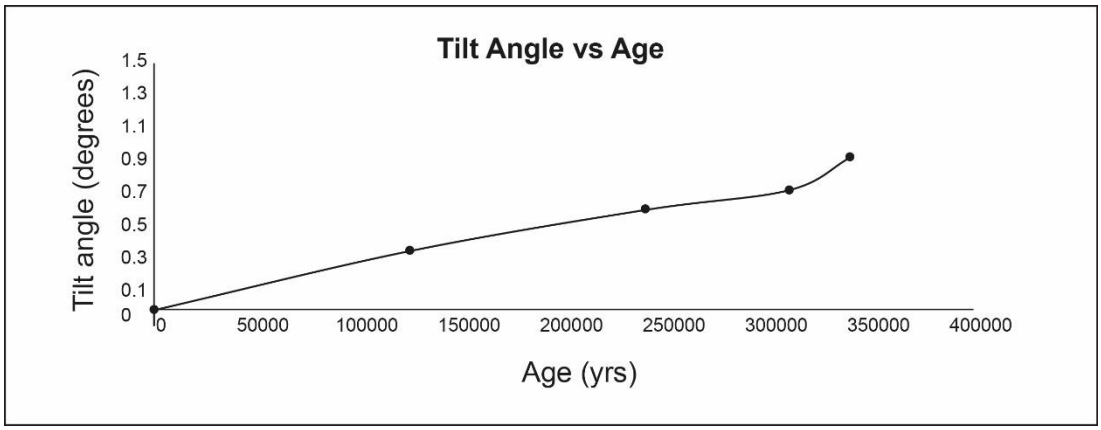

Figure 5.9: *The faulting activity of the Capo D'Orlando Fault over the Late Quaternary has tilted the investigated marine terraces; in fact, older and higher palaeoshorelines show higher tilt angle values because they have been experiencing a longer history of faulting activity.*

Another stratigraphic evidence consistent with the spatially-varying fault-controlled uplift field mapped along-strike the fault is that higher uplift rates close and beyond the fault tip has allowed the preservation of more palaeoshorelines with respect to the centre of the fault (Figure 5.7). This is to be expected due to the overprinting problem (Westaway, 1993; Roberts *et al.*, 2013) which will obliterate some marine terraces if the uplift rate is low. This implies that increase of tilt angle values and increase of the number of preserved marine terraces are diagnostic of incremental fault-controlled deformation, with deformation rates decreasing from the centre of the fault towards the tip as shown for other areas deformed by active normal faults in Greece (Armijo *et al.*, 1996; Roberts *et al.*, 2009) and the Calabrian Arc (Roberts *et al.*, 2013).

Figure 5.7 shows a "tip zone" defined by: (i) field-based evidence where no evidence for a fault scarp has been preserved at the surface, (ii) higher number of preserved marine terraces, and (iii) a shallowing of the long-term tilt angle value recorded by palaeoshorelines from NE to SW. This zone in Figure 5.2b lies where the red-coloured dashed line defines the SW fault tip. Identification of the tip zone is crucial because it provides the opportunity to correlate palaeoshorelines mapped in the hangingwall with those on the footwall by mapping them around the fault tip zone. In turn, this allows an estimate of the slip-rate on the Capo D'Orlando Fault, a value that has not previously been reported. In particular, a correlation is suggested herein between the oldest hangingwall palaeoshoreline with an age defined herein of 340 ka and a palaeoshoreline, mapped at 291 in the tip zone, mapped round the tip onto the footwall to the NE at an elevation of 345 m near the centre of footwall of the fault (see Figure 5.7). In other words, a correlation of a palaeoshoreline with a refined age is proposed across the fault. In particular, (i) taking into account the displacement implied by the difference in elevation between the location in the centre of the hangingwall of the fault (129 m) and the location within the tip zone (291 m), and (ii) applying a long-term uplift/subsidence ratio of 1/3.5 along Profile 7 at the centre of fault, intercepting the WCP mapped in the footwall to predict the footwall elevation of the 340 ka palaeoshoreline, a footwall palaeoshoreline elevation is "predicted" at 335 m which is suggested herein to be associated with the 345 m high palaoeshoreline mapped on the footwall. The implied 216 m vertical offset implies a constant long-term fault slip rate of 0.63 ± 0.02 mm/yr, derived by dividing the fault offset of 216 m by 340 kyrs (Figure 5.8). Note that the uncertainty has been estimated by applying a formula to calculate error propagation as follows: $dTR = |TR|*sqrt[(dD/D)^2 + (dt/T)^2]$ where dTR is the calculated uncertainty, TR (0.63 mm/yr) is the throw rate, D (216 m = 216000 mm) is the measured vertical offset and T (340 kyr = 340000 yr) is the time over the offset occurred.

Furthermore, the error value associated with the vertical offset (dD) is 5000 mm which is derived by barometric altimeter error resolution; error value associated with the age of highstand (dT) is 4000 yr (Siddall *et al.*, 2003; Rohling *et al.*, 2014). These results are consistent with the notion that the Capo D'Orlando Fault has been offsetting the investigated palaeoshorelines at the surface over the Late Quaternary, which in turn suggests that this fault is not a blind fault. Furthermore, these interpretations suggest that if a "regional" uplift signal exists, it has to be measured at a point beyond the fault tip-zone of the Capo D'Orlando Fault, implying a value of ~ 0.9 mm/yr. However, it is important to note that more detailed studies are needed to ascertain whether the above-value is valid, or in fact affected by possible active faults offshore.

5.5. Discussion

This chapter details an investigation of the relationship between active normal faulting, historical seismicity, "regional" uplift, and a sequence Late Quaternary palaeoshorelines. The obtained results suggest that the Capo D'Orlando fault is active and a potential source of historical earthquakes. In addition, the data suggest a constant long-term fault slip-rate and related fault-modified uplift, rather than a fluctuating uplift rate through time as suggested by other authors (Figure 5.10). These results are discussed in more detail below.

That the Capo D'Orlando is active is, perhaps, not surprising given that NE Sicily has experienced historical damaging earthquakes as shown in Figure 2.1 and 5.1. The close proximity for these events to the study area, and the lack of other potential seismic source suggest that these earthquakes may have occurred on the Capo D'Orlando fault. Thus, this

thesis suggests that the Capo D'Orlando Fault should be added within the DISS, at least as a "Debated Seismogenic Source" to improve the geography of the seismic hazard associated with the NE Sicily.

Figure 5.10 suggests that the fault-related uplift rate has been constant through time; it is suggested herein that this implies a constant fault slip-rate through time of 0.63 ± 0.02 mm/yr for the Capo D'Orlando Fault. This result is again perhaps not surprising because fault slip-rate values measured for other active normal faults, which have been accommodating the Plio-Pleistocene crustal extension along the Italian Apennines and the Calabrian Arc, are within the range 0.3 mm/yr to 2.0 mm/yr (Jacques *et al.*, 2001; Galli and Bosi, 2002; Roberts and Michetti, 2004). Also, well-known empirical correlations between fault length, maximum expected magnitude and maximum expected displacement (Wells and Coppersmith, 1994; Galli, Galadini and Pantosti, 2008) allow calculation, for the first time, of an estimated earthquake recurrence interval or T_{mean} for the Capo D'Orlando Fault. Taking into account the length of the fault mapped onshore (~ 15 km) which could be capable of earthquakes with maximum magnitude (m) of 6.4, to produce a fault slip-rate of 0.63 ± 0.02 mm/yr given 62 cm maximum slip seismic events in Mw 6.4 earthquakes implies a T_{mean} of ~ 1000 years. This value is similar to those described for other active normal faults along the Italian peninsula (Jacques *et al.*, 2001; Galli, Galadini and Pantosti, 2008; Roberts *et al.*, 2013). However, it is important to highlight the fact that the NE tip of this fault has not been identified in this or other studies. It is suggested herein that if the NE fault tip is offshore, a longer fault length, larger maximum magnitude, and hence different recurrence interval are implied (depending on the maximum earthquake magnitude chosen for the calculation of recurrence interval).

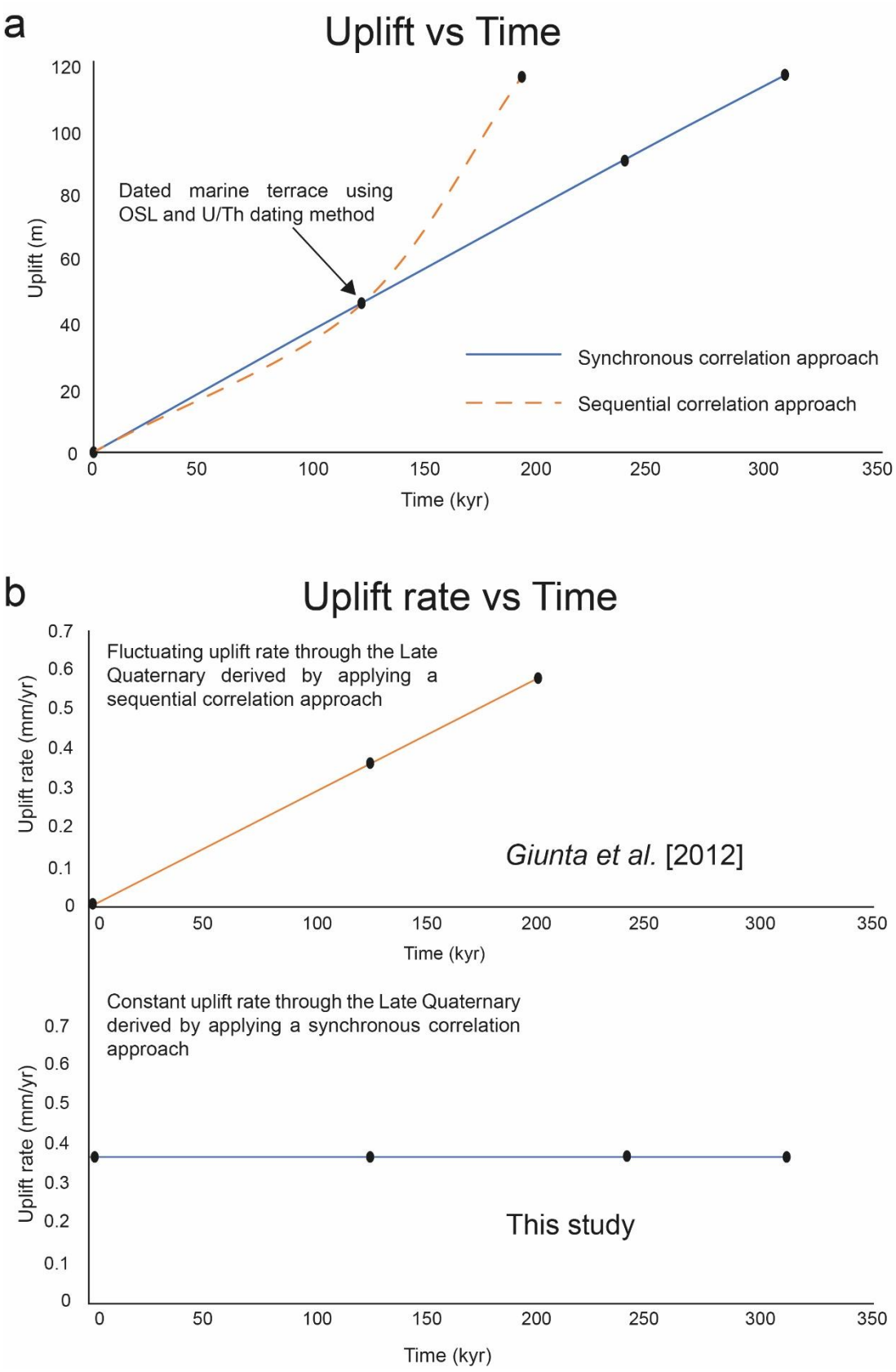

Figure 5.10: *In (a) uplift gradients are shown derived from Giunta et al., (2012) (orange-coloured dashline) and this study (blue line). The orange-coloured dash line shows an exponential growth of the uplift gradient through time driven by an absolutely-dated palaeoshoreline (125 ka). Instead, the blue-coloured line shows a constant growth of the uplift gradient through time also driven by an absolutely-*

dated palaeshoreline (125 ka). Note that changing uplift rates through time is also shown in Figure 7 (section 2) in Giunta et al., (2012).

For example, if the Capo D'Orlando Fault is longer that 15 km, this increases the possible maximum earthquake magnitude to > Mw 6.4; this, in turn, implies larger slip events and hence longer earthquake recurrence intervals; this needs further study of the extent of the offshore fault. However, it is important to note that the above assumes one scenario where a maximum magnitude earthquake is caused by earthquake rupture along the entire length of the Capo D'Orlando Fault; other scenarios are possible if only part of the fault ruptures (e.g. Roberts, 1996).

5.6. Conclusion

This chapter presents a new model for the activity and seismic hazard associated with the Capo D'Orlando fault. In contrast to previous studies, the fault is suggested to be active, responsible for historical earthquakes, and deforming at a constant rate through time. This fault activity occurs in the uplifting upper plate of the Ionian Subduction Zone, and hence the previously-suggested "regional" uplift signal has in fact been influenced by upper plate normal faulting. Also, for the first time, a long-term slip-rate for the Capo D'Orlando Fault has been calculated, with a value of 0.63 ± 0.02 mm/yr, with regional tectonic implications that will be discussed in Chapter 9. For the above reasons, the Capo D'Orlando Fault should be added to the DISS, at least as "Debated Seismogenic Source", suggesting a review of the geography of the seismic hazard in NE Sicily is required.

Chapter 6: Deformation of a foreland forebulge through time constrained by investigating differentially-uplifted Late Quaternary palaeoshorelines; the foreland Hyblean Plateau, SE Sicily.

6.1. Abstract

In this chapter, uplift rates spanning the Late Quaternary have been investigated by modelling a tectonically-deformed sequence of uplifted marine terraces. This is a crustal response due to a forebulge process occurring in the Hyblean Plateau (HP), SE Sicily, because of the ongoing Africa-Eurasia collision. Indeed, this region has historically hit by damaging earthquakes such as the "1693 SE-Sicily Earthquake" (Mw 7.4), however, long-term crustal deformation rates are poorly constrained and, consequently, the long-term seismic hazard approach. By investigating Late Quaternary marine terraces by using a synchronous correlation approach driven by new obtained absolute ages controls ($^{234}U/^{230}Th$ dating and ^{36}Cl cosmogenic dating) alongside those available in the literature, new ages for un-dated marine terraces have been refined. This has allowed the calculation of refined new uplift rates along a N-S oriented transect within the foreland region of the HP. Changes in rates of uplift constant through time and the geometry of palaeoshorelines along the coastline-parallel transect have been mapped, suggesting decreasing uplift rate values from north to south in the HP. If the uplift and its constant rate over the Late Quaternary is related to the forebulge process, this would suggest that long-term Africa-Eurasia convergence rates are constant through time, highlighting new significant knowledge for the associated long-term seismic hazard approach for one of the most seismically-active region in the Mediterranean Basin.

6.2. Introduction

Within a region of tectonic convergence, where subduction rates exceed convergence rates, a trench-ward migrating collisional thrust belt forms with extension and trans-tension processes occurring behind it; this phenomena is known as trench roll-back and is typical of the Mediterranean Basin (Malinverno and Ryan, 1986; Doglioni *et al.*, 1999; De Celles, 2012). This leads to subsidence of a foreland basin due to the adjacent thrust belt load, with a prominent negative flexure within the foredeep zone, and a positive flexural uplift next to the foredeep basin known as the forebulge zone (De Celles, 2012). The Hyblean Plateau (HP), in SE Sicily in southern Italy, represents the foreland region within the converging plate boundary between Africa and Eurasia (Malinverno and Ryan, 1986; Palano *et al.*, 2012; Chiarabba and Palano, 2017) (Figure 6.1). This region is one of the most seismically active areas in the Mediterranean Basin (Malinverno and Ryan, 1986; Bianca *et al.*, 1999; Musumeci *et al.*, 2014). Indeed, NNW-SSE directed continental convergence between the African plate and Eurasian plate is occurring with a rate of ~ 9-10 mm/yr (Faccenna *et al.*, 2001; Reilinger *et al.*, 2006; Palano *et al.*, 2012). This convergence process is seismically accommodated by two regions containing active thrusts located in the southern Tyrrhenian Sea and in the northern HP (Palano *et al.*, 2012) (Figure 6.1a). In particular, the offshore Southern Tyrrhenian Thrust Zone (STTZ), where the Mw 5.6 2002 Palermo Earthquake occurred (Azzaro *et al.*, 2004), shows a convergence rate of ~4.6 mm/yr (Mattia *et al.*, 2012; Palano *et al.*, 2012). The Sicilian Basal Thrust (SBT), with its surface trace bounding the northern part of the HP from the overthrusting Maghrebide Chain, shows a convergence rate of ~4.4 mm/yr (Lavecchia *et al.*, 2007; Mattia *et al.*, 2009; Palano *et al.*, 2012; Chiarabba and Palano, 2017) (Figure 6.1).

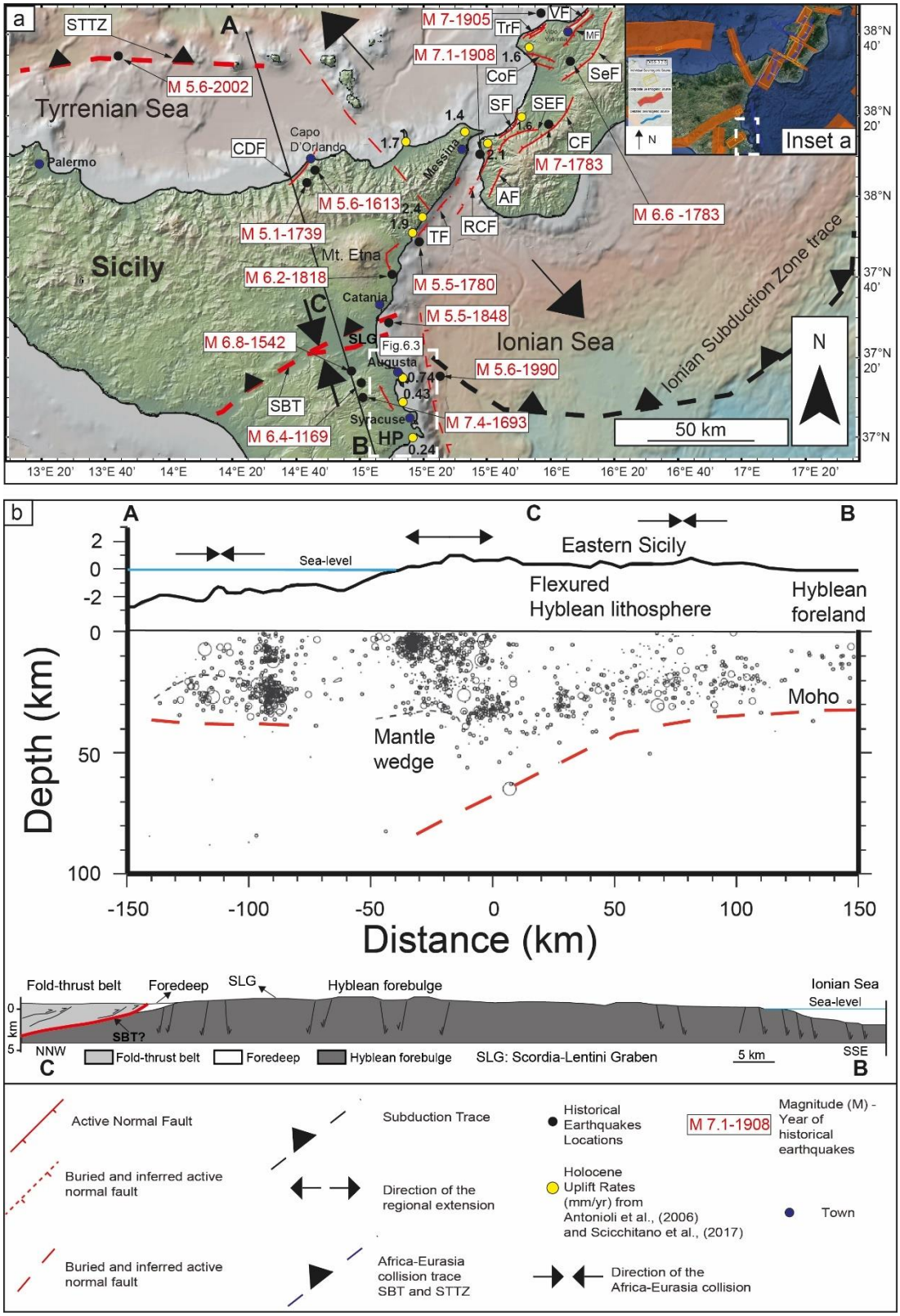

Figure 6.1: *In (a) a tectonic sketch map of the mainland Sicily is shown. The white-coloured dashed square shows the investigated area lying in the HP. Black dots show the location of historical earthquakes; yellow dots show values of Holocene uplift rates. Inset "a" shows a map with the seismogenic sources mapped within the DISS (Basili et al., 2008). In (b) a sketch cross-section shows (i) the seismicity distribution and the Moho discontinuity along the transect A-B adapted from Chiarabba and Palano, (2017). Note that the sketched geological section (adapted from Mattia et al., (2012)) shows the SBT where the Maghrebide Chain is southwardly overthrusting on the HP, producing a forebulge zone.*

The convergence process accommodated in the northern part of the HP is seismically active, and this is confirmed by several damaging earthquakes that have historically occurred in the HP such as the 1169 Mw 6.5, the 1542 Mw 6.68, the 1693 Mw 7.4, the Mw 1818 6.2 and the 1990 Mw 5.6, yet the seismogenic sources associated with these historical earthquakes are still debated (Bianca *et al.*, 1999; Guidoboni *et al.*, 2007; Lavecchia *et al.*, 2007; Visini *et al.*, 2009; Stucchi *et al.*, 2013) (Figure 6.1). For instance, some authors have investigated if the SBT, which represents the north-dipping tectonic structure where the Eurasia plate is southwardly overthrusting the Africa plate with its trace at surface located in the northern rim of the HP (Figure 6.1), could have produced the Mw 7.4 1693 Earthquake (Lavecchia *et al.*, 2007). In particular, it has been shown that: (i) the location of the proposed seismogenic sources for some historical earthquakes, such as the 1169 "Sicilia Orientale" event (Mw 6.4), the 1542 "Siracusano" event (Mw 6.8) and the 1818 Catania event (Mw 6.0), based on the analysis of the distribution of the intensity are in agreement with the geometry of the SBT and that (ii) the "*inferred distribution of the major historical and instrumental seismic activity which occurred above the SBT suggest a northward deepening of the compressional sources*" (Lavecchia *et al.*, 2007). However, some authors (Visini *et al.*, 2009) partly discarded this hypothesis because observed intensities within the HP cannot be fully reproduced by applying a forward modelling technique which estimates the data point intensities at the surface; yet, the same authors show that the SBT can justify the recorded macroseismic field in the northern part of the HP and the expected magnitude (> M 7) (Visini *et al.*, 2009), suggesting that further investigations are needed.

Despite the uncertainty in seismic sources and fault activity, uplift has been mapped within the HP due to the presence of a prominent sequence of uplifted Late Quaternary

palaeoshorelines, stretching from the Augusta peninsula in the north of the HP, to south of Syracuse town (Bianca *et al.*, 1999) (Figure 6.2).

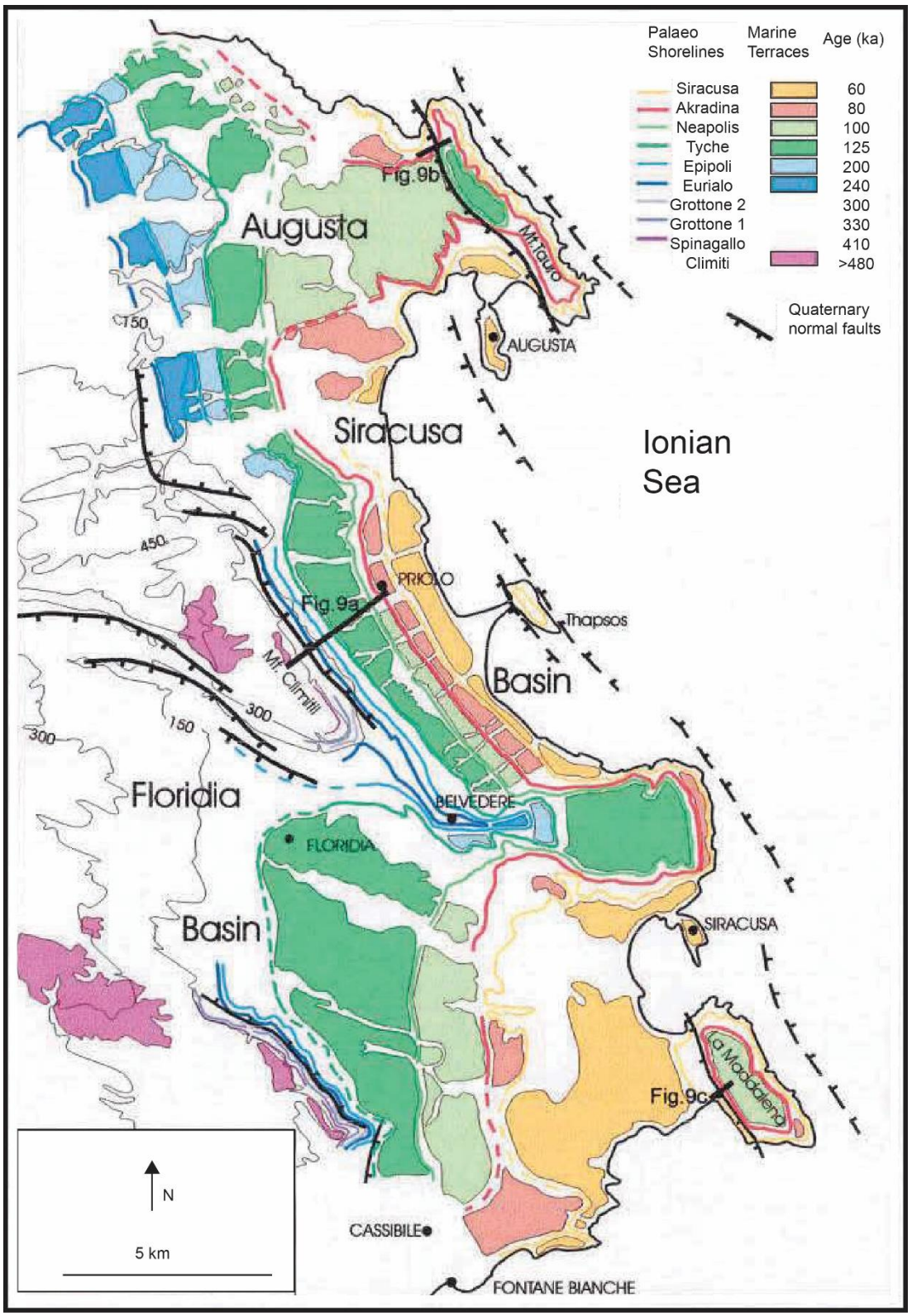

Figure 6.2: *Modified map by Bianca et al., (1999) where marine terraces are mapped and proposed ages for un-dated terraces are assigned by a "sequential" correlation approach.*

Ages of these palaeoshorelines are poorly constrained, due to the lack of abundance of absolute age controls in the region, and hence so are the associated uplift rates over the Late Quaternary. Given the lack of age control, ages for un-dated palaeoshorelines have been derived by applying a "sequential" correlation approach, which does not take into account the overprinting problem in region which is likely to have relative low uplift rates (see Chapter 3 for more details) (Roberts *et al.*, 2013; Meschis *et al.*, 2018; Pedoja *et al.*, 2018). However, it is still unclear, debated and regionally poorly-constrained if and how the uplift and the associated rates are changing spatially along the HP from north to south. Indeed, the cause of the uplift is the subject of debate, with some attributing the uplift process to the normal faulting activity occurring offshore of the HP within the southernmost part of the so-called "Sicilian-Calabrian Rift Zone" (SCRZ) (Bianca *et al.*, 1999; Monaco and Tortorici, 2000). However, recent offshore seismic surveys have mapped a ~ 45 km long, segmented normal fault system, that is east-dipping, located ~ 25 km distant from the present-day coast (Gutscher *et al.*, 2016). This distance suggests the normal fault system, even if active, may be too distant to produce significant uplift onshore. This suggests that the prominent uplift affecting the HP is barely related to the far-field footwall uplift activity of this segmented fault system (Figure 6.1).

The aim of this chapter is to test the following scientific questions:

- Is the ongoing Africa-Eurasia collision controlling the uplift of the HP, representing the foreland region?
- If so, is the uplift varying spatially from the north to the south, controlled by the forebulge process?
- Is the uplift-rate constant over the Late Quaternary?

To answer these scientific questions a field campaign has been undertaken to map uplifted palaeoshorelines and check the reliability and robustness of previous studies. Detailed geomorphological analysis is carried out using a 2 m high resolution Digital Elevation Models that covers the region from the north of the HP near Augusta town to south of Syracuse (Figure 6.3). A synchronous correlation approach has been used to investigate the sequence of palaeoshorelines to overcome the overprinting problem (see Chapter 3, section 3.4 for more details). In particular, the synchronous correlation is driven by: (i) submerged dated palaeoshorelines (Dutton *et al.*, 2009), (ii) new absolute age data from $^{234}U/^{230}Th$ dating of corals from this thesis and (iii) an attempt to use ^{36}Cl cosmogenic dating on WCPs, supported by unpublished data from an existing ^{36}Cl cosmogenic dating attempt on wave-cut platforms (WCPs) cut into Neogene-aged limestones (Spampinato, 2011), all confirming the age of a prominent palaeoshoreline. As for previous chapters, the synchronous correlation exploits knowledge of Quaternary sea-level curves (Siddall *et al.*, 2003; Rohling *et al.*, 2014) and iterates uplift scenarios to find the best match between the iteratively-calculated "predicted" sea-level highstands and the mapped palaeohoreline elevations identified in the field and through GIS analysis of DEMs. This also allows refinement of ages for the un-dated palaeoshorelines and, consequently, derivation of long-term uplift rates over the Late Quaternary. Mapped uplifted palaeoshorelines and the associated shallow marine deposits outcrop parallel to the present-day coastline over a N-S oriented transect that is 35 km in extent, from Augusta town in the north, to the south of Syracuse town. This provides the opportunity to unveil new insights regarding the Africa-Eurasia continental convergence process through time.

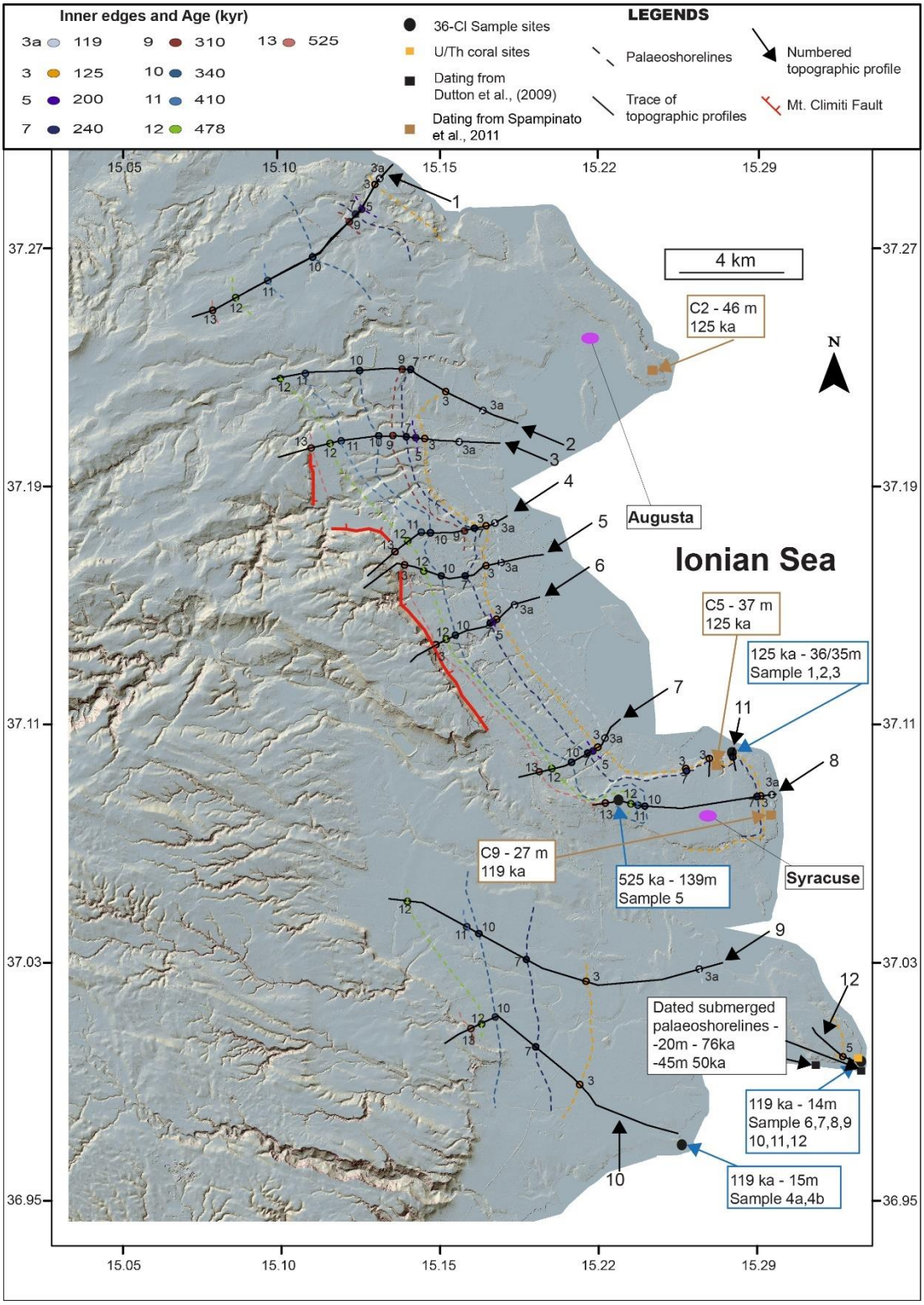

Figure 6.3: *Location maps for palaeoshorelines within the HP, SE Sicily. A 2-m resolution DEM with the associated coloured slope to highlight breaks of slop is used as base-map. Dashed coloured lines represent the inner edge of successive mapped palaeoshorelines. Locations for ^{36}Cl cosmogenic dating are shown alongside the unpublished data from Spampinato, (2011). Locations where corals for U/Th dating have been collected are shown. Numbered black lines indicate the 10 topographic profiles within the investigated area.*

6.2.1 Geological background and available palaeoshoreline ages review

An initial background regarding the HP has been provided in section 2.1.2 (Chapter 2). The HP, representing the "undeformed" foreland of the northern Sicilian Maghrebide chain, lies within the plate boundary where Africa and Eurasia are colliding (Malinverno and Ryan, 1986; Dutton *et al.*, 2009). The northern rim of the HP, where the surface trace of the SBT and the Scordia-Lentini Graben (SLG) are mapped (Figure 6.1), is thought to seismically and partially accommodate (~ 50% of the total 10 mm/yr of convergence rate) the ongoing Africa-Eurasia convergence with a constant rate since the last half million years (Mattia *et al.*, 2012; Palano *et al.*, 2012; Mastrolembo Ventura *et al.*, 2014; DeMets, Iaffaldano and Merkouriev, 2015; Chiarabba and Palano, 2017). This is in agreement with GPS-based horizontal velocity measured along the N-S oriented transect in SE Sicily (Figure 6.4) (Mattia *et al.*, 2012; Palano *et al.*, 2012; Mastrolembo Ventura *et al.*, 2014) showing an ongoing convergence process.

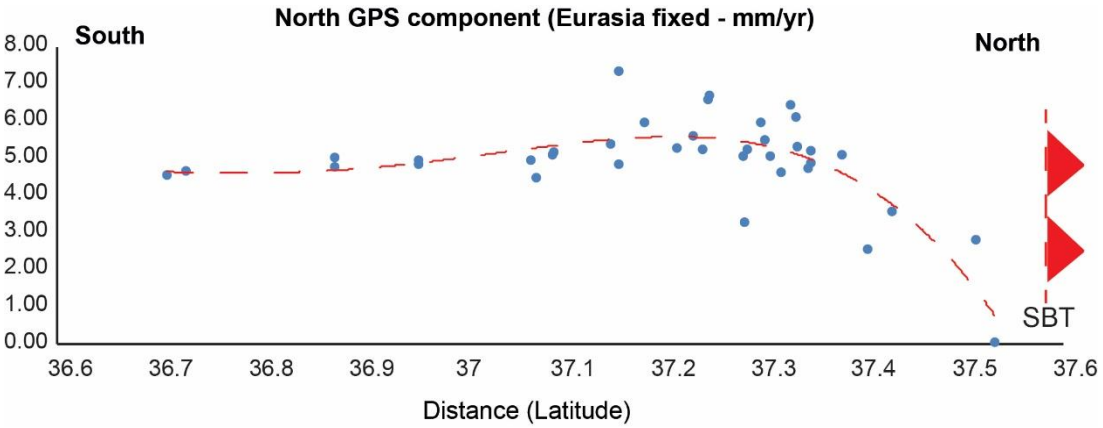

Figure 6.4: *GPS measurements of horizontal velocities* (Mattia *et al.*, 2012; Palano *et al.*, 2012; Mastrolembo Ventura *et al.*, 2014) *along the N-S oriented investigated transect in this thesis showing contraction process near the mapped trace of the SBT.*

This is also in agreement, for instance, with the process of tectonic inversion mapped north of Augusta town within the SLG where extensional faults have been re-activated as high-angle thrust faults since 0.85 ky (Mattia *et al.*, 2012; Mastrolembo Ventura *et al.*, 2014) (Figure 6.1).

For some, the seismogenic source of the 9th January 1693 Earthquake (Mw 6), interpreted as a foreshock of the 11th January 1693 Earthquake (Mw 7.4), could be located within the tectonically-inverted graben north of Augusta (Mastrolembo Ventura *et al.*, 2014). Moreover, distribution of crustal seismicity northwardly deepening show a continental lithospheric bending of the HP beneath the thrust front of the Maghrebide chain (Lavecchia *et al.*, 2007; Musumeci *et al.*, 2014; Chiarabba and Palano, 2017) (Figure 6.1), suggesting that the SBT could have a crucial role for accommodating part of the Africa-Eurasia tectonic convergence. In fact, even though geological (e.g. DeMets, Iaffaldano and Merkouriev, 2015 and this thesis) and geodetic (Reilinger *et al.*, 2006; Mattia *et al.*, 2012; Palano *et al.*, 2012; Mastrolembo Ventura *et al.*, 2014; Musumeci *et al.*, 2014; Chiarabba and Palano, 2017) investigations show a distinct indication of compressive tectonics no prominent seismic events have been recorded, suggesting a possible seismic gap if the mapped prominent shallow crustal deformation is taken into account (Musumeci *et al.*, 2014).

Although the paucity of availability of absolutely-dated marine terraces, previous geoscientists attempted to investigate the uplift process affecting the HP by applying a "sequential" correlation approach (see Chapter 3 for further details on this approach), deriving a poorly-constrained either spatially and temporally uplift rate value of 0.65 mm/yr (Bianca *et al.*, 1999) (Figure 6.2). A successive attempt to refine the uplift rate history of the investigated area has been proposed by dating submerged palaeoshorelines offshore Syracuse town (Dutton *et al.*, 2009) (Figure 6.3). In particular, submerged palaeoshorelines have been mapped respectively at -22 m and – 45 m, and assigned to the 76 ka and 50 ka sea level highstands (Figure 6.3, see section 6.3 for details), suggesting a new uplift scenario. In this

thesis, these absolutely-derived age controls are used to drive a synchronous correlation approach (see section 6.3).

New knowledge about the ages of the investigated sequence of palaeoshorelines in SE Sicily has been attempted by sampling wave-cut platforms (WCPs) cut into Neogene-aged limestone for ^{36}Cl cosmogenic dating along the actual coastline of SE Sicily (Spampinato, 2011) (Figure 6.3). In particular, un-published data from a PhD thesis (Spampinato, 2011) provide exposure ages for WCPs which have been discarded because thought to be affected by high rate of erosion.

Samples	Elevations (m)	36-Cl Conc. (Atoms of 36-Cl/g of sample)	Terrace name and proposed Age (ka) after Bianca et al., (1999) – Figure 6.3	Age (kyrs)	Total uncertainty (kyr)
C2	46	1250000	Neapolis (100 ka)	62.9	6.2
C5	37	1220000	Neapolis (100 ka)	61.8	6.1
C9	27	1090000	Akradina (80 ka)	56.3	5.4

Table 6.1: *Samples from an un-published PhD thesis (Spampinato, 2011) for 36Cl cosmogenic dating but discarded because initially thought to be affected by high erosion rates. These three samples are re-analysed and re-interpreted in this thesis. Sample locations are shown in Figure 6.3.*

Spampinato (2011) provides sampling location information (Figure 6.3), yet, a geomorphological analysis with associated topographic profiles is not shown. In this chapter, some of these un-published data are re-analysed and re-interpreted (Table 6.1), taking into account reasonable erosion rate scenarios, suggested by some (Furlani *et al.*, 2009; Tucker *et al.*, 2011), by using the CRONUSCalc (Marrero *et al.*, 2015, 2016, see Chapter 3 for further details) in order to confirm the age of a prominent palaeoshoreline formed during the Last Interglacial Maximum (LIM). In particular, sampling locations by Spampinato (2011) are checked in the field and topographic profiles using high resolution DEMs are constructed to

show the geomorphological relationship between sampling location and the associated marine terrace inner edges (Figure 6.5). In this thesis, these re-analysed and re-interpreted exposure ages from ^{36}Cl cosmogenic dating are used to drive a synchronous correlation approach.

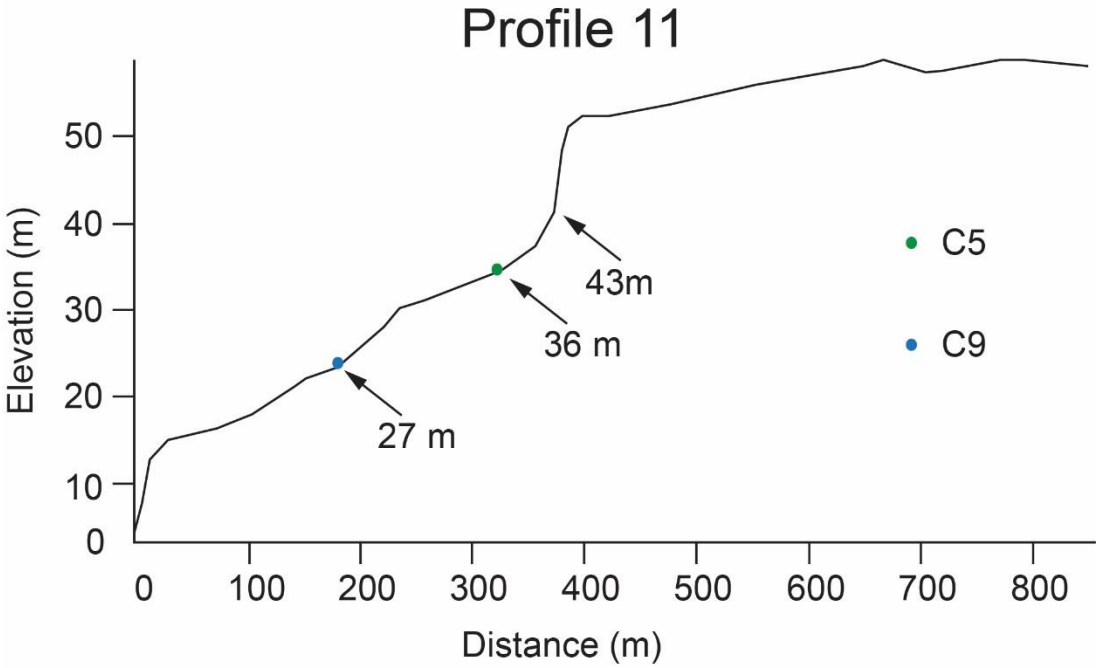

Figure 6.5: *Topographic profile constructed along the sequence of palaeoshorelines attemped to date by Spampinato (2011) and this thesis. The sample location of "C5" from Spampinato, (2011) lies near (~ 300 m apart) where "Sample 1, 2 and 3" are mapped and collected.*

In summary, in this thesis a sequence of uplifted Late Quaternary marine terraces are investigated by applying a synchronous correlation approach which allows to refine uplift rate scenario taking into account the "overprinting problem", typical of regions affected by low uplift rate (Roberts *et al.*, 2013; Meschis *et al.*, 2018; Pedoja *et al.*, 2018). Indeed, this approach is driven by available submerged dated palaeoshorelines offshore of Syracuse (Dutton *et al.*, 2009) (Figure 6.3), re-visited un-published data of ^{36}Cl cosmogenic dating on WCPs in limestone from a PhD thesis (Spampinato, 2011) and a new obtained age control derived by U/Th dating on corals.

In the next section, the approach and further details on the above-mentioned ages are presented.

6.3. Methods and approach

The approach to test the scientific hypotheses mentioned in Section 6.2 has been already described in detail in Chapter 3. Palaeoshoreline elevations have been mapped on 2 m high resolution DEMs by constructing 12 topographic profiles and conducting a detailed topographic analysis along a N-S oriented transect parallel to the actual coastline in SE Sicily (Figure 6.3). The palaeoshorelines mapped on the DEMs have been checked in the field, using as a guide previous mapping by Bianca *et al.*, (1999) (Figure 6.2).

6.3.1. Digital Elevation Models analysis and field mapping of uplifted Late Quaternary palaeoshorelines

Detailed GIS-based geomorphological analysis, by using 2 m high resolution DEMs, alongside field mapping of palaeoshorelines have been described in Chapter 3 (Section 3.1). In particular for this region, 12 topographic profiles have been constructed parallel to the present-day coastline from north to south (Figure 6.3). The field work focussed on checking these profiles and has covered an area from north of Augusta town to south of Syracuse town. By using previous mapping (Bianca *et al.*, 1999) as a guide (Figure 6.2), palaeoshorelines and their associated marine terraces have been re-checked and re-mapped, focussing on the 12 topographic profiles identified on DEMs (Figure 6.3). The field work has also involved sampling wave-cut platforms (WCPs) for *in situ* ^{36}Cl cosmogenic exposure dating (Figure 6.6) and sampling corals from marine terrace deposits for $^{234}U/^{230}Th$ dating (Figure 6.7).

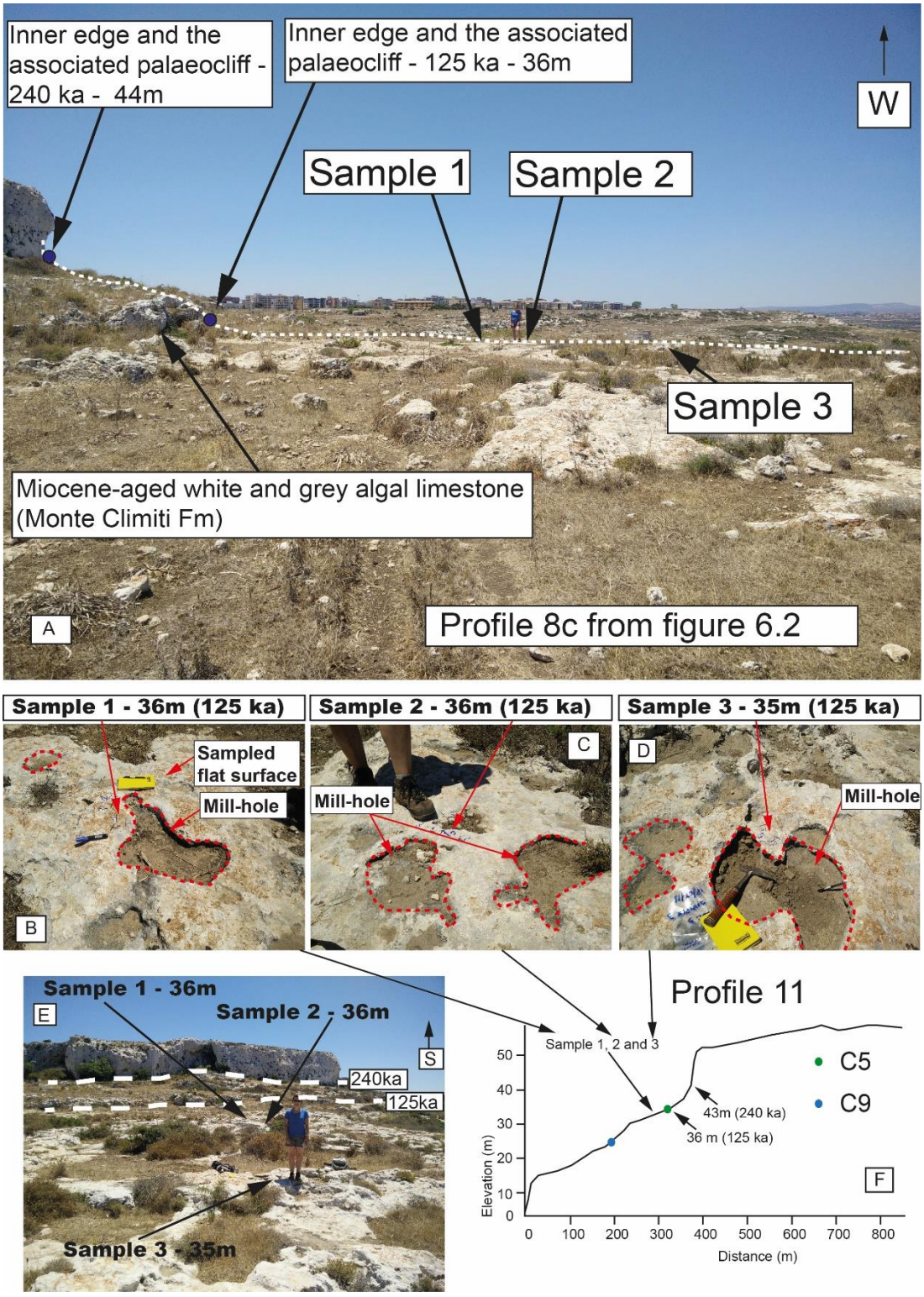

Figure 6.6: *(a) Field photo, locating Samples 1, 2 and 3 for ^{36}Cl cosmogenic dating. Note that these three samples have collected ~300 m away from those unpublished by Spampinato, (2011), and on the same geomorphic surface. Details of geomorphic features of the sampled WCP, confirming wave action, such as mill-holes are shown in (b), (c) and (d). (e) A perspective view of successive marine terrace inner edges is shown. In (f) a profile shows the topography and geomorphology of the sampled palaeoshorelines with associated inner edges and the spatial relationship with samples collected by Spampinato (2011). Note that samples "C5" and "C9" in panel (f) are from Spampinato, (2011) PhD thesis.*

Mapping shows that the wave-cut platforms are essentially the lateral time equivalent of marine terrace deposits, in that they probably formed in the same sea-level highstand, but in some cases the wave-cut platforms are cut into the marine terrace deposits, giving insights into the depositional/erosional history during the sea-level highstand. More detail on the samples collected is given below.

Sampling locations for ^{36}Cl cosmogenic dating have been described in detail in Chapter 3 (section 3.3). For this investigated area 12 samples for ^{36}Cl cosmogenic dating have been collected (Figure 6.6 - for sample locations see map in Figure 6.3). In particular three samples (Sample 1, 2 and 3 collected between 36 m and 35 m above the sea level) have been collected close to those studied by Spampinato, (2011), but not published, such as "C5" and "C9", respectively at 37 m and 27 m. Spampinato, (2011) also collected sample "C2" close to Augusta town, at 46 m in north of the investigated area, where Profile 1 and 2 have been constructed (Figure 6.3 and Table 6.1).

A coral colony (*Cladocora caespitosa*) has been mapped and collected to be dated by applying $^{234}U/^{230}Th$ dating (See Chapter 3 for more details). In particular, this colony forms a bafflestone, where Quaternary bioclastic calcarenite is trapped within and around the coral colony. After early marine cementation of the bafflestone and surrounding sediment wave action cut a wave-cut platform into the bafflestone (Figure 6.7). This sequence suggests preservation of sub-wave base bioclastic sands cemented by early marine cements during sea-level rise toward the highstand. Then, at the sea-level highstand, or as sea-level fall, wave erosion cut into the lithified sediments containing the corals forming the wave-cut platform.

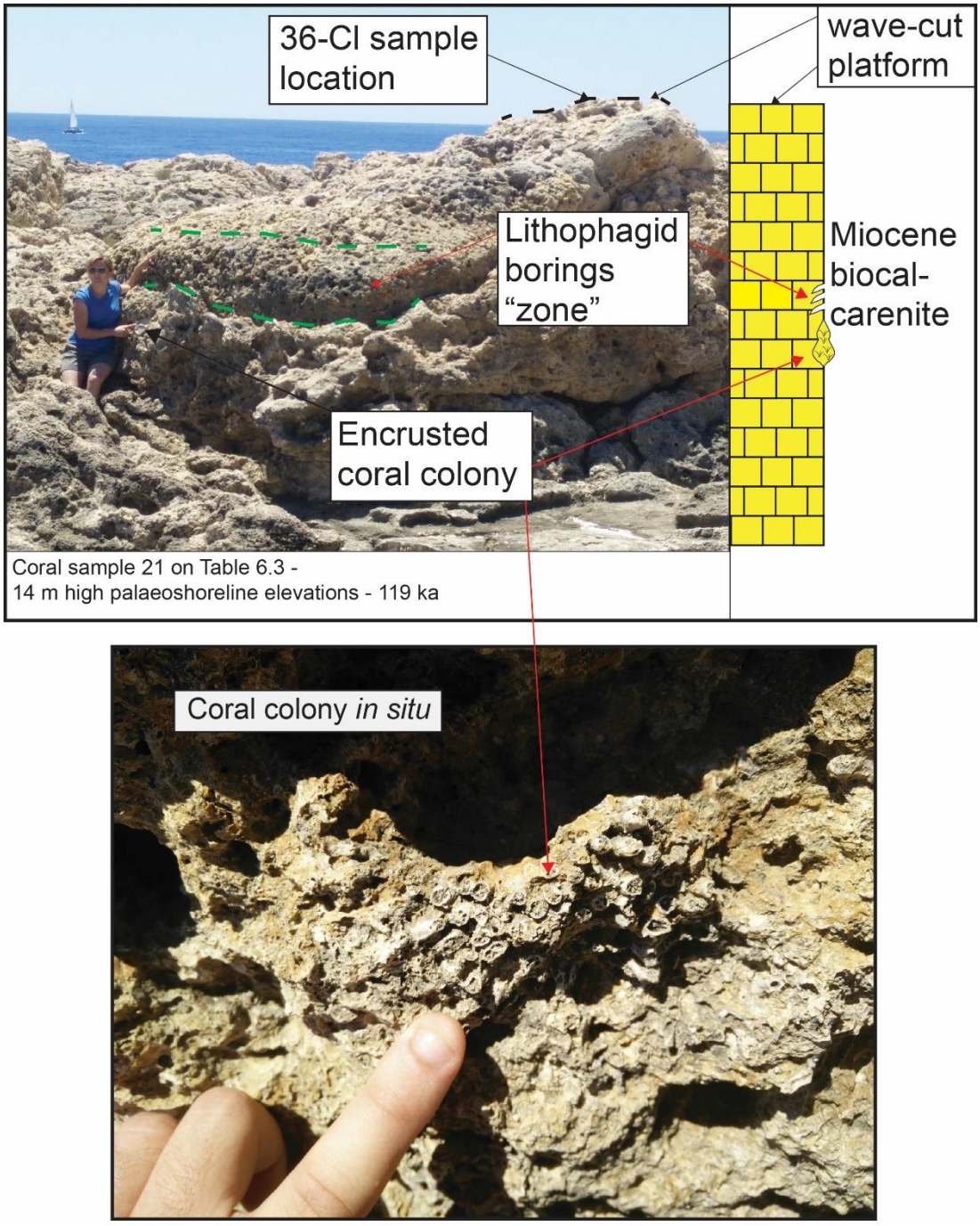

Figure 6.7: *Top image shows a perspective view of the area where a coral colony has been sampled for U/Th age determination, with a sketch stratigraphic log. Bottom image shows details of the coral colony in-situ.*

6.3.2. Age constraints to drive the synchronous correlation technique

In this chapter, new ages from $^{234}U/^{230}Th$ dating on corals and from unpublished ^{36}Cl cosmogenic dating on WCPs cut into limestones (this thesis, and Spampinato, 2011) have been obtained and used, alongside ages available in the literature (Dutton *et al.*, 2009). Table 6.2

shows absolute age data from offshore caves dated by U-series on speleothem calcite and ^{14}C dating on layers of calcite serpulid encrusting the speleothems when the cave was flooded (Dutton *et al.*, 2009) that allowed the dating of two submerged palaeoshorelines offshore south of Syracuse; the locations of these submerged palaeoshorelines are shown in Figure 6.3. This also suggests, for instance, that the "Akradina terrace" (pink terrace in Bianca's map in Figure 6.2) could belong to the MIS 5e (125 ka) (Dutton *et al.*, 2009), suggesting an older age with respect to the proposed age of 80 ka by Bianca et al., (1999).

Reference	**Dating Method**	**Dated sample description**	**Profile number**	**Assigned Highstand (ka)**	**Palaeo-shoreline Elevation (m a.s.l)**
Dutton et al., 2009	U/Th	*"Three specimens of stalagmite."*	9a	76	-22
Dutton et al., 2009	U/Th	*"A specimen of stalactite."*	9a	50	-45

Table 6.2: *Age controls derived from two submerged palaeoshorelines available in the literature. Locations are shown in Figure 6.3.*

A new age from U/Th dating technique on corals has allowed to confirm that the age of a prominent palaeoshoreline cannot be younger than MIS 5c (100 ka), in agreement with those proposed by Dutton et al., (2009) (Table 6.3).

Sample	(230Th/234U)	Uncertainty (2 s.e.)	(234U/238U)	Uncertainty (2 s.e.)	Age (ka)	+	-
21	0.6610	0.00425	1.1032	0.008	102	1.7	1.7

Table 6.3: *Measurements of U/Th isotope ratios of a coral sample collected near Syracuse town. The location of the collected corals is shown in Figure 6.3 and 6.7*

As described and illustrated in Chapter 3, ^{36}Cl cosmogenic dating has been attempted to date WCPs mapped along the N-S oriented transect attempting to gain more ages to drive the synchronous correlation technique, alongside the available age controls shown in Table 6.2. In particular, Table 6.4 shows 12 WCPs that have been sampled from field campaign which three of them (Sample 1, 2 and 3) lies near to those mapped and sampled by

Spampinato, (2011) (Table 6.1), which are not published but herein this thesis re-analysed and re-interpreted in the next section (section 6.4) (C5 and C9 in Table 6.1 - Figure 6.3 and 6.5). However, it is shown that some of sampling locations (Samples 5-12) appear to have been subject to high erosion as the obtained exposure ages are low (Table 6.4); it may be that these ages need to be discarded for present purposes.

Sample	36-Cl Conc. (Atoms of 36-Cl/g of sample)	Erosion rate (mm/ky)	Exposure Age (kyr)	Total uncertainty (kyr)	Elevation (m)	Expected Age (ka)
1	444512.7971	8	31.1	7.4	36	125
2	501752.7274	8	35.2	8.6	36	125
3	529940.5325	8	35.7	8.6	35	125
5	377426.451	8	22.5	5.5	139	525
6	435056.1338	8	29.1	6.5	14	119
7	378052.1812	8	25.1	5.6	14	119
8	144167.6404	8	14.3	3.2	14	119
9	452615.3345	8	32.5	7.5	14	119
10	113835.1077	8	10.7	2.3	14	119
11	413138.7467	8	27.7	6.3	14	119
12	444512.7971	8	31.1	7.4	14	119

Table 6.4: *Exposure ages from ^{36}Cl cosmogenic dating are shown in the table. Sampling locations are shown in Figure 6.3 and in Chapter 3.*

New (U/Th dating), re-interpreted un-published age data (Spampinato, 2011) and already-published age controls (Dutton *et al.*, 2009) have been used to drive the synchronous correlation approach between "predicted" sea-level highstand elevations synchronously-calculated and "measured" palaeoshoreline elevations mapped in the field and on high-resolution DEMs. As in previous chapters (4 and 5), a correlation between multiple "predicted" sea-level highstands and multiple "measured" uplifted Late Quaternary marine terrace elevations have been derived, which forces one to maximise the coefficient of determination R^2 through a linear regression.

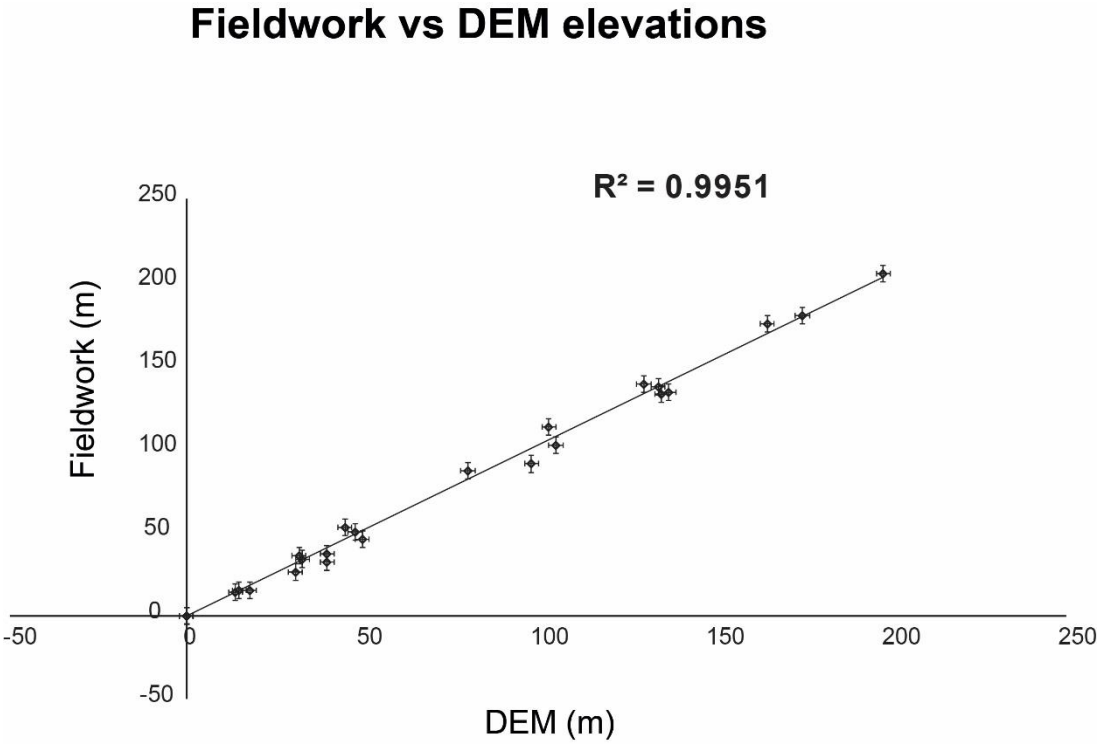

Figure 6.8: *Graph showing the relationship between field-based and DEM-based inner edge elevation measurements. The R^2 value > 0.99 confirms a very robust relationship suggesting that elevations measured elsewhere in the DEM are likely to be accurate.*

Mapped palaeoshoreline elevations that are used to derive uplift rates were derived both from field observations using a hand-held barometric altimeter and DEMs-based observations. Note that using data from high resolution DEMs was critical due to the fact that thick vegetation and private lands did not allow to check all field locations. In particular, inner edges of marine terraces have been checked in the field and compared with those mapped in the DEMs. A correlation between field and DEMs-based elevation data proves that GIS-based geomorphological analysis appears to be robust to use in uplift rate calculations (Figure 6.8).

6.4. Results

In this section, obtained results describing observations of the marine terraces are shown. By using a synchronous correlation approach, identified palaeoshorelines correlated

with sea-level highstands are shown; this correlation is driven by re-assessing un-published data (Spampinato, 2011) which attempt to date WCPs by using ^{36}Cl cosmogenic dating, a new coral age by using U/Th dating technique alongside available submerged dated palaeoshorelines (Dutton *et al.*, 2009). Then spatial and temporal constraints on this sequence of uplifted Late Quaternary palaeoshorelines are used to derive a new uplift rate scenario from the north to south within the HP.

Table 6.5 shows all mapped palaeoshoreline elevations with refined age by applying a synchronous correlation approach; it is critical to highlight that because of heavy vegetation and limited access for private houses, not all palaeoshoreline elevations were checked in the field. However, a comprehensive and exhaustive GIS-based topographic analysis using 2 m high resolution DEMs has been carried out which shows, as in the previous chapters, gently sloping terraced surfaces bounded by steeper scarp-like palaeo-seacliffs as marine terraces, as previous shown by others (e.g. Armijo *et al.*, 1996; Roberts *et al.*, 2013; Meschis *et al.*, 2018).

Palaeoshoreline (Profile number)	**DEMs Elevations (m)**	**Expected Elevations (m)**	**Field Elevations (m)**	**Our proposed Age (ky)**	**Age proposed by Bianca et al., 1999 (ky)**	**UTM Coordinate**
3a (1)	39	44	32	119	60	33 S 0511798 4128664
3 (1)	53	56	-	125	80	33 S 0511552 4128355
5 (1)	73	77	-	200	-	33 S 0510992 4127423
7 (1)	92	93	-	240	100	33 S 0510876 4127282
9 (1)	110	105	-	310	-	33 S 0510678 4127069
10 (1)	143	144	-	340	125	33 S 0509179 4125651
11 (1)	164	163	-	410	-	33 S 0507622 4124802
12 (1)	205	196	-	478	200	33 S 0506230 4124048
13 (1)	235	235	-	525	240	33 S 0505295 4123550
3a (2)	30	37	-	119	60	33 S 0515345 4119964

3 (2)	48	49	-	125	80	33 S 0514217 4120518
7 (2)	78	79	-	240	100	33 S 0512863 4121361
9 (2)	89	87	-	310	-	33 S 0512577 4121369
10 (2)	124	124	-	340	125	33 S 0511095 4121342
11 (2)	149	139	-	410	-	33 S 0509086 4121288
12 (2)	180	167	-	478	200	33 S 0508187 4121081
3a (3)	33	35	-	119	60	33 S 0514208 4118690
3 (3)	45	47	-	125	80	33 S 0513463 4118739
5 (3)	63	62	-	200	-	33 S 0512975 4118790
7 (3)	80	75	-	240	100	33 S 0512874 4118797
9 (3)	87	82	-	310	-	33 S 0512465 4118832
10 (3)	114	119	-	340	125	33 S 0511617 4118857
11 (3)	142	132	-	410	-	33 S 0510498 4118726
12 (3)	157	160	-	478	200	33 S 0509978 4118590
13 (3)	198	196	205	525	240	33 S 0509238 4118419
3a (4)	25	31		119	60	33 S 0515954 4115491
3 (4)	41	43	-	125	80	33 S 0515706 4115434
7 (4)	64	67	-	240	100	33 S 0515298 4115351
9 (4)	79	71	-	310	-	33 S 0514853 4115267
10 (4)	115	107	-	340	125	33 S 0513649 4115181
11 (4)	120	118	-	410	-	33 S 0513067 4115071
12 (4)	135	143	-	478	200	33 S 0512748 4114826
13 (4)	172	178	-	525	240	33 S 0512365 4114546
3a (5)	28	28	-	119	60	33 S 0516074 4114009
3 (5)	40	40	-	125	80	33 S 0515745 4113944
7 (5)	66	62	-	240	100	33 S 0514956 4113539
10 (5)	96	100	-	340	125	33 S 0514144 4113529
12 (5)	135	134	133	478	200	33 S 0513225 4113844

13 (5)	175	167	180	525	240	33 S 0512742 4113972
3a (6)	30	28	-	119	60	33 S 0516603 4112325
3 (6)	40	40	37	125	80	33 S 0516210 4111940
5 (6)	51	51	-	200	-	33 S 0516074 4111853
7 (6)	60	62	-	240	100	33 S 0515909 4111750
10 (6)	105	100	-	340	125	33 S 0514740 4111378
12 (6)	134	134	137	478	200	33 S 0514325 4111194
13 (6)	165	167	175	525	240	33 S 0513822 4110995
3a (7)	20	21	-	119	60	33 S 0520284 4107458
3 (7)	33	33	34	125	80	33 S 0520014 4107098
5 (7)	36	39	-	200	-	33 S 0519936 4107052
7 (7)	48	48	50	240	100	33 S 0519682 4106913
10 (7)	80	80	87	340	125	33 S 0519037 4106554
12 (7)	105	105	102	478	200	33 S 0518482 4106306
13 (7)	137	136	134	525	240	33 S 0517809 4106154
3a (8)	18	21	27	119	60	33 S 0526586 4105288
3 (8)	32	32	36	125	80	33 S 0526126 4105231
7 (8)	50	47	46	240	100	33 S 0525975 4105215
10 (8)	76	78	-	340	125	33 S 0523251 4104783
11 (8)	86	83	-	410	-	33 S 0521890 4104843
12 (8)	98	103	91	478	200	33 S 0521306 4104935
13 (8)	130	133	139	525	240	33 S 0520334 4104971
3a (9)	15	18	15	119	60	33 S 0523728 4098645
3 (9)	31	29	26	125	80	33 S 0518752 4098441
7 (9)	45	42	53	240	100	33 S 0517210 4099084
10 (9)	68	71	-	340	125	33 S 0515619 4099905
11 (9)	76	75	-	410	-	33 S 0514704 4100423
3 (10)	26	25	-	125	80	33 S 0519260 4094329

7 (10)	38	33	-	240	100	33 S 0517321 4095976
10 (10)	61	59	-	340	125	33 S 0516110 4096899
12 (10)	76	76	-	478	200	33 S 0515678 4096690

Table 6.5: *All mapped inner edges from DEM and fieldwork with age assigned via synchronous correlation are shown. Note that not all the locations for inner edges mapped by DEM analysis have been checked with GPS in the field because the investigated area is in places thickly-vegetated and densely-populated with private properties. However, see Figure 6.5 for a check of consistency between the two databases.*

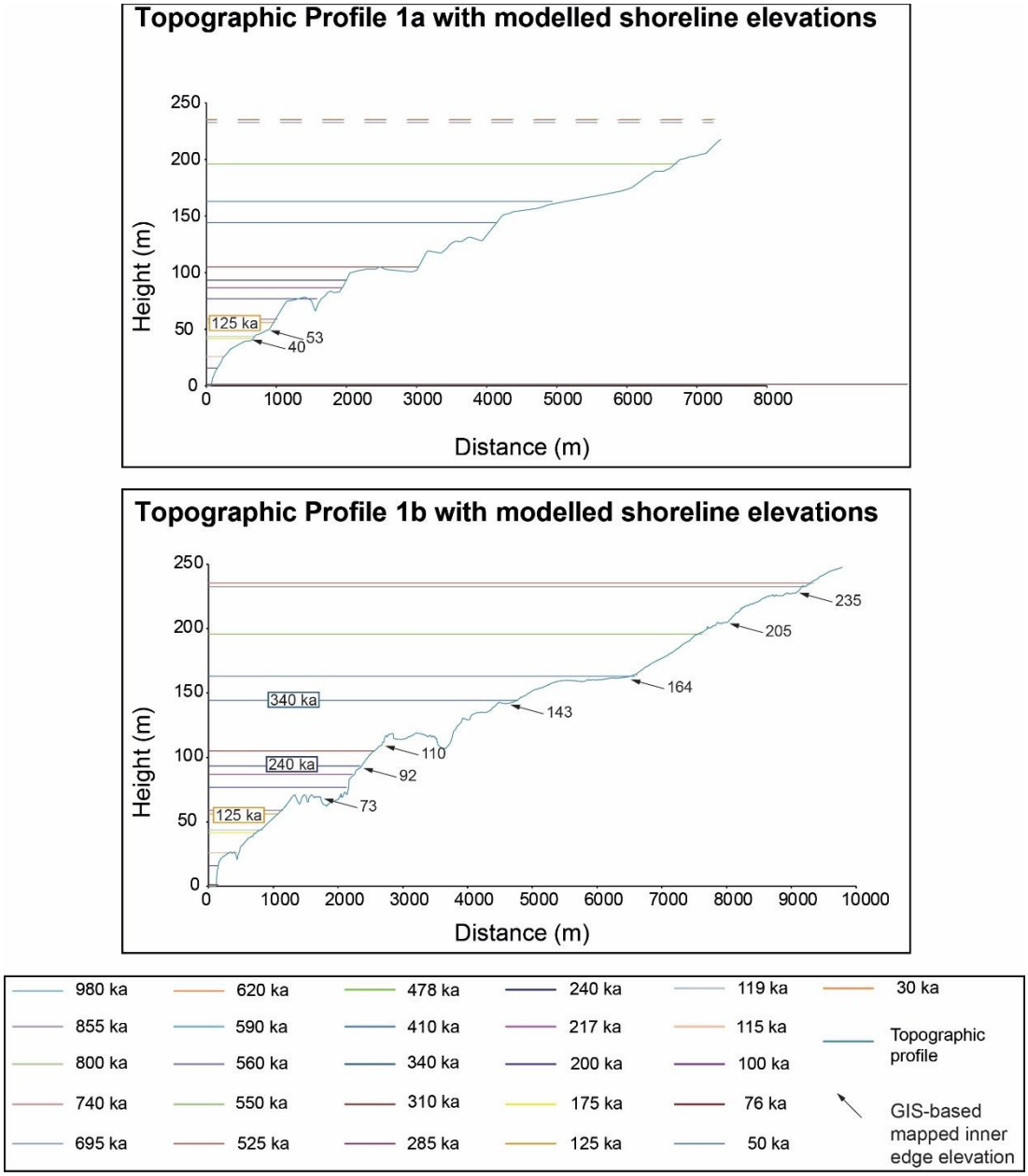

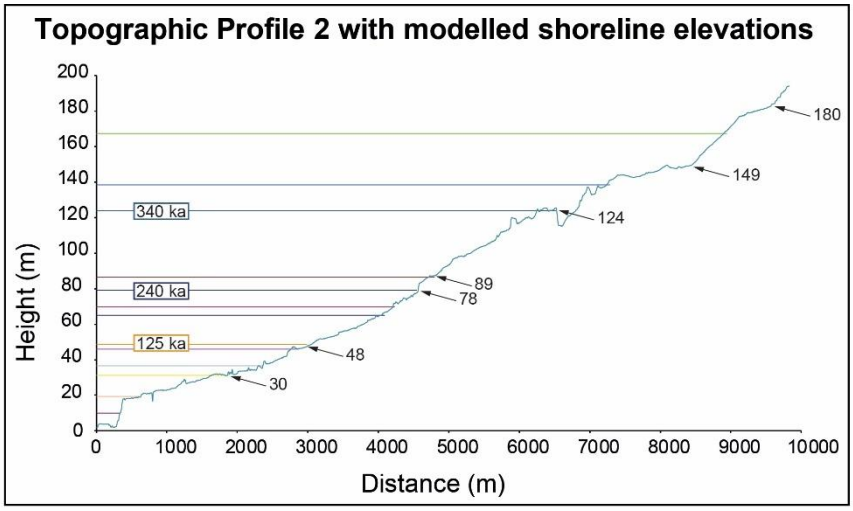
Topographic Profile 2 with modelled shoreline elevations
Height (m)
Distance (m)
340 ka
240 ka
125 ka
180
149
124
89
78
48
30

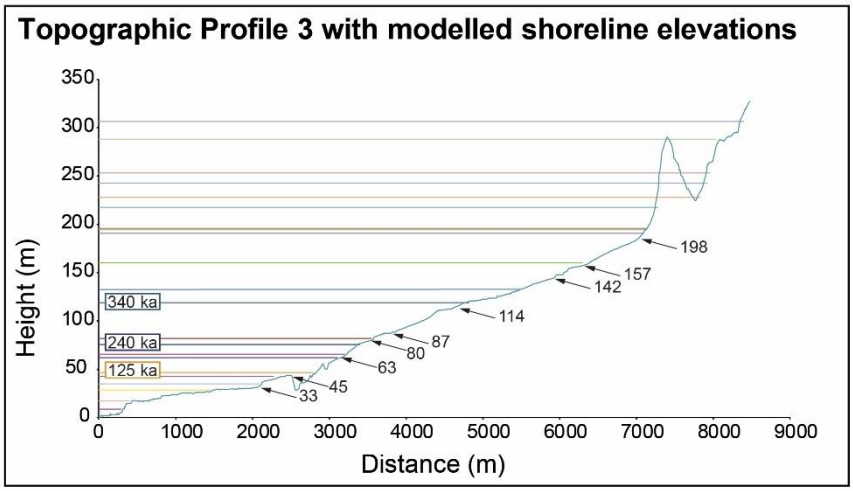
Topographic Profile 3 with modelled shoreline elevations
Height (m)
Distance (m)
340 ka
240 ka
125 ka
198
157
142
114
87
80
63
45
33

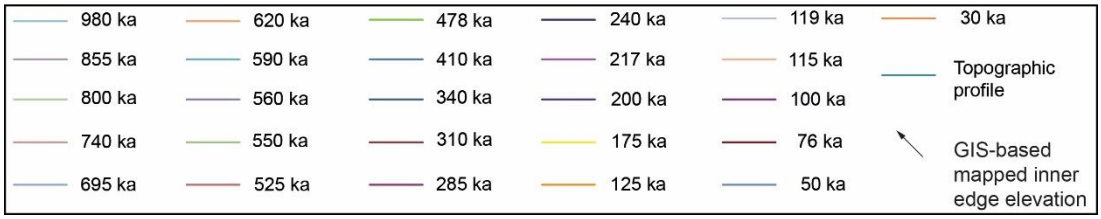
980 ka
855 ka
800 ka
740 ka
695 ka
620 ka
590 ka
560 ka
550 ka
525 ka
478 ka
410 ka
340 ka
310 ka
285 ka
240 ka
217 ka
200 ka
175 ka
125 ka
119 ka
115 ka
100 ka
76 ka
50 ka
30 ka
Topographic profile
GIS-based mapped inner edge elevation

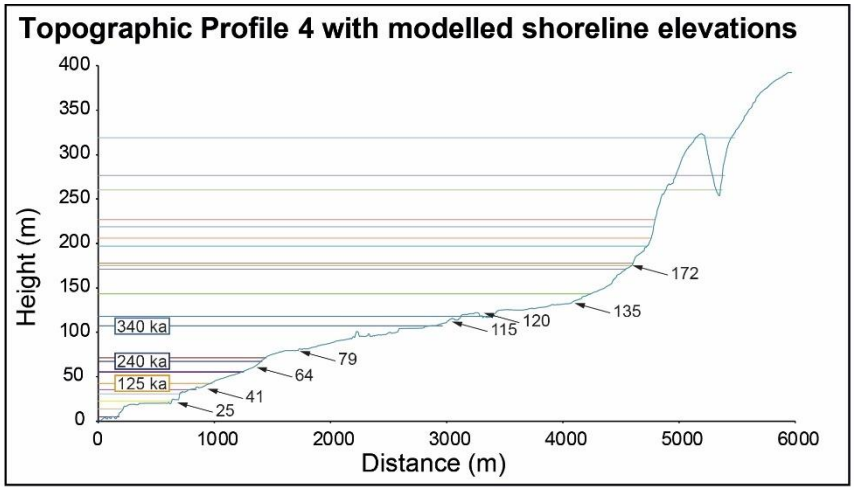
Topographic Profile 4 with modelled shoreline elevations
Height (m)
Distance (m)
340 ka
240 ka
125 ka
172
135
120
115
79
64
41
25

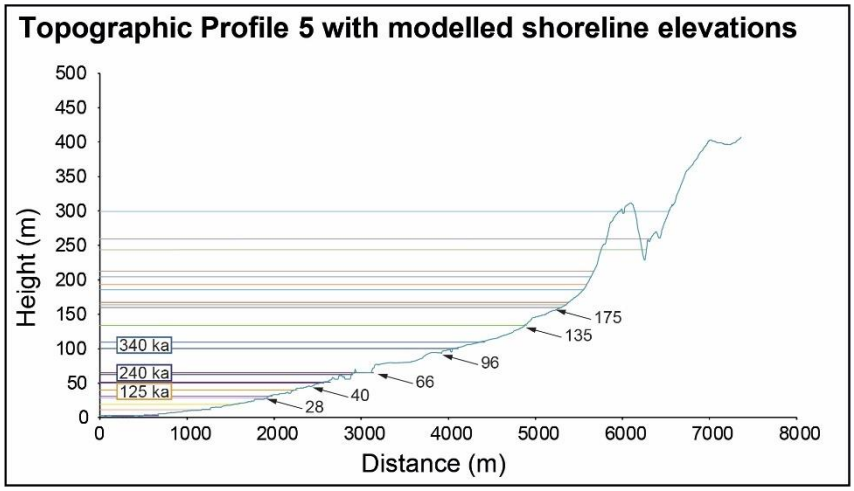
Topographic Profile 5 with modelled shoreline elevations
Height (m)
Distance (m)
340 ka
240 ka
125 ka
175
135
96
66
40
28

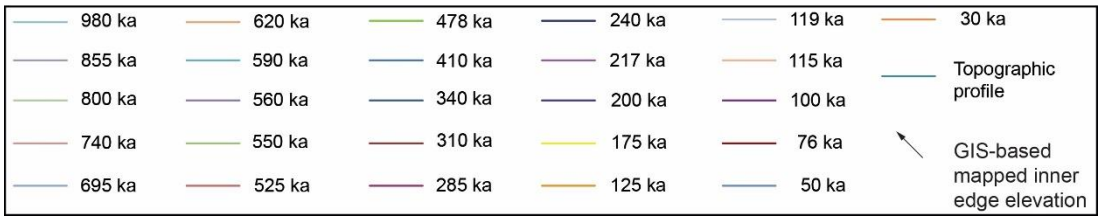
980 ka
855 ka
800 ka
740 ka
695 ka
620 ka
590 ka
560 ka
550 ka
525 ka
478 ka
410 ka
340 ka
310 ka
285 ka
240 ka
217 ka
200 ka
175 ka
125 ka
119 ka
115 ka
100 ka
76 ka
50 ka
30 ka
Topographic profile
GIS-based mapped inner edge elevation

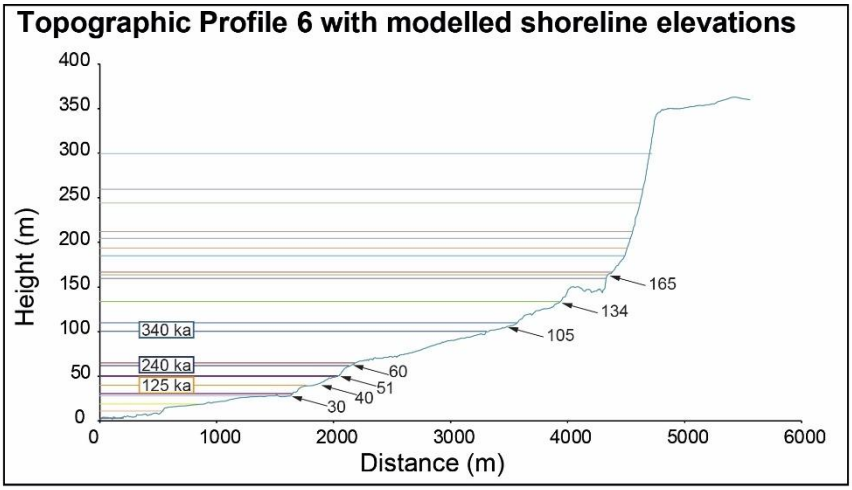
Topographic Profile 6 with modelled shoreline elevations
Height (m)
Distance (m)
340 ka
240 ka
125 ka
165
134
105
60
51
40
30

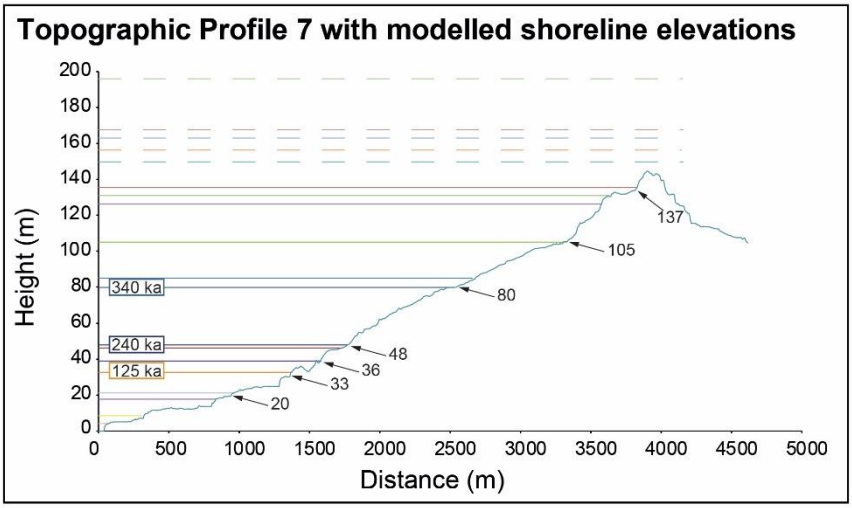
Topographic Profile 7 with modelled shoreline elevations
Height (m)
Distance (m)
340 ka
240 ka
125 ka
137
105
80
48
36
33
20

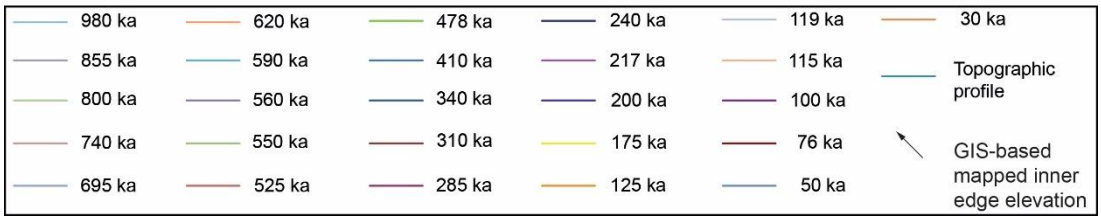
980 ka
855 ka
800 ka
740 ka
695 ka
620 ka
590 ka
560 ka
550 ka
525 ka
478 ka
410 ka
340 ka
310 ka
285 ka
240 ka
217 ka
200 ka
175 ka
125 ka
119 ka
115 ka
100 ka
76 ka
50 ka
30 ka
Topographic profile
GIS-based mapped inner edge elevation

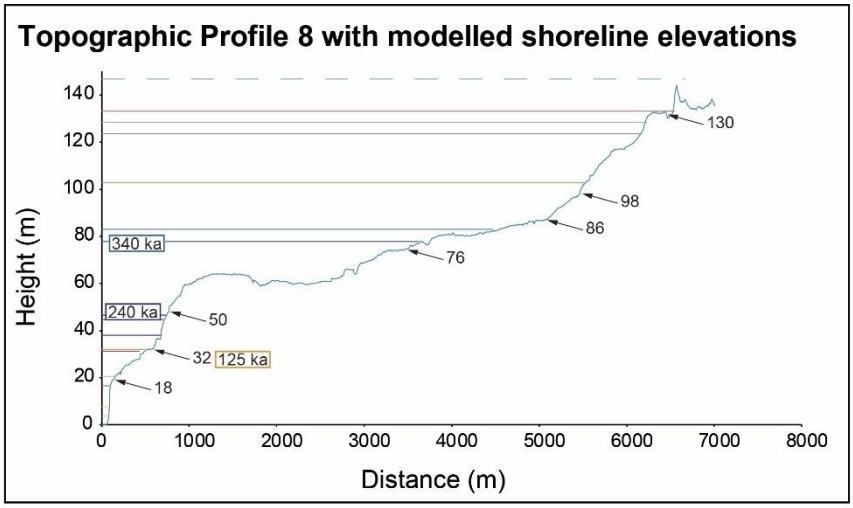
Topographic Profile 8 with modelled shoreline elevations
Height (m)
Distance (m)
340 ka
240 ka
125 ka
130
98
86
76
50
32
18

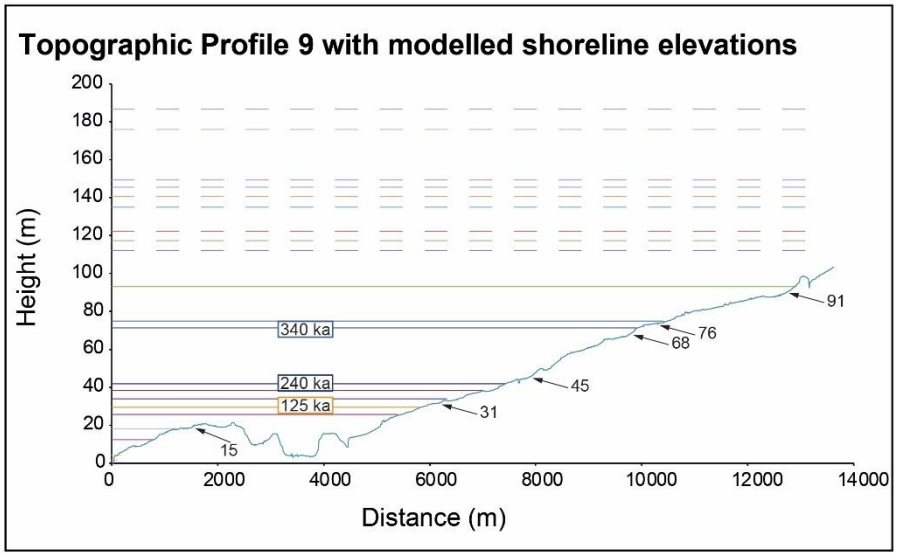
Topographic Profile 9 with modelled shoreline elevations
Height (m)
Distance (m)
340 ka
240 ka
125 ka
91
76
68
45
31
15

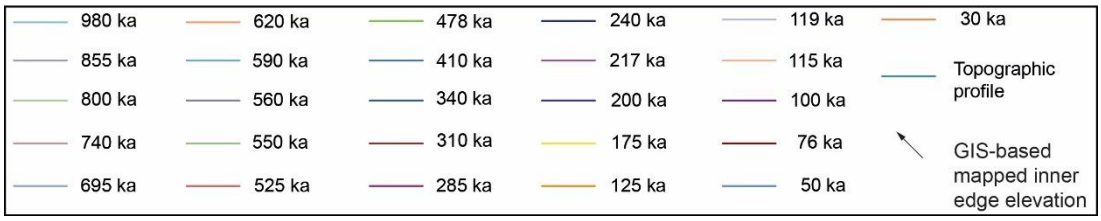
980 ka
855 ka
800 ka
740 ka
695 ka
620 ka
590 ka
560 ka
550 ka
525 ka
478 ka
410 ka
340 ka
310 ka
285 ka
240 ka
217 ka
200 ka
175 ka
125 ka
119 ka
115 ka
100 ka
76 ka
50 ka
30 ka
Topographic profile
GIS-based mapped inner edge elevation

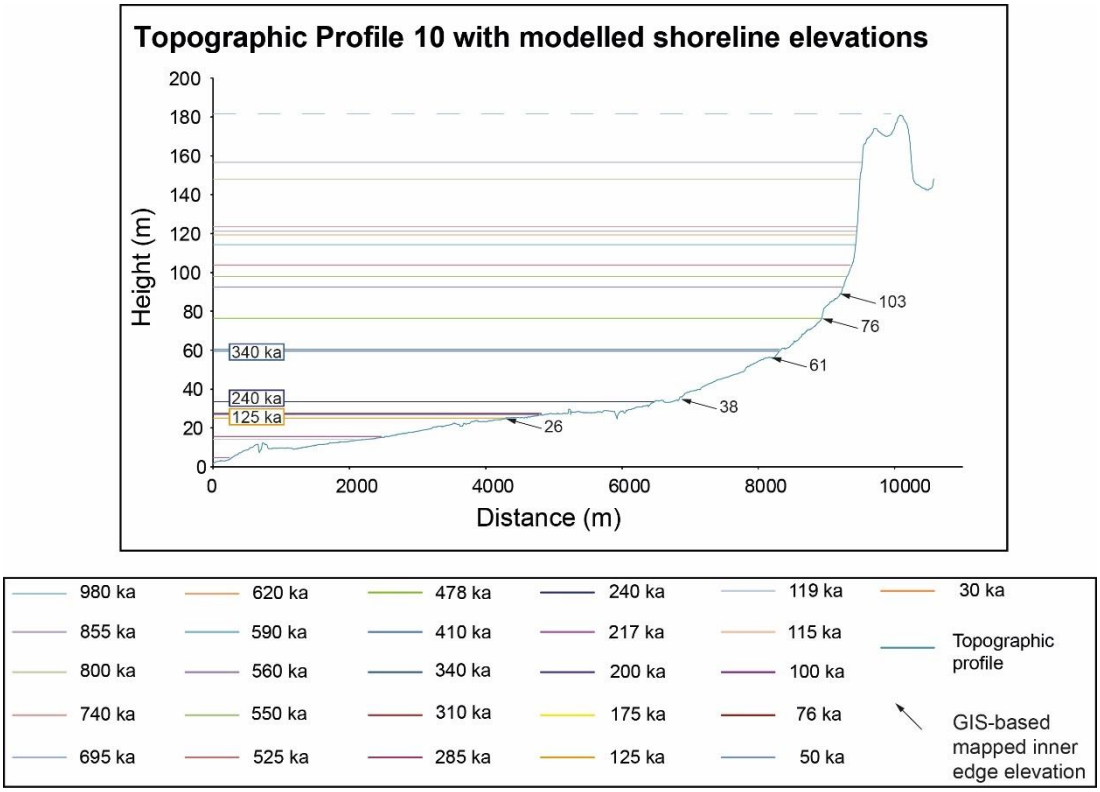

Figure 6.9: *Profiles showing mapped and modelled palaeoshoreline elevations. The topographic profiles are from the 2 m DEM. The numbers with arrows mark the elevations of palaeoshorelines mapped in the field. The coloured lines indicate palaeoshoreline elevations predicted by an uplift rate that has been changed iteratively to produce the best match with the mapped palaeoshorelines; goodness of fit is indicated by the value for the R^2 value in Figure 6.10. Profiles are located on Figure 6.3.*

Figure 6.9 presents interpreted marine terrace locations on each topographic profile. It is important to note that mapped palaeoshorelines are in very good agreement with those mapped by Bianca et al., 1999, yet, palaoeshoreline ages needed to be reviewed by investigating them applying a synchronous correlation approach. By linear regression analysis is assessed and shown the robustness and reliability of the synchronous correlation approach between the "measured" palaeoshoreline elevations in the field and DEMs and the "predicted" elevations iteratively-calculated given: (i) fixed values for sea-level relative to today for several highstands presented by Siddall et al., (2003 and Rohling et al., (2014) (Table 2.1, Chapter 2) and (ii) an uplift rate driven by ages controls described in section 6.3.2. Indeed, Figure 6.10 shows values of R^2 >0.99 between "predicted" and "measured" elevations, also implying that the uplift rate has been constant through time for the last half million years.

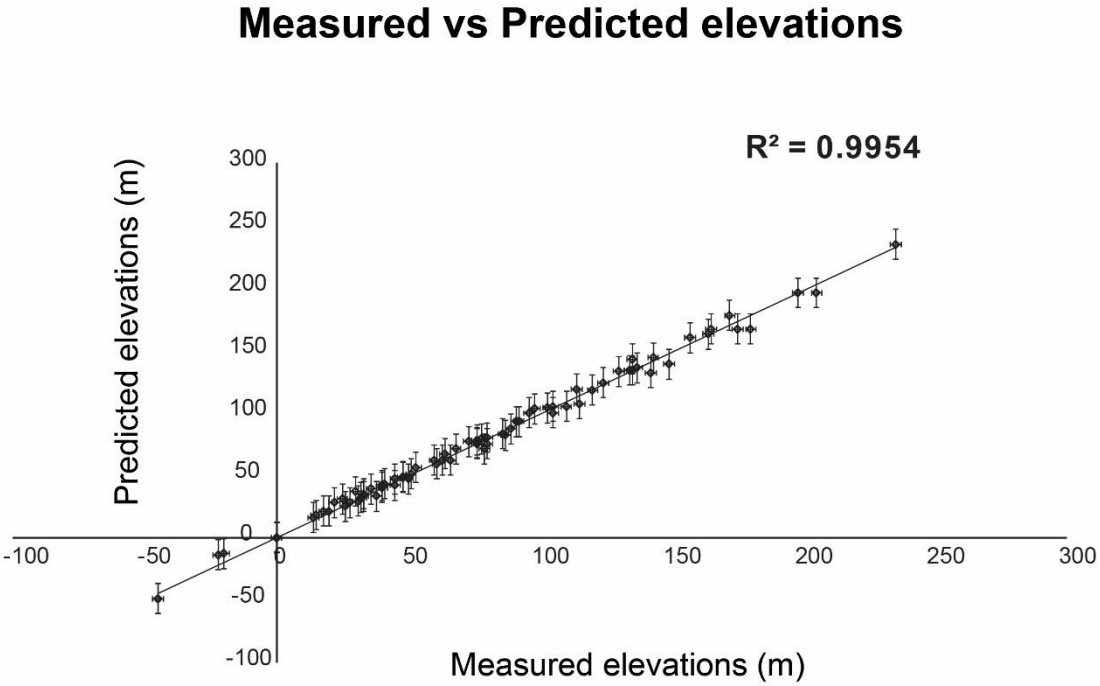

Figure 6.10: *Graph showing linear regression analysis between our measured and predicted elevations. The predicted elevations, representing the synchronously-calculated sea-level highstand elevations, have been derived by defining a constant uplift rate through time, and iterating this value to find the best match to the measured and mapped palaeoshorelines. Note that "measured" elevations represent palaeoshoreline elevations mapped in the 2-m high resolution DEMs. Coefficient of determination, R^2 value, has been used between these two datasets to quantify the best fit for all 15 topographic profiles with a value > 0.99.*

The synchronous correlation presented in this chapter, confirming that a constant uplift rate over the Late Quaternary has to be claimed, has been driven by different age controls. For instance, by using available age controls from submerged palaeoshorelines (Dutton *et al.*, 2009) a sequence of uplifted palaeoshorelines is modelled by claiming an uplift rate of 0.195 mm/yr, confirming the age of a prominent palaeoshoreline formed during the LIM (Figure 6.11). Indeed, Dutton et al., (2009) by dating the two submerged palaeoshorelines (Table 6.2) had suggested that the "Akradina Terrace", aged 80 ka from Bianca et al., (1999), could belong to older sea-level highstands such as either the MIS 5c (100 ka) or the MIS 5e (125 ka). However, the presented synchronous correlation in this thesis finally confirms and refines that the "Akradina Terrace" belongs to the 125 ka sea-level highstands (Figure 6.11). This is also supported by a new age control from U/Th dating on a coral sampled at 14 m in

the same topographic profile presented in Figure 6.11. In particular, the synchronous correlation approach applied along the Profile 12 confirms that the "Siracusa Terrace" mapped by Bianca et al., (1999) with a proposed age of 60 ka (yellow-coloured terrace in Figure 6.2) is actually older, with an age of 119 ka and surely not younger than 102 ka according to the new coral age (102 ka, Table 6.3, section 6.3.2).

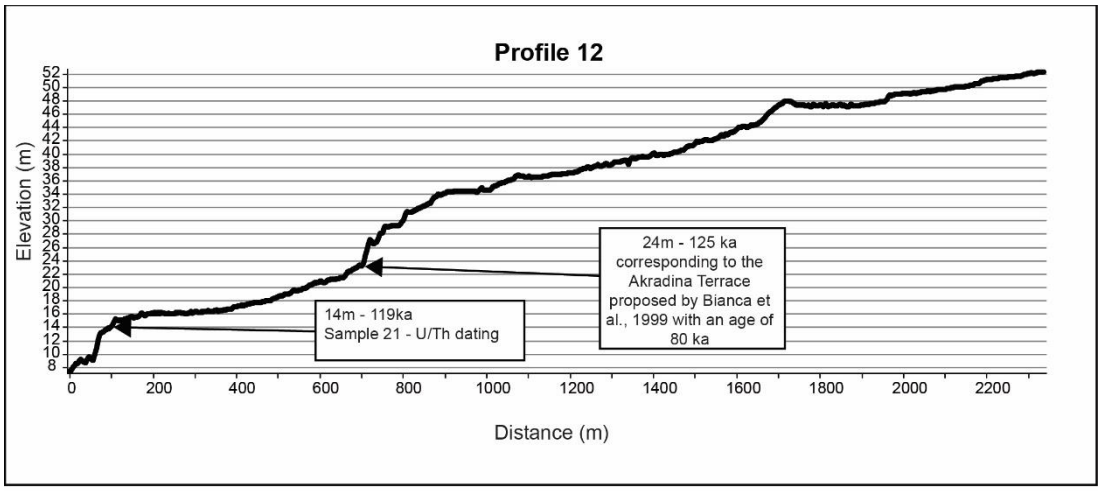

Uplift (mm/yr)	Highstands (ka)	Highstand elevations (m)		R^2 (Predicted vs measured)
		Predicted (Terrace Calc)	Measured (Field/DEM)	
0.195	50	-50	-45	0.99
	76.5	-15	-22	
	119	18	15	
	125	29	24	

Figure 6.11: *On top a topographic profile is constructed onshore with respect the locations of the dated submerged palaeoshorelines by Dutton et al., (2009). On the bottom, outcomes of a synchronous correlation approach which models the un-dated mapped palaeoshorelines, claiming a constant uplift rate through time, showing a robust linear regression analysis ($R^2 > 0.99$). Red coloured values are the age controls from the submerged dated palaeoshoreline. Note that the dated coral presented in Table 6.3 has been sampled along the same topographic profile, at 14 m. Sample 21 location is shown in Figure 6.3 and 6.7.*

Furthermore, as stated in the previous section, an attempt to date WCPs by using the ^{36}Cl cosmogenic dating is applied as shown: (i) in Figure 6.3 where all sample locations are shown and (ii) in Table 6.4 with the obtained exposure ages. Even though, all the obtained exposure

ages from this thesis (Table 6.4) are not matching the expected palaeoshoreline ages derived by a synchronous correlation approach, some un-published data from a previous PhD project in Catania University (Italy) (Spampinato, 2011) which have been re-analysed and re-interpreted support the idea that the before-mentioned "Akradina Terrace" mapped at 36 m near Syracuse town (Figure 6.3) belongs to the LIM. In particular, the initial exposure ages from Spampinato, (2011) derived using an excel spreadsheet calculator by Schimmelpfennig *et al.*, (2009) show low exposure ages (Table 6.1 – Spampinato's ages); even though, Spampinato, (2011) proposed an uplift rate scenario where an erosion rate of 11 mm/ka is taken into account, the "sequential" correlation approach used for deriving ages of un-dated palaeoshorelines implies, as shown in Chapter 4 and 5, that the investigated marine terraces need a further re-interpretation. Indeed, some sample locations from Spampinato, (2011) (Sample C5 and C9 – Figure 6.3) have been checked in the field and lie near WCP locations from this thesis (Sample 1, 2 and 3 in Figure 6.6). A further sample "C2" is used to derive the exposure age in the north of the investigated area (Figure 6.3 near Profile 2). Table 6.6 shows the obtained exposure ages re-analysing these un-published data by: (i) using the CRONUSCalc (Marrero *et al.*, 2015; Marrero, Phillips, Caffee, *et al.*, 2016) presented in Chapter 3 and (ii) assuming an erosion rate of 8mm/ky, a value in agreement with previous erosion rate estimations (Furlani *et al.*, 2009; Tucker *et al.*, 2011). Moreover, Figure 6.12 shows, for the first time, a topographic profile where Spampinato, (2011) sampled "C5" and "C9", confirming that the previously-mapped "Akradina Terrace" and the "Siracusa Terrace" (pink and yellow colours in Figure 6.2) are older than ages proposed by Bianca et al., (1999), with new refined ages of 125 ka and 119 ka respectively. Furthermore, an exposure age (Sample

"C2" – Figure 6.3 for location) in agreement with the age of the LIM is also derived in the north of the investigated area, where the "Akradina Terrace" is mapped at 46 m.

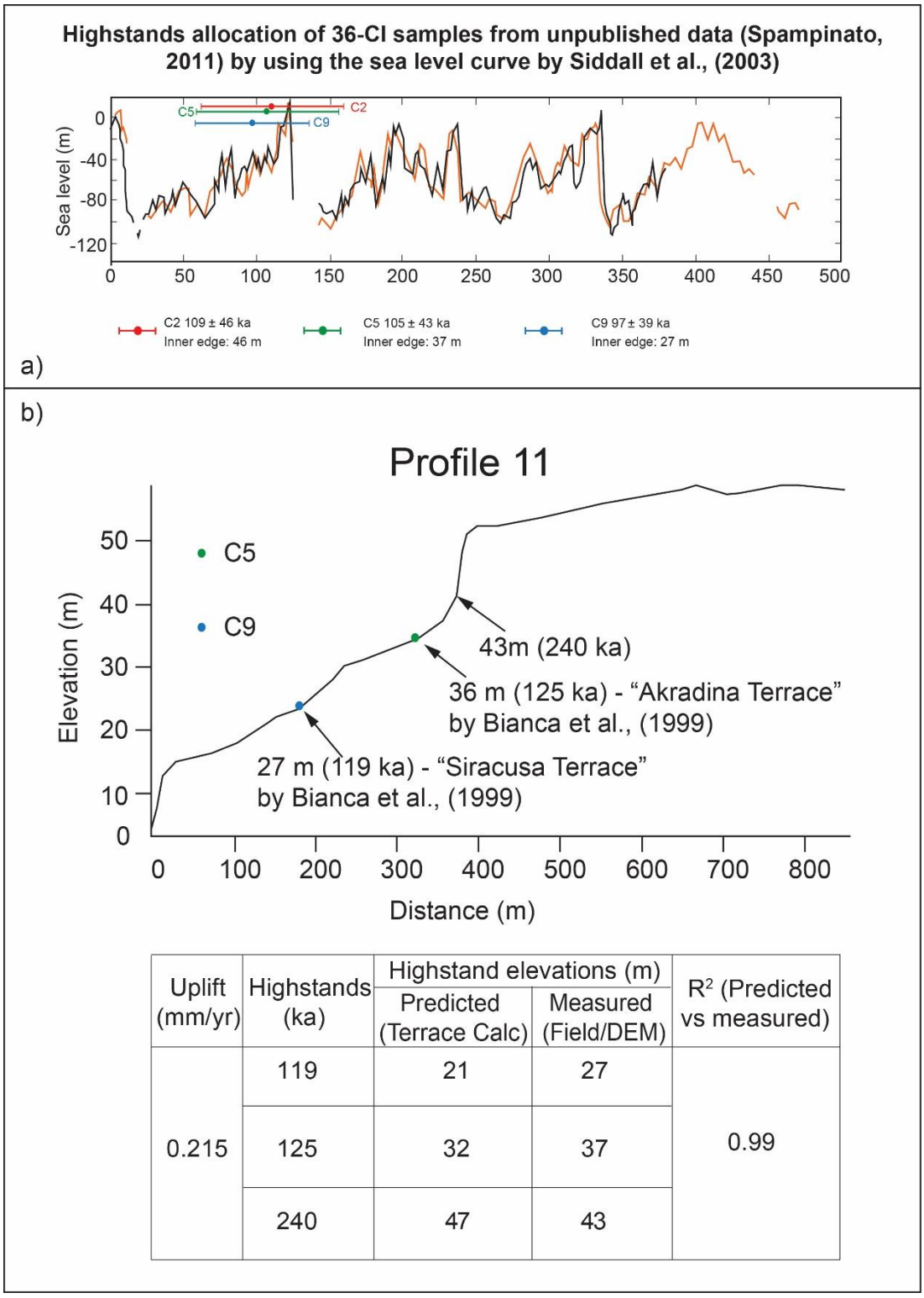

Uplift (mm/yr)	Highstands (ka)	Highstand elevations (m)		R^2 (Predicted vs measured)
		Predicted (Terrace Calc)	Measured (Field/DEM)	
0.215	119	21	27	0.99
	125	32	37	
	240	47	43	

Figure 6.12: *The top panel (a) shows calculated exposure ages, from the unpublished data (Spampinato, 2011), within the sea level curve by Siddall et al., (2003). Note that, even though the relatively large uncertainty, all these ages lie close to the age of the LIM, confirming the age of a prominent palaeoshoreline in the geomorphology which is most likely to be that from MIS 5e. derived by using different age controls. In panel (b) a topographic profile derived from*

2m high resolution DEMs data, and located on Figure 6.3 shows the inner edge of mapped palaeoshorelines in details. Note that in the table outcomes results from a synchronous correlation are shown, by using these new exposure ages.

Sample	36-Cl Conc. (Atoms of 36-Cl/g of sample)	Erosion rate (mm/ky)	Age (kyr)	Internal uncertainty (kyr)	Total uncertainty (kyr)	Elevation (m)	Assigned highstand (ka)
C2	1250000	8	109	9.7	46	46	125
C5	1220000	8	105	9.1	43	37	125
C9	1090000	8	97	7.0	39	27	119

Table 6.6: *Exposure ages from ^{36}Cl cosmogenic dating are shown in the table. These samples have been collected by Spampinato, (2011) but never published. Sampling locations are shown in Figure 6.2 and in Chapter*

A synchronous correlation approach driven by different age controls has allowed to refine ages for un-dated palaeoshorelines proposed by Bianca et al., (1999) and consequently the derived uplift rate scenario over the Late Quaternary. Figure 6.13 presents, for the first time, a new uplift scenario shows changing palaeoshoreline elevations with values higher from north to south.

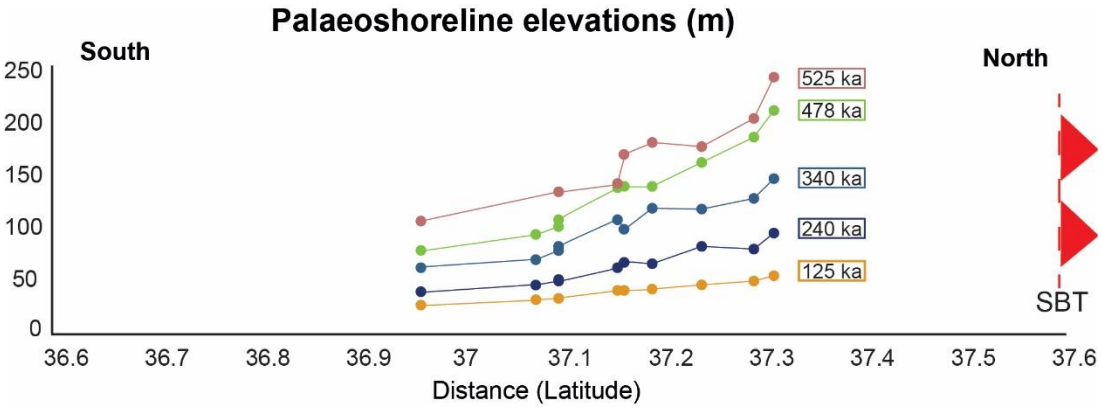

Figure 6.13: *Profiles showing tilting of palaeoshorelines whose ages are defined by the modelling in Figures 6.9 and 6.10. Solid lines show extrapolations between modelled topographic profiles 1-10.*

Similarly, for the first time, Figure 6.14 shows a spatial variation of a constant uplift rate through time with values of 0.16 mm/yr in the south and 0.41 mm/yr in the north. Furthermore, as shown in previous chapters, the tilt angle is mapped with higher values belonging to older palaeoshorelines as shown in Figure 6.15, implying that older palaeoshorelines have experienced a longer history of crustal deformation.

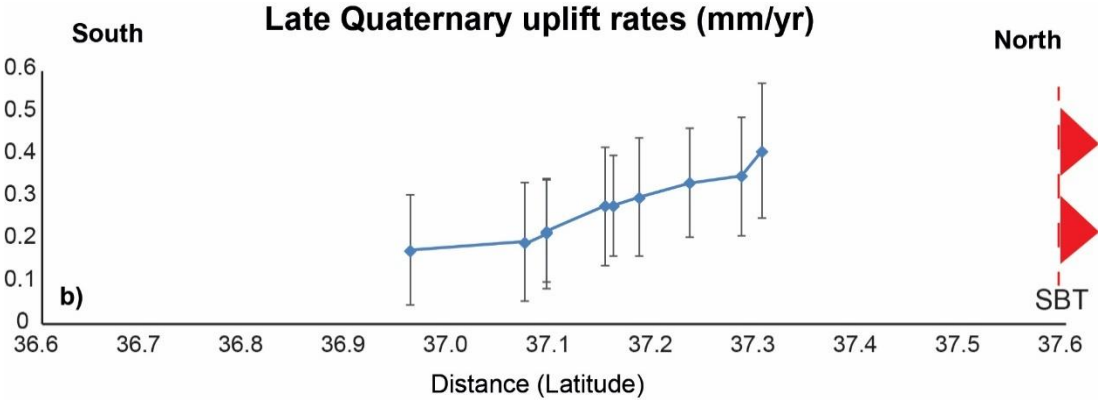

Figure 6.14: *Profile showing that uplift rates vary spatially along the N-S oriented transect within the HP.*

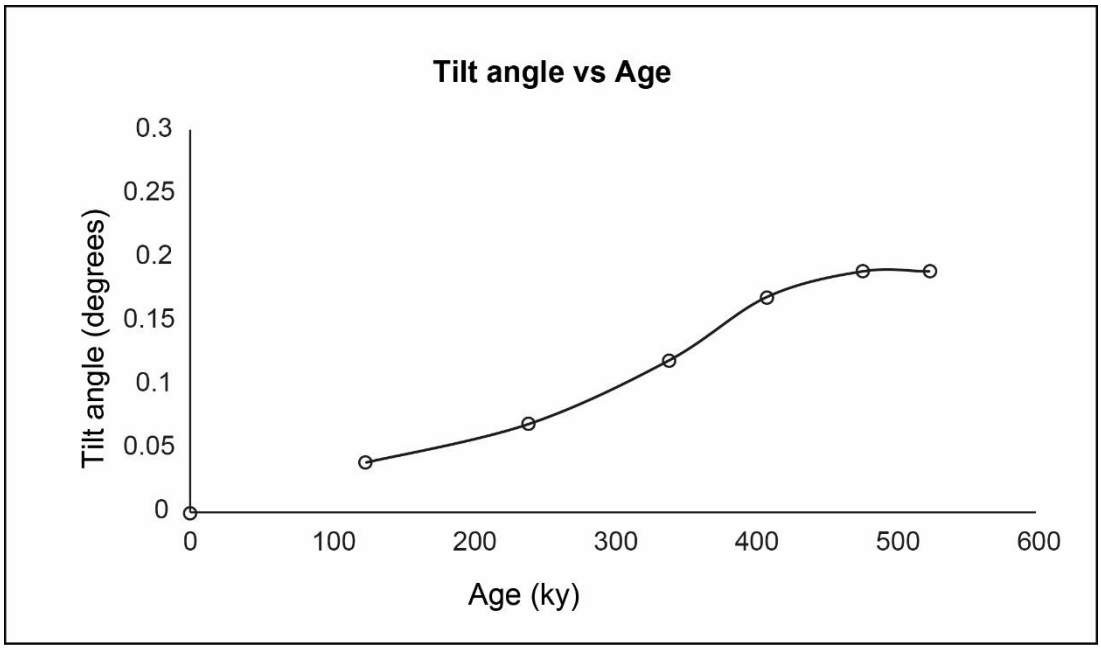

Figure 6.15*: Tilt angle values are calculated for each mapped palaeoshorelines in this chapter, where older and higher palaeoshorelines show higher tilt angle values because they have been experiencing a longer history of crustal deformation.*

Due to the overprinting problem explained in detail in Chapter 3, some palaeoshorelines will be obliterated where uplift rates are low; this implies a diagnostic stratigraphic evidence that higher uplift rate allows the preservation of a higher number of palaeoshorelines (Figure 6.16).

In the next section, all presented results are discussed, suggesting that the HP in SE Sicily has been affected since 525 ka by a forebulge process due to the tectonic convergence between Africa and Eurasia plates.

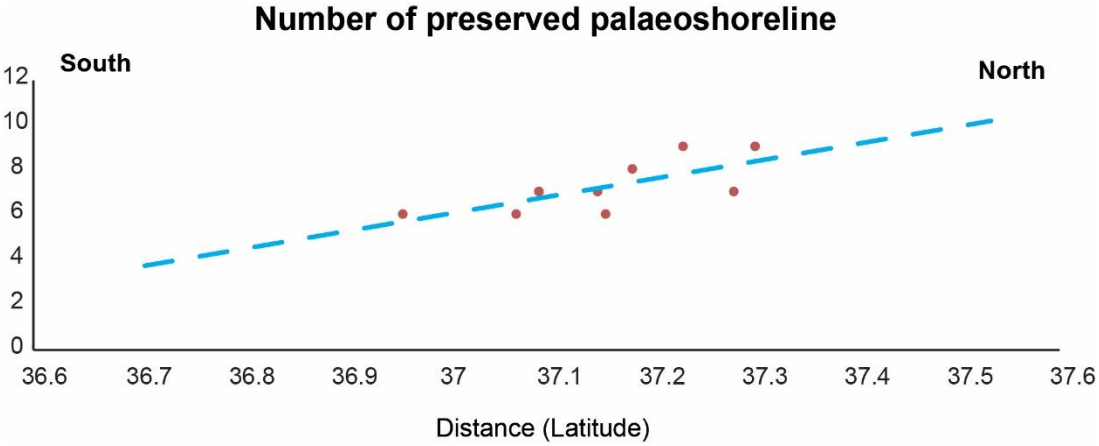

Figure 6.16: *Number of preserved palaeoshorelines from south to north. Note that where higher uplift rates are mapped a higher number of palaeoshorelines is preserved.*

6.5. Discussion

This chapter has investigated the relationship between uplifted Late Quaternary palaeoshorelines and forebulge process within the Africa-Eurasia convergence zone. The results suggest a constant uplift rate over the Late Quaternary, with the rate of uplift varying from the north to south (Figure 6.13, 6.14 and 6.17a, b). For the first time, spatially-changing uplift and its rates are discussed in terms of crustal response to a forebulge process; indeed, it is not surprising that mapping higher uplift rates nearer the trace of the SBT which bounds the northern rim of the HP, where the foredeep region is mapped. Ongoing tectonic convergence between Africa and Eurasia plates is partially accommodated by the SBT where the Africa plate is underthrusting beneath the Maghrebide chain in the northern rim of the HP, in agreement with (i) the northwardly deepening of the Moho discontinuity (Figure 6.17 c) (Neri *et al.*, 2002) and (ii) the GPS-based horizontal velocities (Figure 6.17d) (Palano *et al.*, 2012; Mastrolembo Ventura *et al.*, 2014) showing lower values nearer the SBT surface trace. This is in agreement with an ongoing forebulge process where higher uplift rates are mapped where lower GPS velocities and thicker continental crust are mapped (Figure 6.17).

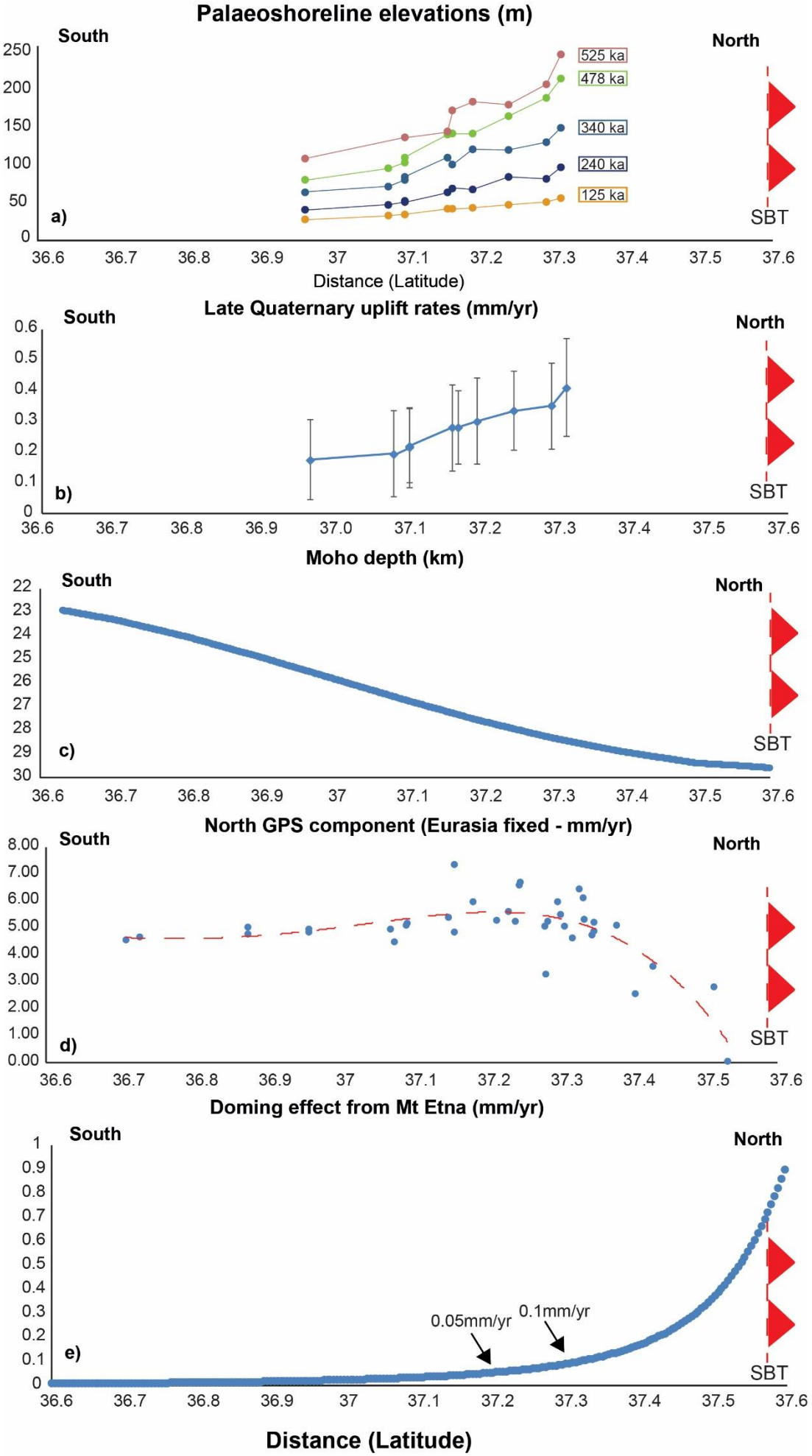
Palaeoshoreline elevations (m)
South
North
525 ka
478 ka
340 ka
240 ka
125 ka
a)
SBT
Distance (Latitude)
Late Quaternary uplift rates (mm/yr)
South
North
b)
SBT
Moho depth (km)
South
North
c)
SBT
North GPS component (Eurasia fixed - mm/yr)
South
North
d)
SBT
Doming effect from Mt Etna (mm/yr)
South
North
0.05mm/yr
0.1mm/yr
e)
SBT
Distance (Latitude)

Figure 6.17: *Higher values of uplift (a) and uplift rates (b) are mapped northwardly where deeper values of Moho discontinuity are mapped (c) and lower values of horizontal GPS velocities (d) are mapped. Note that the uplift is slightly affected by the doming effect from Mt Etna (e), suggesting that the differential uplifting process is describing a forebulge process affecting the HP.*

Furthermore, some can argue that the crustal uplift in the northern rim of the HP could be affected by the deep magmatic processes associated with the Etna volcano; however, Figure 6.17e shows that taking into account the long-term magmatic source with the associated "doming effect" suggested by some (De Guidi *et al.*, 2014), it is possible to show that the "doming effect" contribute is not prominently affecting the forebulge-related uplift in the north of the HP.

Presented results can be briefly discussed in terms of seismic hazard affecting the SE Sicily, one of the most seismically-active region during the historical time. Indeed, the results shown in this chapter suggest that the normal faulting activity mapped offshore SE Sicily (Gutscher *et al.*, 2016) still raises a high seismic hazard in its own, however, it is demonstrated that the differential uplift mapped in the HP in this thesis cannot be related to that as proposed by some (Bianca *et al.*, 1999). Note that the investigated region has been hit by damaging historical earthquakes (Bianca *et al.*, 1999; Lavecchia *et al.*, 2007) and yet, seismogenic sources are still debated (Lavecchia *et al.*, 2007; Visini *et al.*, 2009), suggesting that more investigations including vertical crustal movements spanning the Late Quaternary are needed.

6.6. Conclusion

In this chapter, new rates of uplift constant through time spanning the Late Quaternary has been presented within the foreland (HP) related to the Africa-Eurasia convergence. By applying a synchronous correlation approach, driven by different age controls, a sequence of uplifted Late Quaternary marine terraces has been investigated within

the “undeformed” foreland in the HP, Se Sicily. It has been shown that: (i) higher uplift rates are mapped in the northern rim of the HP, (ii) palaeoshoreline elevations change from north to south and (iii) their tilt angle shows higher values for the older and higher ones, suggesting that the rate of the forebulge process has been constant through time. This new knowledge related to the convergence-related crustal deformation highlight new insights for the long-term seismic hazard approach for one of the most seismically active regions in the Mediterranean Basin.

Chapter 7: Long-term interaction between active normal faults in the upper plate of subduction zones revealed by investigating tectonically-deformed Late Quaternary marine terraces: the Messina Strait, southern Italy

7.1. Abstract

In this chapter, results are presented of an investigation regarding the relationship between climate, sea-level changes and tectonics through time through study of tectonically-deformed uplifted Late Quaternary palaeoshorelines in the Messina Strait, southern Italy. A synchronous correlation approach is applied to investigate palaeoshorelines outcropping on the uplifting coastlines of the Strait, on the footwall of the offshore Messina Strait Fault, close to Sicily, and on the hangingwalls of the Reggio Calabria Fault and the Armo Fault in Calabria. In this region as well as others studied in this thesis, the uplift of a "regional" nature outpaced the local subsidence in the hangingwalls of the Reggio Calabria Fault and the Armo Fault allowing the preservation above present-day sea-level of a dramatic sequence of palaeoshorelines. Spatial and temporal correlation of palaeoshorelines across and along-strike faults are demonstrated, indicating that, for the first time in this thesis, and for the Messina Strait region, long-term uplift rates fluctuated through time. The results suggest a change in uplift rates for both uplifting coastlines of the Strait at ~50 ka. Also, uplift rates vary along strike, with increasing values of uplift rate from the centres of the hangingwalls of the Reggio Calabria Fault and the Armo Fault towards their tips; decreasing values are mapped approaching fault tips on the footwall of Messina Strait Fault. These fault-controlled uplift rates, changing spatially and temporally, suggest activity on the investigated faults and possible

evidence for fault interaction over the Late Quaternary to accommodate the ongoing crustal extension occurring within the Strait. Spatial and temporal changes in uplift mapped within active fault systems are key-step to identify active faults, their deformation rates and the associated seismic hazard above subduction zones.

7.2 Introduction

The Messina Strait is located on the extending upper plate of the Ionian Subduction Zone (ISZ) (southern Italy), within an area of active convergence between the African and Eurasian plates, and is considered one of the most tectonically-active region of the entire Mediterranean (Monaco and Tortorici, 2000; D'Agostino and Selvaggi, 2004; Serpelloni *et al.*, 2010) (Figure 7.1). However, details of the deformation are debated. For instance, uplifted Late Quaternary palaeoshorelines suggest active deformation (Valensise and Pantosti, 1992; Stewart *et al.*, 1997; Monaco and Tortorici, 2000; Catalano *et al.*, 2003; De Guidi *et al.*, 2003; Ferranti *et al.*, 2007; Pavano, Pazzaglia and Catalano, 2016), rates of activity through time and the possible effects of interaction on the closely-spaced faults are still unclear; indeed, some have even questioned if the faults are still active (Miyauchi, Dai Pra and Sylos Labini, 1994; Dumas, Guérémy and Raffy, 2005; Argnani *et al.*, 2008, 2009). For example, a ~ 20-year long debate is still ongoing concerning the existence, the location and the activity through time of a normal fault herein named "The Messina Strait Fault" after Doglioni et al., (2012) (previously named "The Taormina Fault", see Stewart *et al.*, 1997; Monaco and Tortorici, 2000; Catalano *et al.*, 2003; De Guidi *et al.*, 2003; Pavano, Pazzaglia and Catalano, 2016) (Figure 7.1). Uplifted Late Quaternary palaeoshorelines have been mapped along the strike of the footwall of the debated Messina Strait Fault, between Messina town and Taormina town (Figure 7.1),

suggesting possible long-term faulting activity (Stewart *et al.*, 1997; Catalano *et al.*, 2003; De Guidi *et al.*, 2003; Pavano, Pazzaglia and Catalano, 2016). Moreover, recent detailed and improved seismic surveys have shown that a normal faulting-related structure exists and its long-term activity can be linked with the tectonically-deformed palaeoshorelines outcropping on the eastern Sicilian coast (Doglioni *et al.*, 2012) (Figure 7.1), even if its faulting history through time is not described in detail in that study. Likewise, major normal faults and their long-term activity through time onshore on the Calabrian side such as the Reggio Calabria Fault and the Armo Fault, have been previously investigated by studying sequences of uplifted Late Quaternary palaeoshorelines both on their footwalls and hangingwalls (Valensise and Pantosti, 1992; Miyauchi, Dai Pra and Sylos Labini, 1994; Monaco and Tortorici, 2000; Catalano *et al.*, 2003; Aloisi *et al.*, 2013). However, again details of how deformation rates varied through time are not known in detail.

A key issue that earlier chapters in this thesis have raised is whether existing uplift rates scenarios are robust, given that investigations of uplifting coastlines around the Messina Strait (Valensise and Pantosti, 1992; Catalano *et al.*, 2003; De Guidi *et al.*, 2003; Pavano, Pazzaglia and Catalano, 2016) used a sequential correlation approach, and so have not taken into account the possibility that low uplift rates may have made such studies prone to the "overprinting problem" mentioned earlier in the thesis (section 2.5 – Chapter 2). This implies that a review of the long-term crustal deformation rates within the Messina Strait may be needed. As noted in previous chapters, the paucity of absolute ages for palaeoshorelines is a common problem (Roberts *et al.*, 2013; Pedoja *et al.*, 2018; Meschis et al., 2018), and this is true of the Messina Strait. In turn, the necessity to derive ages for un-dated palaeoshorelines by applying a "sequential" correlation approach by some in the past (Balescu *et al.*, 1997;

Catalano and De Guidi, 2003; Catalano *et al.*, 2003; De Guidi *et al.*, 2003; Pavano, Pazzaglia and Catalano, 2016) may well have affected the correlation between multiple palaeoshoreline ages and multiple sea level highstands (Westaway, 1993; Roberts *et al.*, 2013; Meschis et al., 2018). Consequently, it may be that poorly-constrained long-term uplift-rates have had a detrimental effect on the understanding of: (i) subduction/thrusting processes and the seismic hazard associated with megathrust events and tsunamis, and (ii) earthquakes within the upper plate of the ISZ involving active normal faults.

Existing absolute age controls for the palaeoshorelines from the literature are reviewed below. An age control to model the sequence of palaeoshorelines outcropping on the footwall of the Messina Strait Fault is derived by using an Electron Spin Resonance (ESR) dating technique applied on fossiliferous shells remains which has allowed to date a prominent palaeoshorelines belonging to the Last Interglacial Maximum (LIM) (Antonioli, Kershaw, *et al.*, 2006) (Figure 7.1). Another age control from the Calabrian coast, north of Reggio Calabria town, is used to drive the synchronous correlation applied to a sequence of marine terraces outcropping on the hangingwall of the Reggio Calabria Fault (Figure 7.1). In particular, Thermo-Luminescence (TL) dating technique is applied on some non-fossiliferous deposits made of dune aeolian sand at 34 m and assigned to the 50 ka sea level highstand (Balescu *et al.*, 1997). Finally, some geoscientists have correlated to the LIM fossiliferous terraced deposits containing "Strombus Bubonius" mapped on the hangingwall of the Armo Fault at 140 m, in southern Calabria (Miyauchi, Dai Pra and Sylos Labini, 1994; Antonioli, Ferranti, *et al.*, 2006; Aloisi *et al.*, 2013). All these available ages are recalled later in this chapter in section 7.3.

Vertical motions associated with the Messina Strait may be particularly complicated given that faults are closely-spaced across strike (<10 km across strike at depth), forming an

overall graben structure. It may be that the close fault proximity, especially at depth due to the inward dipping nature of the faults, may promote fault interaction, which could in turn produce temporal changes in deformation rates as the faults share the work of extending the region. For example it is well-known regional crustal extension and the associated rates constant through time, within tectonic plate margins, need to be accommodated by activity on normal fault systems (Gupta et al. 1998, Cowie 1996, Roberts *et al.*, 2002). This implies that summed deformation rates, for instance slip rates on faults, across all the involved faults: (i) will be constant through time if all the involved structures persist in being active through time, and (ii) will be roughly equal to the rates of regional deformation associated with the plate motions (Roberts *et al.*, 2002). However, it has been suggested that a more likely scenario is that fault slip rates change through time within normal fault systems (Cowie et al. 2005; McLeod et al. 2000; Cowie and Roberts, 2001; Roberts *et al.*, 2002, 2009; Nixon *et al.*, 2016; Cowie et al. 2017), with activity alternating on faults located across strike on a 10^3-10^6 year timescale. This suggests that acceleration of deformation rates on some active faults implies synchronous deceleration on other faults if the regional deformation rates are to be maintained (Dawers and Underhill, 2000; Roberts *et al.*, 2002; Bennett, Friedrich and Furlong, 2004; McLeod, Dawers and Underhill, 2008). For example, in the Gulf of Corinth in Greece it has been demonstrated by investigating tectonically-deformed palaeoshorelines that normal fault slip rates on one fault can accelerate up to a factor of ~3 when faults across strike cease activity, to maintain the regional deformation (Roberts *et al.*, 2009), (see also Nixon *et al.*, 2016). For the Messina Strait, GPS investigations show NW-SE oriented crustal extension with rates ~ 2.5 mm/yr (Serpelloni *et al.*, 2005), quasi-perpendicular to the strikes of the major Quaternary normal faults affecting the region and investigated in this thesis. In the Strait, these

faults have been seismically accommodating the extension process, producing damaging earthquakes (e.g. 1908 Messina Earthquake – Mw 7.1) (Monaco and Tortorici, 2000; Catalano *et al.*, 2008). However, it is still unclear and poorly-understood if the major Quaternary normal faults such as the Messina Strait Fault, the Reggio Calabria Fault and the Armo Fault are all synchronously active over longer time periods than that constrained with GPS and seismicity (less than ~1 century), and if their related long-term rates have been constant over the Late Quaternary or fluctuating.

The aim of this chapter is to address the following scientific questions:

- Is the uplift process, recorded in the Sicilian and Calabrian coastlines, controlled by upper plate active faults?
- Are the ages assigned in previous studies to un-dated palaeoshorelines affected by the "overprinting problem", which may not be considered when a "sequential approach technique" is applied?
- Are the Messina Strait Fault, the Armo Fault and the Reggio Calabria Fault active, and if so, have their activity rates been constant through time?

In a similar manner to the previous chapters, these scientific questions are examined by undertaking new detailed topographic analysis, taking advantage of a 10 m high resolution Digital Elevation Model (Tarquini *et al.*, 2012), combined with new field mapping to check and collect palaeoshoreline elevations previously mapped by others (Catalano *et al.*, 2003; De Guidi *et al.*, 2003), supported by review existing age controls (Balescu *et al.*, 1997; Antonioli *et al.*, 2003; Catalano *et al.*, 2003; Antonioli, Ferranti, *et al.*, 2006; Antonioli, Kershaw, *et al.*, 2006; Aloisi *et al.*, 2013), and an attempt to gain new absolute ages from U/Th determinations on

corals, and *in situ* ^{36}Cl cosmogenic exposure ages, which are used to drive a "synchronous correlation" approach.

7.3 Methods and approach

In a similar manner to previous chapters, the approach undertaken to test the scientific hypotheses was to map as many palaeoshoreline elevations as possible on DEMs by creating a number of topographic profiles (13 for the Sicilian coast and 9 for the Calabrian coast) (Figure 7.1). These topographic profiles covered the along strike extent of the major Quaternary normal faults such as the Messina Strait Fault, the Reggio Calabria Fault and the Armo Fault (Figure 7.1). Then, elevations of marine terrace inner edges mapped on DEMs were checked in the field for each investigated fault, using as a guide previous mapping (Catalano *et al.*, 2003; De Guidi *et al.*, 2003; Aloisi *et al.*, 2013). Newly-obtained age control (Table 7.1) alongside to those available in the literature (Table 7.2) were then used to drive the synchronous correlation approach (Roberts *et al.*, 2013; Pedoja *et al.*, 2018).

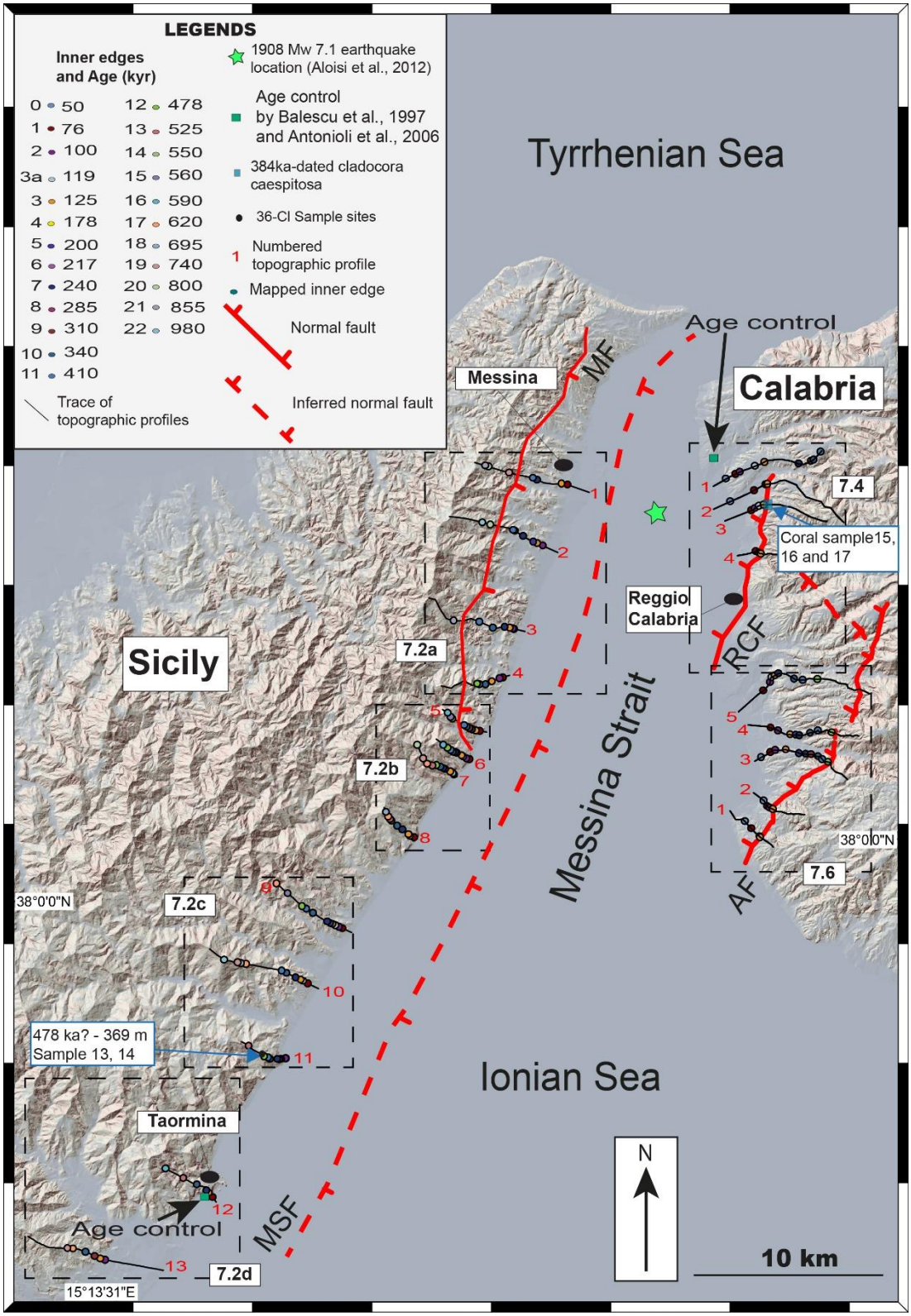

Figure 7.1: *Location map showing the major Quaternary normal faults bordering the Messina Strait. The black dashed-squares outline locations of subsequent figures (see labels). Coloured dots represent mapped palaeoshorelines with newly-assigned ages from synchronous correlation. MSF: Messina Strait Fault; AF: Armo Fault; RCF: Reggio Calabria Fault; MF: Messina Fault.*

7.3.1. Topographic analysis: DEMs and fieldwork to map marine terraces

Detailed topographic analysis has been carried out by using 10 m high resolution DEMs (Tarquini *et al.*, 2007, 2012) aimed to create consecutive topographic profiles along the strikes of the Messina Strait Fault (Figures 7.2 a, b, c, and d), the Reggio Calabria Fault (Figure 7.3) and the Armo Fault (Figure 7.4). Mostly, these topographic profiles are chosen where the geomorphology of palaeoshorelines is appropriate due to their preservation from erosion and also to run close to locations revealed in previous maps (Balescu *et al.*, 1997; Catalano *et al.*, 2003; De Guidi *et al.*, 2003; Antonioli, Kershaw, *et al.*, 2006; Aloisi *et al.*, 2013). These profiles have been derived from the centre of faults towards their tips for the Reggio Calabria Fault and the Armo Fault (Figure 7.3 and 7.4); for the Messina Strait Fault have been derived from the supposed northern tip area close to Messina town towards the southern tip area close to Taormina town (Figure 7.2 a, b, c and d).

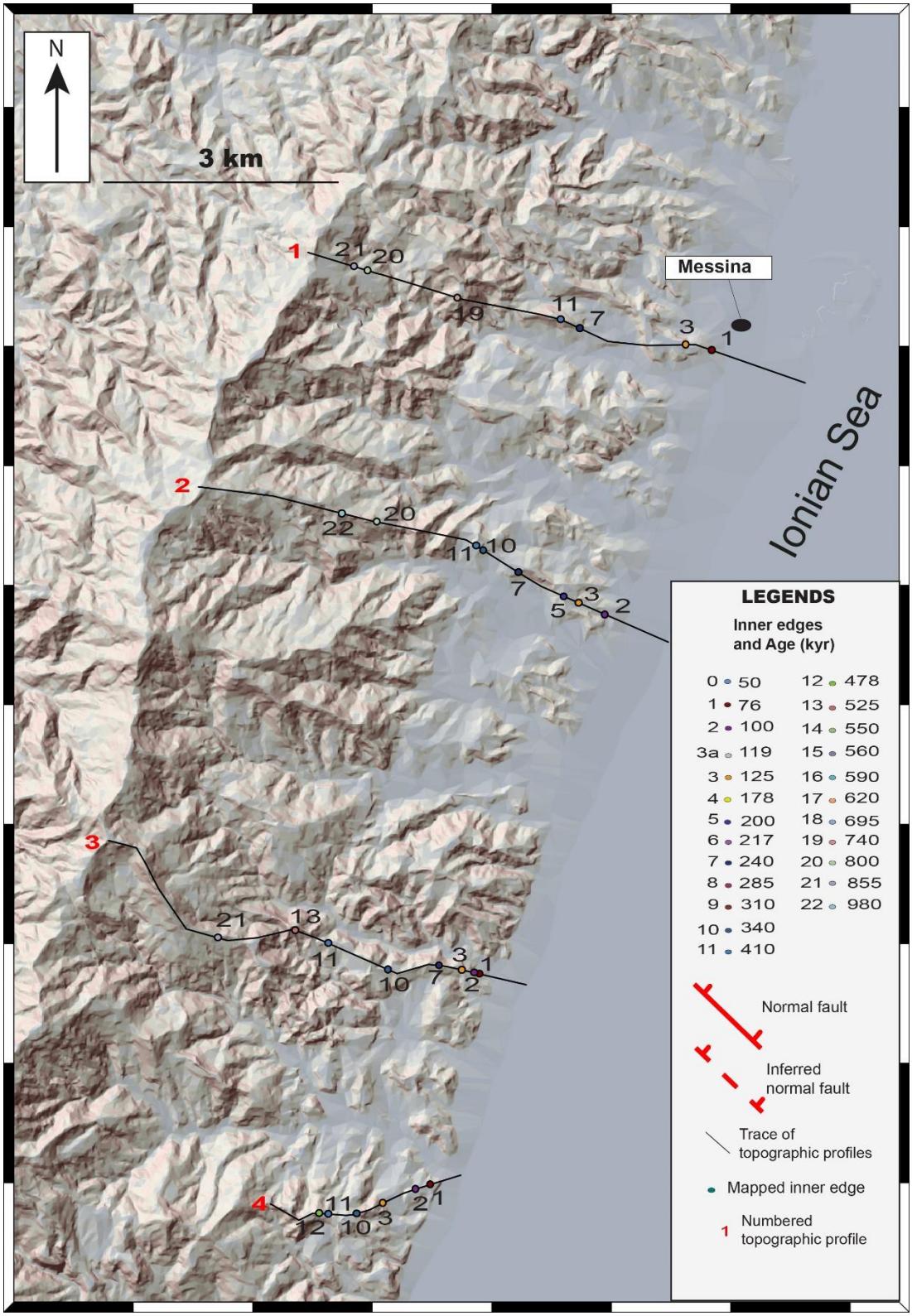
N
3 km
Messina
Ionian Sea
1
21
20
19
11
7
3
1
2
22
20
11
10
7
5
3
2
3
21
13
11
10
7
3
2
1
4
12
11
10
3
2
1
LEGENDS
Inner edges and Age (kyr)
0 50
1 76
2 100
3a 119
3 125
4 178
5 200
6 217
7 240
8 285
9 310
10 340
11 410
12 478
13 525
14 550
15 560
16 590
17 620
18 695
19 740
20 800
21 855
22 980
Normal fault
Inferred normal fault
Trace of topographic profiles
Mapped inner edge
1 Numbered topographic profile

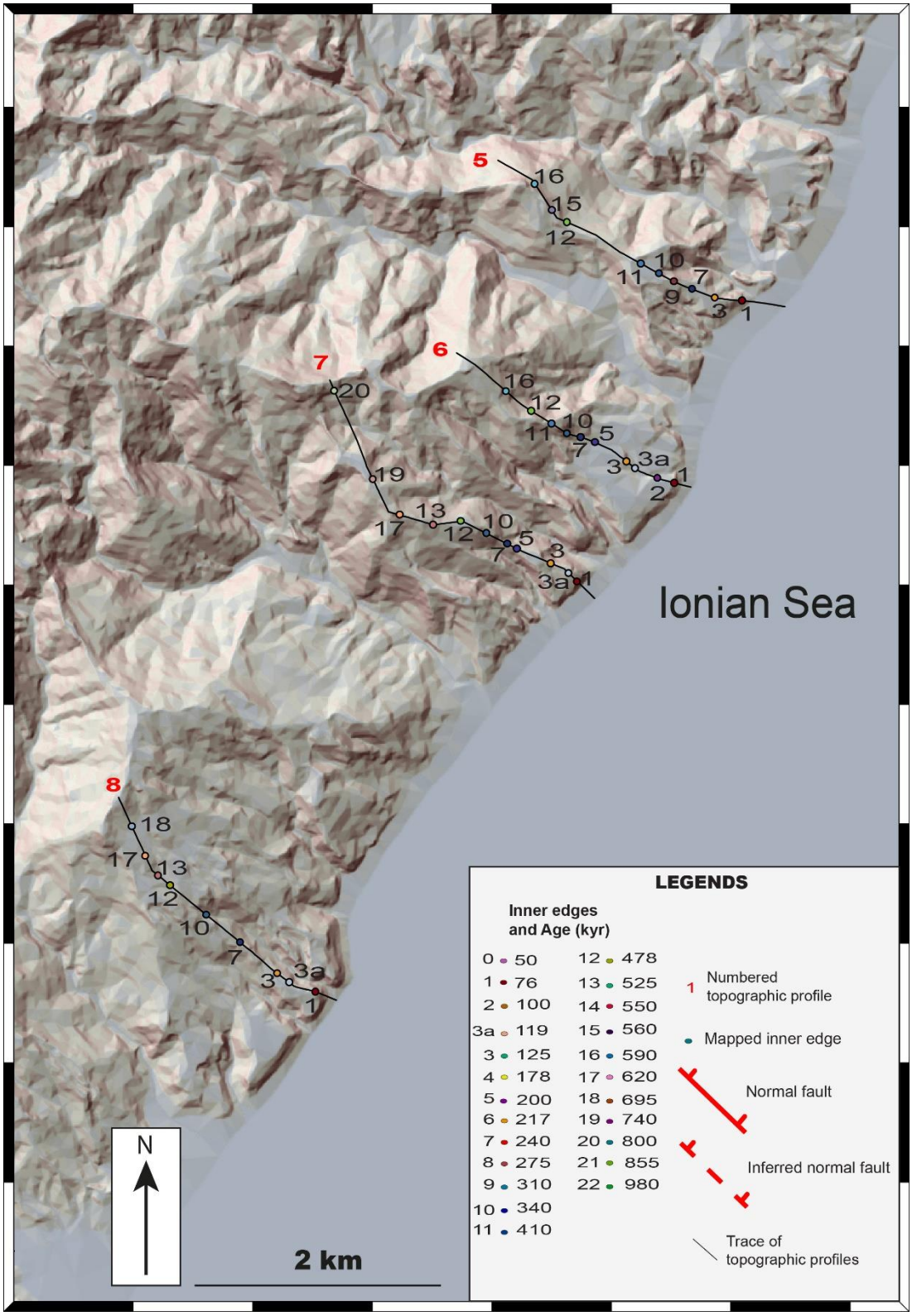
5
16
15
12
11
10
9
7
3
1
6
16
12
11
10
7
5
3
3a
2
1
7
20
19
17
13
12
10
7
5
3
3a
1
8
18
17
13
12
10
7
3
3a
1
Ionian Sea
N
2 km
LEGENDS
Inner edges and Age (kyr)
0 • 50
1 • 76
2 • 100
3a • 119
3 • 125
4 • 178
5 • 200
6 • 217
7 • 240
8 • 275
9 • 310
10 • 340
11 • 410
12 • 478
13 • 525
14 • 550
15 • 560
16 • 590
17 • 620
18 • 695
19 • 740
20 • 800
21 • 855
22 • 980
1 Numbered topographic profile
Mapped inner edge
Normal fault
Inferred normal fault
Trace of topographic profiles

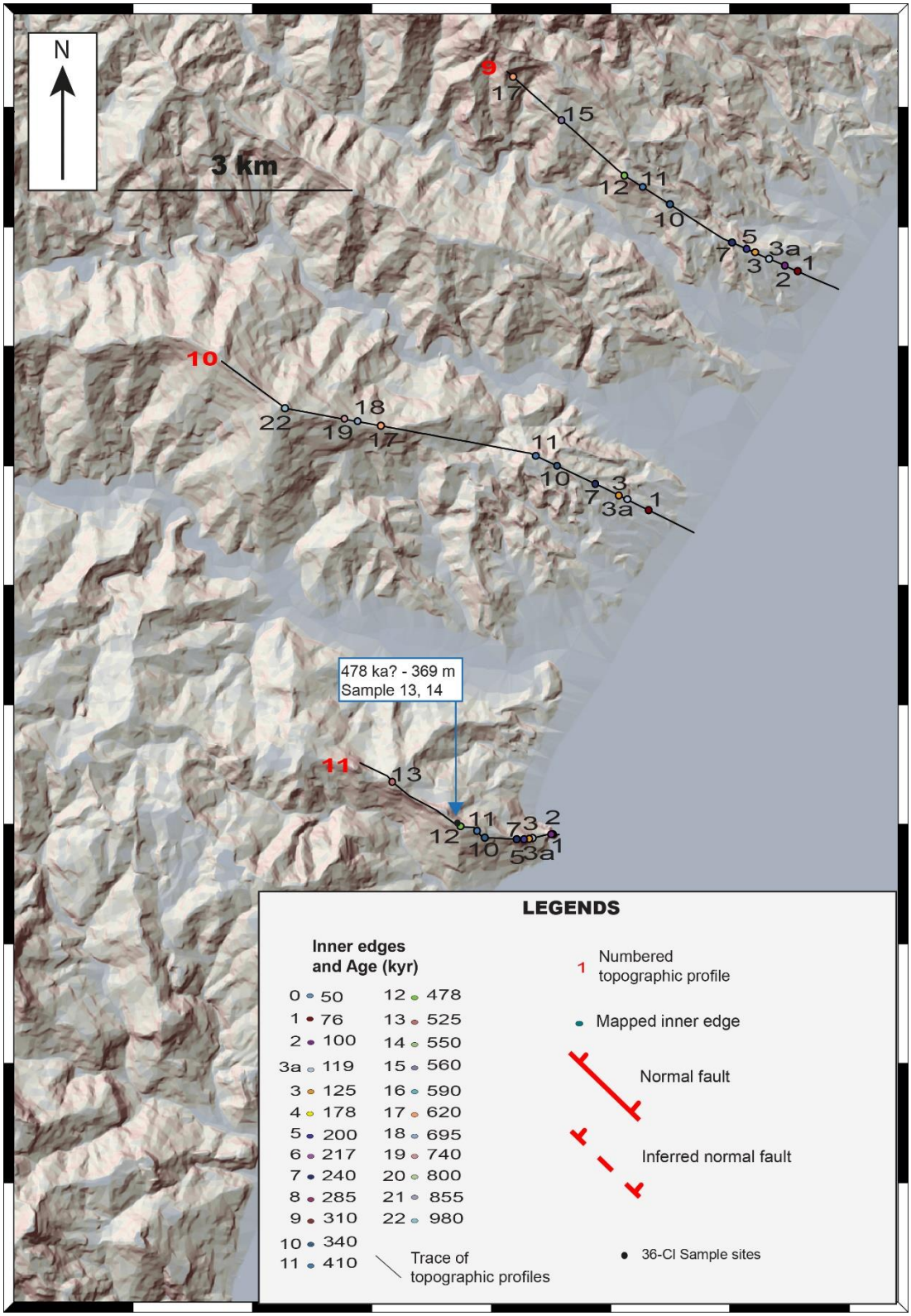
N
3 km
9
17
15
12
11
10
5
7
3a
3
1
2
10
22
18
19
17
11
10
7
3
3a
1
478 ka? - 369 m
Sample 13, 14
11
13
12
11
10
7
5
3
3a
2
1
LEGENDS
Inner edges and Age (kyr)
0 50
1 76
2 100
3a 119
3 125
4 178
5 200
6 217
7 240
8 285
9 310
10 340
11 410
12 478
13 525
14 550
15 560
16 590
17 620
18 695
19 740
20 800
21 855
22 980
Trace of topographic profiles
1 Numbered topographic profile
Mapped inner edge
Normal fault
Inferred normal fault
36-Cl Sample sites

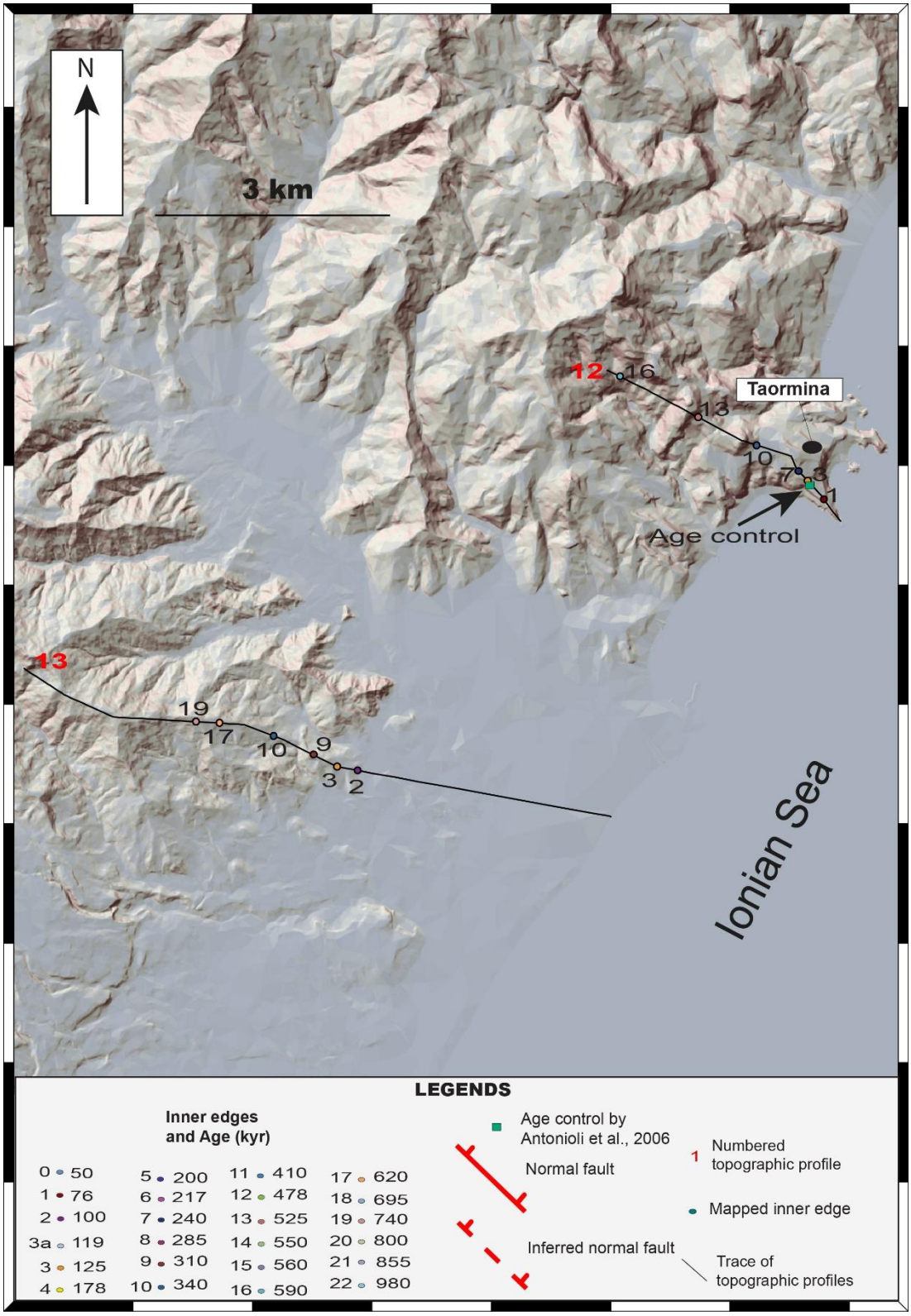

Figure 7.2abcd: *Location maps for palaeoshorelines within the footwall of the offshore Messina Strait Fault. A 10-m resolution DEM with the associated shaded relief to highlight breaks of slope is used as base-map. Panels a,b,c and d show palaeoshorelines with newly-assigned ages (see numbered dots and the associated age within Legends panel) and the 13-topographic profile locations from Messina town in the northern fault tip to Taormina town in the southern tip, E Sicily.*

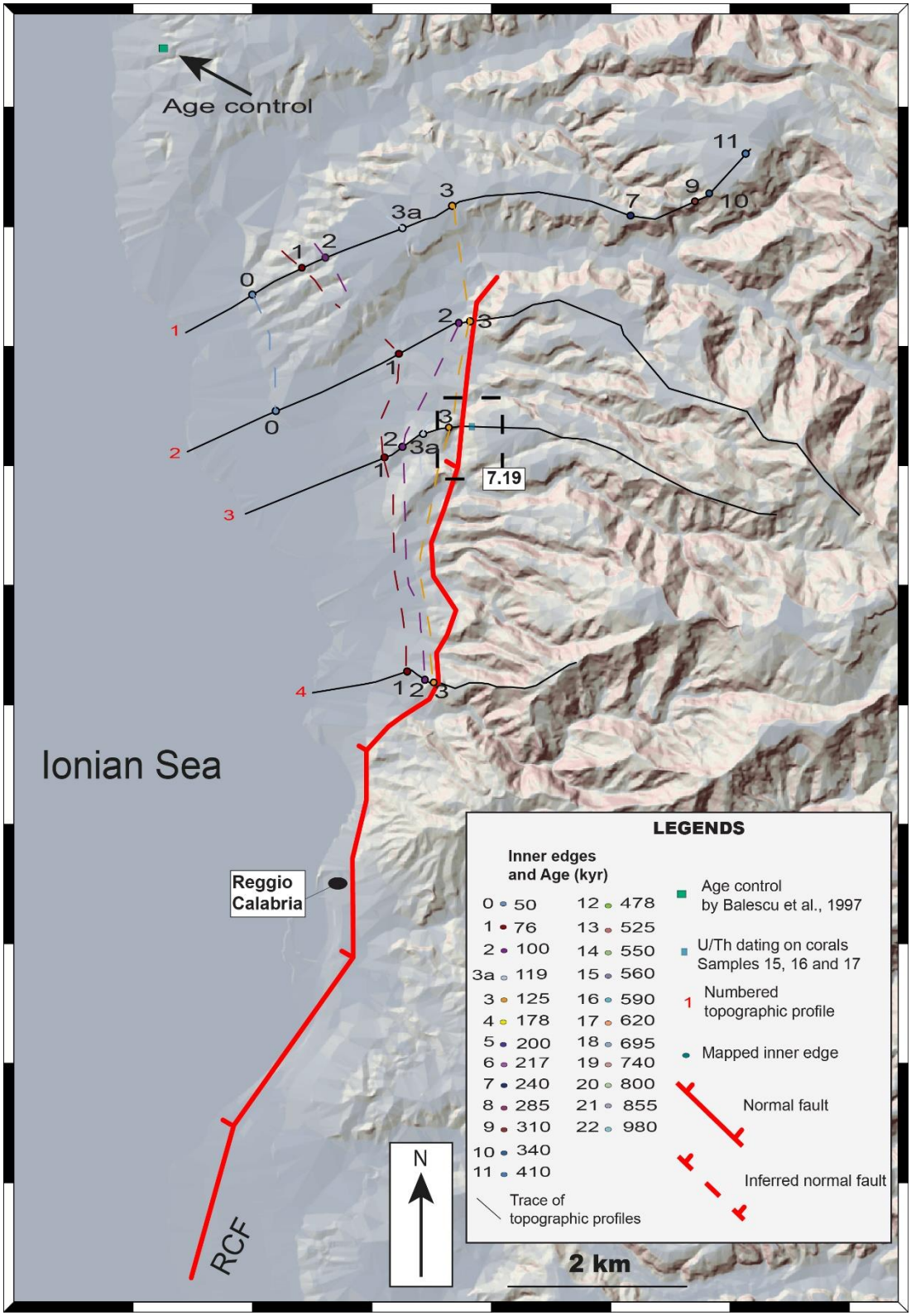

Figure 7.3: *Location map for palaeoshorelines within the hangingwall of the Reggio Calabria Fault. A 10-m resolution DEM with the associated shaded relief, used to highlight breaks of slope is used as base-map. Palaeoshorelines with reviewed ages (see numbered dots and the associated age within Legends panel) and 4-topographic profile locations along the strike of this fault, S Calabria, are shown from this thesis. "7.19" refers to Figure 7.19 which shows where a marine terrace is offset by the RCF in the field.*

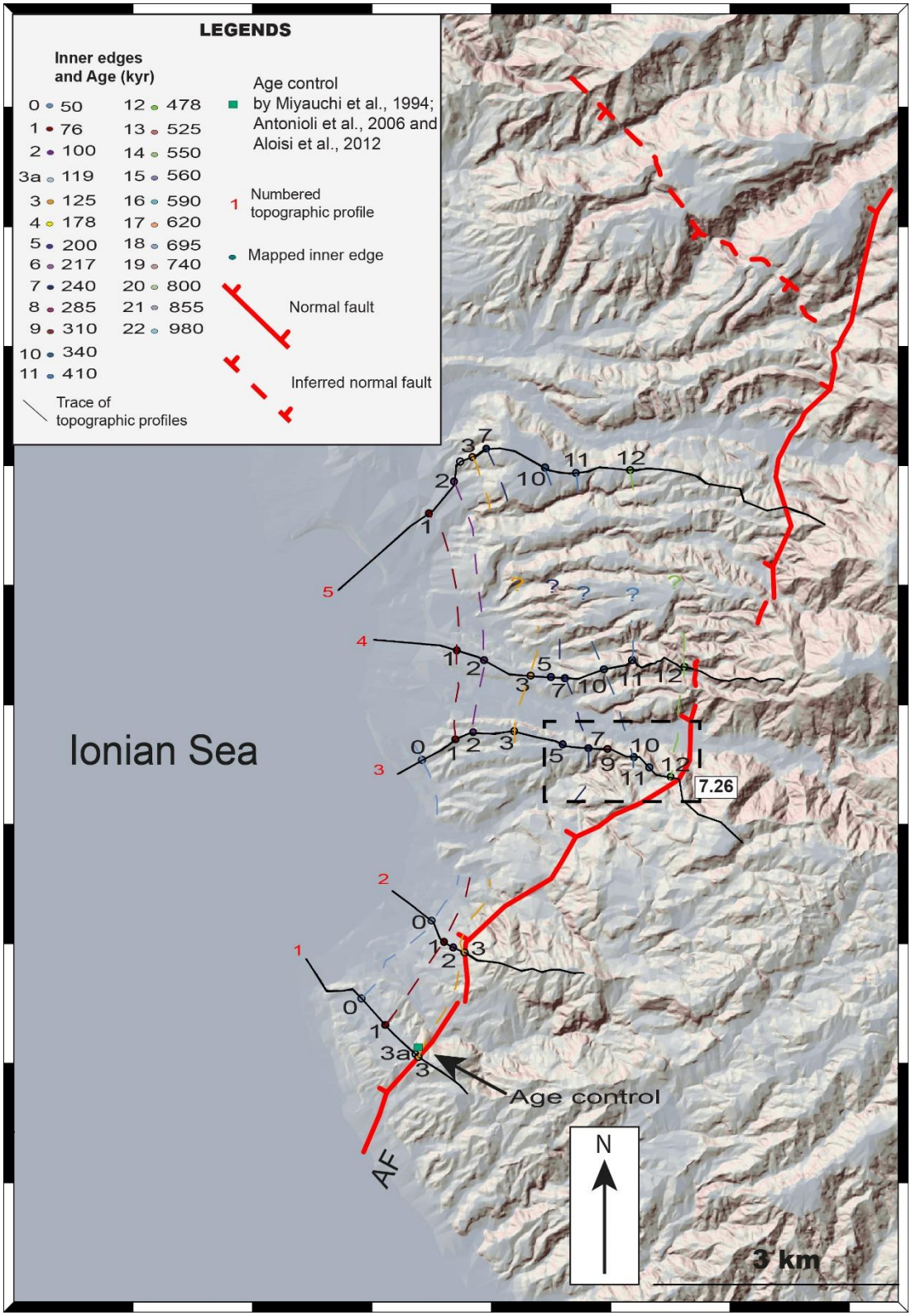

Figure 7.4: *Location map for palaeoshorelines within the hangingwall of the Armo Fault. A 10-m resolution DEM with the associated shaded relief, used to indicate breaks of slopes, is used as base-map. Inner edges of marine terraces with reviewed ages (see numbered dots and the associated age within Legends panel) and 5-topographic profile locations along the strike of this fault, S Calabria, are shown from this thesis. "7.26" refers to Figure 7.26 which shows where a marine terrace is offset by the RCF in the field.*

7.3.2. U/Th dating on corals and available dated terraces used as age controls to drive the synchronous correlation approach

A detailed and complete description of the synchronous correlation approach has been done in the Methods chapter (see Section 3.2). The correlation between multiple uplifted Late Quaternary palaeoshoreline elevation (or measured elevations) and multiple sea-level highstands (or predicted elevations) imposes the need for the user to obtain the highest R^2 value through a linear regression. This has been produced for all investigated areas of this chapter. The uplift rate iteration is driven by absolute age controls, as described below.

For the Reggio Calabria Fault, existing age controls have been described in Section 7.2. New age controls have been obtained through dating of corals with the U/Th dating technique (Figure 7.3). In particular, dated corals allow one to assign an age for a prominent marine terrace on the footwall of the Reggio Calabria Fault (Figure 7.3). Indeed, this terrace is thought to have been faulted and mapped in the hangingwall of the same fault (Catalano *et al.*, 2003). These authors have been mapping palaeoshorelines along the strike of the Reggio Calabria Fault and by using previous age controls (Balescu *et al.*, 1997) assign to the highest terrace mapped on the hangingwall the age of 125 ka, assuming that the terrace mapped on the footwall cut-off has the same age (Catalano *et al.*, 2003). Indeed, the corals were collected from a calcarenite-made boulder within shallow marine terraced deposits, from the same footwall terrace mapped by previous geoscientists mentioned above (Catalano *et al.*, 2003). The absolute age from the dated corals ranges 384 - 480 ka. It is plausible to think that this age can be correlated to prominent sea-level highstands such as those known from 340 and 478 ka (Table 7.1). However, because the corals were sampled from within a detrital boulder, made of cemented bioclastic sands, with a death assemblage or corals, that was embedded within

shallow marine terrace deposits, the age of the terrace is constrained to be not older than 384 ka, but may be younger. It is important to note that these corals are the only material available to sample for obtaining new age controls in this region.

Sample	Sample wt (mg)	U (ppm)	232 Th (ppm)	(234U/238U)	Uncertainty (2 s.e.)	Age (ka)	+	-
15	22.85	3.47	0.002	1.0150	0.003	449.068	17.342	17.342
16	5.32	2.82	0.003	1.0230	0.004	384.123	11.465	11.465
17	8.31	3.84	0.009	1.0158	0.004	480.295	25.100	25.100

Table 7.1: *Measurements of U/Th isotope ratios of coral sample collected near Reggio Calabria town. Location of collected corals is shown in Figure 7.1 and 7.3*

This is consistent with the suggestion that this terrace is related to the 125 ka sea-level highstand (Balescu *et al.*, 1997; Catalano *et al.*, 2003), which they mapped on the hangingwall of the Reggio Calabria Fault; the footwall location from the corals were sampled is suggested herein to be the faulted equivalent of that described by Balescu *et al.*, (1997) and Catalano *et al.*, (2003). This correlation has been used to drive the synchronous correlation approach alongside available age controls from literature shown in Table 7.2, allowing the identification of new ages for the un-dated palaeoshorelines and suggesting a new uplift history over the Late Quaternary (see Section 7.4). Moreover, the correlation between Late Quaternary palaeoshorelines outcropping both on the hangingwall and footwall of this fault has allowed an improved estimation of throw and throw-rate for the Reggio Calabria Fault through time (see Sections 7.4 and 7.5). Nonetheless, a further death assemblage made of fossiliferous shallow marine material such as corals (Cladocora caespitosa and solitary corals), echinoid spines and bivalve shells was mapped and collected on the Reggio Calabria Fault plane, suggesting that these material could represent the lower deposits of the terrace mapped on the footwall, and offset by the Reggio Calabria Fault (Catalano *et al.*, 2003). Another hypothesis

was that this fossiliferous material could be older than the actual age of terrace (older than 125 ka), suggesting that this terrace could be a "composite" terrace like other dated terrace examples mapped in the Mediterranean Basin (e.g. Roberts *et al.*, 2009). However, these further sampled corals were not able to be dated due to open system isotope exchange during diagenesis (See Table 3.1 in Chapter 3 and Appendix 3.2 – Sample 1-14).

Reference	**Dating Method**	**Dated sample description**	**Profile number**	**Reported Age (ky)**	**Assigned Highstand (ka)**	**Palaeo-shoreline Elevation (m a.s.l)**
Antonioli, Kershaw et al., 2006	ESR technique	*"Based on ESR methodology applied to a Patella and venerupid shells (sample nos. K-4343 and K-4244, University of Koln) collected at +105 m, we obtained ages of 76.477.2 and 103.3712.5 ka. If the age is calculated using a constant Uranium-uptake model, the value is 124.5715.0 ka. We attribute these terraces to MIS 5, probably MIS 5.5 (Figs. 3C, D and 6)."*	12 – the Messina Strait Fault	100-125	125	130
Balescu et al., 1997	TL dating	*"Non-fossiliferous eolian sand from a dune associated*	1 – the Reggio Calabria Fault	59 ± 7	50	34

		with a post-last interglacial paleoshoreline culminating at an altitude of 43 m a.s.l.. The latter is correlated by Dumas and Raffy (1993) with Oxygen Isotope Stage 3 (Chappell and Shackleton, 1986).”				
Miyauchi et al., 1994; Antonioli et al., 2006 and Aloisi et al., 2012	Geomorphic and S. bubonius	*“In southernmost Calabria, the terrace attributed to the Marine Isotopic Stage (MIS) 5.5, which is dated at 125 ka BP and can be fairly well recognized due to its palaeontological content (Ferranti et al. 2006), has its inner margin, a close proxy for the palaeo-sea level, lying at elevations between ~130 and ~180 m (Dumas and Raffy 2004)”*	3 – the Armo Fault	125	125	140

Table 7.2: *Available well-accepted age controls from literature. Locations of age controls are shown in figures 7.1, 7.2, 7.3 and 7.4.*

7.4 Results

In this section, results obtained by studying the correlation between multiple mapped elevations of marine terrace inner edges and iteratively-calculated multiple sea-level highstands applying a synchronous correlation are presented. This correlation has been driven by new obtained age controls and those well-accepted and available in the literature. This allows derivation of new, refined uplift rates and how these are related to long-term fault displacements on the Messina Strait Fault (Section 7.4.1), the Reggio Calabria Fault (Section 7.4.2) and the Armo Fault (Section 7.4.3).

7.4.1. The Messina Strait Fault

As for other chapters in thesis, it was not possible to check all marine terraces mapped through GIS analysis in the field due to heavily-vegetated areas and partial access on private land, a common problem for marine terrace investigations (Roberts *et al.*, 2013) (Table 7.3). However, Figure 7.5 shows detailed topographic analysis through 13 topographic profiles, spanning ~ 60 km along the strike of the offshore Messina Strait Fault (Figure 7.1 and 7.2), shows gently seaward-dipping terraced surfaces which have been interpreted as palaeshoreface surfaces cut by wave-action. In places, marine, shallow water, palaeo-beach deposits have been deposited on these terraced surfaces (Figure 7.6), as described by previous studies (Bianca *et al.*, 1999; Catalano *et al.*, 2003; De Guidi *et al.*, 2003; Giunta *et al.*, 2012; Roberts *et al.*, 2013; Gallen *et al.*, 2014). Up dip of these deposits and wave-cut platforms are breaks of slope interpreted as palaeo-sea cliffs, the bases of which are interpreted, herein as palaeoshorelines.

Palaeoshoreline (Profile number)	DEM Elevations (m)	Expected Elevations (m)	Field Elevations (m)	Proposed Age (ka)	UTM Coordinate
1 (1)	49	43	-	76	33 S 0548109 4226786
3 (1)	106	103	-	125	33 S 0547784 4226847
7 (1)	140	150	-	240	33 S 0546450 4227164
11 (1)	230	235	-	410	33 S 0546234 4227257
19 (1)	408	410	-	740	33 S 0545033 4227549
20 (1)	458	455	-	800	33 S 0543821 4228040
21 (1)	487	487	-	855	33 S 0543645 4228146
2 (2)	65	60	-	100	33 S 0546538 4223495
3 (2)	103	103	107	125	33 S 0546212 4223662
5 (2)	135	130	-	200	33 S 0546020 4223740
7 (2)	144	150	145	240	33 S 0545475 4224092
10 (2)	203	210	190	340	33 S 0545066 4224403
11 (2)	245	235	245	410	33 S 0544964 4224469
20 (2)	451	455	-	800	33 S 0543709 4224854
22 (2)	531	550	-	980	33 S 0543263 4225009
1 (3)	55	51	-	76	33 S 0544636 4219045
2 (3)	71	69	80	100	33 S 0544558 4219045
3 (3)	114	113	120	125	33 S 0544424 4219106
7 (3)	155	165	-	240	33 S 0544151 4219170
10 (3)	220	229	-	340	33 S 0543477 4219168
11 (3)	255	256	-	410	33 S 0542755 4219538
21 (3)	518	522	-	855	33 S 0541347 4219715
1 (4)	55	55	-	76	33 S 0543853 4216396
2 (4)	81	79	-	100	33 S 0543657 4216361
3 (4)	119	116	-	125	33 S 0543215 4216202

10 (4)	235	235	-	340	33 S 0542883 4216095
11 (4)	261	263	-	410	33 S 0542527 4216106
12 (4)	300	305	-	478	33 S 0542413 4216117
701 (5)	52	57	-	76	33 S 0542390 4213537
3 (5)	114	120	-	125	33 S 0542162 4213570
7 (5)	170	176	170	240	33 S 0541973 4213662
9 (5)	205	199	210	310	33 S 0541819 4213735
10 (5)	245	243	-	340	33 S 0541697 4213807
11 (5)	280	274	280	410	33 S 0541555 4213895
12 (5)	315	318	320	478	33 S 0540944 4214296
15 (5)	379	368	-	560	33 S 0540827 4214396
16 (5)	400	402	-	590	33 S 0540700 4214634
1 (6)	70	67	70	76	33 S 0541118 4211552
2 (6)	88	87	85	100	33 S 0541571 4212081
3a (6)	110	120	110	119	33 S 0541403 4212174
3 (6)	125	135	130	125	33 S 0541325 4212245
5 (6)	180	176	180	200	33 S 0541075 4212412
7 (6)	203	203	-	240	33 S 0540951 4212465
10 (6)	273	281	-	340	33 S 0540849 4212508
11 (6)	335	318	-	410	33 S 0540702 4212602
12 (6)	380	370	-	478	33 S 0540550 4212712
16 (6)	450	466	-	590	33 S 0540343 4212898
1 (7)	60	71	-	76	33 S 0540829 4211262
3a (7)	132	126	-	119	33 S 0540767 4211332
3 (7)	146	141	138	125	33 S 0540629 4211433
5 (7)	195	184	-	200	33 S 0540354 4211570
7 (7)	203	212	-	240	33 S 0540271 4211615
10 (7)	293	286	-	340	33 S 0540113 4211731

12 (7)	376	386	375	478	33 S 0539901 4211824
13 (7)	441	440	-	525	33 S 0539670 4211819
17 (7)	517	507	-	620	33 S 0539365 4211905
19 (7)	585	577	-	740	33 S 0539176 4212247
20 (7)	647	635	-	800	33 S 0538895 4212998
1 (8)	91	86	90	76	33 S 0538404 4207920
3a (8)	138	145	-	119	33 S 0538186 4208020
3 (8)	160	160	-	125	33 S 0538101 4208095
7 (8)	238	242	-	240	33 S 0537794 4208392
10 (8)	328	332	-	340	33 S 0537526 4208634
12 (8)	450	437	-	478	33 S 0537243 4208906
13 (8)	483	495	-	525	33 S 0537133 4208989
17 (8)	565	571	-	620	33 S 0537042 4209164
18 (8)	605	621	-	695	33 S 0536946 4209421
1 (9)	77	86	-	76	33 S 0534134 4203177
2 (9)	101	110	-	100	33 S 0533969 4203270
3a (9)	150	145	-	119	33 S 0533784 4203368
3 (9)	173	160	180	125	33 S 0533598 4203466
5 (9)	204	210	-	200	33 S 0533517 4203530
7 (9)	239	242	-	240	33 S 0533304 4203610
10 (9)	336	332	-	340	33 S 0532554 4204160
11 (9)	385	378	-	410	33 S 0532245 4204392
12 (9)	438	437	-	478	33 S 0532005 4204553
15 (9)	513	506	-	560	33 S 0531248 4205315
17 (9)	570	571	-	620	33 S 0530678 4205893
1 (10)	75	73	75	76	33 S 0532055 4200306
3a (10)	132	129	-	119	33 S 0531816 4200409
3 (10)	147	143	-	125	33 S 0531687 4200497

7 (10)	212	217	-	240	33 S 0531388 4200659
10 (10)	292	299	-	340	33 S 0530915 4200935
11 (10)	330	340	320	410	33 S 0530672 4201093
17 (10)	526	517	-	620	33 S 0528707 4201593
18 (10)	564	562	-	695	33 S 0528425 4201643
19 (10)	600	589	-	740	33 S 0528276 4201668
22 (10)	790	783	-	980	33 S 0527522 4201891
1 (11)	71	71	-	76	33 S 0530561 4196241
2 (11)	99	93	-	100	33 S 0530542 4196245
3a (11)	120	126	115	119	33 S 0530297 4196212
3 (11)	132	140	130	125	33 S 0530298 4196229
5 (11)	180	183	165	200	33 S 0530189 4196208
7 (11)	207	211	220	240	33 S 0530094 4196212
10 (11)	287	291	290	340	33 S 0529688 4196254
11 (11)	330	330	330	410	33 S 0529598 4196352
12 (11)	387	382	375	478	33 S 0529388 4196416
13 (11)	440	435	445	525	33 S 0528566 4197040
1 (12)	48	53	53	76	33 S 0526025 4188873
3 (12)	122	118	-	125	33 S 0525844 4189113
7 (12)	173	177	177	240	33 S 0525726 4189254
10 (12)	255	247	245	340	33 S 0525242 4189615
13 (12)	375	373	-	525	33 S 0524521 4190029
16 (12)	405	412	-	590	33 S 0523551 4190611
2 (13)	58	59	-	100	33 S 0519946 4185828
3 (13)	102	101	-	125	33 S 0519653 4185868
9 (13)	158	162	-	310	33 S 0519358 4186056
10 (13)	201	204	-	340	33 S 0518890 4186329
17 (13)	349	353	-	620	33 S 0518174 4186534

19 (13)	393	396	-	740	33 S 0517893 4186605

Table 7.3: *Data collected for the Messina Strait Fault. All mapped inner edges from DEM and fieldwork with ages assigned via synchronous correlation. Note that not all the locations for inner edges mapped by DEM have been checked analysis with GPS in the field because the investigated area is in places thickly-vegetated and densely-populated with private properties.*

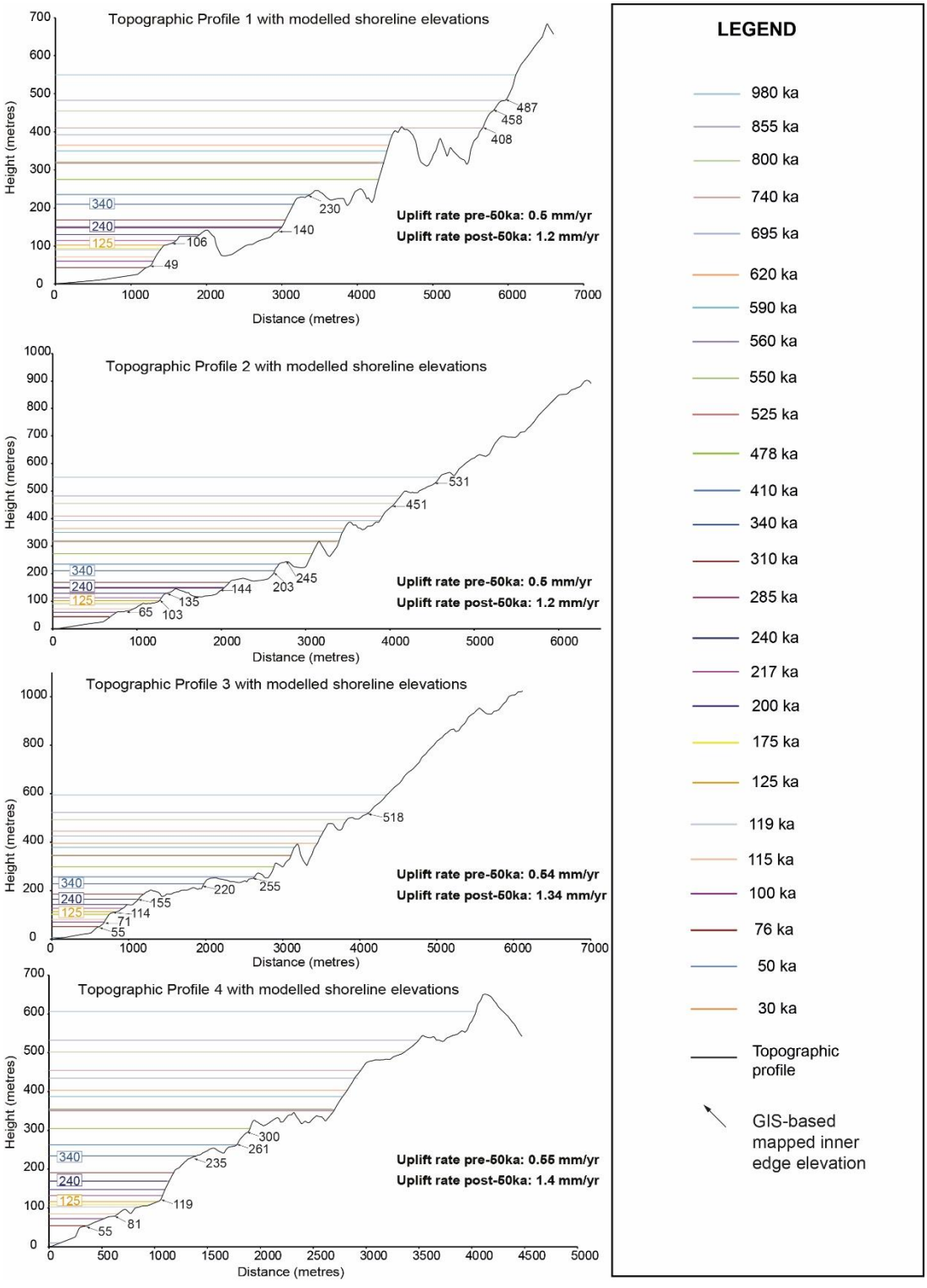

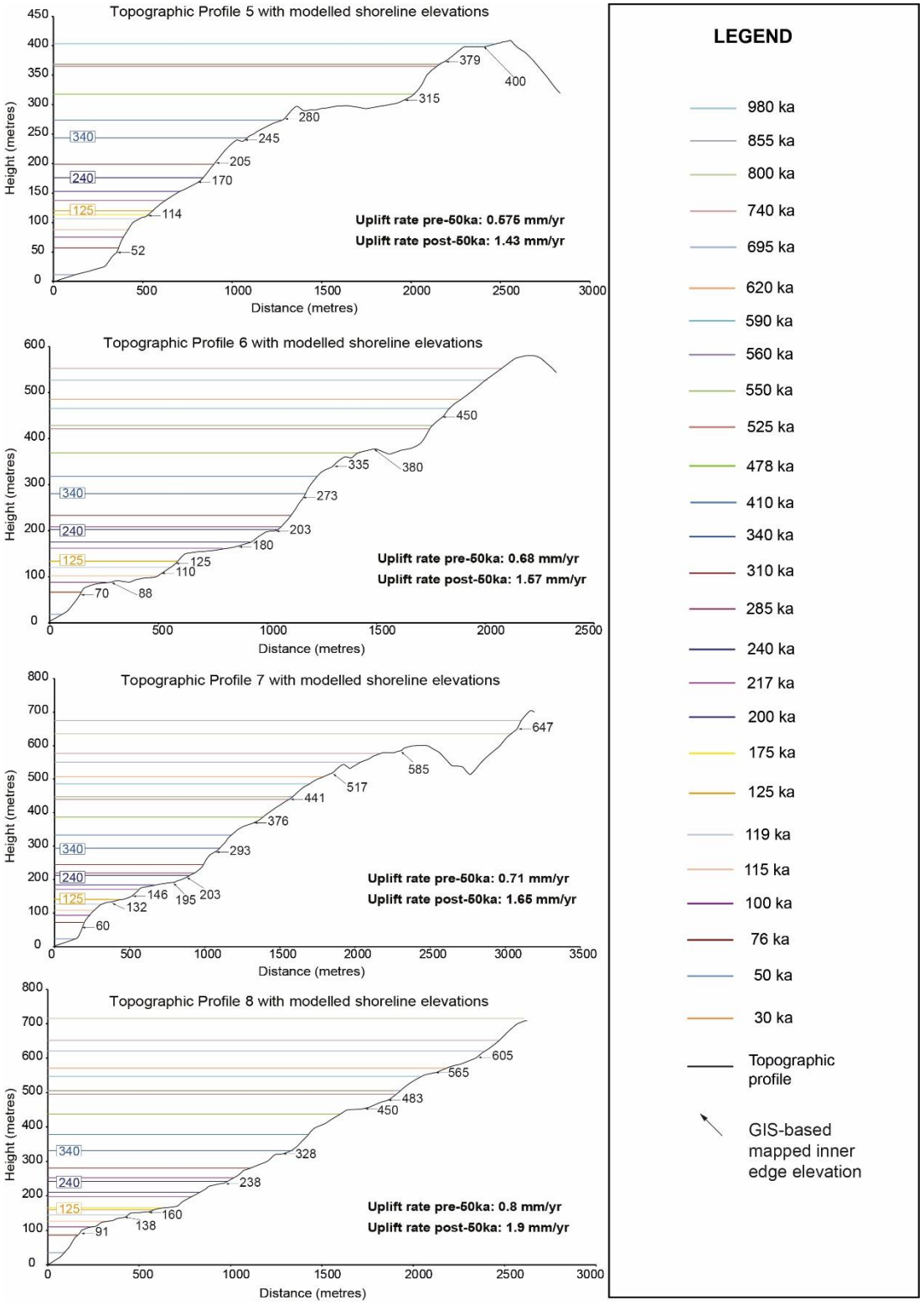
Topographic Profile 5 with modelled shoreline elevations
Height (metres)
Distance (metres)
379
400
315
280
340
245
205
240
170
125
114
52
Uplift rate pre-50ka: 0.575 mm/yr
Uplift rate post-50ka: 1.43 mm/yr
Topographic Profile 6 with modelled shoreline elevations
450
335
380
340
273
240
203
180
125
110
70
88
Uplift rate pre-50ka: 0.68 mm/yr
Uplift rate post-50ka: 1.57 mm/yr
Topographic Profile 7 with modelled shoreline elevations
647
585
517
441
376
340
293
240
146
195
203
125
132
60
Uplift rate pre-50ka: 0.71 mm/yr
Uplift rate post-50ka: 1.65 mm/yr
Topographic Profile 8 with modelled shoreline elevations
605
565
483
450
340
328
240
238
125
160
138
91
Uplift rate pre-50ka: 0.8 mm/yr
Uplift rate post-50ka: 1.9 mm/yr
LEGEND
980 ka
855 ka
800 ka
740 ka
695 ka
620 ka
590 ka
560 ka
550 ka
525 ka
478 ka
410 ka
340 ka
310 ka
285 ka
240 ka
217 ka
200 ka
175 ka
125 ka
119 ka
115 ka
100 ka
76 ka
50 ka
30 ka
Topographic profile
GIS-based mapped inner edge elevation

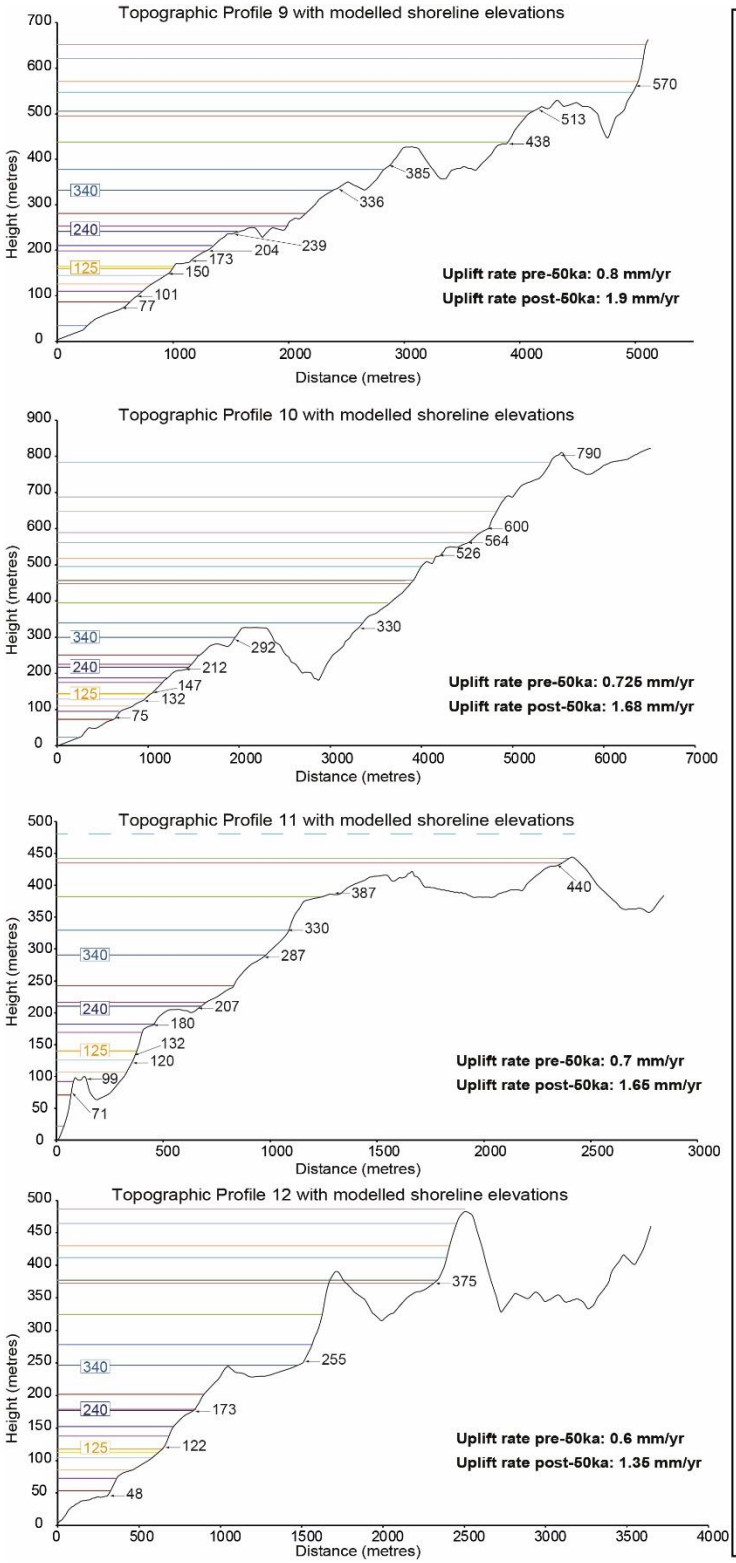
Topographic Profile 9 with modelled shoreline elevations
Height (metres)
Distance (metres)
570
513
438
385
336
340
240
239
204
173
150
125
101
77
Uplift rate pre-60ka: 0.8 mm/yr
Uplift rate post-60ka: 1.9 mm/yr
Topographic Profile 10 with modelled shoreline elevations
790
600
564
526
330
340
292
240
212
147
132
125
75
Uplift rate pre-60ka: 0.725 mm/yr
Uplift rate post-60ka: 1.68 mm/yr
Topographic Profile 11 with modelled shoreline elevations
440
387
330
340
287
240
207
180
132
125
120
99
71
Uplift rate pre-60ka: 0.7 mm/yr
Uplift rate post-60ka: 1.65 mm/yr
Topographic Profile 12 with modelled shoreline elevations
375
340
255
240
173
125
122
48
Uplift rate pre-60ka: 0.6 mm/yr
Uplift rate post-60ka: 1.35 mm/yr
LEGEND
980 ka
855 ka
800 ka
740 ka
695 ka
620 ka
590 ka
560 ka
550 ka
525 ka
478 ka
410 ka
340 ka
310 ka
285 ka
240 ka
217 ka
200 ka
175 ka
125 ka
119 ka
115 ka
100 ka
76 ka
50 ka
30 ka
Topographic profile
GIS-based mapped inner edge elevation

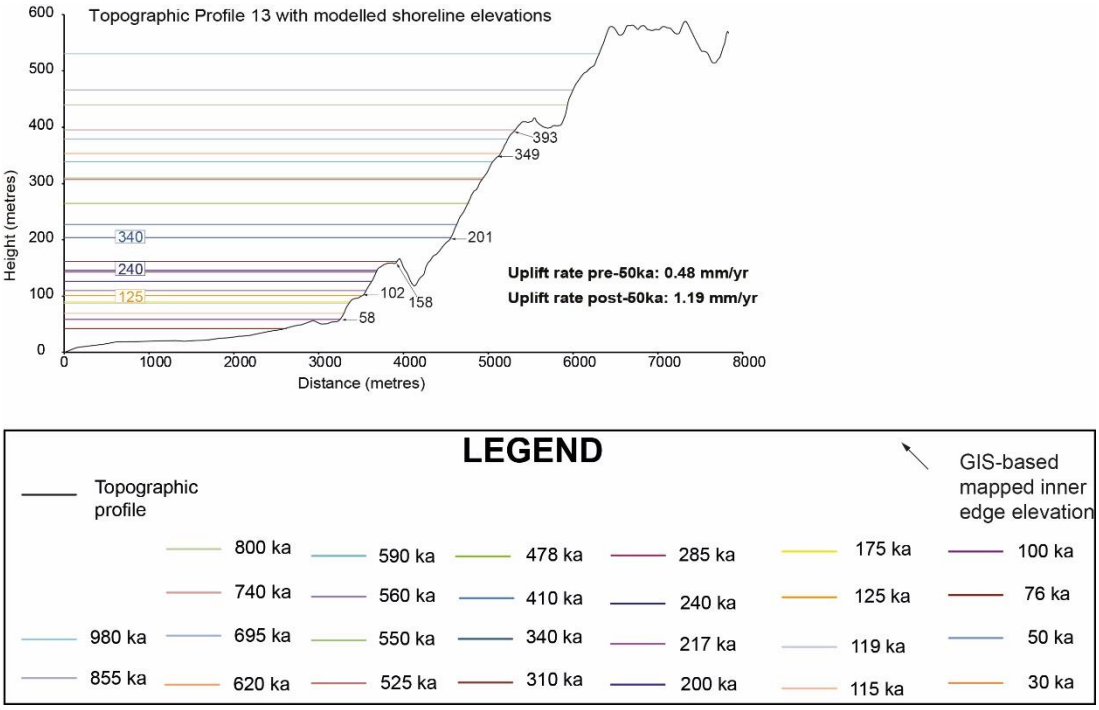

Figure 7.5: *Profiles showing mapped and modelled palaeoshoreline elevations along the strike of the offshore Messina Strait Fault. The topographic profile is from a 10 m DEM. The numbers with arrows mark the elevations of palaeoshorelines mapped in the field. The coloured lines indicate palaeoshoreline elevations predicted by an uplift rate that has been changed iteratively to produce the best match with the mapped palaeoshorelines; goodness of fit is indicated by the value for slope and the R^2 values in Figure 7.8. Profiles are located in Figure 7.1 and 7.2.*

Sample	36-Cl Conc. (Atoms of 36-Cl/g of sample)	Erosion rate (mm/ky)	Age (kyr)	Total uncertainty (kyr)	Elevation (m)	Expected Age (ka)
15	97743.14203	8	5.5	1.2	335	340
16	98034.67934	8	5.3	1.1	335	340

Table 7.4: *Exposure ages from in situ ^{36}Cl cosmogenic exposure dating are shown in the table. Sampling locations are shown in Figure 7.1, 7.2c and in Chapter 3*

As shown in Chapter 3, ^{36}Cl cosmogenic dating has been used to attempt to date a wave-cut platform mapped in the footwall of the Messina Strait Fault to resolve the uplift-rate. However, because of the prominent erosion affecting the area the obtained exposure ages are low and hence discarded (Table 7.4). In particular, a Mesozoic limestone-made WCP was sampled from the terrace where Forza D'Agro' town is built, shown in Figure 7.6a at 335m (see sample locations in Figure 7.1 and 7.2c). Even though a flat surface was mapped and sampled, the results obtained in Table 7.4 show lower ages than the expected one for that

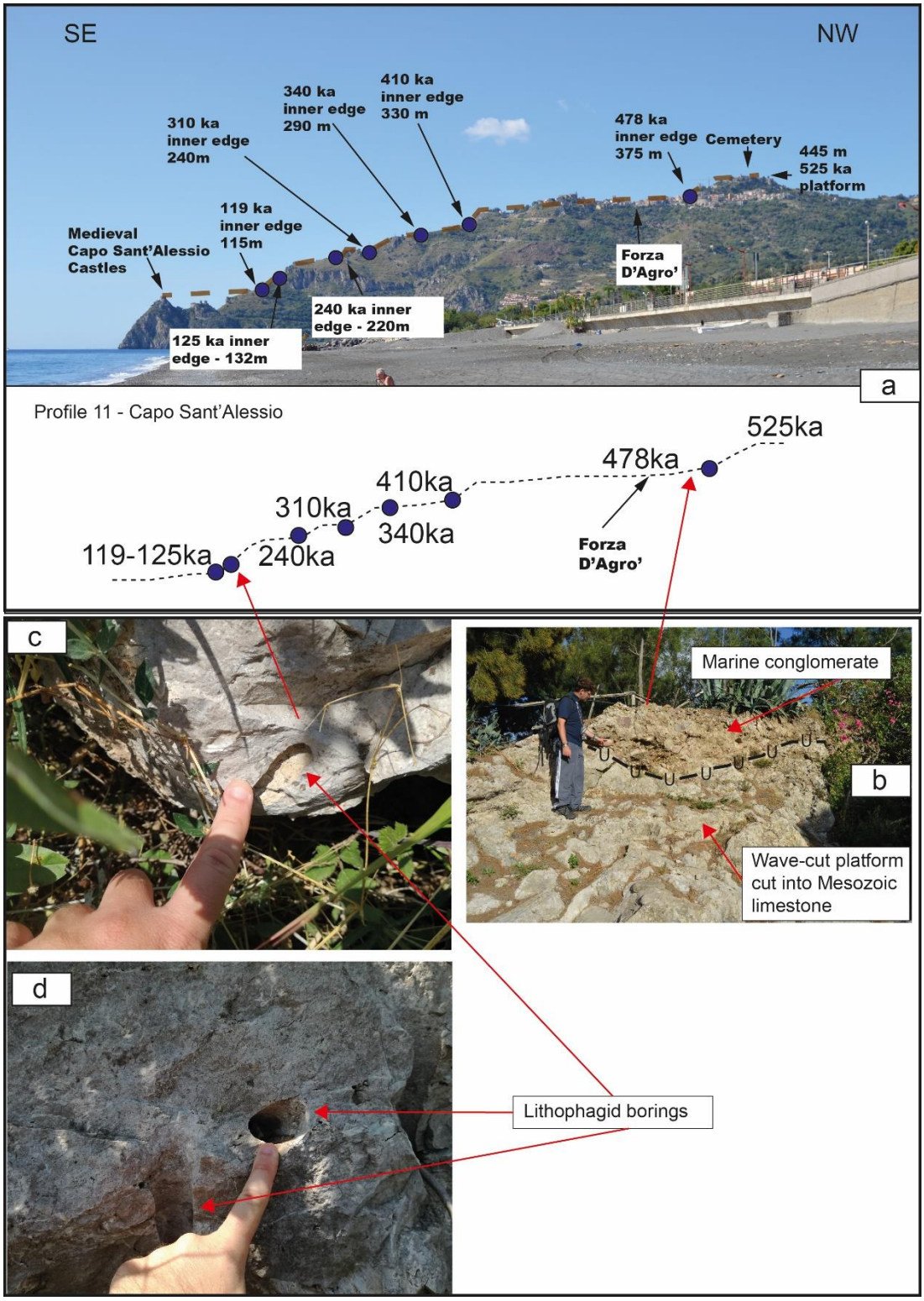

Figure 7.6: *(a) A sequence of uplifted marine terraces is shown on the Sicilian coast. Marine terrace inner edges have been mapped (blue dots) and refined ages are assigned using a synchronous correlation approach. In places, shallow marine deposits have been mapped unconformably overlying wave-cut platforms (b). In (c) and (d) lithophagid borings in Mesozoic limestone formation have been mapped close to inner edge of the 125 ka-dated palaeoshoreline.*

palaeoshoreline (478 ka), suggesting perhaps that topographically-lower wave-cut platforms cut into Mesozoic limestone should be investigated to attempt gaining new age controls by using the ^{36}Cl cosmogenic dating.

Figure 7.7 shows a strong correlation between DEMs-based palaeoshoreline elevations and field-based palaeoshoreline elevations, with R^2 values >0.99, suggesting that: (i) elevations measured elsewhere in the DEM are likely to be reliable and (ii) mapping from previous geoscientists (Catalano *et al.*, 2003; De Guidi *et al.*, 2003) is accurate and strong but ages of un-dated marine terraces needed to be reviewed. This has allowed to correlate multiple "measured" palaeoshoreline elevations from DEMs and checked in the field and "predicted" sea level highstands iteratively-calculated by applying a synchronous correlation approach.

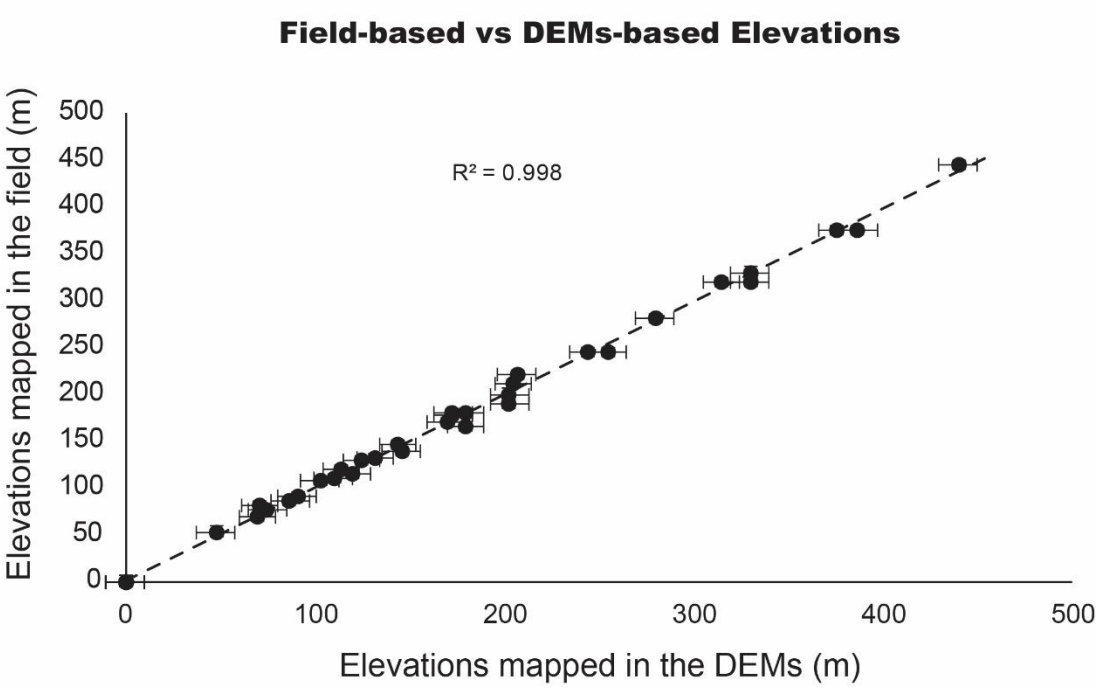

Figure 7.7: *The graph shows the relationship between field-based and DEM-based inner edge elevations. The R^2 value > 0.99 confirms a very robust relationship suggesting that elevations measured elsewhere in the DEM are likely to be accurate.*

Indeed, in a similar manner to other chapters in this thesis, past sea-level interpretations (Figure 7.5) has been made for the elevation dataset, through synchronous correlation, with linear regression analysis used to validate the robustness of the correlation between

"measured" palaeoshorelines and "predicted" past sea-level highstand elevations. The approach already presented in Chapters 4, 5 and 6 (Roberts *et al.*, 2009; Roberts *et al.*, 2013; Meschis *et al.*, 2018; Pedoja *et al.*, 2018) is applied to all 13 topographic profiles to assess whether variations of uplift/subsidence along the strike of the Messina Strait Fault can be mapped due to the long-term faulting activity. At first a constant uplift rate through time was attempted, but a convincing correlation between measured and predicted palaeoshoreline elevations was not achieved. Thus, an attempt was made to vary the uplift rate through time. For time varying uplift, with a change in uplift rate at ~50 kyrs, linear regression analysis between "measured" and "predicted" palaeoshoreline elevations (see Chapter 3 – Methods for more details) shows R^2 values >0.99, indicating a robust synchronous correlation between multiple sea level highstands and multiple Late Quaternary palaeoshoreline elevations (Figure 7.8).

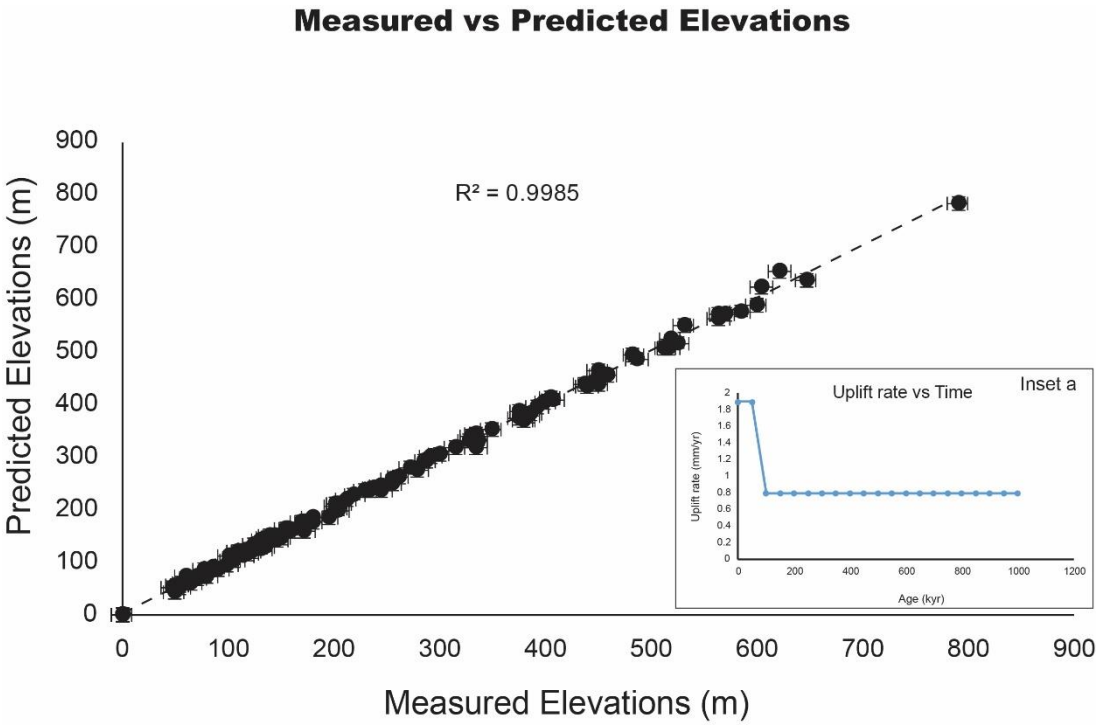

Figure 7.8: *Graph showing linear regression analysis between measured and predicted elevations. The predicted elevations, representing the synchronously-calculated sea-level highstand elevations, have been derived by defining a fluctuating uplift rate through time (increase in rate at ~50 ka), and iterating this value to find the best match to the measured and mapped palaeoshorelines. Note that "measured" elevations represent palaeoshoreline elevations mapped in the 10-m high resolution DEMs. Coefficient of determination, R^2 value, has been used between these two*

datasets to quantify the best fit for all 13 topographic profiles with a value > 0.99 achieved. Inset "a" shows the changing uplift rate through time measured in the centre of fault.

The following palaeoshorelines were identified with this approach; 76 ka, 100 ka, 125 ka, 200 ka, 240 ka, 310 ka, 340 ka, 410 ka, 478 ka, 525 ka, 560 ka, 590 ka, 620 ka, 695 ka, 740 ka, 800 ka, 855 ka and 980 ka., In turn, this suggests long-term faulting activity since at least 1 Ma.

Elevations of marine terraces have been interpreted and correlated with sea-level highstands in Figure 7.5. Figure 7.9 shows spatial variations of uplift along the strike of the Messina Strait Fault affecting the geometry of the palaeoshorelines, suggesting faulting activity spanning the Late Quaternary for this fault.

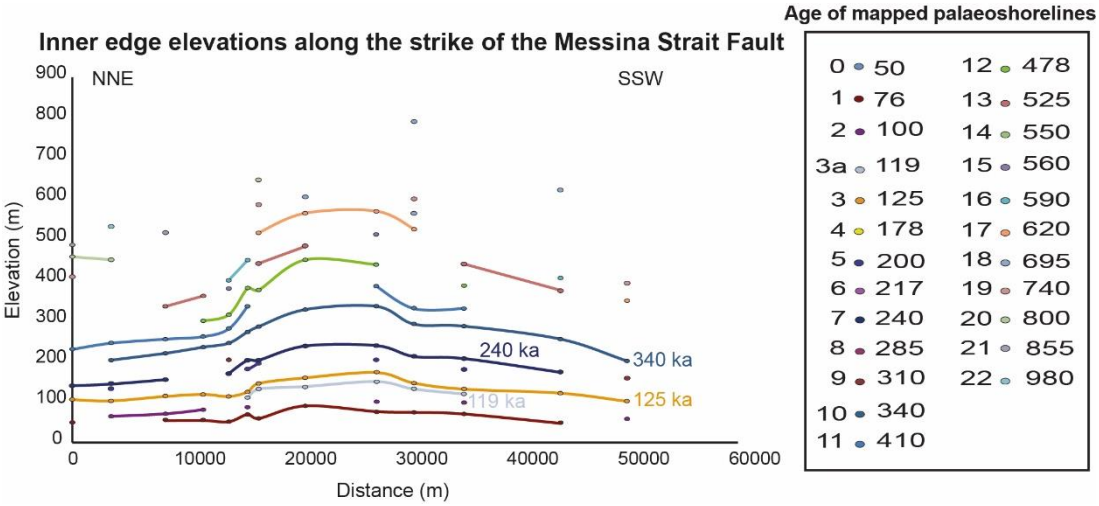

Figure 7.9: *Profiles showing tilting of palaeoshorelines whose ages are defined by the modelling in Figure 7.2 and 7.5. Solid lines represent mapped and measured palaeoshoreline elevations mapped by using DEMs and checked in the field across topographic profiles 1-13. Profile locations shown in Figure 7.1 and 7.2.*

Moreover, this synchronous correlation shows that uplift rates change both spatially along the strike of the offshore Messina Strait Fault (Figure 7.10) and temporally with uplift rates changing at ~ 50 ka, accelerating of a factor of ~ 2.4 (Inset "a" in Figure 7.8). In detail, values of uplift rate vary from ~ 0.5 mm/yr in the NNE tip zone to ~ 0.8 mm/yr in the centre of the fault before 50 ka; after 50 ka the values are ~ 1.3 mm/yr in the NNE tip zone to ~ 2.0 mm/yr in the centre of the fault. This spatially-changing uplift rate identifies a long-term faulting activity where mapped uplift changes along the strike of the Messina Strait Fault.

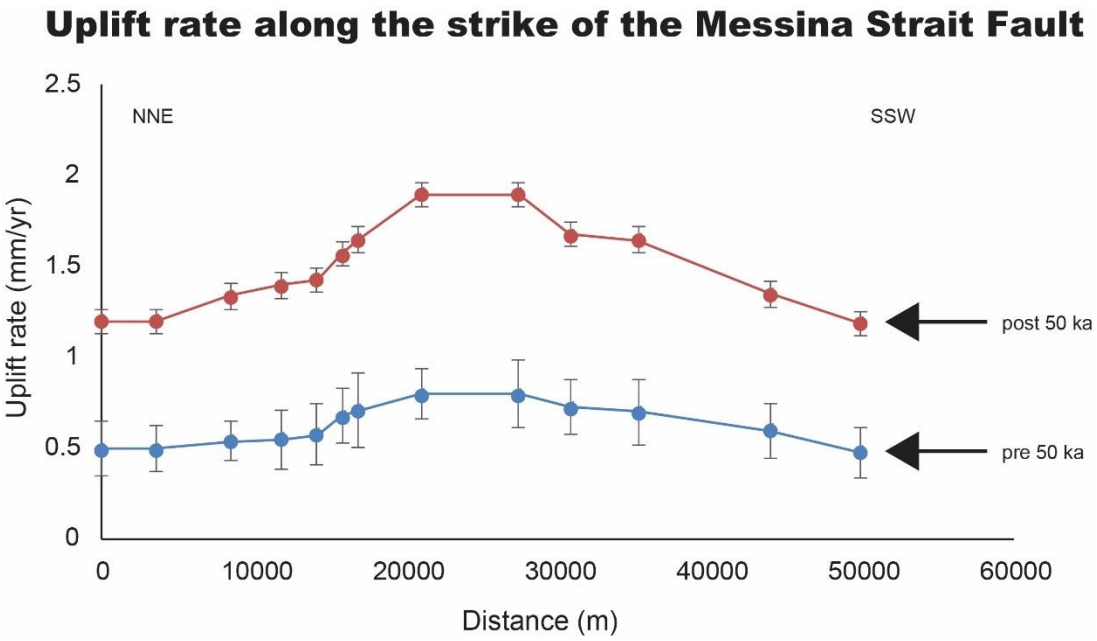

Figure 7.10: *Profile showing that uplift rates are spatially varying along the strike the offshore Messina Strait Fault, both before and after 50 ka.*

Furthermore, progressive deformation throughout the last ~1 Myrs is confrmed by along-strike tilt-angles for palaeoshorelines. Higher and older palaeoshorelines show higher tilt angles, implying that: (i) they have experienced a longer faulting history (Figure 7.11) and that (ii) the Messina Strait Fault is active.

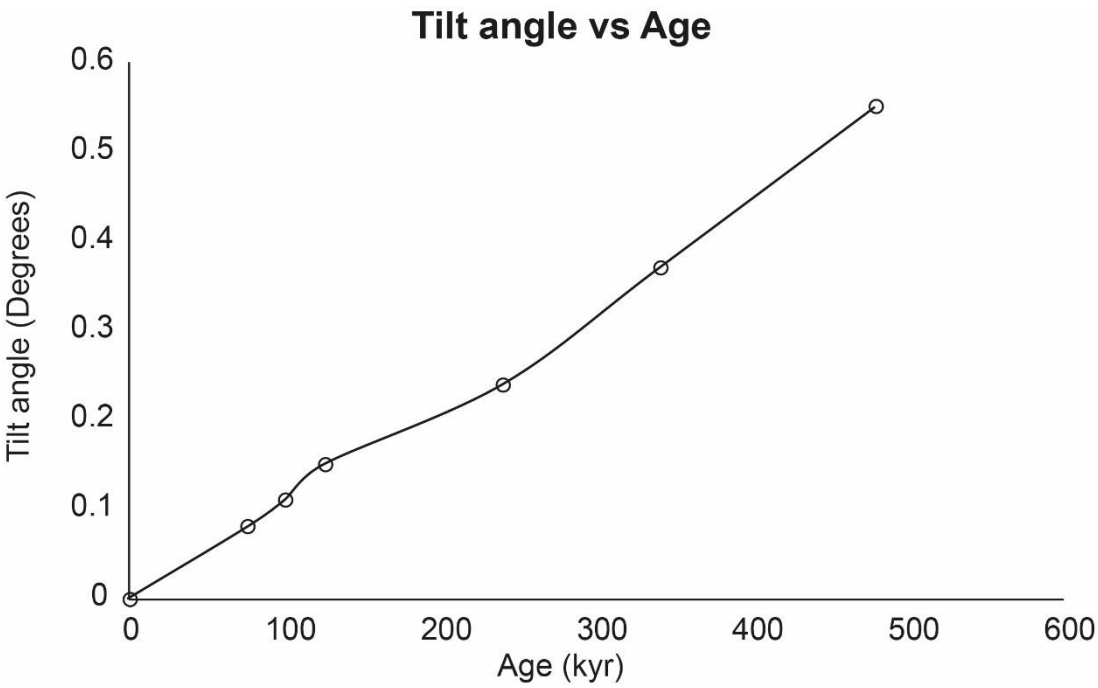

Figure 7.11: *The faulting activity of the Messina Strait Fault over the Late Quaternary has tilted the investigated palaeoshorelines; in fact, older and higher palaeoshorelines show higher tilt angle values because they have experienced a longer history of faulting activity.*

It is important to note that tilt angle values for each investigated palaeoshoreline have been calculated, as a $\tan^{-1}$ of a gradient "m" of straight line equation (y=mx) (Meschis *et al.*, 2018). It is important to highlight that these values have been derived considering the tilting action parallel to the strike of the fault.

Spatially-changing uplift rates along the strike of the Messina Strait Fault have controlled the number of preserved palaeoshorelines; indeed, as already shown by others (Westaway, 1993; Roberts *et al.*, 2009, 2013; Meschis *et al.*, 2018), where higher uplift rates are mapped, a higher number of preserved palaeoshorelines is recorded (Figure 7.12). This is to be expected because of the "overprinting problem" already explained in this thesis and overcome by applying a synchronous correlation approach. Consequently, an increase of tilt angle vales and an increase of the number of preserved palaeoshorelines are indicative of incremental deformation over the last ~1 Myrs.

Even though more studies would be needed to better understand the relationship between uplift rates spanning over the Late Quaternary and those spanning the Holocene, some observation can be done, taking into account these new results. Previous authors have studied Holocene uplift rates by looking at some coastal notches outcropping between Taormina and Capo Sant'Alessio (Stewart et al., 1997; De Guidi et al., 2003; Antonioli et al., 2006), where profiles 11 and 12 are constructed. It is remarkable that independent investigations looking at marine terraces spanning the Late Quaternary like this thesis and investigations on coastal notches spanning the Holocene show similar results in terms of uplift rates with value between 1.5 mm/yr and 2 mm/yr. Moreover, as shown by changing Late Quaternary palaeoshoreline

elevations along the strike of the fault, elevations of Holocene coastal notches are changing along the strike of the fault as shown by previous studies (De Guidi et al., 2003).

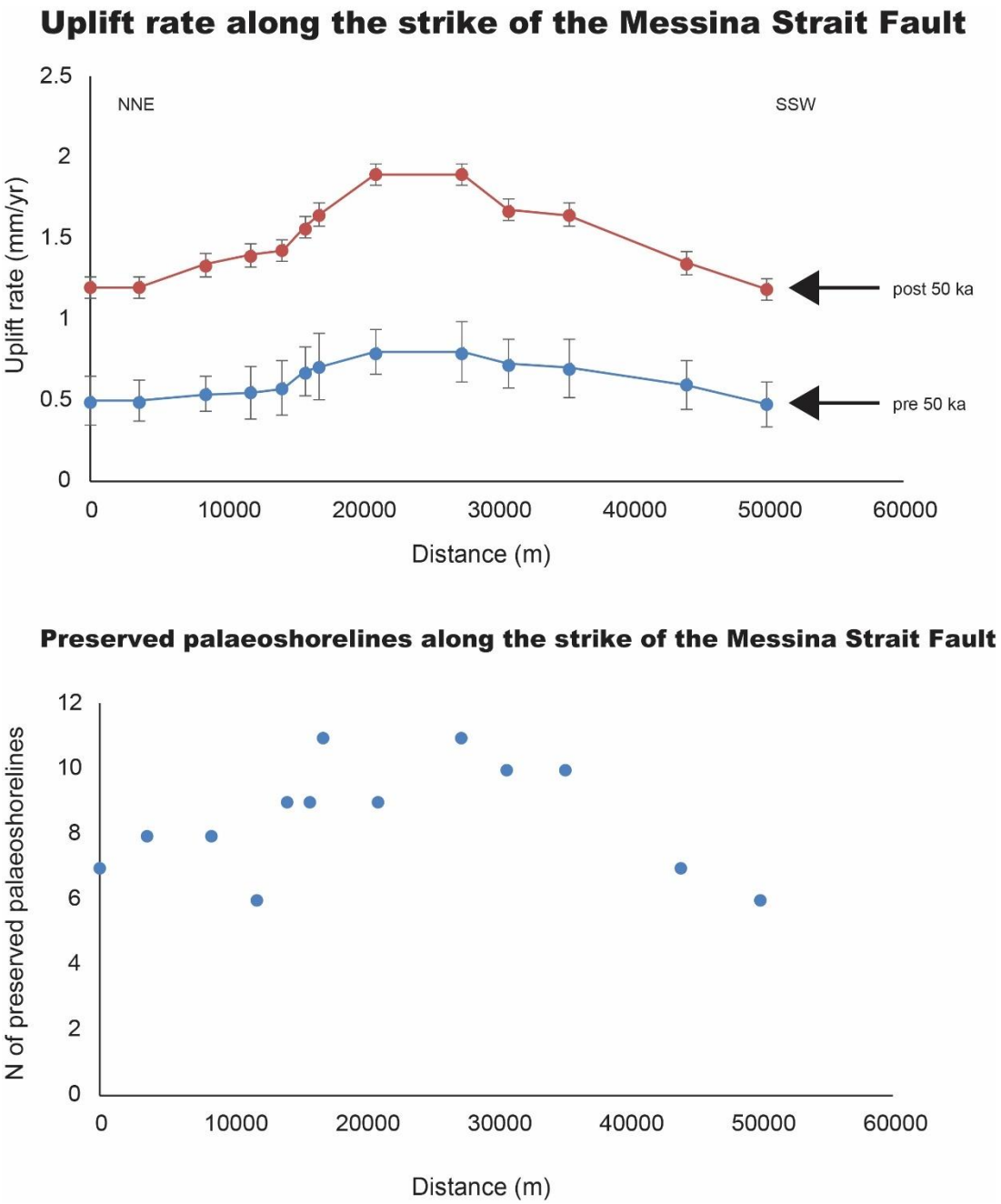

Figure 7.12: *X-Y graphs showing good match between uplift rates and the number of preserved palaeoshorelines along the strike of the Messina Strait Fault; higher uplift rates allow*

7.4.2. The Reggio Calabria Fault

The same approach used for previous locations in this thesis is applied to the sequence of Late Quaternary palaeoshorelines outcropping on the hangingwall of the Reggio Calabria

Fault (Figure 7.3). A synchronous correlation approach has allowed the investigation of multiple mapped marine terraces and multiple sea-level highstands along the strike of the Reggio Calabria Fault. Then, spatial and temporal constraints on the geometry of the palaeoshorelines are used to estimate long-term uplift rates and their relationship with Reggio Calabria Fault displacement.

Table 7.5 shows all mapped palaeoshoreline elevations with refined ages; note that not all palaeoshorelines mapped in the DEMs were checked in the field because of thick vegetation and limited access on private houses.

Palaeoshoreline (Profile number)	DEM Elevations (m)	Expected Elevations (m)	Field Elevations (m)	Proposed Age (ka)	UTM Coordinate
0 (1)	34	40	30	50	33 S 0556796 - 4226515
1 (1)	97	94	-	76	33 S 0557360 - 4226749
2 (1)	115	120	112	100	33 S 0557599 - 4226872
3a (1)	150	157	150	119	33 S 0558440 - 4227121
3 (1)	174	173	174	125	33 S 0558999 - 4227289
7 (1)	270	263	-	240	33 S 0560866 - 4227076
9 (1)	312	312	-	310	33 S 0561574 - 4227195
10 (1)	362	366	-	340	33 S 0561738 - 4227283
11 (1)	420	419	-	410	33 S 0562119 - 4227661
0 (2)	25	23	-	50	33 S 0556979 - 4225258
1 (2)	71	70	-	76	33 S 0558322 - 4225768
2 (2)	99	91	-	100	33 S 0558985 - 4226063
3 (2)	135	138	-	125	33 S 0559098 - 4226092
1 (3)	51	56	-	76	33 S 0558085 - 4224704
2 (3)	78	75	82	100	33 S 0558289 - 4224793
3a (3)	104	106	110	119	33 S 0558522 - 4224917
3 (3)	123	119	110	125	33 S 0558807 - 4224969

1 (4)	57	51	-	76	33 S 0558189 - 4222423
2 (4)	72	69	-	100	33 S 0558376 - 4222319
3 (4)	113	113	-	125	33 S 0558465 - 4222285

Table 7.5: *Data collected for the Reggio Calabria Fault. All mapped inner edges from DEM and fieldwork with age assigned via synchronous correlation are shown. Note that not all the locations for inner edges mapped by DEM analysis with GPS in the field have been checked because the investigated area is in places thickly-vegetated and densely-populated with private properties.*

The data on palaeoshorelines in Table 7.5 underpin the plots in Figure 7.13 which shows 4 profiles across the hangingwall of the fault. Figure 7.14 shows a robust correlation between DEMs-based palaeoshoreline elevations and field-based palaeoshoreline elevations, with R^2 values >0.99, suggesting that: (i) elevations measured elsewhere in the DEM are likely to be reliable and (ii) mapping from previous geoscientists (Catalano *et al.*, 2003; De Guidi *et al.*, 2003) is accurate and strong but ages of un-dated marine terraces needed to be reviewed.

In the same way to previous chapters in this thesis, uplift rates were iterated and linear regression was used to assess the robustness of correlations between (a) the predicted elevations iteratively calculated given (i) an uplift rate value driven by new age controls and (ii) fixed values for sea-level relative to present-day sea-level for several highstands well-known by *Siddall et al.*, (2003) and *Rohling et al.*, 2014 (Table highstands, Chapter 2) and (b) those mapped in the DEMs (Figure 7.15). Initially, constant uplift rates through time were iterated, but correlations between measured and predicted palaeoshorelines elevations provided R^2 values that were relatively low. Thus, a range of temporally-varying uplift rates was attempted. The most successful attempts involved an uplift rate that increasedat ~50 ka. Values for the coefficient of determination close to 1 ($R^2 > 0.99$) were obtained, confirming that the uplift rate has been changing through time (Figure 7.15).

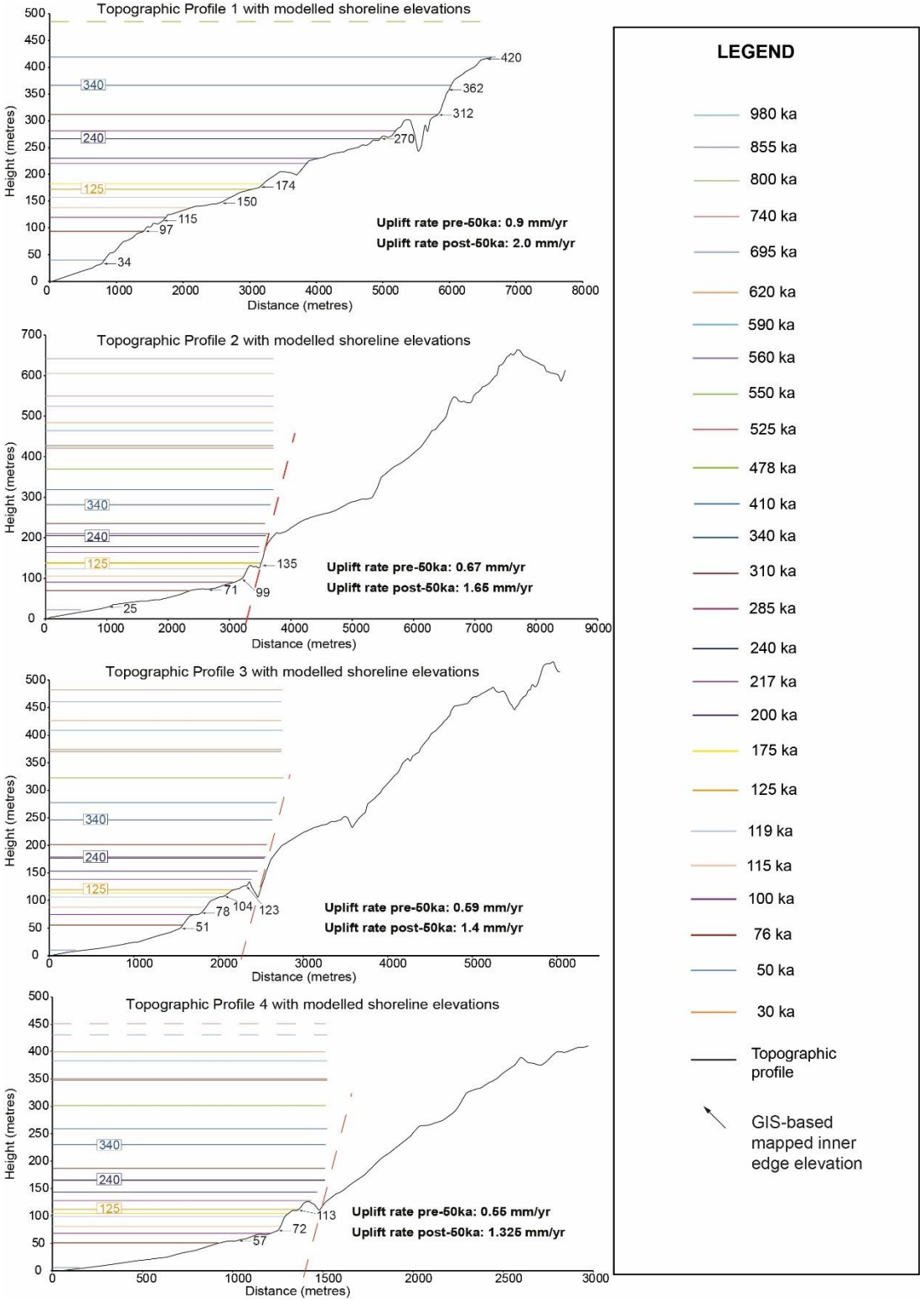

Figure 7.13: *Profiles showing mapped and modelled palaeoshoreline elevations along the strike of the Reggio Calabria Fault. The topographic profiles are from a 10 m DEM. The numbers with arrows mark the elevations of palaeoshorelines mapped in the field and DEMs. The coloured lines indicate palaeoshoreline elevations predicted by an uplift rate that has been changed iteratively to produce the best match with the mapped palaeoshorelines; goodness of fit is indicated by the value for slope and the R^2 values in Figure 7.15. Profiles are located on Figure 7.3.*

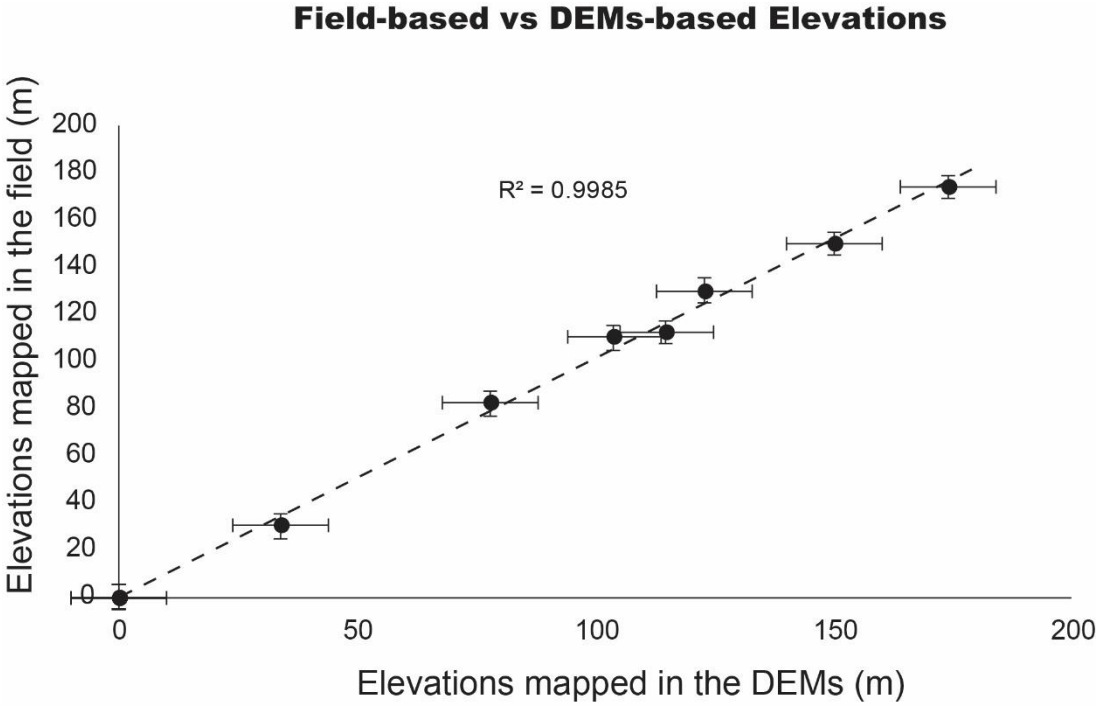

Figure 7.14: *Graph showing the relationship between field-based and DEM-based inner edge elevations. The R^2 value > 0.99 confirms a very robust relationship suggesting that elevations measured elsewhere in the DEM are likely to be robust.*

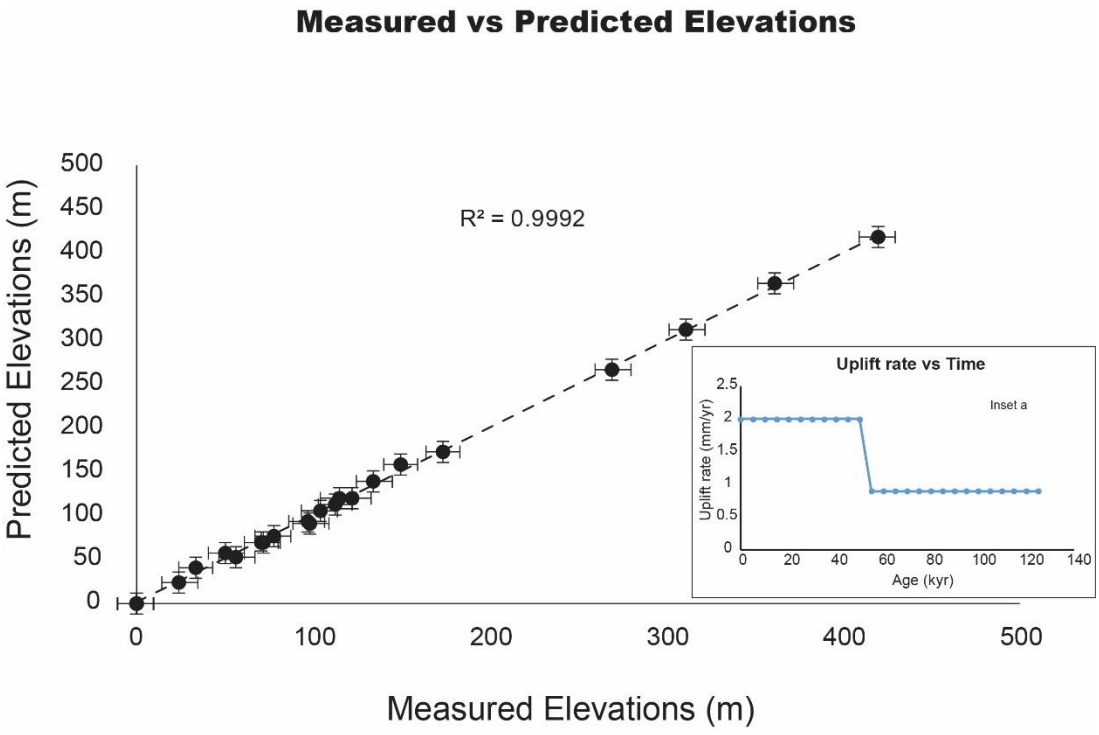

Figure 7.15: *Graph showing linear regression analysis between measured and predicted elevations. The predicted elevations, representing the synchronously-calculated sea-level highstand elevations, have been derived by defining a fluctuating uplift rate through time, and iterating this value to find the best match to the measured and mapped palaeoshorelines. Note that "measured" elevations represent palaeoshoreline elevations mapped in the 10-m high resolution DEMs. Coefficient of determination, R^2 value, has been used between these two datasets to quantify the best fit for all 4 topographic profiles with a value > 0.99. Inset "a" shows the uplift rate versus time measured along Profile 1.*

Figure 7.16 shows a variation in palaeoshoreline elevations along the strike of the Reggio Calabria Fault, suggesting that this fault is active.

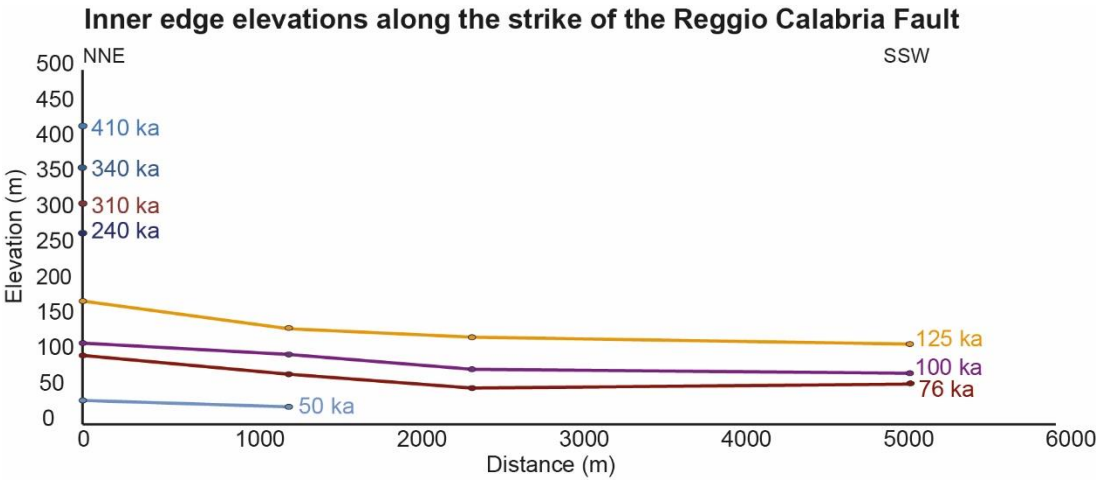

Figure 7.16: *Palaeoshoreline elevations vary along the strike of the Reggio Calabria Fault. Solid lines represent mapped and measured palaeoshoreline elevations mapped by using DEMs and checked in the field across topographic Profiles 1-4 shown in Figure 7.3.*

Moreover, Figure 7.17 shows results revealing spatially-changing uplift rates along the strike of the Reggio Calabria Fault on its hangingwall. This is clear evidence that this fault is active with vertical motions related to the fault decreasing along strike. The mapped uplift is presumably the result of a combination between the local fault-controlled tectonic subsidence and the "regional" uplift signal. Before ~50 ka, values of uplift rates are 0.9 mm/yr beyond the NNE tip zone and 0.55 mm/yr in the centre of the hangingwall of the fault. After ~50 ka, there is a clear acceleration in uplift rate on the hangingwall of the fault with values of 2 mm/yr beyond the tip zone and 1.325 mm/yr in the centre of the fault (Figure 7.17). At the centre of the fault the uplift accelerates by a factor of ~2.4 at ~50 ka. It is also clear that tilt angles for palaeoshorelines along the strike of the fault are greater for progressively older palaeoshorelines (Figure 7.18). However, note that the progressive increases show the effect of the uplift-rate change at 50 ka. The tilt angle values thus confirm progressive deformation associated with the Reggio Calabria fault through the Late Quaternary, but with the signature of the uplift-rate change superimposed on the general increase in tilt angle with age.

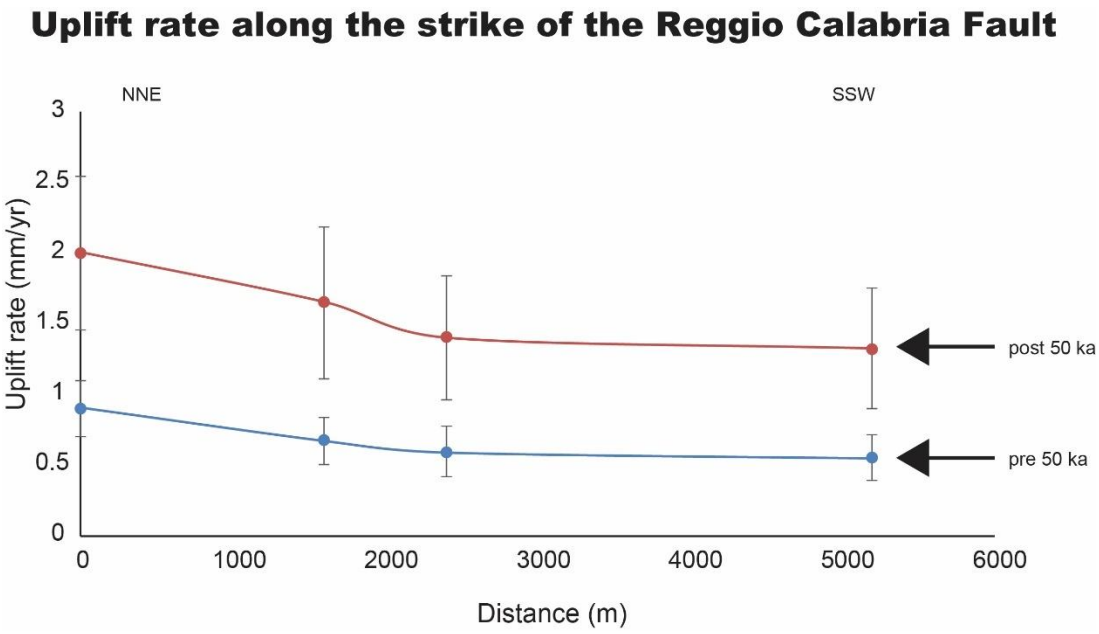

Figure 7.17: *Profile showing that uplift rates are spatially varying along the strike of the Reggio Calabria Fault before and after 50 ka.*

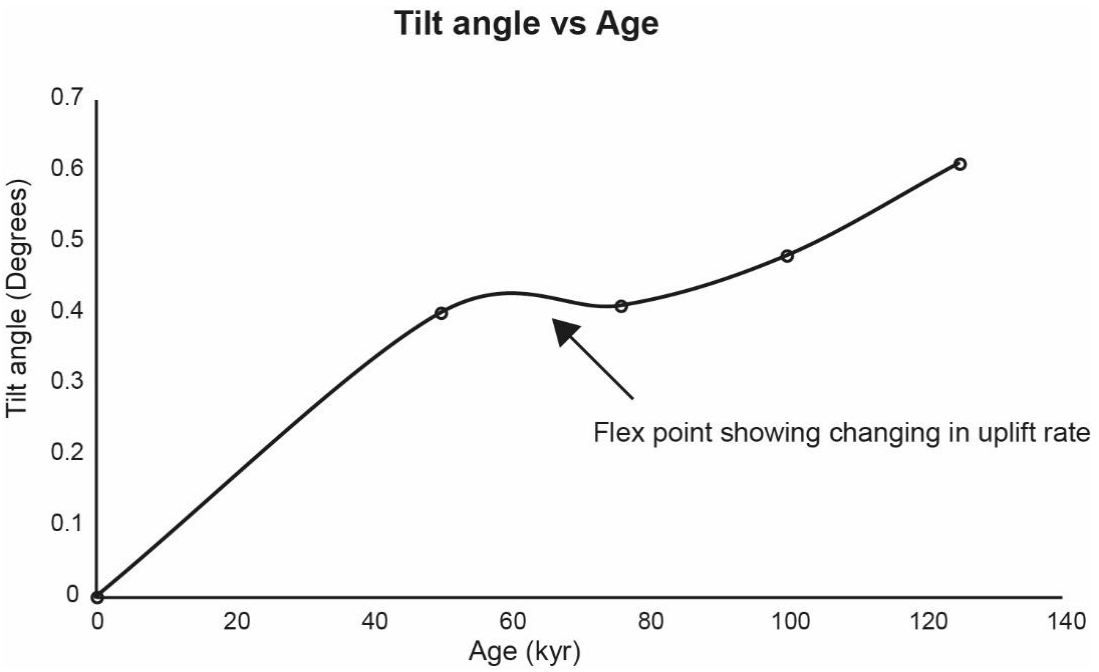

Figure 7.18: *The faulting activity of the Reggio Calabria Fault over the Late Quaternary has tilted the investigated marine terraces; in fact, older and higher palaeoshorelines show higher tilt angle values because they have been experiencing a longer history of faulting activity. Note that a flex point is shown, suggesting a changing uplift rate through time.*

It is important to consider that the acceleration in uplift at ~50 ka for the centre of fault reflects the interplay between fault-related vertical motions and vertical motions that are presumably more "regional" in nature. Herein, it is suggested that if regional uplift stayed constant through time, then it is implied that the hangingwall subsidence on the Reggio Calabria fault decelerated at ~50 ka; in other words, the fault slip rate decreased at ~50 ka. It is interesting to note that (a) Section 7.4.1 shows that the fault slip rate on Messina Strait Fault accelerated at ~50 ka, and (b) the uplift in the footwall of the Messina Strait fault increased by a factor ~2.4 at that time. The Messina Strait Fault and the Reggio Calabria Fault are located across strike from each other and are closely-spaced, with the distance being probably less than 10 km at depth (Figure 7.1). The close proximity, and coincidence in the magnitude and timing of the slip–rate changes on these two faults suggests they may be interacting. This is discussed later in Section 7.5.

Furthermore, the slip-rate on the Reggio Calabria Fault can be constrained due to the mapped offset of a marine terrace associated with what U/Th ages suggest may be the 125 ka palaeoshoreline. In particular, within the youngest and topographically-lowest terrace related to the 125 ka highstand outcropping on its footwall, a marine conglomerate deposit, indicating shallow marine deposit environment, has been mapped at ~ 190 m (Figure 7.19). U/Th dates were achieved for death assemblage of detrital corals contained within a boulder of cemented shallow marine sands in this conglomerate of 448 ± 17 ka, 384 ± 11.5 ka and 480 ± 25 ka (see Table 3.1 and Table 7.1). These ages suggest a maximum age of formation of this boulder of 384 ± 11.5 ka (implying the 448 ±17 ka and 480 ±25 ka corals are detrital ages for corals inherited from a previous highstand at 384 ±11.5 ka). However, the boulder itself is detrital, and its age could be older than the terrace deposits within which it is found. Thus, 384 ±11.5 ka is the maximum age of the marine terrace deposit containing the boulder, with the actual

age possibly younger. It is suggested its age is 125 ka because a very similar layer of marine conglomerate caps marine terrace related to the 125 ka highstand (Balescu *et al.*, 1997; Catalano *et al.*, 2003), which has been mapped on the hangingwall of the same fault at ~ 110 m. If the terraces are one and the same, this implies a vertical offset across the fault of 80 m over 125 ka (Figure 7.19). This implies a long-term fault throw-rate averaged over 125 kyrs of 0.64 ± 0.04 mm/yr, in agreement with previous studies (Monaco and Tortorici, 2000). However, the interpreted decrease in slip-rate at ~50 ka described above means that the 125 kyrs average throw-rate cannot be used over shorter time intervals. If the slip-rate decreased by a factor ~2.4 at ~50 ka, then ~75 kyrs of the 125 kyrs involved a slip-rate that was ~2.4 times faster than that which applies over the following ~50 kyrs. This implies that the throw-rate was 0.83 mm/yr from 125 ka to 50 ka and 0.35 mm/yr from 50 ka to the present day.

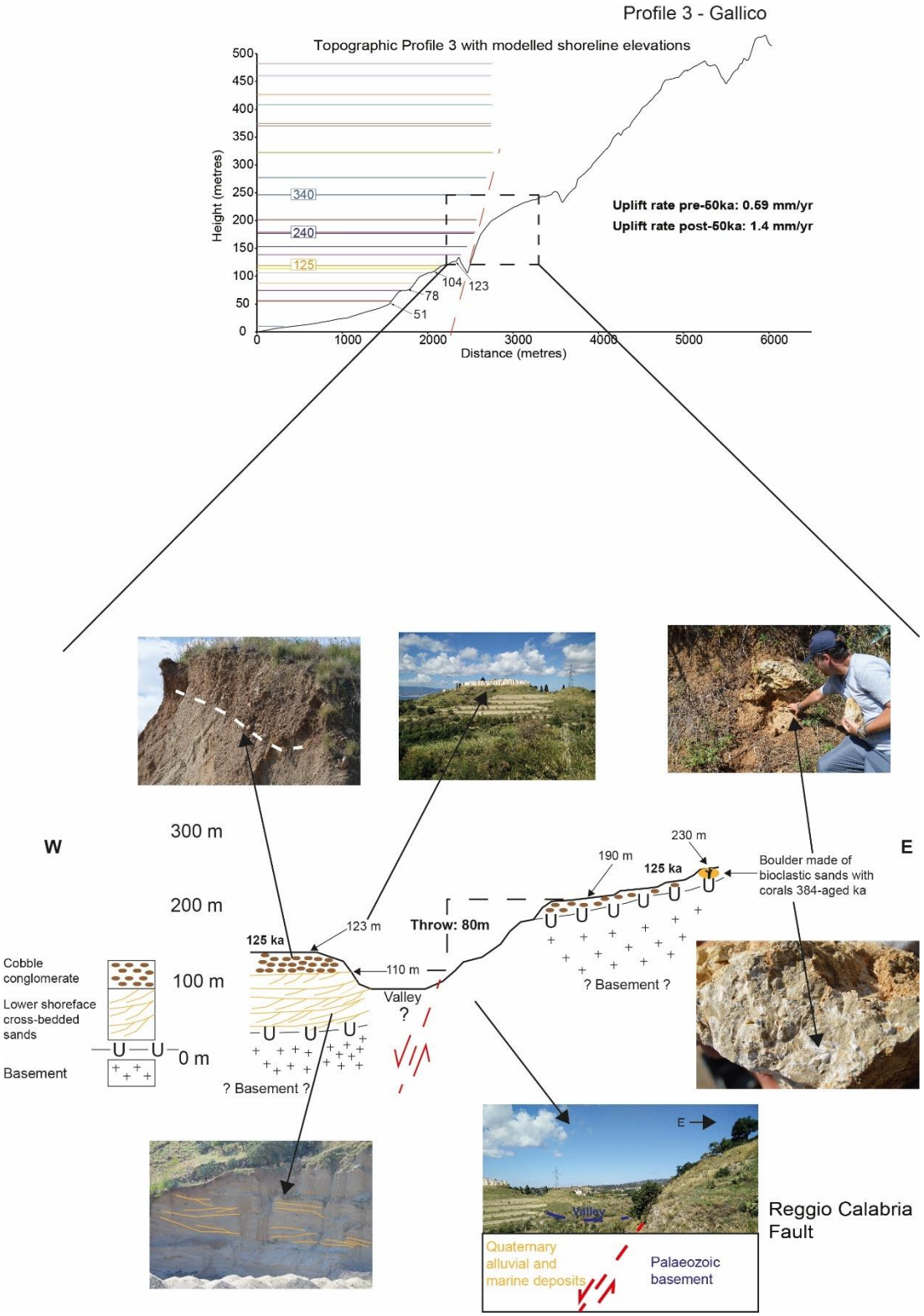

Figure 7.19: *Cartoon sketch showing the Reggio Calabria Fault offsetting terraced shallow marine deposits over 125 ka. On the footwall terrace a boulder made of cemented bioclastic sands containing corals with ages given in Table 3.1 (Samples 15,16 and 17) and Table 7.1, and the significance of the ages described in the text.*

In summary, changes in uplift rates along the strike of the Reggio Calabria Fault have controlled the geometry of the uplifted Late Quaternary palaeoshorelines outcropping on its

hangingwall. In particular, palaeoshoreline elevations are higher beyond the NNE tip zone and lower in the centre of the fault (Figure 7.17). Moreover, values for tilt angle show that higher and older palaeoshorelines have higher tilt angle value, implying progressive deformation since ~1 Ma (Figure 7.18). The slip-rate on the fault is constrained by the offset of a marine terrace associated with the 125 ka palaeoshoreline. The offset of 80 m in 125 kyrs implies a rate of vertical offset (throw-rate) of 0.64 mm/yr, but this value does not apply over shorter time intervals. Given the slip-rate change at ~50 ka and the 80 m offset over 125 kyrs, the throw-rate was 0.83 mm/yr from 125 ka to 50 ka and 0.35 mm/yr from 50 ka to the present day. All these lines of evidence suggest that the Reggio Calabria Fault is active and is controlling the geomorphology of the southern Calabrian coastline.

7.4.3. The Armo Fault

A sequence of uplifted palaeshorelines outcropping on the hangingwall of the Armo Fault has been investigated by applying a synchronous correlation approach to investigate if this fault is active over the Late Quaternary, as previously carried out with other locations in this thesis. As for other investigated locations in this thesis, spatial and temporal constraints on the geometries of the uplifted palaeoshorelines are applied to derive knowledge on the long-term fault displacement.

Table 7.6 shows all measured palaeoshoreline elevations mapped on a DEM and checked in the field; it also shows refined ages for previously un-dated palaeoshorelines, suggesting new scenario for the long-term uplift.

Palaeoshoreline (Profile number)	DEM Elevations (m)	Expected Elevations (m)	Field Elevations (m)	Proposed Age (ka)	UTM Coordinate

0 (1)	54	50	50	50	33 S 0556638 - 4207631
1 (1)	100	103	-	76	33 S 0556962 - 4207191
3a (1)	163	164	157	119	33 S 0557383 - 4206748
3 (1)	180	179	175	125	33 S 0557433 - 4206708
0 (2)	28	35	-	50	33 S 0557753 - 4208702
1 (2)	78	85	-	76	33 S 0557920 - 4208377
2 (2)	110	108	-	100	33 S 0558053 - 4208283
3 (2)	158	156	-	125	33 S 0558202 – 4208194
0 (3)	29	25	-	50	33 S 0557767 - 4211086
1 (3)	81	72	-	76	33 S 0558360 - 4211362
2 (3)	97	93	-	100	33 S 0558550 - 4211458
3 (3)	140	139	-	125	33 S 0559175 - 4211417
5 (3)	176	178	-	200	33 S 0559873 - 4211187
7 (3)	200	204	205	240	33 S 0560244 - 4211110
9 (3)	225	232	230	310	33 S 0560512 - 4211073
10 (3)	274	279	270	340	33 S 0560926 - 4210934
11 (3)	320	314	-	410	33 S 0561086 - 4210765
12 (3)	355	363	350	478	33 S 0561431 - 4210585
1 (4)	61	65	-	76	33 S 0558388 - 4212677
2 (4)	89	84	-	100	33 S 0558788 - 4212503
3 (4)	132	129	135	125	33 S 0559457 - 4212227
5 (4)	156	164	156	200	33 S 0559740 - 4212193
7 (4)	172	188	180	240	33 S 0559960 - 4212168
10 (4)	255	258	259	340	33 S 0560536 - 4212257
11 (4)	284	290	290	410	33 S 0560981 - 4212355
12 (4)	345	336	-	478	33 S 0561742 - 4212200
1 (5)	54	57	-	76	33 S 0558088 - 4214726
2 (5)	81	76	-	100	33 S 0558514 - 4215190

3a (5)	107	106	-	119	33 S 0558611 - 4215468
3 (5)	125	120	126	125	33 S 0558794 - 4215520
7 (5)	165	174	168	240	33 S 0559028 - 4215626
10 (5)	245	240	250	340	33 S 0559867 - 4215297
11 (5)	272	269	-	410	33 S 0560304 - 4215184
12 (5)	306	312	320	478	33 S 0561116 - 4215169

Table 7.6: *Data collected for the Armo Fault. All mapped inner edges from DEM and fieldwork with age assigned via synchronous correlation are shown. Note that not all the locations for inner edges mapped by DEM analysis with GPS in the field have been checked because the investigated area is in places thickly-vegetated and densely-populated with private properties.*

Figure 7.20 shows GIS-based geomorphological analysis through 5 topographic profiles, spanning ~ 15 km along the strike of the Armo Fault with marine terraces mapped on its hangingwall (Figure 7.1 and 7.4), showing gently seaward-dipping terraced surfaces which have been interpreted as palaeshoreface surfaces cut by wave-action. In places, marine, shallow water, palaeo-beach deposits have been deposited on these terraced surfaces, as described by previous studies (Bianca *et al.*, 1999; Catalano *et al.*, 2003; De Guidi *et al.*, 2003; Giunta *et al.*, 2012; Roberts *et al.*, 2013; Gallen *et al.*, 2014). Up dip of these deposits and wave-cut platforms are breaks of slope interpreted as palaeo-sea cliffs, the bases of which are interpreted, herein as palaeoshorelines.

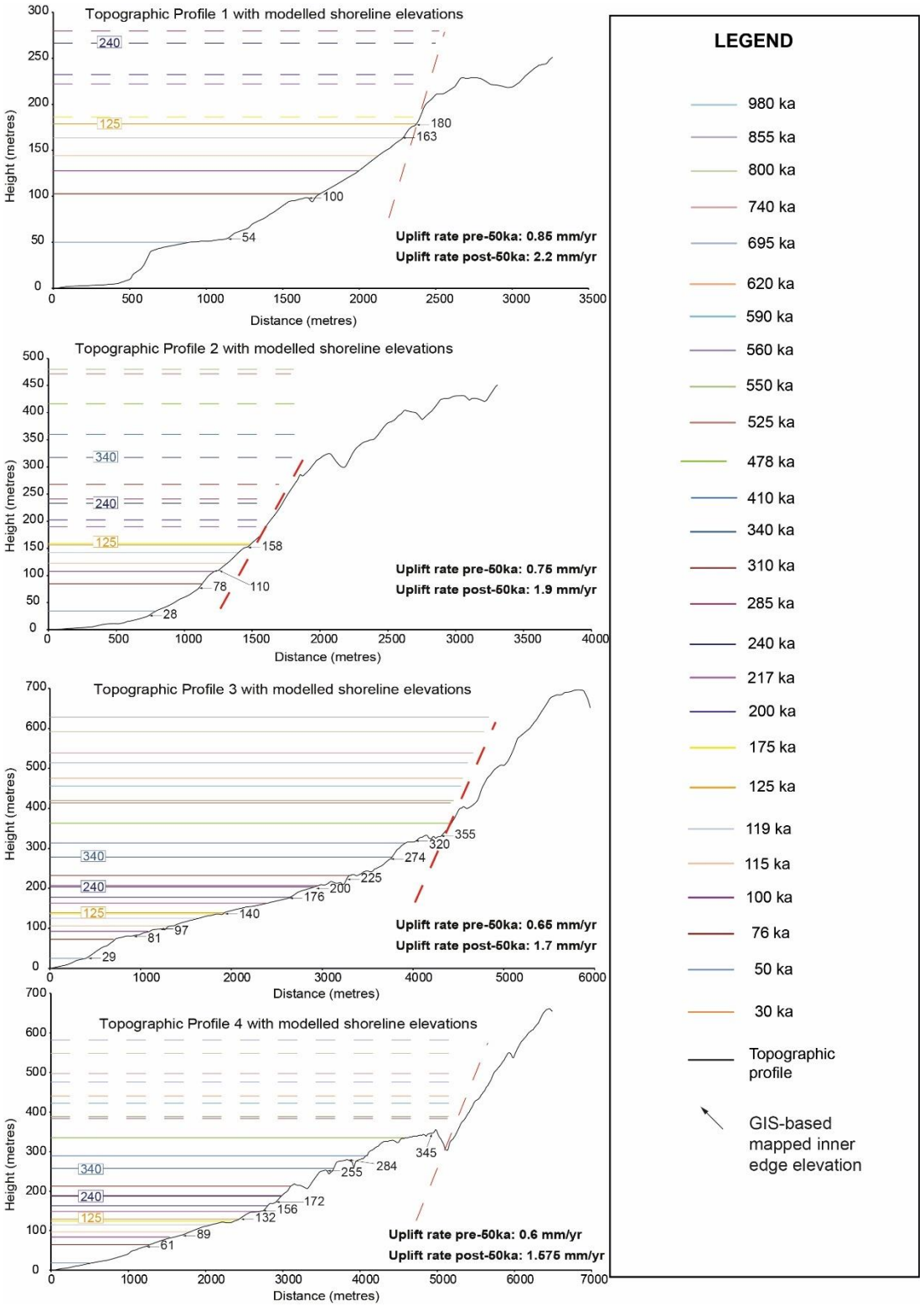
Topographic Profile 1 with modelled shoreline elevations
Height (metres)
Distance (metres)
240
125
180
163
100
54
Uplift rate pre-50ka: 0.85 mm/yr
Uplift rate post-50ka: 2.2 mm/yr
Topographic Profile 2 with modelled shoreline elevations
340
240
125
158
78
110
28
Uplift rate pre-50ka: 0.75 mm/yr
Uplift rate post-50ka: 1.9 mm/yr
Topographic Profile 3 with modelled shoreline elevations
355
320
340
274
240
225
200
176
125
140
97
81
29
Uplift rate pre-50ka: 0.65 mm/yr
Uplift rate post-50ka: 1.7 mm/yr
Topographic Profile 4 with modelled shoreline elevations
345
340
284
255
240
172
156
132
125
89
61
Uplift rate pre-50ka: 0.6 mm/yr
Uplift rate post-50ka: 1.675 mm/yr
LEGEND
980 ka
855 ka
800 ka
740 ka
695 ka
620 ka
590 ka
560 ka
550 ka
525 ka
478 ka
410 ka
340 ka
310 ka
285 ka
240 ka
217 ka
200 ka
175 ka
125 ka
119 ka
115 ka
100 ka
76 ka
50 ka
30 ka
Topographic profile
GIS-based mapped inner edge elevation

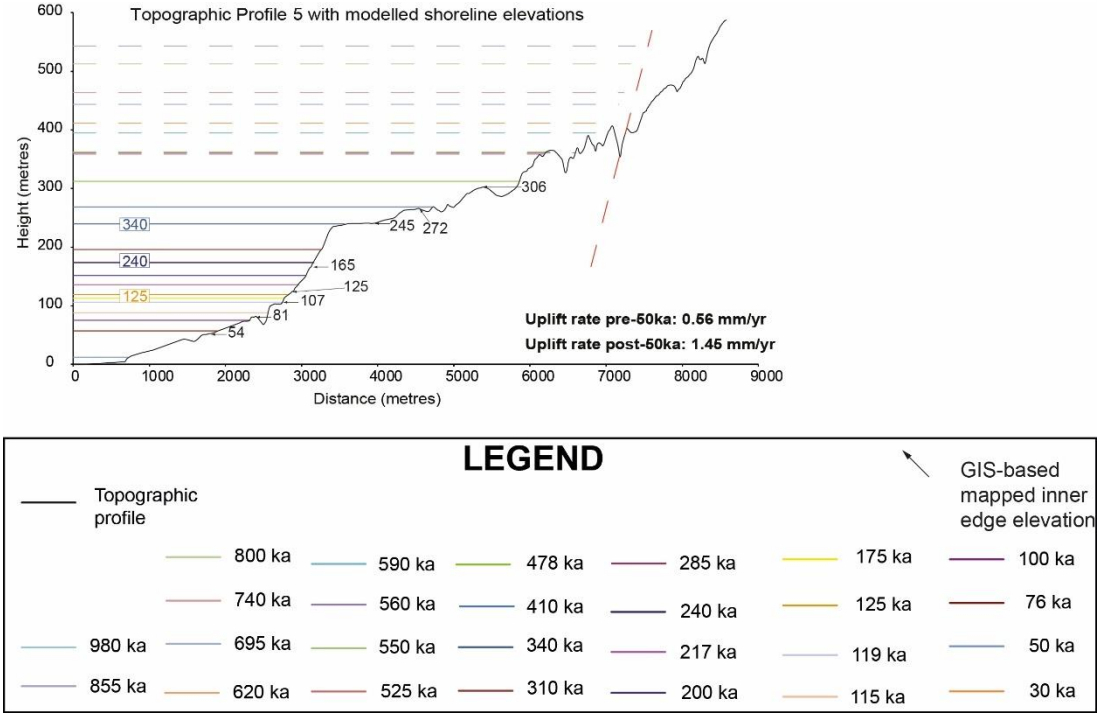

Figure 7.20: *Profiles showing mapped and modelled palaeoshoreline elevations along the strike of the Armo Fault. The topographic profile is from a 10 m DEM. The numbers with arrows mark the elevations of palaeoshorelines mapped in the field and on DEMs. The coloured lines indicate palaeoshoreline elevations predicted by an uplift rate that has been changed iteratively to produce the best match with the mapped palaeoshorelines; goodness of fit is indicated by the value for slope and the R^2 values in Figure 7.22. Profiles are located on Figure 7.1 and 7.4.*

To ensure that elevations measured on the DEM were robust, a linear regression analysis was performed which reveals that a robust correlation exists between palaeoshoreline elevations mapped in the field and those mapped on the DEM, suggesting that the detailed topographic analysis undertaken by using a high 10 m resolution is likely to be robust (R^2>0.99) (Figure 7.21). Following application of the synchronous correlation approach to assign ages to mapped palaeoshorelines, linear regression analysis was used to evaluate the robustness between the measured palaeoshoreline elevations and the predicted sea-level highstand elevations iteratively-calculated by applying a synchronous correlation approach driven by well-accepted age controls available in the literature (Figure 7.22) (Monaco and Tortorici, 2000; Aloisi *et al.*, 2013). After having tested the simplest hypothesis of a constant uplift rate through time, where low values of coefficient of determination are found a changing

uplift rate through time was investigated. After iteration, the best fit between measured and predicted palaeoshoreline elevations was achieved with a change in uplift rate at ~50 ka, producing an R^2 close to 1 (>0.99)

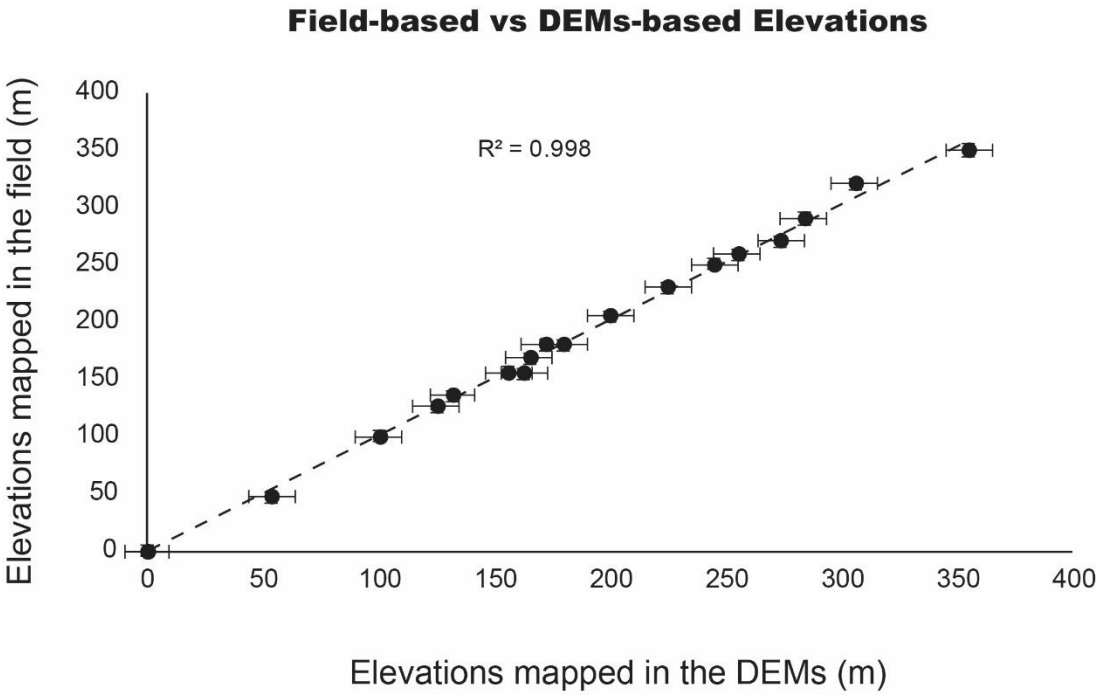

Figure 7.21: *Graph showing the relationship between field-based and DEM-based inner edge elevations. The R^2 value > 0.99 confirms a very robust relationship suggesting that elevations measured elsewhere in the DEM are likely to be accurate.*

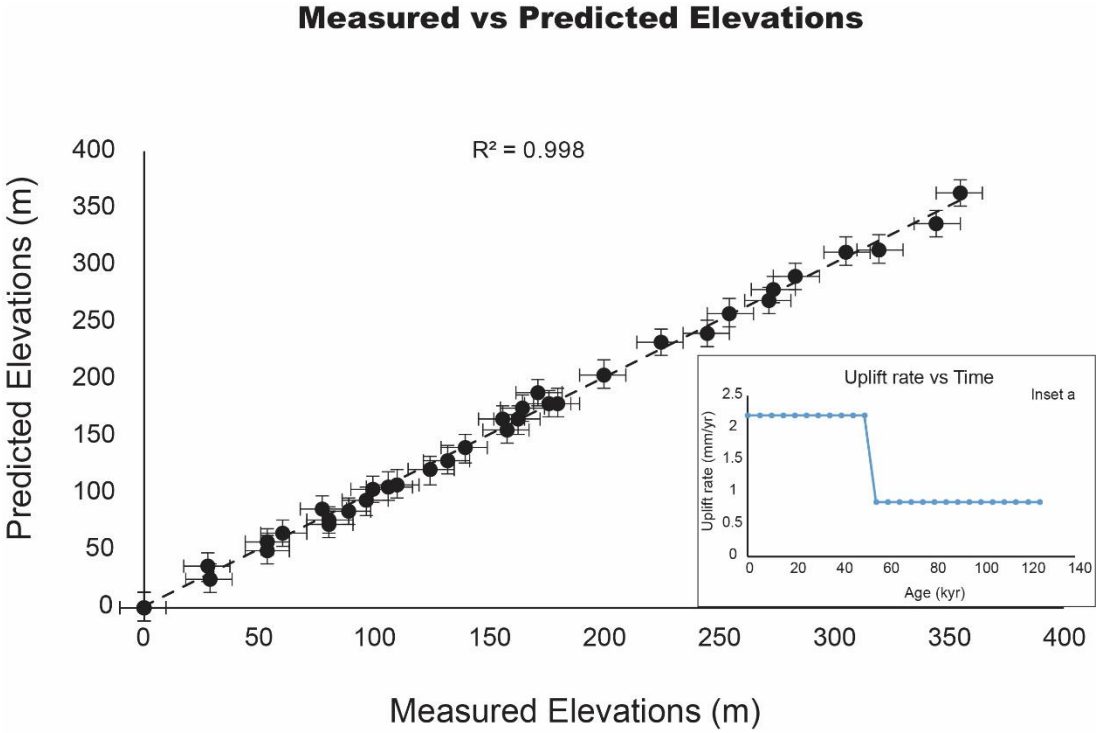

Figure 7.22: *Graph showing linear regression analysis between measured and predicted elevations. The predicted elevations, representing the synchronously-calculated sea-level highstand elevations, have been derived by defining a*

fluctuating uplift rate through time, and iterating this value to find the best match to the measured and mapped palaeoshorelines. Note that "measured" elevations represent palaeoshoreline elevations mapped in the 10-m high resolution DEMs. Coefficient of determination, R^2 value, has been used between these two datasets to quantify the best fit for all 4 topographic profiles with a value > 0.99. Inset "a" shows the changing uplift rate through time measured along the Profile 1.

Combining the results for the individual profiles by correlating along the fault strike, the spatial variation in uplift rates can be determined. Mapped elevations of palaeoshorelines are higher close to the onshore southern tip and lower in the centre of the fault (Figure 7.23).

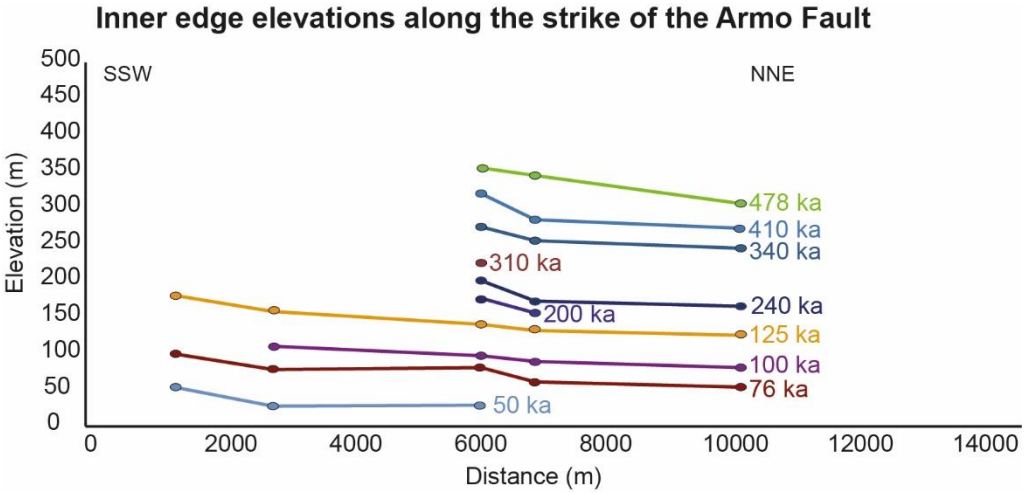

Figure 7.23: *Palaeoshoreline elevations along the strike of the Armo Fault. Solid lines represent mapped and measured palaeoshoreline elevations mapped by using DEMs and checked in the field across Topographic Profiles 1-4 shown in Figure 7.1 and 7.4.*

In terms of actual values of uplift rate, values for prior to ~50 ka vary along the fault from between 0.85 mm/yr close to the onshore southern tip and 0.56 mm/yr in the centre of the fault. Uplift rate values after ~50 ka are between 2.2 mm/yr close to the onshore southern tip and 1.45 mm/yr in the centre of the fault (Figure 7.24). This implies an acceleration in uplift rate by a factor of ~ 2.5, which is a similar value to that obtained for the Messina Strait Fault and for the Reggio Calabria Fault. As for these faults, this change in uplift rate involves a change in the relationship between uplift of a "regional" nature, and local fault-related vertical motions. Assuming that the "regional" rate is constant through time, it is implied that the fault there has been a deceleration in the related long-term fault slip rate.

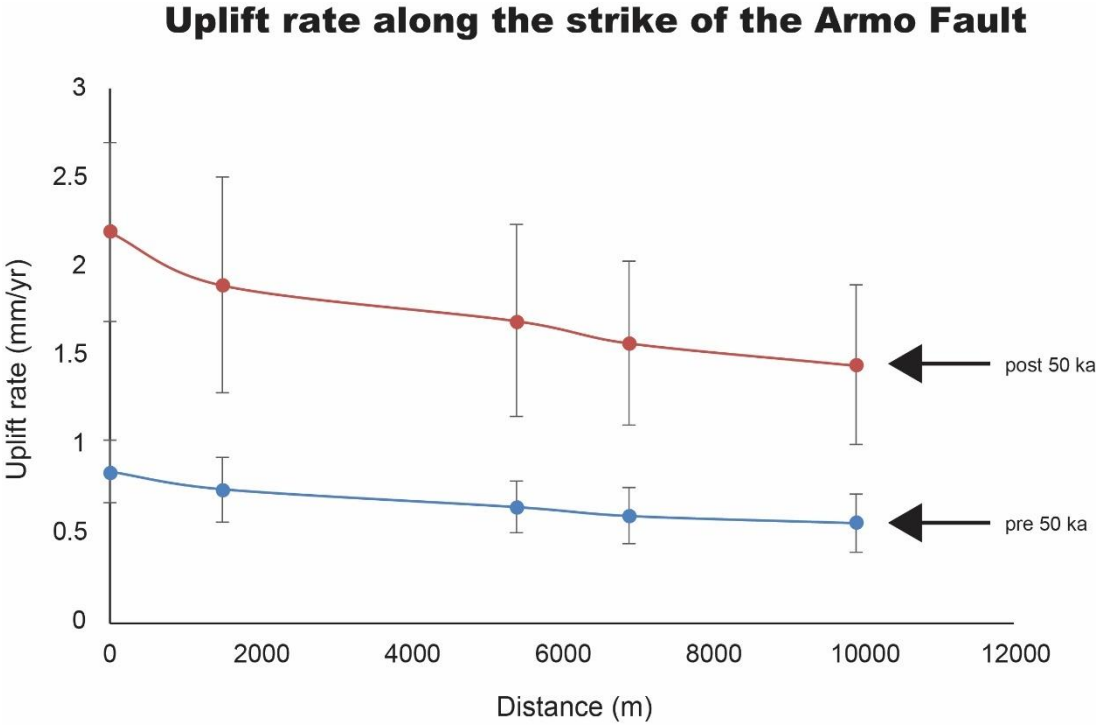

Figure 7.24: *Profile showing that uplift rates are spatially varying along the strike of the Armo Fault, but with higher rates after 50 ka.*

Figure 7.25 shows tilt angle values have been calculated showing that higher and older palaeoshorelines present a higher tilt angle values, suggesting that they have experienced a longer faulting history (Figure 7.22). Note that the graph in Figure 7.25 shows a "point of flex" indicating a changing uplift rate over the Late Quaternary.

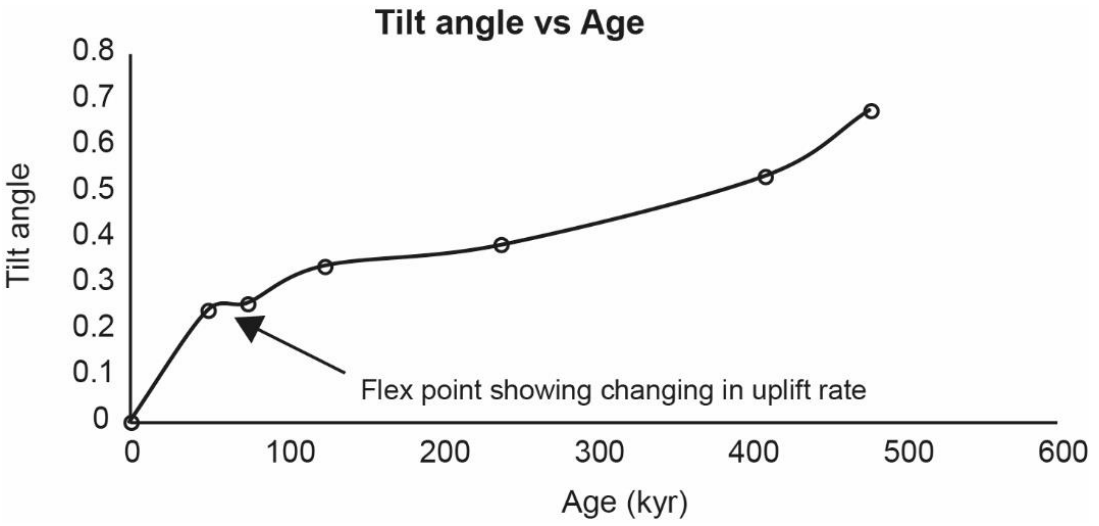

Figure 7.25: *The faulting activity of the Armo Fault over the Late Quaternary has tilted the investigated palaeoshorelines; older and higher palaeoshorelines show higher tilt angle values because they have been experiencing a longer history of faulting activity. Note that a flex point is shown, suggesting a change in uplift rate through time.*

Furthermore, the throw-rate on the Armo Fault can be constrained due to the mapped offset of a marine terrace associated to the 478 ka sea level highstand, a refined age derived by applying a synchronous correlation approach along the Profile 3. In particular, Figure 7.26 shows a tectonic sketch where the topographically-highest and oldest terrace mapped on the hangingwall of the Armo Fault at 355 m is 478 ka-aged. This terrace, as well as all the lower terraces mapped along the Profile 3 shown in in Figure 7.26, is cut into Plio-Pleistocene clastic marine sandy deposits. A flat terraced surface on the footwall cut-off of the Armo Fault is mapped at ~700 m cut into the Palaeozoic basement. If the footwall terrace is assumed to be coeval and with the same age of the hangingwall terrace mapped at 355 m with a synchronouscly-derived age of 478 ka, this implies a vertical displacement of 345 m and a throw-rate of 0.72 ± 0.12 mm/yr averaged over 478 kyrs in agreement with other geoscientists that have studied this fault (Roda-Boluda and Whittaker, 2017). However, the interpreted decrease in slip-rate at ~50 ka described in this section suggests that the 478 kyrs average throw-rate cannot be used over shorter temporal windows. Indeed, if the slip-rate decrease by a factor ~ 2.5 at ~50 ka, then ~428 kyrs of the 478 kyrs implied a slip-rate that was ~ 2.5 times faster than that which applies over the following ~50 kyrs. Consequently, this implies that from 478 ka to 50 ka the throw-rate was 0.77 mm/yr and from 50 ka to present day 0.31 mm/yr for 345 m of offset (see Appendix 7.4 for Throw-rate calculator).

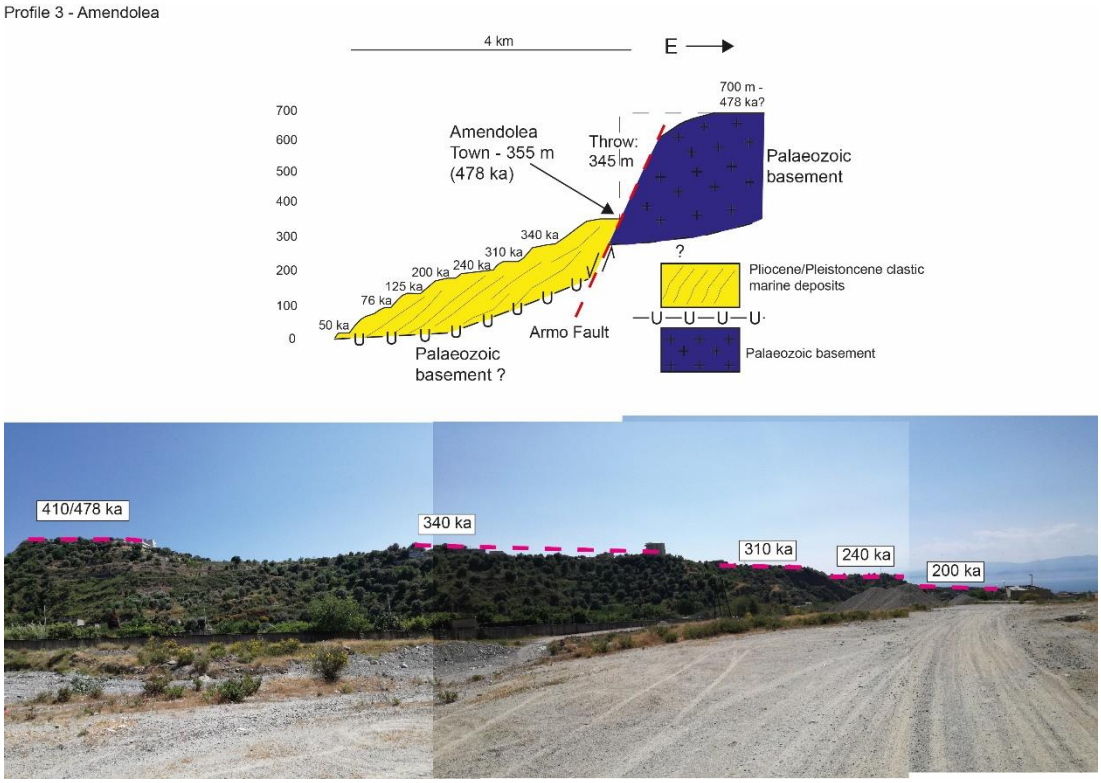

Figure 7.26: *Photograph showing mapped uplifted palaeoshorelines on the hangingwall of the Armo Fault cut into Plio-Pleistocene marine deposits. It is also shown the Armo Fault offsetting the sycnrhonously-derived 478-aged marine terrace, suggesting faulting activity over the Late Quaternary. Bottom photo shows some of the palaeoshorelines mapped on the hangingwall of the Armo Fault along the Profile 3 "Amendolea". Profile location is shown in Figure 7.4.*

7.5 Discussion

Results obtained from an investigation of sequences of uplifted Late Quaternary palaeoshorelines outcropping along the coastlines of the Messina Strait, synchronously-correlated to the iteratively-calculated sea-level highstands, suggest a revised chronology of palaeoshorelines, and a changing uplift-rate through time. In particular, "acceleration" of uplift rates by a factor of ~2.4-2.5 at ~50 ka affecting the coastlines of the Messina Strait is mapped. Moreover, spatial variation in uplift is controlled by the lateral decrease in fault slip toward the tips of the investigated faults implying faulting activity over the Late Quaternary. This is no surprise given the fact that the Messina Strait has been affected by historical

earthquakes that produced widespread damage and a high death tolls (e.g. 1908 Messina earthquake).

In the Sicilian coastline, spatial variation in uplift rates have been mapped from Messina town to Taormina town (Figure 7.1 and Figure 7.10), implying that the offshore Messina Strait Fault is active. Furthermore, an acceleration in uplift rate at 50 ka has been mapped; because these values of uplift rate have been mapped on the footwall of the ~ 58 km long fault, this implies an acceleration of the fault slip-rate over the last 50 kyrs. Seismic profiles have shown long-term throw for the Messina Strait Fault close to the northern tip (offshore Messina town), where the mapped uplift rate is 0.5 mm/yr before 50 ka, of ~ 300 m over the last ~ 3 My, suggesting a long-term fault slip rate of 0.1 mm/yr (Doglioni *et al.*, 2012). However, similarly for the Reggio Calabria Fault and the Armo Fault, the interpreted increase in slip-rate at ~ 50 ka described in Section 7.4.1 suggests that the ~ 3 My average throw-rate cannot be used over shorter timescales. In fact, if the slip-rate increase by a factor of ~ 2.45 at ~ 50 ka, then ~ 2.95 My of the 3 My implied a slip-rate that was ~ 2.45 slower than that which applies over the following 50 kyrs. Therefore, this suggests that from 3 Ma to 50 ka the throw-rate was 0.1 mm/yr and from 50 ka to present is 0.24 mm/yr (see Appendix 7.4). However, as said above, this throw-rate of 0.24 mm/yr is measured near the tip of the fault. Assuming a constant fault displacement gradient along the strike of the Messina Strait Fault, an implied throw-rate of 0.38 mm/yr can be estimated in centre of the fault where an uplift rate of 0.8 mm/yr is mapped over the 50 kyrs. Acceleration showing a factor of ~ 2.45 is a value comparable to the one mapped in other part of the Mediterranean such as the Gulf of Corinth (Roberts *et al.*, 2009), in the last 178 kyrs. The throw-rate value of 0.38 mm/yr across the Messina Strait Fault is contributing to accommodate the crustal extension across the Messina

Strait given that GPS investigations indicate ~ 2.5 mm/yr extension (Serpelloni *et al.*, 2005). A throw-rate of 0.38 mm/yr is typical considering that values measured for the other faults in the Apennines and in the Calabrian Arc lie in the range 0.3 – 2.0 mm/yr (Jacques *et al.*, 2001; Galli and Bosi, 2002; Roberts *et al.*, 2004, 2013; Meschis *et al.*, 2018). Furthermore, in Chapter 8 will be shown that the 1908 Messina Earthquake seems to be produced by the Messina Strait Fault with a slip at depth of 5000 mm, with the 10% of this amount (500 mm) assumed at surface. If the assumed value of 500 mm of slip event at surface is correct, then to produce a throw-rate of 0.38 mm/yr given a maximum 500 mm slip events in M >7 earthquakes implies a T_{mean} of ~ 1315 years over the last 50 kyrs. This is no surprising because similar values have been estimated for active normal faults characterizing the Italian peninsula (Jacques *et al.*, 2001; Galli, Galadini and Pantosti, 2008; Roberts *et al.*, 2013; Meschis *et al.*, 2018). However, (i) for ~ 60-km long normal faults and (ii) potential associated earthquakes with M >7, higher maximum values of slip event at surface can be estimated such as 2000 mm (Wells and Coppersmith, 1994), suggesting longer T_{mean} (over 5000 yrs) for a given throw-rate of 0.38 mm/yr.

In the Calabrian coastline, spatial variation in uplift rates have been mapped in the hangingwalls of two faults, the Reggio Calabria Fault and the Armo Fault (Figure 7.1, Figure 7.17 and Figure 7.24), suggesting that these faults are active. Furthermore, an acceleration in uplift rates has been mapped at ~ 50 ka on their hangingwalls, suggesting a "deceleration" of their fault slip-rates. Fault slip rates of 0.35 mm/yr and 0.31 mm/yr over the last 50 ka respectively. These values of throw-rate suggest that the Reggio Calabria Fault and the Armo Fault are contributing with their faulting activity, along the Messina Strait Fault, to accommodate the ongoing extension occurring in the Messina Strait. Furthermore, for the

first time, values of T_{mean} have been estimated for these faults controlling the coastal geomorphology of the Messina Strait. Indeed, a value of 0.35 mm/yr of throw-rate for the Reggio Calabria Fault, 15 km long for its onshore segment, given a maximum 300 mm slip events in M 6 earthquakes (Wells and Coppersmith, 1994) implies a T_{mean} of ~ 850 years; if the length of the Reggio Calabria Fault is 25 km as claimed by some for its continuation offshore (Monaco and Tortorici, 2000), this suggests a maximum of 1000 mm slip events in M 6.5 earthquakes, implying a T_{mean} of ~ 2850 years. Similarly for the Armo Fault, where its onshore segment is 17 km long, a maximum of 400 mm slip events in M 6.3 earthquakes (Wells and Coppersmith, 1994) is estimated, implying a T_{mean} of ~ 1300 years. Again, these values are comparable to those mapped for the Italian peninsula (Jacques *et al.*, 2001; Galli, Galadini and Pantosti, 2008; Roberts *et al.*, 2013; Meschis *et al.*, 2018).

An open question that it requires more investigations is related to the fault interaction mapped in this Chapter where a synchronous change in fault throw-rates with an associated very similar factor of ~2.4-2.5 is mapped within the Messina Strait with the Messina Strait Fault accelerating its fault throw-rate and the Reggio Calabria Fault and the Armo Fault decelerating their throw-rate since 50 ka. For instance, more Coulomb Stress Change modelling is suggested to test if when the Messina Strait Fault slips, such as during the 1908 Messina Earthquake discussed in Chapter 8, it decreases the stress on the Reggio Calabria Fault and the Armo Fault across-strike, suggesting a new geography of the seismic hazard associated with the Messina Strait.

7.6 Conclusion

A new uplift rate scenario has been presented within the tectonically-extending Messina Strait, southern Italy, on the upper plate of the ISZ by refining ages of tectonically-deformed Late Quaternary marine terraces. Palaeoshorelines investigated on the Sicilian coast, lying on the footwall of the offshore Messina Strait Fault, show an along-strike deformed geometry implying faulting activity over the Late Quaternary. Similarly, long-term faulting activity is implied for the Reggio Calabria Fault and the Armo Fault by showing along-strike deformed geometries of palaeoshorelines. Changes of uplift rates along-strike the investigated faults confirm: (i) the hangingwalls tectonic subsidence, which is presumably counteracting the "regional" uplift signal possibly associated either with the Ionian subduction process (Malinverno and Ryan, 1986; Tortorici *et al.*, 2003) or with mantle upwelling (Gvirtzman and Nur, 1999b), and (ii) the footwall tectonic uplift.

Synchronous correlations, driven by new dated corals in agreement with well-accepted age controls available in the literature, between multiple, tectonically-deformed, Late Quaternary palaeoshorelines with global sea-level highstands, reinforced by detailed terraces mapping in the field and on 10 m high-resolution DEMs unravel that the Messina Strait Fault have been active over the Late Quaternary with a throw-rate value of 0.38 mm/yr after 50 ka. Similarly, the Reggio Calabria Fault and the Armo Fault show values of throw-rates of 0.35 mm/yr and 0.31 mm/yr respectively over the last 50 ka. Indeed, acceleration of uplift rates have been mapped on both coastlines of the Strait by factor of ~ 2.4-2.5 at 50 ka by applying a synchronous correlation approach. Because this acceleration has been mapped on the footwall of the Messina Strait Fault and on the hangingwalls of the Reggio Calabria Fault and the Armo Fault, it implies a synchronous-temporally change on throw-rates of these faults; indeed, acceleration on the throw-rate for the Messina Strait Fault and deceleration on throw-rates for

the Reggio Calabria Fault and the Armo Fault have been mapped. This also suggests that the investigated faults are partially accommodating the ongoing extension occurring in the Messina Strait with a rate of ~ 2.5 mm/yr (Serpelloni *et al.*, 2005), implying that activity on other active faults has to be claimed within the Strait.

This new scenario of temporally-changing fault throw-rates has critical tectonic implications and effect on the long-term seismic hazard approach for the Messina Strait region. This rises the necessity to gain more detailed tectonic data about mapping active faults and the related seismic hazard affecting the Messina Strait.

Chapter 8: The 1908 Mw 7.1 Messina Earthquake Italy revealed: 5m rupture of an offshore 70° east-dipping normal fault.

8.1. Abstract

Elastic half-space modelling has been used to reproduce levelling data from 1907 – 1909, and aspects of the geology and the geomorphology, in order to constrain the geometry and kinematics of the 28th December 1908 Messina Earthquake (Mw 7.1). This damaging earthquake caused > 80000 deaths and transformed earthquake science by activating the study of earthquake environmental effects worldwide, although its seismic source is still debated. Slip along a well-known offshore fault (The Messina Strait Fault) is revealed by modelling the levelling data, with a dip to the east of 70° and 5 m dip-slip at depth, with slip propagating to the surface on the seabed. Furthermore, the question of whether the 1908 Messina Earthquake could be considered as a "characteristic earthquake" is investigated. If the earthquake is characteristic, then repetition of the event would successfully reproduce the elevations of measured uplifted marine terraces described in Chapter 7. It is reported herein that repetition of the 1908 Messina earthquake cannot reproduce the long-term uplift, and this is discussed in terms of fault interaction.

In terms of the wider significance of this study, it is notable that ~110 years were needed to unveil the long-debated seismogenic source for this earthquake despite the fact that the coseismic uplift is shown to be typical of the other large normal faulting earthquakes. It is typical because the earthquake ruptured a known active fault, producing a clear geological and geomorphic expression, with uplift showing the typical asymmetric pattern of coseismic hangingwall subsidence and footwall uplift. Overall, it is suggested that geomorphological and

geological observations supporting maps of "capable faults" should not be ignored when attempting to identify the seismic sources of damaging major earthquakes. A manuscript has been prepared for submission to an international journal on this subject, but a publication decision is not available at the time of writing.

8.2. Introduction

The 28th December 1908 Mw 7.1 earthquake is the most destructive earthquake known for Europe. It occurred in the Messina Strait southern Italy, with >80000 deaths (Mercalli, 1909; Baratta, 1910), yet the geometry and kinematics of the seismogenic source is still debated after ~ 110 years. The 1908 Messina Earthquake was one of the first seismic event in the instrumental period, with seismograms available (but of low quality by modern standards, as discussed below), and it transformed the study of seismicity by triggering attention on earthquake environmental effects which we now know are critical for a better understanding of the geometry and kinematics of coseismic faulting (Comerci *et al.*, 2015). Based on the deformed Late Quaternary and Holocene geology and mapped environmental effects, the epicentre is known to have been located in the Messina Strait graben (Loperfido, 1909; Mercalli, 1909; Platania, 1909; Valensise and Pantosti, 1992; Monaco and Tortorici, 2000; Ferranti *et al.*, 2007; Doglioni *et al.*, 2012; Ridente *et al.*, 2014) (Figure 8.1). However, the lack of a clear surface rupture (Comerci *et al.*, 2015) and a robust focal mechanism (Amoruso, Crescentini and Scarpa, 2002; Aloisi *et al.*, 2014) has led to numerous suggestions for the seismogenic source (details are shown in Figure 2.17 in Chapter 2), including (a) a NNW-SSE fault crossing the coast of Sicily, (b) both high and low angle east dipping emergent or blind normal faults, and (c) a high-angle west-dipping fault outcropping in Calabria (Amoruso,

Crescentini and Scarpa, 2002; Valensise, Basili and Burrato, 2008; Aloisi *et al.*, 2013). Notably, the blind low-angle east dipping and perhaps high-angle west-dipping sources lack clear evidence from mapped geological offsets over the long-term, contrasting the high-angle east-dipping models that may well explain the uplift and deformation of the palaeoshorelines described in Chapter 7. Moreover, it has been claimed that the blind low-angle east-dipping fault is controlling the topography and the geology of the Messina Strait, by producing repeated 1908-characteristic Messina earthquake (Schwartz and Coppersmith, (1984) *sensu stricto*) through time (Valensise and Pantosti, 1992). However, the proposed blind low-angle east-dipping seismic source for the earthquake has not been mapped or imaged, and the long-term repetition of slip on this seismic source has not been modelled, suggesting a review is required of this hypothesis.

A key insight that has emerged since earlier studies is the existence of well-mapped onshore and offshore high-angle east-dipping faults such as the "Messina Strait Fault" (MSF) and the "Messina Fault" (MF) (Figure 8.1). These have been shown to produce kilometre-scale offsets of basement stratigraphy and control the location of sedimentary basins of the Messina Strait (Monaco *et al.*, 1996; Doglioni *et al.*, 2012). Given that normal faulting earthquakes typical rupture faults with clear geomorphic and geological expressions (Stein and Barrientos, 1985; Jacques *et al.*, 2001; Papanikolaou *et al.*, 2010), it would be surprising if the 1908 Messina Earthquake had behaved differently. A second key insight is that the coseismic vertical motions for 1908 earthquake, constrained by geodetic levelling data spanning 1907 – 1909, strongly resemble the asymmetric pattern of hangingwall subsidence and footwall uplift measured from more recent earthquakes where the dip direction of the ruptured fault is well-constrained by the existence of mapped surface ruptures and epicentral location (Figure 8.2).

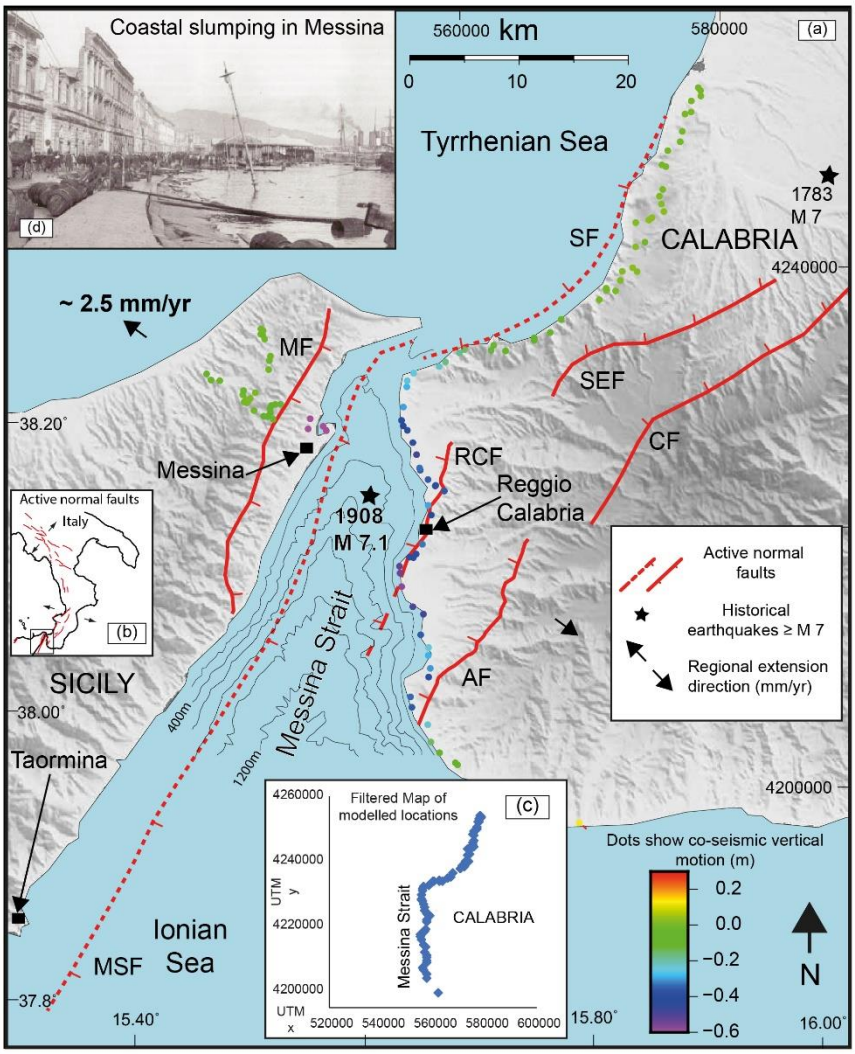

Figure 8.1: *Map showing a tectonic sketch of the Messina Strait with well-known Quaternary normal faults (Monaco and Tortorici, 2000; Doglioni et al., 2012). Coloured dots represent the coseismic vertical movement mapped by Loperfido, (1909). Messina Fault (MF); Messina Strait Fault (MSF); Armo Fault (AF); Reggio Calabria Fault (RCF); Sant'Eufemia Fault (SEF); Cittanova Fault (CF); Scilla Fault (SF). Panel (a) is located in (b). (c) Levelling data used in the modelling. (d) Port of Messina town affected by coastal slumping after the earthquake.*

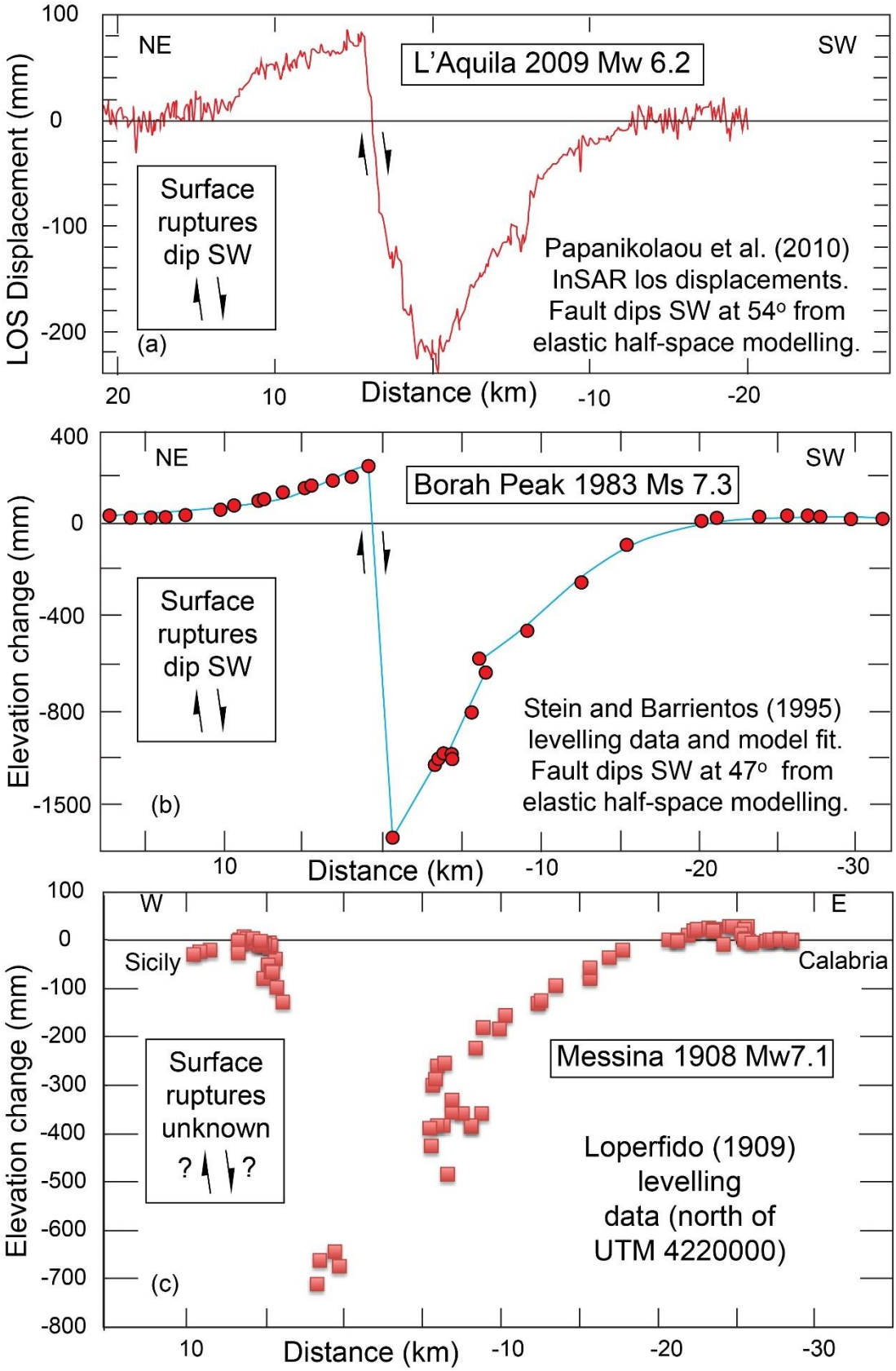

Figure 8.2: *Comparison of observed coseismic elevation changes for three normal faulting earthquakes, where the dip direction of the surface rupture is known for only two of the examples. (a) The 2009 L'Aquila Earthquake; (b) the 1983 Borah Peak Earthquake; (c) the 1908 Messina Earthquake.*

The resemblance is striking, suggesting that the ruptured fault dips to the right in Figure 8.2, that is, to the east; this chapter contains the results of iterative elastic half-space modelling that attempts to replicate the modelled uplift and hence recover the dip direction, the amount of dip of the ruptured fault, and the 1st-order pattern of the coseimsic slip disribution. Furthermore, in a previous chapter (Chapter 7), it has been shown that uplifted Late Quaternary palaeoshorelines have been tectonically-deformed by the seismic activity of the ~58 km long MSF, outcropping on its footwall, possibly due to repeated seismic events through time. Furthermore, an accelerated slip on fault of ~ 0.38 mm/yr has been derived for the last 50 ky. These features are used to investigate whether the slip distribution recovered from the elastic half-space modelling can replicate the long-term Quaternary footwall uplift, if repeated through time.

The aim of this chapter is the investigation of the following scientific questions:

- Did the 1908 Messina Earthquake rupture the Messina Strait Fault or are other models more appropriate?
- If so, has the Messina Strait Fault ruptured along-strike entirely?
- Can the 1908 Messina Earthquake be assumed as a "characteristic earthquake", occurring on the Messina Strait Fault, controlling the geology of the Messina Strait?

The above-stated scientific questions are investigated by attempting to constrain the location, slip and dip of the seismogenic source producing the earthquake using levelling measurements from 1907 – 1909 (Loperfido, 1909; Costanzi, 1910; De Stefani, 1910). These levelling data (Loperfido, 1909) have been already used to model faults embedded in elastic half-spaces in previous studies, either concluding that these data alone (i) cannot be used for producing slip distributions on presumed faults where no fault has been mapped (Amoruso, Crescentini and

Scarpa, 2002), or (ii) are "not capable of discriminating between the two oppositely dipping fault models" (Aloisi *et al.*, 2013).

In this chapter, new insight is shown from plotting the levelling data as a function of distance E-W (Figure 8.2). This reveals, even before modelling, a pattern of uplift and subsidence that strongly resembles that of other large normal faulting earthquakes whose source fault dip and dip direction are well known from mapped surface ruptures (Stein and Barrientos, 1985; Papanikolaou et al., 2010) (Figure 8.2). By applying a fault embedded in an elastic half-space, iterating the fault geometry, fault location, fault slip, and fault dip it has been attempted to reproduce the observed surface deformation, earthquake magnitude, geology and geomorphology, and the environmental effects (Figure 8.2).

8.3. Geological and seismological background

The Messina Strait separates Calabria from Sicily, and represents a fault-bounded graben area between inward-dipping Quaternary normal faults (Ghisetti and Vezzani, 1982; Monaco and Tortorici, 2000; Doglioni *et al.*, 2012; Ridente *et al.*, 2014). In general, thrust sheets of Palaeozoic igneous and metamorphic rock formations that were interposed during Alpine orogenic phase during and after the Oligocene-Miocene, are revealed by over-thrusts of gneiss and schists onto Oligocene-Miocene flysch sediments, which are in turn offset by the Quaternary normal faults (Ghisetti and Vezzani, 1982; Malinverno and Ryan, 1986; Roberts *et al.*, 2013). Capable normal faults onshore are well-mapped, and those offshore are constrained with seismic reflection and bathymetric data. Some studies suggest the existence of an offshore "Taormina Fault" that offsets the pre-Pleistocene basement, and propagated upwards to produce a fault-related syncline along part of its trace (herein named "The Messina

Strait Fault, MSF, after Doglioni et al. (2012)), (Stewart *et al.*, 1997; Monaco and Tortorici, 2000; De Guidi *et al.*, 2003; Ridente *et al.*, 2014; Pavano, Pazzaglia and Catalano, 2016). In contrast, other previous studies advocated less confidence concerning offshore fault locations (Argnani *et al.*, 2009). However, due to the ongoing NW-SE oriented extension across the Messina Strait implied by GPS investigations showing ~2.5 mm/yr (Serpelloni *et al.*, 2005), offshore Quaternary active normal faults appear likely because they are required to: (i) produce the spatially-variable uplift of mapped palaeoshorelines onshore and (ii) accommodate the above-mentioned crustal extension (Valensise and Pantosti, 1992; Catalano and De Guidi, 2003; Pavano, Pazzaglia and Catalano, 2016).

The 28th December 1908 Messina earthquake (Mw 7.1; 05:20.27 CET) affected the area, including the cities of Messina and Reggio Calabria, with devastating MCS intensities up to XI (Oddone, 1909; Rizzo, 1909; Comerci *et al.*, 2015). A tsunami inundated both sides of the Messina Strait with run-up reaching 13 m in places (Comerci *et al.*, 2015). Environmental effects have been investigated such as surface ruptures, coastal retreat, gas emission, liquefaction and landsliding process both on land and offshore; no clear surface ruptures were identified (Comerci *et al.*, 2015).

The main evidence of primary co-seismic effects is ground elevation changes in Calabria and Sicily (Figure 8.1 and 8.2c) due to the lack of clear evidence for surface rupture. It has been suggested that many levelling benchmarks were reached by the tsunami, raising concerns that some may have been disturbed (De Stefani, 1910). Indeed, synchronously to the earthquake, coastal slumping can have affected the coastline as shown in the port of Messina (Figure 8.1 inset d; see also Aloisi *et al.*, 2014 for further details). Furthermore, landsliding processes and slumping are well-documented in historical times, affecting the mountains

along the Sicilian coastline (Goswami, Mitchell and Brocklehurst, 2011; ISPRA, 2016) (Figure 8.1). However, overall, referring to the 1907 – 1909 levelling data, it has been shown that there is "good coherence amongst the data" (Comerci *et al.*, 2015), a conclusion that is supported by the systematic changes in uplift/subsidence with distance shown in Figure 8.2c. This consistency has been interpreted as a primary signal of the co-seismic motions produced by the 1908 Messina Earthquake. This thesis presents new elastic half-space modelling, utilising recently acquired knowledge of the offshore faulting (Doglioni et al. 2012), that attempts to replicate the coseismic vertical motions from the levelling data.

Furthermore, the question of whether the 1908 Messina Earthquake can be considered as a "characteristic earthquake" is examined. The concept of a "characteristic earthquake" suggests that one scenario is that seismic events repeat, with the same magnitude, and same slip distribution, occurring on the same fault through time. The concept was developed following studies of the Wasatch Fault, in the Basin and Range province (USA) (Schwartz and Coppersmith, 1984) (Figure 8.3a). In particular, for the Wasatch Fault, it was suggested that the displacement per single earthquake derived by palaeoseismological investigations in trenches was constant (average of 2.0 m per event). However, elsewhere this hypothesis is not supported because it has been observed that mapped surface ruptures to some historical earthquakes rupture on part of the entire trace of mapped faults. For instance, by investigating the surface ruptures of the 1981 Corinth earthquake, the South Alkyonides Fault seems to have grown by several non-characteristic earthquakes (Roberts, 1996) (Figure 8.3b). One way to investigate whether characteristic earthquakes typify rupture of a fault is to examine whether vertical motions produced by one earthquake can replicate the vertical motions measured over many earthquakes. To this end, this chapter attempts to replicate the mapped pattern of

uplifted Quaternary palaeoshorelines described in Chapter 7 by repeating the vertical motions implied by the elastic half-space modelling of the 1907-1909 levelling data.

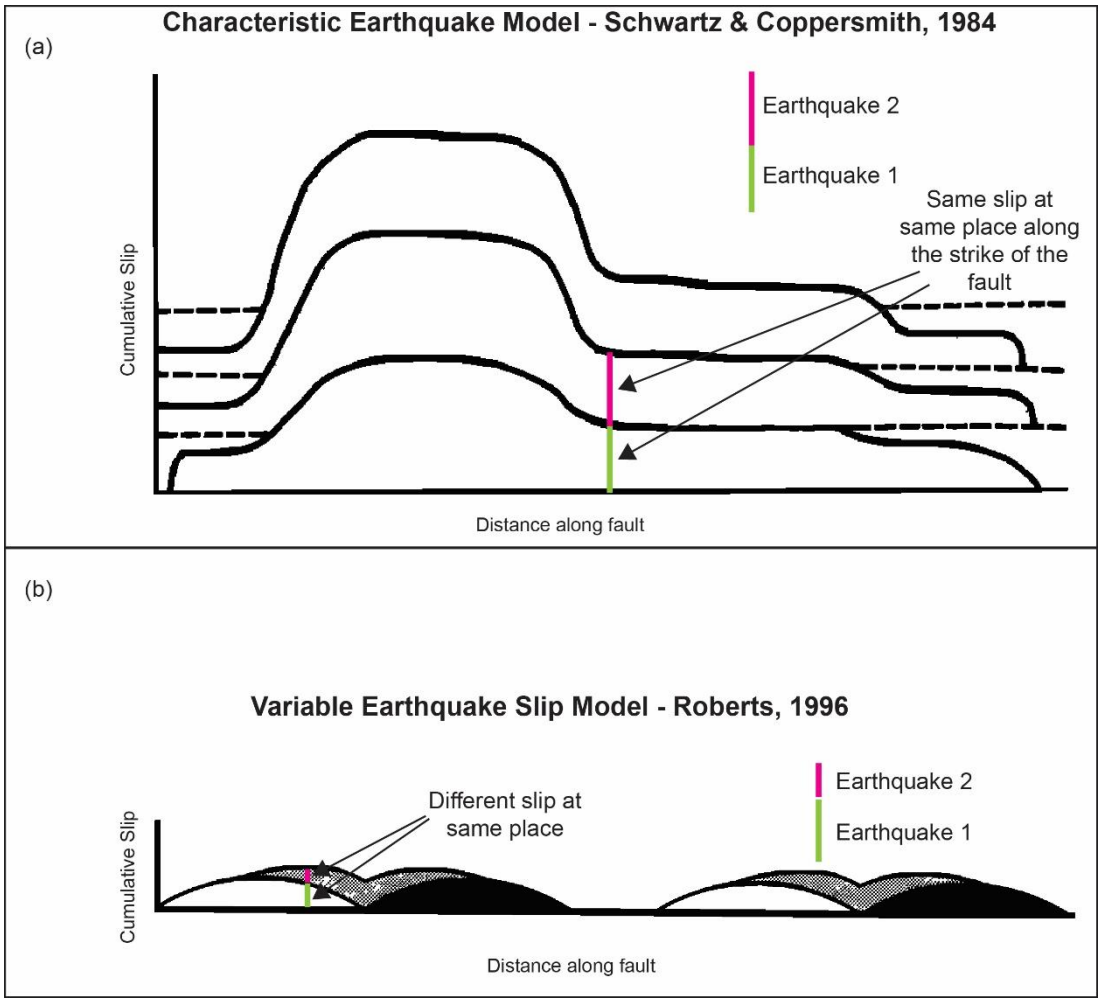

Figure 8.3: *In (a) the characteristic earthquake model is shown where the same amount of slip occurs along the strike of the fault on successive earthquakes. In (b) the variable earthquake slip model is shown where successive earthquakes can rupture partially the same fault and with a different amount of slip along-strike.*

8.4. Methods and approach

8.4.1. Fault-embedded half-space modelling by using Coulomb 3.3 software

Levelling data constraining finite ground motions from 1907 – 1909 have been projected on an E-W section, quasi perpendicular to the ~NNE-SSW strike of the mapped Quaternary normal faults (Figure 8.1 and 8.2c). This E-W section has been chosen due to the fact that faults have curvilinear traces and there is *no a priori* knowledge of which one or which

part of them ruptured during the earthquake. Moreover, this E-W oriented section is chosen to test the simplest hypotheses of whether: (i) the ruptured fault has a high or low dip angle and (ii) whether the ruptured fault dips to the west or east. Furthermore, for the reason that the mountains west of Messina town are strongly affected by slumping and landsliding processes (Goswami, Mitchell and Brocklehurst, 2011; ISPRA, 2016) a filtering step has been made to remove potentially disturbed benchmarks from the levelling data (Figure 8.1). In detail the method is that the curvilinear traces of the mapped normal faults are input into the Coulomb 3.3 software (Toda *et al.*, 2011) using the Matlab code provided by Mildon *et al.*, (2016). The down-dip extent of the fault was set at 15 km, mimicking the expected thickness of the seismogenic layer (Cowie *et al.*, 2013; Valoroso *et al.*, 2013; Mildon *et al.*, 2016). Iterations of the location of the fault, the dip and dip direction of the fault, and the amount of slip at depth and the surface have been carried out. In particular, dip angles ranging from 30 to 90°, and the amount of slip from 3 to 7 m have been iterated. The absolute misfit between modelled and measured vertical motions for each of the modelled levelling location has been calculated for each model run; the preferred model minimizes the misfit in the filtered sub-set of the data. Note that the absolute misfit represents the difference between the measured elevations by Loperfido, (1909) and the modelled elevations for each considered model; linear regression between these two datasets have been derived to assess the robustness of this correlation.

8.4.2. Long-term "characteristic earthquake" simulation as a result of repeated 1908-Messina-Earthquake event.

The hypothesis that the 1908 Messina Earthquake could be considered as a "characteristic earthquake" (Schwartz and Coppersmith, 1984, *sensu strictu*) is tested by simulating repeated earthquakes through time which rupture the entire length of the MSF, trying to match the uplifted Late Quaternary palaeoshoreline elevations outcropping on the footwall of the fault. In particular, iterated multiplications between a number of 1908-earthquakes-like and the measured co-seismic uplift produced by the 1908 earthquake are carried out; these iterations are constrained by the "m" value of the y=mx equation (m=1) calculated between the measured and modelled elevations.

In the next section results of half-space modelling are presented showing, for the first time, that a seismogenic source already mapped and available in the literature is the fault capable of producing the 1908 Messina Earthquake.

8.5. Results

8.5.1. The "Messina Strait Fault" as a seismogenic source for the 1908 Messina Earthquake

Figure 8.2c shows the profile of the co-seismic ground deformation, suggesting even before modelling, that an east-dipping seismogenic source is likely to be responsible for the 1908 Messina Earthquake; this is due to the strong similarity of the co-seismically-measured vertical motions with those for earthquakes with known surface dip directions. Candidate east-dipping faults are (a) the offshore MSF mapped by Doglioni et al. (2012) using seismic

reflection data and sea-bed bathymetry, deforming uplifted palaeoshorelines as shown in Chapter 7, and (b) the onshore MF that dips east, separating Palaeozoic basement metamorphic rocks from Miocene-recent sediments (Ghisetti and Vezzani, 1982; Monaco and Tortorici, 2000; Aloisi *et al.*, 2013) (Figure 8.1). The MF was initially modelled even though there is no field evidence suggesting co-seismic vertical deformation associated with it (Comerci *et al.*, 2015), in case that the rupture was missed during field surveys in this densely-populated region. However, by modelling the MF it was not possible to reproduce the magnitude and location of the co-seismic deformation recorded by the levelling data (See Appendix 8.1). Furthermore, the well-accepted earthquake magnitude (Mw 7.1) associated with the 1908 Messina Earthquake (Amoruso, Crescentini and Scarpa, 2002; Aloisi *et al.*, 2013) could not be reproduced by using the MF as a seismogenic source, because a rupture along its entire length (~ 25 km) could not equal that earthquake magnitude. After the MF was rejected, the ~ 58 km long offshore MSF was modelled. The preferred model with the lowest misfit value (3.9 cm – Figure 8.4) and high R^2 value between "predicted" co-seismic movements and "measured" co-seismic ground changes (Loperfido, 1909) (Figure 8.5), has 70° dip and 5 m dip-slip, with slip reaching and offsetting the sea-bed, with a 15 km down-dip width as shown in Figure 8.6.

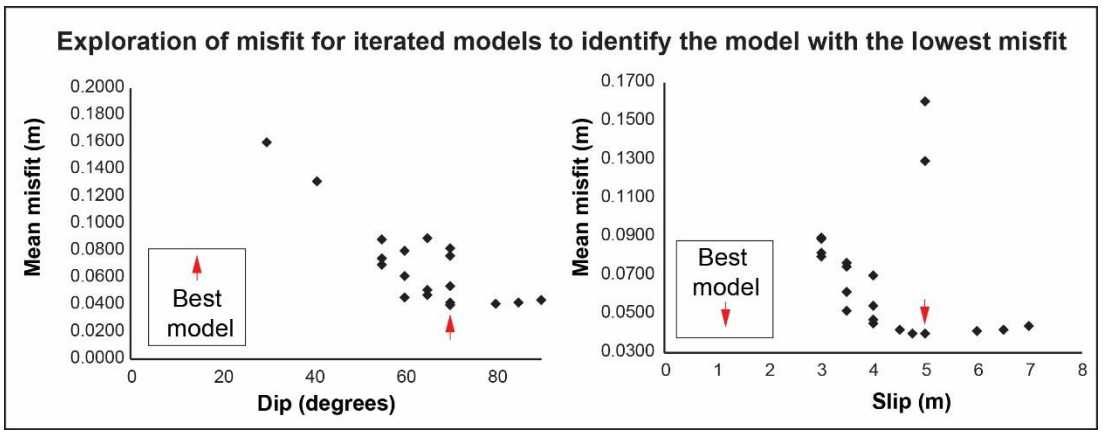

Figure 8.4: *Well-plots showing misfits for various models and the preferred model.*

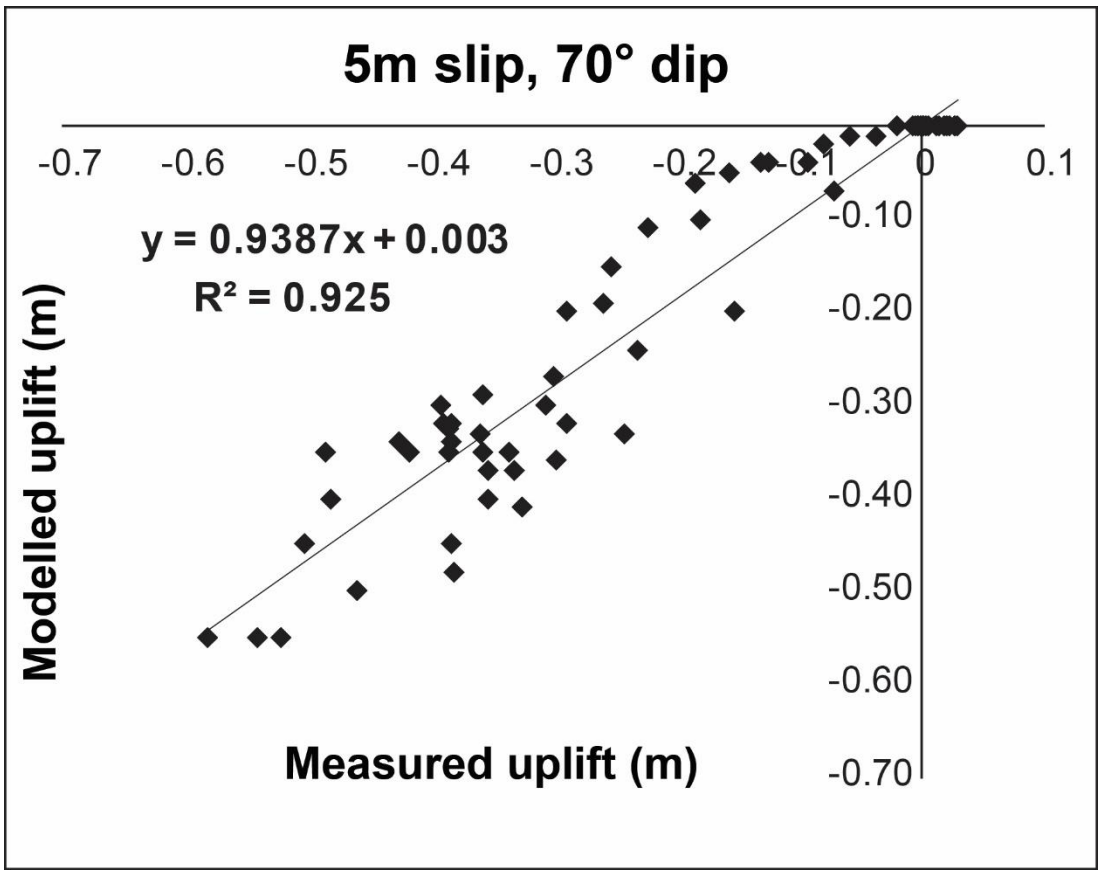

Figure 8.5: *Regression analysis to compare measured and modelled values of co-seismic elevation change for the preferred model; R^2 value = 0.925.*

Furthermore, this model produces a Mw 7.06 earthquake, similar to the widely accepted magnitude of the 1908 earthquake. Other models produce larger values for misfit (Figure 8.4) and are hence rejected. The well-plots of misfit show that iterations cover the range of plausible dip values and slip values. It is important to note that this model, unveiling for the first time that the 1908 Messina Earthquake occurred on the Messina Strait Fault rupturing entirely along its length, offsets the pre-Pleistocene basement, produces uplift of the Sicilian coast consistent with the uplifted marine terrace data mapped in Chapter 7 to a 1st order (Figures 8.6 and 8.7). The model implies rupture on the sea-bed along the trace of the MSF. However, unfortunately, sea-bed ruptures are likely to be hard to find due to their small size, the ~200-1000m water depth, and intense marine erosion and sedimentation (Ridente et al. 2014), so this scenario is hard to support with observations of surface ruptures.

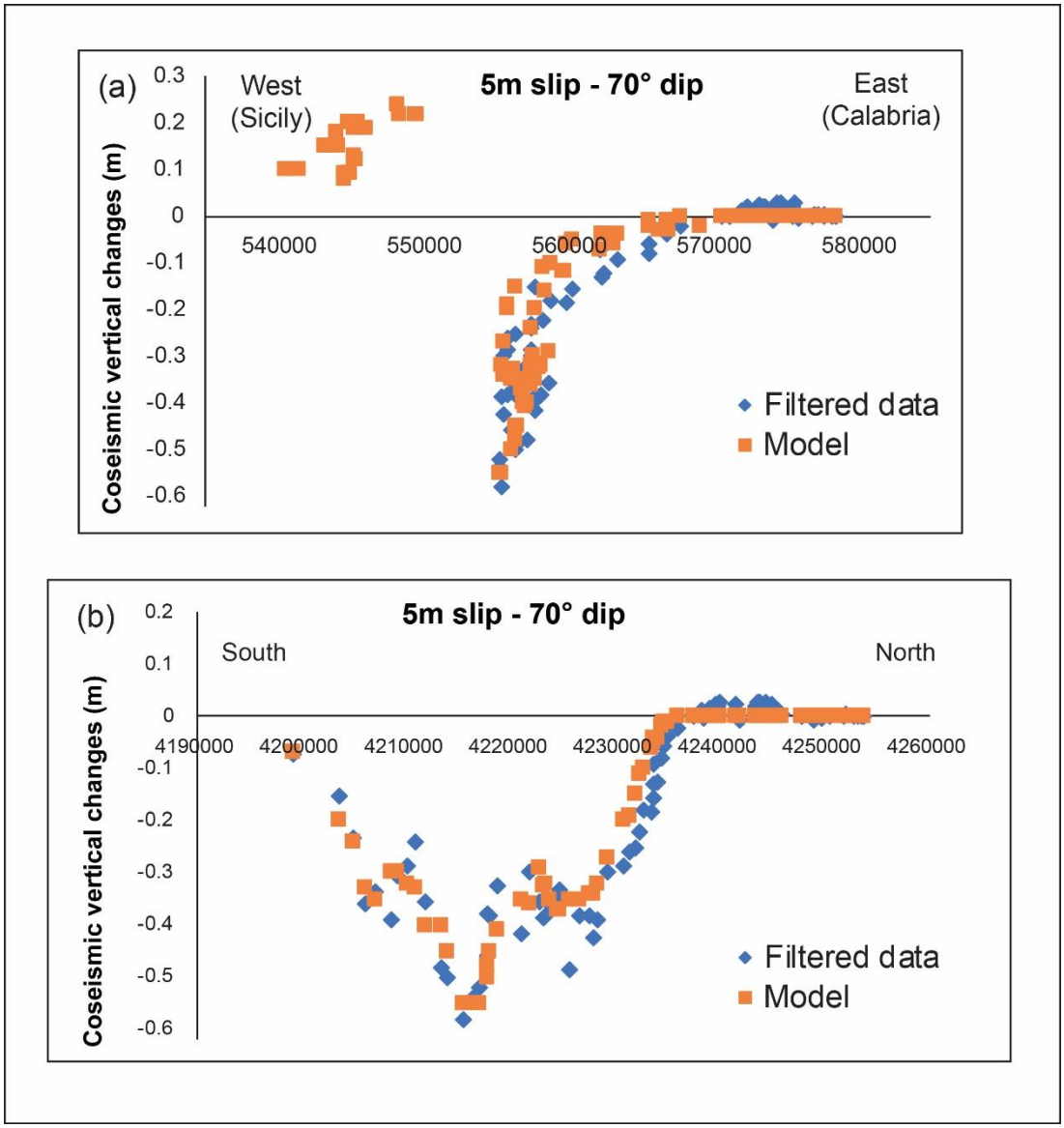

Figure 8.6: *(a) Coseismic elevation changes projected onto an E-W transect. (b) Coseismic elevation changes projected onto a N-S transect. Elevation changes for other dip and slip scenarios are shown in Appendix 8.1, but all show higher values of misfit and hence have been rejected.*

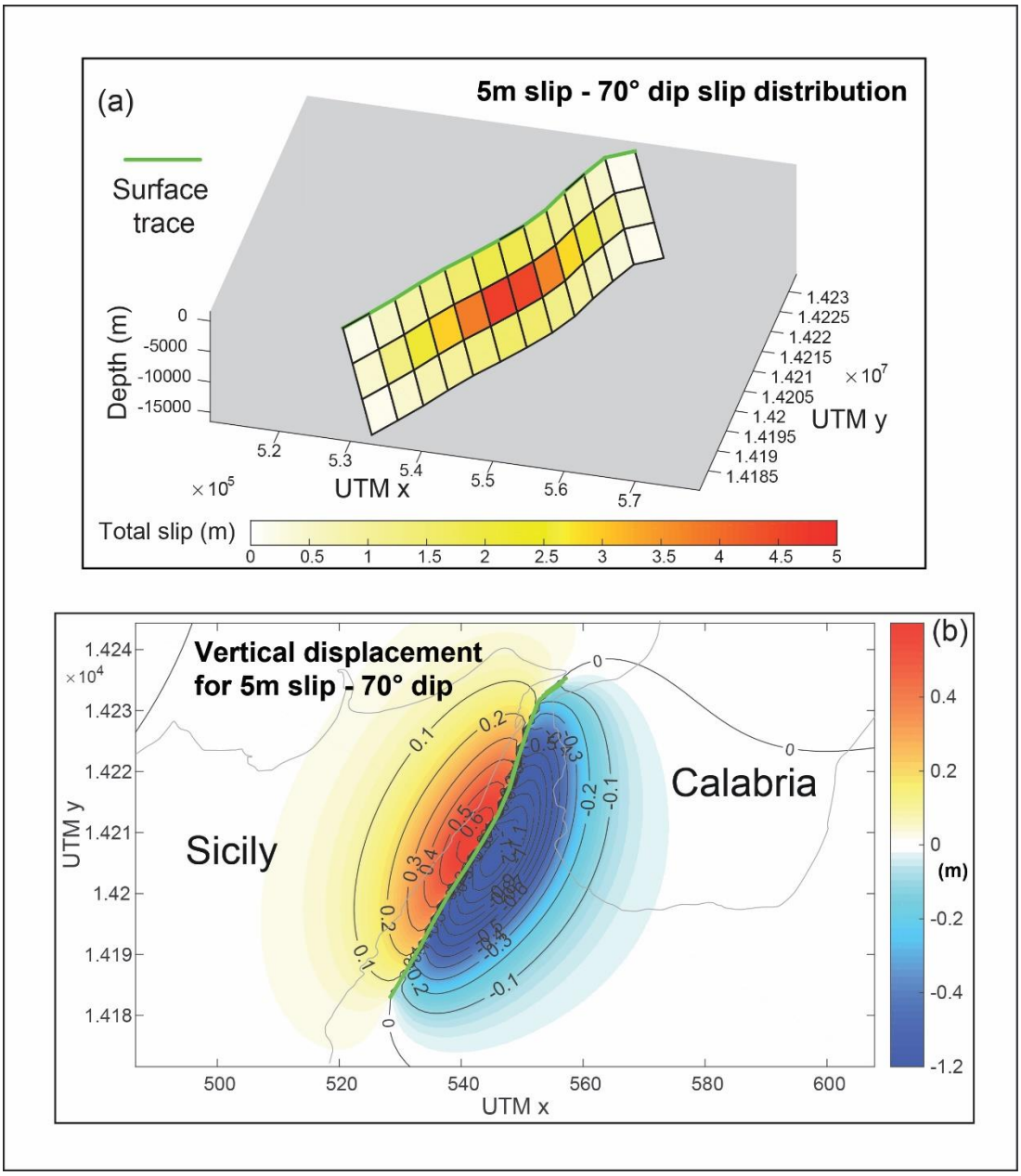

Figure 8.7: *(a) 3D view of the slip distribution for the preferred model of the Messina Strait Fault. (b) Co-seismic uplift/subsidence contours produced by the preferred model.*

The preferred model shown in Figures 8.6 and 8.7 provides a 1st order solution to the earthquake slip distribution. However, it is clear that some misfit remains. Although gaining a better model with a more sophisticated slip-distribution, for example with multiple high slip patches or asymmetric slip contours on the fault plane, might reduce the misfits, it is suggested herein that landsliding and slumping processes affecting the Sicilian coastline with the

associated mass wasting on steep slopes will have degraded the levelling data to an extent; the misfits in the preferred model may simply reflect this data degradation. This raises the question of whether a more sophisticated model is justified, due to the fact that this simple model already explains the primary observations of the earthquake and background geology and geomorphology. It was decided that for the purposes of this thesis, the simple model was adequate for requirements as it already produces a model of the deformation that out-performs published models in that it has lower misfits, and uses a fault geometry that is consistent with observations from seismic reflection data and mapped geology.

The rake has been iterated, for the 70° and 5 m slip model, from -95° to -135° to investigate whether dextral slip was involved, bearing in mind that the error on the original vertical measurements is stated to be ±0.005 m (Aloisi et al., 2012). Although the mean misfit for a rake of -105° was lower than that for -90° by 0.002 m, this is smaller than the uncertainty of the measurements, so the results are indistinguishable. Thus, the effect of changing the rake appears not to be resolvable and, although it cannot be excluded a dextral slip component, the -90° rake results is reported as the preferred model (see Appendix 8.1).

Scientific Reports has accepted for a publication a paper showing the results of this chapter.

8.5.2. Modelling the 1908 Messina Earthquake as a "characteristic earthquake"

In this section results are presented from the analysis of testing if the 1908 Messina Earthquake can be considered a "characteristic earthquake" (Schwartz and Coppersmith, 1984). In particular, from Chapter 7 values of palaeoshoreline elevations from topographic profiles (Table 8.1a), along the strike of the Messina Strait Fault (Table 8.1b – Latitude values), belonging to the 76 ka, 125 ka, 240 ka and 340 ka sea level highstands have been collected in Table 8.1c, d, e and f. These palaeoshoreline elevation values represent the "measured" elevations of the modelling explained as follows. Note that these "measured" palaeoshoreline

elevations already take into account the changing fault-related uplift rates by a factor of ~2.45 since 50 ka explained in the previous chapter (Chapter 7).

Values of coseismic uplift, from elastic half-space modelling from the preferred fault geometry for the MSF (70º dip and 5 m dip-slip) shown in the previous section, are mapped where the 76 ka, 125 ka, 240 ka and 340 ka palaeoshoreline elevations overlap on the footwall and along the strike of the Messina Strait Fault (Table 8.1g, h, i and j). Table 8.1 o, p, q and r shows all calculated values of "predicted" long-term uplift if the 1908 Messina Earthquake is assumed to be a "characteristic earthquake" occurring on the MSF, rupturing the entire fault length, through time. This has been carried out iterating the number of earthquakes (Table 8.1k, l, m and n) with the coseismic uplift values trying to match the mapped and "measured" palaeoshoreline elevations in Chapter 7 (column "c", "d", "e" and "f" in Table 8.1). This iteration is carried out till the value of m=1 from y=mx between the "predicted" and measured elevations is obtained as shown in Figure 8.8.

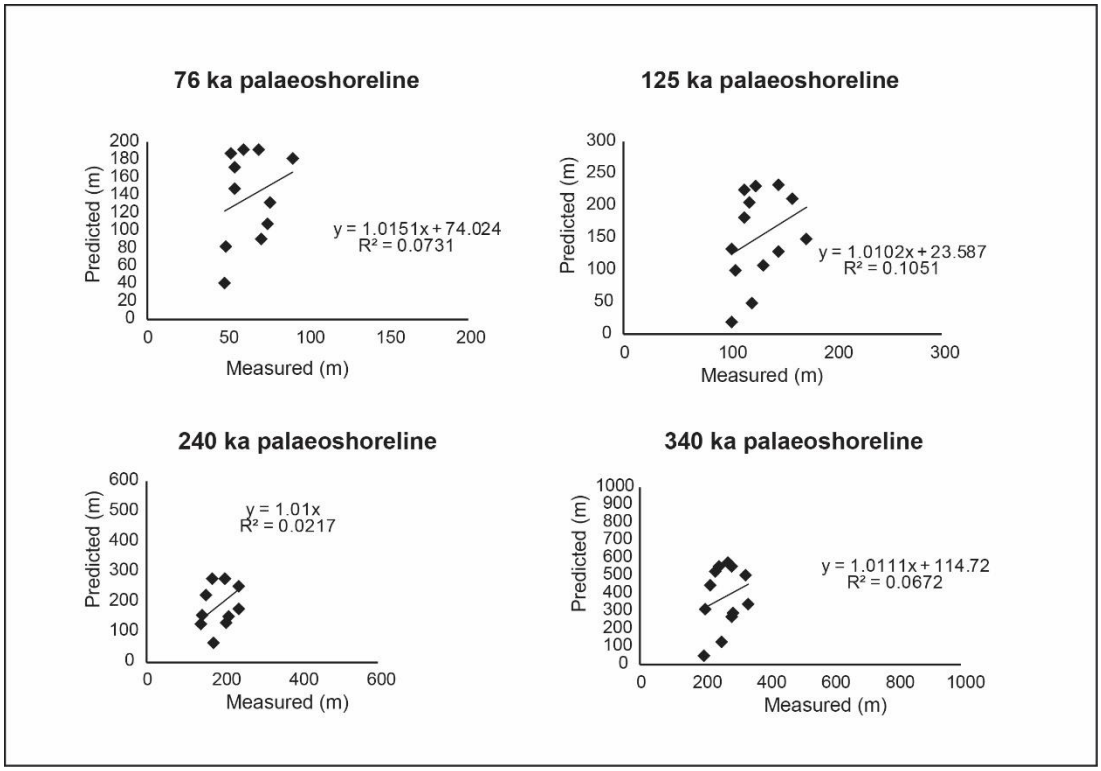

Figure 8.8: *Calculated linear regressions between "predicted" uplift elevations and "measured" elevations to drive the characteristic earthquake modelling, showing the "m" value from the y=mx equation equals to 1.*

A	B	C (m)	D (m)	E (m)	F (m)	G (mm)	H (mm)	I (mm)	J (mm)	K	L	M	N	O (m)	P (m)	Q (m)	R (m)
1	4226847	49	106	140	-	250	250	250	-	330	405	510	1050	82.5	86.625	127.5	-
2	4223662	-	103	144	203	-	330	310	300	330	405	510	1050	-	-	158.1	315
3	4219106	55	114	155	220	450	450	440	425	330	405	510	1050	148.5	155.925	224.4	446.25
4	4216202	55	119	-	235	520	510	-	500	330	405	510	1050	171.6	180.18		525
5	4213570	52	114	170	245	570	560	550	530	330	405	510	1050	188.1	197.505	280.5	556.5
6	4212245	70	125	203	273	580	570	550	550	330	405	510	1050	191.4	200.97	280.5	577.5
7	4211433	60	146	203	286	580	575	550	530	330	405	510	1050	191.4	200.97	280.5	556.5
8	4208095	91	160	238	328	550	525	500	480	330	405	510	1050	181.5	190.575	255	504
9	4203466	77	173	239	336	400	370	350	325	330	405	510	1050	132	138.6	178.5	341.25
10	4200497	75	147	212	292	330	320	300	280	330	405	510	1050	108.9	114.345	153	294
11	4196229	71	132	207	287	275	270	260	260	330	405	510	1050	90.75	95.2875	132.6	273
12	4189113	48	122	173	255	125	125	125	125	330	405	510	1050	41.25	43.3125	63.75	131.25
13	4185868	-	102	-	201	-	50	-	50	330	405	510	1050	-	-	-	52.5

Table 8.1: *(A) Profile numbers from Chapter 7, (B) Latitude in UTM, (C) Elevation of the 76 ka palaeoshoreline (m), (D) Elevation of the 125 ka palaeoshoreline (m), (E) Elevation of the 240 ka palaeoshoreline (m), (F) Elevation of the 340 ka palaeoshoreline (m), (G) Uplift from best fit elastic model for the 76 ka palaeoshoreline (mm), (H) Uplift from best fit elastic model for the 125 ka palaeoshoreline (mm), (I) Uplift from best fit elastic model for the 240 ka palaeoshoreline (mm), (J) Uplift from best fit elastic model for the 340 ka palaeoshoreline (mm), (K) Number of earthquakes needed to replicate the 76 ka data, (L) Number of earthquakes needed to replicate the 125 ka data, (M) Number of earthquakes needed to replicate the 240 ka data, (N) Number of earthquakes needed to replicate the 340 ka data, (O) Predicted uplift (m) for the 76 ka data by multiplying the number of earthquakes to the co-seismic uplift (mm) in column G, (P) Predicted uplift (m) for the 125 ka data by multiplying the number of earthquakes to the co-seismic uplift (mm) in column H, (Q) Predicted uplift (m) for the 240 ka data by multiplying the number of earthquakes to the co-seismic uplift (mm) in column I, (R) Predicted uplift (m) for the 340 ka data by multiplying the number of earthquakes to the co-seismic uplift (mm) in column*

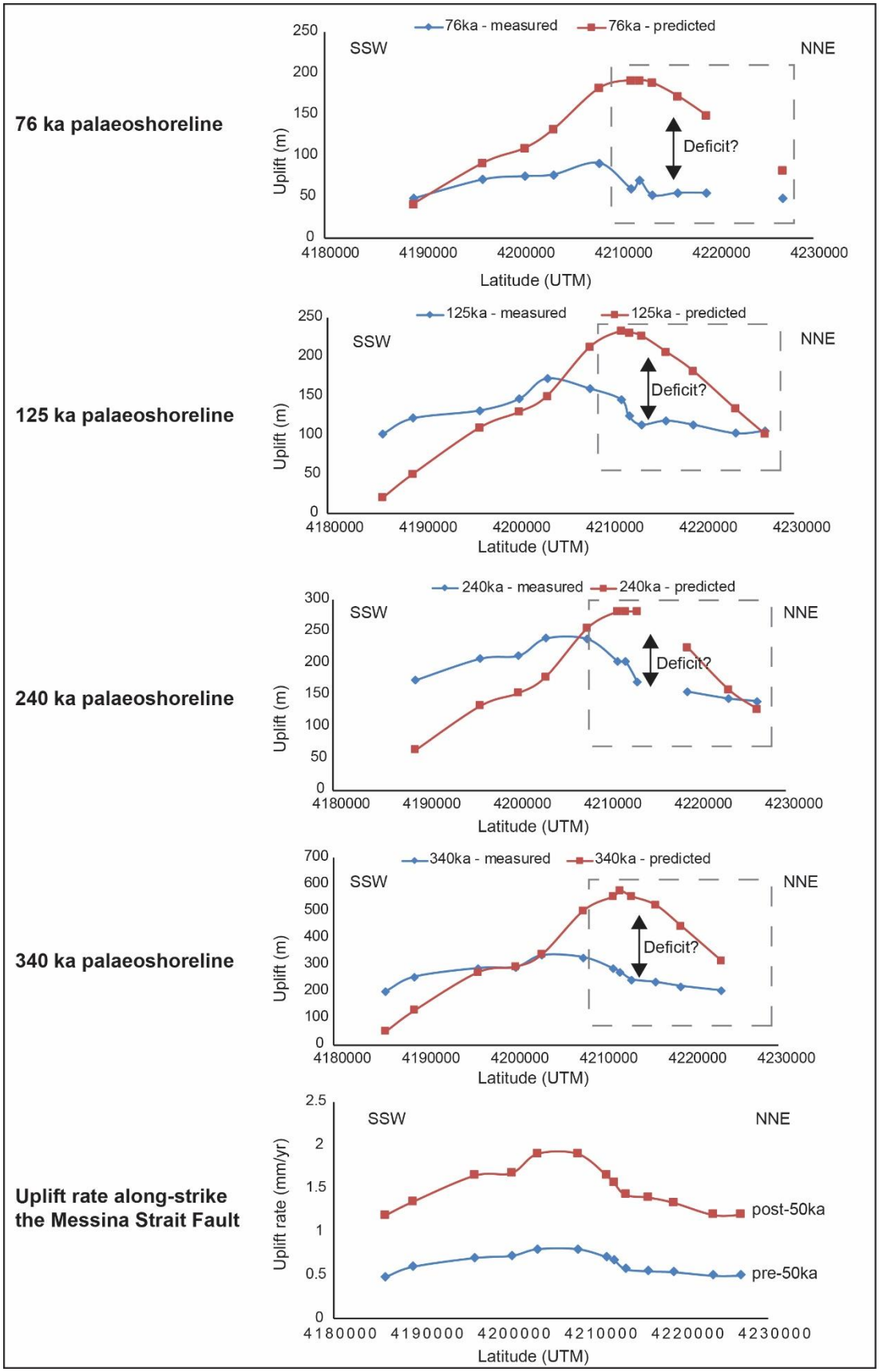

Figure 8.9: *Graphs showing, along-strike the Messina Strait Fault, (i) the "measured" elevations in blue representing the palaeoshoreline elevations mapped in Chapter 7 and (ii) the "predicted" elevations in red representing the*

iteratively-calculated elevations iterating the number of earthquakes through time to find the best match with the "measured" ones. From NNE (near Messina town) to SSW (near Taormina town) "measured" and "predicted" elevations are changing along the strike of the Messina Strait Fault. Black arrows highlight the difference in uplift in northern part of the fault, suggesting deficit affected the "measured" elevations.

Figure 8.9 shows changes along the strike of the MSF of the "predicted" and "measured" uplift elevations, however, different geometries of deformation are shown. A consistent higher uplift is shown by the predicted elevations with respect to the measured elevations on the northern part of the fault through time, suggesting that the hypothesis of considering the 1908 Messina Earthquake as a characteristic earthquake by Valensise and Pantosti, (1992) needs to be reviewed.

In Chapter 7 has been shown a synchronous change of slip rates since 50 ka on the closely-spaced Messina Strait Fault and the antithetic Reggio Calabria Fault, suggesting possible faulting interaction through time in order to accommodate the ongoing extension affecting the Messina Strait (Serpelloni *et al.*, 2005). This faulting interaction is discussed in the next section in order to explain if the 1908 Messina Earthquake could be considered a "characteristic earthquake" *sensu-stricto.*

8.6. Discussion

8.6.1. Using "already-mapped" Quaternary active faults to reconcile palaeogeodetic and geological data; crucial implications.

Levelling data from 1907 – 1909 resemble vertical ground motions from other normal faulting earthquakes if projected onto an E-W transect (Figure 8.1) rather than being plotted by levelling location number (Amoruso, Crescentini and Scarpa, 2002; Aloisi *et al.*, 2013). Furthermore, a known east-dipping fault located offshore has been identified as the source of

the 1908 Messina Earthquake, with a 70° dip, and 5 m slip with slip reaching the surface on the sea bed (Figure 8.6 and 8.7).

It is notable that ~110 years that have elapsed since the earthquake, during which time the source was debated (see Figure 2.17 for proposed models review in Chapter 2) (Schick, 1977; Boschi, Pantosti and Valensise, 1989; Valensise and Pantosti, 1992; Amoruso, Crescentini and Scarpa, 2002; Aloisi *et al.*, 2013). Indeed, it is remarkable because clear mapped active faults were known in the literature onshore and offshore, but not fully used in previous models. By obtaining these new insights, it is important to stress that that modelling of historical datasets should exploit all data including the mapped geology and geomorphology, rather than proposing fault models that do not have a clear geological or geomorphic expression. With this approach in mind, the breakthrough came simply from re-plotting the data to show variation in vertical motions with distance across the strike of the mapped Quaternary active faults (Figure 8.1 and 8.2). Indeed, it is debatably a simpler scientific scenario to propose known mapped capable faults as potential earthquake sources than proposing previously-unknown sources. This also has implications when investigations of "characteristic earthquakes", thought to occur on a fault, are carried out controlling the geology of a region. Clearly it will be advantageous to use a fault geometry that is mapped, rather than using a notional fault geometry that is not supported by observations of offsets of the long-term geology, as discussed below.

8.6.2. The 1908 Messina Earthquake as a "characteristic earthquake"

Figure 8.9 suggests that the 1908 Messina Earthquake was not a "characteristic earthquake" for the MSF using the definition of a "characteristic earthquake" where the same

amount of co-seismic slip occurs at same place along the strike of a fault through successive seismic events (Schwartz and Coppersmith, 1984) (Figure 8.3a). One interpretation of the deficit through time shown in Figure 8.9 could be that a "variable earthquake slip model" is more consistent with the data, where successive earthquakes partially rupture along the strike of the fault with different amount of slip (Roberts, 1996) (Figure 8.3b). However, this interpretation is thought herein to be unsatisfactory for two reasons. Firstly, it has been demonstrated in this chapter that the 1908 Messina Earthquake ruptured the entire length of the MSF. Secondly, it is hard to envisage how a slip deficit of tens to hundreds of metres can be maintained in the long-term, because this implies storage of elastic strain over many thousands of years. An alternative interpretation is preferred, involving across-strike fault interaction as described below.

In Chapter 7 it has been demonstrated that the Reggio Calabria Fault (RCF) is active through the Late Quaternary, deforming sequences of uplifted marine terraces on its hangingwall. This ~25-30 km long fault lies parallel to and antithetic to the MSF with a distance less than 15 km (Figure 8.10). This would suggest that fault activity on the RCF would affect the footwall uplift of the Messina Strait Fault with a counteracting fault-related hangingwall subsidence. Furthermore, the MF offsets Quaternary deposits west of Messina, counteracting the footwall uplift of the MSF with a fault-related hangingwall subsidence (Figure 8.10). The geometry of the map traces of the MSF, RCF and MF mean that they are in closest proximity in the region where the deficit in predicted uplift is shown in Figure 8.9. For these reasons it is not surprising that a deficit in uplift has been identified between "predicted" uplift and "measured" uplift in the northern part of the MSF, close and around Messina town (Figure 8.9). It is implied that the RCF and the MF could have disrupted the long-term tectonic footwall uplift of the MSF due to repeated "characteristic" seismic events like the 1908 Messina

Earthquake. This implies that the hypothesis that the 1908 Messina Earthquake could be assumed as a "characteristic earthquake" cannot be resolved until details of the interaction between the MSF, MF and RCF are resolved in detail.

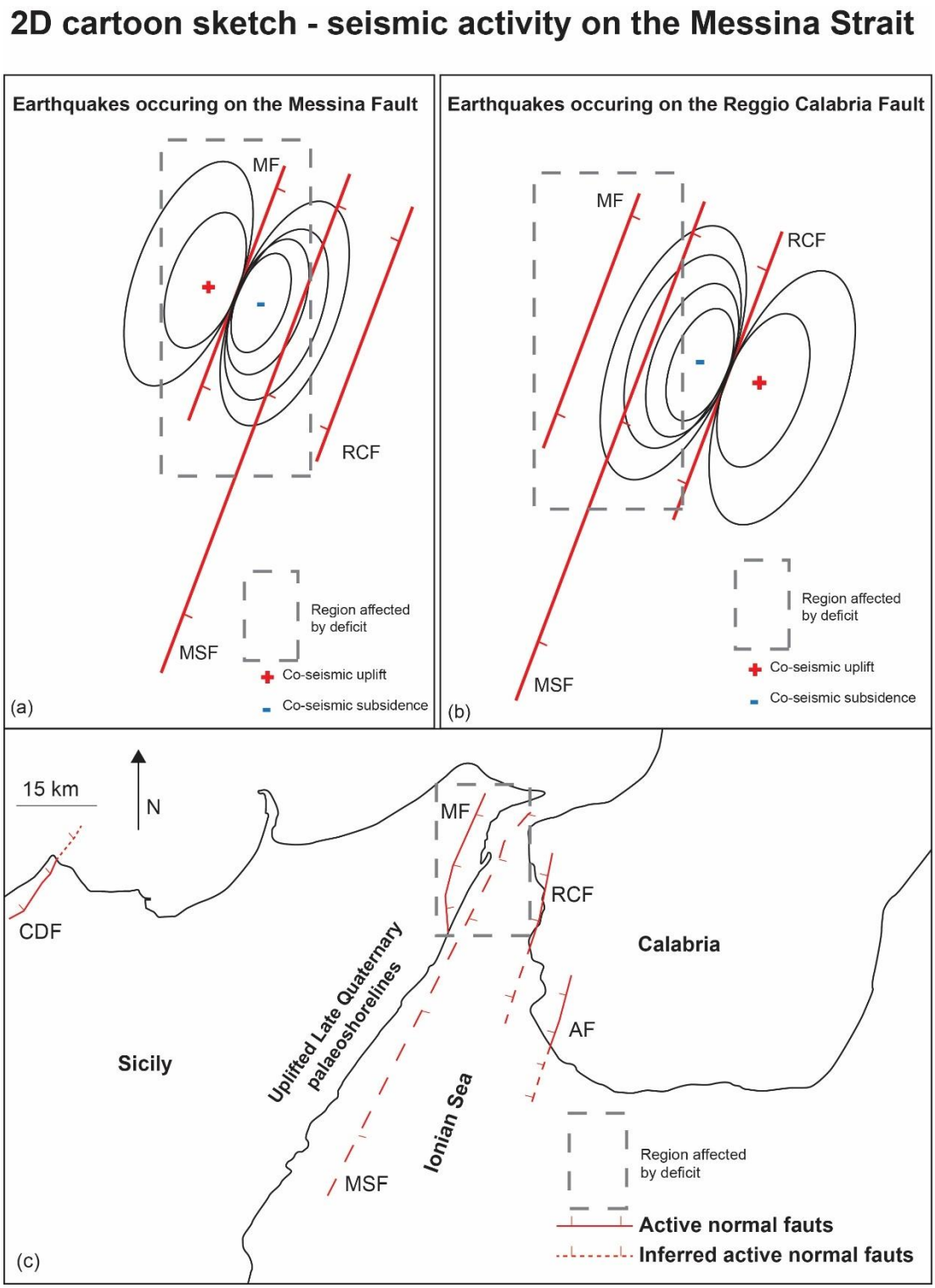

Figure 8.10: *Cartoon sketch showing disturbance of the long-term footwall uplift of the MSF by the tectonic subsidence produced by the MF (a) and the RCF (b). (c) Tectonic sketch of the Messina Strait where the deficit shown in Figure 8.9 is mapped (dashed-grey square).*

It is suggested that more studies offshore and onshore are needed to better understand the palaeoseismic activity that occurred on the MSF, MF, RCF, their interaction, and all the active faults that are accommodating the crustal extension affecting the Messina Strait.

Overall, the study of the 1908 Mw 7.1 Messina earthquake has revealed that the MSF is the best candidate for rupture in that earthquake. The earthquake provides a snapshot of the deformation from a single earthquake that can be multiplied through time to model the expected uplift over the long-term. The implied uplift does not match the measured uplift, in turn suggesting that fault interaction may well be an important process. This is consistent with the notion that fault interaction may have caused a change in uplift rate through time (Chapter 7). The outcome is that fault interaction is an important process to consider when studying the deformation in the upper plate of subduction zones. This is discussed in more detail in the next chapter.

8.*7. Conclusions*

Levelling data from 1907 – 1909 have been re-investigated revealing that the Mw 7.1 1908 Messina Earthquake ruptured a 70° east-dipping normal fault with 5 m dip-slip at depth, and slip at the surface, 15 km down-dip width, with the surface rupture located offshore on a mapped Quaternary active fault, the Messina Strait Fault. After ~ 110 years the long-debated seismic source has been identified, by using and modelling a clearly-mapped fault. This result should stimulate the drive to link historical earthquakes with capable faults, instead of ignoring the valuable insights that geomorphology and geology can bring. Finally, it is not possible to resolve the initial hypothesis that the 1908 Messina Earthquake can be assumed as a "characteristic earthquake" because further and more detailed studies are needed on adjacent

and parallel active faults to better understand their palaeoseismic activity. Surely, this earthquake has not occurred on a blind low-angle east-dipping fault, which has never mapped or imaged, implying that the idea of a "characteristic earthquake" occurring on this latter fault proposed by Valensise and Pantosti, (1992) cannot be explained.

Chapter 9: Discussion

In this chapter results obtained in Chapter 4, 5, 6, 7 and 8, using the approach and methods explained in Chapter 3, will be discussed in order to highlight: (i) the implied wider tectonic implications, (ii) an improved long-term seismic hazard approach, and (iii) some future scientific questions which can be tested based on findings from this thesis. Emphasis will be placed on: (i) critically-assigning ages to the un-dated palaeoshorelines with the associated tectonic implications, and (ii) mapping crustal deformation with associated rates through time on upper plates of subduction zones. Finally, these results will be discussed in order to address to the scientific questions presented in Chapter 1.

9.1. Long-term intracrustal deformation mapped within the Calabria Arc: wider tectonic implications

Uplift of the forearc of the Ionian Subduction Zone and the Calabrian Arc has occurred synchronously with the Ionian subduction process and the associated rollback of the Ionian slab (Goes *et al.*, 2004), and the asthenospheric upwelling beneath the Calabrian forearc (Gvirtzman and Nur, 1999b; Wortel and Spakman, 2000). However, a key finding of this thesis is confirmation of an old, but unclearly-expressed idea where the Calabrian Arc, representing the upper plate of the ISZ, shows prominent internal crustal deformation due to the active normal faulting, presented in this thesis and in the papers already published (Roberts *et al.*, 2013; Meschis *et al.*, 2018); this thesis develops this finding from previous workers by providing a new assessment of the regional geometry and rates of deformation, including a compilation of uplift rates published by others from GPS observations (Figure 9.1a) and

Quaternary uplift (Figure 9.1b). This thesis shows that topographic highs and spatial varying uplift implied by sloping planar surfaces occur because of the active tectonic uplift of footwalls

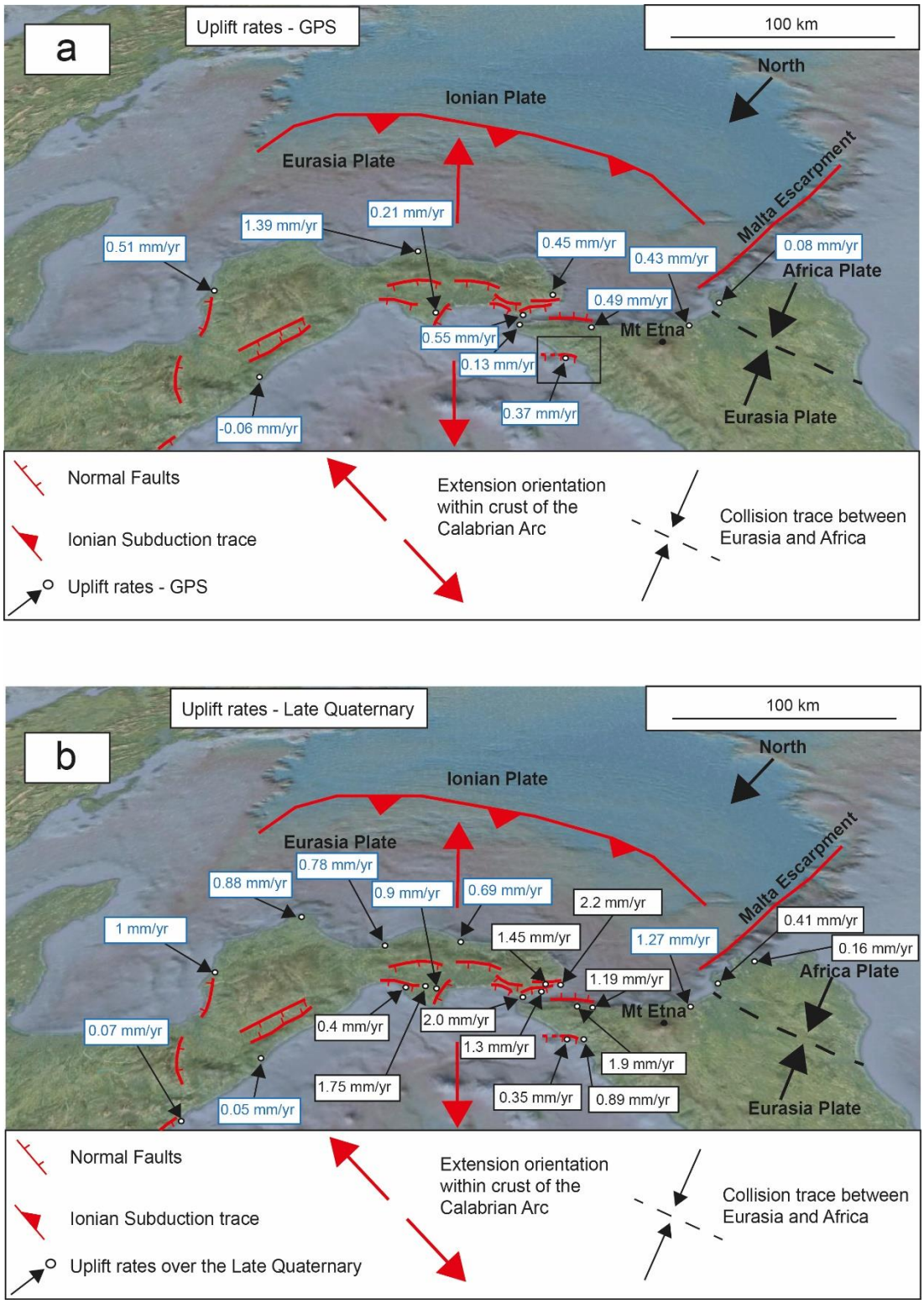

Figure 9.1: *Regional extension accommodated by normal faults within the upper plate of the Ionian Subduction Zone, along the geological domain of Calabrian Arc. (a) Spatially-varying uplift rates from GPS analysis (light blue values; Serpelloni et al., 2013) are shown along the Calabrian Arc. (b) Spatially-varying Late Quaternary uplift rates change by up to a factor of 4 across the Calabrian Arc, with large variations between the footwalls and hangingwalls of faults,*

and along the strike of faults toward fault tips. Light blue values in (b) are reported by Catalano and De Guidi, (2003) and Ferranti et al., (2006), and black values are reported from this thesis, Roberts et al. (2013) and Meschis et al. (2018).

of the active normal faults, and the interplay between hangingwall subsidence and uplift associated with more "regional" processes, such as the Maratea Fault (e.g. Papanikolaou and Roberts, 2007), the Vibo Fault (e.g. Roberts *et al.*, 2013), the Cittanova Fault (Jacques *et al.*, 2001; Galli and Bosi, 2002; Roda-Boluda and Whittaker, 2017), the Messina Strait Fault (e.g. Spampinato *et al.*, 2012 and this thesis) and the Capo D'Orlando Fault (e.g. Meschis *et al.*, 2018) (Figure 9.1). Ongoing crustal extension on the Calabrian Arc has been accommodated by these normal faults. However, this thesis places emphasis on the observation that changing uplift rates along the strike of these normal faults spanning the Late Quaternary (Antonioli, Ferranti, *et al.*, 2006; Antonioli, Kershaw, *et al.*, 2006; Ferranti *et al.*, 2006; Roberts *et al.*, 2013; Meschis *et al.*, 2018 and this thesis) and the last few decades by using GPS investigations (Serpelloni *et al.*, 2013) occur on the same length-scale as the lengths of normal faults (Figure 9.1), suggesting that the uplift signal is not simply controlled either by mantle upwelling or the subduction process which would be expected to produce spatial variations over greater length-scales. Thus, normal faults and their seismic activity are strongly influencing the so-called "regional" uplift signal over wavelengths of a few tens of kilometres within the Calabrian forearc (Meschis *et al.*, 2018). This has major seismic hazard implications for calculating slip distributions on subduction interfaces, which will be discussed later in this chapter.

This thesis also emphasises for the first time that within the same overriding upper plate, crustal deformation rates can be either constant (Chapter 4 and 5) or fluctuating (Chapter 7) through time, and these will be discussed in turn.

Firstly, in terms of faults with constant slip-rates, recognizing that the Vibo Fault (Chapter 4) and the Capo D'Orlando Fault (Chapter 5) are active and their slip-rates have

been constant over the Late Quaternary, but the rates are too low to explain the regional extension rate measured with GPS (Vibo Fault with 1 mm/yr of slip rate shown in Chapter 4 and Capo D'Orlando Fault with 0.63 mm/yr of slip rate shown in Chapter 5 and regional GPS-based extension rates of ~ 2.5 mm/yr) may have important tectonic implications. If the GPS rates, which are measured over only a few decades, are typical of longer-term rates, other active faults must be active across strike accommodate the regional extension (Roberts *et al.*, 2002, 2013; Meschis *et al.*, 2018). For instance, seismic profiles offshore quasi-perpendicular to the coastlines of Vibo Marina town in Calabria (Pepe *et al.*, 2014) and Capo D'Orlando town in NE Sicily (Nigro and Sulli, 1995) suggest the presence of offshore normal faulting activity; interesting future scientific questions, which can be tested, would be to investigate if these offshore normal faults have constant throw-rates spanning the same investigated time for the Vibo Fault and the Capo D'Orlando Fault. Presumably, the offshore faults would have to be only weakly-interacting with Vibo and Capo D'Orlando faults so that activity on one would not suppress activity on the other (e.g. see Cowie *et al.*, 2005); this could, for example, be due to a relatively large across-strike distance, but clearly this needs further study.

Secondly, in terms of faults with time-varying slip-rates, the active fault system characterizing the Messina Strait has been shown to be accommodating ongoing extension within the Strait (Chapter 7) with rates varying over the Late Quaternary. In particular, the MSF has accelerated its fault slip rate since 50 ka by a factor of ~2.45; this implies that other active faults had to "decelerate" across-strike at the same time to maintain a constant regional extension rate (e.g. see Cowie *et al.*, 2005). This idea is consistent with the observation in this thesis that a synchronous "deceleration" in fault slip-rate by a very similar factor (~2.45) has been mapped on two antithetic faults, namely the RCF and the AF. These faults are closely-

spaced across strike. The across strike distance is much less than 10-15 km at the base of the seismogenic layer, where large earthquake probably nucleate, due to the inward-dipping graben structure formed by the MSF and MF compared to the antithetic RCF and AF (Figure 8.10c). This distance is much less than half a fault length (~29 km for the MSF which is 58 km in length), a distance which as a rule of thumb is that within which fault interaction is expected. which may well be the reason that promotes their interaction.

Across-strike interaction for active normal faults is a well-known process, but not one that has been discussed in detail for the Calabrian Arc. For example, other locations within the Mediterranean Basin exhibit active normal fault systems where crustal extension across-strike is associated varying rates on individual faults through time. For instance, by mapping tectonically-deformed marine terraces in the Gulf of Corinth (Greece), and examining hangingwall stratigraphy, varying long-term fault throw-rates have been described, suggesting a synchronous change in faulting activity across-strike active faults (Roberts et al. 2009; Nixon *et al.*, 2016). In detail, the South Alkyonides Fault has been investigated, showing an accelerated fault slip-rate since 175 ka, with the rate changing by a factor of ~3.2, at a time when other faults across strike to the south appear to have ceased activity (Figure 9.2; Roberts *et al.*, 2009). The across strike fault spacing is again less than half a typical fault length in places, suggesting proximity may play a role in fault interaction. It is suggested in this thesis that the eastern Gulf of Corinth and the Messina Strait are examples where active faults are arranged across-strike, and seismically interacting, so that long-term faulting activity switches across strike over the Late Quaternary, so as to maintain constant rates of regional crustal extension. This is similar to the findings for other authors (Roberts *et al.*, 2002; Bennett, Friedrich and Furlong, 2004; Cowie *et al.*, 2005; Dolan, Bowman and Sammis, 2007; Nixon *et al.*, 2016;

Meschis *et al.*, 2018), but the first time this has been reported in the Calabrian Arc. In turn this implies a new and refined seismic hazard scenario is needed that must account for the regional balance of extension rates across active faults. This is important for the Messina Strait region when it is considered that a prominent engineering project was previously planned by Italian Government such as "Il Ponte sullo Stretto" (*the bridge on the Strait*), linking Sicily island with the Italian peninsula.

Turning this to a broader point of view related to the seismic hazard affecting the Calabrian Arc, the newly-refined long-term fault slip-rates in this thesis, and the associated T_{mean} values, play a crucial role for the ongoing seismic hazard calculations of "conditional probability" (P(t)) of occurrence of a seismic event for a given fault for the Italian territory presented in the Chapter 2 (Section 2.6). For the Messina Strait example, using a slip-rate on the MSF over, for example, 125 kyrs would provide a misleadingly long value for T_{mean}, because the slip-rate accelerated by a factor of ~2.45 at ~50 ka (slip-rate over 125 ka = 0.16 mm/yr; assuming 1000 mm slip events imply a T_{mean} of 6250 years or 2000 mm slip events imply a T_{mean} of 12500; slip-rate over 50 ka = 0.38 mm/yr; assuming 1000 mm slip events imply a T_{mean} of 2631 years or 2000 mm slip events imply a T_{mean} of 5263 years). For the RCF fault, using a slip-rate over, for example, 125 kyrs would provide a misleadingly short value for T_{mean}, because the slip-rate decelerated by a factor of ~2.45 at ~50 ka (slip-rate over 125 ka = 0.83 mm/yr; assuming 1000 mm slip events imply a T_{mean} of 1204 years; slip-rate over 50 ka = 0.35 mm/yr; assuming 1000 mm slip events imply a T_{mean} of 2857 years). Thus, this thesis emphasises that it is vital to assess not just the slip-rate, but also the slip-rates history on a fault so that an appropriate slip-rate can be used in seismic hazard calculations of the type described in Section 2.6. However, to do this, one must identify the correct ages of geological markers used in

defining slip-rates. In the next section, the importance of properly-assigning ages for un-dated palaeoshorelines will be discussed and how a different and un-correct age can lead to different seismic hazard and tectonic implications.

9.2. The synchronous correlation approach: a new "modus operandi" to investigate uplifted Quaternary palaeoshorelines and long-term crustal deformation rates

In this thesis, the synchronous correlation approach to study uplifted Late Quaternary palaeoshorelines tectonically-deformed by active faults has been applied for the first time in Italy (Roberts *et al.*, 2013; Meschis *et al.*, 2018), after being applied in the Gulf of Corinth, in Greece (Houghton et al. 2003; Roberts *et al.*, 2009). The work on Italian faults in this thesis has provided revised ages for un-dated palaeoshorelines, outcropping in the hangingwalls and footwalls of normal faults, allowing a refinement of uplift-rate histories (either constant rate, Chapter 4, 5 and 6, or fluctuating rate Chapter 7). Also, new and refined ages for un-dated palaeoshorelines have been assigned within the foreland region in SE Sicily, allowing refinement of knowledge of forebulge-related uplift rates over the Late Quaternary (Chapter 6). The results achieved using the "synchronous correlation" approach differ significantly from those using the "sequential correlation" approach used by others in the same area. This thesis suggests the results from the "synchronous correlation" approach are preferred because (a) they do not suffer from the "overprinting problem", especially at low uplift rates, so that highstands are not missed during correlation between palaeoshorelines and sea-level highstands, (b) the results can be assigned a quality control value, such as the R^2 value for linear correlation between measured and predicted palaeoshoreline elevation, or the number of palaeoshorelines that can be identified within any individual topographic profiles, with

higher numbers of palaeoshorelines correlated indicating a higher quality correlation, especially if all major highstands (e.g. 125 ka, 240 ka, 340 ka) are accounted for (Meschis *et al.*, 2018).

Given that the results from the "synchronous correlation" approach are preferred, this suggests that a worldwide review of palaeoshoreline ages assigned by applying a "sequential" correlation approach is needed (e.g. Armijo *et al.*, 1996; Grant *et al.*, 1999; Saillard *et al.*, 2011; Gallen *et al.*, 2014). For example, this thesis suggests that erroneous uplift histories are implied where the "sequential correlation" approach has been applied. For instance, in Chapter 4 and 5, previous authors (e.g. Bianca *et al.*, 2011; Giunta *et al.*, 2012) after having absolutely-dated a prominent palaeoshoreline, 125 ka, "sequentially" assigned the age of 200 ka to the next topographically higher and older terrace, resulting in a claim of fluctuating uplift rates through time. In fact, the age of the next higher terraces is shown in this thesis to be more likely 240 ka, implying a constant uplift rate through time. This has led Bianca *et al.* (2011) and Giunta *et al.* (2012) to derive incorrect fault-related uplift rates and, consequently, incorrect fault slip-rates over the Late Quaternary. Similarly, new ages for un-dated palaeoshorelines have been synchronously derived in SE Sicily (Chapter 6), obtaining different and refined ages and associated uplift rates with respect to previous geoscientists (Bianca *et al.*, 1999). For example, "geomorphic correlation" suggested that the "Akradina terrace" belonged to the 80 ka sea level highstand, suggesting higher uplift rate. In Chapter 6 it has been demonstrated that the "Akradina terrace" belongs to the 125 ka sea level highstand, suggesting a lower and refined uplift rate.

This thesis strongly emphasises that the step of assigning ages for un-dated palaeoshorelines is very important if long-term crustal deformation rates are derived for an

improved long-term seismic hazard approach. This thesis has also demonstrated that a synchronous correlation approach has to be applied to critically assign ages for un-dated palaeoshorelines even though only a few marine terraces have been absolutely-dated. In fact, if ages of un-dated palaeoshorelines are "sequentially" assigned, long-term uplift rates (either constant or fluctuating through time) will be affected by that. Consequently, for instance, if a normal fault is being investigated by looking at deformed palaeoshorelines, incorrect fault slip-rates will be derived due to the fact the oldest mapped palaeoshorelines in a normal fault hangingwall will have an incorrect age, which will lead to incorrect rates through time, implying incorrect T_{mean} for a given fault. Finally, the seismic hazard values and tectonic implications derived from that will have to be reviewed.

For this reason, an example of palaeoshoreline investigations from a tectonically-active region affected by uplifting process is reviewed and discussed below showing how different the derived uplift rate scenario can be if uplifted marine terraces are not "synchronously" investigated.

9.2.1 Uplifted palaeoshorelines tectonically-deformed by the Xylokastro Fault, Gulf of Corinth (Greece): constant or fluctuating uplift rates through time?

One of most studied region within the Mediterranean Basin investigated using uplifted palaeoshorelines that are tectonically-deformed by active faulting is the Gulf of Corinth in Greece (Figure 9.2). The Gulf of Corinth, within the Aegean region, is a young and rapidly-evolving rift basin with extension rates up to 10 mm/yr (Armijo *et al.*, 1996; Roberts *et al.*, 2009). Previous geoscientists have been debating the evolution of this fault-bounded basin rift and in particular if the active faults accommodating the ongoing extension have

slipped with constant (Armijo *et al.*, 1996) or fluctuating (Roberts *et al.*, 2009; Nixon *et al.*, 2016) rates through time.

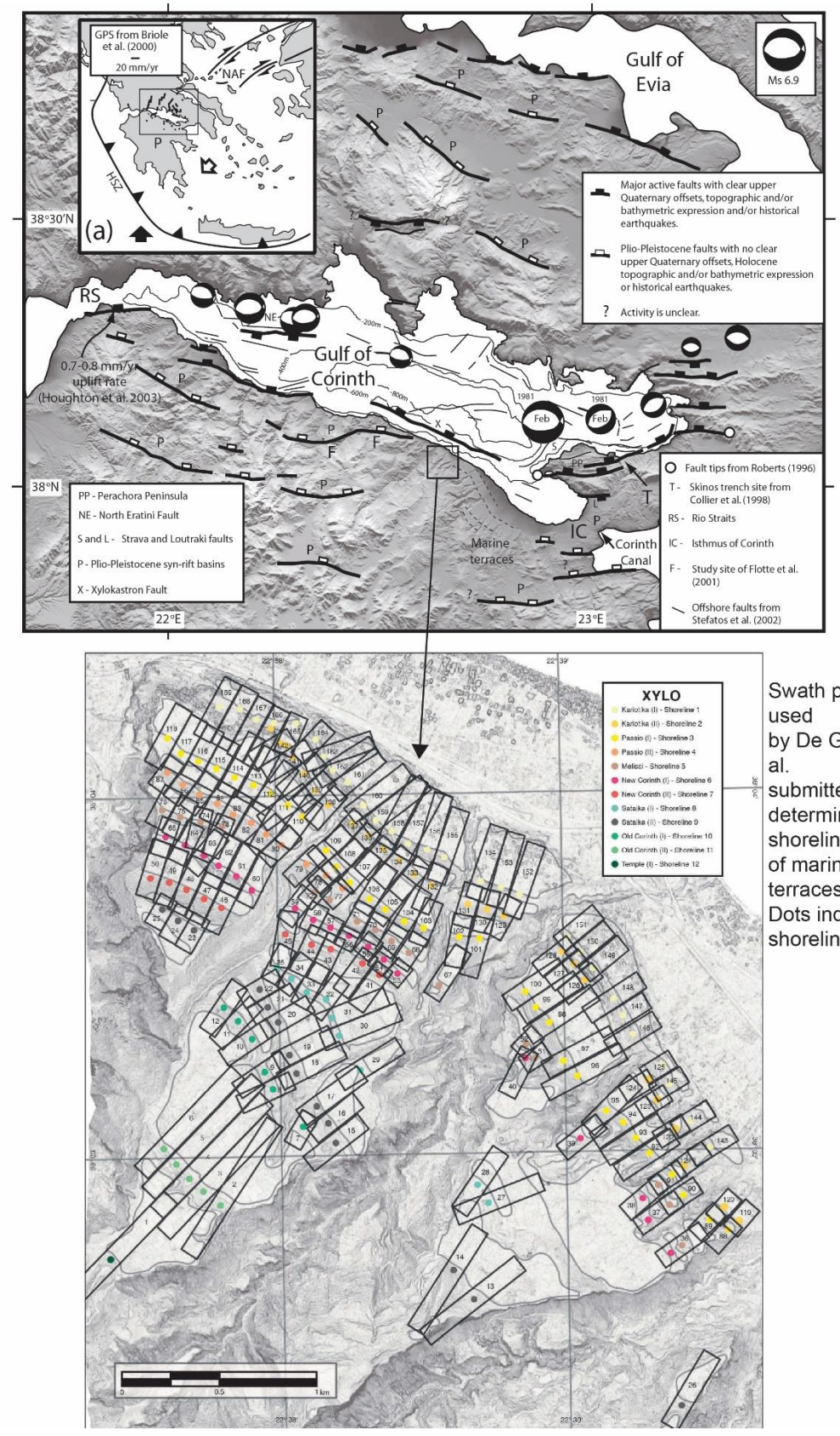

Swath profiles used by De Geder et al. submitted to determine shoreline angles of marine terraces. Dots indicate shoreline angles.

Figure 9.2: *Top map shows a tectonic map modified from Roberts et al., (2009) for the Gulf of Corinth. The black square indicates the location of marine terraces mapped by De Gelder et al. (submitted). Bottom map shows detailed swath profiles mapping the inner edges of marine terraces on the footwall of the Xylokastro Fault.*

The southern part of the gulf is bounded by a ~ 130-km long north-dipping active normal fault system, composed of 30-40 km long individual faults, tectonically-deforming uplifted palaeoshorelines outcropping on the footwalls and hangingwalls of these faults (Armijo *et al.*, 1996; McNeill and Collier, 2004; McNeill *et al.*, 2005; Roberts *et al.*, 2009).

These palaeoshorelines have been mapped and investigated to derive long-term crustal deformation rates to: (i) better understand the faulting activity accommodating the ongoing extension of the gulf through time and (ii) improve the associated seismic hazard of this region, which have been historically hit by damaging earthquakes (e.g. 1981 Corinth, Perachora, and Kaparelli Mw 6.7, 6.4 and 6.2) (Armijo *et al.*, 1996; Roberts *et al.*, 2009). In particular, uplifted palaeoshorelines outcropping on the footwall of the Xylokastro Fault (Figure 9.2) have been re-mapped by using very high-resolution detailed Digital Elevation Models (from Pleiades Satellite Images; De Gelder *et al.*, submitted) using as a guide a previous map by Armijo et al. (1996). De Gelder et al., following Armijo et al. (1996), suggested an averaged constant uplift rate through time of 1.3 mm/yr. This new study (De Gelder *et al.*, submitted), however, does not resolve the problem that this area lacks strong age controls for palaeoshorelines and their associated marine terrace deposits. Furthermore, ages for un-dated palaeoshorelines have been estimated by using a "sequential" correlation approach instead of the "synchronous" correlation. In other words, this thesis suggests that it is useful to test the constant uplift rate hypothesis by assessing whether it is also supported by the "synchronous correlation" approach. In this section an alternative plausible uplift rate scenario is presented using the detailed GIS-based mapped inner edges (Table 9.1) (De Gelder *et al.*, submitted).

Measured Palaeoshoreline (m)	Age controls
44	
72	
101	
112	
155	New Corinth (125 ka)
177	
205	
232	
268	
317	
368	

Table 9.1: *Elevation of mapped inner edges shown in Figure 9.2 (bottom) by using a very high resolution DEMs (De Gelder et al., submitted), confirming and updating a previous mapping (Armijo et al., 1996). Age control is from Armijo et al., (1996).*

Table 9.1 shows palaeoshoreline elevations mapped near the centre of the Xylokastro Fault by using GIS-based topographic analysis (De Gelder *et al.*, submitted) (Figure 9.2), in agreement with previous mapping shown by Armijo et al. (1996). Some geoscientists have dated shallow marine deposits, between Corinth and Loutraki towns, ~ 20 km east from the investigated area (Collier *et al.*, 1992; Dia *et al.*, 1997). A geomorphic correlation to link these previously-obtained dates with the investigated terraces by De Gelder et al. (submitted) following Armijo et al. (1996) is proposed. This leads to use a weak age control, also presented by Armijo et al. (1996), where the "New Corinth" terrace mapped at 155 m is associated to the

125 ka highstand; a "synchronous correlation" approach is applied trying to model the sequence of marine terraces presented in Table 9.1.

As explained in Chapter 3, the "synchronous correlation" approach always starts testing the simplest idea of a constant uplift rate through time in this case driven by the "New Corinth" terrace belonging to the 125 ka sea level highstand. Thus, an initial correlation was attempted using a constant uplift rate (Figure 9.3). A single uplift rate can be applied to all the palaeoshoreline elevations because they are all located within <5 km of the Xylokastro Fault trace, a distance that is small compared to the fault length of ~30 km reported by Armijo et al. (1996); uplift will not vary to an extent that will invalidate this assumption over this relatively short distance of <5km. The results show that although Figure 9.3 shows a reasonably-good correlation between GIS-based "measured" palaeoshoreline elevations and "predicted" iteratively-calculated sea level highstand elevations, only 9 out of 11 palaeoshorelines could be modelled, suggesting that perhaps a changing uplift rate through time can better model the geomorphology of this area.

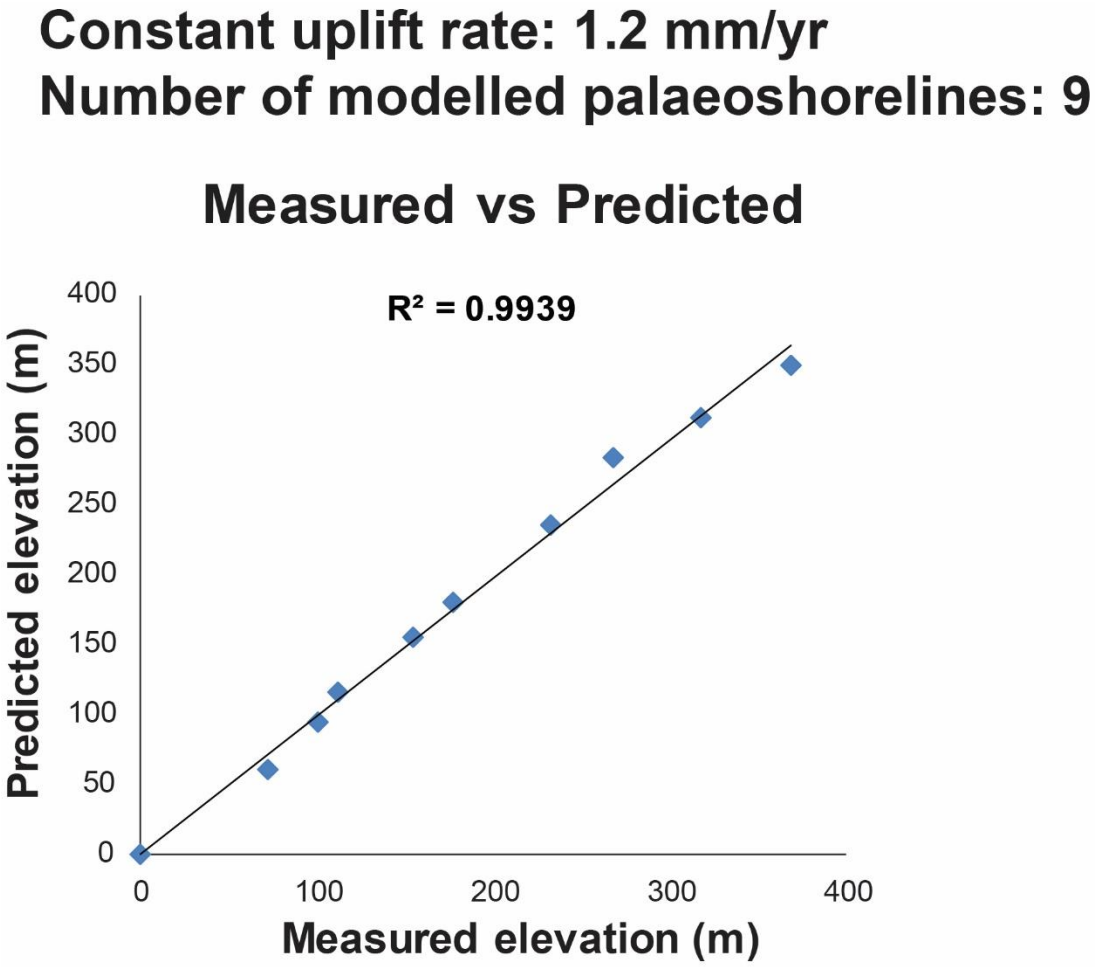

Figure 9.3: *Linear regression between "predicted" and "measured" elevations by applying a synchronous correlation approach to model the sequence of marine terraces presented in Table 9.1 and Figure 9.2. Note that 9 palaeoshorelines out of 11 are modelled assuming a constant uplift rate through time as initial hypothesis.*

Indeed, Table 9.2 shows modelled palaeoshoreline elevations with a constant uplift rate through time (1.2 mm/yr). However, it is important to note that not all the mapped palaeoshoreline elevations could be modelled. For example, the 340 ka sea level highstand, that is commonly mapped in the Mediterranean due to its geomorphic prominence (Roberts *et al.*, 2009; Roberts *et al.*, 2013; Meschis *et al.*, 2018), is not recognized.

Measured Palaeoshoreline (m)	Predicted Elevations (m)	Age of highstands (ka)
44	Not modelled	?
72	62	76.5
101	95	100
112	117	115
155	155	125

177	180	175
205	Not modelled	?
232	235	200
268	283	240
317	312	285
368	350	310

Table 9.2: *"Predicted" and "measured" elevations are shown with an assigned age assuming a constant uplift rate through time of 1.2 mm/yr. Note that two palaeoshorelines could not be modelled with the assumed constant uplift rate scenario. Red coloured elevation represents the age control used to drive the synchronous correlation. Note that it was not possible to identify the 340 ka palaeoshoreline using constant uplift rates.*

In an attempt to refine the modelling, for example to include the 340 ka palaeoshoreline, a changing uplift rate through time was tested for the same sequence of mapped terraces, iterating "predicted" sea level highstand elevations with a change in uplift rate at 175 ka. It is important to note that this time of uplift-rate change (175 ka) is not chosen randomly; a study of uplifted palaeoshorelines tectonically-deformed by a north-dipping active fault (South Alkyonides Fault) which lies a few tens of kilometres to the ENE of the Xylokastro Fault, has been suggested to exhibit a changing fault-related uplift rate at 175 ka (Roberts *et al.*, 2009) (Figure 9.2). Figure 9.4 shows the results of the changing uplift rate synchronous correlation. It is suggested that this shows an improved correlation with a higher R^2 value between "measured" and "predicted" elevations, allowing modelling of 10 out of 11 palaeoshorelines, with an uplift rate of 0.35 mm/yr pre-175 ka and 1.2 mm/yr post-175 ka, (Table 9.3). Importantly, the important sea-level highstand and palaeoshoreline at 340 ka is modelled because it is predicted to lie at 273 m elevation, almost coincident with a measured palaeoshoreline at 268 m elevation (Table 9.3), instead of at an elevation of 408 m where no palaeoshorelines have been mapped, as implied if a constant 1.2 mm/yr uplift rate is used (e.g. (De Gelder *et al.*, submitted). This suggests that a "changing" uplift rate scenario appears to better explain the palaeoshoreline sequence this region. Note that it is implied that the uplift

rate has accelerated by a factor of ~ 3.4, producing a rather dramatic difference in the uplift rate history compared to the constant uplift rate model, as illustrated in Figures 9.5a and 9.5b.

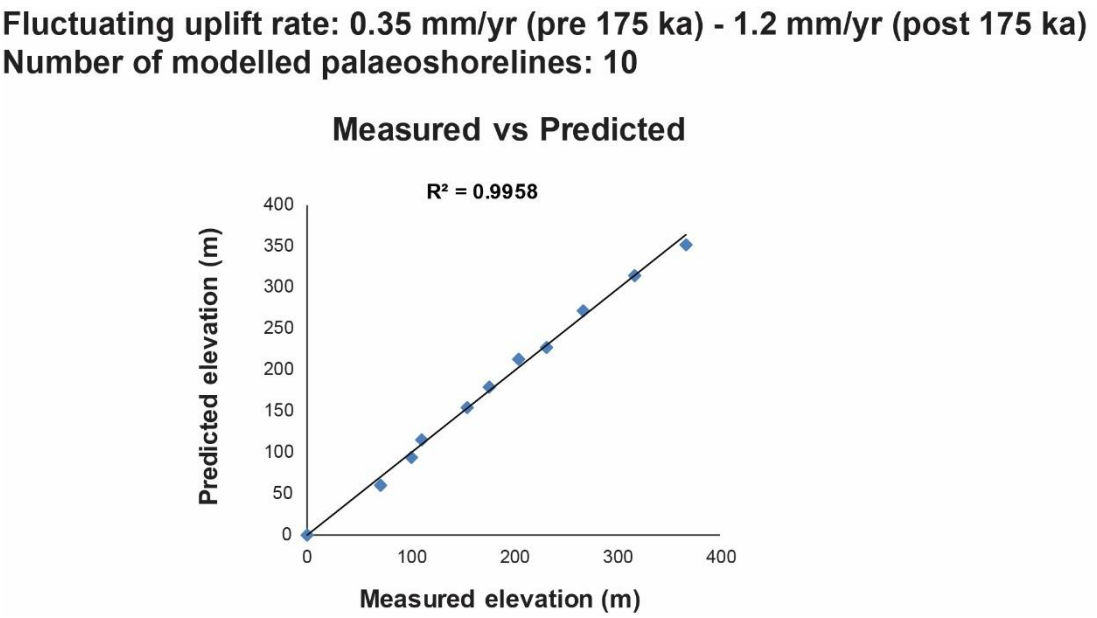

Figure 9.4: *Linear regression between "predicted" and "measured" elevations by applying a synchronous correlation approach to model the sequence of marine terraces presented in Table 9.1 and Figure 9.2. Note that 10 palaeoshorelines out of 11 are modelled assuming a changing uplift rate through time as second tested hypothesis.*

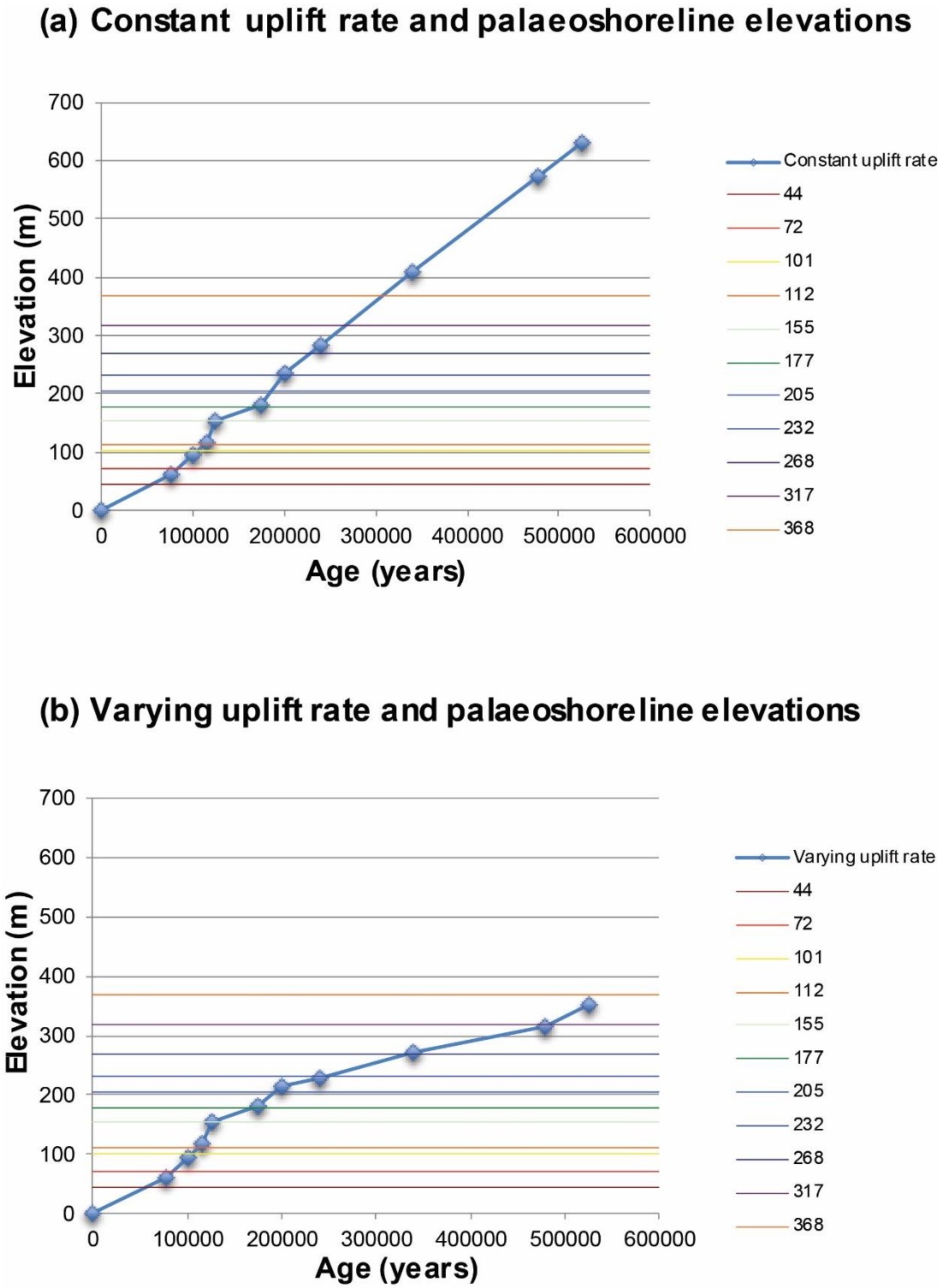

Figure 9.5: *The difference between constant (a) and time-varying uplift rates (b). Coloured horizontal lines show the elevations of mapped palaeoshorelines from De Gelder et al. (submitted). Blue lines show the uplift rate histories with with diamond symbols showing the expected elevations for expected palaeoshorelines.*

Table 9.3 shows modelled palaeoshoreline elevations with a changing uplift rate over the Late Quaternary. This thesis emphasises that the varying uplift rate scenario allows one to model marine terraces with ages that are commonly mapped in the Mediterranean Basin such as the

125 ka, 240 ka and 340 ka, representing prominent sea level highstands mapped previously by some in the Mediterranean Basin (Roberts *et al.*, 2009; Roberts *et al.*, 2013; Meschis *et al.*, 2018) and in this thesis.

Measured Palaeoshoreline (m)	Predicted Elevations (m)	Age of highstands (ka)
44	Not modelled	?
72	62	76.5
101	95	100
112	117	115
155	155	125
177	180	175
205	214	200
232	228	**240**
268	273	**340**
317	316	478
368	353	525

Table 9.3: *"Predicted" and "measured" elevations are shown with an assigned age assuming a changing uplift rate through time (0.35 mm/yr pre-175ka and 1.2 mm/yr post 175 ka). Red coloured elevation represents the age control used to drive the synchronous correlation approach. Importantly, the prominent highstand at 340 ka is successfully modelled, in contrast to the results in Table 9.2.*

Even though future works are needed for this location on (a) gaining more reliable age controls and (b) testing if the "changing" uplift rate scenario is spatially and laterally applicable along the strike of the Xylokastro Fault, by using: (i) the previously-suggested age control for this sequence (New Corinth terrace – 125 ka) (Armijo *et al.*, 1996) and (ii) the new detailed mapping by De Gelder et al., it has been possible to show a plausible fault-related uplift rate scenario in agreement with other fault slip-rate histories through time investigated within the Gulf of Corinth (Roberts *et al.*, 2009; Nixon *et al.*, 2016). In particular, by applying a synchronous correlation approach for the first time a changing uplift rate at 175 ka is mapped, suggesting an "acceleration" by a factor of ~ 3.4; the acceleration factor for the north-dipping South Alkyonides active fault at the same time is 3.2 ±0.2 at 175 ±75 ka (Roberts *et al.*,

2009), a remarkably similar result for two neighbouring faults that have been modelled independently.

The question arises of how the above slip-rate acceleration would impact on seismic hazard assessments if it were not recognised. Consider what would happen in the future if absolute age control were to be gained for other palaeoshorelines in the Xylokastro Fault example; this thesis suggests it is likely that the older, higher palaeoshorelines mapped by De Gelder et al. (submitted) will prove to be <525 ka in age. This is important because, if, for example, the uplift rate for the highest palaeoshoreline was calculated without recognising the change in uplift noted in this thesis, the uplift would be calculated as 368 m uplift in 525 kyrs, that is 0.7 mm/yr at a constant rate; the implied throw rate given a 1:3 uplift to subsidence ratio is 0.7 x 4, that is 2.8 mm/yr, which in turn implies a T_{mean} of 357 years given 1m slip increments (1000 mm divided by 2.8). However, given the 1.2 mm/yr uplift rate suggested by the time-varying uplift-rate model advocated in this thesis (Table 9.3, Figure 9.5b), the T_{mean} would be 208 years given that the throw rate would be 1.2 mm/yr x 4 = 4.8 mm/yr, and assuming 1m slip events (1000 mm divided by 4.8). This dramatic difference in T_{mean} underlines the importance of gaining an appropriate slip-rate on a fault prior to calculating seismic hazard using the approach outlined in Section 2.6 of this thesis.

In summary, this section has shown long-term seismic hazard calculations and tectonic implications spanning the Late Quaternary are strongly and directly affected by ages that are assigned to un-dated palaeoshorelines.

9.3. "Regional" uplift perturbed by "local" upper plates active faults: seismic implications for slip distribution calculation on subduction interfaces.

By synchronously-investigating tectonically-deformed marine terraces within the Calabrian Arc it has been possible to unveil new insights into: (i) the relationship between multiple Late Quaternary marine terraces, active normal faulting, and "regional" uplift, and (ii) the long-term faulting activity within the upper plate of the Ionian Subduction Zone (ISZ). This thesis has been demonstrated that if a "regional" uplift exists, it has been perturbed by "local" active faults which are seismically accommodating the ongoing extension within the Calabrian Arc (Serpelloni *et al.*, 2005), with important implications for the geography of seismic hazard in southern Italy. For instance, in this thesis values of uplift rates have been mapped (a) in the centre of normal fault hangingwalls, (b) in footwalls, and (c) beyond the fault tips. The values in these locations vary markedly (Figure 9.1), suggesting that if a "regional" uplift signal exists, it has to be measured where no "local" perturbation from upper plate active faults can be mapped; it is suggested in this thesis that in practice this will be extremely challenging to achieve due to the closely-spaced nature of the active faults and the fact that fault-controlled spatial variation in uplift appears to extend beyond fault tips for several kilometres (Figure 4.10). This also has wider seismic implications in terms of calculating slip distributions on subduction interfaces using observations of uplift in the upper plate of subduction zones. If the "regional" signal is assumed to be a product of slip on the subduction interface it will be challenging to infer the latter from the former. This is important because it is common for data on uplift in upper plates of subduction zones to be used to estimate slip distributions along the subduction interface (McCloskey, Nalbant and Steacy, 2005; Meltzner *et al.*, 2006, 2015; Nalbant *et al.*, 2013; Nic Bhloscaidh *et al.*, 2015), and these

studies commonly do not identify, extract and discard the signal from internal deformation due to faulting in the upper plate. Indeed, this thesis emphasises that the effect of internal deformation in the upper plate on uplift can be large compared to that expected from slip on the subduction interface. Figure 9.6 shows some examples of co-seismic uplift due to subduction earthquakes from different active subduction zones worldwide measured in the upper plates.

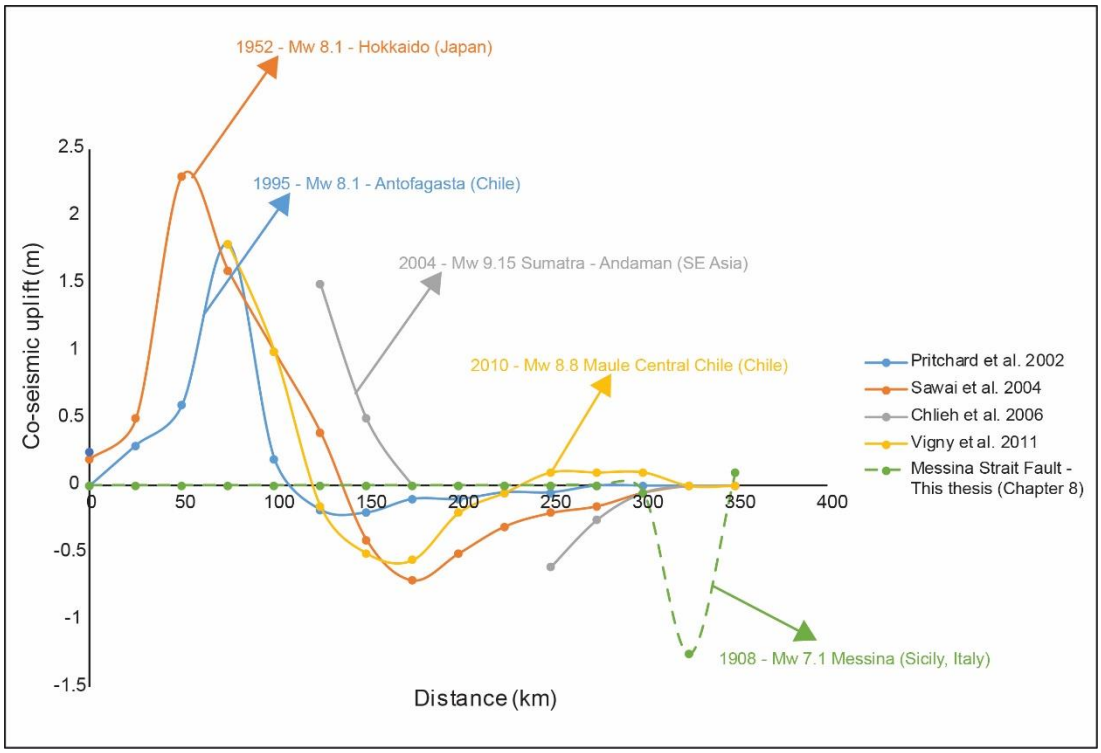

Figure 9.6: *Coseismic surface uplift variation with distance from the subduction interface after different megathrust earthquakes occurring in active subduction zones. Dashed green line shows the co-seismic subsidence modelled after the 1908 Messina earthquake shown in Chapter 8 at the same scale.*

The coseismic vertical motions from the subduction zone earthquakes are typified by uplift of < ~2.5 m amplitude for a distance < ~100-175 km, with subsidence of < ~1 m stretching from ~100-175 km to < ~300-350 km from the subduction interface. This thesis emphasises that coseismic subsidence measured for internal deformation due to normal faulting in the upper plate of subduction zones can have an amplitude of ~1.0-1.5 m, exemplified by the 1908 Mw 7.1 Messina Earthquake (green dashed line in Figure 9.6). In other words, the amplitude of

internal deformation due to normal faulting in the upper plate of subduction zones can be larger than the signal expected from the subduction interface, and so the former may well overwhelm the latter. It is therefore vital that deformation due to upper plate normal faulting earthquakes is identified, extracted and discarded if observations from upper plates of subduction zones are used to infer slip distribution on the subduction interface (Meschis *et al.*, 2018). It is vital because if the spatial variation in uplift rates due to the upper plate active faulting is not recognized and removed from the subduction slip calculations, this could lead to: (i) flawed interpretations about the mantle upwelling-related dynamic topography and (ii) excessively intricate and ambiguous subduction interface slip distributions. This thesis emphasises that future work should involve a worldwide review of subduction zone slip distributions based on uplift, including subduction zones affecting Greece and Crete (Armijo *et al.*, 1996; Vacchi *et al.*, 2012; Gallen *et al.*, 2014), Japan (Hasegawa *et al.*, 2000), California (Grant *et al.*, 1999) and South America (Saillard *et al.*, 2011 and Binnie *et al.*, 2016). This is especially important as some subduction zone earthquakes are thought to involve synchronous slip on upper plate normal faults (McKenzie and Jackson, 2012).

9.4. Coulomb Stress interaction between potential subduction earthquake occurring on the ISZ and active normal faulting affecting the upper plate: tectonic and seismic implications.

This section investigates the possibility of interaction between the subduction interface and upper plate normal faults using elastic half-space modelling. The reason for this work is that this thesis presents data that could underpin a new geography for seismic hazard in southern Italy, in that normal faults have been shown to be active with their slip rate histories constrained, when previously, they were thought not to be active, due to the lack of

mapped Holocene deformation (e.g. Monaco and Tortorici, 2000; Tortorici *et al.*, 2003; Bianca *et al.*, 2011; Giunta *et al.*, 2012). A further variable that ought to be constrained is the potential for seismic activity of the Ionian Subduction Zone (ISZ) to affect the seismic cycle of upper plate normal faults; this has not been studied to date. Although the process of subduction zone occurring in the Ionian Sea is thought to have slowed down since the Middle Pleistocene by some authors (Goes *et al.*, 2004; Serpelloni *et al.*, 2005, 2007; Palano *et al.*, 2012), new seismic reflection investigations offshore show wide-spread folding and thrusting process in the Ionian Sea, throughout the entire Calabrian accretionary wedge, suggesting an ongoing active subduction (Gallais *et al.*, 2012; Gutscher *et al.*, 2017).

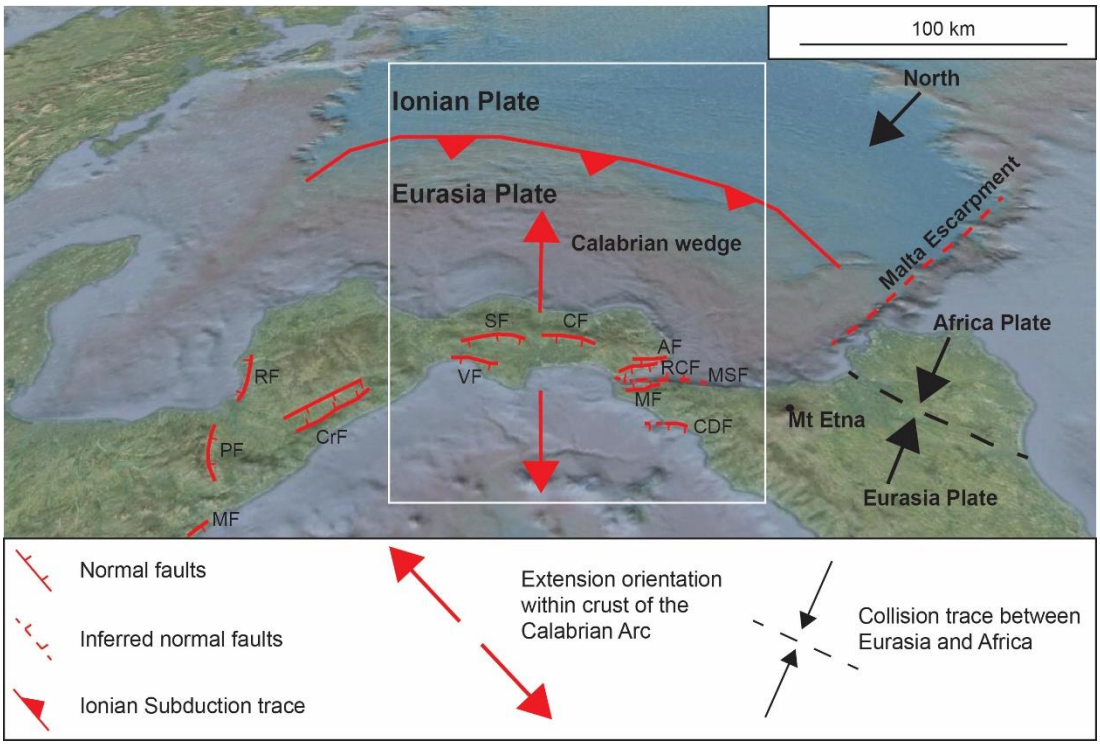

Figure 9.7: *Tectonic sketch of the Calabrian Arc showing the Ionian slab trace and the normal faults modelled for Coulomb Stress Changes calculations (white square).*

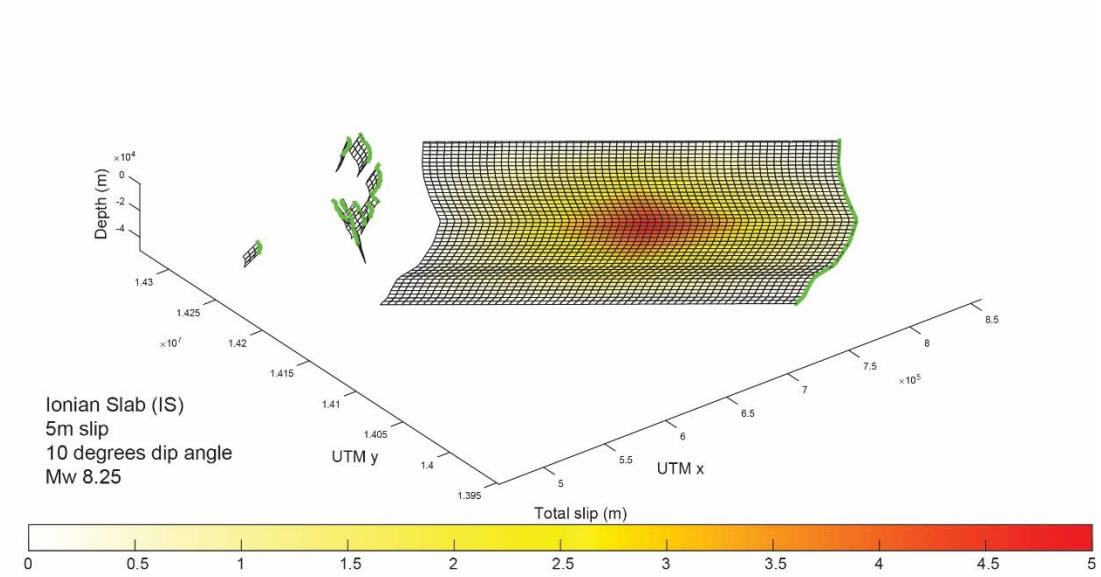
Depth (m)
UTM y
UTM x
Ionian Slab (IS)
5m slip
10 degrees dip angle
Mw 8.25
Total slip (m)
0
0.5
1
1.5
2
2.5
3
3.5
4
4.5
5

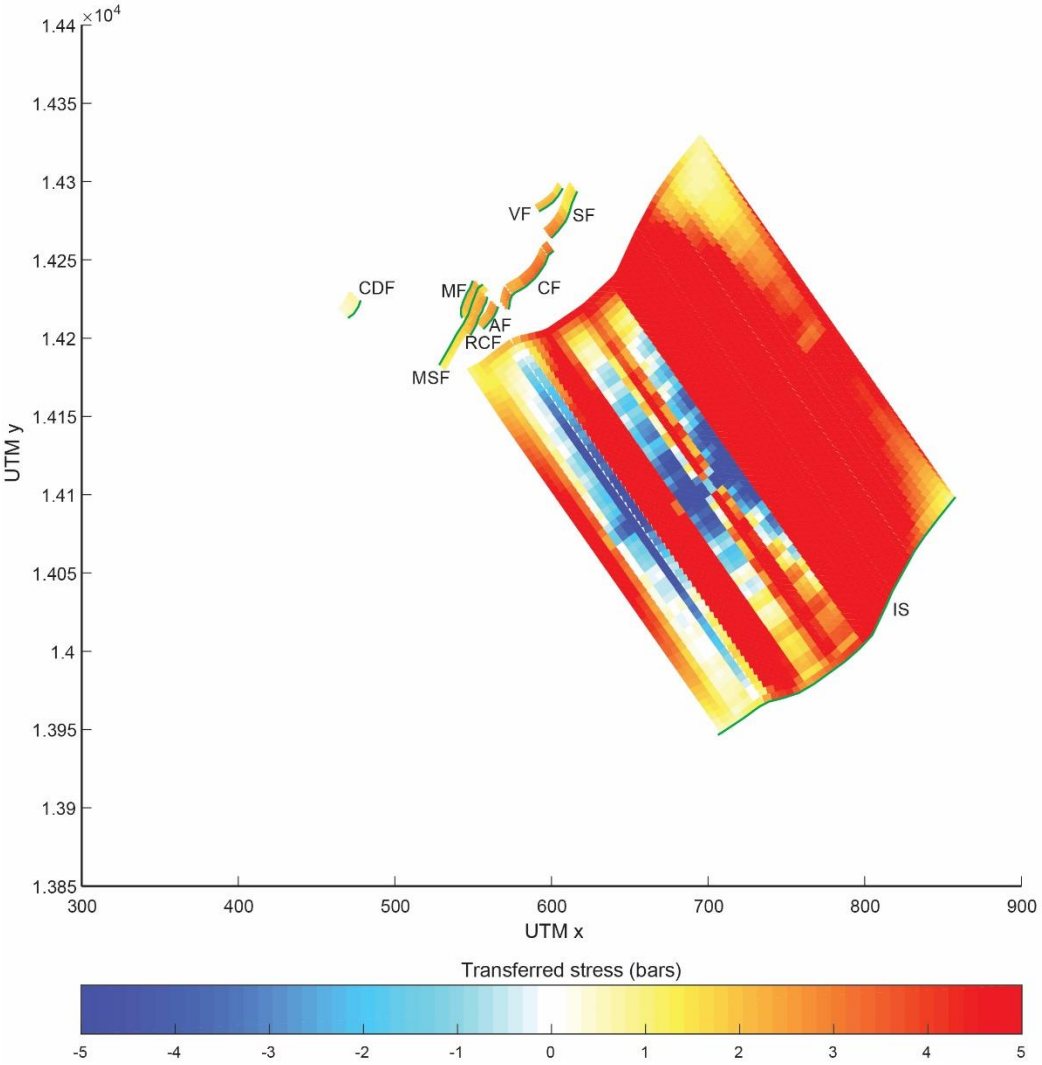
UTM y
UTM x
VF
SF
CF
MF
AF
RCF
CDF
MSF
IS
Transferred stress (bars)
-5
-4
-3
-2
-1
0
1
2
3
4
5

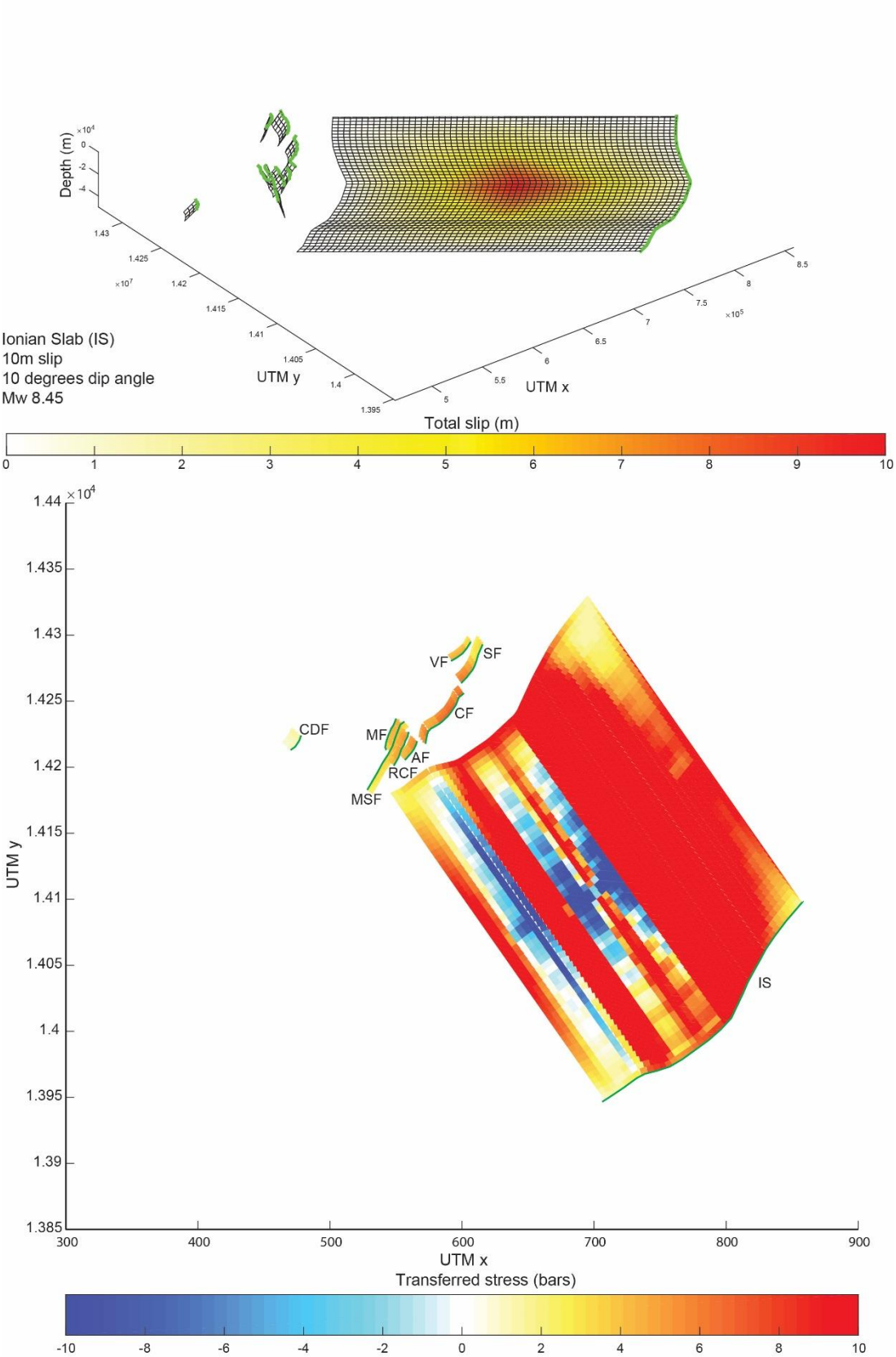
Depth (m)
UTM y
UTM x
Ionian Slab (IS)
10m slip
10 degrees dip angle
Mw 8.45
Total slip (m)
VF
SF
CF
CDF
MF
AF
RCF
MSF
IS
UTM y
UTM x
Transferred stress (bars)

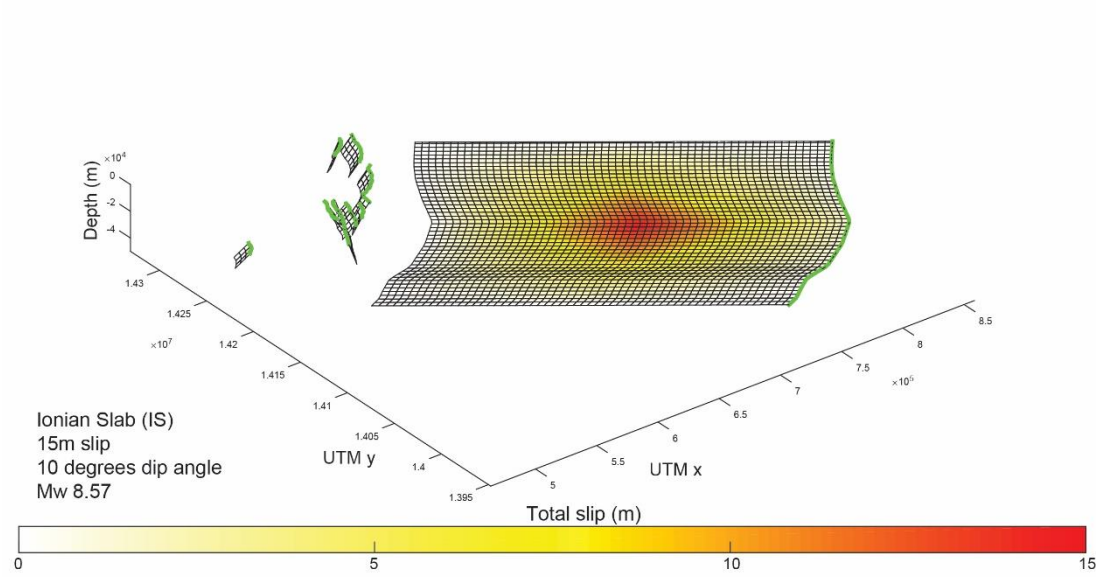
Depth (m)
UTM y
UTM x
Ionian Slab (IS)
15m slip
10 degrees dip angle
Mw 8.57
Total slip (m)
0
5
10
15

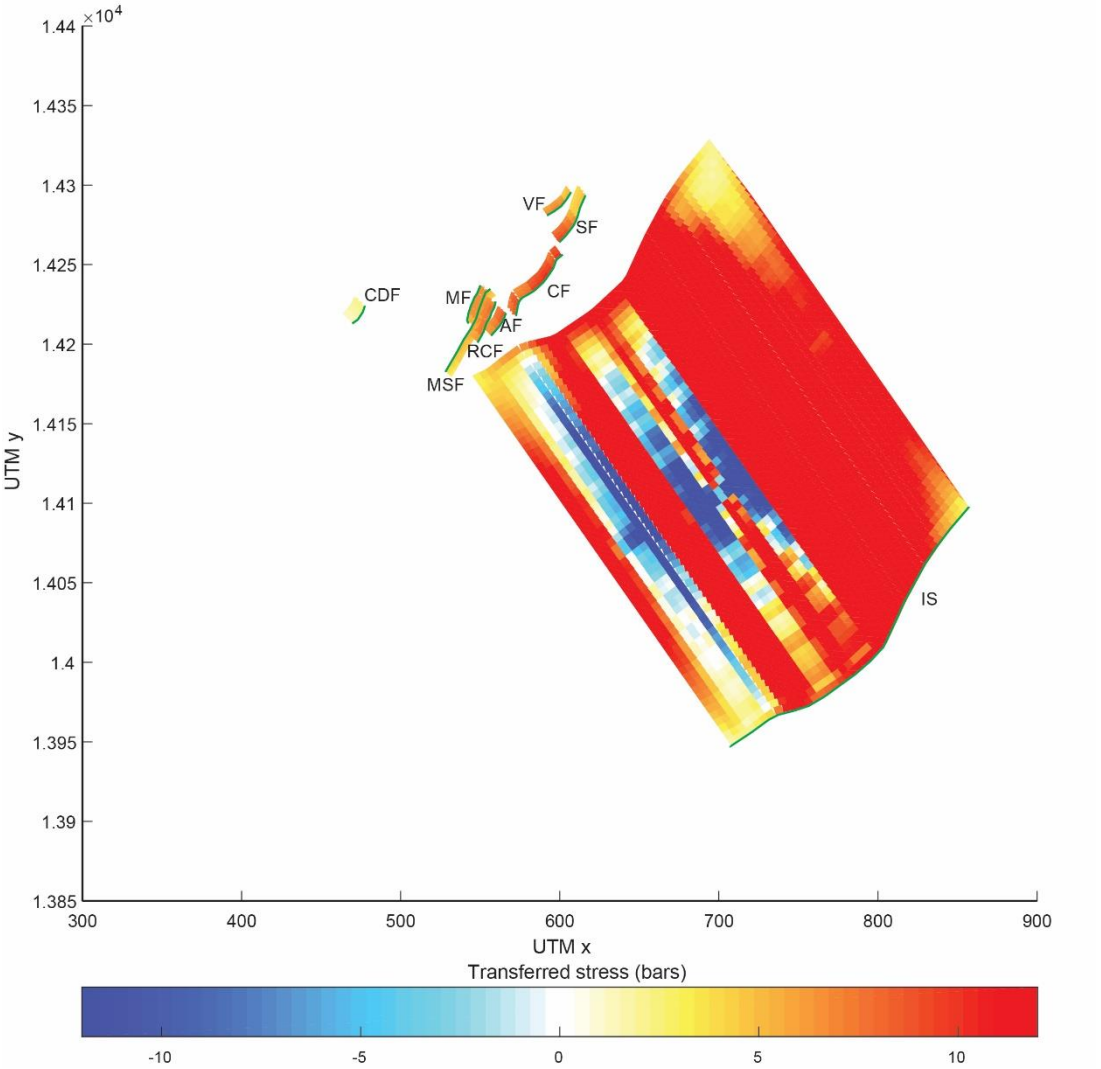
VF
SF
CF
MF
AF
RCF
MSF
CDF
IS
UTM y
UTM x
Transferred stress (bars)
-10
-5
0
5
10

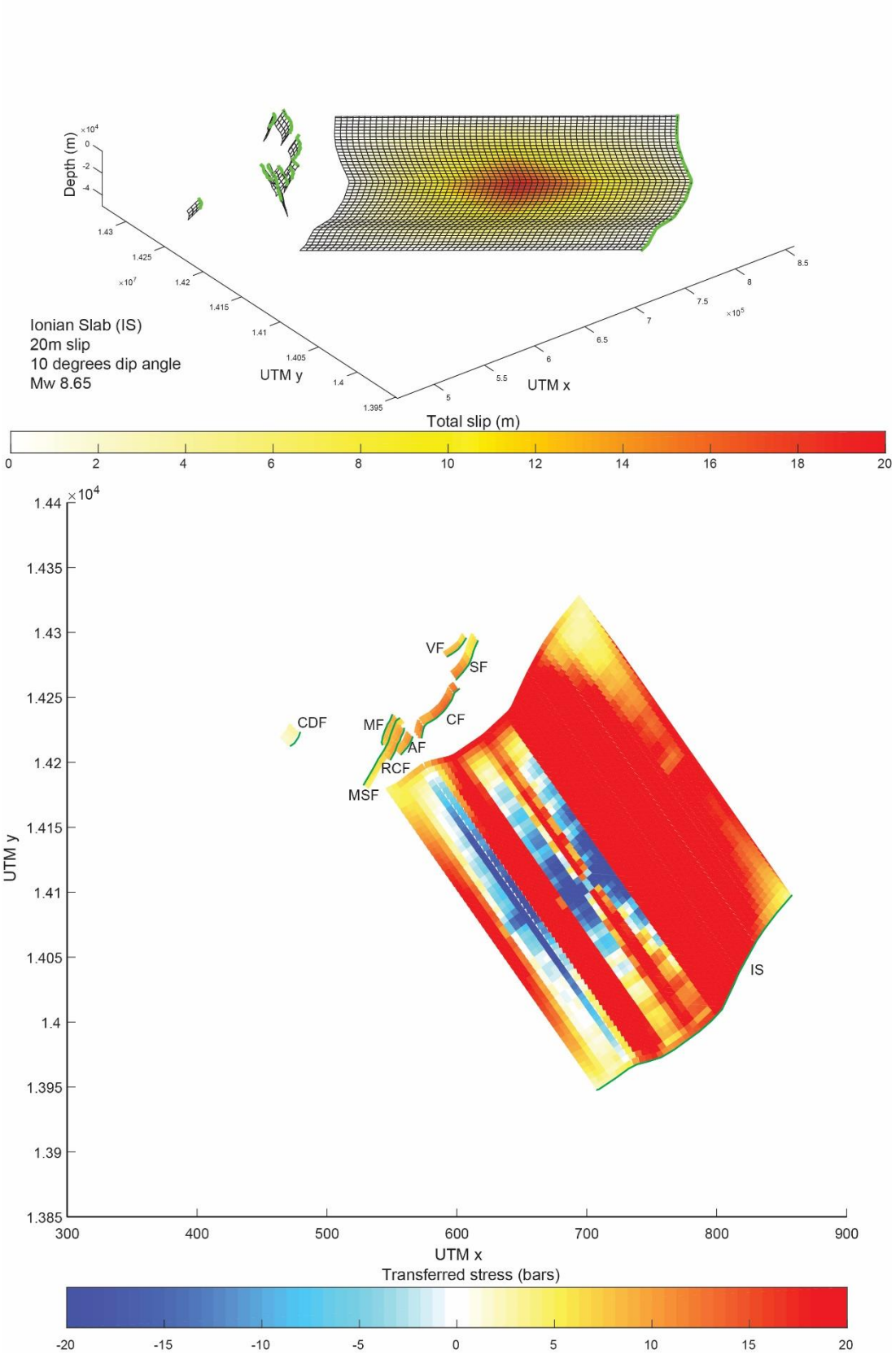

Figure 9.8: *Coulomb Stress Change calculations showing different megathrust earthquakes scenarios with differing slip at depth (5 m to 20 m, increased of 5 m per model). Note that an increasing magnitude is derived for each change in slip at depth. The upper panels show the slip distribution. The lower panels show Coulomb stress transfer onto receiver normal faults in the upper plate and stress transferred onto un-slipped or weakly-slipped patches on the subduction interface. The result is that upper plate normal faults are positively stressed with values of 0.5 bars to 20*

bars. IS: Ionian Slab, CDF: Capo D'Orlando Fault, MSF: Messina Strait Fault, RCF: Reggio Calabria Fault, AF: Armo Fault, CF: Cittanova Fault, SF: Serre Fault, VF: Vibo Fault, MF: Messina Fault.

Furthermore, potential seismic activity of the ISZ has been studied through an attempt to estimate a possible "long-term" slip-rate for the Ionian slab, with a value of 20 mm/yr, even though there are no known earthquakes with shallow dipping thrust focal mechanisms (Gutscher *et al.*, 2017); it has been concluded that there is a potential "seismic gap". The question arises as to what effect slip in this seismic gap would have on the upper plate normal faults described in this thesis.

In this section, by using the Coulomb 3.3 software (Toda *et al.*, 2011) and a new code for Coulomb Stress Change calculations (Mildon *et al.*, 2016), an attempt is made to model the Coulomb Stress Changes on the upper plate active normal faults mapped in this thesis if a subduction-related earthquake occurred on the Ionian slab (Figure 9.7). The method utilised is that map geometries from Google Earth were transferred into the Coulomb software using an approach developed by Mildon et al. (2016) that allows along-strike bends in faults to be included, in contrast to previous models that have only used planar fault geometries.

Figure 9.8 shows how active normal faults in southern Calabria and NE Sicily are positively stressed if an earthquake occurred in the Ionian slab (IS). Indeed, different seismic scenarios have been modelled assuming a 10 degrees dip angle for the IS as proposed by some (Selvaggi and Chiarabba, 1995; Chiarabba, Jovane and DiStefano, 2005b). The trace of the IS for Coulomb modelling was obtained from published works (Polonia *et al.*, 2013; Gutscher *et al.*, 2017). In particular, by assuming different slip at depth (5 m to 20 m) associated with different implied earthquake magnitudes, upper plate normal faults are positively stressed with values ranging between 0.5 bar and 15 bars. The overall outcome is that it appears that failure on the upper plate normal faults would be encouraged if a megathrust earthquake

occurred in the IS. This can also explain the overall uplift of the Calabrian Arc with marine terraces exceptionally outcropping on hangingwalls of normal faults as shown in this thesis, if the uplift is related to successive seismic events on the subduction interface.

The increase in Coulomb stress for upper crustal normal faults when the subduction interface slips has important implications for the seismic hazard. Positive transferred Coulomb stress is generally thought to bring earthquakes forward in time, affecting the T_{mean} which is an important parameter to calculate the "conditional probability" of having an earthquake (Pace, Bocchini and Boncio, 2014) explained in Chapter 2. This information should be combined with data on the elapsed time since the last earthquake on the upper plate normal faults. However, unfortunately this is poorly known for some of the faults, with perhaps only the 1905 earthquake on the Vibo Fault mentioned in the literature (see Chapter 4), the 1739 earthquake on the Capo D'Orlando Fault (see Chapter 5), and 1908 earthquake on the Messina Strait Fault (see Chapter 8) constrained to an extent. Future investigations such as palaeoseismological trenching is needed to further refine and improve the seismic hazard of the Calabria and NE Sicily.

In summary, it has been demonstrated that subduction-related earthquakes produced by the IS can bring upper plate active normal faults mapped in this thesis closer to failure, influencing the time-dependent seismic hazard of southern Italy. Suggested future works such as palaeoseismological investigations to unveil when the last earthquake occurred on these faults is suggested to improve the knowledge of seismic hazard for this region.

9.5. Future works

In this section, suggested future work will be stated based on findings from this thesis.

This thesis has demonstrated the importance of critically investigating the ages of palaeoshorelines if tectonic implications and the associated seismic hazard for a subduction zone and the associated deforming overriding plate are to be derived by studying sequences of deformed palaeoshorelines. A common problem when sequences of deformed palaeoshorelines are studied is the lack of dated horizons (Roberts *et al.*, 2013; Meschis *et al.*, 2018; Pedoja *et al.*, 2018). Clearly more absolute dating is needed. A combined approach using OSL dates on marine terrace sediments, U/Th determinations of corals in those sediments, and *in situ* ^{36}Cl cosmogenic exposure dating of wave-cut platforms is perhaps the only way to provide regional coverage of absolute ages, although this thesis has illustrated the problems and advantages of using U/Th and ^{36}Cl. However, perhaps more importantly in the short term, there is an urgent need to review of ages of palaeoshorelines defined using a "sequential correlation" approach, by adopting the "synchronous correlation" approach, which is considered herein to be more robust because (a) it assigns ages to un-dated palaeoshorelines taking into account the "overprinting problem" in regions with low uplift rates (see Chapter 2 for further details), (b) has quality control built in, with values of R^2 for linear correlation between measured and predicted palaeoshorelines elevations, and the check that prominent sea-level highstands ought to be included in any correlation. This "synchronous correlation" approach is relatively easy to use and major new insights into active uplift and tectonic deformation could be made rapidly, whilst waiting for absolute age controls from OSL, U/Th and ^{36}Cl.

The thesis has also emphasised the important role played by fault interaction. It is suggested that future work should move away from studying individual faults in isolation, and

move towards assessing how neighbouring faults interact, and modify their slip-rates through time to accommodate the regional extension, which is presumably constant in rate over time scales such as the late Quaternary. For example, it has been demonstrated that the Vibo Fault (Chapter 4) and the Capo D'Orlando Fault (Chaper 5) have constant slip-rates over the Late Quaternary, shown by studying tectonically-deformed marine terraces on their hangingwalls and footwalls. Because of their rates only partially accommodate the regional rate of ongoing extension within the Calabrian Arc (Serpelloni *et al.*, 2005), more normal faulting activity is implied only faults across strike which are at present poorly known. This suggest more investigations of offshore faults is needed when planning additional seismic surveys to image crustal deformation offshore. A point of interest is that the constant slip-rates measured on the Vibo and Capo D'Orlando faults may suggest relatively weak interaction with any fault that are found offshore. For another example, presented in Chapter 7, it has been demonstrated for the first time that slip rates on the Messina Strait Fault, the Reggio Calabria Fault and the Armo Fault have changed through time (since 50 ka) in order to partially accommodate the ongoing extension of the Messina Strait (Serpelloni *et al.*, 2005) where a prominent engineering project such as "il Ponte sullo Stretto" (*the Bridge on the Strait*) have been planned. This thesis shows for the first time that slip-rates on these faults have changed synchronously, showing an acceleration of slip for the Messina Strait Fault at ~50 ka, concomitant with a slip-rate deceleration for the Reggio Calabria Fault and the Armo Fault. This is suggested to provide evidence for relatively strong interaction within the fault system. For this reason, more investigations offshore with detailed seismic surveys across-strike these faults can help to understand if other active faults have been accommodating the ongoing extension with rates varying through time. Moreover, Coulomb stress changes investigations

are needed to better understand if the above-mentioned fault interaction is, for instance, due to slip on the Messina Strait Fault negatively stressing the Reggio Calabria Fault and the Armo Fault, implying a decreasing of fault slipping on these faults and *vice versa*, Finally, a speculative relationship ought to be investigated. It is interesting to note that the slip-rate on the Messina Strait Fault increased at ~50 ka, at a time (~100-50) ka when mapped eruptive deposits from Mt. Etna become more "island-arc magmatic source" (more "explosive" activity) compared to mantle-plume type (Schiano *et al.*, 2001). This may suggest a relationship between the ongoing extension on the Messina Strait possibly due to the mantle-upwelling under the continental crust (Gvirtzman and Nur, 1999b), the slab rollback and the volcanic activity of the most active volcano in Europe, but study of this has been beyond the scope of this thesis.

Furthermore, although there is an ongoing debate about the potential seismic activity of the Ionian Slab (Goes *et al.*, 2004; Serpelloni *et al.*, 2005, 2007; Palano *et al.*, 2012; Gutscher *et al.*, 2017) (Section 9.4), it has been demonstrated that if a mega-thrust earthquake occurred on the Ionian Slab, the active normal faults of the upper plate studied in this thesis would be positively stressed and brought closer to failure, affecting the T_{mean} of each fault. This suggests that more investigations such as palaeoseismological studies (trenches for instance) are needed in order to find the elapsed time for each fault (the time since the investigated fault has produced the last earthquake). This would strongly improve calculations for the seismic hazard, explained in Chapter 2, suggesting a new geography of the seismic hazard in southern Italy.

Also, in this thesis not all of the major active Quaternary faults in the Calabrian arc have been investigated. For instance, in Figure 2.1 (Chapter 2), major Quaternary normal

faults are stated such as the Cittanova Fault (CF), the Serre Fault (SF), the Crati Fault (CrF) and the Maratea Fault (MrF), however, it is still unclear if their rates are constant (or fluctuating) through time. This could suggest new investigations of palaeoshorelines outcropping on their footwalls and hangingwalls, considering that are located within the Calabrian Arc, which is an uplifting region since the Lower/Middle Pleistocene (Malinverno and Ryan, 1986).

A final point is that this thesis has shown that a great deal of information can be gleaned from study of sequences of deformed palaeoshorelines. Despite the fact that many coastal regions in the Mediterranean and elsewhere have their geomorphology and stratigraphic development controlled by active faults, seismic hazard studies and studies of tectonic processes are dominated by concentration on datasets mainly comprised of historical earthquake data and geodetic measurements. Such data are valuable, but it is important to note that they only cover a few decades to a few centuries at best, and in many examples lack the detail that can provide information on spatial variability in deformation rates at the scale of individual active faults. It is crucial to understand this spatial variation, such as that mapped in this thesis (Figure 9.1), because without it understanding of the full tectonic and seismic hazard significance of mapped uplift rates values is not possible. This thesis suggests that sequences of deformed palaeoshorelines are relatively under-studied compared with datasets dealing with historical earthquake data and geodetic measurements. This is perhaps mainly due to the lack of absolute dates and relatively poor correlations between sea-level highstands and mapped palaeoshoreline made using a "sequential correlation" approach. The overall impact of this thesis is that it has provided a new approach, combining novel absolute dating from U/Th and ^{36}Cl with "synchronous correlation". It is hoped that this thesis will promote

work on deformed palaeoshorelines using this approach, so that this avenue of research is no longer under-studied.

Chapter 10: Conclusions

In this thesis, a number of topics have been addressed relating to the active tectonics of the Calabrian Arc (southern Italy). In particular, attention has focussed on active crustal deformation in the form of normal faulting and forebulge uplift, with measurements made of the rates of deformation over the Late Quaternary. In this chapter, conclusions are briefly presented recalling the initial scientific questions stated in Chapter 1.

Active normal faulting and ongoing continental convergence activity have been mapped by investigating tectonically-deformed uplifted Late Quaternary palaeoshorelines and their associated marine terraces within the Calabrian Arc, which represents the overriding plate of the Ionian Subduction Zone in southern Italy. By attempting to gain absolute dates for palaeoshorelines using techniques such as U/Th dating on corals, and *in situ* ^{36}Cl cosmogenic exposure dating on wave-cut platforms cut into limestone, alongside utilisation of available dated palaeoshorelines in the literature, it has been possible to drive a synchronous correlation approach that allows refinement of ages for un-dated palaeoshorelines, and consequently, uplift rates associated with long-term slip-rates on faults.

This thesis has demonstrated that uplift rates mapped within the upper plate of the Ionian Subduction Zone (ISZ) are dominated by the crustal deformation in the overriding plate of the ISZ, in the form of active normal faults such as the Vibo Fault (Chapter 4), the Capo D'Orlando Fault (Chapter 5), the Messina Strait Fault, the Reggio Calabria Fault and the Armo Fault (Chapter 7). Furthermore, it has been demonstrated the uplift rates within the foreland region are affected by forebulge process (Chapter 6) due to the ongoing active convergence between Africa and Eurasia occurring in SE Sicily.

This thesis has demonstrated that uplift rate values vary along the strike of major Quaternary faults within the Calabrian Arc, implying that these faults ought to be considered active, even though no Holocene activity has been mapped.

Values of fault-related uplift rates have been mapped over the Late Quaternary. Constant fault-related uplift rates through time have been mapped in Chapter 4, 5, and 6. For these examples the measured rates of deformation are not great enough to accommodate the extension measured with GPS. If deformation rates measured over a few decades with GPS represent longer-term activity, other active faults are required across strike. However, no active faults are obvious in close proximity across strike, suggesting that constant slip-rates may be the results of relatively weak across strike fault interaction. The location of the implied across strike active faults remains a subject for future work. In contrast, varying fault-related uplift rates through time (since 50 ka) have been mapped within the Messina Strait, which contains the closely-spaced MSF, MF and AF, implying faulting interaction over the Late Quaternary (Chapter 7).

Elastic half-space modelling of a 1907-1909 geodetic levelling dataset has identified the fault that ruptures, and allowed its dip and coseismic slip to be determined. The Messina Strait Fault, ruptured with the modelling implies complete rupture of the 53 km fault length, with a 70^{o} dip to the east and 5 m slip maximum at depth.

Finally, this thesis has demonstrated that prominent crustal deformation due to the seismic activity of major Quaternary faults in the upper plates of subduction zones has to be taken into account and subtracted if observations of uplift from upper plates are used to estimate slip distribution on subduction interfaces (Chapter 8 and 9).

Further detailed conclusions are summarised below:

1. Values of uplift rates that are constant through time have been mapped in the hangingwall of the Vibo Fault. These values vary along the strike of the fault from ~0.45 mm/yr in centre of the fault to ~1.75 mm/yr beyond the tip, implying that the Vibo Fault is active (Chapter 4)
2. For the first time, a long-term fault slip-rate of ~1 mm/yr has been derived for the Vibo Fault by correlating a palaeoshoreline from the hangingwall to the footwall (Chapter 4). Furthermore, a new T_{mean} of ~ 1000 years has been calculated for this fault.
3. Refined uplift rates have been mapped in the hangingwall of the Capo D'Orlando Fault, NE Sicily, with values of ~ 0.35 mm/yr in centre of the fault to 0.89 mm/yr beyond the tip, implying that this fault is active (Chapter 5).
4. For the first time, a slip-rate for the Capo D'Orlando Fault of ~ 0.63 mm/yr has been estimated over the last 340 ka, again by correlating a palaeoshoreline from the hangingwall to the footwall, and an associated Tmean of ~ 820 years is calculated (Chapter 5).
5. For the first time, forebulge-related uplift rates have been mapped in the foreland region of SE Sicily. Constant uplift rates through time are constrained, with rates varying from north, with values of ~ 0.41 mm/yr to the south and values of 0.16 mm/yr in the south, suggesting that the convergence between Africa and Eurasia is active and partially accommodated by the Sicilian Basal Thrust (Chapter 6).
6. Uplift rate values varying along the strike of the Messina Strait Fault, the Reggio Calabria Fault and the Armo Fault have been mapped. For the first time, changing uplift rates through time, since 50 ka, have been mapped for these faults. In

particular, data from the footwall of Messina Strait fault suggest along strike variation in uplift rate of 0.5 mm/yr to 0.8 mm/yr before 50 ka; since 50 ka along strike variation of 1.3 mm/yr to 2 mm/yr is implied. In the hangingwall of the Reggio Calabria Fault uplift of 0.55 mm/yr to 0.9 mm/yr is implied before 50 ka, with 1.325 mm/yr to 2mm/yr after 50 ka. In the hangingwall of the Armo Fault, 0.56 mm/yr to 0.85 mm/yr uplift rate if implied before 50 ka, with 1.45 mm/yr to 2.2 mm/yr after 50 ka (Chapter 7).

7. For the first time, slip-rates on the Messina Strait Fault, the Reggio Calabria Fault and the Armo Fault have been mapped with the associated T_{mean}. In particular, a slip-rate value of 0.38 mm/yr has been derived for the Messina Strait Fault over the last 50 ka with an associated T_{mean} of ~ 1315 years. A slip rate value of 0.35 mm/yr has been derived for the Reggio Calabria Fault over the last 50 ka with associated T_{mean} of (i) ~850 years if only the onshore segment is considered and ~2850 years if the possible offshore continuation (~25 km long) is considered. A slip rate value of 0. 31 mm/yr has been derived for the last 50 ka for the Armo Fault with an associated T_{mean} of ~ 1300 years (Chapter 7).
8. A 1907 – 1909 geodetic levelling datasets has been modelled using a fault embedded in half-elastic space using Coulomb 3.3 software. The results show that the Messina Strait Fault seems to be the seismogenic source of the 1908 Mw 7.1 earthquake, most destructive earthquake recorded in Europe last century. For the first time, after a ~110 yrs long debate, it has been demonstrated that the 1908 Messina Earthquake has been produced by a normal fault with a dip angle of 70 degrees to the east and 5 m of slip at depth (Chapter 8).

9. This thesis has shown that a great deal of information can be gleaned from study of sequences of deformed palaeoshorelines, however seismic hazard studies and studies of tectonic processes are dominated by concentration on datasets mainly comprised of historical earthquake data and geodetic measurements. This thesis suggests that sequences of deformed palaeoshorelines are relatively under-studied compared with historical and geodetic datasets. However, the overall impact of this thesis is that it has provided a new approach, combining novel absolute dating from U/Th and ^{36}Cl with "synchronous correlation". It is hoped that this thesis will promote work on deformed palaeoshorelines using this approach, so that this avenue of research is no longer under-studied.

Bibliography

Akinci, A., Malagnini, L. and Sabetta, F. (2010) 'Characteristics of the strong ground motions from the 6 April 2009 L'Aquila earthquake, Italy', *Soil Dynamics and Earthquake Engineering*. Elsevier, 30(5), pp. 320–335. doi: 10.1016/j.soildyn.2009.12.006.

Aloisi, M., Bruno, V., Cannavo, F., Ferranti, L., Mattia, M. and Monaco, C. (2013) 'Are the source models of the M 7.1 1908 Messina Straits earthquake reliable? Insights from a novel inversion and sensitivity analysis of levelling data" by Aloisi et al. (2012)", *Geophysical Journal International*, 192, pp. 1025–1041. doi: https://doi.org/10.1093/gji/ggs062.

Aloisi, M., Bruno, V., Cannavo, F., Ferranti, L., Mattia, M. and Monaco, C. (2014) 'Reply to "Comments on the paper 'Are the source models of the M 7.1 1908 Messina Straits earthquake reliable? Insights from a novel inversion and sensitivity analysis of levelling data' by Aloisi et al. (2012)"', *Geophysical Journal International*, 197(3), pp. 1403–1409. doi: 10.1093/gji/ggu116.

Amoruso, A., Crescentini, L. and Scarpa, R. (2002) 'Source parameters of the 1908 Messina Straits, Italy, earthquake from geodetic and seismic data', *Journal of Geophysical Research: Solid Earth*, 107(B4), p. ESE 4-1-ESE 4-11. doi: 10.1029/2001JB000434.

Andersen, M. B., Stirling, C. H., Potter, E.-K., Halliday, A. N., Blake, S. G., McCulloch, M. T., Ayling, B. F. and O'Leary, M. (2008) 'High-precision U-series measurements of more than 500,000 year old fossil corals', *Earth and Planetary Science Letters*, 265(1–2), pp. 229–245. doi: 10.1016/j.epsl.2007.10.010.

Anderson, H. and Jackson, J. (1987) 'The deep seismicity of the Tyrrhenian Sea', *Geophysical Journal International*, 91(3), pp. 613–637. doi: 10.1111/j.1365-246X.1987.tb01661.x.

Antonioli, F., Ferranti, L., Lambeck, K., Kershaw, S., Verrubbi, V. and Dai Pra, G. (2006)

'Late Pleistocene to Holocene record of changing uplift rates in southern Calabria and northeastern Sicily (southern Italy, Central Mediterranean Sea)', *Tectonophysics*, 422(1–4), pp. 23–40. doi: 10.1016/j.tecto.2006.05.003.

Antonioli, F., Kershaw, S., Renda, P., Rust, D., Belluomini, G., Cerasoli, M., Radtke, U. and Silenzi, S. (2006) 'Elevation of the last interglacial highstand in Sicily (Italy): A benchmark of coastal tectonics', *Quaternary International*, 145–146, pp. 3–18. doi: 10.1016/j.quaint.2005.07.002.

Antonioli, F., Kershaw, S., Rust, D. and Verrubbi, V. (2003) 'Holocene sea-level change in Sicily and its implications for tectonic models: New data from the Taormina area, northeast Sicily', *Marine Geology*, 196(1–2), pp. 53–71. doi: 10.1016/S0025-3227(03)00029-X.

Argnani, A., Brancolini, G., Bonazzi, C., Rovere, M., Accaino, F., Zgur, F. and Lodolo, E. (2009) 'The results of the Taormina 2006 seismic survey: Possible implications for active tectonics in the Messina Straits', *Tectonophysics*, 476(1–2), pp. 159–169. doi: 10.1016/j.tecto.2008.10.029.

Argnani, A., Brancolini, G., Rovere, M., Accaino, F., Zgur, F., Grossi, M., Fanzutti, F., Visnovic, P., Sorgo, D., Lodolo, E., Bonazzi, C. and Mitchell, N. (2008) 'Hints on active tectonics in the southern Messina Straits: Preliminary results from the TAORMINA-2006 seismic cruise', *Bollettino di Geofisica Teorica ed Applicata*, 49(2), pp. 163–176.

Armijo, R., Lyon-Caen, H. and Papanastassiou, D. (1992a) 'East-west extension and Holocene normal-fault scarps in the Hellenic arc', *Geology*, 20(6), pp. 491–494. doi: 10.1130/0091-7613(1992)020<0491:EWEAHN>2.3.CO;2.

Armijo, R., Lyon-Caen, H. and Papanastassiou, D. (1992b) 'East-west extension and

Holocene normal-fault scarps in the Hellenic arc', *Geology*, 20(6), p. 491. doi: 10.1130/0091-7613(1992)020<0491:EWEAHN>2.3.CO;2.

Armijo, R., Meyer, B., King, G. C. P., Rigo, A. and Papanastassiou, D. (1996) 'Quaternary evolution of the Corinth Rift and its implications for the Late Cenozoic evolution of the Aegean', *Geophysical Journal International*. Blackwell Publishing Ltd, 126(1), pp. 11–53. doi: 10.1111/j.1365-246X.1996.tb05264.x.

Azzaro, R., Barbano, M. S., Camassi, R., D'Amico, S., Mostaccio, A., Piangiamore, G. and Scarfì, L. (2004) 'The earthquake of 6 September 2002 and the seismic history of Palermo (Northern Sicily, Italy): Implications for the seismic hazard assessment of the city', *Journal of Seismology*, 8(4), pp. 525–543. doi: 10.1007/s10950-004-8930-2.

Balescu, S., Dumas, B., Guérémy, P., Lamothe, M., Lhénaff, R. and Raffy, J. (1997) 'Thermoluminescence dating tests of Pleistocene sediments from uplifted marine shorelines along the southwest coastline of the Calabrian Peninsula (southern Italy)', *Palaeogeography, Palaeoclimatology, Palaeoecology*, 130(1–4), pp. 25–41. doi: 10.1016/S0031-0182(96)00119-8.

Bally, A. . (1983) 'Seismic expression of structural styles', *AAPG Studies in geology*, 15(3).

Baratta, M. (1910) 'La catastrofe sismica calabro-messinese (28 dicembre 1908): relazione alla Società geografica italiana'. La Società Geografica Italiana.

Basili, R., Valensise, G., Vannoli, P., Burrato, P., Fracassi, U., Mariano, S., Tiberti, M. M. and Boschi, E. (2008) 'The Database of Individual Seismogenic Sources (DISS), version 3: Summarizing 20 years of research on Italy's earthquake geology', *Tectonophysics*, 453(1–4), pp. 20–43. doi: 10.1016/j.tecto.2007.04.014.

Bebout, E., Scholl, W., Kirby, H. and Platt, P. (1996) *Subduction Top to Bottom*. Edited by G.

E. Bebout, D. W. Scholl, S. H. Kirby, and J. P. Platt. Washington, D. C.: American Geophysical Union (Geophysical Monograph Series). doi: 10.1029/GM096.

Ben-Avraham, Z. and Grasso, M. (1991) 'Crustal structure variations and transcurrent faulting at the eastern and western margins of the eastern Mediterranean', *Tectonophysics*, 196(3–4), pp. 269–277. doi: 10.1016/0040-1951(91)90326-N.

Benioff, H. (1949) 'Seismic evidence for the fault origin of oceanic deeps', *Geological Society of America Bulletin*, 60(12), pp. 1837–1856. doi: 10.1130/0016-7606(1949)60[1837:SEFTFO]2.0.CO;2.

Bennett, R. A., Friedrich, A. M. and Furlong, K. P. (2004) 'Codependent histories of the San Andreas and San Jacinto fault zones from inversion of fault displacement rates', *Geology*, 32(11), p. 961. doi: 10.1130/G20806.1.

Bennett, R. A., Wernicke, B. P., Niemi, N. A., Friedrich, A. M. and Davis, J. L. (2003) 'Contemporary strain rates in the northern Basin and Range province from GPS data', *Tectonics*, 22(2). doi: 10.1029/2001TC001355.

Bianca, M., Catalano, S., De Guidi, G., Gueli, A. ., Monaco, C., Ristuccia, G. M., Stella, G., Tortorici, G., Tortorici, L. and Troja, S. O. (2011) 'Luminescence chronology of Pleistocene marine terraces of Capo Vaticano peninsula (Calabria, Southern Italy)', *Quaternary International*. Elsevier Ltd and INQUA, 232(1–2), pp. 114–121. doi: 10.1016/j.quaint.2010.07.013.

Bianca, M., Monaco, C., Tortorici, L. and Cernobori, L. (1999) 'Quaternary normal faulting in southeastern Sicily (Italy): a seismic source for the 1693 large earthquake', *Geophysical Journal International*, 139(2), pp. 370–394. doi: 10.1046/j.1365-246x.1999.00942.x.

Billi, A., Porreca, M., Faccenna, C. and Mattei, M. (2006) 'Magnetic and structural

constraints for the noncylindrical evolution of a continental forebulge (Hyblea, Italy)', *Tectonics*, 25(3), p. n/a-n/a. doi: 10.1029/2005TC001800.

Binnie, A., Dunai, T. J., Binnie, S. A., Victor, P., González, G. and Bolten, A. (2016) 'Accelerated late quaternary uplift revealed by 10 Be exposure dating of marine terraces, Mejillones Peninsula, northern Chile', *Quaternary Geochronology*, 36, pp. 12–27. doi: 10.1016/j.quageo.2016.06.005.

Bloom, A. L. (1974) 'Geomorphology of reef complexes', *The Society of economic paleontologists and mineralogists (SEPM)*, SP18. Available at: http://archives.datapages.com/data/sepm_sp/SP18/Geomorphology_of_Reef_Complexes.htm.

Boccaletti, M., Ciaranfi, N., Cosentino, D., Deiana, G., Gelati, R., Lentini, F., Massari, F., Moratti, G., Pescatore, T., Ricci Lucchi, F. and Tortorici, L. (1990) 'Palinspastic restoration and paleogeographic reconstruction of the peri-Tyrrhenian area during the Neogene', *Palaeogeography, Palaeoclimatology, Palaeoecology*, 77(1), pp. 41-IN13. doi: 10.1016/0031-0182(90)90097-Q.

Bordoni, P. and Valensise, G. (1998) 'Deformation of the 125 ka marine terrace in Italy: tectonic implications', *Geological Society, London, Special Publications*, 146(1), pp. 71–110. doi: 10.1144/GSL.SP.1999.146.01.05.

Boschi, E., Pantosti, D. and Valensise, G. (1989) 'Modello di sorgente per il terremoto di Messina del 1908 ed evoluzione recente dell'area dello Stretto', *Atti VIII Convegno GNGTS, Roma 1989 (1989)*, pp. 245–258.

Bosi, C., Carobene, L. and Sposato, A. (1996) 'Il ruolo dell'eustatismo nella evoluzione geologica nell'area mediterranea', *Memorie della Societa' Geologica Italiana*, 51, pp. 363–

382.

Bottari, A., Carapezza, E., Carapezza, M., Carveni, P., Cefali, F., Lo Giudice, E. and Pandolfo, C. (1986) 'The 1908 Messina Strait earthquake in the regional geostructural framework', *Journal of Geodynamics*, 5(3–4), pp. 275–302. doi: 10.1016/0264-3707(86)90010-4.

Boulton, S. J. and Stewart, I. S. (2015) 'Holocene coastal notches in the Mediterranean region: Indicators of palaeoseismic clustering?', *Geomorphology*. Elsevier B.V., 237, pp. 29–37. doi: 10.1016/j.geomorph.2013.11.012.

Burchfiel, B. C. (1980) 'Eastern European Alpine system and the Carpathian orocline as an example of collision tectonics', *Tectonophysics*, 63(1–4), pp. 31–61. doi: 10.1016/0040-1951(80)90106-7.

Burollet, P. F., Mugniot, J. M. and Sweeney, P. (1978) 'The Geology of the Pelagian Block: The Margins and Basins off Southern Tunisia and Tripolitania', in *The Ocean Basins and Margins*. Boston, MA: Springer US, pp. 331–359. doi: 10.1007/978-1-4684-3039-4_6.

Capuano, B. Y. P., Natale, G. D. E., Gasparini, P., Pingue, F. and Scarpa, R. (1988) 'A model for the 1908 Messina Straits (Italy) earthquake by inversion of levelling data', *Bulletin of the Seismological Society of America*, 78(6), pp. 1930–1947. Available at: https://pubs.geoscienceworld.org/ssa/bssa/article-abstract/78/6/1930/119128.

Caputo, R. (2007) 'Sea-level curves: Perplexities of an end-user in morphotectonic applications', *Global and Planetary Change*, 57(3–4), pp. 417–423. doi: 10.1016/j.gloplacha.2007.03.003.

Carobene, L. and Dai Pra, G. (1991) 'Middle and Upper Pleistocene sea level highstands along the Tyrrhenian coast of Basilicata (Southern Italy)', *Il Quaternario*, 4, pp. 173–202. Available at: http://www.aiqua.it/images/directory/1327416874Quaternario41apag.173-

202.pdf.

Catalano, R. and Sulli, A. (2006) 'Crustal image of the Ionian basin and accretionary wedge', *Bollettino di Geofisica Teorica ed Applicata*, 47(September), pp. 343–374.

Catalano, S. and De Guidi, G. (2003) 'Late Quaternary uplift of northeastern Sicily: Relation with the active normal faulting deformation', *Journal of Geodynamics*, 36(4), pp. 445–467. doi: 10.1016/S0264-3707(02)00035-2.

Catalano, S., De Guidi, G., Monaco, C., Tortorici, G. and Tortorici, L. (2003) 'Long-term behaviour of the late Quaternary normal faults in the Straits of Messina area (Calabrian arc): Structural and morphological constraints', *Quaternary International*, 101–102(1), pp. 81–91. doi: 10.1016/S1040-6182(02)00091-5.

Catalano, S., De Guidi, G., Monaco, C., Tortorici, G. and Tortorici, L. (2008) 'Active faulting and seismicity along the Siculo-Calabrian Rift Zone (Southern Italy)', *Tectonophysics*, 453(1–4), pp. 177–192. doi: 10.1016/j.tecto.2007.05.008.

Chapman, N., Berryman, K., Villamor, P., Epstein, W., Cluff, L. and Kawamura, H. (2014) 'Active Faults and Nuclear Power Plants', *Eos, Transactions American Geophysical Union*, 95(4), pp. 33–34. doi: 10.1002/2014EO040001.

Chappell, J. and Shackleton, N. J. (1986) 'Oxygen isotopes and sea level', *Nature*, 324(6093), pp. 137–140. doi: 10.1038/324137a0.

Chiarabba, C., De Gori, P. and Speranza, F. (2008) 'The southern Tyrrhenian subduction zone: Deep geometry, magmatism and Plio-Pleistocene evolution', *Earth and Planetary Science Letters*, 268(3–4), pp. 408–423. doi: 10.1016/j.epsl.2008.01.036.

Chiarabba, C., Jovane, L. and DiStefano, R. (2005a) 'A new view of Italian seismicity using 20 years of instrumental recordings', *Tectonophysics*, 395(3–4), pp. 251–268. doi:

10.1016/j.tecto.2004.09.013.

Chiarabba, C., Jovane, L. and DiStefano, R. (2005b) 'A new view of Italian seismicity using 20 years of instrumental recordings', *Tectonophysics*, 395(3–4), pp. 251–268. doi: 10.1016/j.tecto.2004.09.013.

Chiarabba, C. and Palano, M. (2017) 'Progressive migration of slab break-off along the southern Tyrrhenian plate boundary: Constraints for the present day kinematics', *Journal of Geodynamics*. Elsevier Ltd, 105, pp. 51–61. doi: https://doi.org/10.1016/j.jog.2017.01.006.

Chmeleff, J., von Blanckenburg, F., Kossert, K. and Jakob, D. (2010) 'Determination of the 10Be half-life by multicollector ICP-MS and liquid scintillation counting', *Nuclear Instruments and Methods in Physics Research Section B: Beam Interactions with Materials and Atoms*. Elsevier B.V., 268(2), pp. 192–199. doi: 10.1016/j.nimb.2009.09.012.

Cinque, A., De Pippo, T. and Romano, P. (1995) 'Coastal slope terracing and relative sea-level changes: deductions based on computer simulations', *Earth Surface Processes & Landforms*, 20(1), pp. 87–103. Available at: http://www.sciencedirect.com/science/article/B6WPY-3V4P94M-2M8/1/5c858b39c2b9d7d5332009e93f3e82a9.

Clarke, G. K. C. and Marshall, S. J. (2002) 'Isotopic balance of the Greenland Ice Sheet: modelled concentrations of water isotopes from 30,000 BP to present', *Quaternary Science Reviews*, 21(1–3), pp. 419–430. doi: 10.1016/S0277-3791(01)00111-1.

Collier, R. E. L., Leeder, M. R., Rowe, P. and Atkinson, T.C. (1992) 'Rates of tectonic uplift in the Corinth and Megara Basins, central Greece', *Tectonics*, 11(6), pp. 1159–1167.

Comerci, V., Vittori, E., Blumetti, A. M., Brustia, E., Di Manna, P., Guerrieri, L., Lucarini, M.

and Serva, L. (2015) 'Environmental effects of the December 28, 1908, Southern Calabria–Messina (Southern Italy) earthquake', *Natural Hazards*, 76(3), pp. 1849–1891. doi: 10.1007/s11069-014-1573-x.

Costanzi, G. (1910) *I risultati della revisione della livellazione in Calabria e in Sicilia dopo il terremoto del 1908*. Edited by Premiata tip. successori Fusi.

Cowgill, E., Gold, R. D., Xuanhua, C., Xiao-Feng, W., Arrowsmith, J. R. and Southon, J. (2009) 'Low Quaternary slip rate reconciles geodetic and geologic rates along the Altyn Tagh fault, northwestern Tibet', *Geology*, 37(7), pp. 647–650. doi: 10.1130/G25623A.1.

Cowie, P. A. and Roberts, G. P. (2001) 'Constraining slip rates and spacings for active normal faults', *Journal of Structural Geology*, 23(12), pp. 1901–1915. doi: 10.1016/S0191-8141(01)00036-0.

Cowie, P. a., Roberts, G. P., Bull, J. M. and Visini, F. (2012) 'Relationships between fault geometry, slip rate variability and earthquake recurrence in extensional settings', *Geophysical Journal International*, 189(1), pp. 143–160. doi: 10.1111/j.1365-246X.2012.05378.x.

Cowie, P. A. and Scholz, C. H. (1992) 'Displacement-length scaling relationship for faults: data synthesis and discussion', *Journal of Structural Geology*, 14(10), pp. 1149–1156. doi: 10.1016/0191-8141(92)90066-6.

Cowie, P. a., Scholz, C. H., Roberts, G. P., Faure Walker, J. P. and Steer, P. (2013) 'Viscous roots of active seismogenic faults revealed by geologic slip rate variations', *Nature Geoscience*. Nature Publishing Group, 3(November), pp. 10–14. doi: 10.1038/ngeo1991.

Cowie, P. A. and Shipton, Z. K. (1998) 'Fault tip displacement gradients and process zone dimensions', *Journal of Structural Geology*, 20(8), pp. 983–997. doi: 10.1016/S0191-

8141(98)00029-7.

Cowie, P., Underhill, J., Behn, M., Lin, J. and Gill, C. (2005) 'Spatio-temporal evolution of strain accumulation derived from multi-scale observations of Late Jurassic rifting in the northern North Sea: A critical test of models for lithospheric extension', *Earth and Planetary Science Letters*, 234(3–4), pp. 401–419. doi: 10.1016/j.epsl.2005.01.039.

Crémière, A., Lepland, A., Chand, S., Sahy, D., Condon, D. J., Noble, S. R., Martma, T., Thorsnes, T., Sauer, S. and Brunstad, H. (2016) 'Timescales of methane seepage on the Norwegian margin following collapse of the Scandinavian Ice Sheet', *Nature Communications*, 7(May), p. 11509. doi: 10.1038/ncomms11509.

Cucci, L. and Cinti, F. R. (1998) 'Regional uplift and local tectonic deformation recorded by the Quaternary marine terraces on the Ionian coast of northern Calabria (southern Italy)', *Tectonophysics*, 292(1–2), pp. 67–83. doi: 10.1016/S0040-1951(98)00061-4.

Cucci, L., Tertulliani, A., Nazionale, I., Sismologia, S. and Murata, V. (2006) 'I Terrazzi Marini Nell ' Area Di Capo Vaticano (Arco Calabro): Solo Un Record Di Sollevamento Regionale O Anche Di Deformazione Cosismica ?', *Il Quaternario*, 19(1), pp. 89–101.

Cultrera, F., Barreca, G., Scarfì, L. and Monaco, C. (2015) 'Fault reactivation by stress pattern reorganization in the Hyblean foreland domain of SE Sicily (Italy) and seismotectonic implications', *Tectonophysics*. Elsevier B.V., 661, pp. 215–228. doi: 10.1016/j.tecto.2015.08.043.

D'Agostino, N., Cheloni, D., Fornaro, G., Giuliani, R. and Reale, D. (2012) 'Space-time distribution of afterslip following the 2009 L'Aquila earthquake', *Journal of Geophysical Research: Solid Earth*, 117(B2), p. n/a-n/a. doi: 10.1029/2011JB008523.

D'Agostino, N., Jackson, J. A., Dramis, F. and Funiciello, R. (2001) 'Interactions between

mantle upwelling, drainage evolution and active normal faulting: an example from the central Apennines (Italy)', *Geophysical Journal International*, 147(2), pp. 475–497. doi: 10.1046/j.1365-246X.2001.00539.x.

D'Agostino, N. and Selvaggi, G. (2004) 'Crustal motion along the Eurasia-Nubia plate boundary in the Calabrian Arc and Sicily and active extension in the Messina Straits from GPS measurements', *Journal of Geophysical Research: Solid Earth*, 109(B11), p. n/a-n/a. doi: 10.1029/2004JB002998.

Darvill, C. M. (2013) 'Cosmogenic nuclide analysis', *Geomophological techniques*, 10(2008), pp. 1–25.

Dawers, N. and Underhill, J. (2000) 'The Role of Fault Interaction and Linkage in Controlling Synrift Stratigraphic Sequences: Late Jurassic, Statfjord East Area, Northern North Sea1', *AAPG Bulletin*, 84(1), pp. 45–64. doi: 10.1306/C9EBCD5B-1735-11D7-8645000102C1865D.

DeCelles, P. G. (2012) 'Foreland basin systems revisted: variations in response to tectonic settings', in Busby, C. and Azor, A. (eds) *Tectonics in Sedimentary Basins: Recent Advances*, p. 405–426. doi: https://doi.org/10.1002/9781444347166.ch20.

DeCelles, P. G. and Giles, K. A. (1996) 'Foreland basin systems', *Basin Research*, 8(2), pp. 105–123. doi: 10.1046/j.1365-2117.1996.01491.x.

Deligiannakis, G., Papanikolaou, I. D. and Roberts, G. (2018) 'Fault specific GIS based seismic hazard maps for the Attica region, Greece', *Geomorphology*. Elsevier B.V., 306, pp. 264–282. doi: 10.1016/j.geomorph.2016.12.005.

DeMets, C., Iaffaldano, G. and Merkouriev, S. (2015) 'High-resolution Neogene and Quaternary estimates of Nubia-Eurasia-North America Plate motion', *Geophysical*

Journal International, 203(1), pp. 416–427. doi: 10.1093/gji/ggv277.

De Stefani, C. (1910) 'La livellazione sul litorale calabro-siculo dopo il terremoto del 1908', *Bollettino della Società Geologica Italiana*, 29, pp. 223–231.

Dewey, J. F., Helman, M. L., Knott, S. D., Turco, E. and Hutton, D. H. W. (1989) 'Kinematics of the western Mediterranean', *Geological Society, London, Special Publications*, 45(1), pp. 265–283. doi: 10.1144/GSL.SP.1989.045.01.15.

Dia, A. ., Cohen, A. ., O'Nions, R. . and Jackson, J. . (1997) 'Rates of uplift investigated through 230Th dating in the Gulf of Corinth (Greece)', *Chemical Geology*, 138(3–4), pp. 171–184. doi: 10.1016/S0009-2541(97)00010-7.

Doglioni, C. (1995) 'Geological remarks on the relationships between extension and convergent geodynamic settings', *Tectonophysics*, 252(1–4), pp. 253–267. doi: 10.1016/0040-1951(95)00087-9.

Doglioni, C., Carminati, E., Cuffaro, M. and Scrocca, D. (2007) 'Subduction kinematics and dynamic constraints', *Earth-Science Reviews*, 83(3–4), pp. 125–175. doi: 10.1016/j.earscirev.2007.04.001.

Doglioni, C., Harabaglia, P., Merlini, S., Mongelli, F., Peccerillo, A. and Piromallo, C. (1999) 'Orogens and slabs vs. their direction of subduction', *Earth-Science Reviews*, 45(3–4), pp. 167–208. doi: 10.1016/S0012-8252(98)00045-2.

Doglioni, C., Ligi, M., Scrocca, D., Bigi, S., Bortoluzzi, G., Carminati, E., Cuffaro, M., D'Oriano, F., Forleo, V., Muccini, F. and Riguzzi, F. (2012) 'The tectonic puzzle of the Messina area (Southern Italy): Insights from new seismic reflection data', *Scientific Reports*, 2(1), p. 970. doi: 10.1038/srep00970.

Dolan, J. F., Bowman, D. D. and Sammis, C. G. (2007) 'Long-range and long-term fault

interactions in Southern California', *Geology*, 35(9), pp. 855–858. doi: 10.1130/G23789A.1.

Dumas, B., Gueremy, P., Hearty, P. J., Lhenaff, R. and Raffy, J. (1988) 'Morphometric analysis and amino acid geochronology of uplifted shorelines in a tectonic region near reggio Calambria, South Italy', *Palaeogeography, Palaeoclimatology, Palaeoecology*, 68(2–4), pp. 273–289. doi: 10.1016/0031-0182(88)90045-4.

Dumas, B., Gueremy, P., Lhenaff, R. and Raffy, J. (1981) 'Le soulèvement quaternaire de la Calabre méridionale', *Revue de Géologie Dynamique et de Géographie Physique Paris*, 23, pp. 27–40.

Dumas, B., Guérémy, P. and Raffy, J. (2005) 'Evidence for sea-level oscillations by the "characteristic thickness" of marine deposits from raised terraces of Southern Calabria (Italy)', *Quaternary Science Reviews*, 24(18–19), pp. 2120–2136. doi: 10.1016/j.quascirev.2004.12.011.

Dunai, T. (2010) *Cosmogenic Nuclides: Principles, concepts and applications in the Earth surface sciences*. Cambridge University Press.

Dutton, A., Scicchitano, G., Monaco, C., Desmarchelier, J. M., Antonioli, F., Lambeck, K., Esat, T. M., Fifield, L. K., McCulloch, M. T. and Mortimer, G. (2009) 'Uplift rates defined by U-series and 14C ages of serpulid-encrusted speleothems from submerged caves near Siracusa, Sicily (Italy)', *Quaternary Geochronology*, 4(1), pp. 2–10. doi: 10.1016/j.quageo.2008.06.003.

Edwards, R. L. (1988) *High precision thorium-230 ages of corals and the timing of sea level fluctuations in the late Quaternary*. California Institute of Technology. Available at: http://thesis.library.caltech.edu/4031/.

Edwards, R. L., Beck, J. W., Burr, G. S., Donahue, D. J., Chappell, J. M. A., Bloom, A. L., Druffel, E. R. M. and Taylor, F. W. (1993) 'A Large Drop in Atmospheric 14C/12C and Reduced Melting in the Younger Dryas, Documented with 230Th Ages of Corals', *Science*, 260(5110), pp. 962–968. doi: 10.1126/science.260.5110.962.

Ellsworth, W. L., Matthews, M. V., Nadeau, R. M., Nishenko, S. P., Reasenberg, P. A. and Simpson, R. . (1999) *A physically-based earthquake recurrence model for estimation of long-term earthquake probabilities*. US Geological Survey.

Faccenna, C., Becker, T. W., Miller, M. S., Serpelloni, E. and Willett, S. D. (2014) 'Isostasy, dynamic topography, and the elevation of the Apennines of Italy', *Earth and Planetary Science Letters*. Elsevier B.V., 407, pp. 163–174. doi: 10.1016/j.epsl.2014.09.027.

Faccenna, C., Funiciello, F., Giardini, D. and Lucente, P. (2001) 'Episodic back-arc extension during restricted mantle convection in the Central Mediterranean', *Earth and Planetary Science Letters*, 187(1–2), pp. 105–116. doi: 10.1016/S0012-821X(01)00280-1.

Faccenna, C., Molin, P., Orecchio, B., Olivetti, V., Bellier, O., Funiciello, F., Minelli, L., Piromallo, C. and Billi, A. (2011) 'Topography of the Calabria subduction zone (southern Italy): Clues for the origin of Mt. Etna', *Tectonics*, 30(1), pp. 1–20. doi: 10.1029/2010TC002694.

Faure Walker, J. P., Roberts, G. P., Cowie, P. A., Papanikolaou, I., Michetti, A. M., Sammonds, P., Wilkinson, M., McCaffrey, K. J. W. and Phillips, R. J. (2012) 'Relationship between topography, rates of extension and mantle dynamics in the actively-extending Italian Apennines', *Earth and Planetary Science Letters*. Elsevier B.V., 325–326, pp. 76–84. doi: 10.1016/j.epsl.2012.01.028.

Faure Walker, J. P., Roberts, G. P., Sammonds, P. R. and Cowie, P. (2010) 'Comparison of

earthquake strains over 10 2 and 10 4 year timescales: Insights into variability in the seismic cycle in the central Apennines, Italy', *Journal of Geophysical Research*, 115(B10), p. B10418. doi: 10.1029/2009JB006462.

Ferranti, L., Antonioli, F., Mauz, B., Amorosi, A., Dai Pra, G., Mastronuzzi, G., Monaco, C., Orrù, P., Pappalardo, M., Radtke, U., Renda, P., Romano, P., Sansò, P. and Verrubbi, V. (2006) 'Markers of the last interglacial sea-level high stand along the coast of Italy: Tectonic implications', *Quaternary International*, 145–146, pp. 30–54. doi: 10.1016/j.quaint.2005.07.009.

Ferranti, L., Monaco, C., Antonioli, F., Maschio, L., Kershaw, S. and Verrubbi, V. (2007) 'The contribution of regional uplift and coseismic slip to the vertical crustal motion in the Messina Straits, southern Italy: Evidence from raised Late Holocene shorelines', *Journal of Geophysical Research*, 112(B6), p. B06401. doi: 10.1029/2006JB004473.

Ferrario, M. F. and Livio, F. (2018) 'Characterizing the Distributed Faulting During the 30 October 2016, Central Italy Earthquake: A Reference for Fault Displacement Hazard Assessment', *Tectonics*, 37(5), pp. 1256–1273. doi: 10.1029/2017TC004935.

Firth, C. and Stewart, I. (1996) 'Coastal elevation changes in eastern Sicily: implications for volcano instability at Mount Etna', *Geological Society, …*, (110), pp. 153–167. doi: 10.1144/GSL.SP.1996.110.01.12.

Fowler, C. M. . (1990) *The solid earth: an introduction to global geophysics*. Cambridge University Press.

Friedrich, A. M., Wernicke, B. P., Niemi, N. A., Bennett, R. A. and Davis, J. L. (2003) 'Comparison of geodetic and geologic data from the Wasatch region, Utah, and implications for the spectral character of Earth deformation at periods of 10 to 10 million

years', *Journal of Geophysical Research: Solid Earth*, 108(B4), p. 2199. doi: 10.1029/2001JB000682.

Furlani, S., Cucchi, F., Forti, F. and Rossi, A. (2009) 'Comparison between coastal and inland Karst limestone lowering rates in the northeastern Adriatic Region (Italy and Croatia)', *Geomorphology*. Elsevier B.V., 104(1–2), pp. 73–81. doi: 10.1016/j.geomorph.2008.05.015.

Gallais, F., Gutscher, M. A., Klaeschen, D. and Graindorge, D. (2012) 'Two-stage growth of the Calabrian accretionary wedge in the Ionian Sea (Central Mediterranean): Constraints from depth-migrated multichannel seismic data', *Marine Geology*. Elsevier B.V., 326–328, pp. 28–45. doi: 10.1016/j.margeo.2012.08.006.

Gallen, S. F., Wegmann, K. W., Bohnenstiehl, D. R., Pazzaglia, F. J., Brandon, M. T. and Fassoulas, C. (2014) 'Active simultaneous uplift and margin-normal extension in a forearc high, Crete, Greece', *Earth and Planetary Science Letters*. Elsevier B.V., 398, pp. 11–24. doi: 10.1016/j.epsl.2014.04.038.

Galli, P. and Bosi, V. (2002) 'Paleoseismology along the Cittanova fault: Implications for seismotectonics and earthquake recurrence in Calabria (southern Italy)', *Journal of Geophysical Research*, 107(B3), p. 2044. doi: 10.1029/2001JB000234.

Galli, P., Galadini, F. and Pantosti, D. (2008) 'Twenty years of paleoseismology in Italy', *Earth-Science Reviews*, 88(1–2), pp. 89–117. doi: 10.1016/j.earscirev.2008.01.001.

Galli, P., Giaccio, B. and Messina, P. (2010) 'The 2009 central Italy earthquake seen through 0.5 Myr-long tectonic history of the L'Aquila faults system', *Quaternary Science Reviews*. Elsevier Ltd, 29(27–28), pp. 3768–3789. doi: 10.1016/j.quascirev.2010.08.018.

De Gelder, G., Fernandez-Blanco, D., Melnick, D., Duclaux, G., Bell, R. E., Jara-Muñoz, J., Armijo, R. and Lacassin, R. (no date) 'Fault flexure and lithosphere rheology set from

climate cycles record in the Corinth Rift', *Nature Geoscience*.

Ghisetti, F. (1981) 'Upper Pliocene-Pleistocene uplift rates as indicators of neotectonic pattern: an example from southern Calabria (Italy)', *Z. Geomorphol*, 40, pp. 93–118.

Ghisetti, F. (1984) 'Recent deformations and the seismogenic source in the Messina Strait (southern Italy)', 109, pp. 191–208. doi: https://doi.org/10.1016/0040-1951(84)90140-9.

Ghisetti, F. and Vezzani, L. (1982) 'Different styles of deformation in the calabrian arc (Southern Italy): Implications for a seismotectonic zoning', *Tectonophysics*, 85(3–4), pp. 149–165. doi: 10.1016/0040-1951(82)90101-9.

Giardini, D. and Woodhouse, J. H. (1986) 'Horizontal shear flow in the mantle beneath the Tonga arc', *Nature*, 319(6054), pp. 551–555. doi: 10.1038/319551a0.

Giunta, G., Gueli, A. M., Monaco, C., Orioli, S., Ristuccia, G. M., Stella, G. and Troja, S. O. (2012) 'Middle-Late Pleistocene marine terraces and fault activity in the Sant'Agata di Militello coastal area (north-eastern Sicily)', *Journal of Geodynamics*, 55, pp. 32–40. doi: 10.1016/j.jog.2011.11.005.

Goes, S., Giardini, D., Jenny, S., Hollenstein, C., Kahle, H.-G. and Geiger, A. (2004) 'A recent tectonic reorganization in the south-central Mediterranean', *Earth and Planetary Science Letters*, 226(3–4), pp. 335–345. doi: 10.1016/j.epsl.2004.07.038.

Gosse, J. C. and Phillips, F. M. (2001) 'Terrestrial in situ cosmogenic nuclides:theory and application', *Quaternary Science Reviews*, 20, pp. 1475–1560. doi: 10.1016/S0277-3791(00)00171-2.

Goswami, R., Mitchell, N. C. and Brocklehurst, S. H. (2011) 'Distribution and causes of landslides in the eastern Peloritani of NE Sicily and western Aspromonte of SW Calabria, Italy', *Geomorphology*, 132(3–4), pp. 111–122. doi: 10.1016/j.geomorph.2011.04.036.

Grant, K. M., Rohling, E. J., Bar-Matthews, M., Ayalon, A., Medina-Elizalde, M., Ramsey, C. B., Satow, C. and Roberts, A. P. (2012) 'Rapid coupling between ice volume and polar temperature over the past 150,000 years', *Nature*. Nature Publishing Group, 491(7426), pp. 744–747. doi: 10.1038/nature11593.

Grant, L. B., Mueller, K. J., Gath, E. M., Cheng, H., Lawrence Edwards, R., Munro, R. and Kennedy, G. L. (1999) 'Late Quaternary uplift and earthquake potential of the San Joaquin Hills, southern Los Angeles basin, California', *Geology*, 27(11), p. 1031. doi: 10.1130/0091-7613(1999)027<1031:LQUAEP>2.3.CO;2.

Grasso, M., Miuccio, G., Maniscalco, R., Garofalo, P., La Manna, F. and Stamilla, R. (1995) 'Plio-Pleistocene structural evolution of the western margin of the Hyblean Plateau and the Maghrebian foredeep, SE Sicily. Implications for the deformational history of the Gela Nappe', *Annales tectonicae*, 9, pp. 7–21.

De Guidi, G., Catalano, S., Monaco, C. and Tortorici, L. (2003) 'Morphological evidence of Holocene coseismic deformation in the Taormina region (NE Sicily)', *Journal of Geodynamics*, 36(1–2), pp. 193–211. doi: 10.1016/S0264-3707(03)00047-4.

De Guidi, G., Imposa, S., Scudero, S. and Palano, M. (2014) 'New evidence for Late Quaternary deformation of the substratum of Mt. Etna volcano (Sicily, Italy): clues indicate active crustal doming', *Bulletin of Volcanology*, 76(5), p. 816. doi: 10.1007/s00445-014-0816-8.

Guidoboni, E., Ferrari, G., Mariotti, D., Comastri, A., Tarabusi, G. and Valensise, G. (2007) 'Catalogue of Strong Earthquakes in Italy (461 BC-1997) and Mediterranean Area (760 BC-1500)'.

Gutscher, M.-A., Dominguez, S., de Lepinay, B. M., Pinheiro, L., Gallais, F., Babonneau, N.,

Cattaneo, A., Le Faou, Y., Barreca, G., Micallef, A. and Rovere, M. (2016) 'Tectonic expression of an active slab tear from high-resolution seismic and bathymetric data offshore Sicily (Ionian Sea)', *Tectonics*, 35(1), pp. 39–54. doi: 10.1002/2015TC003898.

Gutscher, M.-A., Kopp, H., Krastel, S., Bohrmann, G., Garlan, T., Zaragosi, S., Klaucke, I., Wintersteller, P., Loubrieu, B., Le Faou, Y., San Pedro, L., Dominguez, S., Rovere, M., Mercier de Lepinay, B., Ranero, C. and Sallares, V. (2017) 'Active tectonics of the Calabrian subduction revealed by new multi-beam bathymetric data and high-resolution seismic profiles in the Ionian Sea (Central Mediterranean)', *Earth and Planetary Science Letters*. Elsevier B.V., 461, pp. 61–72. doi: 10.1016/j.epsl.2016.12.020.

Gvirtzman, Z. and Nur, A. (1999a) 'Plate detachment, asthenosphere upwelling, and topography across subduction zones', *Geology*, 27(6), p. 563. doi: 10.1130/0091-7613(1999)027<0563:PDAUAT>2.3.CO;2.

Gvirtzman, Z. and Nur, A. (1999b) 'The formation of Mount Etna as the consequence of slab rollback', *Nature*, 401(October), pp. 782–785. doi: 10.1038/44555.

Gvirtzman, Z. and Nur, A. (2001) 'Residual topography, lithospheric structure and sunken slabs in the central Mediterranean', *Earth and Planetary Science Letters*, 187(1–2), pp. 117–130. doi: 10.1016/S0012-821X(01)00272-2.

Hasegawa, A., Yamamoto, A., Umino, N., Miura, S., Horiuchi, S., Zhao, D. and Sato, H. (2000) 'Seismic activity and deformation process of the overriding plate in the northeastern Japan subduction zone', *Tectonophysics*, 319(4), pp. 225–239. doi: 10.1016/S0040-1951(99)00296-6.

Haug, G. H. and Tiedemann, R. (1998) 'Effect of the formation of the Isthmus of Panama on Atlantic Ocean thermohaline circulation', *Nature*, 393(6686), pp. 673–676. doi:

10.1038/31447.

Hays, J. D., Imbrie, J. and Shackleton, N. J. (1976) 'Variations in the Earth's orbit: pacemaker of the ice ages', *American Association for the Advancement of Science*.

Hearty, P. J., Hollin, J. T., Neumann, A. C., O'Leary, M. J. and McCulloch, M. (2007) 'Global sea-level fluctuations during the Last Interglaciation (MIS 5e)', *Quaternary Science Reviews*, 26(17–18), pp. 2090–2112. doi: 10.1016/j.quascirev.2007.06.019.

Hellstrom, J., McCulloch, M. and Stone, J. (1998) 'A Detailed 31,000-Year Record of Climate and Vegetation Change, from the Isotope Geochemistry of Two New Zealand Speleothems', *Quaternary Research*, 50(1998), pp. 167–178. doi: https://doi.org/10.1006/qres.1998.1991.

Hiess, J., Condon, D. J., McLean, N. and Noble, S. R. (2012) '238U/235U Systematics in Terrestrial Uranium-Bearing Minerals', *Science*, 335(6076), pp. 1610–1614. doi: 10.1126/science.1215507.

Houghton, S. L. (2010) *Rates of extensional deformation for the Gulf of Corinth, Greece from U-series dating of marine terraces*. Birkbeck University.

Houghton, S. L., Roberts, G. P., Papanikolaou, I. D. and McArthur, J. M. (2003) 'New 234 U-230 Th coral dates from the western Gulf of Corinth: Implications for extensional tectonics', *Geophysical Research Letters*, 30(19), p. 2013. doi: 10.1029/2003GL018112.

http://www3.telus.net/lejgeology/etrain/htmls/36cl.htm (2008). Available at: http://www3.telus.net/lejgeology/etrain/htmls/36cl.htm.

Ingleby, T. and Wright, T. J. (2017) 'Omori-like decay of postseismic velocities following continental earthquakes', *Geophysical Research Letters*, 44(7), pp. 3119–3130. doi: 10.1002/2017GL072865.

INGV - DISS Working Group (2018) 'Database of Individual Seismogenic Sources (DISS), Version 3.2.1: A compilation of potential sources for earthquakes larger than M 5.5 in Italy and surrounding areas'. doi: 10.6092/INGV.IT-DISS3.2.1.

ISPRA (2016) 'Progetto IFFI: Inventario dei fenomeni franosi in Italia'. Available at: http://www.isprambiente.gov.it/it/progetti/suolo-e-territorio-1/iffi-inventario-dei-fenomeni-franosi-in-italia.

Ivanovich, M. and Harmon, R. S. (1982) *Uranium series disequilibrium: applications to environmental problems*. Oxford University Press.

Ivy-Ochs, S. and Kober, F. (2008) 'Surface exposure dating with cosmogenic nuclides', *Quaternary Science Journal (Eiszeitalter und Gegenwart)*, 57, pp. 157–189.

Jackson, J. (2001) 'LIVING WITH EARTHQUAKES: KNOW YOUR FAULTS', *Journal of Earthquake Engineering*, 5(sup001), pp. 5–123. doi: 10.1080/13632460109350530.

Jackson, J. A. and White, N. J. (1989) 'Normal faulting in the upper continental crust: observations from regions of active extension', *Journal of Structural Geology*, 11(1–2), pp. 15–36. doi: 10.1016/0191-8141(89)90033-3.

Jacques, E., Monaco, C., Tapponnier, P., Tortorici, L. and Winter, T. (2001) 'Faulting and earthquake triggering during the 1783 Calabria seismic sequence', *Geophysical Journal International*, 147(3), pp. 499–516. doi: 10.1046/j.0956-540x.2001.01518.x.

Jara-Muñoz, J. and Melnick, D. (2015) 'Unraveling sea-level variations and tectonic uplift in wave-built marine terraces, Santa María Island, Chile', *Quaternary Research*, 83(1), pp. 216–228. doi: 10.1016/j.yqres.2014.10.002.

Jarrard, R. D. (1986) 'Relations among subduction parameters', *Reviews of Geophysics*, 24(2), p. 217. doi: 10.1029/RG024i002p00217.

Kearey, P., Klepeis, K. A. and Vine, F. J. (2013) *Global tectonics*. John Wiley & Sons.

Kent, E., Boulton, S. J., Stewart, I. S., Whittaker, A. C. and Alçiçek, M. C. (2016) 'Geomorphic and geological constraints on the active normal faulting of the Gediz (Alaşehir) Graben, Western Turkey', *Journal of the Geological Society*, pp. jgs2015-121. doi: 10.1144/jgs2015-121.

King, G. C. P., Stein, R. S. and Rundle, J. B. (1988) 'The Growth of Geological Structures by Repeated Earthquakes 1. Conceptual Framework', *Journal of Geophysical Research: Solid Earth*, 93(B11), pp. 13307–13318. doi: 10.1029/JB093iB11p13307.

Korschinek, G., Bergmaier, A., Faestermann, T., Gerstmann, U. C., Knie, K., Rugel, G., Wallner, A., Dillmann, I., Dollinger, G., von Gostomski, C. L., Kossert, K., Maiti, M., Poutivtsev, M. and Remmert, A. (2010) 'A new value for the half-life of 10Be by Heavy-Ion Elastic Recoil Detection and liquid scintillation counting', *Nuclear Instruments and Methods in Physics Research Section B: Beam Interactions with Materials and Atoms*. Elsevier B.V., 268(2), pp. 187–191. doi: 10.1016/j.nimb.2009.09.020.

Ku, T. L., Knauss, K. G. and Mathieu, G. G. (1977) 'Uranium in open ocean: concentration and isotopic composition', *Deep-Sea Research*, 24(11), pp. 1005–1017. doi: 10.1016/0146-6291(77)90571-9.

Lajoie, K. R. (1986) 'Coastal Tectonics', in *Active Tectonics: Impact on Society*, pp. 95–124. Available at: http://books.google.com/books?hl=en&lr=&id=qaz9KnE2lxQC&pgis=1.

Lambeck, K., Esat, T. M. and Potter, E.-K. (2002) 'Links between climate and sea levels for the past three million years', *Nature*, 419(6903), pp. 199–206. doi: 10.1038/nature01089.

Langmuir, D. (1978) 'Uranium solution-mineral equilibria at low temperatures with applications to sedimentary ore deposits', *Geochimica et Cosmochimica Acta*, 42(6), pp.

547–569. doi: 10.1016/0016-7037(78)90001-7.

Lavecchia, G., Ferrarini, F., de Nardis, R., Visini, F. and Barbano, M. S. (2007) 'Active thrusting as a possible seismogenic source in Sicily (Southern Italy): Some insights from integrated structural–kinematic and seismological data', *Tectonophysics*, 445(3–4), pp. 145–167. doi: 10.1016/j.tecto.2007.07.007.

Lawrence Edwards, R., Chen, J. H. and Wasserburg, G. J. (1987) '238U234U230Th232Th systematics and the precise measurement of time over the past 500,000 years', *Earth and Planetary Science Letters*, 81(2–3), pp. 175–192. doi: 10.1016/0012-821X(87)90154-3.

Lentini, F., Di Geronimo, I., Grasso, M., Carbone, S., Sciuto, F., Scamarda, G., Cugno, G., Iozzia, S., Bommarito, S. and La Rosa, N. (1987) 'Carta geologica della Sicilia sud-orientale. Università di Catania, Istituto di Scienze della Terra, 1987.' S.EL.CA. Ed, Florence.

Loperfido, A. (1909) 'Livellazione geometrica di precisione eseguita dall'IGM sulla costa orientale della Sicilia, da Messina a Catania, a Gesso ed a Faro Peloro e sulla costa occidentale della Calabria da Gioia Tauro a Melito di Porto Salvo', *Relazione della Commissione Reale incaricata di designare filezone più adatte per la ricostruzione degli abitati colpiti dal terremoto del 28 dicembre 1908 o da altri precedenti (1909)*, pp. 131–156.

Loreto, M. F., Fracassi, U., Franzo, A., Del Negro, P., Zgur, F. and Facchin, L. (2013) 'Approaching the seismogenic source of the Calabria 8 September 1905 earthquake: New geophysical, geological and biochemical data from the S. Eufemia Gulf (S Italy)', *Marine Geology*. Elsevier B.V., 343(December 1908), pp. 62–75. doi: 10.1016/j.margeo.2013.06.016.

Lucente, F. P., Margheriti, L., Piromallo, C. and Barruol, G. (2006) 'Seismic anisotropy

reveals the long route of the slab through the western-central Mediterranean mantle', *Earth and Planetary Science Letters*, 241(3–4), pp. 517–529. doi: 10.1016/j.epsl.2005.10.041.

Magni, V., Faccenna, C., van Hunen, J. and Funiciello, F. (2014) 'How collision triggers backarc extension: Insight into Mediterranean style of extension from 3-D numerical models', *Geology*, 42(6), pp. 511–514. doi: 10.1130/G35446.1.

Malinverno, A. and Ryan, W. B. F. (1986) 'Extension in the Tyrrhenian Sea and shortening in the Apennines as result of arc migration driven by sinking of the lithosphere', *Tectonics*, 5(2), pp. 227–245. doi: 10.1029/TC005i002p00227.

Marrero, S. M., Phillips, F. M., Borchers, B., Lifton, N., Aumer, R. and Balco, G. (2015) *http://cronus.cosmogenicnuclides.rocks/2.0/*.

Marrero, S. M., Phillips, F. M., Borchers, B., Lifton, N., Aumer, R. and Balco, G. (2016) 'Cosmogenic nuclide systematics and the CRONUScalc program', *Quaternary Geochronology*. Elsevier B.V, 31, pp. 160–187. doi: 10.1016/j.quageo.2015.09.005.

Marrero, S. M., Phillips, F. M., Caffee, M. W. and Gosse, J. C. (2016) 'CRONUS-Earth cosmogenic 36 Cl calibration', *Quaternary Geochronology*. Elsevier B.V, 31, pp. 199–219. doi: 10.1016/j.quageo.2015.10.002.

Massonnet, D. and Feigl, K. L. (1995) 'Satellite radar interferometric map of the coseismic deformation field of the M = 6.1 Eureka Valley, California Earthquake of May 17, 1993', *Geophysical Research Letters*, 22(12), pp. 1541–1544. doi: 10.1029/95GL01088.

Mastrolembo Ventura, B., Serpelloni, E., Argnani, A., Bonforte, A., Bürgmann, R., Anzidei, M., Baldi, P. and Puglisi, G. (2014) 'Fast geodetic strain-rates in eastern Sicily (southern Italy): New insights into block tectonics and seismic potential in the area of the great 1693

earthquake', *Earth and Planetary Science Letters*. Elsevier B.V., 404, pp. 77–88. doi: 10.1016/j.epsl.2014.07.025.

Mattia, M., Bruno, V., Cannavò, F. and Palano, M. (2012) 'Evidences of a contractional pattern along the northern rim of the Hyblean plateau (Sicily, Italy) from GPS data', *Geologica Acta*, 10(1), pp. 63–70. doi: 10.1344/105.000001705.

Mattia, M., Palano, M., Bruno, V. and Cannavò, F. (2009) 'Crustal motion along the Calabro-Peloritano Arc as imaged by twelve years of measurements on a dense GPS network', *Tectonophysics*, 476(3–4), pp. 528–537. doi: 10.1016/j.tecto.2009.06.006.

McCloskey, J., Nalbant, S. S. and Steacy, S. (2005) 'Indonesian earthquake: Earthquake risk from co-seismic stress', *Nature*, 434(7031), pp. 291–291. doi: 10.1038/434291a.

McClusky, S., Reilinger, R., Mahmoud, S., Ben Sari, D. and Tealeb, A. (2003) 'GPS constraints on Africa (Nubia) and Arabia plate motions', *Geophysical Journal International*, 155(1), pp. 126–138. doi: 10.1046/j.1365-246X.2003.02023.x.

McElhinny, M. W. and McFadden, P. L. (1997) 'Palaeosecular variation over the past 5 Myr based on a new generalized database', *Geophysical Journal International*, 131(2), pp. 240–252. doi: 10.1111/j.1365-246X.1997.tb01219.x.

McKenzie, D. and Jackson, J. (2012) 'Tsunami earthquake generation by the release of gravitational potential energy', *Earth and Planetary Science Letters*. Elsevier, 345–348, pp. 1–8. doi: 10.1016/j.epsl.2012.06.036.

McLeod, A. E., Dawers, N. H. and Underhill, J. R. (2008) 'The propagation and linkage of normal faults: insights from the Strathspey-Brent-Statfjord fault array, northern North Sea', *Basin Research*, 12(3–4), pp. 263–284. doi: 10.1111/j.1365-2117.2000.00124.x.

McNeill, L. C. and Collier, R. E. L. (2004) 'Uplift and slip rates of the eastern Eliki fault

segment, Gulf of Corinth, Greece, inferred from Holocene and Pleistocene terraces', *Journal of the Geological Society*, 161(1), pp. 81–92. doi: 10.1144/0016-764903-029.

McNeill, L. C., Cotterill, C. J., Henstock, T. J., Bull, J. M., Stefatos, A., Collier, R. E. L., Papatheoderou, G., Ferentinos, G. and Hicks, S. E. (2005) 'Active faulting within the offshore western Gulf of Corinth, Greece: Implications for models of continental rift deformation', *Geology*, 33(4), p. 241. doi: 10.1130/G21127.1.

Melnick, D. (2016) 'Rise of the central Andean coast by earthquakes straddling the Moho', *Nature Geoscience*, 9(5), pp. 401–407. doi: 10.1038/ngeo2683.

Meltzner, A. J., Sieh, K., Abrams, M., Agnew, D. C., Hudnut, K. W., Avouac, J.-P. and Natawidjaja, D. H. (2006) 'Uplift and subsidence associated with the great Aceh-Andaman earthquake of 2004', *Journal of Geophysical Research: Solid Earth*, 111(B2), p. n/a-n/a. doi: 10.1029/2005JB003891.

Meltzner, A. J., Sieh, K., Chiang, H., Wu, C., Tsang, L. L. H., Shen, C., Hill, E. M., Suwargadi, B. W., Natawidjaja, D. H., Philibosian, B. and Briggs, R. W. (2015) 'Time-varying interseismic strain rates and similar seismic ruptures on the Nias e Simeulue patch of the Sunda megathrust', *Quaternary Science Reviews*. Elsevier Ltd, 122, pp. 258–281. doi: 10.1016/j.quascirev.2015.06.003.

Menard, H. W. (1964) 'Marine geology of the Pacific'.

Mercalli, G. (1909) 'Contributo allo studio del terremoto calabro-messinese del 28 dicembre 1908.', *Cooperativa tipografica*.

Meschis, M., Roberts, G. P., Robertson, J. and Briant, R. M. (2018) 'The relationships between regional Quaternary uplift, deformation across active normal faults and historical seismicity in the upper plate of subduction zones: The Capo D'Orlando Fault,

NE Sicily.', *Tectonics*. doi: 10.1029/2017TC004705.

Mildon, Z. K., Toda, S., Faure Walker, J. P. and Roberts, G. P. (2016) 'Evaluating models of Coulomb stress transfer: Is variable fault geometry important?', *Geophysical Research Letters*, 43(24), p. 12,407-12,414. doi: 10.1002/2016GL071128.

Miller, W. R. and Mason, T. R. (1994) 'Erosional Features of Coastal Beachrock and Aeolianite Outcrops in Natal and Zululand, South Africa', *Journal of Coastal Research*, 10(2), pp. 374–394. doi: 10.2307/4298223.

Mix, A. (1985) 'Structure and timing of the last deglaciation: Oxygen-isotope evidence', *Quaternary Science Reviews*, 4(2), pp. 59–108. doi: 10.1016/0277-3791(85)90015-0.

Miyauchi, T., Dai Pra, G. and Sylos Labini, S. (1994) 'Geochronology of Pleistocene marine terraces and regional tectonics in the Tyrrhenian coast of South Calabria, Italy', *Il Quaternario*, 7, pp. 17–34.

Molnar, P. and Chen, W.-P. (1983) 'Focal depths and fault plane solutions of earthquakes under the Tibetan Plateau', *Journal of Geophysical Research*, 88(B2), p. 1180. doi: 10.1029/JB088iB02p01180.

Monaco, C., Barreca, G., Di Stefano, A. and Ristuccia, G. (2014) 'Quaternary marine terraces and fault activity in the northern sector of the Messina Straits (southern Italy)', in *GNGTS 2014*, pp. 85–90.

Monaco, C., Bianca, M., Catalano, S., De Guidi and Tortorici, L. (2002) 'Sudden change in the Late Quaternary tectonic regime in eastern Sicily : evidences from geological and geomorphological features', *Bollettino della Societa Geologica Italiana*, 1(January), pp. 901–913.

Monaco, C. and Tortorici, L. (2000) 'Active faulting in the Calabrian arc and eastern Sicily',

Journal of Geodynamics, 29(3–5), pp. 407–424. doi: 10.1016/S0264-3707(99)00052-6.

Monaco, C., Tortorici, L., Nicolich, R., Cernobori, L. and Costa, M. (1996) 'From collisional to rifted basins: an example from the southern Calabrian arc (Italy)', *Tectonophysics*, 266(1–4), pp. 233–249. doi: 10.1016/S0040-1951(96)00192-8.

Morley, C. K., Nelson, R. A., Patton, T. L. and Munn, S. G. (1990) 'Transfer zones in the East African rift system and their relevance to hydrocarbon exploration in rifts (1)', *AAPG Bulletin*, 74(8), pp. 1234–1253.

Mouslopoulou, V., Nicol, A., Begg, J., Oncken, O. and Moreno, M. (2015) 'Clusters of megaearthquakes on upper plate faults control the Eastern Mediterranean hazard', *Geophysical Research Letters*, 42(23), p. 10,282-10,289. doi: 10.1002/2015GL066371.

Mouslopoulou, V., Oncken, O., Hainzl, S. and Nicol, A. (2016) 'Uplift rate transients at subduction margins due to earthquake clustering', *Tectonics*, 35(10), pp. 2370–2384. doi: 10.1002/2016TC004248.

Mulargia, F. and Boschi, E. (1983) '"The 1908 Messina earthquake and related seismicity', *Earthquakes: observation, theory and interpretation*, pp. 493–518.

Musumeci, C., Scarfì, L., Palano, M. and Patanè, D. (2014) 'Foreland segmentation along an active convergent margin: New constraints in southeastern Sicily (Italy) from seismic and geodetic observations', *Tectonophysics*, 630(C), pp. 137–149. doi: 10.1016/j.tecto.2014.05.017.

Nalbant, S., McCloskey, J., Steacy, S., NicBhloscaidh, M. and Murphy, S. (2013) 'Interseismic coupling, stress evolution, and earthquake slip on the Sunda megathrust', *Geophysical Research Letters*, 40(16), pp. 4204–4208. doi: 10.1002/grl.50776.

Nalin, R., Massari, F. and Zecchin, M. (2007) 'Superimposed Cycles of Composite Marine

Terraces: The Example of Cutro Terrace (Calabria, Southern Italy)', *Journal of Sedimentary Research*, 77(4), pp. 340–354. doi: 10.2110/jsr.2007.030.

De Natale, G. and Pingue, F. (1991) 'A Variable Slip Fault Model For the 1908 Messina Straits (Italy) Earthquake, By Inversion of Levelling Data', *Geophysical Journal International*, 104(1), pp. 73–84. doi: 10.1111/j.1365-246X.1991.tb02494.x.

Nehme, C., Verheyden, S., Noble, S. R., Farrant, A. R., Sahy, D., Hellstrom, J., Delannoy, J. J. and Claeys, P. (2015) 'Reconstruction of MIS 5 climate in the central Levant using a stalagmite from Kanaan Cave, Lebanon', *Climate of the Past*, 11(12), pp. 1785–1799. doi: 10.5194/cp-11-1785-2015.

Neri, G., Barberi, G., Orecchio, B. and Aloisi, M. (2002) 'Seismotomography of the crust in the transition zone between the southern Tyrrhenian and Sicilian tectonic domains', *Geophysical Research Letters*, 29(23), pp. 50-1-50–4. doi: 10.1029/2002GL015562.

Neumann, E. R. and Ramberg, I. . (2012) *Petrology and Geochemistry of Continental Rifts*. Springer Science & Business Media.

Nic Bhloscaidh, M., McCloskey, J., Naylor, M., Murphy, S. and Lindsay, A. (2015) 'Reconstruction of the slip distributions in historical earthquakes on the Sunda megathrust, W. Sumatra', *Geophysical Journal International*, 202(2), pp. 1339–1361. doi: 10.1093/gji/ggv195.

Nicol, A. and Beavan, J. (2003) 'Shortening of an overriding plate and its implications for slip on a subduction thrust, central Hikurangi Margin, New Zealand', *Tectonics*, 22(6), p. n/a-n/a. doi: 10.1029/2003TC001521.

Nicolich, R., Laigle, M., Hirn, A., Cernobori, L. and Gallart, J. (2000) 'Crustal structure of the Ionian margin of Sicily: Etna volcano in the frame of regional evolution', *Tectonophysics*,

329(1–4), pp. 121–139. doi: 10.1016/S0040-1951(00)00192-X.

Nigro, F. and Sulli, A. (1995) 'Plio-Pleistocene extensional tectonics in the Western Peloritani area and its offshore (northeastern Sicily)', *Tectonophysics*, 252(1–4), pp. 295–305. doi: 10.1016/0040-1951(95)00096-8.

Nixon, C. W., McNeill, L. C., Bull, J. M., Bell, R. E., Gawthorpe, R. L., Henstock, T. J., Christodoulou, D., Ford, M., Taylor, B., Sakellariou, D., Ferentinos, G., Papatheodorou, G., Leeder, M. R., Collier, R. E. L., Goodliffe, A. M., Sachpazi, M. and Kranis, H. (2016) 'Rapid spatiotemporal variations in rift structure during development of the Corinth Rift, central Greece', *Tectonics*, 35(5), pp. 1225–1248. doi: 10.1002/2015TC004026.

Oddone, E. (1909) 'Appunti fisici per lo studio del terremoto di Sicilia e Calabria', *Annali della Societa' degli Ingegneri ed Architetti Italiani*, 7.

Oskin, M., Perg, L., Shelef, E., Strane, M., Gurney, E., Singer, B. and Zhang, X. (2008) 'Elevated shear zone loading rate during an earthquake cluster in eastern California', *Geology*, 36(6), p. 507. doi: 10.1130/G24814A.1.

Pace, B., Bocchini, G. M. and Boncio, P. (2014) 'Do static stress changes of a moderate-magnitude earthquake significantly modify the regional seismic hazard? Hints from the L'Aquila 2009 normal-faulting earthquake (Mw 6.3, central Italy)', *Terra Nova*, 26(6), pp. 430–439. doi: 10.1111/ter.12117.

Pace, B., Peruzza, L., Lavecchia, G. and Boncio, P. (2006) 'Layered Seismogenic Source Model and Probabilistic Seismic-Hazard Analyses in Central Italy', *Bulletin of the Seismological Society of America*, 96(1), pp. 107–132. doi: 10.1785/0120040231.

Palano, M., Ferranti, L., Monaco, C., Mattia, M., Aloisi, M., Bruno, V., Cannav??, F. and Siligato, G. (2012) 'GPS velocity and strain fields in Sicily and southern Calabria, Italy:

Updated geodetic constraints on tectonic block interaction in the central Mediterranean', *Rendiconti Online Societa Geologica Italiana*, 21(PART 1), pp. 235–237. doi: 10.1029/2012JB009254.

Papanikolaou, D., Alexandri, M. and Nomikou, P. (2006) 'Active faulting in the north Aegean basin', in *Special Paper 409: Postcollisional Tectonics and Magmatism in the Mediterranean Region and Asia*. Geological Society of America, pp. 189–209. doi: 10.1130/2006.2409(11).

Papanikolaou, I. D., Foumelis, M., Parcharidis, I., Lekkas, E. L. and Fountoulis, I. G. (2010) 'Deformation pattern of the 6 and 7 April 2009, M_W=6.3 and M_W=5.6 earthquakes in L'Aquila (Central Italy) revealed by ground and space based observations', *Natural Hazards and Earth System Science*, 10(1), pp. 73–87. doi: 10.5194/nhess-10-73-2010.

Papanikolaou, I. D. and Roberts, G. P. (2007) 'Geometry, kinematics and deformation rates along the active normal fault system in the southern Apennines: Implications for fault growth', *Journal of Structural Geology*, 29(1), pp. 166–188. doi: 10.1016/j.jsg.2006.07.009.

Papanikolaou, I. D., Roberts, G. P. and Michetti, A. M. (2005) 'Fault scarps and deformation rates in Lazio–Abruzzo, Central Italy: Comparison between geological fault slip-rate and GPS data', *Tectonophysics*, 408(1–4), pp. 147–176. doi: 10.1016/j.tecto.2005.05.043.

Papanikolaou, I. D., Roberts, G. P., Deligiannakis, G., Sakellariou, A. and Vassilakis, E. (2013) 'The Sparta Fault, Southern Greece: From segmentation and tectonic geomorphology to seismic hazard mapping and time dependent probabilities', *Tectonophysics*, 597–598, pp. 85–105. doi: 10.1016/j.tecto.2012.08.031.

Pavano, F., Pazzaglia, F. J. and Catalano, S. (2016) 'Knickpoints as geomorphic markers of active tectonics: A case study from northeastern Sicily (southern Italy)', *Lithosphere*, 8(6),

pp. 633–648. doi: 10.1130/L577.1.

Peacock, S. M. (1986) 'Thermal and Petrologic Structure of Subduction Zones', in, pp. 119–133. doi: 10.1029/GM096p0119.

Pedoja, K., Husson, L., Johnson, M. E., Melnick, D., Witt, C., Pochat, S., Nexer, M., Delcaillau, B., Pinegina, T., Poprawski, Y., Authemayou, C., Elliot, M., Regard, V. and Garestier, F. (2014) 'Coastal staircase sequences reflecting sea-level oscillations and tectonic uplift during the Quaternary and Neogene', *Earth-Science Reviews*, 132, pp. 13–38. doi: 10.1016/j.earscirev.2014.01.007.

Pedoja, K., Jara-Muñoz, J., De Gelder, G., Robertson, J., Meschis, M., Fernandez-Blanco, D., Nexer, M., Poprawski, Y., Dugué, O., Delcaillau, B., Bessin, P., Benabdelouahed, M., Authemayou, C., Husson, L., Regard, V., Menier, D. and Pinel, B. (2018) 'Neogene-Quaternary slow coastal uplift of Western Europe through the perspective of sequences of strandlines from the Cotentin Peninsula (Normandy, France)', *Geomorphology*. Elsevier B.V., 303, pp. 338–356. doi: 10.1016/j.geomorph.2017.11.021.

Pedoja, K., Ortlieb, L., Dumont, J. F., Lamothe, M., Ghaleb, B., Auclair, M. and Labrousse, B. (2006) 'Quaternary coastal uplift along the Talara Arc (Ecuador, Northern Peru) from new marine terrace data', *Marine Geology*, 228(1–4), pp. 73–91. doi: 10.1016/j.margeo.2006.01.004.

Peltier, W. R. (1998) 'Postglacial variations in the level of the sea: Implications for climate dynamics and solid-Earth geophysics', *Reviews of Geophysics*, 36(4), pp. 603–689. doi: 10.1029/98RG02638.

Peltier, W. R. (1999) 'Global sea level rise and glacial isostatic adjustment', *Global Planetary Change*, 20, pp. 93–123.

Pepe, F., Bertotti, G., Ferranti, L., Sacchi, M., Collura, A. M., Passaro, S. and Sulli, A. (2014) 'Pattern and rate of post-20 ka vertical tectonic motion around the Capo Vaticano Promontory (W Calabria, Italy) based on offshore geomorphological indicators', *Quaternary International*. Elsevier Ltd and INQUA, 332, pp. 85–98. doi: 10.1016/j.quaint.2013.11.012.

Pepe, F., Sulli, A., Agate, M., Di Maio, D., Kok, A., Lo Iacono, C. and Catalano, R. (2003) 'Plio-Pleistocene geological evolution of the northern Sicily continental margin (southern Tyrrhenian Sea): new insights from high-resolution, multi-electrode sparker profiles', *Geo-Marine Letters*, 23(1), pp. 53–63. doi: 10.1007/s00367-003-0124-3.

Peruzza, L., Pace, B. and Cavallini, F. (2010) 'Error propagation in time-dependent probability of occurrence for characteristic earthquakes in Italy', *Journal of Seismology*, 14(1), pp. 119–141. doi: 10.1007/s10950-008-9131-1.

Platania, G. (1909) 'Il maremoto dello Stretto di Messina del 28 Dicembre 1908', *Bollettino della Societa Geologica Italiana*, 22, pp. 369–458.

Polonia, A., Panieri, G., Gasperini, L., Gasparotto, G., Bellucci, L. G. and Torelli, L. (2013) 'Turbidite paleoseismology in the Calabrian Arc Subduction Complex (Ionian Sea)', *Geochemistry, Geophysics, Geosystems*, 14(1), pp. 112–140. doi: 10.1029/2012GC004402.

Raymo, M. E. (1992) 'Global Climate Change: A Three Million Year Perspective', in *Start of a Glacial*. Berlin, Heidelberg: Springer Berlin Heidelberg, pp. 207–223. doi: 10.1007/978-3-642-76954-2_15.

Rehault, J.-P., Boillot, G. and Mauffret, A. (1984) 'The Western Mediterranean Basin geological evolution', *Marine Geology*, 55(3–4), pp. 447–477. doi: 10.1016/0025-3227(84)90081-1.

Reilinger, R., McClusky, S., Vernant, P., Lawrence, S., Ergintav, S., Cakmak, R., Ozener, H., Kadirov, F., Guliev, I., Stepanyan, R., Nadariya, M., Hahubia, G., Mahmoud, S., Sakr, K., ArRajehi, A., Paradissis, D., Al-Aydrus, A., Prilepin, M., Guseva, T., Evren, E., Dmitrotsa, A., Filikov, S. V., Gomez, F., Al-Ghazzi, R. and Karam, G. (2006) 'GPS constraints on continental deformation in the Africa-Arabia-Eurasia continental collision zone and implications for the dynamics of plate interactions', *Journal of Geophysical Research: Solid Earth*, 111(B5), p. n/a-n/a. doi: 10.1029/2005JB004051.

Ridente, D., Martorelli, E., Bosman, A. and Chiocci, F. L. (2014) 'High-resolution morpho-bathymetric imaging of the Messina Strait (Southern Italy). New insights on the 1908 earthquake and tsunami', *Geomorphology*. Elsevier B.V., 208(March), pp. 149–159. doi: 10.1016/j.geomorph.2013.11.021.

Rizzo, G. B. (1909) *Relazione sul terremoto di Messina e della Calabria nel 28 dicembre 1908.*

Roberts, A. and Yielding, G. (1994) 'Continental extensional tectonics', in Press, P. (ed.) *Continental Deformation*, pp. 223–250.

Roberts, G. G., White, N. J. and Shaw, B. (2013) 'An uplift history of Crete, Greece, from inverse modeling of longitudinal river profiles', *Geomorphology*. Elsevier B.V., 198, pp. 177–188. doi: 10.1016/j.geomorph.2013.05.026.

Roberts, G. P. (1996) 'Noncharacteristic normal faulting surface ruptures from the Gulf of Corinth, Greece', *Journal of Geophysical Research*, 101(B11), p. 25,255-25,267. doi: https://doi.org/10.1029/96JB02119.

Roberts, G. P., Cowie, P., Papanikolaou, I. and Michetti, A. M. (2004) 'Fault scaling relationships, deformation rates and seismic hazards: An example from the Lazio-Abruzzo Apennines, central Italy', *Journal of Structural Geology*, 26(2), pp. 377–398. doi:

10.1016/S0191-8141(03)00104-4.

Roberts, G. P. and Ganas, A. (2000) 'Fault-slip directions in central and southern Greece measured from striated and corrugated fault planes: Comparison with focal mechanism and geodetic data', *Journal of Geophysical Research: Solid Earth*, 105(B10), pp. 23443–23462. doi: 10.1029/1999JB900440.

Roberts, G. P., Houghton, S. L., Underwood, C., Papanikolaou, I., Cowie, P. A., van Calsteren, P., Wigley, T., Cooper, F. J. and McArthur, J. M. (2009) 'Localization of Quaternary slip rates in an active rift in 10 5 years: An example from central Greece constrained by 234 U- 230 Th coral dates from uplifted paleoshorelines', *Journal of Geophysical Research*, 114(B10), p. B10406. doi: 10.1029/2008JB005818.

Roberts, G. P., Houghton, S. L., Underwood, C., Papanikolaou, I., Cowie, P. A., Van Calsteren, P., Wigley, T., Cooper, F. J. and McArthur, J. M. (2009) 'Localization of quaternary slip rates in an active rift in 105 years: An example from central Greece constrained by 234U- 230Th coral dates from uplifted paleoshorelines', *Journal of Geophysical Research: Solid Earth*, 114(10), pp. 1–26. doi: 10.1029/2008JB005818.

Roberts, G. P., Meschis, M., Houghton, S., Underwood, C. and Briant, R. M. (2013) 'The implications of revised Quaternary palaeoshoreline chronologies for the rates of active extension and uplift in the upper plate of subduction zones', *Quaternary Science Reviews*, 78, pp. 169–187. doi: 10.1016/j.quascirev.2013.08.006.

Roberts, G. P. and Michetti, A. M. (2004) 'Spatial and temporal variations in growth rates along active normal fault systems: an example from The Lazio–Abruzzo Apennines, central Italy', *Journal of Structural Geology*, 26(2), pp. 339–376. doi: 10.1016/S0191-8141(03)00103-2.

Roberts, G. P., Michetti, A. M., Cowie, P., Morewood, N. C. and Papanikolaou, I. (2002) 'Fault slip-rate variations during crustal-scale strain localisation, central Italy', *Geophysical Research Letters*, 29(8), pp. 9-1-9–4. doi: 10.1029/2001GL013529.

Roda-Boluda, D. C. and Whittaker, A. C. (2017) 'Structural and geomorphological constraints on active normal faulting and landscape evolution in Calabria, Italy', *Journal of the Geological Society*, pp. jgs2016-097. doi: 10.1144/jgs2016-097.

Rohling, E. J., Fenton, M., Jorissen, F. J., Bertrand, P., Ganssen, G. and Caulet, J. P. (1998) 'Magnitudes of sea-level lowstands of the past 500,000 years', *Nature*, 394(6689), pp. 162–165. doi: 10.1038/28134.

Rohling, E. J., Foster, G. L., Grant, K. M., Marino, G., Roberts, A. P., Tamisiea, M. E. and Williams, F. (2014) 'Sea-level and deep-sea-temperature variability over the past 5.3 million years', *Nature*. Nature Publishing Group, 508(7497), pp. 477–482. doi: 10.1038/nature13230.

Rohling, E. J., Grant, K., Bolshaw, M., Roberts, A. P., Siddall, M., Hemleben, C. and Kucera, M. (2009) 'Antarctic temperature and global sea level closely coupled over the past five glacial cycles', *Nature Geoscience*. Nature Publishing Group, 2(7), pp. 500–504. doi: 10.1038/ngeo557.

Saillard, M., Hall, S. R., Audin, L., Farber, D. L., Regard, V. and Hérail, G. (2011) 'Andean coastal uplift and active tectonics in southern Peru: 10Be surface exposure dating of differentially uplifted marine terrace sequences (San Juan de Marcona, ~15.4°S)', *Geomorphology*. Elsevier B.V., 128(3–4), pp. 178–190. doi: 10.1016/j.geomorph.2011.01.004.

Schiano, P., Clocchiatti, R., Ottolini, L. and Busà, T. (2001) 'Transition of Mount Etna lavas

from a mantle-plume to an island-arc magmatic source', *Nature*, 412(6850), pp. 900–904. doi: 10.1038/35091056.

Schick, R. (1977) 'Eine seismotektonische Bearbeitung des Erdbebens von Messina-im Jahre 1908', *Geologisches Jahrbuch Reihe E, Band E 11*.

Schimmelpfennig, I., Benedetti, L., Finkel, R., Pik, R., Blard, P.-H., Bourlès, D., Burnard, P. and Williams, A. (2009) 'Sources of in-situ 36Cl in basaltic rocks. Implications for calibration of production rates', *Quaternary Geochronology*, 4(6), pp. 441–461. doi: 10.1016/j.quageo.2009.06.003.

Schlagenhauf, A., Gaudemer, Y., Benedetti, L., Manighetti, I., Palumbo, L., Schimmelpfennig, I., Finkel, R. and Pou, K. (2010) 'Using in situ Chlorine-36 cosmonuclide to recover past earthquake histories on limestone normal fault scarps: a reappraisal of methodology and interpretations', *Geophysical Journal International*, 182(1), p. no-no. doi: 10.1111/j.1365-246X.2010.04622.x.

Schlische, R. W., Young, S. S., Ackermann, R. V and Gupta, A. (1996) 'Geometry and scaling relations of a population of very small rift-related normal faults', *Geology*, 24(8), p. 683. doi: 10.1130/0091-7613(1996)024<0683:GASROA>2.3.CO;2.

Schwartz, D. P. and Coppersmith, K. J. (1984) 'Fault behavior and characteristic earthquakes: examples from the Wasatch and San Andreas fault zones (USA).', *Journal of Geophysical Research*, 89(B7), pp. 5681–5698. doi: 10.1029/JB089iB07p05681.

Schwartz, D. P. and Coppersmith, K. J. (1984) 'Fault behavior and characteristic earthquakes - examples form the Wasatch and San-Andreas fault zones', *Journal of Geophysical Research*, 89(NB7), pp. 5681–5698. doi: 10.1029/JB089iB07p05681.

Scicchitano, G., Lo Presti, V., Spampinato, C. R., Gasparo Morticelli, M., Antonioli, F.,

Auriemma, R., Ferranti, L. and Monaco, C. (2011) 'Millstones as indicators of relative sea-level changes in northern Sicily and southern Calabria coastlines, Italy', *Quaternary International*, 232(1–2), pp. 92–104. doi: 10.1016/j.quaint.2010.08.019.

Selvaggi, G. and Chiarabba, C. (1995) 'Seismicity and P-wave velocity image of the Southern Tyrrhenian subduction zone', *Geophysical Journal International*, 121(3), pp. 818–826. doi: 10.1111/j.1365-246X.1995.tb06441.x.

Serpelloni, E., Anzidei, M., Baldi, P., Casula, G. and Galvani, A. (2005) 'Crustal velocity and strain-rate fields in Italy and surrounding regions: new results from the analysis of permanent and non-permanent GPS networks', *Geophysical Journal International*, 161(3), pp. 861–880. doi: 10.1111/j.1365-246X.2005.02618.x.

Serpelloni, E., Bürgmann, R., Anzidei, M., Baldi, P., Mastrolembo Ventura, B. and Boschi, E. (2010) 'Strain accumulation across the Messina Straits and kinematics of Sicily and Calabria from GPS data and dislocation modeling', *Earth and Planetary Science Letters*, 298(3–4), pp. 347–360. doi: 10.1016/j.epsl.2010.08.005.

Serpelloni, E., Faccenna, C., Spada, G., Dong, D. and Williams, S. D. P. (2013) 'Vertical GPS ground motion rates in the Euro-Mediterranean region: New evidence of velocity gradients at different spatial scales along the Nubia-Eurasia plate boundary', *Journal of Geophysical Research: Solid Earth*, 118(11), pp. 6003–6024. doi: 10.1002/2013JB010102.

Serpelloni, E., Vannucci, G., Pondrelli, S., Argnani, A., Casula, G., Anzidei, M., Baldi, P. and Gasperini, P. (2007) 'Kinematics of the Western Africa-Eurasia plate boundary from focal mechanisms and GPS data', *Geophysical Journal International*, 169(3), pp. 1180–1200. doi: 10.1111/j.1365-246X.2007.03367.x.

Seth, B., Thirlwall, M. F., Houghton, S. L. and Craig, C.-A. (2003) 'Accurate measurements

of Th–U isotope ratios for carbonate geochronology using MC-ICP-MS', *J. Anal. At. Spectrom.*, 18(11), pp. 1323–1330. doi: 10.1039/B308908H.

Shackleton, N. J. (1967) 'Oxygen Isotope Analyses and Pleistocene Temperatures Re-assessed', *Nature*, 215(5096), pp. 15–17. doi: 10.1038/215015a0.

Shackleton, N. J. (1987) 'Oxygen isotopes, ice volume and sea level', *Quaternary Science Reviews*, 6(3–4), pp. 183–190. doi: 10.1016/0277-3791(87)90003-5.

Shaw, B., Ambraseys, N. N., England, P. C., Floyd, M. a., Gorman, G. J., Higham, T. F. G., Jackson, J. a., Nocquet, J.-M., Pain, C. C. and Piggott, M. D. (2008) 'Eastern Mediterranean tectonics and tsunami hazard inferred from the AD 365 earthquake', *Nature Geoscience*, 1(4), pp. 268–276. doi: 10.1038/ngeo151.

Shaw, B., Jackson, J. A., Higham, T. F. G., England, P. C. and Thomas, A. L. (2010) 'Radiometric dates of uplifted marine fauna in Greece: Implications for the interpretation of recent earthquake and tectonic histories using lithophagid dates', *Earth and Planetary Science Letters*. Elsevier B.V., 297(3–4), pp. 395–404. doi: 10.1016/j.epsl.2010.06.041.

Siddall, M., Rohling, E. J., Almogi-Labin, A., Hemleben, C., Meischner, D., Schmelzer, I. and Smeed, D. A. (2003) 'Sea-level fluctuations during the last glacial cycle', *Nature*, 423(6942), pp. 853–858. doi: 10.1038/nature01690.

Spampinato, C. R. (2011) *Metodi di analisi delle deformazioni verticali lungo aree costiere della Sicilia orientale e Calabria meridionale*. Università degli studi di Catania.

Spampinato, C. R., Scicchitano, G., Ferranti, L. and Monaco, C. (2012) 'Raised Holocene paleo-shorelines along the Capo Schisò coast, Taormina: New evidence of recent co-seismic deformation in northeastern Sicily (Italy)', *Journal of Geodynamics*. Elsevier Ltd, 55, pp. 18–31. doi: 10.1016/j.jog.2011.11.007.

Stein, R. S. (1999) 'The role of stress transfer in earthquake occurrence', *Nature*, 402(6762), pp. 605–609. doi: 10.1038/45144.

Stein, R. S. and Barrientos, S. E. (1985) 'Planar high-angle faulting in the basin and range: Geodetic analysis of the 1983 Borah Peak, Idaho, earthquake', *Journal of Geophysical Research*, 90(B13), p. 11355. doi: 10.1029/JB090iB13p11355.

Stewart, I. S., Cundy, A., Kershaw, S. and Firth, C. (1997) 'Holocene coastal uplift in the taormina area, northeastern sicily: Implications for the southern prolongation of the calabrian seismogenic belt', *Journal of Geodynamics*, 24(1–4), pp. 37–50. doi: 10.1016/S0264-3707(97)00012-4.

Stirling, C. ., Esat, T. ., Lambeck, K. and McCulloch, M. . (1998) 'Timing and duration of the Last Interglacial: evidence for a restricted interval of widespread coral reef growth', *Earth and Planetary Science Letters*, 160(3–4), pp. 745–762. doi: 10.1016/S0012-821X(98)00125-3.

Stirling, C. H., Andersen, M. B., Potter, E.-K. and Halliday, A. N. (2007) 'Low-temperature isotopic fractionation of uranium', *Earth and Planetary Science Letters*, 264(1–2), pp. 208–225. doi: 10.1016/j.epsl.2007.09.019.

Stone, J., Lambeck, K., Fifield, L. K., Evans, J. M. and Cresswell, R. G. (1996) 'A Lateglacial age for the Main Rock Platform, western Scotland', *Geology*, 24(8), pp. 707–710. doi: 10.1130/0091-7613(1996)024<0707:ALAFTM>2.3.CO;2.

Stone, J. O., Allan, G. L., Fifield, L. K. and Cresswell, R. G. (1996) 'Cosmogenic chlorine-36 from calcium spallation', *Geochimica et Cosmochimica Acta*, 60(4), pp. 679–692. doi: 10.1016/0016-7037(95)00429-7.

Stramondo, S., Tesauro, M., Briole, P., Sansosti, E., Salvi, S., Lanari, R., Anzidei, M., Baldi, P.,

Fornaro, G., Avallone, A., Buongiorno, M. F., Franceschetti, G. and Boschi, E. (1999) 'The September 26, 1997 Colfiorito, Italy, earthquakes: Modeled coseismic surface displacement from SAR interferometry and GPS', *Geophysical Research Letters*, 26(7), pp. 883–886. doi: 10.1029/1999GL900141.

Strobl, M., Hetzel, R., Fassoulas, C. and Kubik, P. W. (2014) 'A long-term rock uplift rate for eastern Crete and geodynamic implications for the Hellenic subduction zone', *Journal of Geodynamics*. Elsevier Ltd, 78, pp. 21–31. doi: 10.1016/j.jog.2014.04.002.

Stucchi, M., Rovida, A., Gomez Capera, A. A., Alexandre, P., Camelbeeck, T., Demircioglu, M. B., Gasperini, P., Kouskouna, V., Musson, R. M. W., Radulian, M., Sesetyan, K., Vilanova, S., Baumont, D., Bungum, H., Fäh, D., Lenhardt, W., Makropoulos, K., Martinez Solares, J. M., Scotti, O., Živčić, M., Albini, P., Batllo, J., Papaioannou, C., Tatevossian, R., Locati, M., Meletti, C., Viganò, D. and Giardini, D. (2013) 'The SHARE European Earthquake Catalogue (SHEEC) 1000–1899', *Journal of Seismology*, 17(2), pp. 523–544. doi: 10.1007/s10950-012-9335-2.

Sulli, A., Lo Presti, V., Gasparo Morticelli, M. and Antonioli, F. (2013) 'Vertical movements in NE Sicily and its offshore: Outcome of tectonic uplift during the last 125 ky', *Quaternary International*. Elsevier Ltd and INQUA, 288, pp. 168–182. doi: 10.1016/j.quaint.2012.01.021.

Tarquini, S., Isola, I., Favalli, M., Mazzarini, F., Bisson, M., Pareschi, M. T. and Boschi, E. (2007) 'TINITALY/01: A new Triangular Irregular Network of Italy', *Annals of Geophysics*, 50(3), pp. 407–425.

Tarquini, S., Vinci, S., Favalli, M., Doumaz, F., Fornaciai, A. and Nannipieri, L. (2012) 'Release of a 10-m-resolution DEM for the Italian territory: Comparison with global-

coverage DEMs and anaglyph-mode exploration via the web', *Computers & Geosciences*, 38(1), pp. 168–170. doi: 10.1016/j.cageo.2011.04.018.

Toda, S., Stein, R. S., Sevilgen, V. and Lin, J. (2011) 'Coulomb 3.3. Graphic-rich deformation & stress-change software for earthquake, tectonic and volcano research and teaching - User Guide', *USGS Open-File Report*, p. 63. Available at: https://pubs.usgs.gov/of/2011/1060/.

Torelli, L., Grasso, M., Mazzoldi, G. and Peis, D. (1998) 'Plio–Quaternary tectonic evolution and structure of the Catania foredeep, the northern Hyblean Plateau and the Ionian shelf (SE Sicily)', *Tectonophysics*, 298(1–3), pp. 209–221. doi: 10.1016/S0040-1951(98)00185-1.

Tortorici, G., Bianca, M., De Guidi, G., Monaco, C. and Tortorici, L. (2003) 'Fault activity and marine terracing in the Capo Vaticano area (southern Calabria) during the Middle-Late Quaternary', *Quaternary International*, 101–102(1), pp. 269–278. doi: 10.1016/S1040-6182(02)00107-6.

Tortorici, L., Monaco, C., Tansi, C. and Cocina, O. (1995) 'Recent and active tectonics in the Calabrian arc (Southern Italy)', *Tectonophysics*, 243(1–2), pp. 37–55. doi: 10.1016/0040-1951(94)00190-K.

Tucker, G. E., McCoy, S. W., Whittaker, A. C., Roberts, G. P., Lancaster, S. T. and Phillips, R. (2011) 'Geomorphic significance of postglacial bedrock scarps on normal-fault footwalls', *Journal of Geophysical Research: Earth Surface*, 116(F1), p. n/a-n/a. doi: 10.1029/2010JF001861.

Vacchi, M., Rovere, A., Zouros, N., Desruelles, S., Caron, V. and Firpo, M. (2012) 'Spatial distribution of sea-level markers on Lesvos Island (NE Aegean Sea): Evidence of differential relative sea-level changes and the neotectonic implications', *Geomorphology*,

159–160, pp. 50–62. doi: 10.1016/j.geomorph.2012.03.004.

Valensise, G. (1988) 'Low angle normal faulting during the 1908, Messina, earthquake revealed by geodetic data analysis.', *Eos Transactions - AGU*, 69.

Valensise, G., Basili, R. and Burrato, P. (2008) 'La sorgente del terremoto del 1908 nel quadro sismotettonico dello Stretto di Messina', in *Il terremoto e il maremoto del 28 dicembre 1908. Analisi sismologica, impatto, prospettive.*, pp. 161–182.

Valensise, G. and Pantosti, D. (1992) 'A 125 Kyr-long geological record of seismic source repeatability: the Messina Straits (southern Italy) and the 1908 earthquake (M s 7/ 2)', *Terra Nova*, 4(4), pp. 472–483. doi: 10.1111/j.1365-3121.1992.tb00583.x.

Valoroso, L., Chiaraluce, L., Piccinini, D., Stefano, R. Di, Schaff, D. and Waldhauser, F. (2013) 'Radiography of a normal fault system by 64 , 000 high-precision earthquake locations : The 2009 L ' Aquila (central Italy) case study', *Journal of Geophysical Research: Solid Earth*, 118(Dd), pp. 1156–1176. doi: doi.org/10.1002/jgrb.50130.

Vermeesch, P., Fenton, C. R., Kober, F., Wiggs, G. F. S., Bristow, C. S. and Xu, S. (2010) 'Sand residence times of one million years in the Namib Sand Sea from cosmogenic nuclides', *Nature Geoscience*, 3(12), pp. 862–865. doi: 10.1038/ngeo985.

Visini, F., De Nardis, R., Barbano, M. S. and Lavecchia, G. (2009) 'Testing the seismogenic sources of the January 11 th 1693 sicilian earthquake (Io X/XI): Insights from macroseismic field simulations', *Bollettino della Societa Geologica Italiana*, 128(1), pp. 147–156. Available at: http://www.scopus.com/inward/record.url?eid=2-s2.0-65349195035&partnerID=40&md5=e67b450fe867d37ff5c1376ab97f4304.

Visini, F. and Pace, B. (2014) 'Insights on a Key Parameter of Earthquake Forecasting, the Coefficient of Variation of the Recurrence Time, Using a Simple Earthquake Simulator',

Seismological Research Letters, 85(3), pp. 703–713. doi: 10.1785/0220130165.

Wadati, K. (1935) 'On the activity of deep-focus earthquakes in the Japan Islands and neighbourhoods', *Geophysical Magazine*, 8, pp. 305–325.

Waelbroeck, C., Labeyrie, L., Michel, E., Duplessy, J. C., McManus, J. F., Lambeck, K., Balbon, E. and Labracherie, M. (2002) 'Sea-level and deep water temperature changes derived from benthic foraminifera isotopic records', *Quaternary Science Reviews*, 21(1–3), pp. 295–305. doi: 10.1016/S0277-3791(01)00101-9.

Walsh, J. J. and Watterson, J. (1991) 'Geometric and kinematic coherence and scale effects in normal fault systems', *Geological Society, London, Special Publications*, 56(1), pp. 193–203. doi: 10.1144/GSL.SP.1991.056.01.13.

Walters, R. J., Elliott, J. R., D'Agostino, N., England, P. C., Hunstad, I., Jackson, J. A., Parsons, B., Phillips, R. J. and Roberts, G. (2009) 'The 2009 L'Aquila earthquake (central Italy): A source mechanism and implications for seismic hazard', *Geophysical Research Letters*, 36(17), p. L17312. doi: 10.1029/2009GL039337.

Ward, S. N. (1998) 'On the consistency of earthquake moment release and space geodetic strain rates: Europe', *Geophysical Journal International*, 135, pp. 1011–1018. doi: 10.1046/j.1365-246X.1998.00658.x.

Wedmore, L. N. J., Faure Walker, J. P., Roberts, G. P., Sammonds, P. R., McCaffrey, K. J. W. and Cowie, P. A. (2017) 'A 667 year record of coseismic and interseismic Coulomb stress changes in central Italy reveals the role of fault interaction in controlling irregular earthquake recurrence intervals', *Journal of Geophysical Research: Solid Earth*, 122(7), pp. 5691–5711. doi: 10.1002/2017JB014054.

Wells, D. L. and Coppersmith, K. J. (1994) 'New empirical relationships among magnitude,

rupture length, rupture width, rupture area, and surface displacement', *Bulletin of the Seismological Society of America*, 84(4), pp. 974–1002. Available at: http://www.bssaonline.org/content/84/4/974.short (Accessed: 18 February 2016).

Westaway, R. (1993) 'Quaternary uplift of southern Italy', *Journal of Geophysical Research*, 98(B12), pp. 741–772. doi: 10.1029/93JB01566.

Whittaker, A. C. and Boulton, S. J. (2012) 'Tectonic and climatic controls on knickpoint retreat rates and landscape response times', *Journal of Geophysical Research: Earth Surface*, 117(F2), p. n/a-n/a. doi: 10.1029/2011JF002157.

Wilkinson, M., McCaffrey, K. J. W., Roberts, G., Cowie, P. A., Phillips, R. J., Michetti, A. M., Vittori, E., Guerrieri, L., Blumetti, A. M., Bubeck, A., Yates, A. and Sileo, G. (2010) 'Partitioned postseismic deformation associated with the 2009 Mw 6.3 L'Aquila earthquake surface rupture measured using a terrestrial laser scanner', *Geophysical Research Letters*, 37(10), p. n/a-n/a. doi: 10.1029/2010GL043099.

Wortel, M. J. and Spakman, W. (2000) 'Subduction and slab detachment in the Mediterranean-Carpathian region.', *Science (New York, N.Y.)*, 290(5498), pp. 1910–1917. doi: 10.1126/science.290.5498.1910.

Yeats, R. (2012) *Active Faults of the World*. Cambridge: Cambridge University Press. doi: 10.1017/CBO9781139035644.

Yeats, R. S. and Prentice, C. S. (1996) 'Introduction to Special Section: Paleoseismology', *Journal of Geophysical Research: Solid Earth*, 101(B3), pp. 5847–5853. doi: 10.1029/95JB03134.

Appendix

In this section, Appendix as digital supplementary material on a CD-ROM is submitted with this thesis. A guide to the submitted material is stated below. A folder named "Appendix" is where all the supplementary material is stored. All digital material is presented as excel files.

Appendix 3.1 shows the 36-Cl analysis for sample 16 samples mapped and collected for this thesis. This data analysis has been used as "input" data for CRONUSCalc (http://cronus.cosmogenicnuclides.rocks/2.0/) explained in Chapter 3.

Appendix 3.2 shows U-Th analysis on corals mapped and sampled in this thesis. Note that 4 corallites are dated and used to constrain palaeoshoreline ages. Sample 15, 16 and 17 are used in Chapter 7. Sample 21 is used in Chapter 6.

Appendix 5 shows the synchronous correlation analysis for the marine terraces modelled on the hangingwall of the Capo D'Orlando Fault. Results from this analysis are shown in Chapter 5 and in the published paper titled "The Relationships Between Regional Quaternary Uplift, Deformation Across Active Normal Faults, and Historical Seismicity in the Upper Plate of Subduction Zones: The Capo D'Orlando Fault, NE Sicily" by Meschis et al. in Tectonics (https://agupubs.onlinelibrary.wiley.com/doi/abs/10.1029/2017TC004705).

Appendix 6 shows the synchronous correlation analysis for the marine terraces modelled on the foreland region, in SE Sicily. Results describes the forebulge process occurring in the region due to the Africa – Eurasia collision over the last 500 kyrs. Results from this analysis are shown in Chapter 6.

Appendix 7.1 shows the synchronous correlation analysis for the marine terraces modelled on the footwall of the Messina Strait Fault, from Messina town to Taormina town. Results from this analysis are shown in Chapter 7.

Appendix 7.2 shows the synchronous correlation analysis for the marine terraces modelled on the hangingwall of the Reggio Calabria Fault, from Sambatello town to Archi town, S Calabria. Results from this analysis are shown in Chapter 7.

Appendix 7.3 shows the synchronous correlation analysis for the marine terraces modelled on the hangingwall of the Armo Fault. Results from this analysis are shown in Chapter 7.

Appendix 7.4 shows a throw rate calculator to estimate the throw-rates of Reggio Calabria Fault and Armo Fault before and after the change in their throw-rate since 50 ka, taking into account the "deceleration factor" of ~2.4-2.5 mapped by investigating tectonically-deformed marine terraces. Furthermore, a throw rate calculator for the Messina Strait Fault (MSF) is shown where an acceleration on the slip rate by a factor of 2.45 is mapped.

Appendix 8.1 shows the analysis to derive the geometry of the possible seismic source for the 1908 Messina Earthquake. The modelled seismic source is the Messina Strait Fault; by using the Coulomb 3.3 software, the function "Vertical Displacement" has been used to reproduce the co-seismic uplift-subsidence to find the best match (lowest misfit) between the "measured" benchmark elevations by Loperfido, (1909) and the "predicted" elevations from the model. Results of this analysis is shown in Chapter 8.

Appendix 8.2 shows the analysis to test if the 1908 Messina Earthquake could be assumed as a "characteristic earthquake" to explain the footwall uplift deforming the palaeoshorelines discussed in Chapter 7.

Appendix 9 shows the synchronous correlation analysis for the marine terraces modelled on the footwall of the Xylokastro Fault, in gulf of Corinth (Greece). This analysis is presented to show the importance of: (i) stressing a worldwide review of all marine terraces

investigations carried out by applying a “sequential” correlation approach and (ii) a critically-assigning of ages for un-dated palaeoshorelines.